Structural, Magnetic and Micromechanical Properties of Multifunctional Ni-Mn-Ga Heusler Alloys Influenced by Elemental Doping

AMADEUSZ ŁASZCZ

A dissertation submitted in partial fulfilment of the requirements
for the degree of

Doctor of Philosophy in Materials Engineering

Wrocław University of Science and Technology
Department of Mechanics, Materials and Biomedical Engineering

December 2022

Abstract

Magnetic shape memory alloys (MSMAs) have recently emerged as one of the most extensively researched groups of modern functional smart materials. This is due to the fact that their complex magnetostructural nature is very often associated with a variety of significant properties that may be influenced by different stimuli, including thermal, magnetic and mechanical field. Among the relatively narrow group of MSMAs, NiMnGa-based Heusler alloys stand out as one of the post promising candidates for many future multifunctional applications, due to the numerous magneto-thermo-mechanical properties, including magnetic field-induced strains, thermal and magnetic pseudoelasticity, giant magnetoresistance, magneto- and mechanocaloric effects or exchange bias. All of the multifunctional properties of Ni-Mn-Ga alloys stem from the reversible first-order martensitic transformation and the reversible second-order magnetic transformation. The martensitic transformation undergoes from high-symmetry austenite phase to low-symmetry martensite phase, whereas the magnetic transformation undergoes from paramagnetic to ferromagnetic state. The main characteristic feature of the Ni-Mn-Ga compound is that both transformations are independent and can be shifted individually through compositional tunning, introduction of additional alloying elements or proper heat treatment. As a result the functional properties of the final material may be adjusted to the particular application, which is the main idea of modern material engineering. However, in order to establish the consistent designing rules for some future potential applications, a detailed knowledge of the complex magnetostructural behaviour of doped Ni-Mn-Ga compounds is required.

The purpose of this thesis is to investigate the influence of elemental doping and atomic ordering on the magneto-thermo-structural behaviour of NiMnGa-based magnetic shape memory alloys. To achieve this, the series of polycrystalline Ni-Mn-Ga alloys doped with Co and/or Fe were produced by the arc-melting technique. All samples were carefully annealed and subjected to a cooling procedure involving three different cooling rates realized by water, air and furnace cooling, which simulates the different atomic ordering. The presented comprehensive characterization of microstructure, magnetic and micromechanical properties of the produced multifunctional alloys is carried out in terms of the electronic parameters, including the valence electron concentration and the non-bonding electrons concentration.

In the presented dissertation, two main parts can be distinguished: the theoretical framework and the experimental part. The theoretical part provides an introduction to the topic of multifunctional NiMnGa-based magnetic shape memory Heusler alloys. This part mainly focuses on microstructural features of the investigated materials and the corresponding complex nature of the reversible martensitic transformation. Furthermore, the introduction includes detailed information on the major functional properties of Ni-Mn-Ga compounds, including thermal and magnetic shape memory, giant magnetoresistance, exchange bias and mechanocaloric effects. Particular emphasis is also placed on the compositional dependence of off-stoichiometric alloys and the influence of selective alloying elements. The last parts of the theoretical introduction presents the different forms of Ni-Mn-Ga materials and describes some recent advanced promising applications of different types of NiMnGa-based Heusler alloys.

The research part of the dissertation is divided into two areas. The first one includes the characterisation of the production process of the polycrystalline NiMnGa-based materials, as well as the description of the characterization methods used in the presented studies. The second part of the research area is entirely devoted to the presentation of the investigation results and the broad discussion of the emerging outcomes.

The first section of the research chapter is dedicated to microstructural and crystallographic investigations conducted on polarised optical microscope, SEM/EDS, XRD and AFM. These studies reveal the single phase microstructure for all fabricated materials and confirm the obtained chemical composition with the designed ones, which validates the production process of NiMnGa-based materials in bulk polycrystalline form. The detailed temperature dependent Rietveld refinement analysis allows to identify the crystal lattice parameters for cubic austenite, tetragonal non-modulated martensite and five-layered modulated martensite, and demonstrates the clear dependence of structural properties of Ni-Mn-Ga Heusler alloys on the considered electronic parameters. The additional, supporting, AFM investigation reveals the complex microstructure of self-accommodated martensitic structures observed at three different length scales and manifested by various twinning models. Moreover, a quantitative approach to the analysis of AFM profiles for martensitic relief is also proposed to distinguish the non-modulated and modulated types of martensite.

The second section of the research chapter is focused on both the reversible martensitic transformation and magnetic transformation observed in the fabricated multifunctional alloys. In this case, the magneto-thermo-structural behaviour of the produced samples was investigated with the help of DSC, M-TG and VSM, which allows for extensive characterization of first- and second-order transformations. These studies clearly show that the structural transformation in Ni-Mn-Ga-Fe-Co system is strongly dependent on the elemental doping and can alter over a wide range of temperature, independently of the magnetic transformation. Moreover, it is also demonstrated that the temperature of martensitic transformation may be predicted by the electronic parameters, regardless of the type of dopant.

The third part of the research chapter is strictly focused on the magnetic properties of the studied alloys estimated on the basis of VSM measurements carried out at wide ranges of temperatures and external magnetic fields. In this section, the atomic ordering of differently cooled samples is discovered to greatly influence the magnetic properties of the samples, such as coercivity. Moreover, the investigation of the martensite and austenite hysteresis loops clearly depicts the considerable magnetostructural anisotropy of the low-symmetry martensite phase in comparison to the high-symmetry austenite phase. To quantitatively describe the observed differences, the low of approach to magnetic saturation model were used to estimate the energy of magnetocrystalline anisotropy in all fabricated NiMnGa-based materials. The strong relationship between magnetocrystalline anisotropy, chemical composition and electronic parameters is also described in detail in this section.

The last part of the research chapter considers the micromechanical properties of the produced polycrystalline samples investigated by instrumented nanoindentation mapping. The presented studies reveal considerable anisotropy of the elastic and plastic properties of neighbouring grains and twins in the austenite and martensite phase, respectively. The statistical approach based on the 2D Gaussian mixture model used for clustering, labelling and calculating the mechanical parameters of individual grains is also proposed and comprehensively discussed in this section. In the case of micromechanical properties, the obtained vales of hardness, elastic modulus and elastic energy ratio are once again discussed with respect to the examined electronic parameters. Lastly, the additional AFM investigation of the residual imprints displays two significant phenomena: reorientation of twins in self-modulated martensite and mechanical stress-induced martensitic transformation, which is widely reviewed in this section.

The submitted dissertation contains a comprehensive and methodological examination of the microstructure and magneto-thermo-mechanical characteristics of Ni-Mn-Ga magnetic shape alloys influenced by Co and Fe doping. The provided results and accompanying discussions demonstrate that correct elemental doping results in a substantial change in all of the crucial multifunctional features of final material, including structural, magnetic and mechanical properties. The established influence of Co and/or Fe on the Ni-Mn-Ga composition, as well as the effect of varied cooling conditions, can be exploited to modify and alter the necessary functional properties of the material to make it suitable for a certain demanding application. Furthermore, in the Ni-Mn-Ga-Co-Fe system investigated in this thesis, the universal approach regarding both the valence electron concentration and the non-bonding electron concentration may be used to determine the specific multifunction functional characteristics. The extensive research presented in this dissertation makes a distinct and original contribution to the future development of polycrystalline NiMnGa-based Heusler alloys, especially in the promising Ni-Mn-Ga-Co-Fe system.

Keywords: *magnetic shape memory alloys*; *multifunctional materials*; *reversible martensitic transformation*; *twinned martensite*; *magnetocrystalline anisotropy*; *nanoindentation mapping*

To my supporting *wife* and *parents*

Table of contents

List of abbreviations

Abbreviations	Description
2D GMM	two-dimensional Gaussian mixture model
3M	three-layered modulated martensite
5M	five-layered modulated martensite
7M	seven-layered modulated martensite
AC	alternating current
AFM	Atomic Force Microscope
BC	barocaloric
BCE	barocaloric effect
BIC	Bayesian Information Criterion
BSE	backscattered electrons
C	commensurate
C-AFM	Contact Atomic Force Microscopy
CDF	cumulative density function
DSC	Differential Scanning Calorimetry
EB	exchange bias
eC	elastocaloric
eCE	elastocaloric effect
EDM	Electrical Discharge Machine
EDX	Energy Dispersive X-Ray Spectroscopy
EM	expectation-maximization
FC	field cooled mode
FIB	Focused Ion Beam
FM	ferromagnetic
FSMA	ferromagnetic shape memory alloy
GMCE	giant magnetocaloric effect
GMM	Gaussian mixture model
GMR	giant magnetoresistance
GOF	goodness of fit

HRTEM	High Resolution Transmission Electron Microscopy
IC	incommensurate
IMT	intermartensitic transformation
IUCr	International Union of Crystallography
L-PBF	Laser Powder Bed Fusion
LMR	large magnetoresistance
LoA	low of approach to magnetic saturation
M-TG	Magnetic Thermogravimetry
MC	magnetocaloric
MCE	magnetocaloric effect
mCE	mechanocaloric effect
MFIS	magnetic field induced strains
MIR	magnetic field induced structure reorientation
MR	magnetoresistance
MSMA	magnetic shape memory alloy
NHT	Nanoindentation Tester
NM	non-modulated martensite
PDF	probability density function
PM	paramagnetic
PSPD	position sensitive photodiode
REE	rare earth elements
SE	secondary electrons
SEB	spontaneous exchange bias
SEM	Scanning Electron Microscope
TG	Thermogravimetry
VSM	Vibrating Sample Magnetometer
XRD	X-Ray Diffraction
ZFC	zero field mode
TB	twin boundary
RT	room temperature

List of symbols

Symbol	Unit	Description
A	nm^3	projected contact area
A_f	K	austenite finish temperature
A_r	-	relative atomic mass
A_s	K	austenite start temperature
at.%	%	atomic percentage
c_p	$\mathrm{J{\cdot}kg^{-1}{\cdot}K^{-1}}$	specific heat capacity
E	-	number of valence electrons
E_i	GPa	elastic modulus of the indenter
E_IT	GPa	elastic modulus of the examined material
e_n	-	number of non-bonding electrons
E_r	GPa	reduced elastic modulus
F_max	N	applied load
G_A	$\mathrm{J{\cdot}K^{-1}{\cdot}mol^{-1}}$	Gibbs free energy of austenite
G_M	$\mathrm{J{\cdot}K^{-1}{\cdot}mol^{-1}}$	Gibbs free energy of martensite
H	A/m	external magnetic field
H_C	A/m	coercivity
h_c	nm	contact depth
H/E	-	elastic deformation index
h_f	nm	final depth
H_IT	MPa	instrumented hardness
h_max	nm	maximum depth
K_eff	$\mathrm{J{\cdot}m^{-3}}$	effective magnetocrystalline anisotropy constant
M	$\mathrm{A{\cdot}m^2{\cdot}kg^{-1}}$	magnetization
M_f	K	martensite finish temperature
M_s	K	martensite start temperature
M_S	$\mathrm{A{\cdot}m^2{\cdot}kg^{-1}}$	magnetization saturation
N_e/a	-	non-bonding electron concentration

N_{WS}	-	corrected electron density parameter
p	Pa	hydrostatic pressure
R_{exp}	-	expected R-factor
R_{wp}	-	weighted profile R-factor
S	$\mathrm{N \cdot m^{-1}}$	stiffness
T	K	temperature
T_{A}	K	austenitic transformation temperature
T_{C}	K	Curie temperature
T_{IMT}	K	intermartensitic transformation temperature
T_{M}	K	martensitic transformation temperature
V	$\mathrm{m^3}$	volume
W_{e}	J	elastic energy
W_{p}	J	plastic energy
wt.%	%	weight percentage
β	-	geometrical correction factor of indenter
ΔE_{mag}	J	magnetic energy
ΔE_{Z}	J	Zeeman energy
ΔS	$\mathrm{J \cdot kg^{-1} \cdot K^{-1}}$	entropy change
ΔS_{mag}	$\mathrm{J \cdot kg^{-1} \cdot K^{-1}}$	magnetic entropy change
ΔT_{ad}	K	adiabatic temperature change
ΔT_{H}	K	thermal hysteresis
ε	-	mechanical strain
η_{IT}	-	elastic energy ratio
μ_0	$\mathrm{N \cdot A^{-2}}$	magnetic permeability constant
ν_{i}	-	Poisson's ratio of the intender
ν_{s}	-	Poisson's ratio of the sample
σ	Pa	mechanical stress
Φ	Wb	magnetic flux

1

Introduction

1.1 The origin of Heusler alloys

1.1.1 Brief history of Heusler alloys

The history of Heusler alloys started in 1903 from the discovery of Cu_2MnSn alloy by German mining engineer and chemist – Friedrich Heusler. He demonstrated that the proper addition of Sn to the Cu-Mn composition changes the magnetic properties of the material [1,2]. The newly discovered alloy appeared to be ferromagnetic, even though it contained only paramagnetic elements. This unusual phenomenon attracted the attention of many other scientists, but the lack of sophisticated measuring techniques had restricted the subsequent development of this group of materials for many years. Later, it was found that the addition of other elements such as Sn, Sb or Bi to the Cu-Mn compound also results in ferromagnetic alloy, but the full explanation of this effect remained unknown. Only the progress of X-ray measurements allowed Potter [3] to discover that the constituent atoms of the Cu-Mn-Al alloy are organized in a four *face-centred cubic* (*fcc*) sublattices. Five years later, the X-ray studies over the Heusler compounds were also substantially extended by Bradley and Rogers [4], who described the Cu_2MnSn compound as fully ordered $L2_1$ structure. The discovery of the crystal structure of Heusler alloys accelerated their future investigations.

In 1983 in the pioneering theoretical work, de Groot *et al.* [5] have shown that many of the potential Mn-based Heusler alloys are half-metals. His predictions were subsequently experimentally confirmed by Hanssen and his research group in 1990 [6]. Today, this class of materials is known as *half*-heusler alloys, since one of the fourth *fcc* sublattices in the *full*-heusler compound remains empty in half-Heusler (**Fig 1.1**). The unoccupied sublattice means that some of the atoms in unit cell are replaced by vacancies, which consequently allows for many compositional alterations between full- and half-Heuslers. The discovery of half-metallic half-

Heusler compositions is accompanied by the development of a brand new branch of physics and electronics, *i.e. spintronics* (or *spin electronics*).

Half-metallic ferromagnetic materials are metallic (conducting) in one spin channel, while insulating in the opposite spin. Consequently, all the electrons at the Fermi level in half-metallic material are spin up or spin down, which results in almost 100% spin polarization (in common ferromagnetic metals like Fe, both spin directions are present at Fermi level, which results in polarisation notably lower than 100%). This phenomenon laid the foundation for a potentially *giant* (or theoretically even infinite) *magnetoresistance* (GMR) of the half-metallic material [7], which is now required in the majority of efficient spintronics applications, including spin filters, tunnel junctions and GMR devices. The discovery of this unusual magnetic behaviour in half-Heusler compounds provided the spark for further intensive research in understanding the nature of the Heusler alloys.

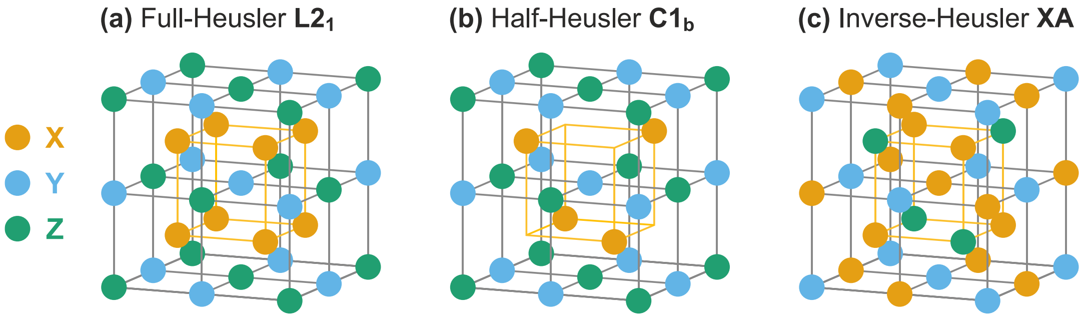

Fig. 1.1. Unit cell structure of **(a)** full-Heusler, **(b)** half-Heusler and **(c)** inverse-Heusler alloys.

From this moment on, three main groups of Heusler alloys emerged:

- » *Full*-Heusler – with the composition of X_2YZ exhibiting $L2_1$ unit cell (**Fig. 1.1(a)**) with $Fm\bar{3}m$ symmetry, e.g. Ni_2TiAl [8]. Full-Heuslers are typically characterised by high magnetic moment and high Curie temperatures.
- » *Half*-Heusler – with the composition of XYZ exhibiting $C1_b$ (**Fig. 1.1(b)**) unit cell with $F\bar{4}3m$ symmetry, e.g. ZrNiSn [9]. Half-Heuslers are characterised by lower magnetic moment and lower Curie temperatures than full-Heusler.
- » *Inverse*-Heusler – with the composition of Y_2XZ exhibiting XA unit cell (**Fig. 1.1(c)**), with $F\bar{4}3m$ symmetry, e.g. Mn_2CoAl [10]. Inverse-Heuslers are characterised by high Curie temperature.

The X and Y in the aforementioned compositions are typically transition metals or lanthanides and Z is the *p*-block element (group III–V). Nevertheless, these rules are not very restrictive, and there are several compositional exceptions, which are graphically summarised in the periodic table presented in **Fig. 1.2**. It is seen that possible combinations of atoms for Heusler compound cover more than a half of periodic table, which leads to a remarkable fact that, until now, theoretical Heusler family contains more than 1500 different compositions [11]. What is more, in the last couple of years the three main groups of Heusler alloys have been extended even more to binary (X_3Z) [12] and quaternary compositions ($XX'YZ$) [13].

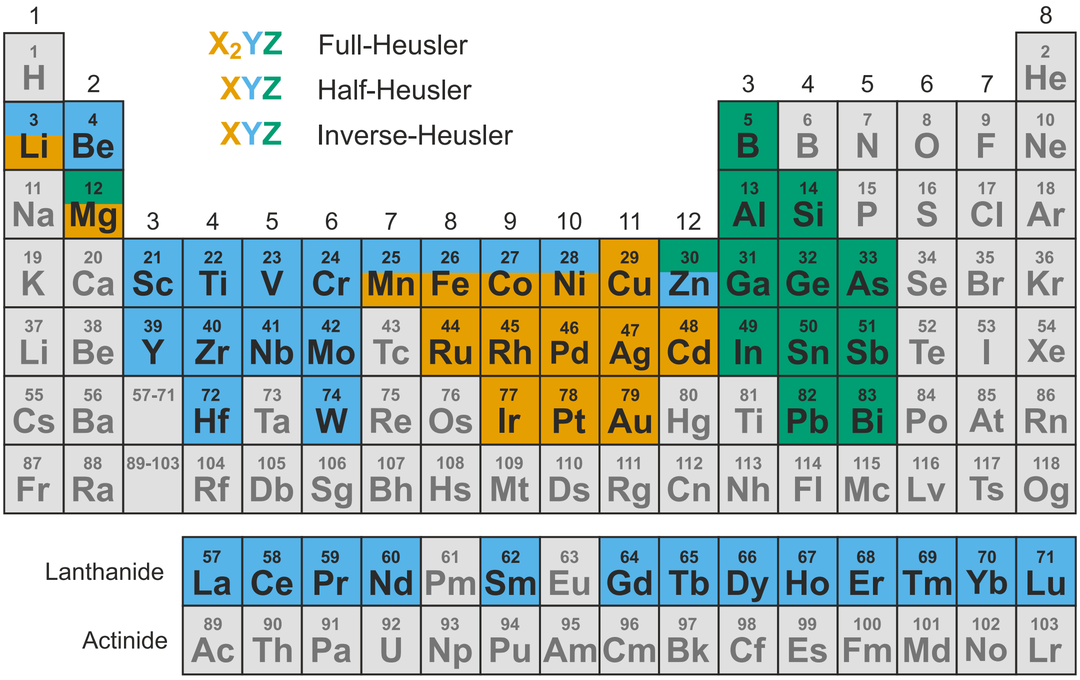

Fig. 1.2. Periodic table of elements. The colour scheme depicts numerous different variations of full-, half- and inverse-Heusler alloys (based on [11,14]).

1.1.2 The development of Ni-Mn-Ga alloys

NiMnGa-based Heusler alloys have been of scientific interest for more than 60 years [15]. However, at the beginning of their development, only some of their potential magnetic and structural properties were studied [16–19]. It can be said that Ni-Mn-Ga alloys were treated just like one of the many possible Heusler compounds. This situation changed radically in 1983, when Webster discovered the reversible martensitic transformation from cubic austenite to tetragonal martensite in full-Heusler Ni_2MnGa alloy [20]. His discovery opens a completely new path for the development of a different types of Heusler alloys, which undergoes the reversible phase transformation. Since then, a number of studies considering the nature of martensitic transition in near-stoichiometric Ni_2MnGa compounds were publish, including the Kokorin [21] and Chernenko [22] work.

However, the most significant breakthrough was presented only 13 years after Webster discovery. In 1996 Ullakko *et al.* reported the reversible magnetically induced strain of 0.15% for the near-stoichiometric single crystal NiMnGa-based alloy [23]. These significant reversible strains in the metallic material were comparable to the giant magnetostriction reported for the smart piezoelectric materials based on intermetallic compounds such as Terfenol-D [24]. From this time on, NiMnGa-based Heuslers started to be classified as *magnetic shape memory alloys*

(MSMAs) or *ferromagnetic shape memory alloys* (FSMAs) – a relatively small group of smart materials already represented by Fe-Pt [25–27] and Fe-Pd [28,29] alloys. As a result, the unusual phenomenon of magnetically induced shape recovery contributed to the great experimental and theoretical interest in NiMnGa-based Heuslers, as until now (September 2022) Ullakko work have been cited more than 3150 times.

The Ulakko discovery has made an impact on the new findings of other group of Heusler-type magnetic shape memory alloys. Today, it is known that at some certain off-stoichiometric compositions, almost every Ni-Mn-based Heusler compound will exhibit martensitic transition, but due to various technological reasons, the most promising one are Ni-Mn-X (X = Ga, In, Sn and Sb) alloys [30,31]. Furthermore, in addition to NiMn-based Heusler alloys, several other Heusler-type systems undergoing martensitic transformation have been reported, including Co-Ni-Al [32,33], Co-Ni-Ga [34–36], Co-Mn-Al [37,38] or Ni-Fe-Ga [39–41]. Despite the development of other compounds, the NiMn-based alloys have been still receiving the greatest research interest and there are a number of reasons to explain this situation.

First of all, the temperature of phase transformation in NiMn-based Heuslers can be easily shifted by altering the Ni-Mn-X composition. Secondly, the martensitic transformation undergoes from the cubic austenite phase to both tetragonal non-modulated martensite or – what is especially important – to 5M or 7M modulated structures [42,43]. Moreover, martensitic structures may exhibit stress-induced *intermartensitic transformation*, resulting in *superelasticity* (or more accurately *pseudoelasticity*), attributed to martensite variant reorientation [44,45]. Thirdly, due to the relatively easy twin boundary motion in the martensitic phase, a large *magnetic field-induced strain* (MFIS) of up to 12% can be generated in the martensitic structure [46], which is not achievable in other MSMAs. In addition, the combination of the reversible martensitic transformation and subsequent MFIS leads to a two-way shape memory effect [47,48]. Finally, in 2001 Hu *et al.* reported a large *magnetocaloric effect* (MCE) in a single-crystal Ni-Mn-Ga alloy, which again attracted the scientific community [49]. Considering the fact that reversible martensitic transition is strongly dependent not only from thermal and magnetic stimulus but also from mechanical stress, in the last couple of years one of the main research topics was focused on other giant caloric effects including elastocaloric [50] and barocaloric [51] effects, which are recently more often summarised as mechanocaloric effects [52]. Lastly, it is worth noting that the strong coupling between structural and magnetic properties of the Ni-Mn-Ga alloys may also be a source of other interesting physical effects not directly related to shape memory, such as previously mentioned *giant magnetoresistance* [53–55], *exchange bias* [56–58], or *strain glass* behaviour [59,60].

This short introduction shows that NiMnGa-based alloys are not ordinary shape memory materials. They combine a unique set of thermally, magnetically and mechanically driven properties (**Fig. 1.3**) that may be altered by chemical composition, alloying additions, manufacturing parameters or post-fabrication heat treatment. On the basis of their versatile properties, they are nowadays more often classified as smart *multifunctional materials*, rather than standard MSMAs.

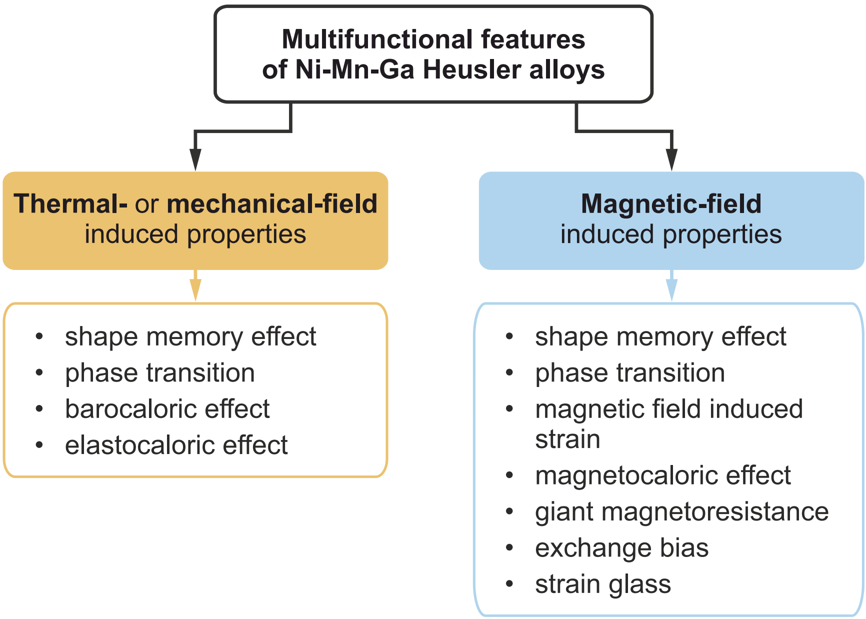

Fig. 1.3. List of numerous multifunctional features of the Ni-Mn-Ga Heusler alloys divided into two groups: (1) thermal- or mechanical field-induced and (2) magnetic field-induced.

The theoretical part of this thesis provides an overview of NiMnGa-based multifunctional Heusler-type alloys. The first part of the theoretical background is focused on atomic structure of both the parent austenite phase and different variations of martensite phase. This part also discussed the nature of the reversible martensitic transformation associated with the premartensitic and intermartensitic transition. Moreover, the magnetic and magnetostructural transitions are also discussed in this section. The second part of the theoretical introduction follows the most significant magnetostructural properties of Ni-Mn-Ga alloys, including shape memory effect, magnetic field-induced strains, pseudoelasticity and mechanocaloric effects. The third section of the theoretical background is mainly focused on the compositional dependence of Ni-Mn-Ga alloys and the influence of alloying additions on their microstructure and magnetomechanical properties. In addition, different modern forms of MSMAs are also briefly discussed in order to show the fabrication versatility of Ni-Mn-Ga compound. The last part of the introduction provides a summary of the recent and possible future applications of the different forms of multifunctional Ni-Mn-Ga alloys.

1.2 Structure of Ni-Mn-Ga alloys

1.2.1 Austenite phase

1.2.1.1 Ordered $L2_1$ phase

At the beginning, it should be clarified that due to the existence of reversible phase transition in Ni-Mn-Ga alloys two main phases are distinguishable in this compound: low temperature martensite and high temperature austenite. *High* and *low temperature phases* are just a common names to describe the structure of alloy before and after martensitic transition, but it does not mean that the particular martensitic transformation temperature is neither low nor high, as it can be altered in a very wide range depending on the chemical composition (for details see **Section 1.3.4**).

It was already mentioned at the beginning of the theoretical introduction that the crystal structure of the stoichiometric Ni_2MnGa alloy was firstly described by Webster *et al.* [20]. Based on the high-resolution neutron powder diffraction measurements, he reported that Ni_2MnGa alloy is characterised by cubic $L2_1$ unit cell with lattice parameter $a = 5.825$ Å and may by explained as four interpenetrating *fcc* sublattices. Further investigations by other researchers [43,61,62] confirmed the $Fm\bar{3}m$ space group (no. 225) for $L2_1$ crystal structure with the following Wyckoff atomic positions: 8*c* (0.25, 0.25, 0.25), 4*a* (0, 0, 0) and 4*b* (0.5, 0.5, 0.5) sites for Ni, Mn and Ga atoms, respectively. What is interesting, the neutron diffraction measurement were crucial for a clear determination of austenite phase in Ni-Mn-Ga alloy, because more popular and accessible X-ray diffraction measurements for these particular Heusler alloys are restricted by similar X-ray scattering factors of Ni, Mn and Ga atoms.

1.2.1.2 Disordered $B2'$ phase

From a technological and fabrication point of view, another significant factor of the crystal structure of the austenite phase is its crystallization behaviour from the liquid state. For the stoichiometric Ni_2MnGa Heusler alloy the melting temperature is 1382 K [63]. During cooling from the liquid state, below the melting temperature, the Ni-Mn-Ga system solidifies in an intermediate $B2'$ phase [63]. The $B2'$ cubic structure with $Pm\bar{3}m$ symmetry is partially ordered, as only Ni atoms are ordered in the crystal lattice, whereas both Mn and Ga atoms randomly occupies their sites as it is depicted in **Fig. 1.4(a)**. During further cooling, the Ni-Mn-Ga alloy undergoes the disorder-order transition from a partially ordered $B2'$ phase into fully ordered $L2_1$ phase (**Fig. 1.4(b)**). For the stoichiometric Ni_2MnGa Heusler the second order $B2' \rightleftarrows L2_1$ transformation takes place at 1071 K [63], but it can vary in non-stoichiometric composition [64–66].

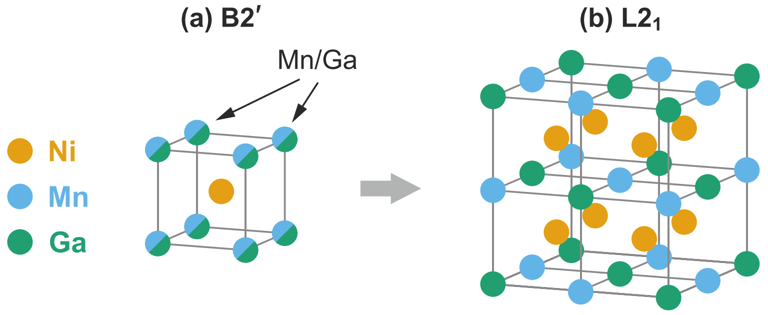

Fig. 1.4. Unit cell model of **(a)** the partially ordered B2′ structure and **(b)** the fully ordered $L2_1$ structure of the Ni-Mn-Ga alloys.

1.2.2 Martensite phase

The crystal structure of low temperature martensite phase is more complex than in the case of the austenite phase. During cooling below the martensitic transformation temperature, the Ni-Mn-Ga alloy undergoes a phase transition involving the lattice deformation (also called *Bain distortion*) from $L2_1$ cubic structure to $L1_0$ tetragonal structure [20]. The orientation of the $L1_0$ unit cell in the parent $L2_1$ cell is presented in **Fig. 1.5(a)** and single $L1_0$ unit cell is also shown separately in **Fig. 1.5(b)**. It is seen that, the symmetry between the $L2_1$ and $L1_0$ unit cell requires the precise correlation between the crystallographic axes of these two structures. Depending on the composition, alloying addition and manufacturing conditions, the tetragonal structure of martensite may be both *non-modulated* (NM) or *modulated* (M). The most commonly observed modulated structures are *five-layered* 5M (also known as 10M) and *seven-layered* 7M (also known as 14M) modulated martensite [43]. It is worth to noting that NM martensite is the most stable low-temperature phase, whereas 5M martensite is the least stable. The stability of 7M martensite is between NM and 5M martensite [67].

1.2.2.1 Non-modulated martensite

Non-modulated martensite is the most simple and stable variant of low temperature phase of Ni-Mn-Ga alloys. The tetragonal crystal structure of the NM martensite is defined by $I4/mmm$ space group with Ni, Mn and Ga atoms occupying the $4d$ (0, 0.5, 0.25), $2b$ (0, 0, 0.5) and $2a$ (0, 0, 0) Wyckoff positions, respectively [68,69]. The microstructure of NM martensite is characterised by internally twinned plates. However, internal twinning is not regular and may vary even in the same main martensite plate [43].

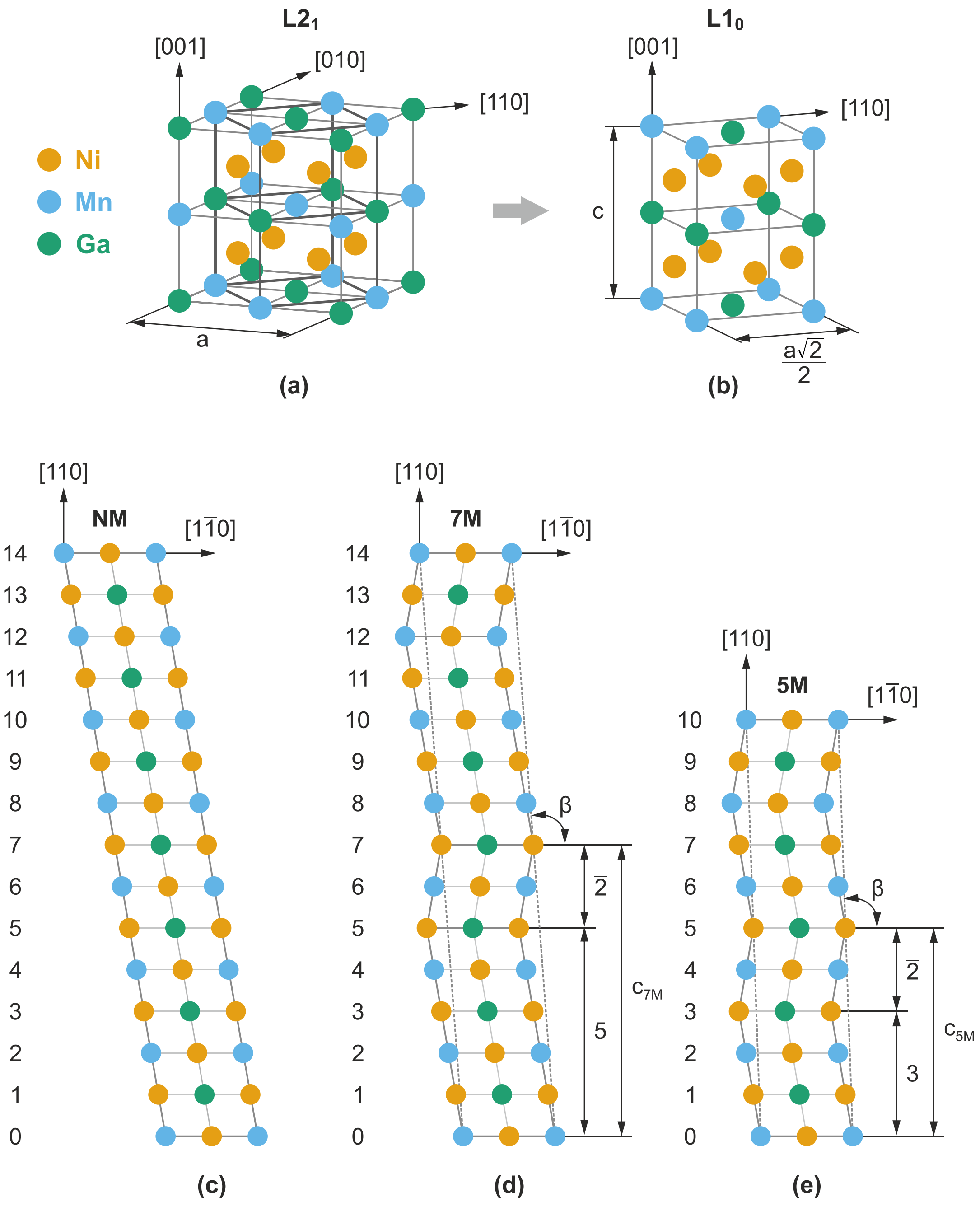

(a) (b)

(c) (d) (e)

Fig. 1.5. Different types of Ni-Mn-Ga alloys structures: **(a)** austenite $L2_1$ cubic cell with marked crystallographic axes, **(b)** martensite $L1_0$ tetragonal cubic cell oriented with respect to the $L2_1$ axes, **(c)** non-modulated martensite, **(d)** 7M and **(e)** 5M modulated martensite marked according to Zhdanov's notation with monoclinic distortion characterised by β angle (based on [70–72]).

1.2.2.2 5M and 7M modulated martensite

In the last 30 years many different theoretical models have been established to explain the nature of martensite modulation in Ni-Mn-Ga alloys. Among them, two main models received the most considerable attention and were verified both theoretically and experimentally.

The first model is based on a specific periodic shuffling of the {110}-type atomic layers (derived from $L2_1$ lattice) along the $[1\bar{1}0]$ direction due to the instability of the cubic phase. In this model, every fifth (for the 5M structure) or every seventh (for the 7M structure) basal plane remains in its initial position, while other planes are subjected to characteristic shift [43,73–75]. As a result, five or seven consecutive unit cells form a characteristic *five-* or *seven-fold superstructure*, respectively.

The second model is based on the approach that was firstly presented for the very similar modulations observed in Ni-Al-Mn Heusler alloys [76] and then successfully adapted in Ni-Mn-Ga alloys [77,78]. In this model basal {110}-type plane from $L2_1$ austenite stacks in regards to the $(3\bar{2})_2$ or $(5\bar{2})_2$ sequence in Zhdanov's notation, which is shown in **Fig. 1.5(d)–(e)**. According to this approach modulated martensite is characterised by a and b axes on the basal plane and c axis along the stacking direction. It is seen in **Fig. 1.5(d)–(e)** that three (3) or five (5) basal planes stacked along the c-axis are shifted in a direction of the a-axis, whereas the two ($\bar{2}$) remaining planes are shifted in the opposite direction. The combination of two neighbouring blocks (referred as subscript in Zhdanov's notation) with two or five differently shifted planes forms the $(3\bar{2})_2$ or $(5\bar{2})_2$ sequence. What is more, this model assume the monoclinic distortion of martensite unit cell with the angle β only slightly higher than 90° (~90.3° for 5M and ~93.3° for 7M [61,78,79] martensite).

To make the structural properties of the martensite variants even more complicated, further comprehensive XRD studies at low temperatures revealed that the modulated structures of martensite may be *commensurate* (C) and *incommensurate* (IC) [79–82]. Righi *et al.* reported that the previously assumed monoclinic distortion of five-layered martensite is valid only for the commensurate structure ($I2/m$ space group), as the 5M incommensurate martensite is more likely orthorhombic ($Pnmn$ space group) than monoclinic [80,82]. In case of seven-layered martensite, only incommensurate structures with monoclinic distortion ($P2/m$ space group) were found in the Ni-Mn-Ga alloys [79]. Later on Glavatskyy *et al.*, based on the neutron diffraction measurements, also suggested the monoclinic distortion of the 5M commensurate structure but with slightly different space group – $P2/m$ [83]. Examples of lattice parameters of different commensurate and incommensurate crystal structures of Ni-Mn-Ga alloys are summarized in **Table 1.1**.

Table 1.1. Examples of the lattice parameters for the austenitic as well as NM, 5M and 7M martensitic structures in different reported crystallographic systems of the Ni-Mn-Ga alloys.

Alloy composition	Cell	Symmetry	Lattice parameters (Å)			Angle (°)
			a	b	c	β
$Ni_{50}Mn_{25}Ga_{25}$ [20]	$L2_1$	Cubic	5.825			
$Ni_{53}Mn_{25}Ga_{22}$ [68]	NM	Tetragonal	3.865		6.596	
$Ni_{49}Mn_{30}Ga_{22}$ [80]	5M(C)	Monoclinic	4.228	5.575	4.200	90.3
$Ni_{50}Mn_{25}Ga_{25}$ [82]	5M(IC)	Orthorhombic	4.219	5.553	4.190	
$Ni_{50}Mn_{30}Ga_{30}$ [79]	7M(IC)	Monoclinic	4.267	5.507	4.223	93.3

What is interesting, the differences between the two presented models are relatively small and may be distinguishable only on the atomic level. The detailed high resolution transmission electron microscopy (HRTEM) investigations of the off-stoichiometric Ni-Mn-Ga alloys shows that in the case of 5M martensite both models (*i.e.* modulation by periodic shuffling and stacking of basal planes) are equally satisfactory, resulting in almost the same atomic positions [77,78,80]. However, the theoretical interpretation of the nature of 5M modulated structures favours the modulation by periodic shuffling due to the existence of a prior pre-martensitic transformation from austenite to an intermediate modulated phase [43]. Consequently, the martensitic transformation follows a reduction in symmetry from cubic to tetragonal structure and subsequent change in the modulation period from 3M (also known as 6M) to 5M [72,84–86].

In contrary, when it comes to the 7M martensite, the second model based on the stacking of close-packed planes seems to be more accurate, as the seven-layered structure is reported to be nanotwinned in nature [77,78]. Following this fact, the existence of the nanotwinned modulated structure may be well explained by the theory of an *adaptive martensite* [72,87–90]. In this theory, *adaptive* nanotwinning is required to balance the energy generated by the elastic stress at the phase boundaries with low nanotwin boundary energy. As a result, the concept of the 7M modulation as an adaptive phase is more probable than the simple modulation by shuffling observed in the 5M martensite.

1.3 Phase transformations in Ni-Mn-Ga alloys

Phase transformations in Ni-Mn-Ga multifunctional alloys can be divided into two main groups: (1) *structural transformations* and (2) *magnetic transformations*. This division is especially important because in NiMn-based Heuslers the magnetic and structural transformation are independent, which is generally a rare phenomenon in solid-state physics. It means that, depending on the chemical composition, both the austenite and martensite phases may be in ferromagnetic or paramagnetic state. Due to that fact, the structural and magnetic transformation will be discussed in separate subsections.

1.3.1 Structural transformations sequence

When it comes to structural phase transformations, the best way to describe the transition behaviour of Ni-Mn-Ga alloys is to follow their transformation sequence from the liquid state up to the low temperature martensite phase. Understanding the complex phase transformation behaviour of Ni-Mn-Ga compounds is necessary to utilize this group of multifunctional materials in modern applications. A schematic representation of phase transformation paths for the Ni-Mn-Ga alloys is presented in **Fig. 1.6**.

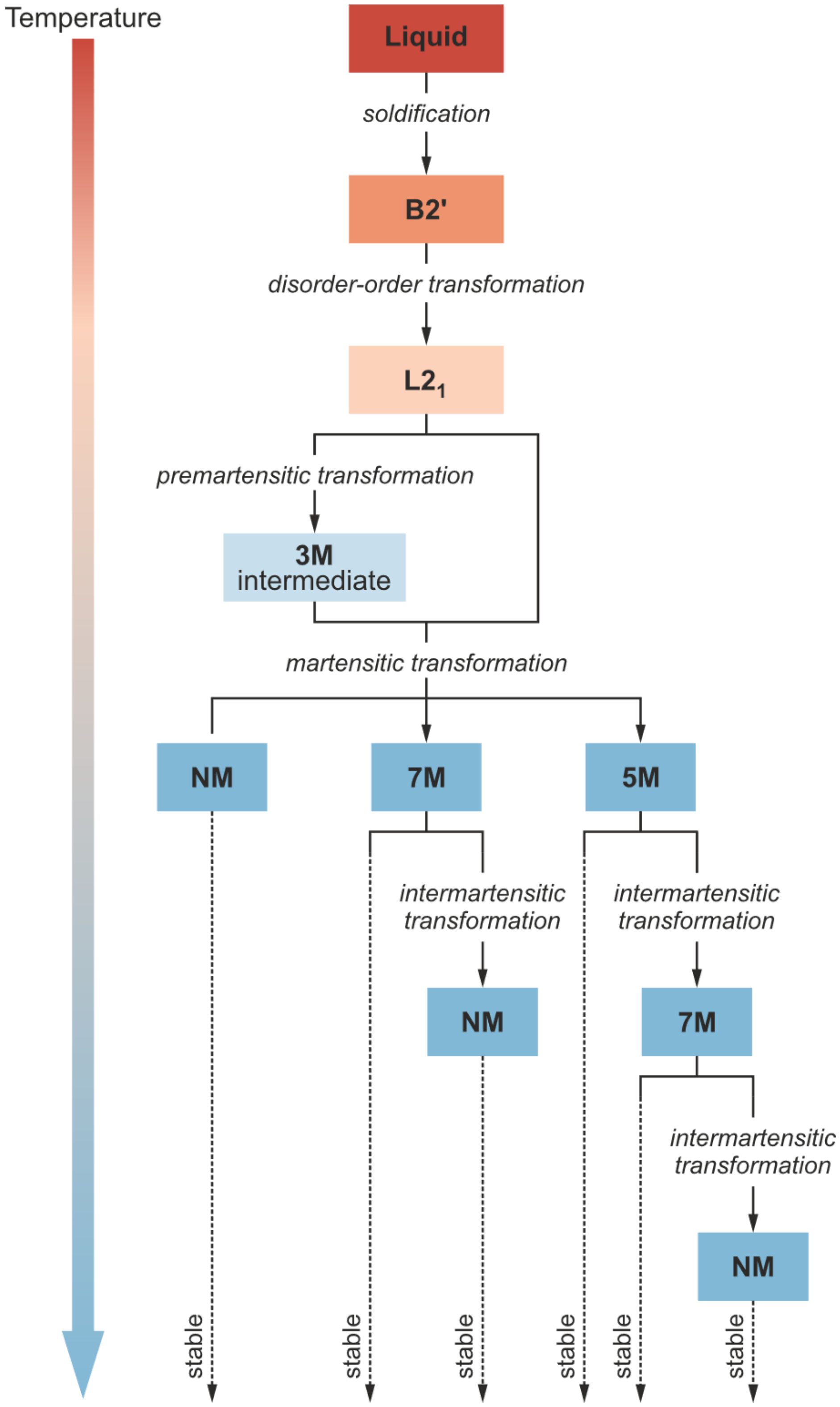

Fig 1.6. Schematic diagram of the sequence of structural transformations in Ni-Mn-Ga alloys during cooling from liquid state (based on [91]).

As seen in **Fig. 1.6**, at the beginning, at a high temperature above 1350°C, the material is in a fully liquid state. During cooling, the first transformation undergoes from liquidus into partially ordered B2′ phase. Further cooling leads to the characteristic *disorder-order transition* from the B2′ phase to the fully ordered $L2_1$ austenitic phase. Close to the martensitic transition temperatures, depending on the chemical composition, some Ni-Mn-Ga alloys may undergo the *premartensitic transition* from the $L2_1$ phase into the intermediate modulated phase. Other Ni-Mn-Ga alloys do not exhibit the premartensitic phase and transform to the martensitic phase directly from the $L2_1$ structure. The *martensitic transformation* is the most complex transition as it may undergo to three different types of martensite phase: (1) non-modulated, (2) 5M and (3) 7M modulated martensite, which were in detail described in previous section (see **Section 1.2.2**). On the basis of the chemical composition and thermal history of the alloy, as well as the additional alloying elements, the resulting martensitic structures may or may not be stable during further cooling. If the martensite modulation is stable enough, it will be present in the material even at very low temperatures. However, in case of unstable modulated structures (5M or 7M) during further cooling the Ni-Mn-Ga alloy undergoes the *intermartensitic transformations* from 5M to 7M martensite and/or from 7M to NM martensite. The detailed description of the above-mentioned transformation will be discussed in the following sections.

1.3.2 Crystallization and disorder-order transformation

It was already mentioned in **Section 1.2.1** that Ni-Mn-Ga alloys solidifies into the partially ordered B2′ phase, where only Ni atoms are ordered in the crystal lattice. Upon further cooling, the material undergoes second order $B2' \rightleftarrows L2_1$ transformation [63]. This transformation is an disorder-order type, as the $L2_1$ austenite phase is a fully ordered structure in which not only Ni, but also Mn and Ga atoms, occupy their final position in the crystal lattice (see **Section 1.2.1**).

The $B2' \rightleftarrows L2_1$ transformation is especially important from a manufacturing point of view. The Ni-Mn-Ga alloys are commonly produced from pure metallic elements, which can be melted using many different fabrication techniques. In the vast majority of cases, during cooling from liquid state, the cooling ratio is so high that it impedes the homogeneous distribution of atoms in the crystal lattice of the alloy. As a result, the produced materials require additional post-fabrication heat treatment to accelerate the diffusion of atoms and homogenize their distribution. For the Ni-Mn-Ga alloys, the most effective annealing temperature is above the disorder-order transformation, where the material still has a B2′ structure. This helps the disordered Mn and Ga atoms to by uniformly spread throughout the crystal lattice of the alloy. In view of the above, accurate estimation of the $B2' \rightleftarrows L2_1$ transformation is crucial for the appropriate determination of the heat treatment conditions for the as-cast Ni-Mn-Ga Heusler alloys.

1.3.3 Premartensitic transition

Premartensitic transformation in Ni-Mn-Ga alloys is a pretransition phenomenon that can occur just before the former martensitic transformation. It is a weak first order transition that stems from the magnetoelastic coupling. It means that the premartensitic transition is a precursor phenomenon that announces the prior martensitic transition by changing the dynamic response of the austenite crystal lattice (known as *phonon softening*) [92]. Remarkably, the premartensitic transition is observed only in specific NiMnGa-based Heuslers, which are usually very close to the stoichiometric Ni_2MnGa composition [93]. As a consequence, the premartensitic transition is only reported for alloys with the martensitic transformation temperature lower than 270 K [94].

The temperature of the premartensitic transformation, T_P, is higher than the temperature of the martensitic transformation, T_M, which means that in the range between T_P and T_M, the Ni-Mn-Ga alloy is in an intermediate phase between austenite and martensite. Detailed studies of neutron powder diffraction and electron diffraction shown that this intermediate phase is characterised by a *commensurate three-layered modulated structure* (3M) with orthorhombic distortion defined by the *Pnnm* space group [85,95–97]. However, several recent researches reported that the 3M intermediate martensitic phase can also be *incommensurate* in nature [86,98].

1.3.4 Martensitic transformation

Historically, martensitic transformation refers to a phase transformation that accompany the quenching process of steel [99]. However, in the course of the development of material engineering, the term *martensitic transformation* broadens its original definition. Today, there is still no clear definition of *martensitic transformation*, though it is usually used to describe diffusionless, reversible phase transformations in metallic alloys, ionic solids and oxides [100].

In case of shape memory materials the martensitic transformation is first order type (as there is latent heat related with this phase transition), diffusionless transformation during which atoms in crystal lattice shift on very short rage in strictly determined pattern [101]. The temperature-induced martensitic transformation is characterized by four temperatures: martensitic transformation start and finish temperature, M_s and M_f, as well as austenitic transformation start and finish temperature, A_s and A_f. **Fig. 1.7(a)** presents an example of the differential scanning calorimetry (DSC) curves recorded for the Ni-Mn-Ga alloy. It is seen that martensitic transformation starts when the alloy is cooled below M_s and ends when temperature is lower than M_f and the whole sample is in martensitic state (**Fig 1.7(b)**). Likewise, the reverse martensitic transformation (austenitic transformation) occurs when the alloy is heated beyond the A_s until the temperature exceeds A_f and the whole material is in the austenitic state (**Fig. 1.7(b)**). The forward transformation from austenite to martensite is *exothermic*, which means that energy is released and the change in enthalpy is negative. On the contrary, the reversible transformation from martensite to austenite is *endothermic*, which means that heat is absorbed by the reaction and therefore the change in enthalpy is positive.

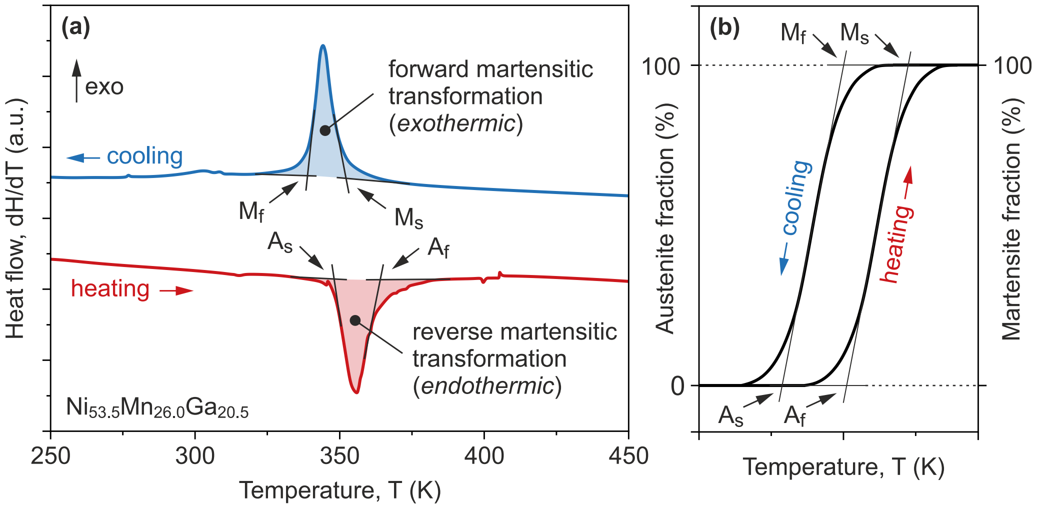

Fig. 1.7. **(a)** Example of the DSC curve for the Ni-Mn-Ga alloy recorded during the heating and cooling cycle (data from [102]). Heating is represented by the red curve, and cooling is represented by the blue curve. The arrows show the estimated start (M_s/A_s) and finish (M_f/A_f) temperatures for the martensitic and austenitic transitions, respectively. The peaks filled with colour are related to the latent heat absorbed (red colour) or released (blue colour) during endothermic or exothermic transitions, respectively. **(b)** Fraction of the austenite and martensite phases as a function of temperature.

In order to compare the transformation temperatures between different shape memory Heusler alloys, the average martensitic transformation temperature T_M is defined as:

$$T_M = \frac{M_s + M_f + A_s + A_f}{4} \tag{1.1}$$

The necessity of using the average martensitic transformation temperature is caused by the characteristic hysteresis observed during heating and cooling of the alloy. According to the basics of thermodynamics, the hysteretic behaviour of the martensitic transition in MSMAs is driven by *Gibbs free energy*. **Fig. 1.8** shows the schematic representation of Gibbs free energy as a function of temperature for both the austenite and martensite phase. Generally, both presented phases are characterised by different entropies and enthalpies, which leads to the two different curves that intersect at specified temperature. At high temperatures (above A_f) the Gibbs free energy of austenite, G_A, is significantly lower than the free energy of martensite, G_M. As a result, the alloy is in austenitic state, since the whole system aims to minimize the Gibbs potential (system energy). An analogous situation is present at low temperatures (below M_f). This time, the G_M is notably lower than G_A, thus martensite is more thermodynamically favoured. The temperature at which Gibbs free energies of the martensite and austenite phases are equal (both phases are equally stable) is identified as the martensitic transformation temperature. In ideal conditions, without thermal hysteresis, the transition should occur at equilibrium temperature T_M. However, due to the contribution of the surface and elastic energy stored during the phase transformation, the martensitic transition requires an additional *driving force* to induce this transformation [103]. In the most simple model, this *driving force* is generally achieved by overcooling for the forward martensitic transition or by overheating during the reverse martensitic transition. The temperature difference ΔT_s between T_M and M_s (during cooling) or A_s (during heating) produces the difference in Gibbs free energy, $\Delta G_{A\text{-}M}$ or $\Delta G_{M\text{-}A}$, which is represented in **Fig. 1.8** by the blue and red arrows, respectively. When the difference in free Gibbs energy exceeds the accumulated surface and elastic energy – the transformation begins.

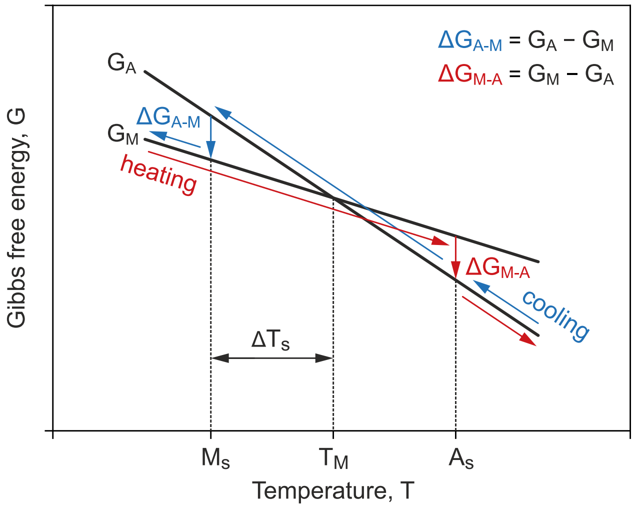

Fig. 1.8. Schematic representation of the Gibbs free energy for the austenite (G_A) and martensite (G_M) phases. The intersection of the curves represents the temperature of martensitic transformation (T_M). ΔT_s is the overcooling or overheating required for the transformation. $\Delta G_{A\text{-}M}$ and $\Delta G_{M\text{-}A}$ is the driving force for the martensite and austenite transformation, respectively (based on [103]).

1.3.5 Intermartensitic transformation

The intermartensitic transformation (IMT) is a first-order transformation between two different type of martensite [104–109]. It was already mentioned and showed in **Fig. 1.6**, that depending on the stability of the modulated martensite structures (7M or 5M), during cooling the modulated martensite may seek to transform into the more stable form. Depending on the chemical composition and internal stress accumulated in the alloy during fabrication [110,111], the intermartensitic transformation may take place between 7M → NM, 5M → NM and 7M → 5M → NM martensite variants (**Fig. 1.6**). The structural details of the modulated and non-modulated martensite structures are explained in **Section 1.2.2**.

The abrupt change of martensite structure results in notable changes in the physical properties of the material, including thermal [106,110,112], electrical [108,109,111], magnetic [106,108,109,111,112] and mechanical [107,110,113] properties. The example of the changes of magnetic properties represented by AC magnetic susceptibility and electrical properties represented by electrical resistivity is presented in **Fig. 1.9**. It is seen that both martensitic and intermartensitic transformations are accompanied by a significant change in magnetic and electrical properties.

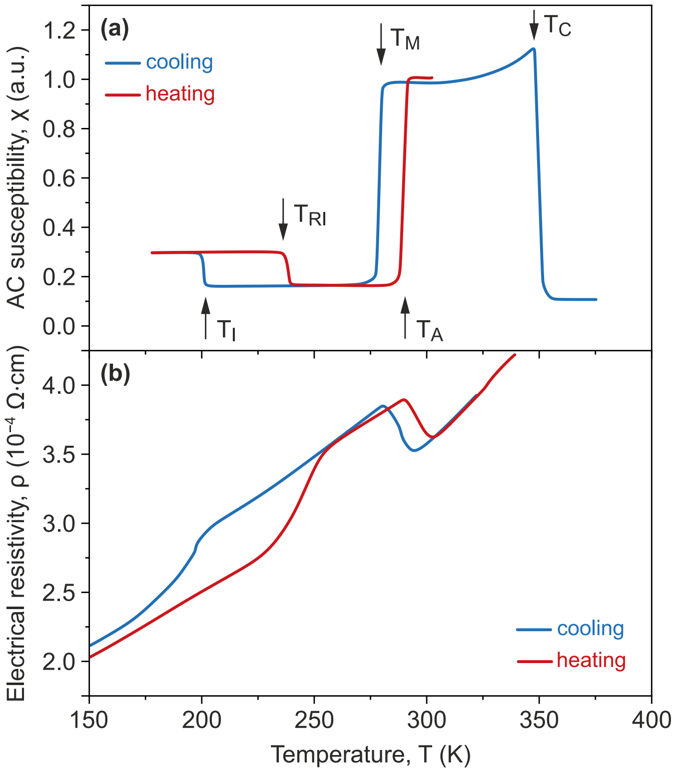

Fig. 1.9. Temperature dependence of **(a)** the AC magnetic susceptibility and **(b)** the electrical resistivity for the single crystal $Ni_{52}Mn_{24}Ga_{24}$ alloy (data from [111]). T_M is the martensitic transformation temperature, T_A is the austenitic transformation temperature, T_I is the intermartensitic transition temperature during cooling, T_{IR} is the reversible martensitic transformation temperature, and T_C is the Curie temperature.

The phenomenon of intermartensitic transformation may be both an advantage and a disadvantage feature in the potential application of the Ni-Mn-Ga alloys. From a positive perspective, it broadens the multifunctional potential of the MSMAs, as each martensite variant, which may be induced in the same specimen, is characterised by their own physical properties. On the other hand, when only one modulated martensite variant is required, the intermartensitic transition sets the lower temperature limit for future applications of the alloy.

1.3.6 Magnetic transformation

The ferromagnetic properties of Ni-Mn-Ga alloys mainly originate from the magnetic moment of the Mn atoms, as Ni atoms carry only a small magnetic moment, whereas the influence of the Ga atoms is negligible [114–116]. This phenomenon is very interesting, because in the normal state Mn is antiferromagnetic. In case of the Ni-Mn-Ga compound, the Mn atoms are placed according to the characteristic $L2_1$ structure in which distances between Mn atoms are increased in comparison to pure metallic Mn. These structural changes between Mn atoms lead to a change of Mn-Mn exchange interaction from antiferromagnetic to ferromagnetic [116]. It illustrates how the strong magnetic properties of the NiMnGa-based alloys are dependant on the chemical composition, since every excess of Ni, Mn or Ga as, well as other alloying elements, introduce extra atoms to the crystal lattice and changes their original stoichiometric occupation [116–118].

Similarly to the other ferromagnetic materials, Ni-Mn-Ga alloys undergo the second order reversible magnetic transformation from a ferromagnetic to a paramagnetic state during heating and from a paramagnetic to a ferromagnetic state during cooling. The temperature at which material loses its ferromagnetic order is called the Curie temperature, T_C, or Curie point and, for example, is clearly visible in **Fig. 1.9** as an abrupt drop of magnetic susceptibility. The T_C is a very essential temperature, as it limits the potential usage of all magnetic-indued effects of ferromagnetic Heusler material. For the stoichiometric Ni_2MnGa alloys the T_C is equal to 376 K [119]. What is interesting, the temperature of magnetic transformation is significantly less dependant on the chemical composition of the alloy than it is for structural transformation [120–123]. This phenomenon is especially evident for ternary Ni-Mn-Ga compositions. **Fig. 1.10** shows the temperature of both structural martensitic and magnetic transformation as a function Ni excess in favour of Ga and Mn for the off-stoichiometric $Ni_{2+x}Mn_{1-x}Ga$ and $Ni_{2+x}MnGa_{1-x}$ alloy. It is clearly seen that structural and magnetic transformations are independent from each other and that the changes of T_M are far more substantial than variations in T_C. In addition, three characteristic regions where (1) $T_M < T_C$, (2) $T_M = T_C$ and (3) $T_M > T_C$ are also distinguishable. In such situations both martensite and austenite phases may be ferromagnetic or paramagnetic, which is very rare feature in solid-state physics. The more substantial alteration of the Curie temperature requires significant deviations from the stoichiometric composition as well as proper alloying additions.

1.3.7 Magnetostructural transformation

In the previous section, it was shown that structural and magnetic transformations are independent and may change separately. Following that fact, it is possible to obtain the material where both transformation temperatures coincide, *i.e.*, $T_C \cong T_M$ (**Fig. 1.10**). This leads to the so-called *magnetostructural transition*, which undergoes between the ferromagnetic martensite and the paramagnetic austenite [124].

The interplay between magnetic and structural properties of the NiMnGa-based Heusler alloys leads to the extraordinary magnetoelastic behaviour of these materials [125–127]. The evolution of the magnetostructural transformation enhances the magnetoelastic interactions in the crystal lattice of alloy and sets the origin for the giant magneto- and mechanocaloric effects [52,125,128], which will be discussed in detailed in **Section 1.5.3**.

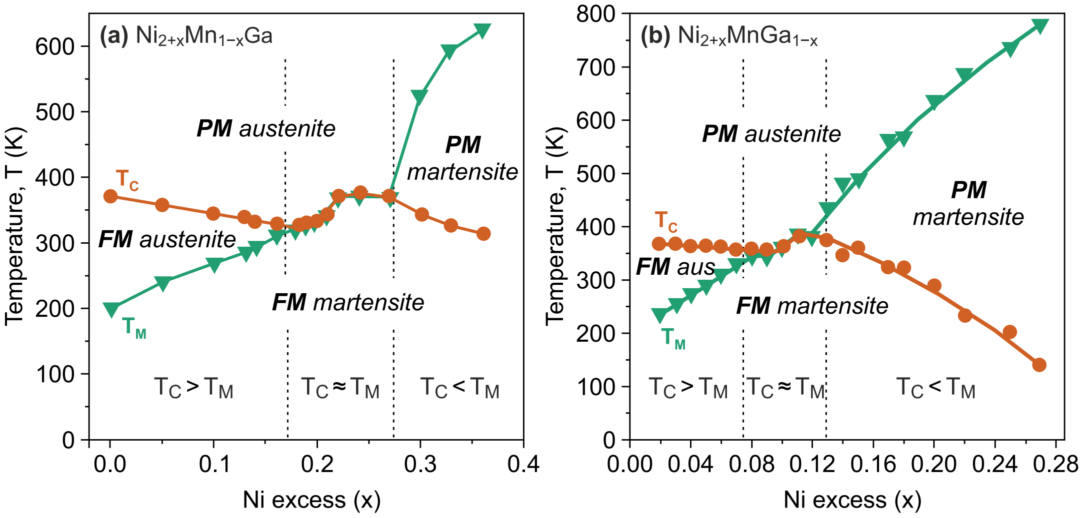

Fig. 1.10. Magnetic phase diagrams for the **(a)** Ni$_{2+x}$Mn$_{1-x}$Ga (based on [121]) and **(b)** Ni$_{2+x}$MnGa$_{1-x}$ (based on [120]) shape memory alloys. T_M corresponds to the martensitic transition temperature and T_C shows the Curie temperatures. The PM and FM abbreviations represent the paramagnetic and ferromagnetic states, respectively. The dashed lines divide the phase diagrams into three regions: (1) $T_M < T_C$, (2) $T_M = T_C$ and (3) $T_M > T_C$.

1.4 Shape memory properties

The Ni-Mn-Ga based alloys have been subjected to very intensive research mainly because of their unique magnetomechanical properties, including magnetoplasticy – responsible for the magnetic shape memory effect, and pseudoelasticity – a phenomenon similar to those observed in other shape memory materials like NiTi alloys. The following section examines a brief explanation of the origin and general features of these uncommon magnetomechanical properties.

1.4.1 Thermal shape memory

Generally, typical shape memory alloys are materials that can recover their original shape after large permanent deformation only by heating above a certain temperature [129]. The origin of the shape recovery stems from the *thermoelastic phase transformation* from a high symmetry austenite phase to a low symmetry martensite phase. The schematic representation of the thermally induced shape memory effect is presented in **Fig. 1.11**. It is seen that due to the low symmetry of martensite phase certain differently oriented martensite variants are present in martensite phase below transformation temperature (to enhance clarity, only two different variants are shown in **Fig. 1.11**). The observed polyvariant structure is the result of self-accommodation of martensite variants minimizing the elastic energy of the crystal lattice. On a macroscopic scale, no significant changes in material shape are observed. Only application of external mechanical stress leads to a *twin boundary motion* according to the currently favourable crystallographic orientation. In other words, the fraction of the martensite variant with the largest strain along the direction of the external stress grows at the expanse of other variants. The structural reorientation of martensite variants is characterised by a flat plateau observed in the stress-strain curve (**Fig. 1.11**). The mechanism of twin boundary motion results in a significantly higher macroscopic change of shape than the martensite transformation. It should be noted that the reorientation of martensite variants occurs within the same martensite modulation (NM, 5M or 7M) and is not connected with previously described intermartensitic transitions. The new crystallographic orientation of martensite variants is stable even after stress removal, so the material will remain in its deformed shape. The corresponding relationship between stress (σ), strain (ε) and temperature (T) during phase transformation and subsequent stress loading is also shown in **Fig. 1.11**.

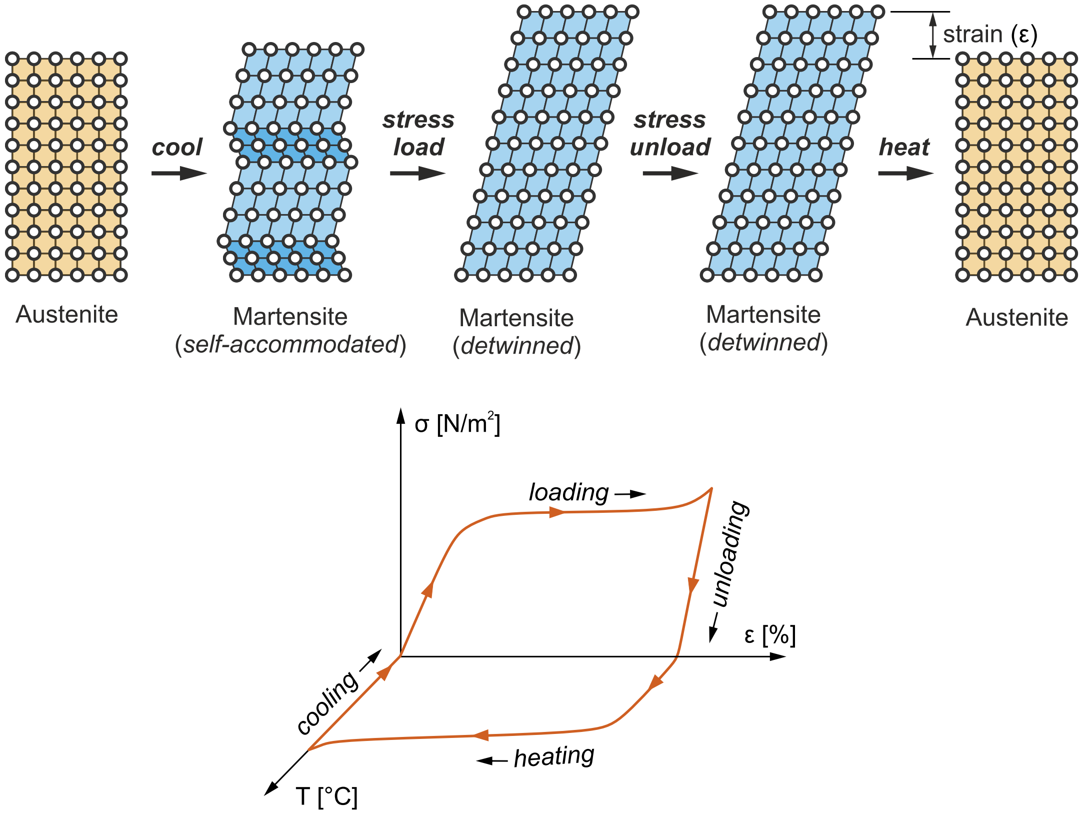

Fig. 1.11. Schematic representation of thermally induced shape memory effect followed by twin boundary motion mechanism induced by mechanical stress. The additional graph shows the corresponding stress-strain-temperature (σ-ε-T) relationship (based on [130,131]).

In order to restore the initial shape, the alloy needs to be heated above the austenite transformation temperature. Above the A_f, the sample transforms back to a parent austenite phase, followed by the upfront deterioration of the martensite variants. The full shape recovery between parent austenite and twinned martensite is achievable due to two main reasons: (1) diffusionless character of martensitic transformation and (2) twin boundary motion mechanism, which in its origin preserved the topological structure of the crystal structure.

1.4.2 Pseudoelasticity

The pseudoelasticity effect is another interesting phenomenon that is strongly related to the reversible martensitic transformation. The origin of pseudoelasticity stems from the fact that diffusionless phase transformation in shape memory materials may be also induced only by external mechanical stress. When the material is in austenitic state, the application of sufficiently high external stress favours the appearance of martensite variant characterised by the higher shear stress, which is schematically presented in **Fig. 1.12**. In contrast to the thermally induced shape memory effect, after phase transition, only one single preferred variant of martensite is induced in the microstructure of the material, directly resulting in significant deformation of the sample (**Fig. 1.12**). After vanishing of mechanical stress, the martensite phase becomes unstable and is no longer the energetically favourable phase. As a result, the sample turns back to a parent austenite phase followed by a full deformation recovery. Moreover, it is worth mentioning that the pseudoelasticity is very often called *superelasticity*. However, in this case, the *pseudo* prefix is more suitable, as it emphasises that the deformation of the alloy is not connected with common plastic deformation mechanisms, which is characteristic to majority of metallic materials.

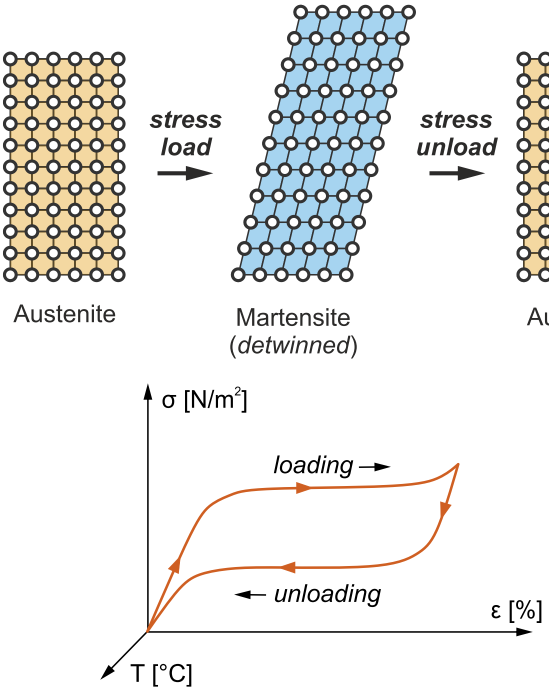

Fig. 1.12. Schematic representation of the pseudoelasticity mechanism with the corresponding stress-strain-temperature (σ-ε-T) graph (based on [131]).

1.4.3 Magnetic shape memory

The discovery of the magnetic shape memory effect was a significant breakthrough in the development of smart shape memory materials. The additional degree of freedom in the form of an external magnetic field opens a completely new way of controlling and understanding the origin of shape memory mechanism. On the other hand, the precise control and alteration of shape memory characteristics of MSMAs are far more complicated than in case of standard shape memory materials, due to the mutual relation between three degrees of freedom: magnetic, thermal and mechanical field. In NiMn-based Heusler alloys the shape memory effect is strictly connected with two interesting separable phenomena: *magnetic field-induced structure reorientation* (MIR) and *magnetic field-induced phase transformation*.

1.4.3.1 Magnetic field-induced structure reorientation

The schematic representation of magnetic shape memory effect is shown in **Fig. 1.13**. The whole mechanism is presented similarly to the thermal shape memory effect from **Fig. 1.11**, but instead of mechanical load the external magnetic field is introduced. It is seen that below the martensitic transformation temperature, the material consists of various structural martensite variants with different crystallographic orientations, separated by twin boundaries. Because of the ferromagnetic nature of magnetic shape memory alloys, below the Curie temperature, each martensite variant is characterised by the easy magnetization axis. In macroscopic scale, all magnetization axes in different martensite variants are ordered to reduce the *magnetostatic energy* (self-energy of the material exposed to an external magnetic field [132]). The application of an external magnetic field leads to the reorientation of magnetic moments along the magnetic field. In standard ferromagnetic materials, due to low magnetic anisotropy, this reorientation occurs within the crystal structure of the material, without any noticeable macroscopic changes. However, Ni-Mn-Ga magnetic shape memory materials are characterized by high magnetic anisotropy, which requires a significant amount of energy to rotate the magnetic domains. If this energy exceeds the elastic energy required for twin boundary motion, magnetically induced reorientation occurs [133–135]. In the simplest model, the magnetic energy ΔE_{mag} needed for the twin boundary motion is defined by the relation [135]:

$$\Delta E_{\mathrm{mag}} \geq \varepsilon_0 \sigma_{\mathrm{tw}} \tag{1.2}$$

where ε_0 is the tetragonal distortion ($\varepsilon_0 = 1 - c/a$) and σ_{tw} is twinning stress. Consequently, after application of external magnetic field the magnetically induce reorientation of twin variants takes place in order to promote the martensite variant favourably oriented with respect to the this magnetic field (**Fig. 1.13**). The lower the twinning stress, the higher the twin mobility. If a single variant of martensite nucleates and grows on the expanse of others, a significant macroscopic change of length will be noticeable. This unique mechanism of strain generation is called *magnetic field-induced strain* (MFIS) and is often investigated on its own, without considering the whole shape memory path.

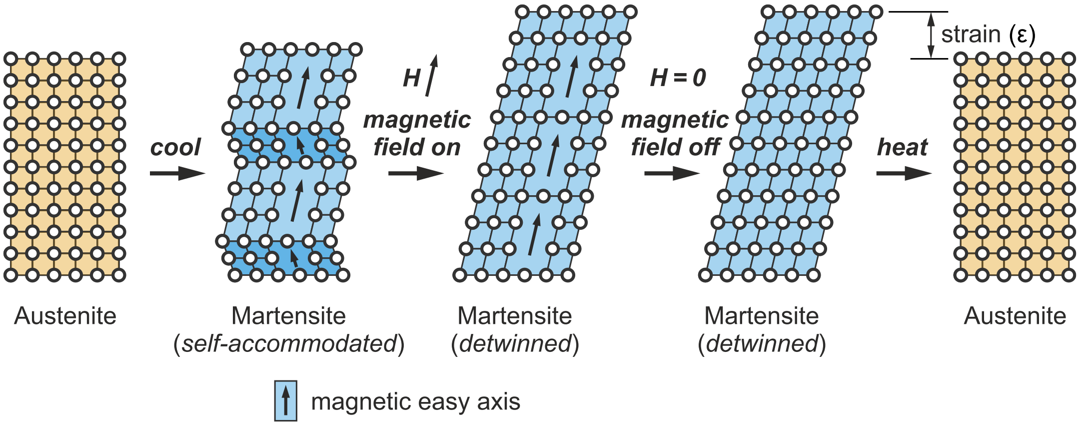

Fig. 1.13. Schematic representation of the magnetic shape memory effect with magnetically induce reorientation of twin variants. The arrows in martensite phase variants represent the easy axis of magnetisation and the arrow next to the *H* shows the direction of an external magnetic field (based on [131]).

When the magnetic field disappears, the induced strains remain in the sample because the structure is still characterised by a single martensite variant. In standard shape memory materials, the strain recovery is achievable only by heating the sample above the austenite transformation temperature. In case of MSMAs additional degrees of freedom broaden the possibilities of strain recovery. First of all, strain recovery may be induced by rotation of the magnetic field, which will induce twin boundary motion according to the new direction of the magnetic field [136–138]. Secondly, the application of mechanical stress perpendicular to the magnetic field will promote the martensite variant favourably oriented with respect to shear stress, not easy magnetization axis, which is schematically depicted in **Fig. 1.14**. In this case, the additional external mechanical stress, σ_{ext}, should be included in the energy model, previously presented in **Eq. 1.2**, by relation [138]:

$$\sigma_{\mathrm{mag}} = \Delta E_{\mathrm{mag}}/\varepsilon_0 \geq \sigma_{\mathrm{tw}} \pm \sigma_{\mathrm{ext}} \tag{1.3}$$

where σ_{mag} is the equivalent magnetic stress, σ_{ext} is the external mechanical stress and the positive or negative sign before σ_{ext} defines if the stress works against or in unison with the magnetic field, respectively.

This model clearly shows that the proper application of both magnetic field and mechanical stress may facilitate or hinder the magnetic field-induced strains. Up to now substantial magnetic field-induced strains exceeding 7% for 5M martensite [139], 9% for 7M martensite [140] and even 12% for NM martensite [46] have been reported for single crystalline NiMnGa-based alloys. Moreover, in principle, the maximum strain limit is only restricted by tetragonal distortion of the crystal lattice, which in the case of the Ni-Mn-Ga compound is even up to 25% [138]. Still, at some point, such high strains are limited by large twinning stress and insufficient magnetic anisotropy, so that condition from **Eq. 1.3** cannot be fulfilled.

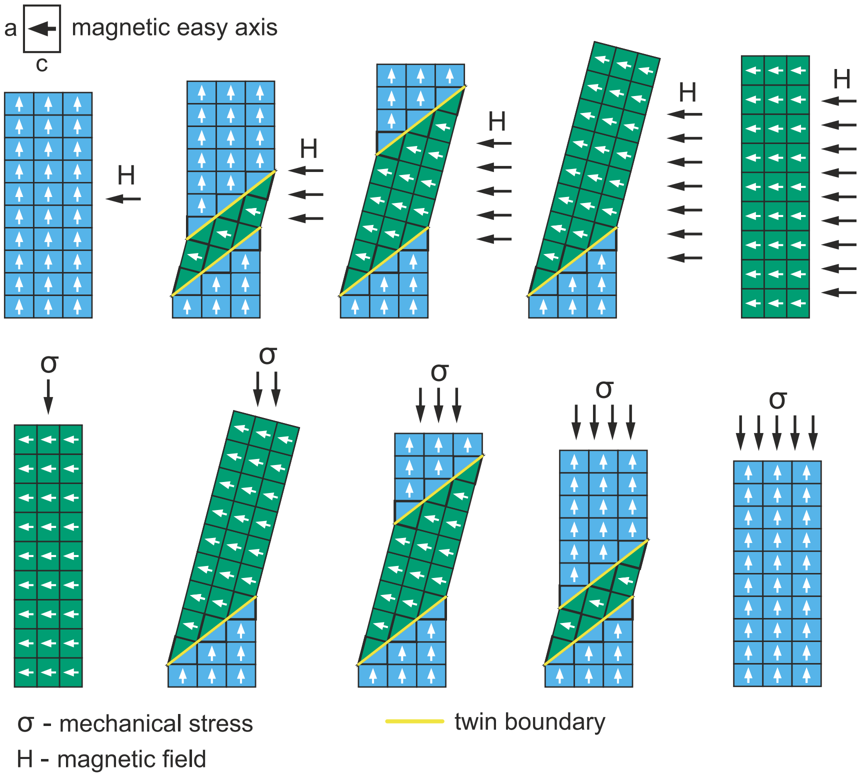

Fig. 1.14. Schematic representation of the magnetic field-induced strains phenomenon controlled by concurrent magnetic field and mechanical stress (based on [141]).

In case of polycrystalline alloys, magnetic field-induced strains are not as impressive because of two main reasons [142]:

- *grain boundaries* (and other lattice imperfections) that are suppressing the twin boundaries mobility,
- *randomly oriented grains* with different types of martensite variants that are averaging the induced strains in different crystallographic directions.

Thereby, the MFIS in bulk polycrystalline Ni-Mn-Ga alloys are currently limited to about 0.2–2% for the directionally solidified samples with highly textured microstructure [143–149]. On the other hand, the abovementioned problems of polycrystalline structure may be overcome by choosing different manufacturing processes. Chmielus and Witherspoon have shown that the introduction of small pores into the microstructure of the material reduces crystallographic constrains, which may increase the MFIS even up to 8.7% [150–153] (see **Section 1.7.6**). Another approach was very recently presented by Laitinen *et al.*, who shown that Ni-Mn-Ga samples produced using an additive manufacturing method called laser powder bed fusion are characterised by repeatable MFIS of 5.8% [154] (see **Section 1.7.9**). Further detailed information about different forms of magnetic shape memory alloys is discussed in **Section 1.7**.

Apart from the MFIS phenomenon in the martensitic phase, full shape recovery to the parent austenite phase is finally achieved by heating the deformed Ni-Mn-Ga material above the austenitic transformation temperature (**Fig. 1.13**). During the whole magnetic shape memory path presented in **Fig. 1.13** the topological structure of the alloy is constantly preserved, which helps to retain the complete shape recovery.

1.4.3.2 Magnetic field-induced phase transformation

It was already explained in **Section 1.4.1** that for standard shape memory materials martensitic phase transformation may be induced only by mechanical stress, which results in so-called pseudoelasticity effect. Considering the additional degree of freedom in magnetic shape memory materials, the same phase transformation may be induced only by an external magnetic field, which in general approach can substitute the mechanical stimuli. The magnetic equivalent of pseudoelasticity effect is called *magnetic pseudoelasticity*, however in the literature considering MSMAs the greater emphasis is put on the *magnetic field-induced transformation* rather than on special *elasticity* behaviour. This is the reason why the term *magnetic field-induced phase transformation* is much more popular than *magnetic pseudoelasticity*. However, it is still worth mentioning that these two terms correspond to the same physical phenomenon.

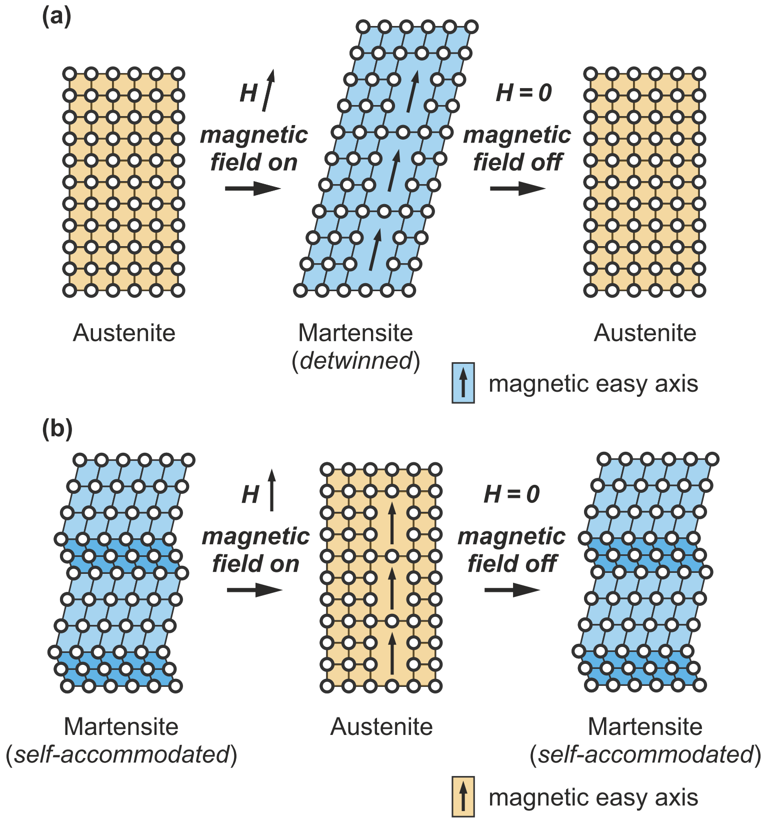

Fig. 1.15. Schematic representation of the magnetic field-induced structural transformation (magneto pseudoelasticity effect). **(a)** The external magnetic field stabilizes the martensitic phase and induces the forward martensitic transition. **(b)** The external magnetic field stabilizes the austenitic phase and induces the reverse martensitic transformation (based on [131]).

The schematic representation of magnetic field-induced phase transformation is presented in **Fig. 1.15**. It is seen that the induced strains are the result of a phase transition instead of a twin boundary motion. At isothermal conditions, close to the martensitic transition, the application of external magnetic field changes the comparative stability between austenite and martensite phases because of the strong magnetostructural coupling existing in MSMAs. In this situation, the external magnetic field will promote the phase characterized by higher magnetization. Thus, the magnetic field may shift the martensitic transformation temperature to higher or lower temperatures depending on whether martensite or austenite have higher magnetization. In case of forward martensitic transformation, the induced strains are significant, as under magnetic field, martensite nucleates only as a single variant (**Fig. 1.15(a)**). On the contrary, in case of reverse martensitic transition, the resultant strains are not so significant, as austenite phase has no preferable crystallographic orientation (**Fig. 1.15(b)**).

The corresponding Gibbs free energy diagram influenced by the magnetic field is presented in **Fig. 1.16**. **Fig. 1.16(a)** shows the situation, where magnetic field stabilizes the martensitic phase, which introduces the additional driving force for transformation in the form of Zeeman energy. As a result, the required energy difference between martensite and austenite is achieved at higher temperatures, which increases the martensitic transformation temperatures. The opposite situation is presented in **Fig. 1.16(b)**, where the external magnetic field stabilizes the parent austenitic phase. In such case, the required energy difference between austenite and martensite is lowered due to the existence of Zeeman energy, which consequently decreases the martensitic transformation temperature.

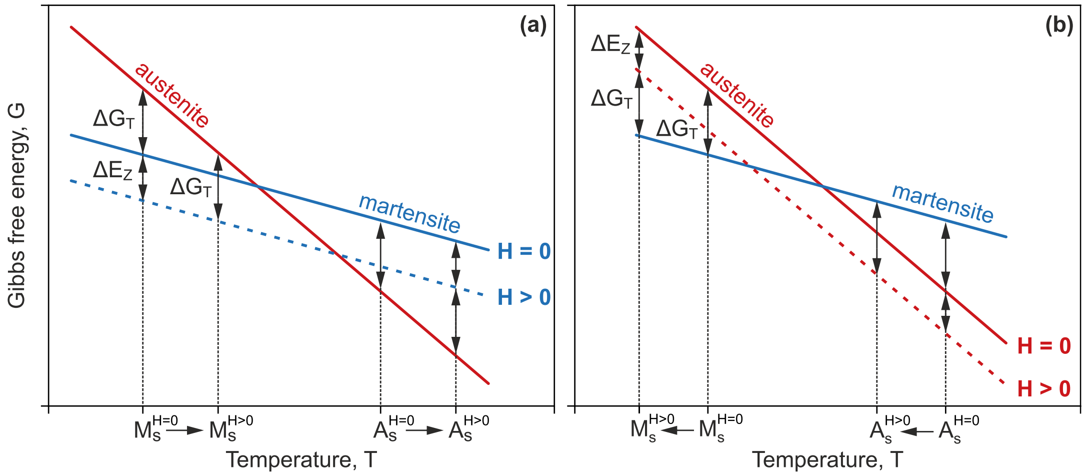

Fig 1.16. Gibbs free energy diagram in the vicinity of the martensitic phase transition influenced by an external magnetic field. The dashed lines represent the free energy under an external magnetic field. ΔG_T is the driving force required to induce the martensitic transition and ΔE_Z is the magnetic Zeeman energy arising from exposition to the magnetic field. **(a)** The external magnetic field stabilize the martensitic phase, thus increasing the martensitic transformation temperature. **(b)** The external magnetic field stabilize the austenitic phase, thus decreasing the martensitic transformation temperature (based on [155]).

The field dependence of the martensitic transformation is strongly dependent on the chemical composition of MSMAs and may significantly differ even in the same NiMn-based group of Heusler alloys. The highest magnetic field dependence of T_M up to about −10 K/T is reported for Ni-Mn-In alloys [156–158]. On the other hand, the weakest rate of change of about −(1–3) K/T is reported for the Ni-Mn-Sn alloys [159–161]. In both Ni-Mn-In and Ni-Mn-Sn compounds, the negative sign before the value means that temperature of martensitic transformation decreases with the increasing field. The different phenomenon is reported for the Ni-Mn-Ga alloys, in which application of the magnetic field shifts the phase transformation to the higher temperature. Interestingly, depending on chemical composition, different magnetic field dependences are reported for NiMnGa-based alloys: from a weak rate of change of about +(0.5–1.5) K/T [162,163], through notably higher rates close to +(6–7) K/T [108,164], up to even +14 K/T for the Co-doped Ni-Mn-Ga alloys [165]. This contrast clearly shows the strong correlation between chemical composition and magnetostructural coupling in the Ni-Mn-Ga system.

1.5 Various multifunctional properties of Ni-Mn-Ga alloys

It was already mentioned that NiMnGa-based alloys owe their attention due to shape memory properties, that are obviously the most spectacular ones, especially when it comes to macroscopic effects. However, the existence of a reversible martensitic transition influenced by three different degrees of freedom stands the basis for other noteworthy multifunctional properties. From the thermodynamic point of view, the strong interplay between mechanical, thermal and magnetic field may promote many other cross-variable phenomena that are schematically summarized in **Fig. 1.17**. As a matter of course, not all of the presented effects are observable in every Ni-Mn-Ga- alloy, but the complexity of the presented relations demonstrates the vast multifunctional potential of magnetic shape memory Heusler alloys. In this section, some interesting functional properties of these materials will be briefly discussed.

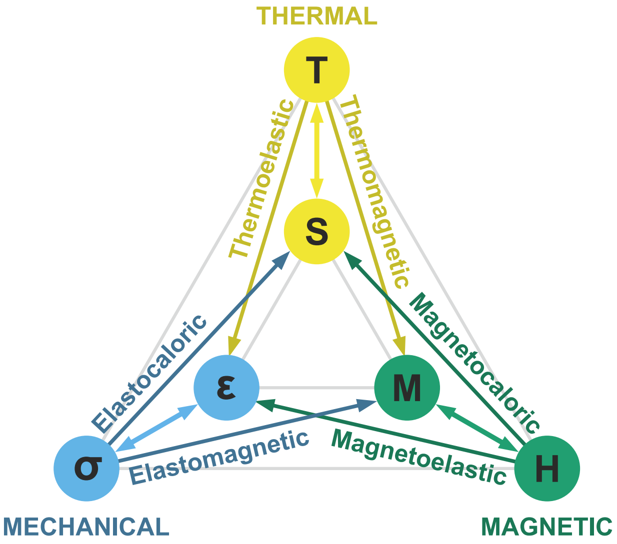

Fig 1.17. Schematic representation of the thermodynamic relations between thermal, mechanical and magnetic variables observed in the multifunctional Ni-Mn-Ga Heusler alloys (adapted from [166]).

1.5.1 Giant magnetoresistance

Magnetoresistance (MR) is a phenomenon that describes the changes in resistance of the material when it is exposed to the external magnetic field [167]. This feature is especially significant in order to define the relations between magnetic and electric properties of the metallic materials, but in the case of large (LMR) or giant (GMR) magnetoresistance, it may also be utilized in modern sophisticated spintronics applications [168].

The NiMn-based Heuslers exhibit negative magnetoresistance in the vicinity of martensitic transition [53,54,169,170]. What is interesting, the explanation of this phenomenon is still not yet fully developed. There are three main mechanisms proposed to explain the MR processes in MSMAs, *i.e.* (1) anisotropic MR, (2) intrinsic magnetic scattering and (3) interface spin scattering [53,169]. Apart form the exact detail explanation of MR origin, the experimental data confirm the existence of large magnetoresistance effect in Ni-Mn-Ga alloys in both in single-crystal and polycrystalline form. In case of polycrystalline structure, about ~5% MR was reported for simple bulk samples [171] and for more structurally sophisticated microwires [172]. For the Ni-Mn-Ga single crystal, even ~25% MR resulting from magnetic field-induced twin boundary reorientation was reported by Zeng *et al.* [173]. The presented interplay between the structural ordering of MSM Heusler alloys and their magnetoresistance properties is a very important topic for some future magnonic applications [53].

1.5.2 Exchange bias

The exchange bias (EB) or exchange anisotropy is another interesting effect that is observed in NiMnGa-based MSMAs. Generally, this phenomenon occurs in layered materials, where one antiferromagnetic layer with a preferred magnetization direction (*pinning layer*) causes shift of the magnetic hysteresis loops of the other soft magnetic layer (*pinned layer*) [174]. This effect normally requires field-assisted cooling below the blocking temperature of ferromagnetic layer due to its remnant magnetization, therefore is usually observed at low temperature. However, in NiMnGa-based Heusler alloys, the EB could be observed during cooling, but without the presence of an external magnetic field. In this case, the unidirectional anisotropy may be created only by the prior phase transition. That is why this phenomenon is sometimes called *spontaneous exchange bias* (SEB) [58]. The first discovery of SEB in the NiMn-based system was reported by Wang *et al.* for the Ni-Mn-In alloys [175]. In later years, due to intensive research, SEB was also observed in other NiMn-based Heusler systems, including Ni-Mn-Ga alloys [56,176–178]. It is worth noticing that the interest in the research of SEB phenomenon is especially important in the development of magnetic recording and sensor applications, as for many years the standard EB restricts the development of currently used solutions [177,179].

1.5.3 Magnetocaloric and mechanocaloric effects

One of the most promising and intensively developing properties of MSMAs are various *caloric effects*, including the standard *magnetocaloric effect* (MCE), but recently also the *mechanocaloric effect* (mCE) manifested by the *elastocaloric* (eC) or *barocaloric* (BC) response of the material. A great deal of attention is focused on this subject due to the emerging need for a potential replacement of current refrigeration technologies based on vapor compression technology, which has a considerable harmful impact on our environment [180]. Following that fact, the Ni-Mn-Ga Heusler materials are a promising candidate for future magneto- and mechanocaloric technologies, due to their complex thermodynamical interplay between magnetic, mechanical and thermal properties (see **Fig. 1.17**).

1.5.3.1 Magnetocaloric effect

The Magnetocaloric effect refers to the thermal response of a solid material when exposed to an external magnetic field. The first explanation of this effect was proposed almost 100 years ago independently by Debye [181] and Giauque [182], but only the discovery of the *giant magnetocaloric effect* (GMCE) in $Gd_5Ge_2Si_2$ [183] makes a significant impact on the ongoing development of magnetocaloric materials.

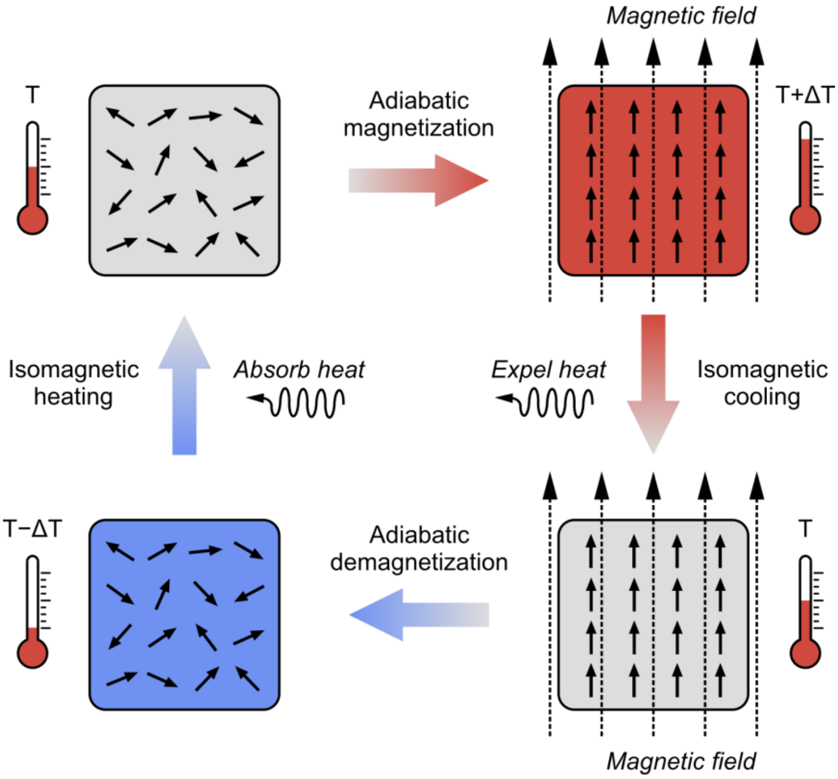

Fig. 1.18. Magnetocaloric cooling cycle divided into four characteristic stages: adiabatic magnetization, isomagnetic cooling, adiabatic demagnetization and isomagnetic cooling. The arrows represent the magnetic moments of atoms that create the crystal lattice of MC material (adapted from [184] and [185]).

The easiest way to explain the magnetocaloric effect is to follow the changes during the magnetocaloric cycle in two different subsystems of solid material, that is, magnetic and structural subsystems (**Fig. 1.18**) [184,186]. When the material is at constant temperature and is not exposed to an external magnetic field, the magnetic moments of the atoms fluctuate and the crystal lattice vibrates in a manner of current temperature. After application of an external magnetic field, the magnetic moments align according to the field direction. To maintain the constant entropy of material under adiabatic conditions, the decrease in the magnetic anisotropy is compensated be an increase in lattice entropy. Consequently, the overall temperature of the material increases during magnetization. In a standard cooling cycle, at this stage, the induced heat is removed from the material by the circulating cooling medium. The reverse situation occurred after removal of an external magnetic field. This time, due to the demagnetization process, the magnetic entropy increases, which implies the decrease in lattice anisotropy and consequently the material is cooled. During the cooling cycle, the heat extracted from the refrigeration system can be cooled by the magnetocaloric material.

From a thermodynamical point of view, MCE may be described by entropy change, ΔS_{M}, and adiabatic temperature change, ΔT_{ad}. The temperature dependence of the entropy as a function of temperature and magnetic field with corresponding ΔS_{M} and ΔT_{ad} is presented in **Fig. 1.19**. Assuming the adiabatic condition, when there is no heat dissipation between the material and the surrounding environment, the magnetic entropy change follows the Maxwell relation [183]:

$$\Delta S_{\mathrm{M}}(T, \Delta H) = -\int_{0}^{H} \left(\frac{\partial M(T,H)}{\partial T}\right) \mathrm{d}H \tag{1.4}$$

where ΔS_{M} is the magnetic entropy change, H is the external magnetic field, M refers to the magnetization of the material, and T is the current temperature.

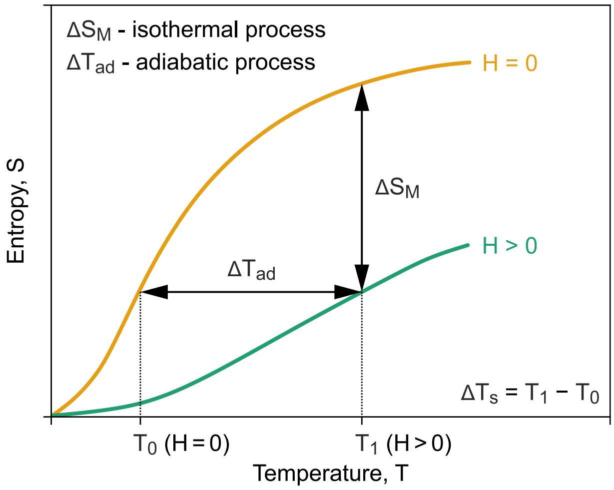

Fig 1.19. Temperature dependence of the entropy of magnetocaloric material with (H > 0) and without (H = 0) the application of the external magnetic field. The corresponding magnetic entropy change, ΔS_{M}, and the adiabatic temperature change, ΔT_{ad}, are presented as vertical and horizontal arrows, respectively (adapted from [187]).

The ΔS_M can be measured indirectly using conventional experimental devices, however, it does not show the real change in the temperature of the material and sometimes differs with direct measurements or theoretical studies [188]. More convenient, but experimentally harder to determine is the adiabatic temperature change ΔT_{ad}, which directly shows the temperature change of the material during the adiabatic magnetization process. The ΔT_{ad} is defined by the relation [184]:

$$\Delta T_{ad} = -\int_{0}^{H} \frac{T}{c_p}\left(\frac{\partial M(T,H)}{\partial T}\right) \mathrm{d}H \tag{1.5}$$

where ΔT_{ad} is the adiabatic temperature change and c_p is the specific heat capacity.

Over the past few years, several metallic-based systems that exhibit a large or giant magnetocaloric effect were found, such as $Gd_5(Si,Ge)_4$ [183], Mn(As,Sb) [189], MnFe(P,Ge) [190], MnCoGe [191], $La(Fe,Si)_{13}$ [192] and finally NiMn-based Heusler alloys [193–195], including the considered Ni-Mn-Ga MSMAs [49,196–199]. The magnetic entropy change in Ni-Mn-Ga system was firstly reported at moderate values between 6–18 $J \cdot kg^{-1} \cdot K^{-1}$ for the external magnetic field up to 5 T [49,127,196,199]. However, due to chemical composition changes and appropriate production technologies, the ΔS was recently increased up to 30 $J \cdot kg^{-1} \cdot K^{-1}$ [197,198,200,201]. Interestingly, the Ni-Mn-Ga alloy is the only NiMn-based Heusler material that exhibits *direct* magnetocaloric effect (above 1 T), whereas other systems like Ni-Mn-In, Ni-Mn-Sn and Ni-Mn-Sb are characterized by *inverse* magnetocaloric effect [202].

Similarly to the other MC materials, the magnetocaloric phenomenon in Ni-Mn-Ga Heusler alloys originates from the reversible structural transformation, which in this case is represented by the austenite ⇄ martensite transition. Furthermore, it was previously mentioned that one of the most unique features of this group of materials is the independence between structural and magnetic transformation, which may be separately tailored by proper compositional changes. Following that fact, the standard MCE can be substantially increased when both transformations overlap, resulting in the so-called magnetostructural transition (see **Section 1.3.7**) [199,200,203]. In such specific situation both structural and magnetic contributions have simultaneous considerable influence on the total entropy change, as ferromagnetic martensite transforms into paramagnetic austenite. What is important, the occurrence of magnetostructural transformation is extended to many different compositions, which is an essential advantage of the Ni-Mn-Ga system [200].

The amount of entropy change during the transition is highly dependent on the structural properties of martensite and austenite phases. The low symmetry of twinned martensite and the high symmetry of regular austenite favour the giant magnetocaloric effect. Moreover, it should be remembered that the symmetry of martensitic phase is governed by magnetocrystalline anisotropy. Similarly to the MFIS, the application of external magnetic field forces the magnetic moment to align according to the field direction, which subsequently results in twin boundary motion. Therefore, the magnetocaloric effect in NiMnGa-based alloys stems from two different factors [131]:

- *magnetostructural coupling* during the martensite ⇄ austenite transformation induced by the change of symmetry,
- strong *magnetocrystalline anisotropy* of martensitic phase that directs the magnetic domains orientation.

Lastly, it should be noted that due to the thermoelastic nature of martensitic transformation, the local thermal hysteresis is also an inherent part of magnetostructural transition [203,204]. For standard MC materials, the existence of thermal hysteresis hinders the effective magnetocaloric effect, which is undesirable in potential applications. However, for the Ni-Mn-Ga-based Heusler alloys, due to their complex structural properties, imminent hysteresis could be successfully narrowed by the introduction of premartensitic/intermartensitic transformation [205] or by the application of other stimuli supporting the magnetic field, *e.g.* hydrostatic pressure [195].

1.5.3.2 Mechanocaloric effects

One of the main disadvantages of magnetocaloric materials, which is still restraining them from wider usage, is the requirement for the relatively high external magnetic field of several tesla. As a result, in the last decade, great attention has been paid to shape memory materials in which magnetic and structural properties may be influenced by mechanical stimuli [206]. One of the first important modern research was published in 2008 by Bonnot *et al.* [207], who reported the giant elastocaloric effect (eCE) in the Cu-Zn-Al single crystal alloy associated with stress-induced martensitic transition. Later on, in 2010 Manosa *et al.* [208] reported the giant barocaloric effect (BCE) in the Ni-Mn-In Heusler alloy. Since these two important discoveries, the development of mechanocaloric materials begins rapidly and NiMn-based Heusler alloys, including the Ni-Mn-Ga compound, have become one of the most promising candidates in this field [209–212].

The origin of the mechanocaloric effect in MSMAs is analogous to the magnetocaloric effect. The only difference is that in the case of the mechanocaloric effect, the isothermal entropy change or the adiabatic temperature change occurs because of the application of the mechanical field instead of an external magnetic field. The same strong coupling between the stimuli (mechanical stress) and crystal lattice is the source of the giant caloric response of the material. It is important to highlight that the magnetothermal properties of Ni-Mn-Ga Heusler alloys have the same foundation as the magnetomechanical properties described in **Section 1.4.3**, *i.e.* magnetic or mechanical field-induced reversible martensitic transformation. When it comes to a distinction between elastocaloric and barocaloric effect, they differ by the form of mechanical stress, which is schematically presented in **Fig. 1.20**. The elastocaloric effect occurs under uniaxial stress $\Delta\sigma$, whereas the barocaloric effect originates from isotropic stress, such as hydrostatic pressure ΔP. For the adiabatically applied mechanical field, the previously mentioned change in temperature (from **Eq. 1.5**) takes the following form [210]:

$$\Delta T_{\mathrm{ad}} = -\int_{0}^{Y} \frac{T}{c_p}\left(\frac{\partial x}{\partial T}\right)\mathrm{d}Y \tag{1.6}$$

The above equation corresponds to the barocaloric response for $Y = p$ and $x = V$ and to the elastocaloric response for $Y = \sigma$ and $x = \varepsilon$, where ΔT_{ad} is the adiabatic temperature change, c_p is the specific heat capacity, p is the hydrostatic pressure, V is volume, σ is the uniaxial stress and ε is the uniaxial strain.

(a) Elastocaloric

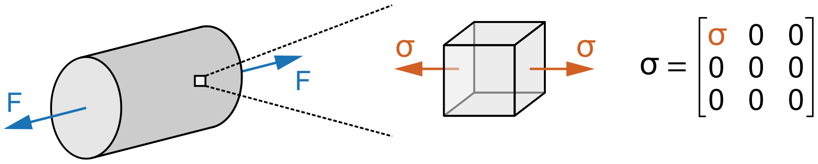

(b) Barocaloric

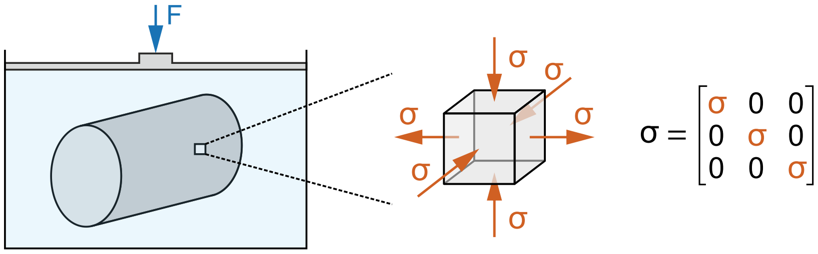

Fig. 1.20. Schematic illustration of mechanical stress, with the corresponding tensor notation showing the difference between **(a)** the elastocaloric and **(b)** the barocaloric effects (adapted from [213]).

The development of the mechanocaloric cooling is in its early stages, nevertheless, there are several promising advantages of mechanocaloric NiMn-based Heusler alloys that surpass the standard magnetocaloric materials. First of all, the wide temperature range of the adiabatic temperature change, effectively extending the working temperature region and thus the application possibilities of these materials [214,215]. Secondly, the variety of available types of mechanical stresses, including tensile, compressive, flexural, shear or bending stress, as well as hydrostatic pressure [213]. Thirdly, the lower cost of obtaining sufficient mechanical field in comparison to the corresponding magnetic field. Last, but not least, the possibility of multicaloric application that will exploit the synergy between mechanical, magnetic and thermal properties of the material during magnetostructural phase transformation [216]. The simultaneous use of more than one stimuli is a very promising opportunity, that may reduce the required driving magnitude of single field, which is schematically depicted in **Fig. 1.21**. Moreover, the proper alteration of different stimulus allows for better reversibility of phase transition and control of thermal hysteresis [217]. What is interesting, most recent advances in this field also report that the typically detrimental hysteresis may be even used as an advantage to reduce the magnitude of the magnetic field in the mechanocaloric cooling cycle [218].

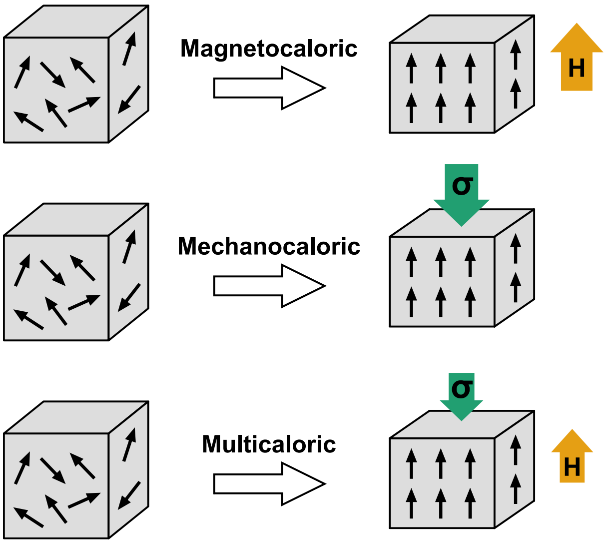

Fig. 1.21. Schematic representation of the synergy between the magnetocaloric and mechanocaloric properties of the magnetic shape memory Heusler alloys manifested as multicaloric effect. The simultaneous application of magnetic and mechanical fields reduces the magnitude of the stimulus in comparison to monocaloric effects (adapted from [216]).

1.6 Compositional dependence and selective alloying elements

The previous sections are devoted to the crystal structure and multifunctional properties of NiMnGa-based Heusler alloys. It was announced that all significant properties are strictly connected with the chemical composition of the material, including the Ni/Mn/Ga ratio in the non-stoichiometric alloy, as well as the influence of additional alloying elements. In this context, the following section will be fully devoted to outline the strong influence of chemical composition on magnetostructural behaviour of Ni-Mn-Ga MSMAs, with particular emphasis on the alloying elements that were used in the experimental part of this thesis, *i.e.* iron (Fe) and cobalt (Co).

1.6.1 Ni/Mn/Ga ratio in non-stoichiometric alloys

In the early stages of the development of Ni-Mn-Ga MSMAs, the main focus waw directed toward non-stoichiometric compositions. Despite the fact that only three elements constitute this subgroup of Heusler alloys, the investigation of the influence of chemical composition on the magnetostructural behaviour of the resulting alloy is still complicated. The main problem is that some of the previously described magnetostructural properties are very sensitive to even slightest deviation from specific chemical composition. Consequently, some unintentional errors in the definition of chemical composition may result in ambiguous results. Secondly, a clear definition of the influence of one element is always connected with the strong influence of other elements. For example, if one wants to define the influence of Ni excess in relation to stoichiometric composition, the increased amount of Ni atoms is always introduced at the expanse of Mn, Ga or both Mn and Ga combined in a different ratio. In every case, the properties of the alloy will be different, due to the different ratio of remaining atoms. By analogy, the same problem occurs for Mn or Ga atoms excess or deficiency studies. Last, but not least, the reversible martensitic transformation in Ni-Mn-Ga system takes place in a wide range of off-stoichiometric chemical compositions, which is unprecedented among other Heusler alloys and, thus, complicates the overall analysis and description of the considered group of MSMAs.

One of the most popular approaches for modifying the Ni-Mn-Ga composition is the introduction of Ni excess. Many researchers report that increasing concentration of Ni in the expanse of Mn increases the martensitic transformation temperature, but simultaneously decreases the Curie temperature [116–118,122,219–226]. Moreover, it should be remembered that the changes in T_M are much more pronounced than changes in T_C. As a result, for Ni-rich non-stoichiometric $Ni_{2+x}Mn_{1-x}Ga$ compositions, the coincidence of T_M and T_C manifested as magnetostructural transition occurs for compositional range $0.18 < x < 0.27$ [225]. The same monotonical increase in the martensitic transformation temperature and a slight decrease in the Curie temperature with the increasing concentration of Ni atoms were also reported for alloys in which Ni atoms were substituted for Ga [118,120,122,224,227] or partially for both Ga and Mn [122,224]. Interestingly, in the case of the Ni/Ga ratio, Singh *et al.* reported the opposite results [228]. In contrary, in his research, the T_M tends to increase, and the T_C tends to decrease with the increasing concentration of Ga at the expanse on Ni. However, the investigated composition $Ni_{2-x}MnGa_{1+x}$ ($0.4 < x < 0.9$) deviates strongly from the stoichiometric Ni_2MnGa compound and was closer to the other theoretical Heusler alloy Ga_2MnNi [229]. This may be the reason for the discrepancies between his findings and other aforementioned research.

When it comes to Mn excess, the majority of published researches are considering the substitution of Mn for Ga in non-stoichiometric $Ni_2Mn_{1+x}Ga_{1-x}$ alloys [117,118,123,219,222,230]. This is due to the fact, that a similar tendency of T_M increasing and T_C decreasing with the increase of Mn concentration is observed in this type of Ni-Mn-Ga MSMAs as it is for Ni-rich compositions. In the less popular approach, when Mn is substituted for Ni, both transformation temperatures behave in the opposite way, that is, the T_M is decreasing, while the T_C increasing [116,231,232].

There are two different origins that are presumably responsible for the transformations temperatures changes with the deviation in the Ni/Mn/Ga ratio. The aforementioned martensitic transformation temperature changes are commonly attributed to the variation in the *valence electron concentration e/a*. The *e/a* parameter arises from the Hume-Rothery mechanism [233] and describes the average number of valence electrons per one atom in the Ni-Mn-Ga composition. Interestingly, the connection between the physical properties of numerous Heusler compounds and the number of their valence electrons is well established for many different groups of Heusler alloys besides MSMAs [11]. In case of Ni-Mn-Ga system the number of valence electrons for Ni, Mn and Ga is 10 ($3d^8 4s^2$), 7 ($3d^5 4s^2$) and 3 ($4s^2 4p^1$), respectively, therefore the *e/a* parameter follows the relation:

$$e/a = \frac{10 \cdot \mathrm{Ni}_{at\%} + 7 \cdot \mathrm{Mn}_{at\%} + 3 \cdot \mathrm{Ga}_{at\%}}{\mathrm{Ni}_{at\%} + \mathrm{Mn}_{at\%} + \mathrm{Ga}_{at\%}} \tag{1.7}$$

where $\mathrm{Ni}_{at\%}$, $\mathrm{Mn}_{at\%}$, $\mathrm{Ga}_{at\%}$ is the atomic concentration of nickel, manganese and gallium, respectively.

The *e/a* parameter is widely used to describe the structural transformation behaviour of different types of Ni-Mn-Ga MSMAs, including Ni-rich and Mn-rich alloys [104,109,120], which is schematically presented in **Fig. 1.22.** It is seen that in each group of alloys the basic tendencies between T_M and *e/a* are similar. However, the evident differences in transformation temperature values are also noticeable, which restricts the use of the *e/a* as a universal parameter [120]. Moreover, it should be noted that the *e/a* parameter has another disadvantage appearing in the vicinity of the magnetostructural transition for the Ni-rich alloys (**Fig. 1.22(a)-(b)**). Close to Curie temperature, the volume magnetostriction increases the crystal lattice parameters, which subsequently exhibits a stronger influence on martensite transformation temperature than *e/a* [219].

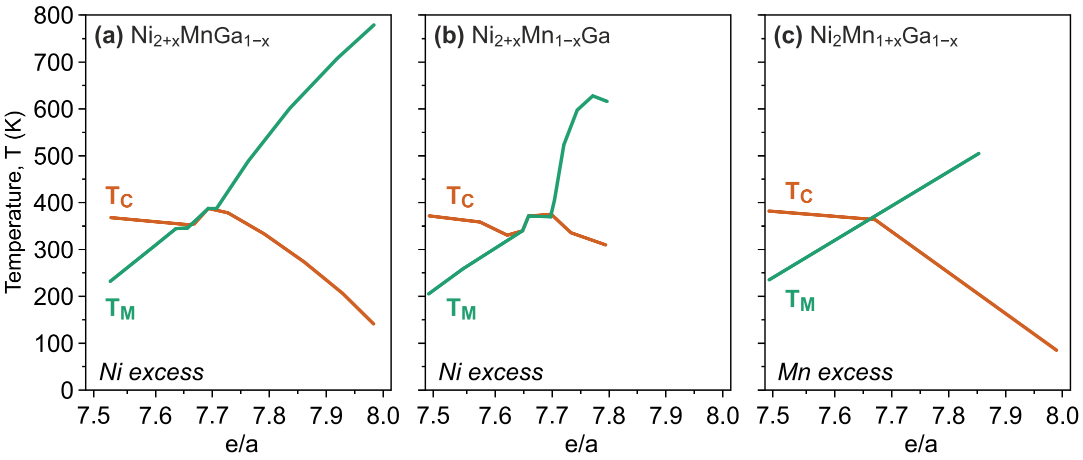

Fig 1.22. The *e/a* dependence of the martensitic (T_M) and magnetic (T_C) transformation temperature for different types of Ni-Mn-Ga compounds: **(a)** $Ni_{2+x}MnGa_{1-x}$, **(b)** Ni_{2+x} $Mn_{1-x}Ga$ and **(c)** $Ni_2Mn_{1+x}Ga_{1-x}$ (derived from data collected in [120]).

When it comes to magnetic transformation temperature, the physical origin of its changes is probably different than in the case of martensitic transition [234]. As mentioned in **Section 1.3.6** the magnetic moment of Ni-Mn-Ga Heusler alloys is mainly based on Mn atoms. Lazpita *et al.* showed that for the non-stoichiometric alloys with Ni excess, Ni atoms occupy Mn sites and some of Mn atoms are forced to move to Ga sites [116]. On the other hand, for the Mn-rich alloys with Ni deficiency, Mn atoms may occupy both Ni and Ga positions. In such off-stoichiometric situations, magnetic coupling of Mn atoms is various at different sites [116,235], which subsequently influences the Curie temperature of alloy.

1.6.2 Selective alloying elements

In addition to the alteration in non-stoichiometric Ni-Mn-Ga composition, one of the main methods to change the magnetostructural properties of MSM Heusler alloys is the introduction of additional alloying elements. Because of the wide range of different atomic elements, the possibility of using dopants is a very broad and complex subject. Considering the already wide group of non-stoichiometric ternary Ni-Mn-Ga compositions, the additional doping elements lead to the existence of countless different chemical composition. In this situation, the majority of researchers are focused on four, five or utmost six element compositions including one, two or three different dopants, respectively. In the following section, due to the strong coupling between magnetostructural properties of Ni-Mn-Ga MSMAs and their electronic structure (e/a parameter), the selective alloying elements were divided into different groups based on their general valence configuration defined by a *p*-, *d*- or *f*-block.

1.6.2.1 p-block elements

The most obvious *p*-block elements that may be used as an alloying addition to the Ni-Mn-Ga composition are In, Sb and Sn. This is due to the fact that these three elements originate from the greater Ni-Mn-X (X = Ga, In, Sn and Sb) group. However, if the In, Sb or Sn are used as the fourth element in the Ni-Mn-Ga system, they should be considered as a standard alloying addition, not as constitutive element.

Early studies showed that the addition of In at the expanse of Ga in the stoichiometric $Ni_2MnGa_{1-x}In_x$ alloy leads to a decrease in both martensitic and magnetic transformation temperatures [236]. Furthermore, the maximum limit for the existence of martensitic transformation was reported to be $x < 0.14$ [236]. Later, other researchers confirms that the substitution of In for Ga significantly stabilizes the austenitic phase in both stoichiometric [237,238] and off-stoichiometric compounds [239,240]. What is more, proper alteration of In concentration allows for the existence of magnetostructural transformation close to room temperature. Interestingly, in the case of In for Ga substitution, the e/a parameter becomes ineffective as both In and Ga are characterized by the same number of valence electrons. Consequently, in this case, significant changes in magnetostructural properties cannot be directly associated with constant *e*/*a*.

Very similar influence on the magnetostructural properties of doped Ni-Mn-Ga-X alloys is reported for Sn and Sb dopants [57,241–244]. In the case of Sn or Sb, even vary small addition of these elements (below 2 at.% [243,244]) leads to a substantial decrease in the martensitic transformation temperature followed by neglected changes in Curie temperature. Again, as in the case of In doping, the reported behaviour of T_M does not follow the *e*/*a* parameter in the same way as for ternary Ni-Mn-Ga alloys.

Another documented *p*-block alloying element is Al. The Al atom contains the same number of valence electrons as the Ga atom and is characterised by a similar atomic radius. It should also be noted that the influence of Al on the Ni-Mn-Ga system is a very complex topic, as Al can completely substitute Ga in the Ni_2MnGa composition by forming another Ni_2MnAl Heusler alloy [245]. Following this topic, Ishikawa *et al.* [246] investigated the Al for Ga substitution in the Ni-Mn-Ga system starting from the Ni_2MnGa and ending in the Ni_2MnAl composition. He reports that the temperature of martensitic transformation decreases monotonically with increasing Al content, whereas the Curie temperature is almost constant and changes only close to the Ni_2MnAl composition. Similar results for a high concentration of Al (4–18 at.%) in the Ni-Mn-Ga-Al composition were also presented by Xin *et al.* [247]. Further detailed studies for the lower concentration of Al (up to 5 at.%) revealed the opposite trend, *i.e.* the T_M increased with increasing Al content [248,249]. Moreover, the reported increase in T_M was non-monotonic and the same complex deviations from the monotonical trend were also observed for other thermal and electrical properties of Al-doped Ni-Mn-Ga alloys [248].

The last interesting *p*-block alloying element is B. Is was reported that substitution of B for Mn in the close stoichiometric $Ni_2Mn_{1-x}GaB_x$ alloy has almost no influence on the martensitic transformation temperature for the B concentration $x < 0.08$ [250]. Surprisingly, for $x > 0.08$ the T_M decreases abruptly with the further increase in the B content. At the same time, the magnetic transformation temperature decreases almost linearly with increasing B content. Following the magnetic behaviour of the Ni-Mn-Ga alloys doped with B, for the Ni-rich off-stoichiometric compositions with a low concentration of B, a significant increase in saturation magnetization was also reported [251]. Additionally, the magnetic coercivity of the material can also increase greatly by proper B doping, which is found to extend the magnetomechanical functionality of the alloy [252,253]. The last significant reported advantage of B addition to Ni-Mn-Ga composition is a notable improvement in the mechanical properties of the doped material [254,255].

1.6.2.2 d-block elements

Among various doping elements, one of the best documented *d*-block alloying additions is Cu. Early research showed that the proper addition of Cu to the Ni-Mn-

Ga compound significantly increases the martensitic transformation temperature, which may overlap with the slightly decreasing Curie temperature, leading to the magnetostructural transition [256–258]. Furthermore, Kataoka *et al.* reported that phase diagrams for the doped $Ni_2Mn_{1-x}GaCu_x$ and ternary $Ni_{2+x}Mn_{1-x}Ga$ alloys are very similar, which may by helpful in predicting the transformation temperatures of Cu-doped MSMAs [259]. Further investigations showed that the addition of Cu has almost no negative influence on the magnetic entropy change for materials exhibiting magnetostructural transition, which is crucial for prospect magnetocaloric applications [256,260]. Recent studies reveal that the giant magnetocaloric effect and overall caloric performance are significantly better in Cu-doped Ni-Mn-Ga alloys, than in standard ternary Ni-Mn-Ga alloys [261–263]. Lastly, researchers focused on the mechanical performance of Ni-Mn-Ga-Cu alloys reported the a significant improvement of mechanical properties of Cu-duped alloys [264]. What is worth noting, Liao *et al.* presented very promising high damping capabilities of Cu-doped Ni-Mn-Ga materials that utilize the twin boundary mobility mechanism enhanced by proper Cu addition [265].

Another important *d*-block alloying element is Co. At the beginning, the main role of Co addition to Ni-Mn-Ga system was an effective increase in Curie temperature, which is required for high-temperature magnetic shape memory alloys [266,267]. More detailed studies confirmed that the T_C increases when Co is added in the expanse of Ni or Ga [266,268]. The unusual non-monotonous trend of T_C was revealed for alloys with Mn substituted by Co [269]. The similar strange non-monotonous behaviour of T_C was also observed for alloys in which Co was added to the overall Ni-Mn-Ga composition, without sacrificing any particular elements [270]. Subsequently, it was also established that substitution of Mn or Ga by Co increases the martensitic transformation temperature [267,271–273], whereas substitution of Ni by Co decreases the T_M [268,272,274,275]. Moreover, the addition of Co was found to increase the magnetic moment of the austenitic phase and decrease the magnetic interaction in the martensitic phase [270,276,277]. As a result, the magnetization change during magnetostructural transformation may be significantly increased for Co-doped Ni-Mn-Ga alloys, which may promote the magnetic field-inducted martensitic transformation (see **Section 1.4.3.2**). It is also worth noting that many researchers present a comparable dependence between the e/a and the temperature of phase transitions for the quaternary Ni-Mn-Ga-Co alloys as for the standard ternary Ni-Mn-Ga alloys [270–272,278]. These similarities may be connected with the close electronic structure of Co, Ni and Mn atoms, which are all attributed to 3*d* transition metals. However, it should be remembered that the number of different non-stoichiometric Ni-Mn-Ga compositions is high and there are several papers [273,275] that report the different dependence of T_M versus e/a, which deviates from general trends characterising other Ni-Mn-Ga-Co and Ni-Mn-Ga compositions. Lastly, a detailed description of Ni-Mn-Ga-Co alloys is also hampered due to the possible dual-phase microstructure of Co-doped MSMAs [274,279–282]. Generally, Co is soluble in Ni-Mn-Ga matrix in a wide range of stoichiometry, but with a proper chemical composition and after careful heat treatment, the additional γ phase may precipitate along the grain boundaries [274,280–282]. The additional phase is ductile, thus it enhances the mechanical properties of the brittle material, but also complicates the investigation of magnetostructural properties of the alloy.

For the same reason as Co, over the last couple of years, a considerable attention has been also devoted to Fe, as one of the possible dopants in the Ni-Mn-Ga system. Fe is another 3*d* transition metal, which has almost the same atomic radius as Co and is also characterised by ferromagnetic properties. From the technological point of view, Fe and Co exhibit similar melting and boiling temperatures, which also suggests the strong similarities between these two dopants. Early researches showed that the substitution of Mn for Fe shifts the martensitic transformation temperature to lower values and stabilizes the austenitic phase [267,283–285]. It was also observed that, at the same time, the Curie temperature increases with increasing Fe content [267,284]. On the other hand, some researchers suggested that the substitution of Mn with Fe has almost no influence on both T_M and T_C [286,287], due to the negligible changes in the *e*/*a* ratio, and only Ni substitution with Fe may significantly decrease the T_M and increase the T_C [286–288]. The opposite effect on transformations behaviour was found for alloys, where Ga was substituted by Fe, which in this case follows the general *e*/*a* ratio tendencies for the Ni-Mn-Ga MSMAs [286,287,289,290]. Remarkably, it is also reported that the addition of Fe to the Ni-Mn-Ga composition may induce the intermartensitic transition [288,291–293] and/or contribute to the formation of the complex martensitic structures [292,294]. When it comes to magnetic properties, despite the fact that Fe is a ferromagnetic element, its introduction to the Ni-Mn-Ga system has a minor influence in enhancing the ferromagnetic properties of the material and may even lower the saturation magnetization [295,296]. In recent years the greatest attention has been paid to the magnetocaloric properties of the doped Ni-Mn-Ga Heusler materials and in this field quaternary Ni-Mn-Ga-Fe alloys exhibit the promising large MCE [297–300]. Lastly, it should be noted that similarly to Co-doped alloys, the sufficiently high addition of Fe to the non-stoichiometric Ni-Mn-Ga composition may promote the precipitation of the additional γ phase [301,302]. This secondary phase leads to an increase in the general ductility of the material and improve its mechanical properties.

There are several others less documented alloying additions from the *d*-block, including Nb [303], Zn [242,304,305], Cr [306,307], V [308–310] or Ti [311–314]. Tian *et al.* [303] reported that the addition of Nb to the Ni-Mn-Ga composition increases the martensitic transformation temperature. However, it also promotes precipitation of the Nb-rich second phase, which is characterised by low ductility and poor mechanical properties. Both experimental [242] and theoretical [304,305] studies suggest that small Zn doping at the Ga site in the Ni-Mn-Ga compound results in an increase in T_M and has a vary slight effect on Curie temperature. A similar notable increase in T_M was also reported for Cr-doped alloys [306,307]. However, this time, the Cr doping also had a strong influence on magnetic transformation, by shifting the T_C to lower values [307]. The opposite influence on the phase transformation of the Ni-Mn-Ga-based materials was obtained by V doping. Several studies reported that Mn or Ga substitution for V significantly decreases the T_M and broadens the thermal hysteresis of phase transformation [308–310]. Some research is also focused on Ti as a possible advantage dopant to the Ni-Mn-Ga system, as its solubility in near-stoichiometric Ni-Mn-Ga alloys is up to approximately 8 at.% [312]. It was reported that Ti substitution for Ga increases the martensitic transformation temperature with a neglected influence on Curie temperature [311,312]. Moreover, the addition of Ti improves the mechanical stability of the material [314] and enhances its mechanical properties, which was also reported in [313] by the Author of this thesis.

1.6.2.3 f-block elements – rare-earth elements

In contrast to *s*-block and *d*-block elements, the *f*-block rare earth elements (REEs) have a large atomic size and considerably complex electronic structure. Because of this fact, the REEs are seen as possible dopants that may induce the precipitation of other phases in normally single-phase MSMAs, which may result in significant changes in magnetomechanical properties of the doped materials. In the last couple of years, many different REEs have been proposed as possible dopants, including Gd [315–319], Ge [320], Tb [321–324], Sm [324], Dy [325–327], Nd [324] or Y[328]. It was reported that that the solubility of RE elements are relatively low [317,324,325,327,328], which leads to the formation of RE-rich phases distributed along the grain boundaries of the Ni-Mn-Ga matrix [315–318,322–328]. The main advantage of the second phase was the effective reduction in material brittleness [318,324,326] and the notable improvement of their mechanical properties [317,322,323,326–328], which was also reported in [315,316] by the Author of this thesis. Moreover, the minor amount of REE in the Ni-Mn-Ga matrix leads to an increase in T_M and a decrease in T_C [320,321,323–325,328]. It is also worth noting that the microstructure of Ni-Mn-Ga-RE alloys is strictly dependent on their thermal history [317,321,326], which was also discussed in [316,319] by the Author of this thesis.

1.6.2.4 Ni/Mn/Ga ratio in doped Ni-Mn-Ga alloys

It was presented in previous subsections that even small addition of an extra alloying element to Ni-Mn-Ga compound may significantly change the magnetostructural properties of the material. It was also shown that regardless of whether the doping element originates from the *s*-, *d*- or *f*-block, the transformation paths become more complex than in the case of ternary Ni-Mn-Ga alloys, and some local anomalous behaviour may appear in doped compositions. Due to that fact, in many cases, the widely used e/a parameter is losing its importance, which is graphically summarized in **Fig. 1.23**. It is seen that, usually, within one group of doped alloys, the transformation temperatures follow some individual trends with respect to the e/a ratio. Unfortunately, the comparison between different compositions is clearly not feasible. Even if the general trends between quaternary and ternary alloys are analogous, the exact comprehensive comparison between these two subsystems is still problematic.

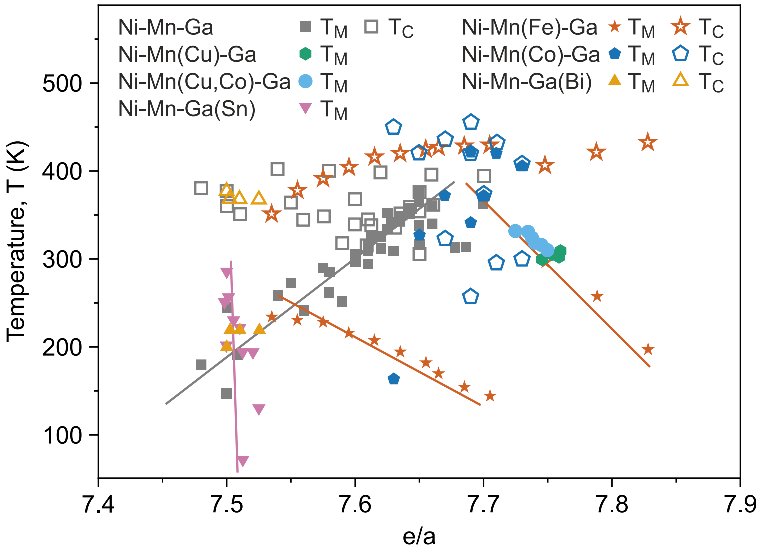

Fig. 1.23. Temperatures of martensitic (T_M) and magnetic (T_C) transformations for different groups of doped Ni-Mn-Ga MSMAs (based on the data summarised in [329]). Solid lines represents some general trends for selective group of materials.

Recently, Ramudu *et al.* [330] presented an alternative way to estimate the valence electrons per atom. He proposed the N_e/a parameter, which represents the average number of empirically derived non-bonding electrons per atom in one formula unit. In this approach, based on Pauling's principle of electroneutrality [331], only non-bonding electrons contribute to the physicochemical properties of the metallic alloy. The number of non-bonding electrons e_n is then defined as [330]:

$$e_n = E - N_{WS} \tag{1.8}$$

where E is the number of valence electrons and N_{WS} is the corrected electron density parameter derived from the Miedema's empirical model [332,333].

The N_{WS} for each element in Ni-Mn-Ga composition is equal to 5.36, 4.17 and 2.25 for the Ni, Mn and Ga, respectively. Taking into account these values and based on **Eq. 1.8** the N_e/a for the ternary Ni-Mn-Ga alloy is as follows:

$$N_e/a = \frac{(10-5.36)\mathrm{Ni}_{at.\%} + (7-4.17)\mathrm{Mn}_{at.\%} + (3-2.25)\mathrm{Ga}_{at.\%}}{\mathrm{Ni}_{at.\%} + \mathrm{Mn}_{at.\%} + \mathrm{Ga}_{at.\%}} \tag{1.9}$$

The advantage of the N_e/a parameter over the e/a ratio was firstly demonstrated for the quaternary Ni-Mn-Ga alloys doped with In or Fe [330]. Later on, several other studies discussed the better correlation of magnetostructural properties of doped Ni-Mn-Ga alloys using the N_e/a parameter rather than the e/a ratio [320,334,335].

Lastly, it should be remembered that all the abovementioned discrepancies between the magnetostructural and thermomechanical properties of the different groups of doped MSM Heusler alloys may also stem from the thermal history of the material inherited during the sample preparation process. It is widely reported [253,336–342] that depending on the processing conditions of the NiMn-based material, the various types of post-fabrication heat treatment result in a different degree of atomic order, which subsequently influences the temperatures of phase transitions.

1.7 Forms of material

All of the multifunctional properties of NiMnGa magnetic shape memory alloys described in **Sections 1.4** and **1.5** are mostly well documented for the single crystal alloys. The absence of grain boundaries in single crystal materials favours the magnetostructural properties that stem from the phase transitions. However, the technology beyond the single crystal fabrication is limited, especially for Ni-Mn-Ga compound characterized by significant segregation of chemical composition [343–346], which hinders the production of uniform bulk material with stable magnetomechanical properties. On the other hand, polycrystalline materials are much cheaper and easier to produce, however, the existence of grain boundaries, as well as the random orientation of grains, impedes the magnetostructural properties of these specimens. Considering the advantages and disadvantages of both single crystal and polycrystalline structures, many different types and forms of NiMnGa-based MSMAs have been fabricated and reported in the literature, which will be briefly described in the following section.

1.7.1 Directional solidification

Directional solidification is one of the most common techniques to produce polycrystalline material with the preferred grain orientation. The alloys produced with favourable crystal orientation using temperature gradient and/or magnetic field are characterised by long columnar austenite grains along the desired direction of solidification (**Fig. 1.24(a)**) [347–349]. Within this microstructure, below the T_M, the martensite twin boundaries can move along the single lamellar grains without major obstacles. Moreover, this production technique allows the elimination of unwanted martensite variants and promotes one certain variant [350–352]. As a result, after proper magnetomechanical training [353–355], the MFIS in directionally solidified Ni-Mn-Ga alloys may reach 1–2% [144,147,148]. Several studies report that directionally solidified alloys are characterised by improved mechanical stability [354–357], high strength [350,354,357] and superior magneto- and mechanocaloric properties [349,356–358].

1.7.2 Ribbons

It was previously mentioned that atomic disorder in the Ni-Mn-Ga system introduced during the fabrication process may significantly influence the magnetostructural properties of the material. In this context, many researches produce and investigate the melt-spun ribbons manufactured by rapid solidification using a melt spinning technique. Generally, NiMnGa-based ribbons exhibit different temperatures of phase transformations than their bulk counterparts with the same chemical composition, which is strongly dependent on the degree of atomic order and internal stresses [359–361]. Subsequent annealing of melt-spun ribbons significantly changes both the T_{M} and T_{C}, due to the atomic segregation and vanishing of internal stresses [360–363]. Hence, Ni-Mn-Ga ribbons are a promising candidate for multifunctional materials, where temperatures of phase transformations may be widely altered only by proper heat treatment. It is also important that rapidly quenched ribbons are characterised by notably finer microstructure than typical bulk materials [359,363–366]. Moreover, the notable preferred orientation of the microstructure inherited from the melt spinning technique is also widely observed for this form of material (**Fig. 1.24(b)**) [360,363,364,367–369]. Finally, very promising magnetocaloric properties of NiMnGa-based ribbons were also reported for samples exhibiting magnetostructural transition [198,368,370].

1.7.3 Microwires and microfibres

Microwires or microfibres are another possible form of NiMnGa-based materials, which are produced by rapid solidification using the melt extraction method. This manufacturing technique is similar to the melt-spinning method, however, this time, the rotating extraction wheel touches the melting pool of the molten alloy [371]. As a result, the Ni-Mn-Ga polycrystalline wires with the diameters of 50–100 μm may be fabricated. Similarly to the aforementioned rapidly cooled ribbons, the rapid solidification technique allows to receive fine grain microstructure [371–373]. It should be noted that sometimes even the oligocrystalline *bamboo-like* grains are reported in Ni-Mn-Ga microwires, which example is depicted in **Fig. 1.24(c)** [374–377]. This very characteristic bamboo-grains microstructure leads to relatively large magnetic field-induced strains up to 1% [376,377], due to the reduction of grain constrains that usually limits the twin boundary motion. Another interesting property of Ni-Mn-Ga microwires that differs them from the other types of Ni-Mn-Ga materials is excellent superelasticity. Recently, many researchers reported that the superelastic strain of non-stoichiometric Ni-Mn-Ga microwires may even be close to 10% [372,375,378–380]. Last, but not least, the fine-grained microstructure of the microwires results in the a significant reduction in thermal and magnetic hysteresis during magnetostructural transformation [300], which is beneficial for the magnetocaloric effect. Following this concept, the exceptional MC properties, exceeding those of bulk polycrystalline alloys, were reported for ternary and doped NiMnGa-based microwires [300,374,381].

1.7.4 Thin films and foils

Films and foils are another group of thin multifunctional structures that can be produced on the basis of the Ni-Mn-Ga compound. There are two main approaches for fabricating very thin NiMnGa-based materials: (1) the epitaxial growth on a specific substrate and (2) machining from the previously produced bulk samples.

When it comes to *epitaxial growth*, this method allows to produce very thin films with thickness varying from several to hundreds of nanometres [382]. Epitaxial growth is considered to be an effective way of fabricating Ni-Mn-Ga films, as the materials are produced in a favourable single crystalline form. Early researches on this topic demonstrated that magnetically induced reorientation, responsible for many functional effects, can be achieved in off-stoichiometric Ni-Mn-Ga compositions, especially in freestanding films released from rigid substrate (**Fig. 1.24(d)**) [383–387]. However, the resulting martensite structure is exceptionally complex, exhibiting different types and variants of martensite [388–391], which may be partially controlled by the crystal orientation of the substrate [392,393]. Despite comprehensive research of NiMnGa-based epitaxial films, a full detailed description of their magnetostructural behaviour is still lacking. Still, recent findings are very promising and show the promising path for new generation of smart nanomaterials suitable for future micromechanical devices [394–397].

The second method for the fabrication of thin Ni-Mn-Ga samples is the machining from the bulk alloy. In this approach, it is much easier to control the chemical composition and final structure of the sample, as the starting materials for the thinning process are in the form of bulk alloy. Typically, the whole machining process includes abrasive and electrochemical thinning [398]. The complexity of the fabrication process depends on the required thickness of the final specimen. Until now, the thinnest foils manufactured by machining were close to 1 μm thick [399], while the standard reported thickness ranges from 80 to 200 μm [398,400–402]. In order to distinguish micrometre-sized specimens fabricated by machining from nanometre-sized epitaxial films, the term foils is used in the literature to describe the first ones. The greatest advantage of foils over freestanding epitaxial films is the possibility of obtaining only one variant of martensite [399–402]. Such microstructure does not inhibit magnetostructural effects characterising Ni-Mn-Ga alloys, including twin boundary motion and magnetic field-induced strains. Consequently, the NiMnGa-based foils are considered as prospect micrometre-sized active elements for different types of sensors and actuators [401,402].

1.7.5 Micropillars

Micropillars, just as abovementioned thin foils, are another form of micrometre-sized materials that can be produced from single crystalline bulk Ni-Mn-Ga samples. The fabrication of micropillars is based on the focused ion beam (FIB) milling, which allows to cut a rectangular samples with dimensions of single to several tens of micrometres (**Fig. 1.24(e)**) [403–405]. Due to the sophisticated FIB technique required for production, very little research is available on this subject. Recent publications suggested the existence of giant magnetic field-induced strains in Ni-Mn-Ga micropillars [404,405]. What is interesting, the actuation speed of manufactured micropillars was found to be higher than that of bulk material, which can extend the working frequencies of some future MEMS devices [404].

1.7.6 Foams and porous structures

One of the most advanced and novel types of Ni-Mn-Ga alloys are foams and porous structures. The idea of introducing porosity to Ni-Mn-Ga material was firstly presented by Boonyongmaneerat *et al.* [406]. He suggested that grain boundary constrains may by reduced by free space pores and demonstrated the Ni-Mn-Ga foam with 76% porosity that exhibit MFIS of 0.12% with excellent mechanical stability exceeding 30 million cycles. The idea of porosity was later developed and improved by Chmielus *et al.*, who in their pioneering work [153], reports a maximum value of MFIS reaching even 8.7%. The unique NiMnGa-based foam characterized by bimodal pore size distribution is presented in **Fig. 1.24(f)**. In microscale it was build from small struts connected together at nodes [150]. Each strut was characterised by bamboo-like grains, so it behaves close to a single crystalline sample. Later on, the idea of foam Ni-Mn-Ga structures was developed and investigated by other researches in the subject of pores architecture [407], porosity level [151,408], magnetomechanical training [151,152] or pore fabrication method [408,409].

1.7.7 Particles and powders

Other forms of Ni-Mn-Ga material that have been greatly studied in the last decade are particles and powders. There are many different techniques to fabricate metallic Ni-Mn-Ga particles, from sophisticated spark-erosion [410–412] or gas atomization [413] methods to more common ball milling [414–418] or even manual grinding [419–421]. From the technological point of view, the most promising method is ball milling, as it is a versatile, repeatable, and cost-effective technique that allows producing mico-, submicro- and nanosized particles (**Fig. 1.24(g)**). What is more, the starting material for the ball milling may be a conventional bulk polycrystalline alloy with formerly designed magnetostructural properties. Certainly, the milling process changes both the structural and magnetic properties of the Ni-Mn-Ga alloy, which are determined by the final size of particles [414–418] and the internal parameters of the milling process [415,416,418]. In comparison to bulk samples, the milled particles are characterised by lower phase transformation temperatures [414,416], higher Curie temperature [414], enhanced saturation magnetization [414,416] and reduced thermal hysteresis [416].

1.7.8 Polymer-based composites

The presented versatility of different forms of Ni-Mn-Ga based alloys encouraged many researchers to utilize these various types of samples as a constituent active element in polymer-based composite materials. It should be recalled that one of the biggest disadvantages of the broader application of Ni-Mn-Ga alloys is their high brittleness and poor workability, which might be significantly improved when combined with the polymer matrix [422,423]. One of the most popular combinations of MSM composite incorporates polycrystalline Ni-Mn-Ga particles mixed with flexible polymer matrix (**Fig. 1.24(h)**) [422,424–431]. In these materials, the polymer matrix is responsible for composite integrity, whereas Ni-Mn-Ga particles provide multifunctional properties. It was reported that particle/polymer composites retain their shape memory behaviour and exhibits MFIS from 0.1% [425] even up to 4.0% [430]. Another important distinctive feature of composite materials are very interesting smart damping properties at temperatures close to the structural transformation of the particles [424,426–429]. What is worth noting, Goswami *et al.* [431] reported the concurrent magnetocaloric effect of Ni-Mn-Ga/polymer composite and, very recently, Gao *et al.* [432] presented promising preliminary studies of porous Ni-Mn-Ga samples filled with epoxy resin.

1.7.9 Additive manufacturing

The additive manufacturing of metallic alloys is one of the most popular technological topics in modern materials engineering [433]. Consequently, magnetic shape memory materials drew the attention of many researchers as they seek the opportunity to print complex structural objects characterised by multifunctional properties. In the case of Ni-Mn-Ga compounds, additive manufacturing is still a fledging topic, however, there are several promising studies showing a completely new way to manufacture MSMAs, such as laser powder bed fusion (L-PBF) [154,434–438] or binder jet 3D printing [439–441]. The best documented method to produce Ni-Mn-Ga alloys by additive manufacturing is laser powder bed fusion, as this method is widely used for other various metallic alloys [433]. For Ni-Mn-Ga compound, L-PBF struggles with many technological problems, including selective evaporation of Mn or significant quenching stresses during material cooling [434–436]. Consequently, the fabrication process introduces many internal defects to the manufactured material, which can be reduced only in some point by additional heat treatment [436]. As a result, very low MFIS of about 0.01% were reported in additively manufactured Ni-Mn-Ga materials [439]. The example of the cubic Ni-Mn-Ga specimen fabricated using L-PBF is depicted in **Fig. 1.24(i)**. Despite the described obstacles, very recently, Laitinen *et al.* [154] proved that all the aforementioned disadvantages of L-PBF can be overcome by proper adjustment of the process parameters. On that basis, he showed the additively manufactured millimetre-sized element that exhibits a repeatable MFIS of 5.8%, which is superior to the standard bulk polycrystalline Ni-Mn-Ga alloy.

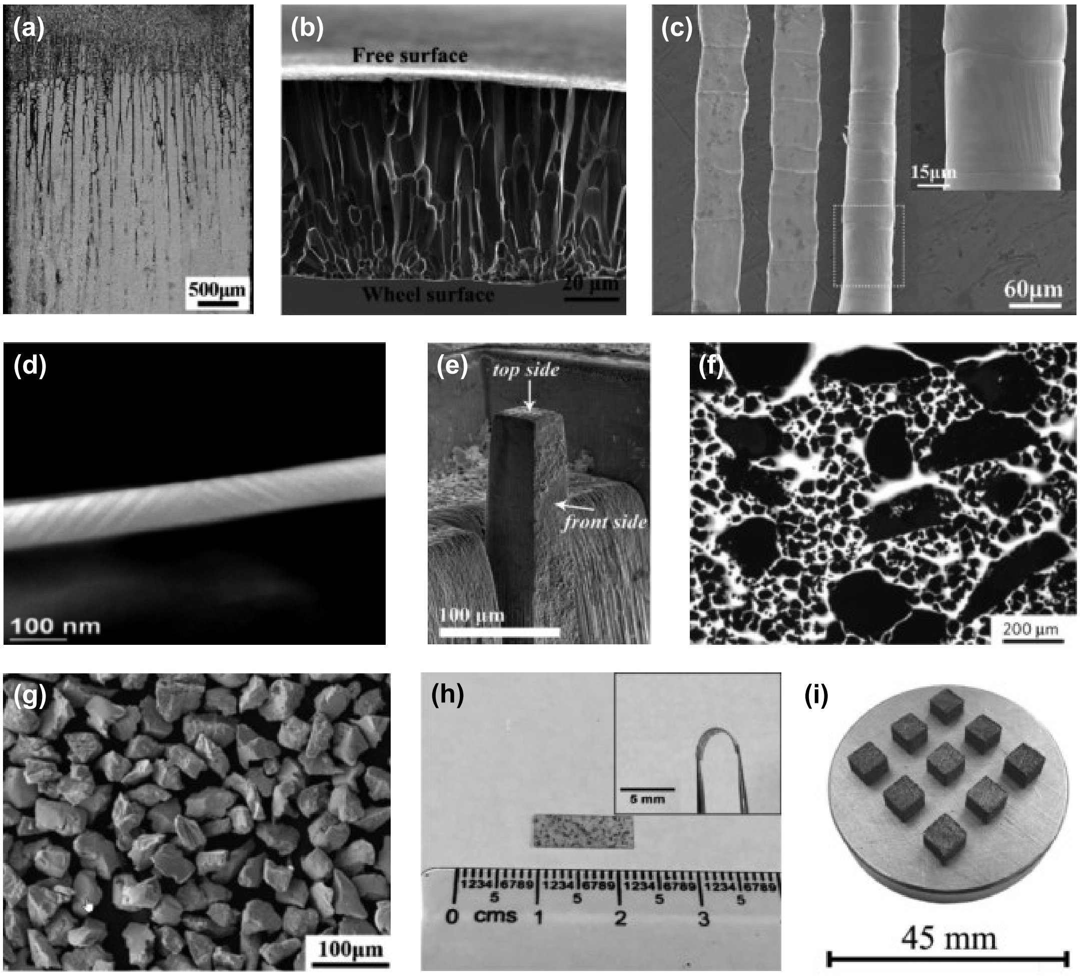

Fig. 1.24. Images of different forms of NiMnGa-based materials: **(a)** directionally solidified the $Ni_{54}Mn_{24}Ga_{22}$ alloy [348], **(b)** cross section of the $Ni_{51}Mn_{27}Ga_{22}$ ribbon [364], **(c)** bamboo grains of the $Ni_{50.5}Mn_{28.0}Ga_{21.4}$ microwires [374], **(d)** cross section of the epitaxial free-standing $Ni_{52.5}Mn_{19.5}Ga_{28.0}$ film [390], **(e)** single crystalline $Ni_{50}Mn_{28.5}Ga_{21.5}$ micropillar [404], **(f)** cross section of the $Ni_{52.0}Mn_{24.4}Ga_{23.6}$ foam [153], **(g)** polycrystalline $Ni_{54.5}Mn_{20.5}Ga_{25}$ micro-particles [421], **(h)** Ni-Mn-Ga/polymer composite based on the $Ni_{52}Mn_{26}Ga_{22}$ particles and polysulfone matrix [431], **(i)** 3D cubic $Ni_{49.7}Mn_{29.1}Ga_{21.2}$ samples fabricated by the additive manufacturing L-PBF method [436].

1.8 Applications and future prospects

Previous chapters describes the nature and variety of different multifunctional properties of Ni-Mn-Ga magnetic shape memory alloys that may be induced by magnetic, thermal or mechanical stimulus. The combination of three different degrees of freedom opens a completely new path for many modern smart applications, which require multifunctionality in order to reduce the number of active and/or sensing elements. Another important aspect of the multifunctional nature of the Ni-Mn-Ga alloys is the synergistic behaviour of stimulating fields that may be exploited in many applications. For example, the high thermal inertia of classic thermally induced shape memory effect may be drastically reduced by application of a fast-switching magnetic field. On the other hand, the high energy required to apply a sufficient external magnetic field might be particularly reduced by additional mechanical stress, which is yet more energy efficient than the magnetic field. Lastly, it should be remembered that Ni-Mn-Ga compounds can be fabricated in many different forms and sizes (see **Section 1.7**), which broadens the possibilities of their feasible applications from common-size electronic devices up to sophisticated submicron or nanoscale solutions. In this section, various potential applications of Ni-Mn-Ga alloys will be discussed, considering their magnetic shape memory behaviour, magnetic field-induced strains, superelasticity phenomenon and giant magneto- and mechanocaloric effects.

1.8.1 Sensing and actuating applications

Sensors and actuators are probably the most obvious application of Ni-Mn-Ga alloys, because of the exceptional shape memory effect and magnetic field-induced strains. Over the last two decades, these uncommon phenomena have drew the attention of many researchers who have tried to exploit and describe these effects for the purpose of future devices.

When it comes to sensing applications, the early experiments reported in [442] showed that there is a clear connection between the inductance of the Ni-Mn-Ga material and the compression strain. The authors suggested that elongation of the MSMA may be defined by simple inductance measurement, however, no detailed model of this dependence was established. In the same time, Sarawate *et al.* [443,444] proposed a similar approach, which was also based on the flux density measurement. Later on, the novel developed idea for strain sensing was also proposed by Stephen *et al.* [445], who reported the linear dependence between the tensile elongation of the Ni-Mn-Ga sample and the magnetic flux density of stray fields. What is interesting, in his concept, presented in **Fig. 1.25**, the strain sensor did not require the electrical contact with the rest of the device and the only part that needs to use electric power was the magnetic field sensor. In the next version of his setup [446], he also reported that the external magnetic bias field may be partially substituted by the thermal field, which notably reduced the size of a large permanent magnet. In a more recent sensing solution, reported in [447], the large permanent magnet required for the bias field was changed to a dual coil system powered by a small AC voltage, significantly reducing the size of the whole device.

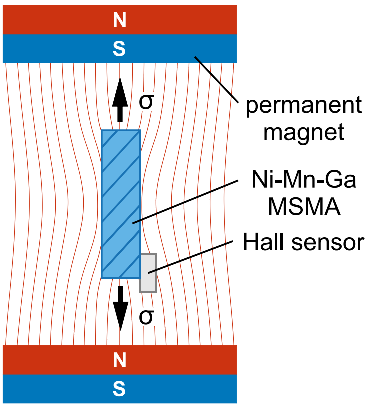

Fig 1.25. Schematic representation of the strain sensor based on Ni-Mn-Ga MSMA. The MSM element is exposed to the bias magnetic field and loaded with mechanical stress, σ. The Hall sensor measures the distorted magnetic stray field close to the elongated MSM element (based on [445]).

In terms of the actuation solutions, it is worth noticing, that this branch of Ni-Mn-Ga applications is far more widely well documented than aforementioned sensors. This is due to the fact, that it is technologically easier to induce stains in active element and simply measure its displacement, rather than measure the magnetic field effects accompanying the deflection of the material. Generally, as a result of complex magnetostructural behaviour of Ni-Mn-Ga alloys, there are several different approaches to design MSM actuator, which differs by excitation and restoring forces acting on active element. Holtz *et al.* [448] proposed five unique *operation modes* characterized by different possibilities to achieve the elongation or contraction of the alloy. Due to technological restrictions the most popular operation mode, investigated by many researchers [449–452], is based on the magnetically induced elongation and mechanically induced contraction generated by a typical spring, which is schematically presented in **Fig 1.26(a)**. The usage of spring in *spring-loaded actuators* reduces the maximum actuation force, narrows the displacement range and demands constant electric power to maintain magnetic field required to hold the MSM element at a given position [453,454]. To overcome theses problems the concept of *push-push actuators* were also discussed in literature [455–457]. The push-push configuration, schematically depicted in **Fig 1.26(b)**, contains two MSM elements working against each other and connected by a movable part. In this case the excitation of single coil elongates only one corresponding MSM element, which subsequently contract the other one. As a result, the MSM elements may work in bidirectional actuation and hold at given position without the redundant electrical power consumption.

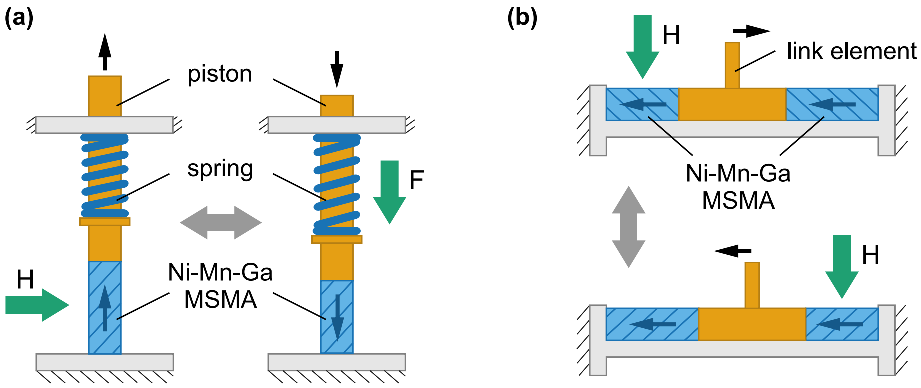

Fig 1.26. Schematic representation and the principle of working of **(a)** spring-loaded and **(b)** push-push actuator constructed on the Ni-Mn-Ga magnetic shape memory alloy (based on [455]).

It is worth noting that Pinneker *et al.* [458] presented a completely different mechanism of linear actuation based on the reversible martensitic transition, not on the magnetic field-induced strains. In his approach, the reproducible strain of about 4.1% was obtained by application of a temperature gradient along the single crystalline Ni-Mn-Ga foil exposed to the bias magnetic field, which subsequently results in the visible movement of the austenite-martensite phase boundary. It must be emphasized that the observed actuation phenomenon was possible due to the usage of thin Ni-Mn-Ga foil instead of bulk alloy. In this context, it should be remembered that thin Ni-Mn-Ga films are considered to be one of the most promising smart actuation materials. Until now, there has been several well-documented studies [459–464] that discussed the sophisticated submicron or nanoscale actuators based on Ni-Mn-Ga alloys.

The majority of the abovementioned actuator solutions are in the laboratory or prototype stage. However, despite many technological drawbacks, very recently ETO Magnetic revealed the first commercial line of innovative actuators named MAGNETOSHAPE® [465], which are based on the Ni-Mn-Ga alloy. The first two available types are linear spring-loaded and push-push actuator.

1.8.2 Hydraulic and pneumatic applications

Very interesting prospect applications of Ni-Mn-Ga magnetic shape memory alloys have been emerging in modern hydraulic and pneumatic designs. This is attributed to the two important features of MSMAs: (1) fast actuation response - excellent for vales designing and (2) complex deformation behaviour that may be used as a pumping mechanism in miniaturized hydraulics.

Generally, pneumatic and hydraulic valves fabricated using MSMAs are the more advanced developed forms of actuators discussed in the previous subsection. The first practical prototypes of pneumatic [466] or hydraulic [467] valves were directly based on spring-loaded or push-push actuators. One of the first unique design for MSM airflow valve was presented by Schiepp *et al.* [468]. In his prototype concept, the actuating MSM element was both elongated and contracted by the sets of two opposite coils. The elimination of the spring allowed for minimization of energy consumption and increased the overall efficiency of the valve. The important aspect of power consumption was also discussed in [469,470], where authors investigated two different valve concepts in order to improve the energy efficiency of future constructions. Lastly, it is worth mentioning that some researchers successfully supported the valve design prototyping with complex numerical simulations [471–473].

Another important prospect application of Ni-Mn-Ga MSMAs in modern hydraulics and pneumatics are precise micropumps. One of the first and most interesting designs of micropump was demonstrated by Ullakko *et al.* [474]. In his concept, presented in **Fig. 1.27**, the active Ni-Mn-Ga element was fixed at both ends, so MSM material cannot change its relative length. After the application of an external magnetic field, the Ni-Mn-Ga element cannot contract, and hence characteristic shrinkage for fluid occurs. The precise control of magnetic field, *e.g.* by diametrically magnetized magnet, allowed to move the shrinkage and the liquid inside from inlet to outlet of the micropump. It is worth highlighting that in this solution the MSM element works as both pumping and valve mechanism. Moreover, the authors suggested that MSMA solution presents advantages over piezoelectric micropumps, as it is more compact, generates higher pressure and may operate at different flow rates, which was later also proved in [475]. The most spectacular use of MSM micropump was reported by Barker *et al.* [476], who used it for the intracranial drug delivery in rats. Recently, Saren *et al.* [477] presented even more sophisticated micropump based on the same working principle, however, manufactured as a precise *lab-on-a-chip* model. In his design, the micropump may work with both gases and liquids with the accuracy of transmitted volumes reaching even single nanolitres.

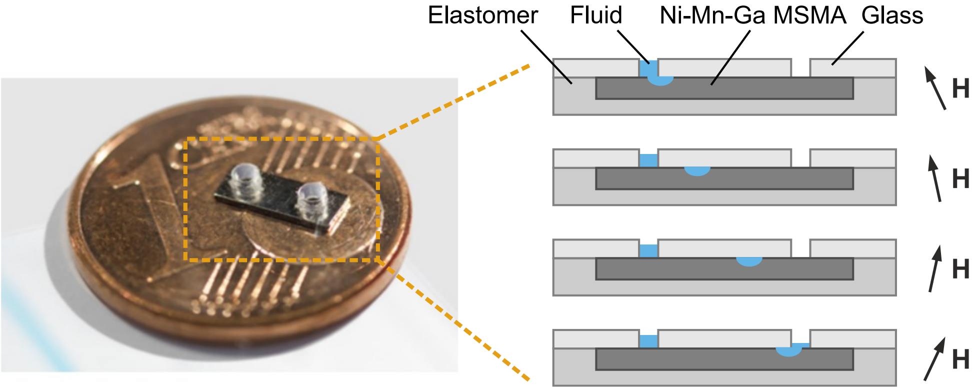

Fig 1.27. Micropump based on the Ni-Mn-Ga magnetic shape memory material (without the sealing base and permanent magnet) compared to 1 euro cent coin (reprinted from [478]) and schematic representation of its working principle (based on [474]).

1.8.3 Energy harvesting

In the last couple of years, due to the worldwide trends for energy efficient applications and renewable sources of energy, the demand for different forms of mobile electricity increased significantly. These mobile sources of electricity are essential in the modern automotive, aerospace or marine industry to power the monitoring and diagnostics devices, which nowadays require micro- or milliwatts of energy [479]. Taking into account these specialistic requirements, the energy harvesting systems are found to be the leading solution that may dominate the market in the near future.

Among the various smart materials that have been developed and investigated for energy harvesting applications, Ni-Mn-Ga MSMAs are evolving as one of the most promising alloys [480]. This is due to the multifunctional nature of the Ni-Mn-Ga compound, that may be influenced by thermal, magnetic and mechanical field, which makes it possible to harvest and convert three different types of energy by only one active element. There are numerous sources of *waste energy* that can be harvested and subsequently reused, however, from the a technological perspective, the greatest attention is currently focused on mechanical vibration, thermal and acoustic energy. It should be emphasized that each aforementioned energy may be supposedly harvested via Ni-Mn-Ga MSMAs.

Generally, the idea of vibration energy harvesting is based on the coupling between mechanical and magnetic properties of the Ni-Mn-Ga alloy, nevertheless, the exact design of the harvester may change depending on application and requirements. In the solution discussed in [481–483], the Ni-Mn-Ga element is fixed with one end of the cantilever beam (**Fig. 1.28**) and the inert mass element is situated at the other end. The vibrating beam generates the strain in the MSM element and consequently stimulates reorientation of the martensite variant. The structural changes of martensite are strongly connected with the magnetization of the Ni-Mn-Ga alloy, therefore, these fluctuations induced the current in a neighbouring pickup coil according to the Faraday's law [484]. In other approaches, discussed in [485–488], the vibrating beam is replaced by strains generated directly in the horizontal direction of the active Ni-Mn-Ga element that simulates the actual vibrating mass. Despite the fact that the working principle of each aforementioned harvester is the same, the trickiest technological aspect is the voltage induction. The voltage induced in the pick-up coils is strongly related to the changes in magnetic flux, which in turn is influenced by structural changes and vibration frequency [489,490]. That is why the further development of NiMnGa-based vibration energy harvesters is still needed to provide a reliable technological solution.

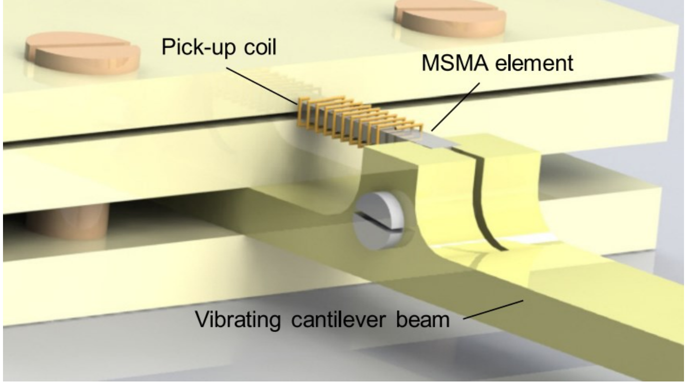

Fig 1.28. 3D model depicting the idea of vibration energy harvester based on the Ni-Mn-Ga MSMA (derived from [483]).

When it comes to prospect thermal energy harvesting via MSMAs, a very interesting solution was proposed by Gueltig *et al.* [491,492]. He demonstrated the thermal energy harvester for low-temperature differences constructed on a polycrystalline NiMn-based thin film attached to the free end of the cantilever. The working principle of this harvester was based on the sudden magnetization change during the magnetostructural transformation of the MSM material. Even small changes of temperature in the vicinity of phase transformation result in significant changes in magnetization of the thin film. As a result, the MSM films were repeatedly attracted to the permanent magnet, causing the oscillation of the flexible beam. These oscillations can be then harvested by a pick-up coil in the same manner as in the case of the vibration energy harvesters.

In terms of acoustic energy harvesting via Ni-Mn-Ga MSMAs, very recently, Farsangi *et al.* [493] presented the acoustic harvester based on the Helmholtz resonator. In his design, the MSM element was fixed to the elastic membrane of the Helmholtz resonator. The enhanced sound pressure generated by the loud environment vibrates this membrane, resulting in the strain generation in the Ni-Mn-Ga element and, therefore, in reorientation of the martensite variants. The structural martensite changes are then converted to a voltage in the surrounding pick-up coils, just like in other harvester solutions.

1.8.4 Magnetocaloric refrigeration

The magnetocaloric as well as mechanocaloric properties of the Ni-Mn-Ga alloys were described in detail in **Section 1.5.3**. It was presented that MSMAs can successfully compete with other well-known magneto- and mechanocaloric materials. Additionally, the magnetocaloric properties of NiMnGa-based Heusler alloys may be tuned by compositional or structural changes, which always limits the usage of other MC materials. When it comes to actual refrigeration application, it must be explained that in this field, the main focus is placed on technological aspects, like cooling cycles, magnetic field generation or control algorithms, rather than on material aspects. Moreover, despite the variety of MC materials, most researchers have been using common Gd as a benchmark element in order to compare different devices, excluding the influence of the MC material [494]. In this context, it should be remembered, that the majority of the magnetocaloric devices may possibly operate equally well on Ni-Mn-Ga alloys as on Gd. The latest comprehensive reviews of magnetocaloric refrigeration prototypes were presented by Kitanovski [180] and Greco *et al.* [494].

In order to show the future magnetocaloric potential of Ni-Mn-Ga alloys, it is worth noting that between 2014 and 2018 General Electric (GE), one of the world's leading energy companies, in cooperation with Oak Ridge National Laboratory, presented several different iterations of prototypes of magnetocaloric refrigeration systems [495]. On of the prototype revealed in 2015 is depicted in **Fig. 1.29**. Their devices were based on magnetocaloric microchanneled elements fabricated from the Ni-Mn-Ga alloy by additive manufacturing technology. Remarkably, the objective of the project was to reduce the energy consumption of refrigeration systems by 20–30% in comparison to conventional vapor compression technology.

Fig. 1.29. Prototype of the magnetocaloric refrigeration system based on the Ni-Mn-Ga alloy developed by General Electric and Oak Ridge National Laboratory (derived from [495]).

1.9 Aim and scope of thesis

The presented theoretical introduction clearly shows the complex magneto-thermo-structural nature of NiMnGa-based magnetic shape memory alloys. Current research in this topic is extensive and focused on many different multifunctional applications of stoichiometric, near-stoichiometric and doped materials, as was discussed in the introduction. Furthermore, the wide variety of Ni-Mn-Ga alloy morphologies, from bulk single crystals to very thin nanometric films, broadens the scope of available research in this area. All of this complicates the uniform and consistent description of this particular group of smart materials, which is one of the main obstacles in their future prospect application.

Many researchers are trying to find the solution to this problem by introducing the universal electronic parameters, such as the well-known valence electron concentration e/a and recently reported non-bonding electrons concentration N_e/a. However, the uncertainties in reported chemical compositions, relying on theoretical estimations of these parameters, rather than calculating them on the basis of the experimental chemical compositions, combining various doping elements with different electronic structures, mixing different heat treatment procedures, and focusing on the particular group of structural, magnetic or mechanical properties significantly reduce the practical usefulness of the e/a or N_e/a parameter.

Taking into account the aforementioned problems, the objective of this thesis is it produce a series of polycrystalline NiMnGa-based materials doped by Co and/or Fe in order to provide fundamental comprehensive research on their structural, thermal, magnetic and mechanical properties. Moreover, the produced series of alloys will be exposed to different cooling conditions to elucidate the role of atomic ordering on the examined magneto-thermo-structural properties. The proposed wide-ranging investigation consists of most important aspects of multifunctional behaviour of magnetic shape memory materials that may be useful in designing their future potential applications. Finally, all of the presented studies are considered with respect to universal electronic parameters, including valence electron concentration and non-bonding electrons concentration, to establish the clear differences between these parameters.

The author of this thesis states that the proper selection of chemical composition, alloying additions and heat treatment conditions allows for the fabrication of multifunctional NiMnGa-based magnetic shape memory alloys characterized by complex magnetomechanical properties, which could be closely correlated with their intrinsic electronic parameters.

2

Experimental procedure

2.1 Preparation of alloys

After careful preliminary studies on the subject of compositionally tuned multifunctional Ni-Mn-Ga Heusler alloys, in part already published in [313,315,316,319], a series of NiMnGa-based polycrystalline alloys doped with Fe and/or Co were chosen as a general group of MSMAs investigated in the presented dissertation. The chemical compositions of the materials were carefully established, with the aim of studying the influence of Co and Fe addition on the magnetomechanical properties of the doped Ni-Mn-Ga alloys, as well as the effects of partial substitution of Co by Fe. Consequently, the following eight compositions were proposed (in at.%):

- $Ni_{48}Mn_{32}Ga_{20}$
- $Ni_{48}Mn_{31}Ga_{20}Co_1$
- $Ni_{48}Mn_{30}Ga_{20}Co_2$
- $Ni_{48}Mn_{28}Ga_{20}Co_4$
- $Ni_{48}Mn_{28}Ga_{20}Co_3Fe_1$
- $Ni_{50}Mn_{25}Ga_{21}Co_2Fe_2$
- $Ni_{48}Mn_{28}Ga_{20}Co_1Fe_3$
- $Ni_{48}Mn_{28}Ga_{20}Fe_4$

It is seen that the reference undoped alloy is an off-stoichiometric Mn-rich composition and the proposed alloying elements are introduced in the Ni-Mn-Ga composition at the expanse of Mn. Generally, for the stoichiometric Ni_2MnGa alloys Ni, Mn and Ga atoms occupies the 8*c*, 4*a* and 4*b* site, respectively, which was described in **Section 1.2**. However, for the Mn-rich alloys with Ga deficiency the extra Mn atoms occupy the free Ga sites. In this situation the structural limit when every unit cell theoretically contains an additional Mn atom is Mn = 31 [126]. Taking this into consideration, the reference undoped composition is in the vicinity of the that limit, which should allow for more controllable Mn substitution towards more stoichiometric Ni/Mn/Ga ratio.

The chemical compositions of the Heusler alloys are always denoted in *atomic percentage* (at.%), which is a well-established practice in material science. However, for production purpose, the atomic percentage must to be converted to the *weight percentage* (wt.%) according to the following relation:

$$\mathrm{wt.\%} = \frac{\mathrm{at.\%} \cdot A_\mathrm{r}}{\sum_{i=1}^{n} \mathrm{at.\%}_i \cdot A_{\mathrm{r}i}} \cdot 100\% \tag{2.1}$$

where A_r is the relative atomic mass, n is the number of different atomic elements in the chemical composition, i indicates the selected element, and wt.% and at.% are weight and atomic percentage, respectively.

The chemical compositions of the abovementioned alloys expressed in at.% and wt.% are summarised in **Table 2.1**. The calculated wt.% were used to weigh the appropriate amount of each alloying element using the electronic scale with the precision of 0.001 g. The materials were prepared from high purity raw elements, including Ni (99.99%), Mn (99.98%), Ga (99.99%), Co (99.95%) and Fe (99.99%) provided by Alfa Aesar (now Thermo Scientific). The preparation of raw Mn required an additional mechanical and chemical cleaning step to remove the inevitable oxidation layer. The final mass of all elements was balanced to be close to 10 g, which is also listed in **Table 2.1**. It should be mentioned that preliminary experimental studies revealed the high, but relatively constant volatility of Mn close to 2 wt.%, which was caused by the significant vapor pressure of Mn. At 1500°C (temperature close to the melting point of Ni, Fe and Co) the vapor pressure of Mn is more than 20 times higher than for other constituent elements [496]. In order to reduce the loss of Mn and maintain the nominal chemical compositions, the final weight of Mn was increased by about 2 wt.% in each fabricated material.

The rest of the fabrication process of the investigated NiMnGa-based alloys was divided into three stages:

1. First melting to receive the homogenous samples from raw elements.
2. Second melting (remelting) to receive the cylindrical specimens from the previously as-cast alloys.
3. Heat treatment procedure followed by three different cooling rates obtained by water, air or furnace cooling.

In the first stage, the prepared raw elements were melted by the use of arc melter (Edmund Bühler GmbH). In this technique, the required heat is produced by an electric arc generated between tungsten electrode and pure metallic elements placed on the water-cooled copper plate, as shown in **Fig 2.1**. Prior to the melting process, the chamber of the furnace was evacuated three times to high vacuum condition, each time subsequently flushed with high purity argon. The fourth evacuation stage was carried out to $5 \cdot 10^{-5}$ mbar and then the chamber was filled back with protective argon to a pressure of 800 mbar. The relatively low DC current of 150 A was used during the melting process to reduce the evaporation of Mn. Each ingot was turned upside down and remelted four times to ensure the good homogeneity of the materials. The final form of the as-cast samples had a button-like shape, which is presented in **Fig. 2.2(a)**.

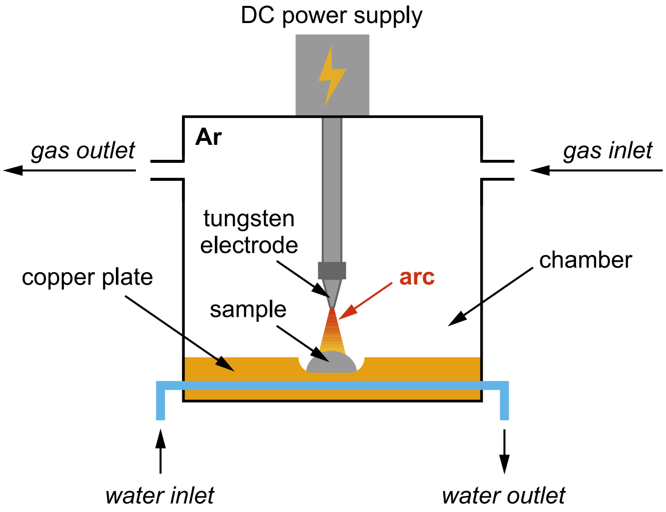

Fig 2.1. Schematical representation of arc melter equipped with water cooled copper plate operating under protective argon atmosphere that were used in the presented studies to produce the polycrystalline bulk Heusler alloys.

After the first melting process,, the button-shaped samples were mechanically crushed into smaller pieces and again placed in the arc melter chamber, this time on the water-cooled copper palate with u-shaped groove. Before the second melting process, the same evacuation and argon flushing procedure was undertaken as in the first melting stage. Mechanical crushing of the as-cast alloys, followed by the second melting procedure, ensures even better chemical homogeneity of the alloys and allowed to receive the materials in a form of ~30 mm long and ~5 mm in diameter cylinders, as depicted in **Fig. 2.2(b)**. The final weight loss after the two-stage melting process is summarized in **Table 2.1**. It is seen that in each alloy, the weight loss was less than 1%, which is a very satisfactory result considering the arc melting technique.

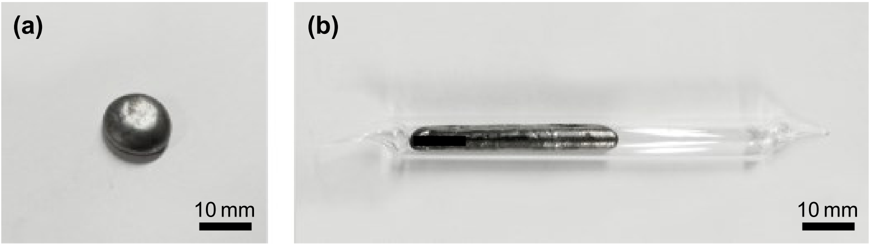

Fig 2.2. The example of the $Ni_{50}Mn_{25}Ga_{21}Co_2Fe_2$ alloy after **(a)** the first melting procedure – button-shaped sample, and **(b)** the second melting procedure – cylindrical sample sealed in an argon filled quartz ampoule.

Table 2.1. The summary of the chemical compositions of the investigated NiMnGa-based alloys expressed by atomic (at.%) and weight (wt.%) percentages, as well as the total masses of the prepared materials before and after the melting procedure with the corresponding weight losses.

Alloy	**El.**	**A_r**	**at.%**	**wt.%**	**Mass before melting (g)**	**Mass after melting (g)**	**Weight loss(%)**
$Ni_{48}Mn_{32}Ga_{20}$	Ni	58.693	48	47.19	10.118	10.043	0.74
	Mn	54.938	32	29.45			
	Ga	69.723	20	23.36			
$Ni_{48}Mn_{31}Ga_{20}Co_1$	Ni	58.693	48	47.16	10.122	10.051	0.70
	Mn	54.938	31	28.51			
	Ga	69.723	20	23.34			
	Co	58.933	1	0.99			
$Ni_{48}Mn_{30}Ga_{20}Co_2$	Ni	58.693	48	47.13	10.022	9.936	0.86
	Mn	54.938	30	27.57			
	Ga	69.723	20	23.33			
	Co	58.933	2	1.97			
$Ni_{48}Mn_{28}Ga_{20}Co_4$	Ni	58.693	48	47.07	10.047	9.976	0.71
	Mn	54.938	28	25.70			
	Ga	69.723	20	23.30			
	Co	58.933	4	3.94			
$Ni_{48}Mn_{28}Ga_{20}Co_3Fe_1$	Ni	58.693	48	47.09	10.090	10.015	0.74
	Mn	54.938	28	25.71			
	Ga	69.723	20	23.31			
	Co	58.933	3	2.96			
	Fe	55.845	1	0.93			
$Ni_{50}Mn_{25}Ga_{21}Co_2Fe_2$	Ni	58.693	50	48.90	10.096	10.012	0.83
	Mn	54.938	25	22.88			
	Ga	69.723	21	24.40			
	Co	58.933	2	1.96			
	Fe	55.845	2	1.86			
$Ni_{48}Mn_{28}Ga_{20}Co_1Fe_3$	Ni	58.693	48	47.14	10.002	9.930	0.72
	Mn	54.938	28	25.74			
	Ga	69.723	20	23.33			
	Co	58.933	1	0.99			
	Fe	55.845	3	2.80			
$Ni_{48}Mn_{28}Ga_{20}Fe_4$	Ni	58.693	48	47.16	10.028	9.950	0.78
	Mn	54.938	28	25.75			
	Ga	69.723	20	23.34			
	Fe	55.845	4	3.74			

In the third manufacturing stage, the as-cast materials were exposed to the heat treatment procedure consisting of high-temperature annealing and the subsequent cooling process. Each alloy was cut into three even pieces assigned to three different cooling conditions: (1) *water cooling*, (2) *air cooling* and (3) *furnace cooling*. To prevent the oxidation of the alloys during high-temperature annealing, the fabricated cylindrical samples were sealed in quartz tubes filled with high purity argon. The stand for vacuum sealing, schematically presented in **Fig. 2.3**, was designed and assembled by the Author of this thesis. The applied solution allowed for the prior air evacuation of the quartz ampoule and subsequent argon filling. The example of the sample sealed in an argon-filled quartz ampoule is shown in **Fig. 2.2(b)**.

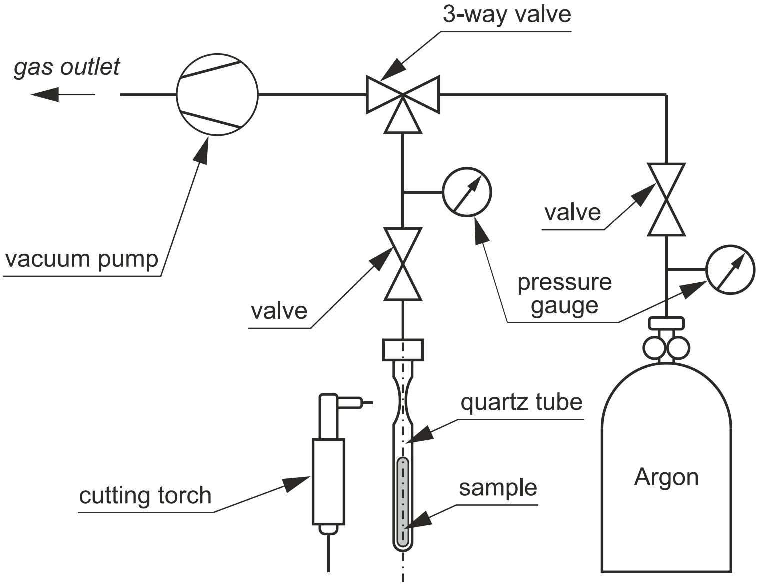

Fig. 2.3. The schematic representation of the self-made stand developed to seal metallic specimens in argon-filled quartz ampoules.

In order to homogenize the samples and increase the degree of atomic order, the Ni-Mn-Ga alloys should be annealed above the $L2_1 \rightleftarrows B2'$ transformation temperature, which was described in detailed in **Section 1.3.2**. To ensure the proper annealing conditions, preliminary differential scanning calorimetry (DSC) measurements of the undoped as-cast $Ni_{48}Mn_{32}Ga_{20}$ sample were carried out. **Fig. 2.4** shows the DSC curve recorder for the aforementioned sample at 10 K/min heating rate. The apparent characteristic small peak starting at $T_{B2'} = 1028$ K is connected with the $L2_1 \rightleftarrows B2'$ order-disorder transformation, whereas the significant endothermic transformation at $T_m = 1362$ K represents the melting process. In both cases the temperature of transformation was evaluated from the onset temperature, as it less dependant on heating rate and mass of the sample [497]. Based on the estimated $T_{B2'}$ and T_m, the temperature for annealing for all fabricated samples was set to 1173 K (900°C), which was above the order-disorder transformation, but still safety below the melting point.

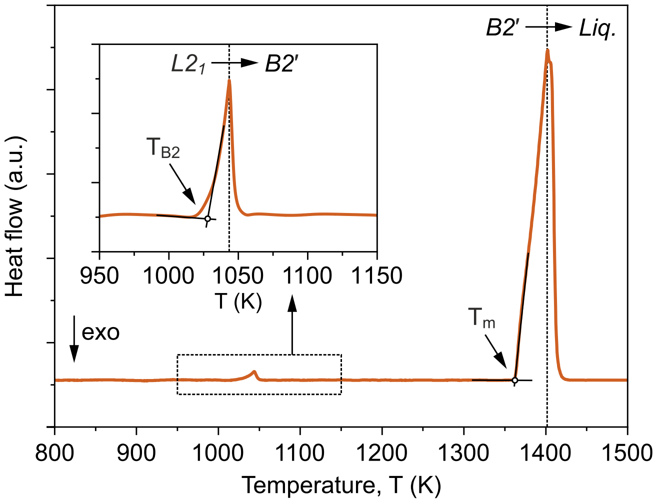

Fig. 2.4. The DSC curve recorder for the as-cast $Ni_{48}Mn_{32}Ga_{20}$ alloy at 10 K/min heating rate. The inset shows the part of the curve with the characteristic distinctive transformation related to the $L2_1 \rightleftarrows B2'$ transformation starting at T_{B2} temperature. The T_m corresponds to the melting point of the alloy.

In the next stage, the sealed specimens were annealed in a muffled furnace (Nabertherm) at an established temperature of 1137 K for 24 h with a 2 h preheating stage. After annealing, the first group of alloys was immediately quenched in ice water, the second group was removed from the furnace and cooled in room temperature conditions and the third group was left inside the chamber to slowly cool in the furnace (~1 K/min). The summary of the applied heat treatment conditions is depicted in **Fig. 2.5**.

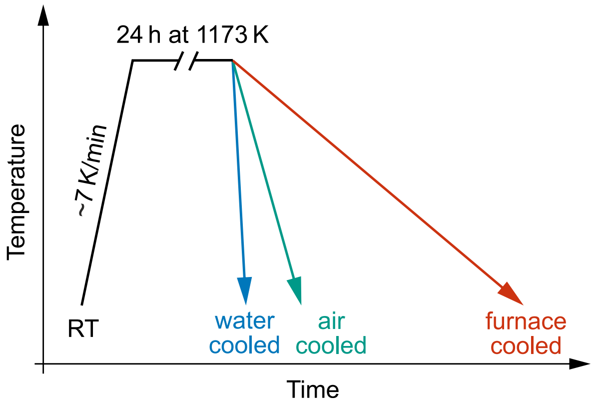

Fig. 2.5. The heat treatment procedures applied for the fabricated NiMnGa-based alloys. The 3 main groups of materials were produced: (1) water cooled, (2) air cooled and (3) furnace cooled.

2.2 Preparation of samples for experiments

After the fabrication process, the samples were removed from quartz tubes and prepared according to the different experimental requirements. For each investigation, the cross-section slices from the cylindrical sample were cut on the wire Electrical Discharge Machine (EDM). This approach ensures that each specimen was exposed to the same temperature gradient during the production process and that it will be characterized by comparable crystallographic texture. The received cross-section slices were initially polished by grinding paper to remove any unwanted oxidation.

For the X-Ray Diffraction (XRD) studies, the prepared slices of materials were first mechanically cut into smaller pieces and then manually grinded using an agate mortar and pestle. The same mass of the received powder was used during the X-ray diffraction.

For the Differential Scanning Calorimetry (DSC) and Magnetic Thermogravimetry (M-TG) measurements, one quarter of each cross-section slice was used. The difference between the mass of the samples was less than 5%.

For the Scanning Electron Microscopy with Energy Dispersive X-ray Spectroscopy (SEM-EDX), Atomic Force Microscopy (AFM) and Instrumented Nanoindentation (NHT) examinations, the cut off slices were mounted in an acrylic resin and then thoroughly polished. To ensure the flat oxide-free surface, the materials were grinded from 800 to 4000 grit sanding paper and subsequently polished using 6 to 0.25 μm diamond suspensions. For the final polishing step, the 0.05 μm colloidal silica suspensions were used. After all polishings steps, the specimens were rinsed with distilled water and cleaned with the help of an ultrasonic cleaner.

For the Vibrating Sample Magnetometer (VSM) investigations, the thin needle-like specimens were cut from the previously prepared samples. The needle shape of the material, with a length to diameter ratio of more than 10, allowed reducing the influence of the demagnetizing field [132].

2.3 Experimental methods

2.3.1 Polarised optical microscopy

The microstructures of the manufactured and thoroughly polished NiMnGa-based materials were investigated by the optical microscope equipped with polarized light and supplied as a module of the Nanoindentation Tester (NHT^2, Anton Paar). To eliminate the influence of the possible uneven thermal history of the heat treated alloys, prior to the observations, all specimens were cooled down to the temperature of liquid nitrogen ($\sim$77 K) and then slowly warmed up to room temperature.

2.3.2 Scanning Electron Microscopy (SEM) and Energy Dispersive X-ray Spectroscopy (EDX)

The detailed microstructure observations were performed using a Scanning Electron Microscope equipped with an Energy Dispersive X-ray Spectroscopy attachment (SEM-EDX Quanta FEG 250, FEI). The SEM images were recorded by both secondary electrons (SE) and backscattered electrons (BSE) detectors.

The SE are low-energy electrons emitted from the shallow surface of the sample through interaction with the high-energy electrons of the primary beam (**Fig 2.6**). The emission of SE electrons is strongly dependent from the incidence angle of the primary beam, therefore, the SE signal is mostly influenced by the topography of the sample. On the contrary, the BSE electrons are high-energy electrons from the primary beam backscattered due to inelastic collisions with atoms from the surface of the investigated specimen (**Fig 2.6**). As the atomic number of atoms from investigated material increases, the energy of the backscattered electrons also increases. Consequently, the BSE emission reveals the variations in specimen atomic number, which is commonly known as material contrast or compositional contrast. However, it is worth noticing that BSE emission is also influenced by other mechanisms including magnetic field or crystallographic orientation [498]. The crystallographic orientation contrast is associated with the diffraction of electrons by the lattice planes of the single grain. The intensity of this signal is weak and considerably dependent on the angular relationship between incident electron beam and observed crystal structure. As a result any changes in sample tilt or rotation allows for identification if the signal originates from variations in atomic number or from crystallographic orientation.

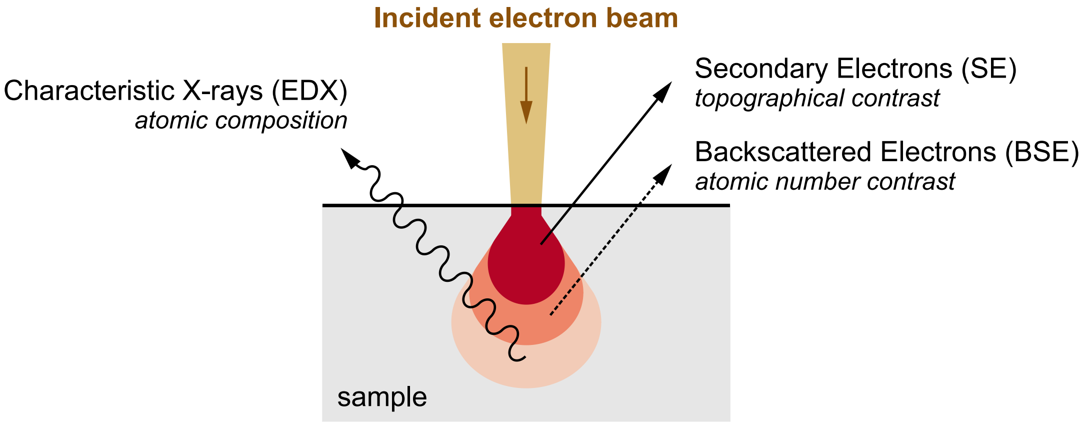

Fig 2.6. The idea of scanning electron microscopy (SEM) and energy dispersive X-ray spectroscopy (EDX). Secondary electrons are low energy electrons from the most shallow penetration depth responsible for the topographic image. Backscattered electrons are high energy electrons reflected or backscattered out of the sample dependent on the atomic number. Characteristic X-rays are emitted from the sample when electrons from outer shell fill a vacancy in the inner shell of an atom. The characteristic X-ray pattern is recorded by EDX detector.

The energy dispersive X-ray spectroscopy detector analyses the X-ray signal emitted from the investigated material due to interaction with the primary electron beam (**Fig 2.6**). The electrons from the primary beam knock out the electrons from the inner shells of atoms, which are subsequently replaced by electrons from outer shells. When a high-energy electron from the outer shell occupies the place of a low-energy electron, the energy difference is emitted in the form of X-ray spectrum. The generated X-rays are characteristics for the elements present in the measured specimen. Hence, the EDS provides qualitative and quantitative information about the chemical composition of the material.

Before the SEM-EDX observations the EDX detector was calibrated using high-quality reference standards. For each investigated specimen the EDX analysis were performed in at least 5 different random areas covering both the central and outer part of the prepared cross sections. The final chemical composition of the manufactured NiMnGa-based alloys was calculated as an arithmetical mean of all conducted EDX analysis.

2.3.3 X-Ray Diffraction (XRD)

The detailed crystal lattice investigations were conducted on an X-Ray Diffractometer (XRD MiniFlex 600, Rigaku) equipped with a monochromator isolating Cu Kα radiation ($\lambda = 1.5406$ Å). The XRD patterns were collected at a Bragg angle 2θ between 20° and 85° with a step size of 0.02°. In order to follow the evolution of the crystal lattice of the investigated samples during phase transformations, the XRD measurements were performed at three different temperatures: 295 K, 320 K and 400 K with the help of supporting heating stage attachment (BTS 500, Anton Paar). The schematic representation of the X-ray diffraction setup utilized in this thesis is presented in **Fig. 2.7**.

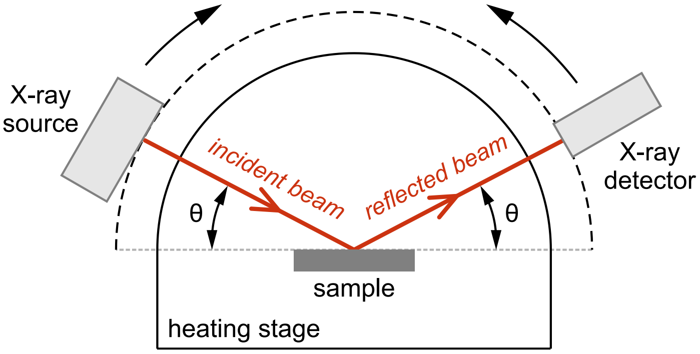

Fig. 2.7. Schematic representation of the X-ray diffraction setup equipped with the additional heating stage.

During the measurement, the X-rays generated by a cathode tube are scattered by atoms from crystal lattice of the samples because of the interactions with encountering electrons. The atomic plane of the crystal causes incident X-ray beams to interfere with each other while leaving the crystal. The constructive interference occurs when the Bragg's Law condition is satisfied [499]:

$$n\lambda = 2d\sin\theta \tag{2.2}$$

where d is the distance between the crystallographic planes, θ is the incident angle, λ is the wavelength of the X-ray beam and n is an integer.

The d-spacing is characteristic to periodic arrangement of the unit cell, and thus it allows for crystal lattice determination, if measured under different incident angles. In the presented studies, the recorded experimental diffraction patterns were subsequently evaluated according to the Rietveld refinement method [500] using Profex software [501] based on the BGMN kernel. The computer-aided Rietveld refinement requires the additional information about the examined crystal lattice to perform the numerical fitting procedure. For the BGMN kernel the crystallographic information is represented in the special crystallography CIF file, which is a standard file format recommended by the International Union of Crystallography (IUCr) [502]. In the presented work, the CIF files for each identified phases were created from scratch on the basics of most recent diffraction studies reviewed in theoretical part of this thesis in **Section 1.2**. The applied CIF files are attached in the **Appendix A**.

The main idea of Rietveld analysis is to refine an ideal diffraction pattern of the modelled sample until the differences between the calculated model and experimental XRD spectra are minimized. In order to estimate and quantify the degree of this convergence, three most commonly used profile agreement indices, *i.e.* R_{wp}, R_{exp} and GoF, were calculated during the refinement control. The first parameter is the *weighted profile R-factor* (R_{wp}) defined as [503]:

$$R_{\mathrm{wp}} = \left[\frac{\sum_i w_i (y_{ci} - y_{oi})^2}{\sum_i w_i\, y_{oi}{}^2}\right]^{\frac{1}{2}} \tag{2.3}$$

where y_{oi} and y_{ci} corresponds to the observed and calculated intensity values at $2\theta_i$, respectively, and w_i is the *weight* described as [503]:

$$w_i = \frac{1}{\sigma^2[y_{oi}]} = \frac{1}{\left\langle (y_{oi} - \langle y_{oi}\rangle)^2 \right\rangle} \tag{2.4}$$

where $\sigma[y_{oi}]$ represents the *standard uncertainty* and angle brackets $\langle\ \rangle$ indicates the expected intensity values.

It is seen in **Eq. 2.3** that R_{wp} compares the calculated model to the experimental data by weighting the residual difference between experimental and calculated diffraction patterns. As a result, during fitting procedure, the high intensity diffraction peaks are more significant than low intensity background, which seems reasonable from the analytical point of perspective.

The second agreement index is the *expected R-factor* (R_{exp}), which assesses the quality of the experimental data according to the following relation [503]:

$$R_{\text{exp}} = \left[\frac{N-P}{\sum_i w_i \, y_{oi}{}^2}\right]^{\frac{1}{2}} \tag{2.5}$$

where N is the number of data points and P is the number of refined parameters.

It should be noted that for the presented powder diffraction data, the overall value of "N—P" is overwhelmingly dominated by N, thus P may be safely ignored. The R_{exp} measure the quality of experimental data limited by the inevitable noise and low peak intensities. From other perspective, it also indicates the best possible R_{wp} that can be theoretically achieved for the particular data, as R_{wp} can converge, but never be lower than the R_{exp}. Considering that fact, the third parameter known as *goodness of fit* (GOF) is introduced to compare the R_{wp} to R_{exp} using the relation [503]:

$$\text{GOF} = \left[\frac{R_{\text{wp}}}{R_{\text{exp}}}\right]^2 \tag{2.6}$$

The GOF estimates how close the refined diffraction pattern is to the ideal expected diffraction pattern considering the quality of experimental data. For the theoretically perfectly converged fit the GOF is equal to 1.

2.3.4 Atomic Force Microscopy (AFM)

The microstructural characterisation was also supported by the comprehensive studies on the Atomic Force Microscope (AFM XE-100, Park System). The surface of the samples were scanned in contact mode (C-AFM) with the help of the PPP-CONTR (NANOSENSORS) cantilever glued on the dedicated alignment chip. According to the specification provided by the manufacturer, the radius of the cantilever tip was less than 7 nm, which ensured reproducible images and superior resolution. The maximum scan area was limited to 45 μm × 45 μm. The additional scanning parameters, such as scan frequency, proportional and integral gains or force set point, were adjusted during measurements, depending on the current surface properties.

In C-AFM, the flexible cantilever with a tip radius of a single nanometre remains in a constant contact with the studied surface, *i.e.* the measurements are carried out in a repulsive interaction regime. The laser beam, directed on the cantilever by the optical system, is reflected on the position-sensitive photodiode (PSPD), which is schematically depicted in **Fig. 2.8**. In this configuration, even slightest deflection of the cantilever, caused by topographical deviations of the sample, is displayed on the PSPD. The measurements are conducted in a feedback loop control, which means that the system keeps a constant interaction between the tip and the sample during scanning. Any topographical changes are compensated by the vertical positioning system (z-drive), as the physical deflection of the cantilever is reckoned as an error signal used for the feedback loop.

The final post-processing and analysis of the collected AFM images was carried out using Gwyddion software [504]. The post-processing includes simple background levelling, height line correction and linear artifacts removal.

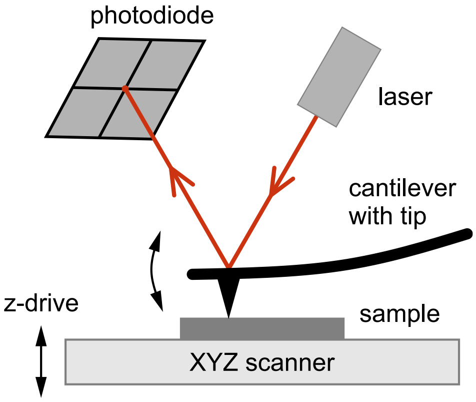

Fig. 2.8. The schematic principle of working of contact AFM (C-AFM) working in feedback loop control.

2.3.5 Differential Scanning Calorimetry (DSC) and Magnetic Thermogravimetry (M-TG)

The martensitic transformation behaviour of the manufactured NiMnGa-based alloys was investigated by the means of the Differential Scanning Calorimeter (DSC 404C Pegasus, Netzsch). The heat flux DSC, schematically presented in **Fig. 2.9(a)**, allows for simultaneous measurement of the temperature difference between the studied sample and the reference side. Due to the different heat capacities of the investigated material and the reference side (*e.g.* empty pan), any first-order transformations are observed as an increase or decrease in the measured temperature difference, which is directly connected to the enthalpy of this transition. As a result, the DSC allows for indirect measurements of endothermic or exothermic transformations undergoing during the heating or cooling process.

In the presented studies, all measurements were performed under a protective argon atmosphere. The measurements were conducted in a heating and cooling loop from 225 K to 425 K and subsequently from 425 K to 225 K with the same heating and cooling rate of 10 K/min. In order to check the thermal stability of the phase transformations, three consecutive loops were measured for each studied alloy. The characteristic temperatures of the forward and reverse martensitic transformations were determined by tangent method using corresponding endothermic and exothermic peaks.

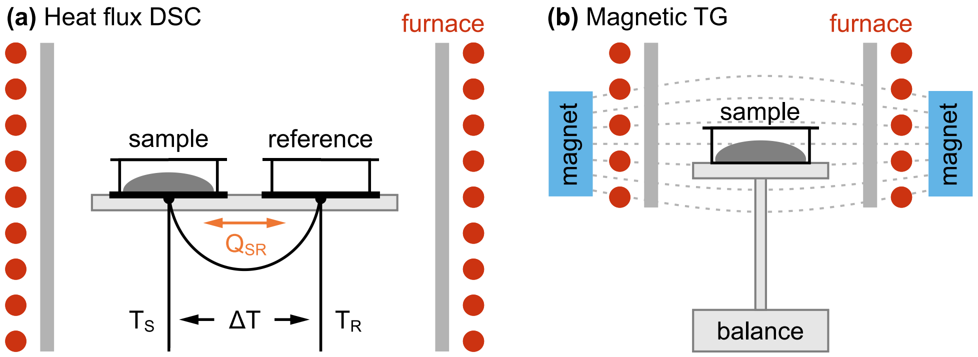

Fig. 2.9. The schematic representation of **(a)** the heat flux differential scanning calorimetry (DSC) and **(b)** the magnetic thermogravimetry (M-TG). T_S and T_R are the temperatures of sample and reference side, respectively; ΔT is the temperature difference between T_S and T_R; Q_{SR} is the resulting heat flow difference.

The DSC technique is suitable for the investigation of the first-order transformations, such as considered martensitic transition, in which the latent heat is evolved. On the contrary, second-order phase transformation, like magnetic transition, does not have accompanying latent heats, which restricts the usage of heat flux DSC. In some systems with strong magnetostructural coupling, abrupt variations in heat capacity can be detected in the DSC signal as λ-shape anomalies observed close to the Curie temperature [505]. However, this is not a reliable universal method for defining the temperature of the magnetic transformation. Taking into account this limitation, additional magnetic thermogravimetry (M-TG) studies were conducted on the Simultaneous Thermal Analyzer (STA 449 F1 Jupiter, Netzsch). In the M-TG method, presented in **Fig. 2.9(b)**, the precise balance measures the relative mass of the sample during the heating or cooling process. If the ferromagnetic material is exposed to the external magnetic field, the magnetic Faraday force acts upon the sample, introducing the magnetic weight. Close to the Curie temperature, the magnetic weight abruptly decreases or increases, which results in substantial change in the TG signal. In the presented studies, the M-TG measurements were carried out in a heating ⇄ cooling loop from 350 K to 425 K and from 425 K to 350 K at the same constant heating/cooling rate of 10 K/min.

2.3.6 Vibrating Sample Magnetometry

The characterization of the magneto-thermo-structural properties of the manufactured magnetic shape memory alloys was carried out using the Vibrating Sample Magnetometer (VSM) unit from the VersaLab System (Quantum Design). The VSM instrument operates according to the Faraday's induction law:

$$V = \frac{\mathrm{d}\Phi}{\mathrm{d}t} = \left(\frac{\mathrm{d}\Phi}{\mathrm{d}z}\right)\left(\frac{\mathrm{d}z}{\mathrm{d}t}\right) \tag{2.7}$$

where V is the induced voltage, t is time, Φ is the magnetic flux and z is the current vertical position of the magnetic sample.

During measurement, the investigated ferromagnetic sample is exposed to an external magnetic field that aligns its magnetization according to the direction of the external field. This specimen, characterized by the magnetic dipole moment, vibrates vertically in a pickup coil in a strictly defined manner (**Fig. 2.10**). As a consequence of a time-dependent position change, the voltage is induced in the pickup coil. Taking into account the **Eq. 2.7**, the induced voltage is proportional to the magnetic moment of the investigated material.

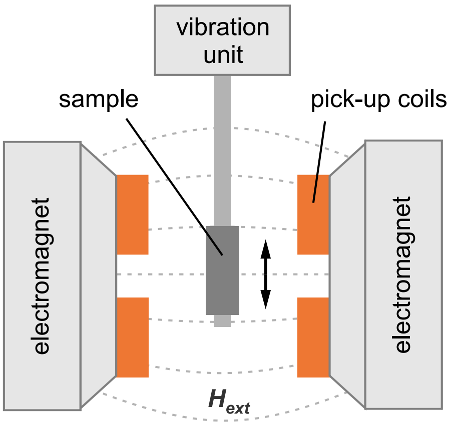

Fig. 2.10. The vibrating sample magnetometer setup operating on the basis of Faraday's induction law. H_{ext} represents the external magnetic field generated by the electromagnet.

In the presented studies the temperature dependence of magnetization under low external magnetic field of 100 mT was collected from 70 K to 370 K following the zero-field cooled (ZFC) and field cooled (FC) protocols with constant heating and cooling rates of 10 K/min. In ZFC mode the investigated specimen was firstly cooled to 70 K without external magnetic field. At 70 K the constant magnetic field of 100 mT was applied and then the measurement were performed following the increasing temperature up to 370 K. Next, in FC mode the magnetization of the sample was measured during cooling from 370 K to 70 K under the same constant external magnetic field of 100 mT. The relatively low magnetic field was chosen to reduce the influence of strong magnetocrystalline anisotropy of the produced multifunctional Heusler alloys on their magnetization process [506].

2.3.6.1 Low of approach to magnetic saturation

The magnetic DC hysteresis loops were also recorded at 100 K and 320 K or 360 K under an external magnetic field of up to 2 T. The selected temperatures were established to cover the magnetization process of both the low-temperature austenite phase and the high-temperature martensite phase.

The recorded hysteresis loops were subsequently used to estimate the *effective magnetocrystalline anisotropy* of each fabricated Heusler alloy in both austenitic and martensitic state according to *the low of approach to magnetic saturation* (LoA) [507]. However, in order to use the LoA model correctly, some important assumptions have been made. First of all, the LoA model refers to the high field magnetization process where $H \gg H_C$, thus only the last 5% of magnetization ($M \geq 0.95M_S$) were used for the actual fitting procedure. The proposed assumption is also supported by the fact that in the selected magnetization range the recorded hysteresis loops were full closed, which suggests that all hysteretic processes can be neglected, as the further increase in magnetization is mainly govern by the rotation of magnetic domains and not by the domain wall movement. The selected high field magnetization curves were then analysed following the low of approach to magnetic saturation model [507]:

$$M(H) = M_s\left(1 - \frac{a}{H} - \frac{b}{H^2}\right) + \chi H \tag{2.8}$$

where M_s is the magnetization saturation, a is the coefficient related to the local structural inhomogeneities (*i.e.* non-magnetic inclusions, point-like defects or internal microstresses) [508], b is the actual coefficient defining the magnetocrystalline anisotropy [508,509], and the last term χH corresponds to the high field spontaneous magnetization (*i.e.* the magnetic moment increases by itself due to Zeeman splitting) [508].

Depend on the magnetization behaviour of investigated hysteresis loop, the **Eq. 2.8** can be expressed in different forms. For the soft magnetic materials with low coercivity and high initial magnetic permeability, the coefficient a may be neglected, as it plays a significant role only in relatively low magnetic fields [507,510]. In such case the **Eq. 2.8** is simplified to:

$$M(H) = M_s\left(1 - \frac{b}{H^2}\right) + \chi H \tag{2.9}$$

On the other hand, for materials with lower permeability, the coefficient a may have considerable influence even at relatively high magnetic fields. In this situation the high field spontaneous magnetization term χH can be ignored, because it becomes dominant at very high magnetic fields [507,510]. As a result, the **Eq. 2.8** is then expressed as:

$$M(H) = M_s\left(1 - \frac{a}{H} - \frac{b}{H^2}\right) \tag{2.10}$$

Depend on the observed magnetization behaviour of high-temperature austenite phase and low-temperature martensite phase, the coefficient b were estimated following the **Eq. 2.9** and **Eq. 2.10**, respectively. The coefficient b and magnetization saturation M_s determined from the applied fitting were subsequently used to calculate the effective magnetic anisotropy constant K_{eff} in terms of the relation:

$$b = c\left(\frac{K_{\mathrm{eff}}}{\mu_0 M_s}\right)^2 \tag{2.11}$$

where c is the constant related to the crystal structure of the investigated material and μ_0 is the magnetic permeability constant.

Knowing the structural anisotropy of the examined alloy from other microstructural studies, the K_{eff} were finally calculated as:

$$K_{\mathrm{eff}} = \mu_0 M_{\mathrm{s}} \sqrt{\frac{b}{c}} \tag{2.12}$$

2.3.7 Nanoindentation (NHT)

The micro- and nanomechanical properties of the produced NiMnGa-based Heusler alloys were investigated in detail with the help of the Nanoindentation Tester (NHT^2, Anton Paar). The selection of this sophisticated characterization technique was forced by the small sizes of the fabricated materials, as conventional methods for examining mechanical properties are commonly destructive and require large bulk samples. Additionally, the NHT method allows for the determination of subtle differences of mechanical properties across the microstructure of the sample that are normally averaged in conventional mechanical testing.

2.3.7.1 The Oliver and Pharr approach

In the traditional hardness test, which forms the basis for the instrumented indentation, the hardness is calculated on the basis of the size of the penetration imprint left by the rigid probe and the applied static load. In this situation, no additional information on the elastoplastic deformation process is provided. In case of *instrumented indentation*, the current applied load and the indentation depth are continuously recorded throughout the loading and unloading sequence. Owing to this, the collected load-displacement curve (**Fig. 2.11(b)**) contains significant information on both plastic and elastic properties of the examined material. The most popular and commonly used method to quantitatively analyse the load-displacement curve is the Oliver and Pharr procedure originally proposed and described in [511] and later developed in [512]. This approach was also applied in the presented studies.

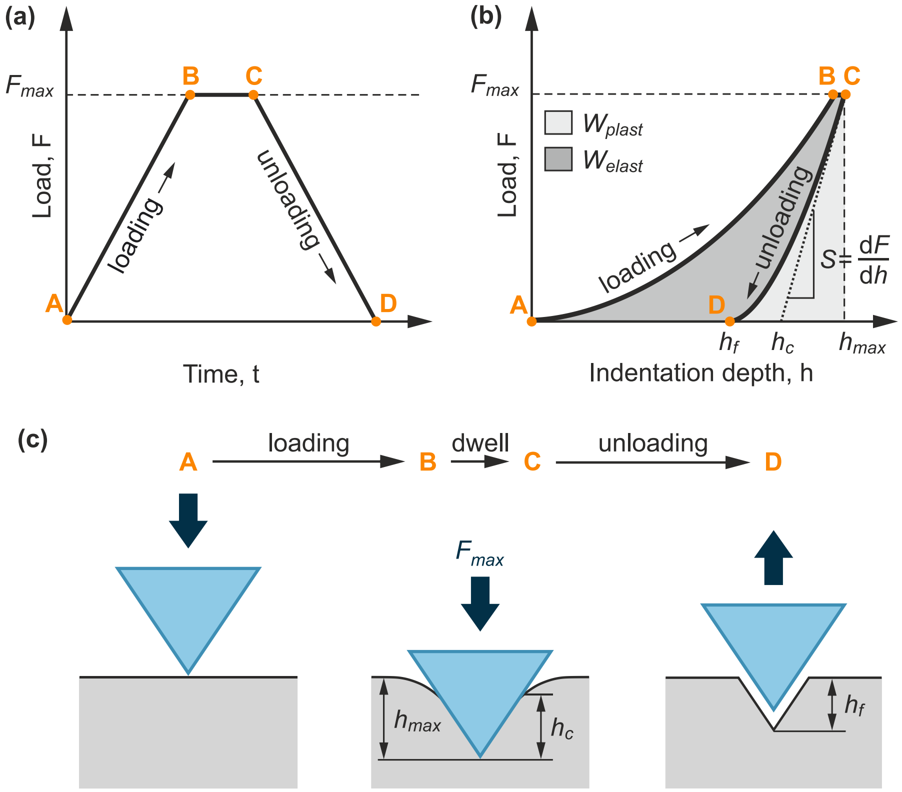

Fig. 2.11. The idea of the instrumented nanoindentation test. **(a)** Dependence of applied load ($F_{\max}$) versus time (t) during the load-control indentation. **(b)** The resultant load-displacement curve recorded during the indentation. **(c)** The corresponding displacement of the indenter during the indentation. The following characteristic stages of the indentation test are distinguished: A-B loading at constant loading rate, B-C dwell at maximum load and C-D unloading at constant unloading rate. The $h_{\max}$ is the maximum depth, h_c is the contact depth and h_f is the final depth. The unloading stiffens is denoted as S ($S = dF/dH$). The plastic and elastic deformation energy is indicated as an area under the corresponding loading and unloading part of the load-displacement curve.

The method proposed by Oliver and Pharr assumes that the loading process is governed by elastic and plastic deformation, whereas the unloading process is dominated only by elastic deformation (**Fig. 2.9(b)**). The characteristic parameters that may be obtained directly from the load-displacement curve are maximum load ($F_{\max}$), maximum depth of indentation ($h_{\max}$), the elastic stiffness (S) defined as an initial slope during unloading ($S = \mathrm{d}F/\mathrm{d}h$) and the final depth of indentation (h_{f}). The noticeable difference between $h_{\max}$ and h_{f} arises from the elastic nature of the material and is observable as a characteristic *sink-in* during maximum load (**Fig. 2.9(c)**). This elastic behaviour requires the introduction of the true corrected contact depth (h_{c}) at which the indenter is in full contact with the sample:

$$h_{\mathrm{c}} = h_{max} - \varepsilon \frac{F_{\max}}{S} \tag{2.13}$$

where ε is a geometry-dependant parameter of the indenter. In the presented studies, the three-sided pyramidal Berkovich indenter characterized by $\varepsilon = 0.75$ was used.

The proper estimation of h_c is essential to calculate the true projected contact area A. The contact area strongly depends on the geometry of the indenter, so any deviations from the ideal shape of the indenter tip must be compensated. To do that, the so-called *area function* is introduced. The area function is established on the basis of the calibration performed on standard fused quartz prior to the actual testing. What is important, the determined area function does not have a physical meaning and describes only the experimental calibration data. In the presented study, the area function is defined as:

$$A = C_0 {h_c}^2 + \sum_{i=1}^{7} C_i {h_c}^{1/2^i} \tag{2.14}$$

where C_0 and C_i ($i = 1$–7) are the polynomial coefficients of the obtained from the calibration data fitting.

The calculated contact area may be finally used to determine the instrumented hardness (H_{IT}) of the sample using the same relation as in case of the traditional hardness measurements, which is:

$$H_{IT} = \frac{F_{max}}{A} \tag{2.15}$$

The estimated hardness is related to the plastic properties of the sample. When it comes to elastic properties, the contact area and stiffness during unloading can be used to calculate the reduced elastic modulus (E_r) defined as:

$$E_r = \frac{S\sqrt{\pi}}{2\beta\sqrt{A}} \tag{2.16}$$

where β is the dimensionless geometrical correction factor equal to 1.034 for the Berkovich indenter.

The reduced elastic modulus specifies the elastic properties of the sample-indenter pair. Knowing the exact elastic properties of the diamond indenter, the elastic modulus of the examined material (E_{IT}) is estimated using the following relation:

$$E_{IT} = \frac{1 - {\upsilon_s}^2}{\frac{1}{E_r} - \frac{1 - {\upsilon_i}^2}{E_i}} \tag{2.17}$$

where ν_s is the Poisson’s ratio of the sample, and ν_i and E_i are the Poisson’s ratio and the elastic modulus of the indenter, respectively.

Further analysis of the load-displacement curve allows for estimation of the energy dissipated during indentation. The plastic energy (W_p) and elastic energy (W_e) correspond to the areas below the loading and unloading part of the curve, respectively (**Fig. 2.9(b)**). The distinction between elastic and plastic deformation energy is important to discuss the deformation behaviour of the investigated material. Considering this, the fraction of elastic energy in total deformation energy is defined as the *elastic energy ratio* (η_{IT}) and is expressed as follows:

$$\eta_{IT} = \frac{W_e}{W_e + W_p} \tag{2.18}$$

2.3.7.2 Nanoindentation mapping

In order to investigate the mechanical properties across the surface of the fabricated materials, the nanoindentation mapping technique was applied. In this technique, the single indentations are arranged in a uniform grid that covers the certain area of the sample. The statistical analysis of the data collected from this grid allowed for subsequent mapping of mechanical properties.

The single nanoindentation test was conducted in the load control mode with a maximum load of 50 mN. The loading and unloading rate was set to 100 mN/min with 10 s dwell at maximum load. The measurements were arranged in a 15 x 15 indentation grid with 15 μm space between neighbouring measurements, which results in a 210 μm × 210 μm map covered with 225 indentations. The preliminary study shows that the applied distance between the indentations prevents the adjacent measurements from having a mutual impact on their mechanical properties. Each single indentation was subsequently analysed according to the aforementioned Oliver and Pharr protocol. Finally, each indentation in a grid was characterized by hardness (H_{IT}), elastic modulus (E_{IT}) and elastic energy ratio (η_{IT}).

The obtained mechanical properties were subsequently subjected to statistical analysis. It is worth mentioning that there is no clear well-established methodology for such evaluation. This situation is caused by the large number of different investigated group materials and their various mechanical properties. In some approaches to indentation mapping, the authors analyse each mechanical property independently [513–516], whereas in other works the analysis is performed considering combined mechanical properties [517–520]. In addition, the statistical tools and methods described in the literature, including histograms [515], probability density functions (PDF) [513], cumulative density functions (CDF) [514,516], or clustering algorithms [517–520], also differ between the numerous studies reported on this topic. After the comprehensive examination of different statistical approaches, the Author of this thesis developed a proprietary methodology adapted to the studied metallic polycrystalline Heusler materials, which is summarized as flow chart in **Fig. 2.12**.

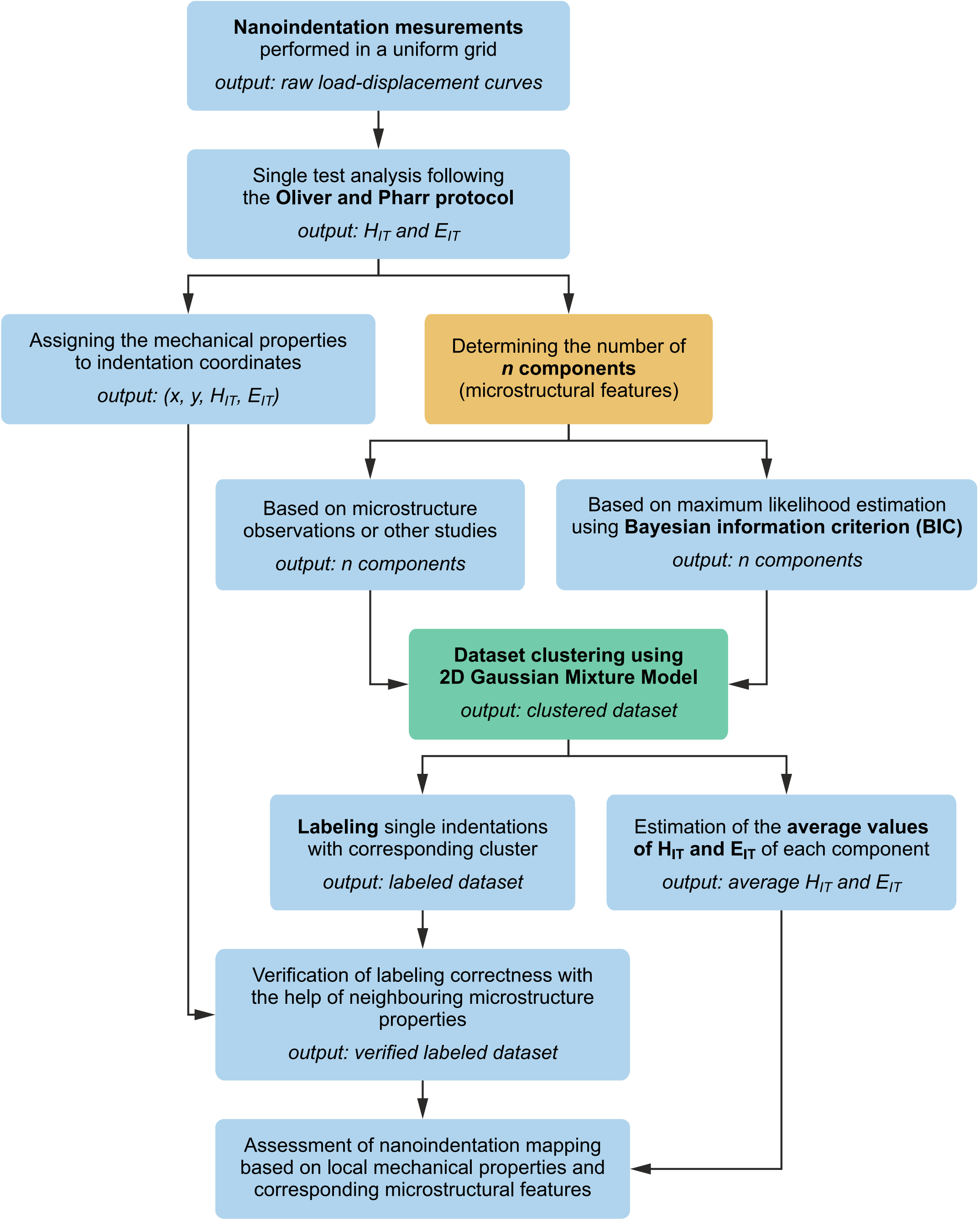

Fig. 2.12. Flow chart representing the nanoindentation mapping analysis methodology developed and applied in the presented thesis.

After preliminary studies, the produced NiMnGa-based alloys were assumed to be single phase materials characterized by austenite or martensite structure at room temperature without unwanted secondary phases. However, the probable different orientations of the austenite grains or the characteristic texture of the martensite laths may influence the distribution of the local mechanical properties of the fabricated materials. To include these deviations in the statistical analysis, the deconvolution method was incorporated into the presented methodology.

The first assumption for the deconvolution process is the strong relationship between the plastic and elastic properties of the materials. It means that each indentation is characterized by two subsidiary values: elastic modulus and hardness that may be plotted against each other (H_{IT} versus E_{IT}). If the mechanical properties of different microstructural features vary, certain groups of points will be observable, each corresponding to a different feature. However, in most situations, the number of groups (microstructural features) is not so evident and requires additional clustering to gain significant information about the dataset. In the proposed methodology, the two-dimensional Gaussian Mixture Model (2D GMM) was used as a probabilistic model for data clustering [521]. In general, the idea behind 2D GMM is to find a two-dimensional Gaussian distributions of probability that best models the input data. On its basis, it assumes that the investigated dataset originates from Gaussian distributions, which is a characteristic distribution for mechanical properties testing. Taking these assumptions into account, each indentation data point is expressed as a mixture of Gaussians with the following probability density function:

$$\begin{gathered} p(x) = \sum_{k=1}^{K} \phi_k \, \mathcal{N}(x. \mu_k, \Sigma_k) \\ \sum_{k=1}^{K} \phi_k = 1 \end{gathered} \tag{2.19}$$

where K is the number of Gaussian components, ϕ_k is the weight of each k-Gaussian, μ_k is the mean of k-Gaussian and Σ_k is the covariance of k-Gaussian.

The first equation shows that each investigated data point is a linear combination of K Gaussian distributions represented by mean and covariance. The second equation indicates that the weight coefficients must sum up to 1. Additionally, the *groupwise covariances* structure assuming the different means and covariances of K Gaussian distributions were used in this studies. In a view of discussed equations, the GMM is a linear superposition of K Gaussian distributions. However, it is also seen that the GMM is a generative probabilistic model for density estimation rather than a pure clustering algorithm. Due to that fact, it requires a determination of the number of Gaussian components (clusters) in the dataset. If the number of components (microstructure features) is known from other studies, it may be used in a model as a recognized known value. The best fitting parameters for each Gaussian will then be evaluated following the Expectation-Maximization (EM) algorithm [522]. However, in many situations, the number of components is unknown. In such a case, since GMM is basically a probability distribution, the likelihood of the optimal number of clusters can be evaluated using some analytic criteria. In the following methodology, the Bayesian Information Criterion (BIC) was used [523]. The BIC compares the models with different numbers of components previously optimized by the EM algorithm. The model characterized by the lowest BIC is considered the best fitting model that indicates the most probable number of clusters. What is especially significant, the use of BIC, instead of assumed number of components, makes the deconvolution results less dependent on the operator.

The proposed methodology for nanoindentation grid data analysis (**Fig. 2.12**) allowed to evaluate the number of different microstructural features on the tested areas of studied samples, as well as determine their corresponding mechanical properties. Furthermore, after clustering, each single indentation was labelled according to the corresponding cluster, allowing the localization and identification of particular microstructural feature. The labelled indentations were also finally used to estimate the average values of the elastic energy ratio for each microstructural component of the studied MSM materials.

3

Results and discussion

3.1 Microstructure and crystallography

3.1.1 Microstructure in macroscale

The first stage of microstructural characterisation of the fabricated NiMnGa-based multifunctional alloys was the microstructural analysis using polarised optical microscopy. The usage of polarised light allows to reveal the microstructural features of the investigated metallic materials without the additional chemical etching process, that is required in case of standard optical microscopy. **Fig. 3.1** presents the images for the water cooled reference undoped $Ni_{48}Mn_{32}Ga_{20}$ alloy and Co-doped $Ni_{48}Mn_{31}Ga_{20}Co_1$, $Ni_{48}Mn_{30}Ga_{20}Co_2$ and $Ni_{48}Mn_{28}Ga_{20}Co_4$ alloys, while **Fig. 3.2** shows the images for the alloys in which Co was gradually substituted by Fe, *i.e.* $Ni_{48}Mn_{28}Ga_{20}Co_3Fe_1$, $Ni_{50}Mn_{25}Ga_{21}Co_2Fe_2$, $Ni_{48}Mn_{28}Ga_{20}Co_1Fe_3$ and $Ni_{48}Mn_{28}Ga_{20}Fe_4$ alloy. The presented micrographs are organized in a way that shows two different areas for the same investigated sample. It is clearly seen in **Fig. 3.1** and **3.2** that due to the exposition to polarized light, the grain boundaries are evident in every investigated alloy. The slight differences in the intensity of the blue colour correspond to the different crystallographic orientation of individual grains of martensite laths. The observable colour contrast is also more noticeable at grain boundaries being the interface between two neighbouring grains. One needs to bear in mind that grain boundaries are classified as defects in the crystal lattice and that defects will be exposed in polarised light microscopy.

(a) $Ni_{48}Mn_{32}Ga_{20}$ **water cooled**

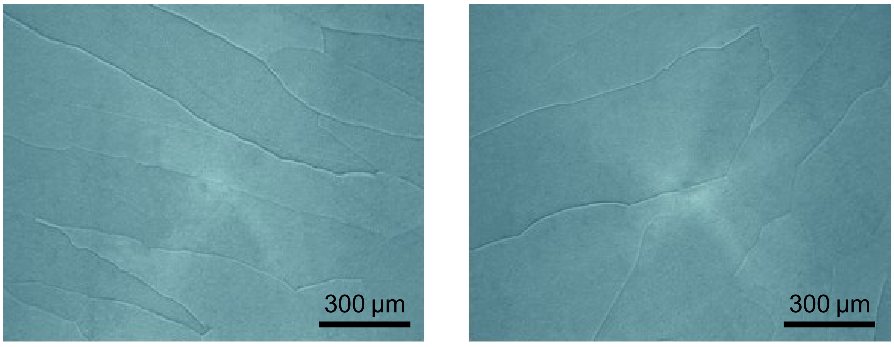

(b) $Ni_{48}Mn_{31}Ga_{20}Co_1$

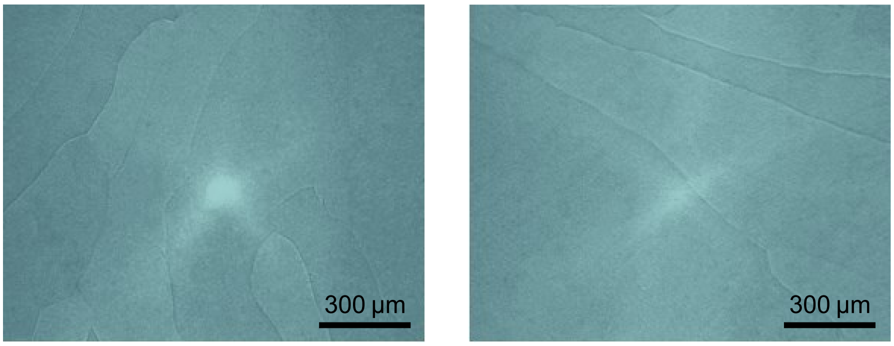

(c) $Ni_{48}Mn_{30}Ga_{20}Co_2$

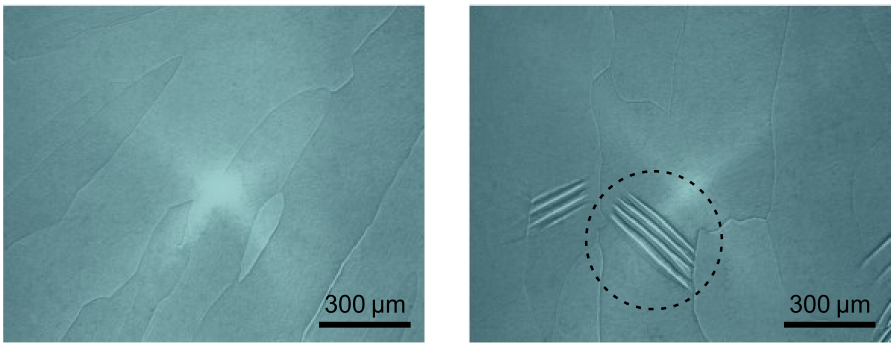

(d) $Ni_{48}Mn_{28}Ga_{20}Co_4$

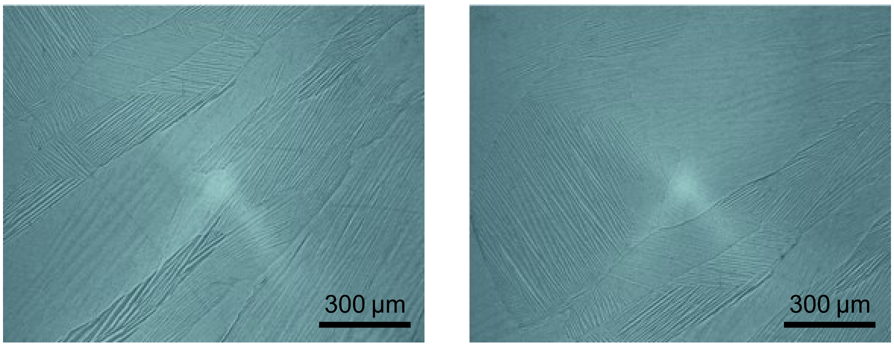

Fig. 3.1. Polarised light microscopy images of the water cooled **(a)** $Ni_{48}Mn_{32}Ga_{20}$, **(b)** $Ni_{48}Mn_{31}Ga_{20}Co_1$, **(c)** $Ni_{48}Mn_{30}Ga_{20}Co_2$ and **(d)** $Ni_{48}Mn_{28}Ga_{20}Co_4$ Heusler alloys.

(a) $Ni_{48}Mn_{28}Ga_{20}Co_3Fe_1$ **water cooled**

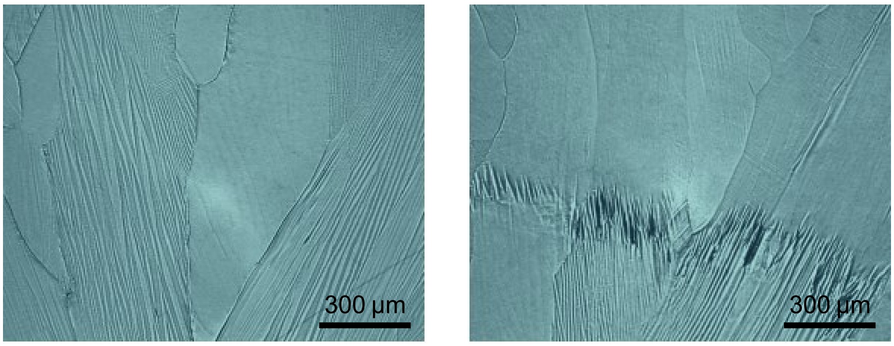

(b) $Ni_{50}Mn_{25}Ga_{21}Co_2Fe_2$

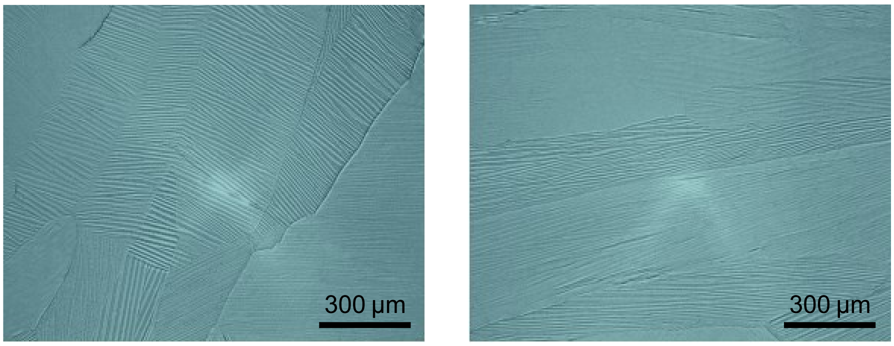

(c) $Ni_{48}Mn_{28}Ga_{20}Co_1Fe_3$

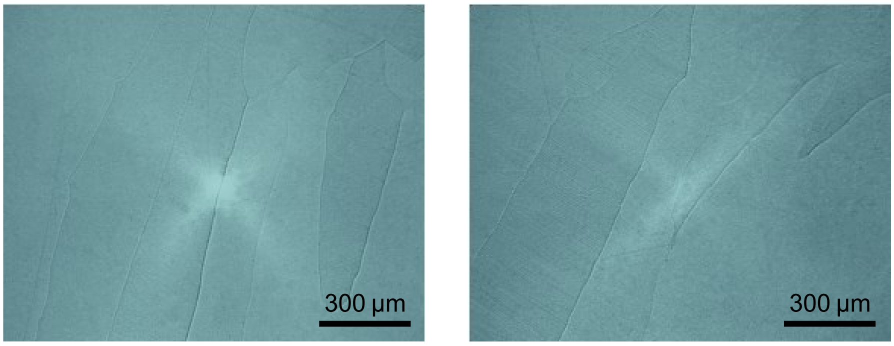

(d) $Ni_{48}Mn_{28}Ga_{20}Fe_4$

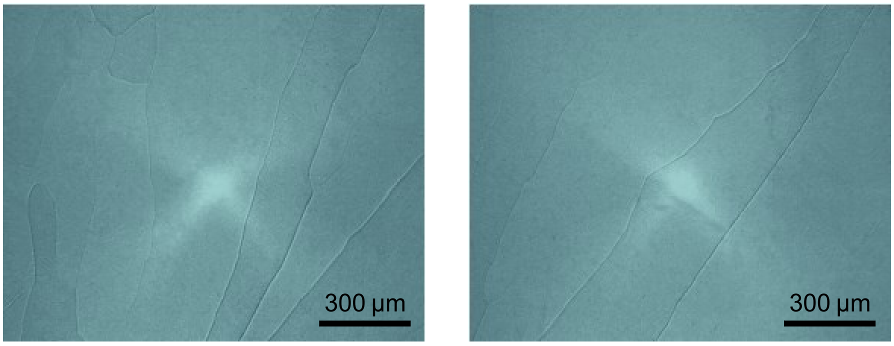

Fig. 3.2. Polarised light microscopy images of the water cooled **(a)** $Ni_{48}Mn_{28}Ga_{20}Co_3Fe_1$, **(b)** $Ni_{50}Mn_{25}Ga_{21}Co_2Fe_2$, **(c)** $Ni_{48}Mn_{28}Ga_{20}Co_1Fe_3$ and **(d)** $Ni_{48}Mn_{28}Ga_{20}Fe_4$ Heusler alloys.

In is seen in **Fig. 3.1** and **3.2** that all fabricated water cooled NiMnGa-based materials are characterised by single phase microstructure free of any additional unwanted phases. It confirms that the addition of Co, Fe, or Co and Fe up to 4 at.% is fully soluble in the proposed Ni-Mn-Ga compositions after the heat treatment procedure. Furthermore, at room temperature, the $Ni_{48}Mn_{32}Ga_{20}$, $Ni_{48}Mn_{31}Ga_{20}Co_1$, $Ni_{48}Mn_{30}Ga_{20}Co_2$, $Ni_{48}Mn_{28}Ga_{20}Co_1Fe_3$ and $Ni_{48}Mn_{28}Ga_{20}Fe_4$ alloys are in the austenitic state, whereas $Ni_{48}Mn_{28}Ga_{20}Co_4$, $Ni_{48}Mn_{28}Ga_{20}Co_3Fe_1$ and $Ni_{50}Mn_{25}Ga_{21}Co_2Fe_2$ are in the martensitic state, which indicates the counter influence of Co and Fe on the martensitic transformation temperature. Interestingly, some post-martensitic textures (marked by a circle in **Fig 3.1(c)**) were also observed for the $Ni_{48}Mn_{30}Ga_{20}Co_2$ alloy. The indicated post martensitic reliefs are located only in some part of austenitic grains and their morphology differs from that of the conventional martensitic structure depicted in **Fig. 3.1(d)** and **3.2(a)-(b)**.

What is worth noticing, both austenitic and martensitic microstructures inherited the characteristic texture created during the cooling process. In all microstructures presented in **Fig 3.1** and **3.2** the individual grains are elongated and arranged along one preferred direction, which reflects the heat gradient propagation during the fast water cooling process. As can be seen in the samples in the austenitic form (**Fig. 3.1(a)–(c)** and **Fig. 3.2(c)–(d)**), the individual grains are relatively large, ranging in width from 100 to 500 μm and length up to a single millimetre. In the case of martensitic alloys, the martensite laths are arranged within the boundaries of the former austenite phase. Depending on the crystallographic features of the prior austenite grains, the martensitic structure is characterized by various morphologies, differing by the specific boundary misorientations and sizes of single laths. No other evident differences between the microstructure of the Co-doped and Co-Fe-doped samples were noticed. However, the gradual substitution of Co by Fe results in the shift of the martensitic transformation temperature, which does not have the substantial influence on the particular austenite or martensite microstructure.

When it comes to air cooled NiMnGa-based Heusler materials, **Fig. 3.3** and **3.4** present the Co-doped and Co-Fe-doped alloys, respectively. The arrangement of these figures is the same, as in case of the water cooled samples (**Fig. 3.1** and **3.2**). Again, it is clear that the same alloys exhibit an austenitic or martensitic microstructure. The austenitic phase is present in the $Ni_{48}Mn_{32}Ga_{20}$, $Ni_{48}Mn_{31}Ga_{20}Co_1$, $Ni_{48}Mn_{30}Ga_{20}Co_2$, $Ni_{48}Mn_{28}Ga_{20}Co_1Fe_3$ and $Ni_{48}Mn_{28}Ga_{20}Fe_4$ alloys, while the martensitic phase is present in the $Ni_{48}Mn_{28}Ga_{20}Co_4$, $Ni_{48}Mn_{28}Ga_{20}Co_3Fe_1$ and $Ni_{50}Mn_{25}Ga_{21}Co_2Fe_2$ alloys. This time, no post-martensitic relief was observed in any air cooled materials, including the $Ni_{48}Mn_{30}Ga_{20}Co_2$ sample.

The sizes of individual austenite or martensite grains of air cooled samples are similar to those of water cooled ones. In contrast, air cooled samples exhibit less of the distinctive texture that is affected by the heat gradient throughout the cooling process. During optical microscopy investigations, the lack of an evident texture direction was mostly apparent in the centre of the austenitic specimens. For instance, this loss of microstructure texture can be seen in the $Ni_{48}Mn_{31}Ga_{20}Co_1$ (**Fig. 3.3(b)**), $Ni_{48}Mn_{30}Ga_{20}Co_2$ (**Fig. 3.3(c)**) and $Ni_{48}Mn_{28}Ga_{20}Co_1Fe_3$ (**Fig. 3.4(c)**) alloys. On the other hand, in the case of air cooled materials in the martensitic state, the strong directional texture is still observed across the whole examined cross sections (**Fig. 1(d)** and **Fig. 2(a)–(b)**). The difference in cooling rates between the water and air medium did not cause any additional noticeable variations in the microstructural properties, despite these minor variations in the texture.

Regarding the slowest cooling alloys, **Fig. 3.5** and **3.6** presents furnace-cooled NiMnGa-based samples arranged similarly to water and air cooled materials, *i.e.* **Fig. 3.5** shows alloys with Co doping and **Fig. 3.4** depicts samples where Fe gradually replacing Co. What is interesting, for the furnace cooled Heusler materials, the variations in microstructural features caused by very slow cooling rate are different for the Co-doped and Fe-Co-doped specimens.

When it comes to Co-doped alloys (**Fig. 3.5**), their microstructures generally looks very similar to the corresponding water and air cooled samples. Despite the extremely slow cooling rate, these specimens still have the distinctive texture, mainly on the outside of the investigated cross sections. Although the observed directional texture is less prominent than in samples that were quickly cooled in water, the elongation of the grains along the radial direction is still visible. The biggest difference in microstructural features between the water or air cooled sample and the furnace cooled Co-doped alloys is found for the $Ni_{48}Mn_{31}Ga_{20}Co_1$ alloy depicted in **Fig. 3.5(a)**. It is seen that the microstructure of this alloy contains significantly larger grains than those in corresponding water or air cooled samples, but also those of other studied materials in austenitic state, regardless of their prior cooling process.

The Co-Fe-doped alloys depicted in **Fig. 3.6** showed the most substantial changes between furnace and water/air cooled NiMnGa-based materials. For example, the $Ni_{48}Mn_{28}Ga_{20}Co_3Fe_1$ specimen, which was characterized by the martensitic structure for the water and air cooled materials, is nearly entire austenitic after furnace cooling (**Fig. 3.6(a)**). Throughout the whole cross section of the investigated alloy, only occasional post martensitic reliefs (depicted by a black circle in **Fig. 3.6(a)**) were identified. The morphology of these post-martensitic structures is very similar to the one observed for the water cooled $Ni_{48}Mn_{30}Ga_{20}Co_2$ sample. It suggests that these post martensitic reliefs appear close to the martensitic transformation temperature and that slow furnace cooling shifts this temperature for the $Ni_{48}Mn_{28}Ga_{20}Co_3Fe_1$ alloy. For the Co-Fe-doped alloys, the fully martensitic structure is only observed for the $Ni_{50}Mn_{25}Ga_{21}Co_2Fe_2$ sample, however, in this case, the microstructural characteristics of martensite also differ from those of other water and air cooled samples. The greatest difference is the size of the prior austenite grains that are significantly larger and less directionally textured in the furnace cooled $Ni_{50}Mn_{25}Ga_{21}Co_2Fe_2$ alloy, resulting in larger and more uniform martensite laths (**Fig. 3.6(b)**). For the furnace cooled $Ni_{48}Mn_{28}Ga_{20}Co_1Fe_3$ and

$Ni_{48}Mn_{28}Ga_{20}Fe_4$ alloys, their microstructure is almost identical to that of the corresponding water and air cooled samples. since they share the same grain sizes and similar directional texture.

(a) $Ni_{48}Mn_{32}Ga_{20}$

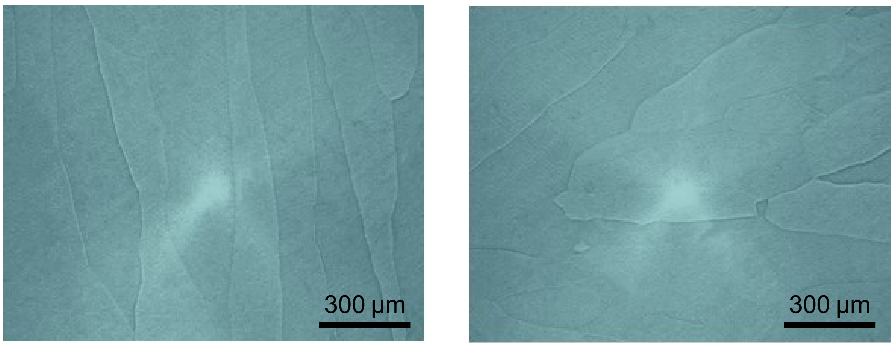

(b) $Ni_{48}Mn_{31}Ga_{20}Co_1$

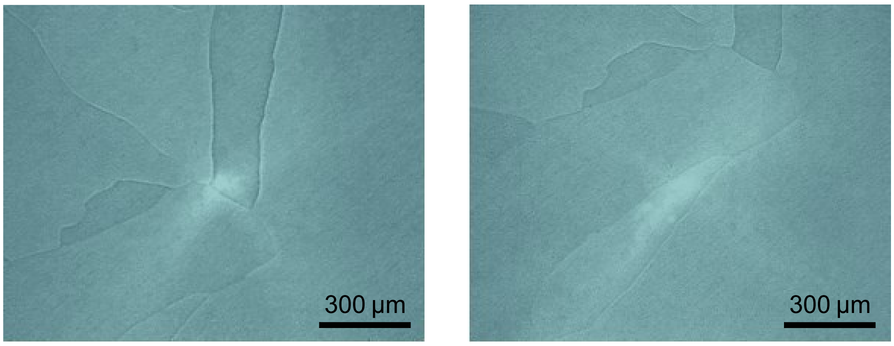

(c) $Ni_{48}Mn_{30}Ga_{20}Co_2$

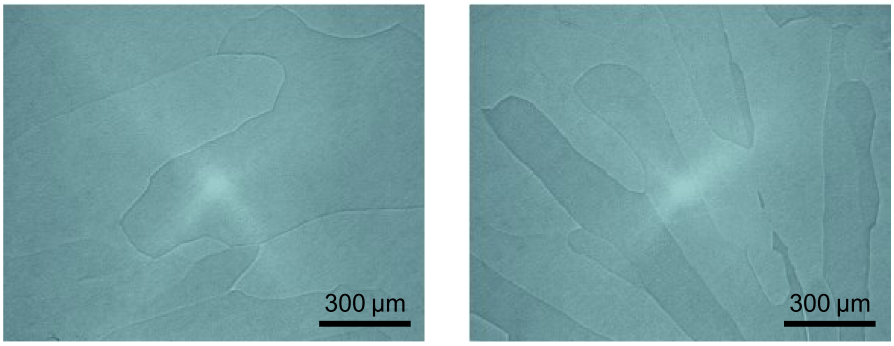

(d) $Ni_{48}Mn_{28}Ga_{20}Co_4$

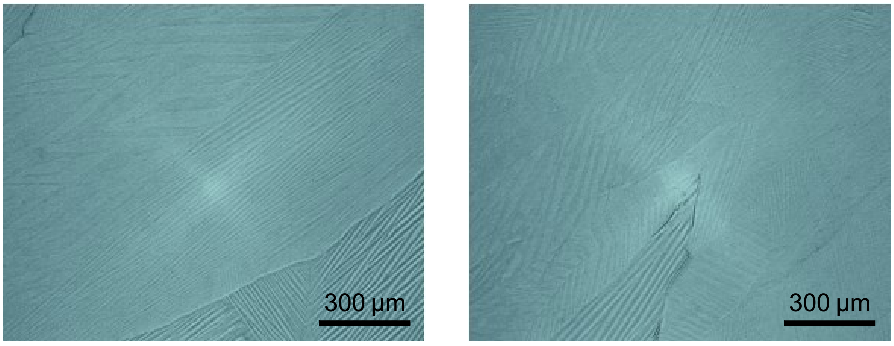

Fig. 3.3. Polarised light microscopy images of the air cooled **(a)** $Ni_{48}Mn_{32}Ga_{20}$, **(b)** $Ni_{48}Mn_{31}Ga_{20}Co_1$, **(c)** $Ni_{48}Mn_{30}Ga_{20}Co_2$ and **(d)** $Ni_{48}Mn_{28}Ga_{20}Co_4$ Heusler alloys.

(a) $Ni_{48}Mn_{28}Ga_{20}Co_3Fe_1$

air cooled

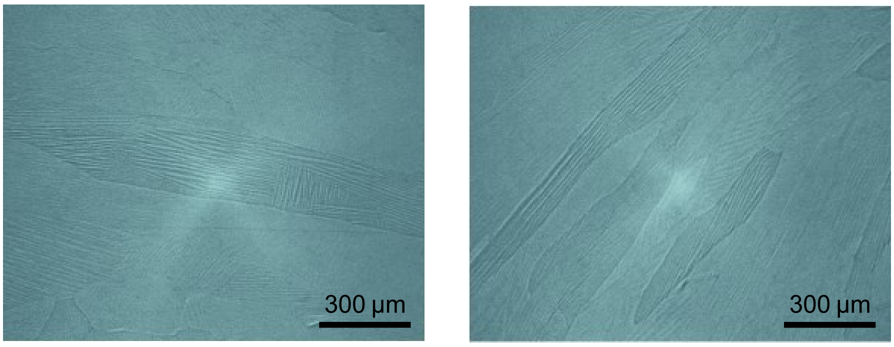

(b) $Ni_{50}Mn_{25}Ga_{21}Co_2Fe_2$

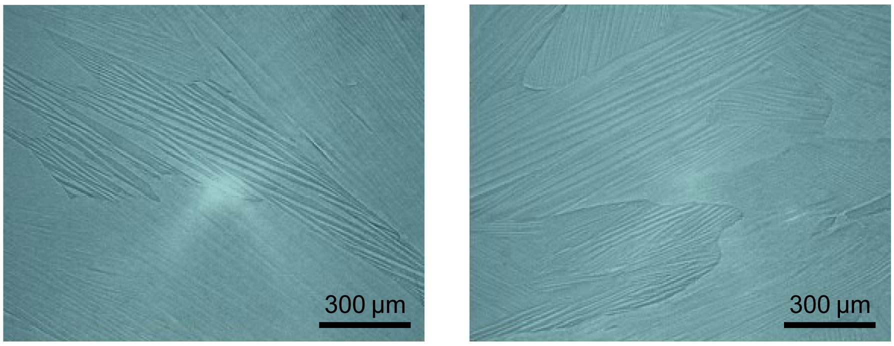

(c) $Ni_{48}Mn_{28}Ga_{20}Co_1Fe_3$

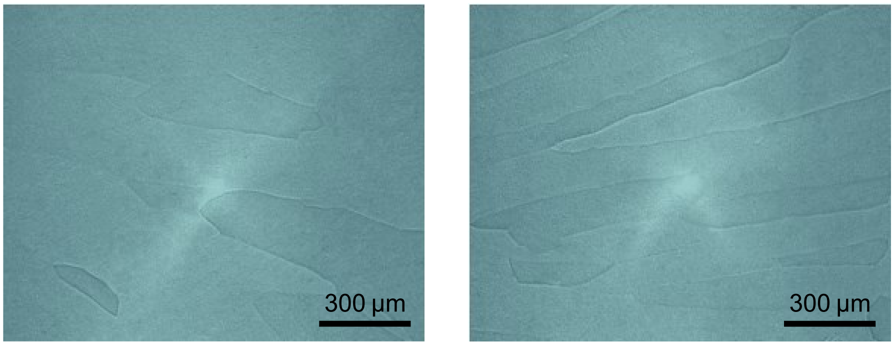

(d) $Ni_{48}Mn_{28}Ga_{20}Fe_4$

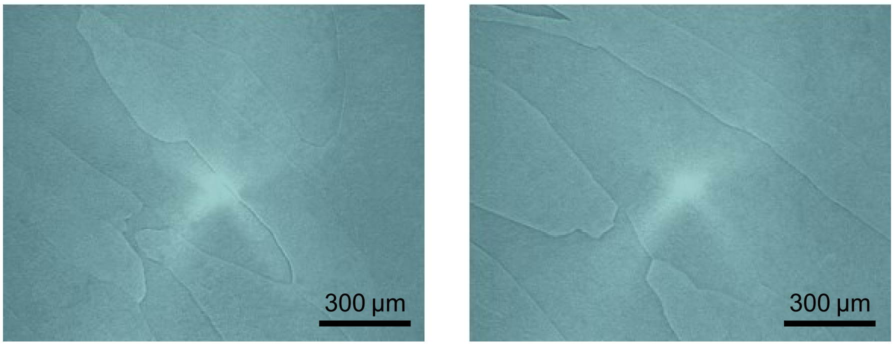

Fig. 3.4. Polarised light microscopy images of the air cooled **(a)** $Ni_{48}Mn_{28}Ga_{20}Co_3Fe_1$, **(b)** $Ni_{50}Mn_{25}Ga_{21}Co_2Fe_2$, **(c)** $Ni_{48}Mn_{28}Ga_{20}Co_1Fe_3$ and **(d)** $Ni_{48}Mn_{28}Ga_{20}Fe_4$ Heusler alloys.

(a) $Ni_{48}Mn_{28}Ga_{20}Co_3Fe_1$ **furnace cooled**

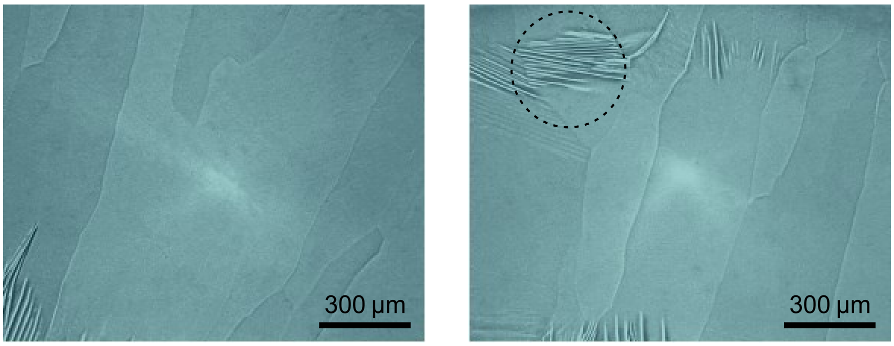

(b) $Ni_{50}Mn_{25}Ga_{21}Co_2Fe_2$

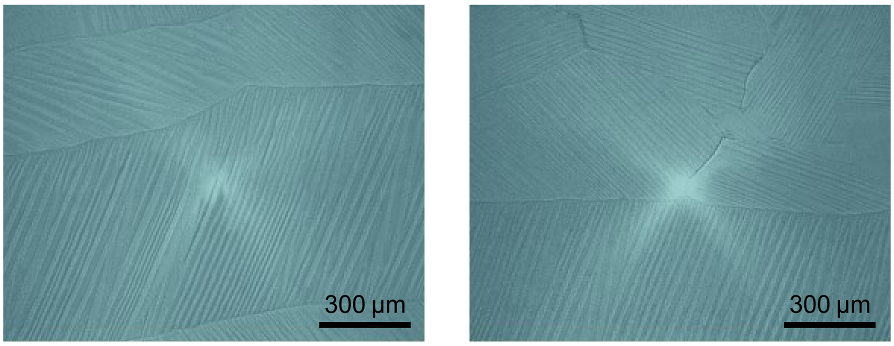

(c) $Ni_{48}Mn_{28}Ga_{20}Co_1Fe_3$

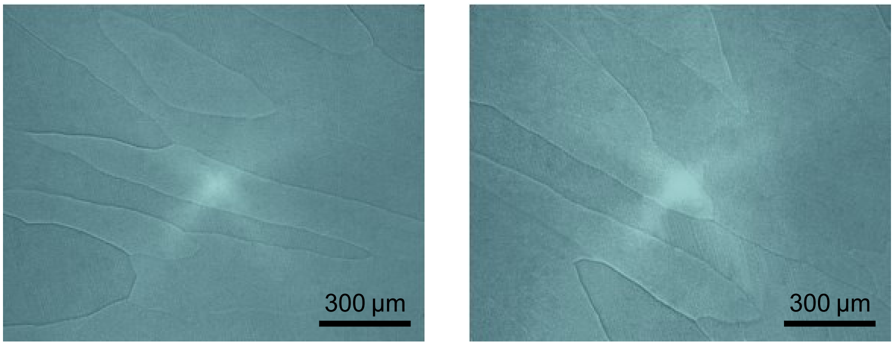

(d) $Ni_{48}Mn_{28}Ga_{20}Fe_4$

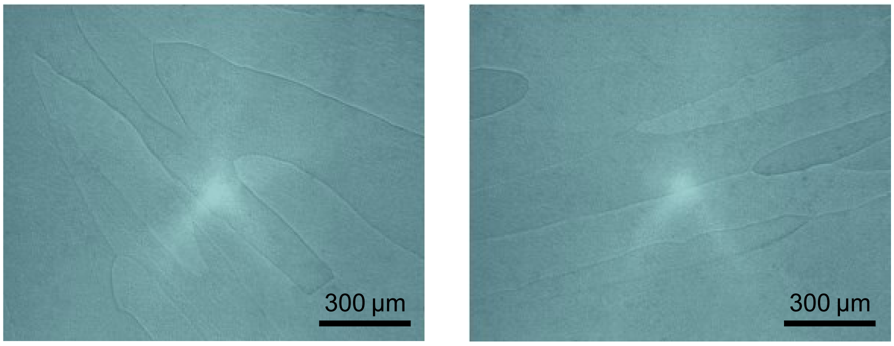

Fig. 3.5. Polarised light microscopy images of the air cooled **(a)** $Ni_{48}Mn_{32}Ga_{20}$, **(b)** $Ni_{48}Mn_{31}Ga_{20}Co_1$, **(c)** $Ni_{48}Mn_{30}Ga_{20}Co_2$ and **(d)** $Ni_{48}Mn_{28}Ga_{20}Co_4$ Heusler alloys.

Fig. 3.6. Polarised light microscopy images of the air cooled **(a)** $Ni_{48}Mn_{28}Ga_{20}Co_3Fe_1$, **(b)** $Ni_{50}Mn_{25}Ga_{21}Co_2Fe_2$, **(c)** $Ni_{48}Mn_{28}Ga_{20}Co_1Fe_3$ and **(d)** $Ni_{48}Mn_{28}Ga_{20}Fe_4$ Heusler alloys.

The figures presented from **Fig. 3.1** to **3.6** focus on the microstructural differences between the NiMnGa-based alloys with different chemical compositions. In order to illustrate and review the differences between various cooling techniques for alloys with the same chemical compositions, the obtained images are also summarized in **Fig. 3.7** and **3.8**. **Fig. 3.7** presents the selected microstructure image of the produced Co-doped Ni-Mn-Ga alloys for each cooling procedure and **Fig. 3.8** depicts the further micrographs of the Fe-Co-doped alloys organise in the exact same way.

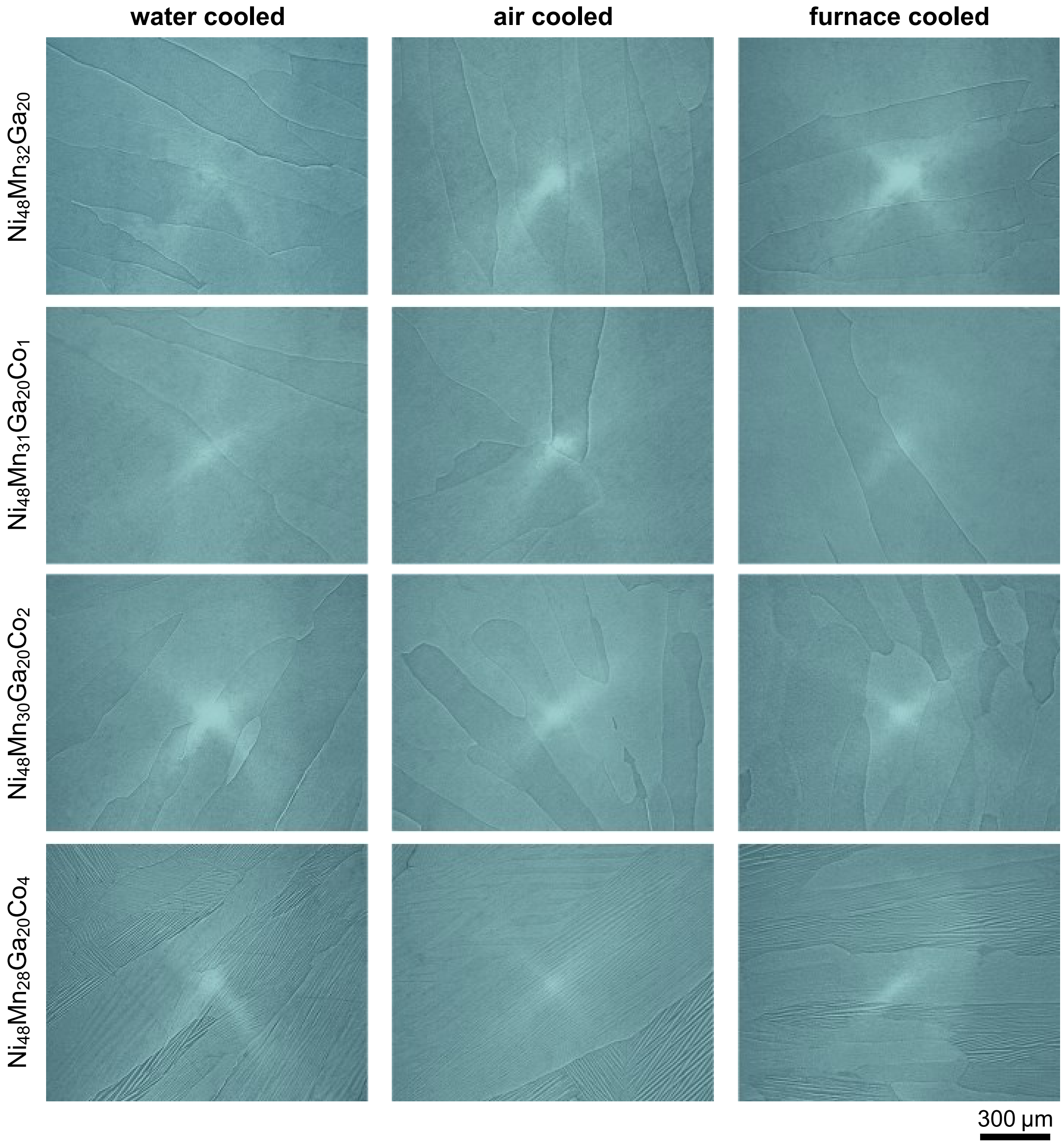

Fig. 3.7. Polarised light microscopy images of the water, air and furnace cooled $Ni_{48}Mn_{32}Ga_{20}$, $Ni_{48}Mn_{31}Ga_{20}Co_1$, $Ni_{48}Mn_{30}Ga_{20}Co_2$ and $Ni_{48}Mn_{28}Ga_{20}Co_4$ Heusler alloys. The uniform scale is presented in the bottom right hand corner.

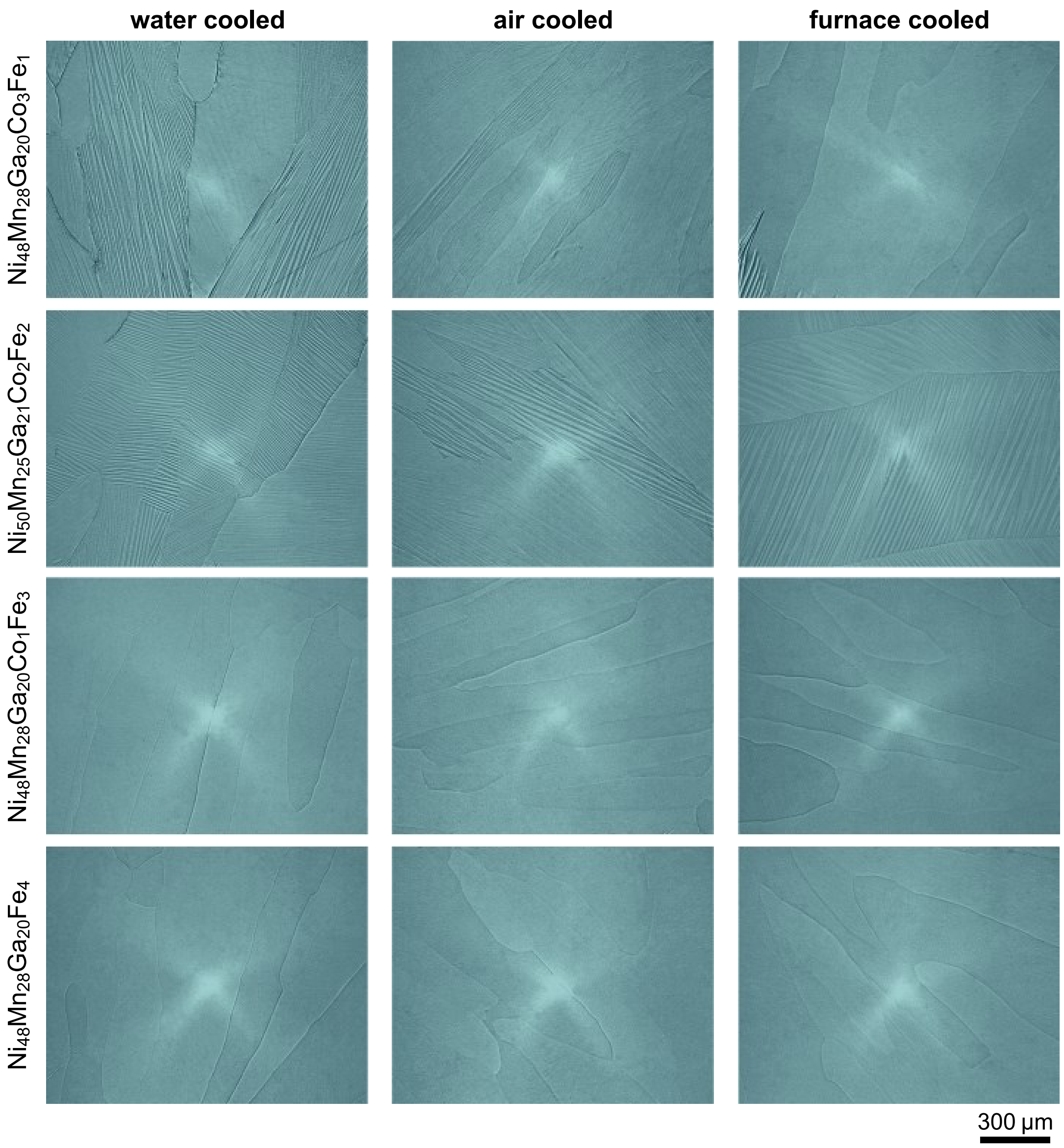

Fig. 3.8. Polarised light microscopy images of the water, air and furnace cooled $Ni_{48}Mn_{28}Ga_{20}Co_3Fe_1$, $Ni_{50}Mn_{25}Ga_{21}Co_2Fe_2$, $Ni_{48}Mn_{28}Ga_{20}Co_1Fe_3$ and $Ni_{48}Mn_{28}Ga_{20}Fe_4$ Heusler alloys. The uniform scale is presented in the bottom right hand corner.

This direct comparison of different cooling procedures in **Fig. 3.7** and **3.8** demonstrates that the aforementioned differences between water, furnace and air cooled samples are not so obvious and require the careful observations to see the discussed changes in microstructural features. Generally, the grain size in all fabricated materials is comparable under different cooling conditions and the only exceptions were found for the austenitic $Ni_{48}Mn_{31}Ga_{20}Co_1$ and martensitic $Ni_{50}Mn_{25}Ga_{21}Co_2Fe_2$ alloys. At room temperature, all water, air and furnace cooled $Ni_{48}Mn_{32}Ga_{20}$, $Ni_{48}Mn_{31}Ga_{20}Co_1$, $Ni_{48}Mn_{30}Ga_{20}Co_2$, $Ni_{48}Mn_{28}Ga_{20}Co_1Fe_3$ and $Ni_{48}Mn_{28}Ga_{20}Fe_4$ alloys are in austenitic state, whereas $Ni_{48}Mn_{28}Ga_{20}Co_4$ and $Ni_{50}Mn_{25}Ga_{21}Co_2Fe_2$ are in martensitic state. The only exception is the

$Ni_{48}Mn_{28}Ga_{20}Co_3Fe_1$ alloy, which remains austenitic after extremely slow furnace cooling but becomes totally martensitic after cooling in water or air.

3.1.2 Microstructure in microscale

Scanning electron microscopy investigations in secondary electrons and backscattered electrons modes were carried out to study the topographical and material (or crystallography) contrast of the produced NiMnGa-based multifunctional alloys. The SEM observations were conducted at magnifications higher than those of optical microscopy, because of the significantly larger magnification capability of this technique. **Fig. 3.9** presents the example SE and corresponding BSE images for the same area of the sample for the reference $Ni_{48}Mn_{32}Ga_{20}$ and Co-doped $Ni_{48}Mn_{31}Ga_{20}Co_1$, $Ni_{48}Mn_{30}Ga_{20}Co_2$ and $Ni_{48}Mn_{28}Ga_{20}Co_4$ alloys. The equivalent SE and BSE images for the Fe-Co-doped $Ni_{48}Mn_{28}Ga_{20}Co_3Fe_1$, $Ni_{50}Mn_{25}Ga_{21}Co_2Fe_2$, $Ni_{48}Mn_{28}Ga_{20}Co_1Fe_3$ and $Ni_{48}Mn_{28}Ga_{20}Fe_4$ alloys are shown in **Fig. 3.10**.

It is important to keep in mind when discussing SE images that the prepared specimens were carefully polished without any additional chemical etching. Because of this, the final topography of the sample should theoretically be perfectly flat, which consequently results in negligible SE contrast. This assumption was confirmed for all water cooled alloys in austenitic state, including $Ni_{48}Mn_{32}Ga_{20}$, $Ni_{48}Mn_{31}Ga_{20}Co_1$ and $Ni_{48}Mn_{30}Ga_{20}Co_2$ samples from **Fig. 3.9**, as well as $Ni_{48}Mn_{28}Ga_{20}Co_1Fe_3$ and $Ni_{48}Mn_{28}Ga_{20}Fe_4$ alloys from **Fig. 3.10**. The slight SE contrast observed for some aforementioned samples is caused by the fact that the SE signal also, to some extent, depends on other local surface properties, such as crystallographic alterations or changes in the atomic number of elements. When topographical features are absent from very flat samples, the typically ignored influence of other elements becomes more apparent and may eventually result in very little contrast that can be still detectable. On the other hand, in the case of specimens in martensitic state, *i.e.* $Ni_{48}Mn_{28}Ga_{20}Co_4$, $Ni_{48}Mn_{28}Ga_{20}Co_3Fe_1$ and $Ni_{50}Mn_{25}Ga_{21}Co_2Fe_2$ alloys, the observed SE contrast may stem from the actual topographical deviations. This is because the martensitic structure is distinguished by specified micrometric relief that affects the completely flat surface due to its crystallographic nature. The intensity of this contrast is obviously affected by the local morphology of the particular martensitic structure, therefore it may differs between the studied samples. For the water cooled alloys, the highest topographical contrast is observed for the $Ni_{48}Mn_{28}Ga_{20}Co_3Fe_1$, sample depicted in **Fig. 3.10(a)**.

The BSE signal, which is mostly influenced by the atomic number of elements and partially by crystallographic orientation, may provide additional information about the microstructure of the material for the flat, unetched metallic samples. For all of the examined water cooled alloys, it is generally observed that material contrast is relatively low. Even at high magnification, there are no unexpected precipitations or secondary phases to be seen in the presented micrographs, which supports the consistent single-phase microstructure of the manufactured materials. The slight contrast observed in the BSE images is related to the different crystallographic orientation of large austenite grains or martensite laths for alloys in the austenitic or martensitic state, respectively. In such a case, the intensity of the BSE contrast depends on the level of crystallographic disorientation between the neighbouring grains. This phenomenon occurs at random across the cross sections of all produced alloys and do not depends on chemical composition or heat treatment conditions. For instance, for the water cooled materials in austenitic state the high BSE contrast is observed for the $Ni_{48}Mn_{31}Ga_{20}Co_1$ (**Fig. 3.9(b)**) or $Ni_{48}Mn_{28}Ga_{20}Fe_4$ (**Fig. 3.10(d)**) alloys, whereas almost unnoticeable contrast is seen for the $Ni_{48}Mn_{32}Ga_{20}$ (**Fig. 3.9(a)**) or $Ni_{48}Mn_{28}Ga_{20}Co_1Fe_3$ (**Fig. 3.10(c)**) sample. It should be emphasized that the images discussed here are consistent with previous polarized light microscopy studies (Section 3.1.1).

In regards to air cooled NiMnGa-based alloys, **Fig. 3.11** and **3.12** shows the SEM images of the air cooled specimens that are presented similarly to **Fig. 3.9** and **3.10**. **Fig. 3.11** depicts the reference and Co-doped alloys, while **Fig 3.12** shows the Fe-Co-doped materials. Again, no additional secondary phases are observed in all studied multifunctional Heuslers, confirming the single-phase microstructure of water cooled materials. Furthermore, the origin of both SE and BSE signals is determined by the same conditions as in the aforementioned water cooled Heuslers. Thus, the SE and BSE images presented in **Fig. 3.11** and **3.12** are mostly influence by the local morphology of the martensite phase or crystallographic misorientation of austenite grains, respectively. The highest SE and the corresponding BSE signal is observed for the $Ni_{48}Mn_{28}Ga_{20}Co_3Fe_1$ alloy (**Fig. 3.12(a)**) characterized by relatively large martensite laths, which form a notable topographic relief and also differs by crystallographic orientation. When it comes to specimens in austenitic state, the majority of the studied alloys reflect almost undetectable BSE contrasts and the most evident difference between the BSE signal of neighbouring grain is seen for the $Ni_{48}Mn_{28}Ga_{20}Co_1Fe_3$ alloy depicted in **Fig. 3.12(c)**. It should be also stressed that no additional significant differences between water and air cooled materials were noticed during the SEM investigation.

Concerning the slowest cooled NiMnGa-based specimens, **Fig. 3.13** and **3.14** presents the furnace cooled Co-doped and Fe-Co-doped alloys, respectively. These figures are arranged in the same way as in the case of water and air cooled samples. It can be observed once more that furnace-cooled alloys are single-phase materials with no unfavourable secondary phases. It demonstrates the good solubility of Co and Fe in Ni-Mn-Ga composition, which does not require the fast cooling to increase the saturation of the alloying elements. In addition, the general microstructure of furnace cooled materials shown in **Fig. 3.13** and **3.14** is comparable to that of water and air cooled materials, demonstrating the differences in crystallographic orientation of large austenite grains.

It is interesting to note that the $Ni_{48}Mn_{28}Ga_{20}Co_{3}Fe_{1}$ alloy is found in an austenitic state after furnace cooling (**Fig. 3.14(a)**), while it is fully martensitic after water (**Fig. 3.10(a)**) or air cooling (**Fig. 12(a)**). The presented SEM findings are in line with optical microscopy investigations.

(a) $Ni_{48}Mn_{32}Ga_{20}$ **water cooled**

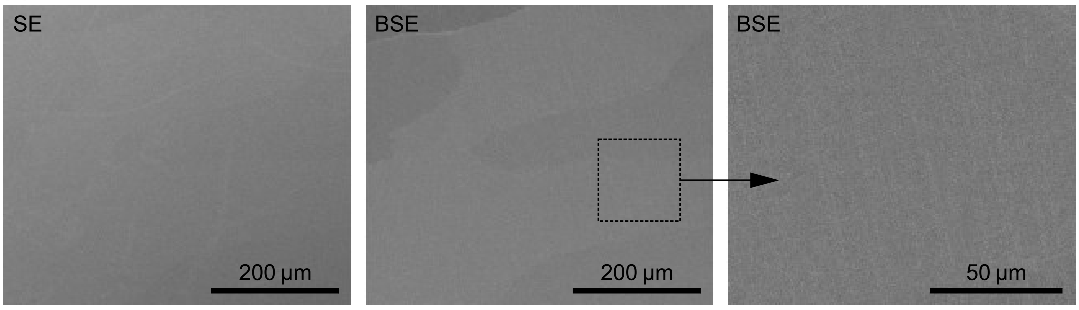

(b) $Ni_{48}Mn_{31}Ga_{20}Co_{1}$

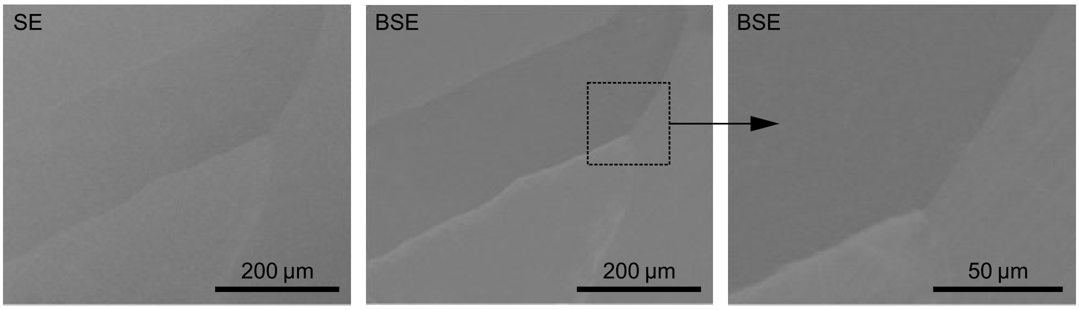

(c) $Ni_{48}Mn_{30}Ga_{20}Co_{2}$

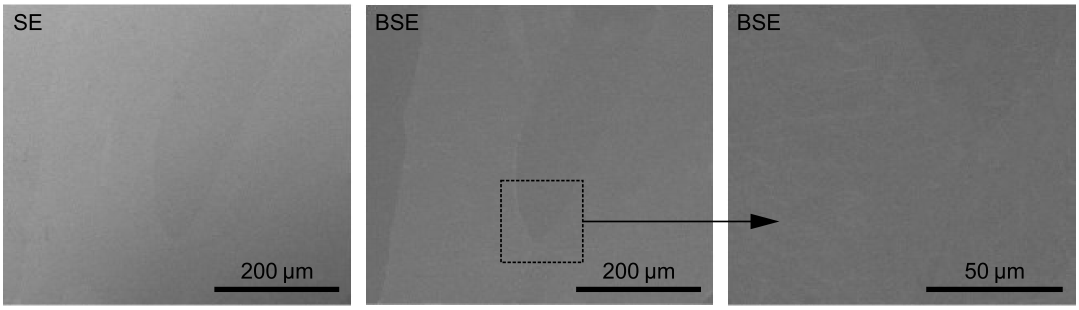

(d) $Ni_{48}Mn_{28}Ga_{20}Co_{4}$

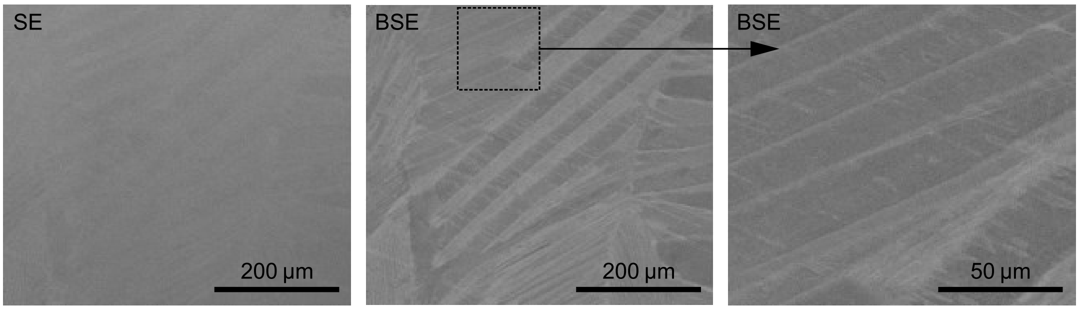

Fig. 3.9. SEM images obtained with the SE and BSE detector for the water cooled **(a)** $Ni_{48}Mn_{32}Ga_{20}$, **(b)** $Ni_{48}Mn_{31}Ga_{20}Co_{1}$, **(c)** $Ni_{48}Mn_{30}Ga_{20}Co_{2}$ and **(d)** $Ni_{48}Mn_{28}Ga_{20}Co_{4}$ magnetic shape memory alloys.

(a) $Ni_{48}Mn_{28}Ga_{20}Co_3Fe_1$

water cooled

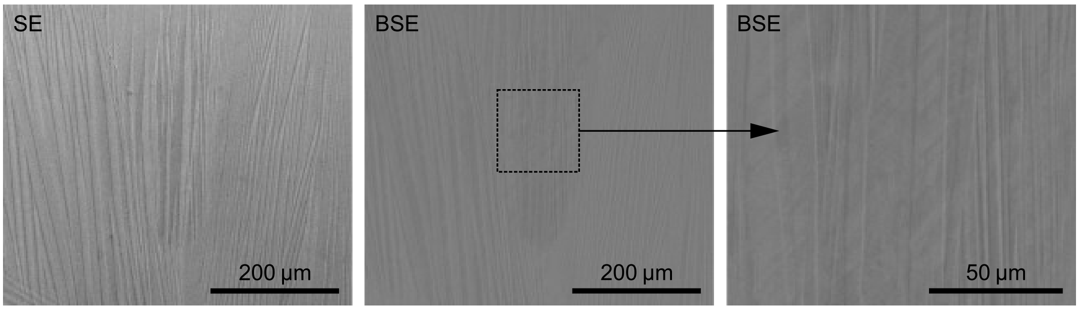

(b) $Ni_{50}Mn_{25}Ga_{21}Co_2Fe_2$

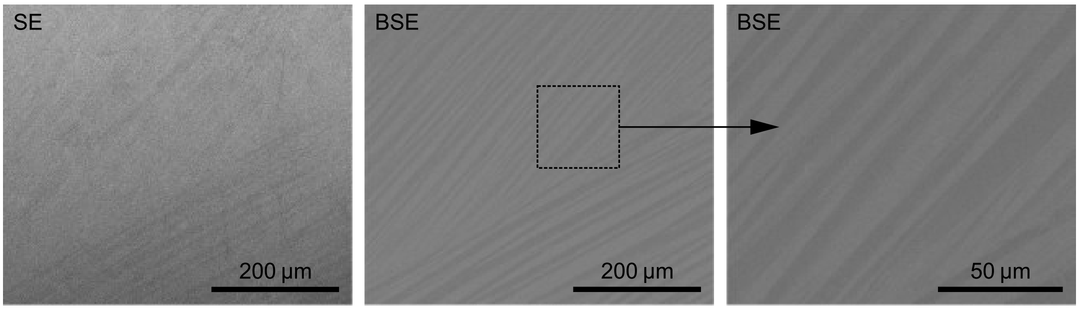

(c) $Ni_{48}Mn_{28}Ga_{20}Co_1Fe_3$

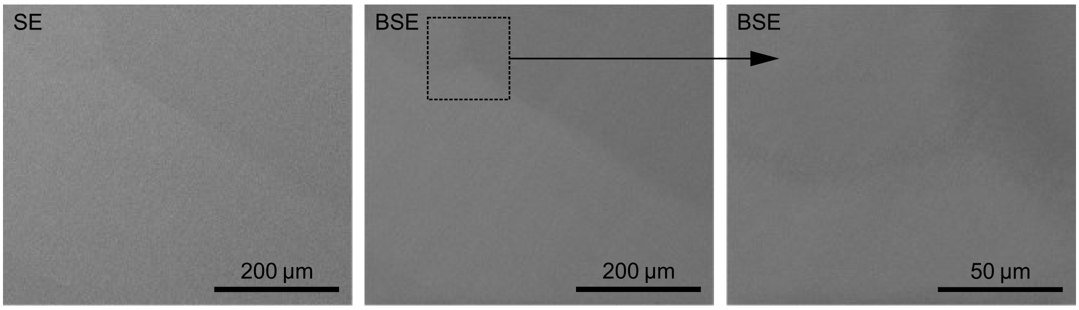

(d) $Ni_{48}Mn_{28}Ga_{20}Fe_4$

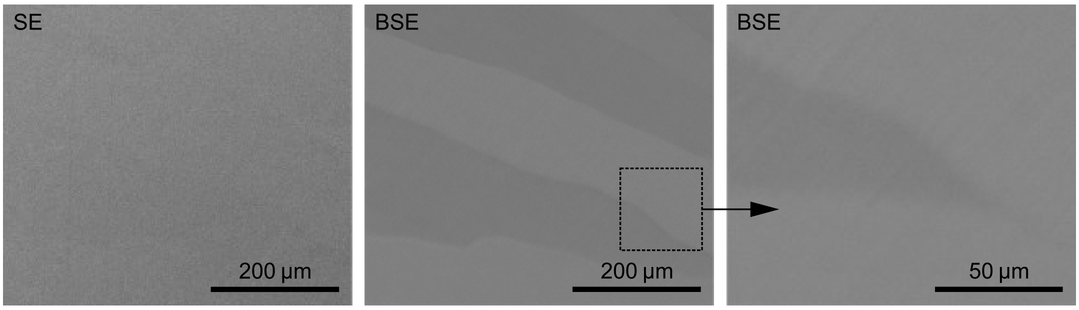

Fig. 3.10. SEM images obtained with the SE and BSE detector for the water cooled **(a)** $Ni_{48}Mn_{28}Ga_{20}Co_3Fe_1$, **(b)** $Ni_{50}Mn_{25}Ga_{21}Co_2Fe_2$, **(c)** $Ni_{48}Mn_{28}Ga_{20}Co_1Fe_3$ and **(d)** $Ni_{48}Mn_{28}Ga_{20}Fe_4$ magnetic shape memory alloys.

(a) $Ni_{48}Mn_{32}Ga_{20}$ **air cooled**

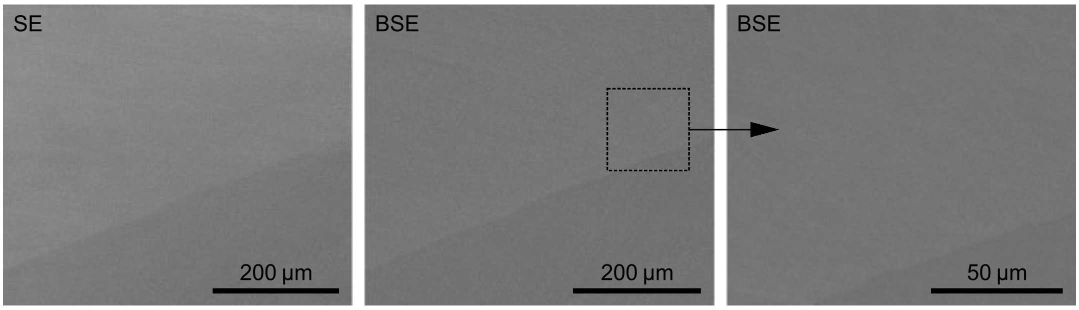

(b) $Ni_{48}Mn_{31}Ga_{20}Co_{1}$

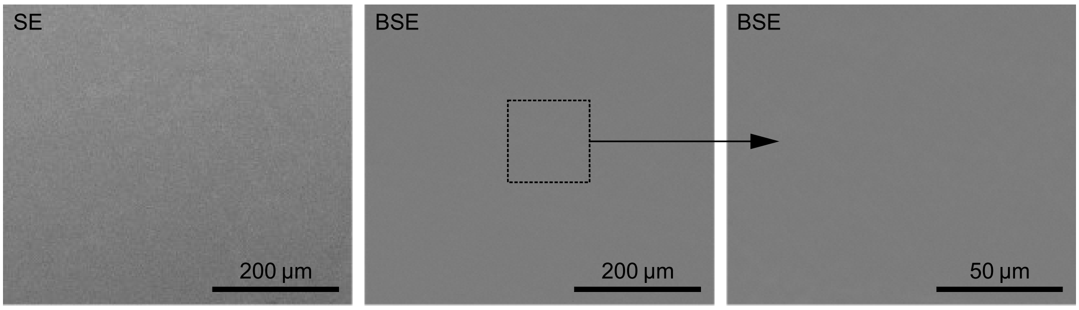

(c) $Ni_{48}Mn_{30}Ga_{20}Co_{2}$

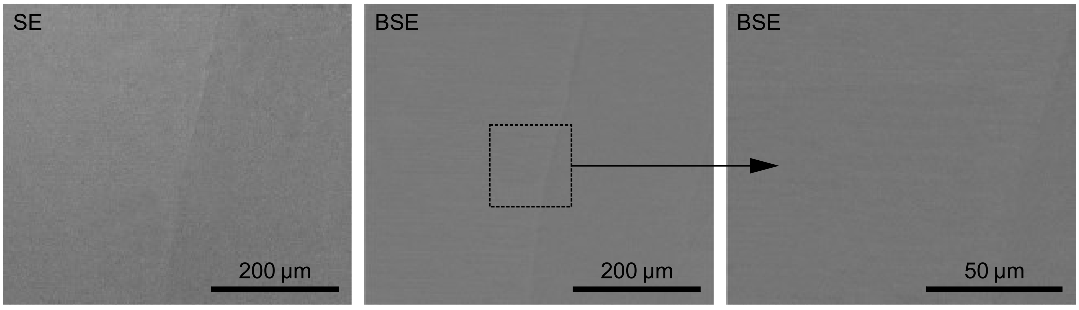

(d) $Ni_{48}Mn_{28}Ga_{20}Co_{4}$

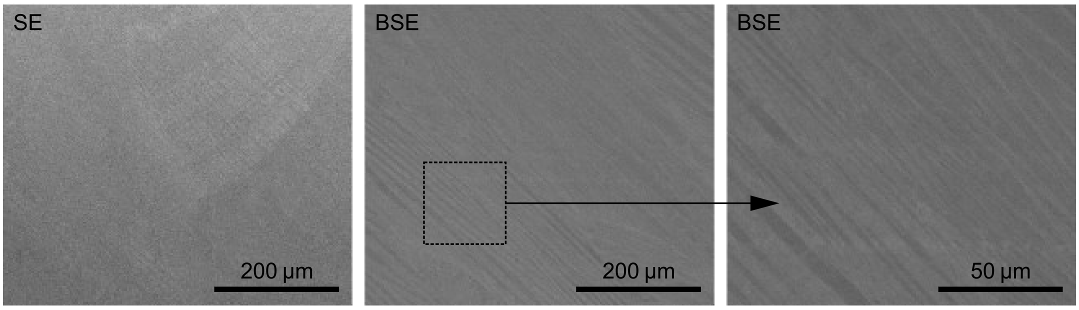

Fig. 3.11. SEM images obtained with the SE and BSE detector for the water cooled **(a)** $Ni_{48}Mn_{32}Ga_{20}$, **(b)** $Ni_{48}Mn_{31}Ga_{20}Co_{1}$, **(c)** $Ni_{48}Mn_{30}Ga_{20}Co_{2}$ and **(d)** $Ni_{48}Mn_{28}Ga_{20}Co_{4}$ magnetic shape memory alloys.

(a) $Ni_{48}Mn_{28}Ga_{20}Co_3Fe_1$

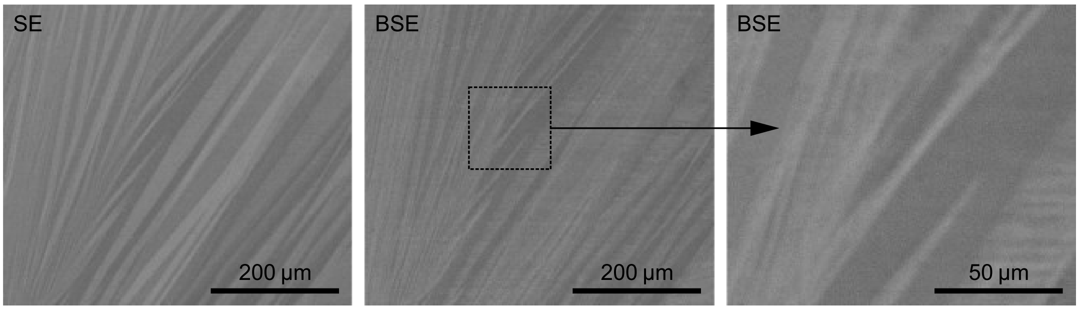

(b) $Ni_{50}Mn_{25}Ga_{21}Co_2Fe_2$

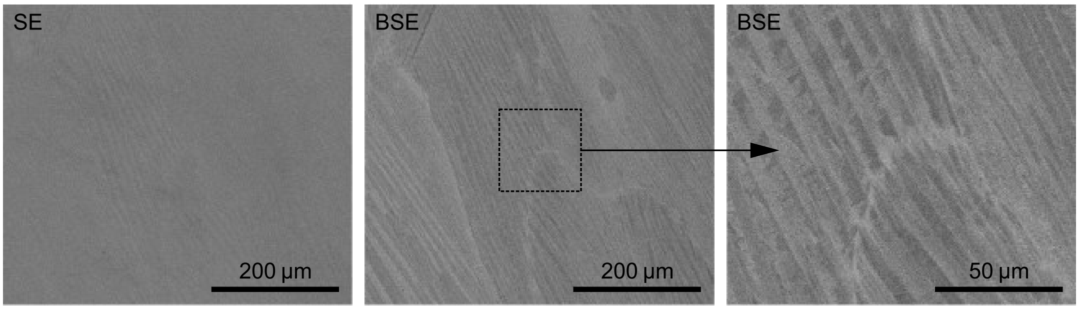

(c) $Ni_{48}Mn_{28}Ga_{20}Co_1Fe_3$

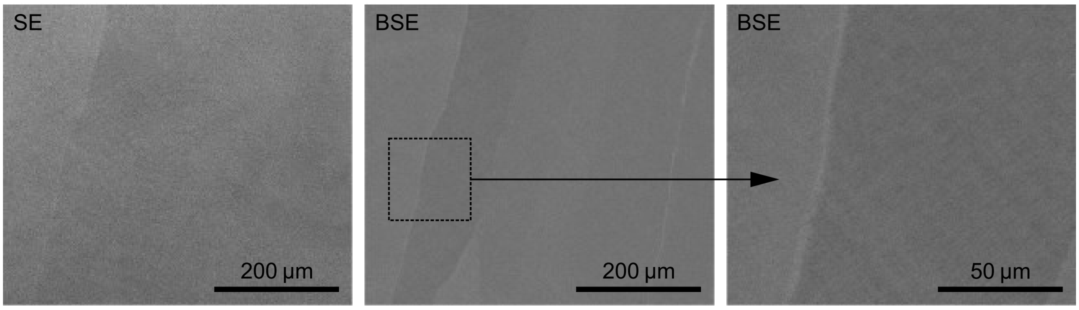

(d) $Ni_{48}Mn_{28}Ga_{20}Fe_4$

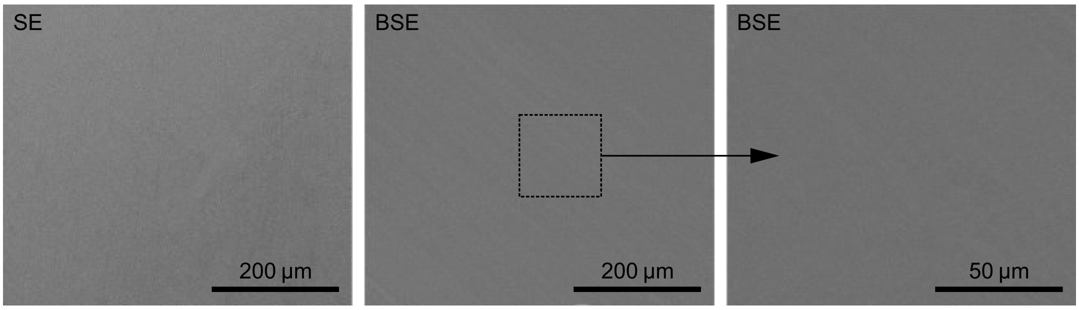

Fig. 3.12. SEM images obtained with the SE and BSE detector for the air cooled **(a)** $Ni_{48}Mn_{28}Ga_{20}Co_3Fe_1$, **(b)** $Ni_{50}Mn_{25}Ga_{21}Co_2Fe_2$, **(c)** $Ni_{48}Mn_{28}Ga_{20}Co_1Fe_3$ and **(d)** $Ni_{48}Mn_{28}Ga_{20}Fe_4$ magnetic shape memory alloys.

(a) $Ni_{48}Mn_{32}Ga_{20}$

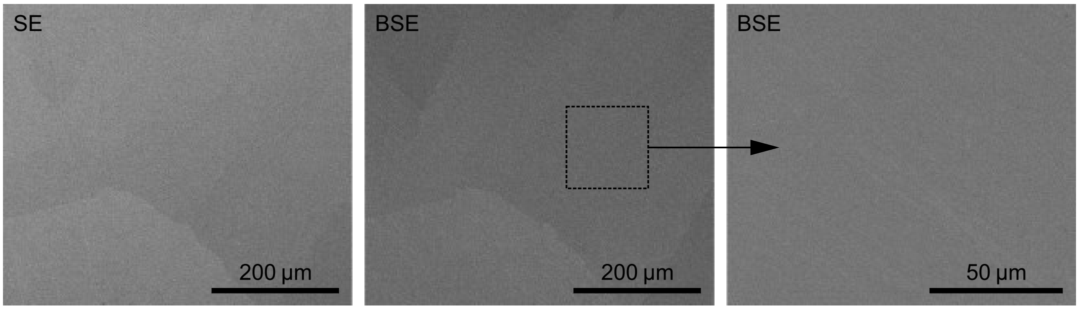

(b) $Ni_{48}Mn_{31}Ga_{20}Co_1$

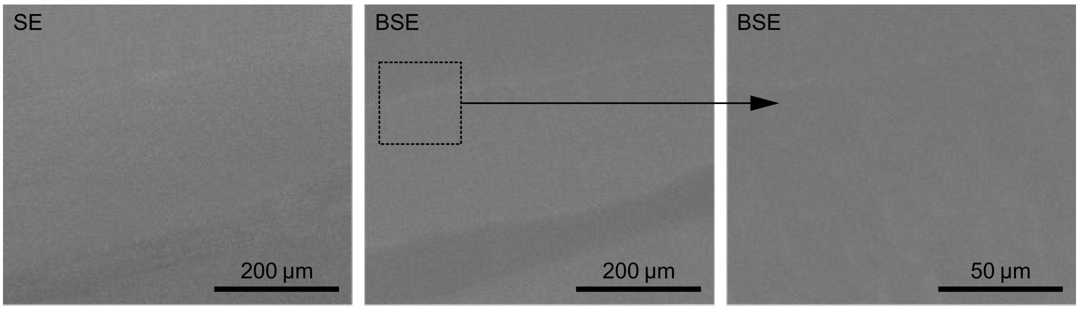

(c) $Ni_{48}Mn_{30}Ga_{20}Co_2$

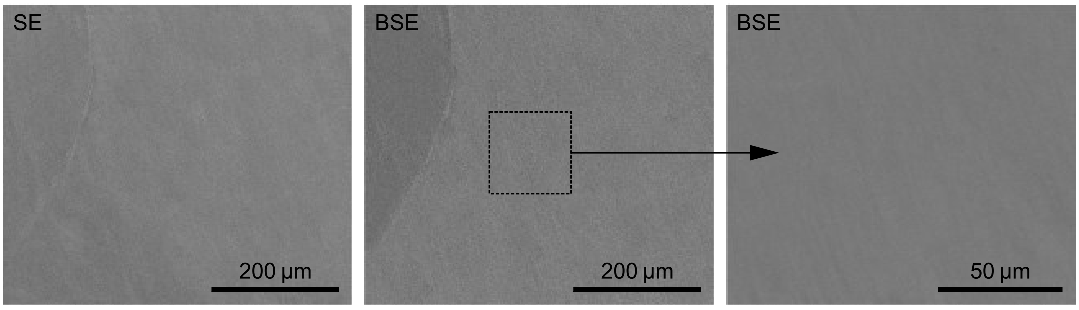

(d) $Ni_{48}Mn_{28}Ga_{20}Co_4$

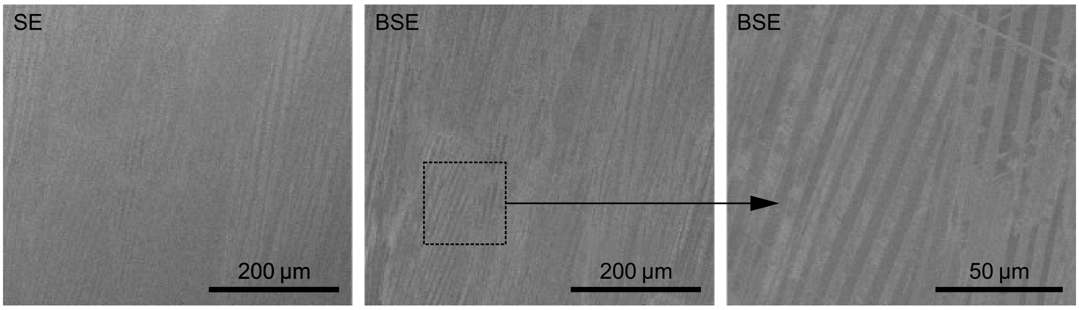

Fig. 3.13. SEM images obtained with the SE and BSE detector for the furnace cooled **(a)** $Ni_{48}Mn_{32}Ga_{20}$, **(b)** $Ni_{48}Mn_{31}Ga_{20}Co_1$, **(c)** $Ni_{48}Mn_{30}Ga_{20}Co_2$ and **(d)** $Ni_{48}Mn_{28}Ga_{20}Co_4$ magnetic shape memory alloys.

(a) $Ni_{48}Mn_{28}Ga_{20}Co_3Fe_1$

furnace cooled

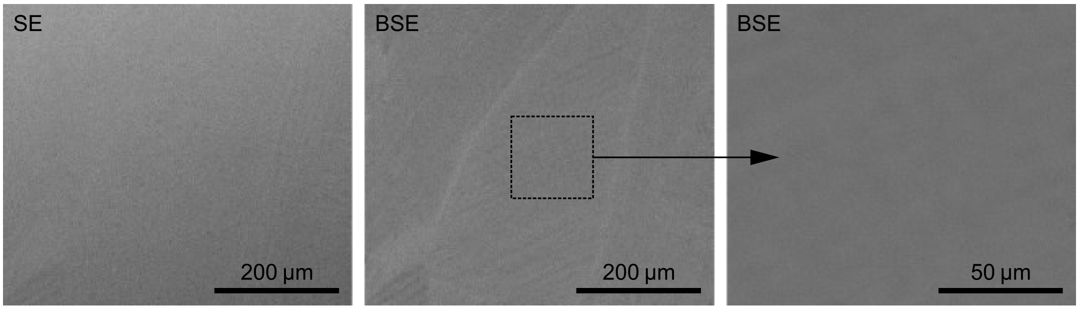

(b) $Ni_{50}Mn_{25}Ga_{21}Co_2Fe_2$

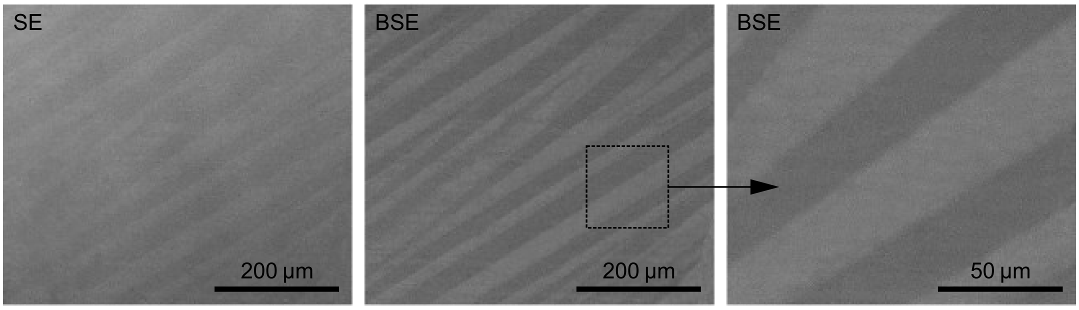

(c) $Ni_{48}Mn_{28}Ga_{20}Co_1Fe_3$

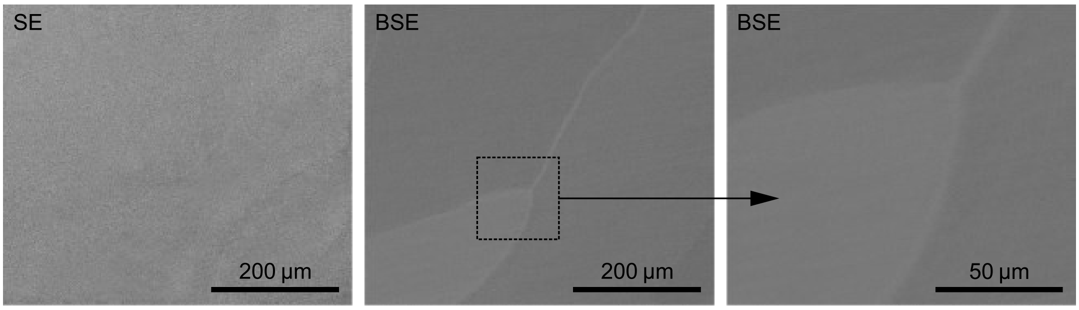

(d) $Ni_{48}Mn_{28}Ga_{20}Fe_4$

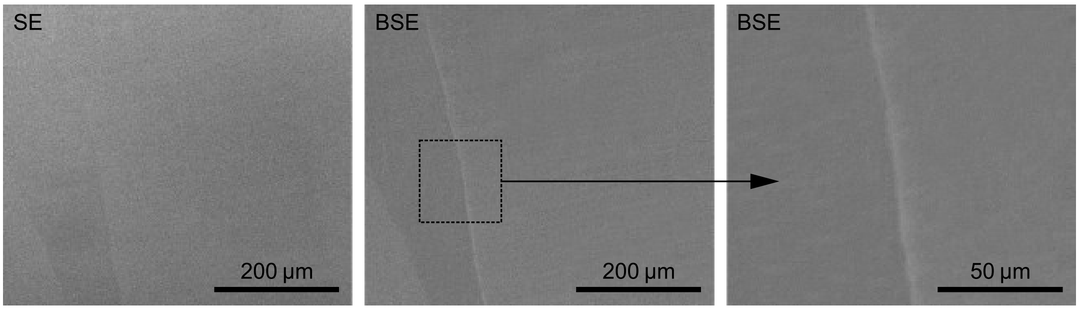

Fig. 3.14. SEM images obtained with the SE and BSE detector for the furnace cooled **(a)** $Ni_{48}Mn_{28}Ga_{20}Co_3Fe_1$, **(b)** $Ni_{50}Mn_{25}Ga_{21}Co_2Fe_2$, **(c)** $Ni_{48}Mn_{28}Ga_{20}Co_1Fe_3$ and **(d)** $Ni_{48}Mn_{28}Ga_{20}Fe_4$ magnetic shape memory alloys.

3.1.3 Chemical compositions

The energy dispersive X-ray detector was used during SEM studies to evaluate the final chemical composition of the fabricated alloys as well as the homogeneity of their chemical compositions. The EDX analysis was performed randomly from different areas of the specimens including both the central and the outer parts of the studied cross sections. It should be noted that the chemical composition for each investigated material was almost constant across the entire studied area and the difference between the atomic percentage was less than 0.2 at.% for all elements used for the particular alloy. The high homogeneity of the chemical composition was observed for all manufactured NiMnGa-based materials. Moreover, neither the low nor high cooling rates achieved by the water/air or furnace cooling process contribute to the segregation of additional doping elements, *i.e.* Fe and/or Co.

Fig. 3.15–3.17 presents the example of recorded EDX spectra for water, air and furnace cooled NiMnGa-based alloys, respectively. In order to highlight the peaks related to the doping elements, the Fe and Co symbols were bolded and underlined. It is clearly seen in all figures that the obtained characteristic X-ray spectra contains only well defined peaks related to the used Ni, Mn, Ga, Co or Fe elements. Furthermore, the continuum X-ray background is comparatively low and no undesired peaks from typical contaminating elements, such as carbon, oxygen or nitrogen, are also observed. For Ni-Mn-Ga Heusler alloys, this is particularly challenging to obtain because of the high oxygen affinity of Mn. The collected EDX spectra confirm that the proposed methodology for the fabrication of NiMnGa-based materials, described in **Section 2.1**, provides the pure uncontaminated bulk alloy characterized by the desired chemical composition.

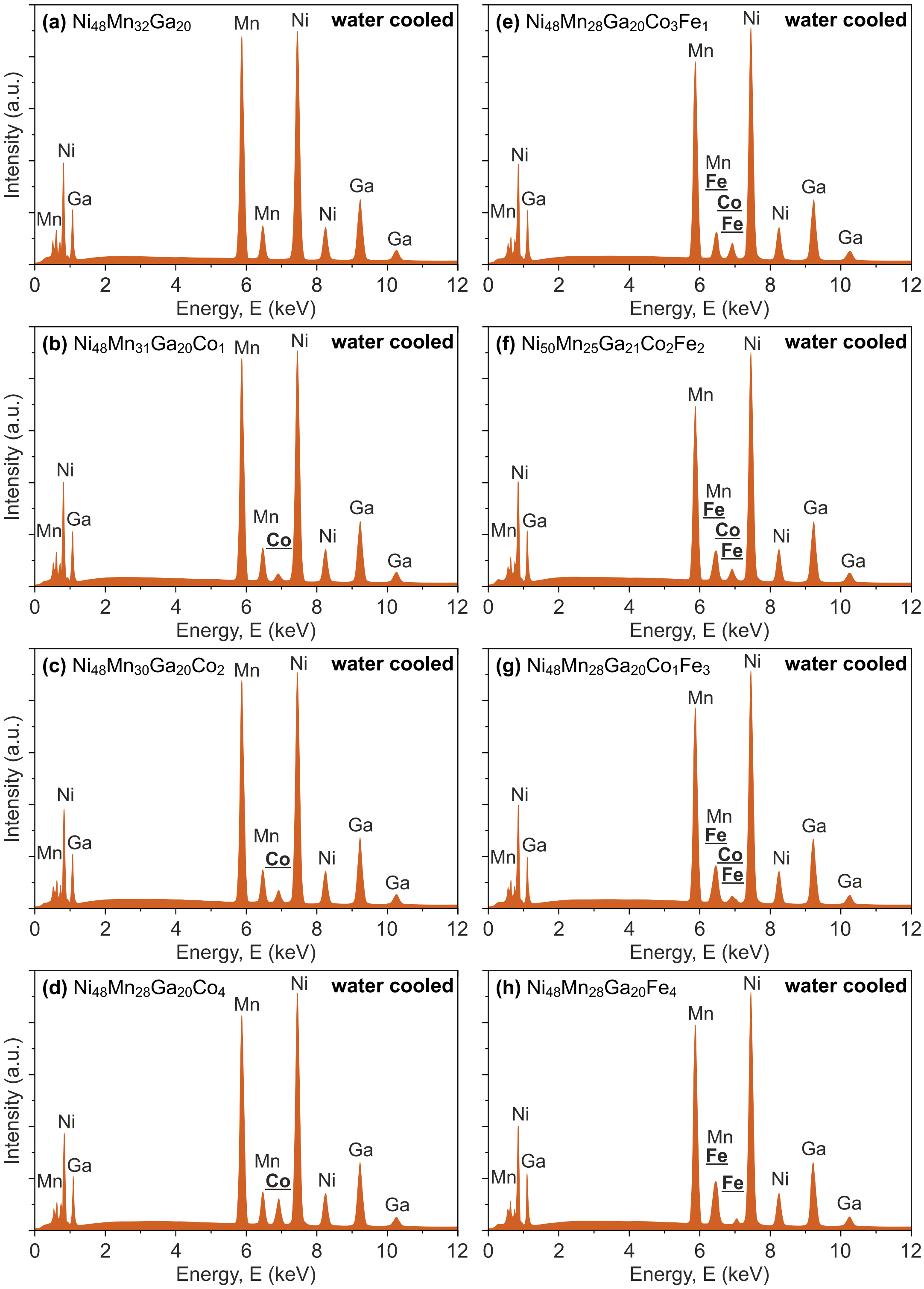

Fig. 3.15. The example of EDX spectra collected for the water cooled **(a)** $Ni_{48}Mn_{32}Ga_{20}$, **(b)** $Ni_{48}Mn_{31}Ga_{20}Co_{1}$, **(c)** $Ni_{48}Mn_{30}Ga_{20}Co_{2}$ **(d)** $Ni_{48}Mn_{28}Ga_{20}Co_{4}$, **(e)** $Ni_{48}Mn_{28}Ga_{20}Co_{3}Fe_{1}$, **(f)** $Ni_{50}Mn_{25}Ga_{21}Co_{2}Fe_{2}$, **(g)** $Ni_{48}Mn_{28}Ga_{20}Co_{1}Fe_{3}$ and **(h)** $Ni_{48}Mn_{28}Ga_{20}Fe_{4}$ magnetic shape memory alloys. The doping elements Co and Fe are bolded and underlined.

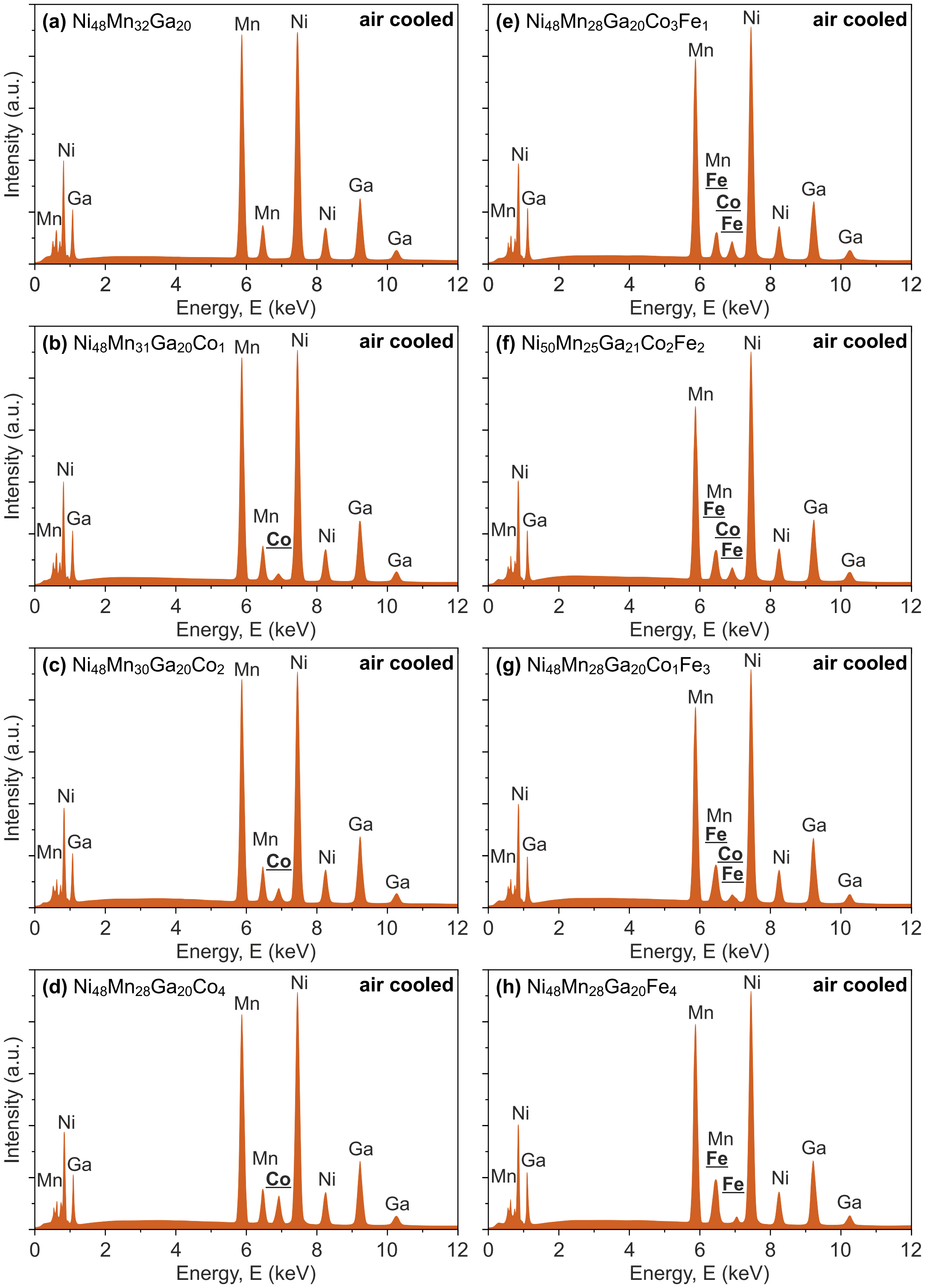

Fig. 3.16. The example of EDX spectra collected for the air cooled **(a)** $Ni_{48}Mn_{32}Ga_{20}$, **(b)** $Ni_{48}Mn_{31}Ga_{20}Co_1$, **(c)** $Ni_{48}Mn_{30}Ga_{20}Co_2$ **(d)** $Ni_{48}Mn_{28}Ga_{20}Co_4$, **(e)** $Ni_{48}Mn_{28}Ga_{20}Co_3Fe_1$, **(f)** $Ni_{50}Mn_{25}Ga_{21}Co_2Fe_2$, **(g)** $Ni_{48}Mn_{28}Ga_{20}Co_1Fe_3$ and **(h)** $Ni_{48}Mn_{28}Ga_{20}Fe_4$ magnetic shape memory alloys. The doping elements Co and Fe are bolded and underlined.

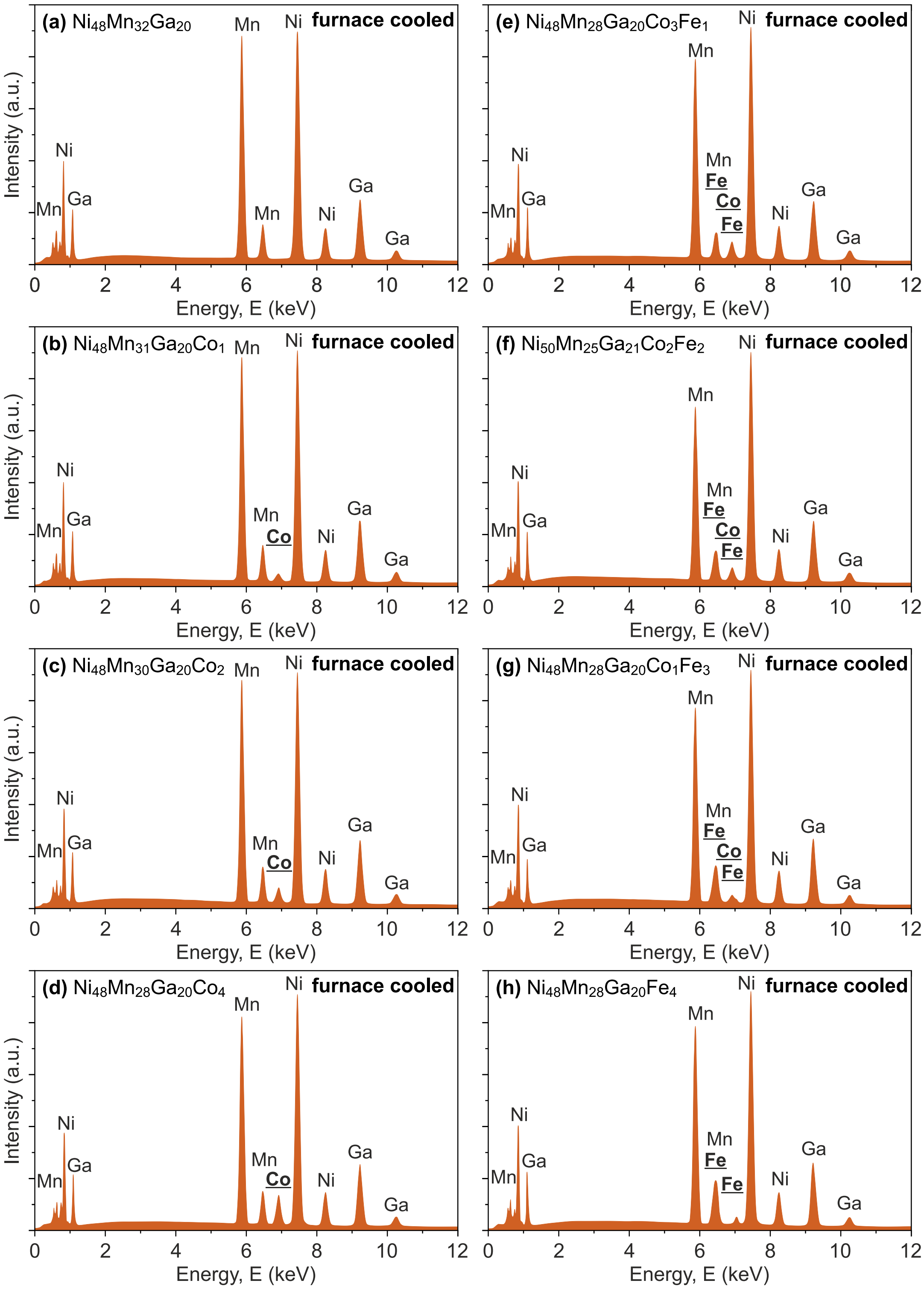

Fig. 3.17. The example of EDX spectra collected for the furnace cooled **(a)** $Ni_{48}Mn_{32}Ga_{20}$, **(b)** $Ni_{48}Mn_{31}Ga_{20}Co_1$, **(c)** $Ni_{48}Mn_{30}Ga_{20}Co_2$ **(d)** $Ni_{48}Mn_{28}Ga_{20}Co_4$, **(e)** $Ni_{48}Mn_{28}Ga_{20}Co_3Fe_1$, **(f)** $Ni_{50}Mn_{25}Ga_{21}Co_2Fe_2$, **(g)** $Ni_{48}Mn_{28}Ga_{20}Co_1Fe_3$ and **(h)** $Ni_{48}Mn_{28}Ga_{20}Fe_4$ magnetic shape memory alloys. The doping elements Co and Fe are bolded and underlined.

The high quality of the X-ray spectra shown in **Fig. 3.15–3.17** ensures the reliable outcome of the quantitative EDX analysis. Due to the aforementioned low deviation of chemical composition of the examined materials, the final chemical composition of individual alloys was evaluated as an arithmetical mean from five different areal EDX analysis. The experimentally determined chemical composition together with the formerly designed composition are summarized in **Table 3.1**. It is seen that the final chemical compositions of alloys fabricated in a two stage melting process followed by high temperature annealing are in good agreement with the designed compositions. Additionally, alloys with the same chemical composition exposed to a different cooling procedures exhibit the same chemical compositions with atomic percentage deviations that do not surpass 0.1 at.%.. These results confirm the good homogeneity of produced alloys in the whole volume of material, as water, air and furnace cooled samples were prepared from the same single specimen produced in a two stage melting procedure. Following a consistent EDX analysis, the valence electron concentration e/a and the non-bonding electrons concentration N_e/a were calculated using the experimentally determined chemical compositions. The average value of at.% from water, air and furnace cooled materials were taken for further calculations, however it should be mentioned that neglectable difference between the at.% did not influence the final value of e/a and N_e/a.

The physical explanation of the valence electron concentration is described in detail in the theoretical part of this thesis in **Section 1.6.1**. For the fabricated NiMnGa-based materials doped by Co and/or Fe, the e/a was calculated according to the following relationship:

$$e/a = \frac{10 \cdot \mathrm{Ni}_{at\%} + 7 \cdot \mathrm{Mn}_{at\%} + 3 \cdot \mathrm{Ga}_{at\%} + 9 \cdot \mathrm{Co}_{at\%} + 8 \cdot \mathrm{Fe}_{at\%}}{\mathrm{Ni}_{at\%} + \mathrm{Mn}_{at\%} + \mathrm{Ga}_{at\%}} \tag{3.1}$$

where 10, 7, 3, 9 and 8 are the number of valence electrons derived for outer electrons configuration of the corresponding Ni ($3d^8 4s^2$), Mn ($3d^5 4s^2$), Ga ($4s^2 4p^1$), Co ($3d^7 4s^2$), and Fe ($3d^6 4s^2$), respectively.

The nature of non-bonding electrons concentration was also comprehensively described in the theoretical part of the thesis in **Section 1.6.2.4**. The calculation of N_e/a parameter required the prior estimation of the number of non-bonding electrons e_n in individual elements expressed as:

$$e_n = E - N_{WS} \tag{3.2}$$

where E is the number of valence electrons and N_{WS} is the corrected electron density parameter derived from the Miedema's empirical model.

The N_{WS} obtained from for the Miedema's model for the used elements is 5.36, 4.17, 2.25, 5.36 and 5.55 for Ni, Mn, Ga, Co and Fe, respectively [332,333]. Taking into account the N_{WS} and abovementioned number of valence electrons for the examined elements, the e_{n} is equal to 4.46, 2.83, 0,75, 3.64 and 2.45 Ni, Mn, Ga, Co and Fe, respectively. Following the obtained values of e_{n}, the N_{e}/a parameter was estimated as follows:

$$N_{\mathrm{e}}/a = \frac{4.64\mathrm{Ni}_{at.\%} + 2.83\mathrm{Mn}_{at.\%} + 0.75\mathrm{Ga}_{at.\%} + 3.64\mathrm{Co}_{at.\%} + 2.45\mathrm{Fe}_{at.\%}}{\mathrm{Ni}_{at.\%} + \mathrm{Mn}_{at.\%} + \mathrm{Ga}_{at.\%}} \tag{3.3}$$

The calculated e/a and N_{e}/a parameters for all produced NiMnGa-based materials are as well listed in **Table 3.1**. These electronic parameters are used in the later part of the thesis to discuss their dependence on the structural, magnetic and mechanical properties of fabricated multifunctional Heusler alloys. Here, it is worth noticing that the alloy defined by $\mathrm{Ni_{50}Mn_{25}Ga_{21}Co_2Fe_2}$ composition were designed with the different Ni/Mn ratio, but still comparable e/a parameter, as rest of the fabricated NiMnGa-based materials. This was done intentionally to determine whether the influence of electronic parameter outweighs the presence of alloying elements represented by both Fe and Co.

Table 3.1. The summary of the chemical compositions determined from EDX analysis for the produced water, air and furnace cooled NiMnGa-based alloys. The electronic parameters e/a and N_e/a were calculated on the basis of the average values of at.% from water, air and furnace cooled samples.

Alloy	**El.**	**Base (at.%)**	**Water (at.%)**	**Air (at.%)**	**Furnace (at.%)**	**e/a**	**N_e/a**
$Ni_{48}Mn_{32}Ga_{20}$	Ni	48	48.2	48.3	48.3	7.67	3.21
	Mn	32	32.3	32.1	32.2		
	Ga	20	19.5	19.6	19.5		
$Ni_{48}Mn_{31}Ga_{20}Co_{1}$	Ni	48	48.4	48.4	48.5	7.70	3.22
	Mn	31	31.0	31.1	31.1		
	Ga	20	19.4	19.4	19.3		
	Co	1	1.2	1.1	1.1		
$Ni_{48}Mn_{30}Ga_{20}Co_{2}$	Ni	48	48.6	48.6	48.7	7.72	3.23
	Mn	30	29.7	29.6	29.6		
	Ga	20	19.5	19.6	19.5		
	Co	2	2.2	2.2	2.2		
$Ni_{48}Mn_{28}Ga_{20}Co_{4}$	Ni	48	48.3	48.3	48.4	7.76	3.25
	Mn	28	28.0	28.0	28.0		
	Ga	20	19.4	19.4	19.4		
	Co	4	4.3	4.3	4.2		
$Ni_{48}Mn_{28}Ga_{20}Co_{3}Fe_{1}$	Ni	48	48.6	48.7	48.6	7.75	3.23
	Mn	28	27.1	27.1	27.1		
	Ga	20	19.7	19.6	19.7		
	Co	3	3.2	3.2	3.1		
	Fe	1	1.4	1.4	1.5		
$Ni_{50}Mn_{25}Ga_{21}Co_{2}Fe_{2}$	Ni	50	50.2	50.2	50.2	7.76	3.23
	Mn	25	24.9	24.9	24.9		
	Ga	21	20.3	20.2	20.3		
	Co	2	2.1	2.2	2.1		
	Fe	2	2.5	2.5	2.5		
$Ni_{48}Mn_{28}Ga_{20}Co_{1}Fe_{3}$	Ni	48	48.6	48.6	48.7	7.73	3.21
	Mn	28	27.1	27.1	27.1		
	Ga	20	19.6	19.6	19.6		
	Co	1	1.1	1.1	1.0		
	Fe	3	3.6	3.6	3.6		
$Ni_{48}Mn_{28}Ga_{20}Fe_{4}$	Ni	48	48.2	48.1	48.2	7.72	3.19
	Mn	28	27.8	27.9	27.8		
	Ga	20	19.4	19.4	19.4		
	Fe	4	4.6	4.6	4.6		

3.1.4 X-Ray crystallography

The strong coupling between crystal lattice and multifunctional properties of Ni-Mn-Ga Heusler alloys are described in the theoretical part of the presented thesis. In light of the foregoing introduction, the detailed X-ray diffraction studies of the produced NiMnGa-based materials were performed at room temperature (295 K) as well as at elevated temperatures equal to 320 K and 400 K. The preliminary studies shows that the structural differences between water, air and furnace cooled alloys with the same chemical compositions are comparable at room temperature and at higher temperatures. In view of this preliminary findings and considering the long measuring times of X-ray patterns, the temperature dependent XRD studies were conducted only for the alloys that were cooled in water. For the air and furnace cooled materials the X-ray spectra were collected only at room temperature. All measurements were performed with the same scanning conditions, which were thoroughly explained in **Section 2.3.3**.

The qualitative and quantitative evaluation of the recorded XRD patterns were carried out following the Rietveld refinement method. **Fig. 3.18–25** presents the results obtained from the Rietveld analysis for the $Ni_{48}Mn_{32}Ga_{20}$, $Ni_{48}Mn_{31}Ga_{20}Co_1$, $Ni_{48}Mn_{30}Ga_{20}Co_2$ $Ni_{48}Mn_{28}Ga_{20}Co_4$, $Ni_{48}Mn_{28}Ga_{20}Co_3Fe_1$, $Ni_{50}Mn_{25}Ga_{21}Co_2Fe_2$, $Ni_{48}Mn_{28}Ga_{20}Co_1Fe_3$ and $Ni_{48}Mn_{28}Ga_{20}Fe_4$ alloys, respectively. All figures are arranged in the same manner, including the XRD spectra for the water cooled samples recorded at 295 K, 320 K and 400 K, as well as corresponding XRD patterns for the air and furnace cooled samples collected at 295 K.

In all fabricated NiMnGa-based magnetic shape memory materials the austenitic phase was characterized by $L2_1$ unit cell arranged in the cubic $Fm\bar{3}m$ space group (no. 225). Moreover, the following Wyckoff atomic positions: 8c (0.25, 0.25, 0.25), 4a (0, 0, 0) and 4b (0.5, 0.5, 0.5) were identified for the main Ni, Mn and Ga atoms, respectively (the crystallography file for the identified phase is attached in the **Appendix A**). What is interesting, no water, air or furnace cooled alloy exhibits a totally austenitic structure at room temperature. This is particularly of concern when viewed in conjunction with the previously discussed microstructural observations suggesting that martensitic phase is present only in $Ni_{48}Mn_{28}Ga_{20}Co_4$, $Ni_{48}Mn_{28}Ga_{20}Co_3Fe_1$ and $Ni_{50}Mn_{25}Ga_{21}Co_2Fe_2$, alloys. In contrary to previous assumptions, the XRD studies performed at room temperature reveal that some amount of the residual martensitic phase exhibits in almost all investigate materials. This is mainly seen close to the highest intensity (220) peak of austenite phase at $2\theta = 44°$, where the characteristic bimodal distribution is observed for all examined samples, except the fully martensitic $Ni_{48}Mn_{28}Ga_{20}Co_4$ alloy. The Rietveld refinement indicates that the low intensity peak responsible for this bimodal distribution is, with the highest likelihood, related to the non modulated martensite phase. This NM martensite is well defined by tetragonal crystal structure of $I4/mmm$ space group (no. 139) in which Ni, Mn and Ga atoms occupies the 4d (0, 0.5, 0.25), 2b (0, 0, 0.5) and 2a (0, 0, 0) Wyckoff positions, respectively (the detailed crystallography file is also attached in the **Appendix A**). On the one hand, the amount of the NM martensite in alloys previously identified as austenitic is relatively low, as it is mainly manifested close to the main (220) austenite peak. On the other hand, the influence of NM martensite peak is clearly visible in the collected XRD spectra and cannot be ignored during further examination. This minor occurrence of NM martensite phase suggests that it may originates from residual microstructural stresses remaining in the sample volume. These residual stresses provides a local driving force for martensitic transformation that may undergo at lower temperatures than in stress-free material. It is important to note that the residual stress may result both from thermal history of the alloy as well as from the repeated forward and backward martensitic transformation. In the presented work, the fabricated alloys were subjected to the same number of several heating and cooling cycles that may induced some local internal stresses in their microstructures. These explanations of the presence of NM martensite is also supported by the fact that the NM martensite (112) peak close to 2θ = 43° is observed to a varying extent for the alloys with the same chemical composition but exposed to the different cooling procedures. This phenomenon is clearly demonstrate by the example of the $Ni_{48}Mn_{32}Ga_{20}$ (**Fig. 3.18**), $Ni_{48}Mn_{28}Ga_{20}Co_1Fe_3$ (**Fig. 3.24**) or $Ni_{48}Mn_{28}Ga_{20}Fe_4$ (**Fig. 3.25**) samples, where the influence of NM martensite component in the overall XRD spectra is noticeably more distinct for the furnace cooled specimens than for the water cooled samples. The presented findings point out that both the thermal and structural transformation history plays an important role in the crystal structure of NiMnGa-based Heusler alloy.

The non-modulated martensite is not the only martensite type that was discovered during the XRD studies. For the neighbouring Co-doped $Ni_{48}Mn_{31}Ga_{20}Co_1$ (**Fig. 3.19**) and $Ni_{48}Mn_{30}Ga_{20}Co_2$ (**Fig. 3.20**) alloys the characteristic additional peaks components close to NM martensite phase peaks at 2θ approximately equals to 45°, 63° and 77° were identified during the Rietveld refinement. These additional components of XRD spectra collected at room temperature cannot be explained only by NM martensite phase, hence implying the existence of modulated structures. The complexity of modulated martensite, for example expressed by the number of Bragg's positions in X-ray spectra (**Fig. 3.19–3.20**), restricts the detail evaluation of this structures with the help of only XRD method and require more sophisticated neutron diffraction techniques. This issue was already introduced and discussed in the theoretical part of the thesis in **Section 1.2.2.2**. However, despite the aforementioned difficulties, both 5M and 7M martensite structures were employed for the preliminary Rietveld refinement analysis. Examinations of both modulated martensite structures showed that 5M modulation significantly better matches the experimental data than 7M modulation. The same reliable fitting outcomes were obtained for the both $Ni_{48}Mn_{31}Ga_{20}Co_1$ (Fig XXX) and $Ni_{48}Mn_{30}Ga_{20}Co_2$ (Fig XXX) alloys after every cooling procedure, which is reflected by the small discrepancy between the observed and theoretically predicted XRD patterns expressed by blue solid line in **Fig. 3.19** and **3.20**, respectively. Taking this fitting consistency into account the 5M modulated structure, defined by monoclinic unit cell of $P2/m$ space group (no. 10), were used in this work to describe the observed modulation of martensite phase (crystallography file is attached in the **Appendix A**). Surprisingly, the modulation of martensite disappears with the further increase of Co addition, because the water, air and furnace cooled $Ni_{48}Mn_{28}Ga_{20}Co_4$ alloy is defined by solely NM tetragonal martensite, as depicted in **Fig. 3.21**. Furthermore, other Co-doped or Fe-Co-doped Heusler materials showed no evidence of martensite modulation.

The vanishing of residual unstable NM martensite phase is clearly observed on the example of the water cooled materials for which the additional XRD spectra were recorded at 320 K and 400 K, and presented in **Fig. 18(a)–25(a)**. It is seen that for all investigated water cooled alloys characterized by small volume of NM martensite at room temperature (295 K), *i.e.* $Ni_{48}Mn_{32}Ga_{20}$, $Ni_{48}Mn_{31}Ga_{20}Co_1$, $Ni_{48}Mn_{30}Ga_{20}Co_2$, $Ni_{48}Mn_{28}Ga_{20}Co_3Fe_1$, $Ni_{50}Mn_{25}Ga_{21}Co_2Fe_2$, $Ni_{48}Mn_{28}Ga_{20}Co_1Fe_3$ and $Ni_{48}Mn_{28}Ga_{20}Fe_4$ alloy, the amount of residual martensitic phase begins to decreases at 320 K and completely disappears at 400 K. The only exception is the $Ni_{48}Mn_{28}Ga_{20}Co_4$ alloy, which is entirely martensitic at room temperature and also at 320 K. For this alloy characterized by the highest amount of Co, the first evident indications of high-temperature austenitic phase is observed at 400 K, however, even at such elevated temperature, the NM martensite still predominates. The stated observations supports the previous findings that the observed bimodal distribution of the main (220) austenite peak is related to the existence of NM tetragonal martensite, which should generally disappears with the increasing temperature as is seen for fabricated NiMnGa-based materials.

Additionally, the temperature dependent XRD studies of the water cooled samples revealed the different thermal stability of the NM and 5M modulated martensite identified for the $Ni_{48}Mn_{31}Ga_{20}Co_1$ (**Fig. 3.19(a)**) and $Ni_{48}Mn_{30}Ga_{20}Co_2$ (**Fig. 3.20(a)**) alloys. In both presented materials, the influence of martensite modulation vanishes completely at 320 K, whereas the NM martensite is still observed at the same temperature and disappears only at 400 K. Furthermore, the direct comparison of XRD patterns for the $Ni_{48}Mn_{31}Ga_{20}Co_1$ (**Fig. 3.19**) and $Ni_{48}Mn_{30}Ga_{20}Co_2$ (**Fig. 3.20**) materials that were cooled in water, air and furnace reveals that the furnace cooled samples have the highest levels of the 5M martensite and the water-cooled samples have the lowest levels. This suggests that high cooling rate stabilizes the NM martensitic structure, while low cooling rates allows for additional structural modulations of martensite. These behaviour is in accordance with general theory indicating the notably better stability of NM martensite in comparison to 5M and 7M modulated structures. The detailed explanation of the martensitic phase stability were provided in theoretical part of the thesis in **Section 1.2.2**.

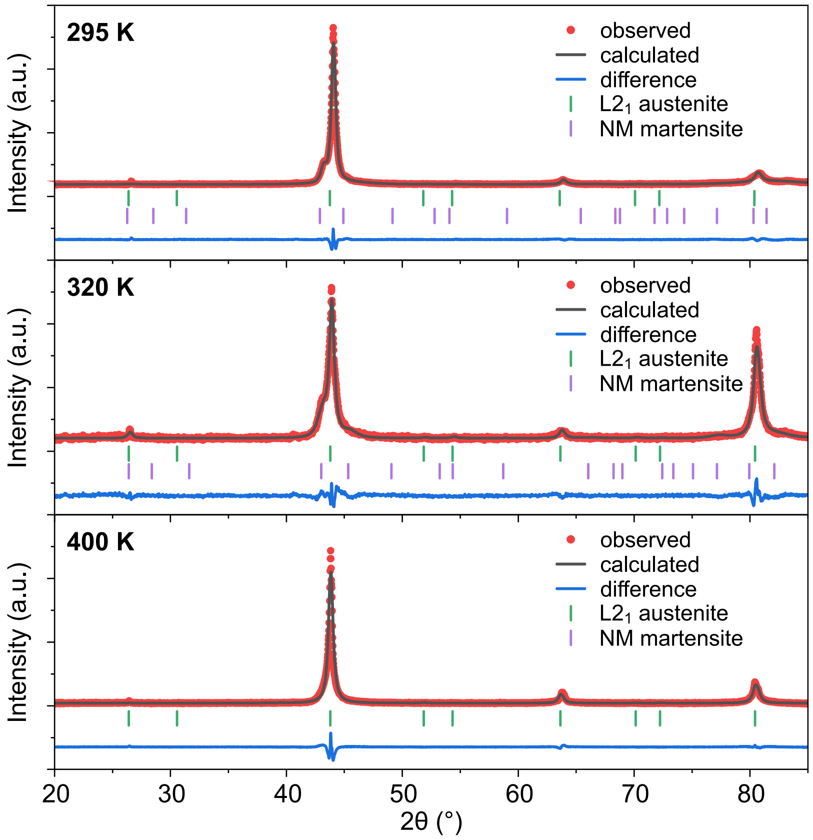

(a) $Ni_{48}Mn_{32}Ga_{20}$ - water cooled

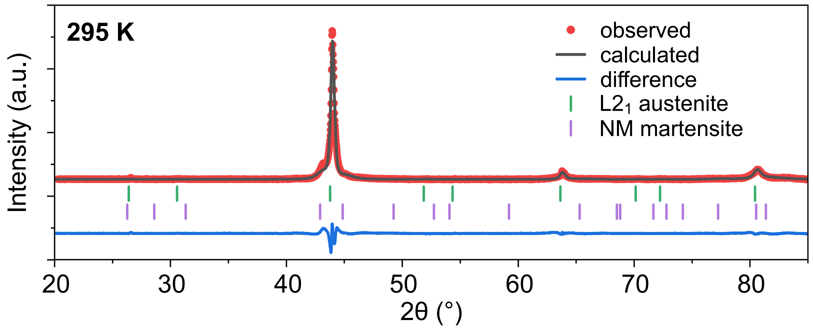

(b) $Ni_{48}Mn_{32}Ga_{20}$ - air cooled

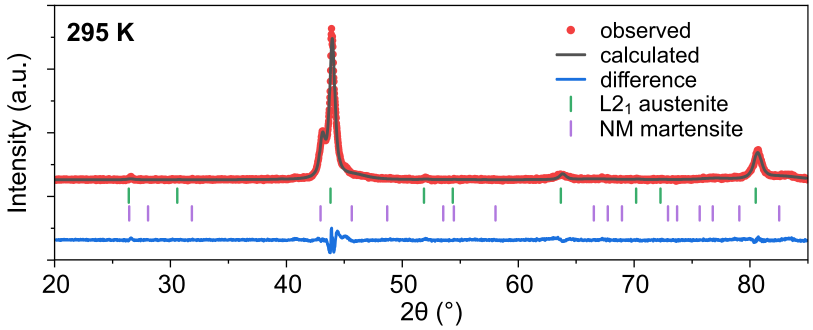

(c) $Ni_{48}Mn_{32}Ga_{20}$ - furnace cooled

Fig. 3.18. Rietveld refinement of XRD patterns recorded at indicated temperatures for the **(a)** water, **(b)** air and **(c)** furnace cooled $Ni_{48}Mn_{32}Ga_{20}$ alloy. The red points, black solid line and blue solid lines represent the observed and calculated XRD spectra of the investigated sample, as well as their difference. The short vertical green and violet lines show the positions of the Bragg reflections for $L2_1$ austenite and NM martensite, respectively.

(a) $Ni_{48}Mn_{31}Ga_{20}Co_1$ - water cooled

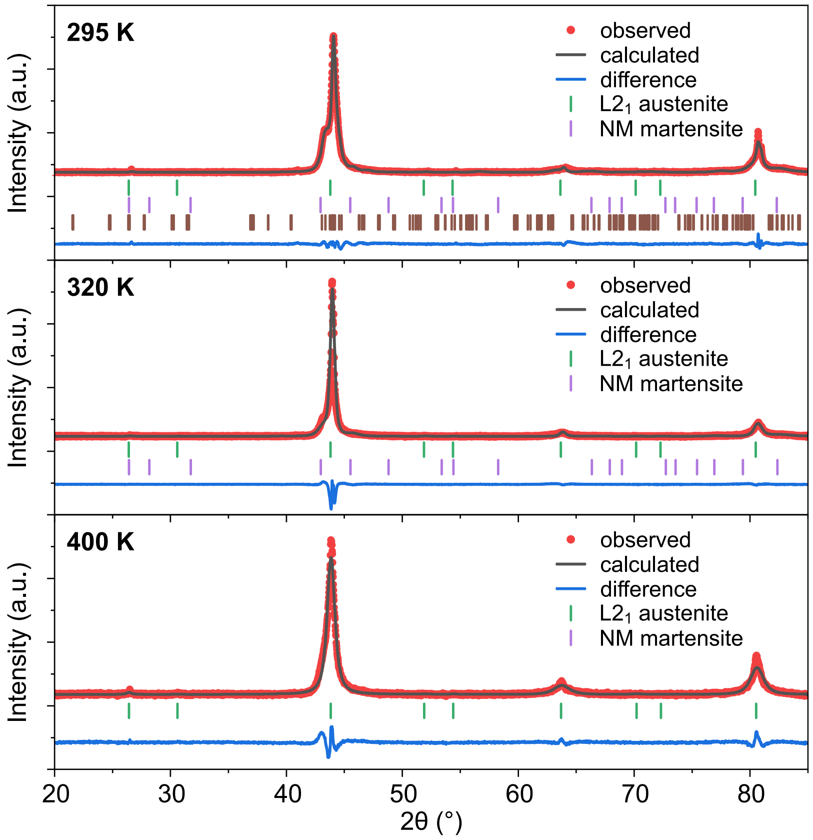

(b) $Ni_{48}Mn_{31}Ga_{20}Co_1$ - air cooled

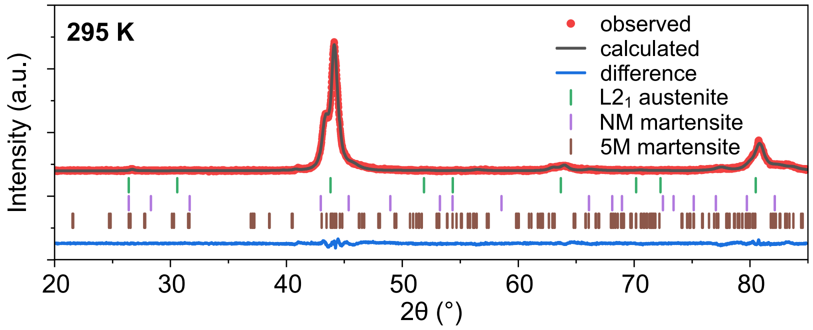

(c) $Ni_{48}Mn_{31}Ga_{20}Co_1$ - furnace cooled

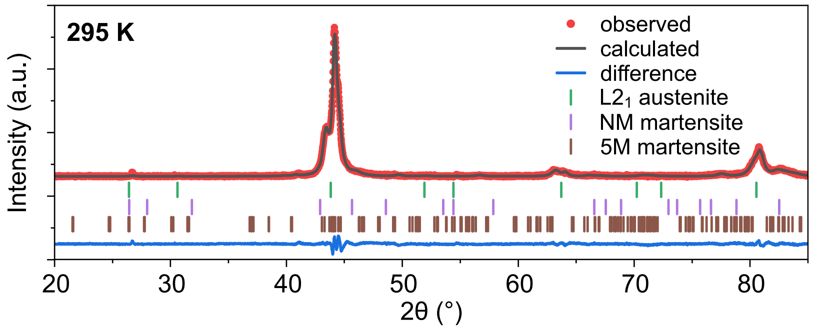

Fig. 3.19. Rietveld refinement of XRD patterns recorded at indicated temperatures for the **(a)** water, **(b)** air and **(c)** furnace cooled $Ni_{48}Mn_{31}Ga_{20}Co_1$ alloy. The red points, black solid line and blue solid lines represent the observed and calculated XRD spectra of the investigated sample, as well as their difference. The short vertical green, violet and brown lines show the positions of the Bragg reflections for $L2_1$ austenite , NM martensite and 5M martensite, respectively.

(a) $Ni_{48}Mn_{30}Ga_{20}Co_2$ - water cooled

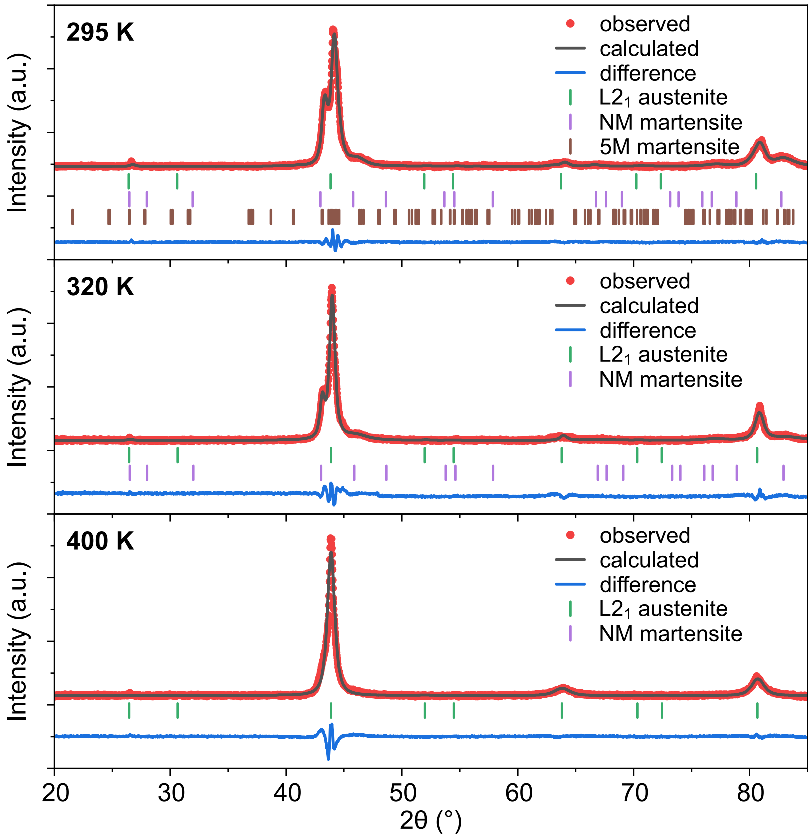

(b) $Ni_{48}Mn_{30}Ga_{20}Co_2$ - air cooled

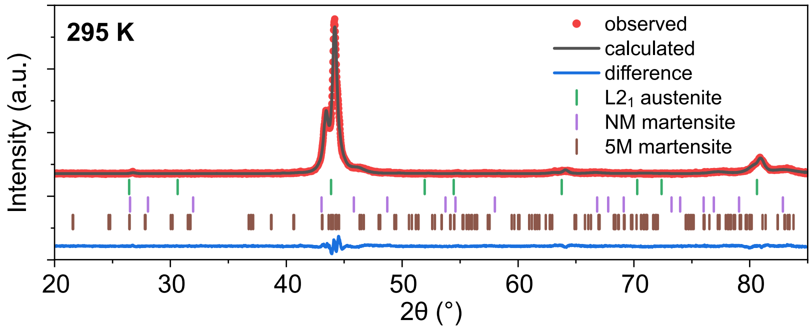

(c) $Ni_{48}Mn_{30}Ga_{20}Co_2$ - furnace cooled

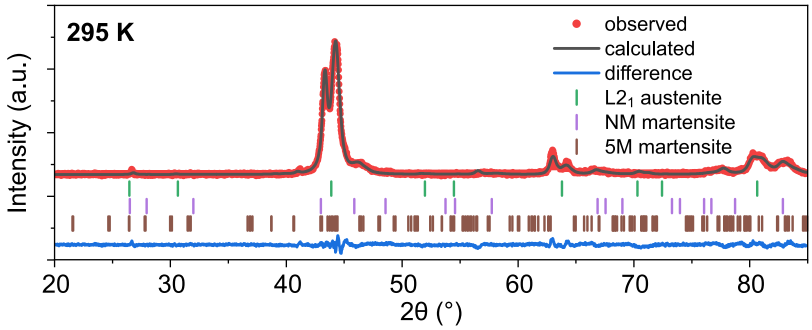

Fig. 3.20. Rietveld refinement of XRD patterns recorded at indicated temperatures for the **(a)** water, **(b)** air and **(c)** furnace cooled $Ni_{48}Mn_{30}Ga_{20}Co_2$ alloy. The red points, black solid line and blue solid lines represent the observed and calculated XRD spectra of the investigated sample, as well as their difference. The short vertical green, violet and brown lines show the positions of the Bragg reflections for $L2_1$ austenite , NM martensite and 5M martensite, respectively.

(a) $Ni_{48}Mn_{28}Ga_{20}Co_4$ - water cooled

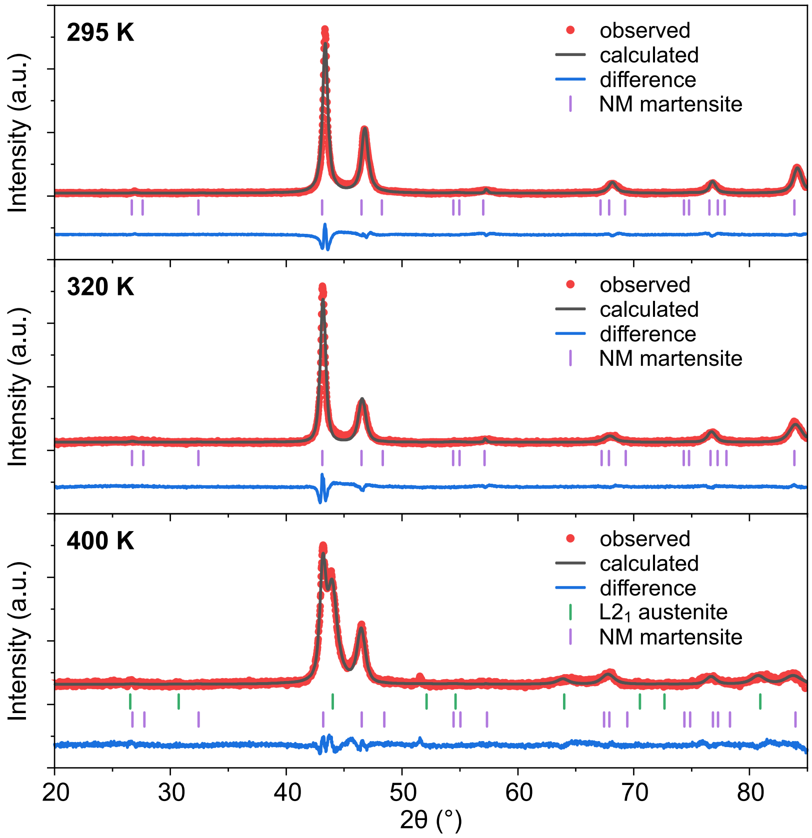

(b) $Ni_{48}Mn_{28}Ga_{20}Co_4$ - air cooled

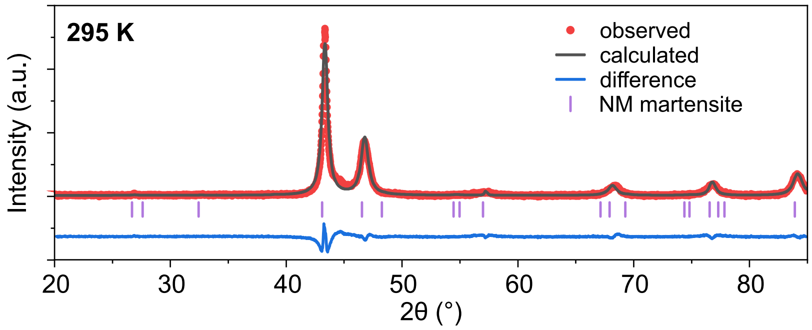

(c) $Ni_{48}Mn_{28}Ga_{20}Co_4$ - furnace cooled

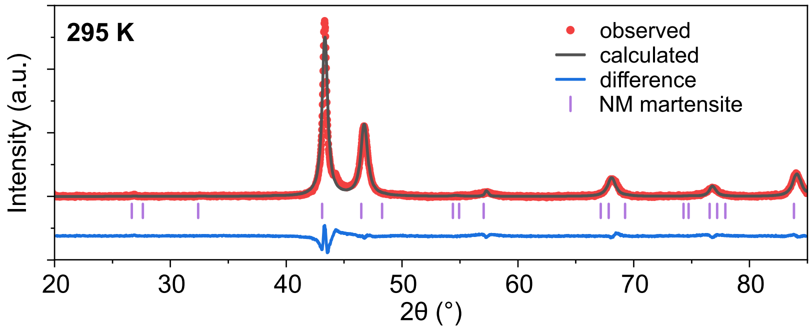

Fig. 3.21. Rietveld refinement of XRD patterns recorded at indicated temperatures for the **(a)** water, **(b)** air and **(c)** furnace cooled $Ni_{48}Mn_{28}Ga_{20}Co_4$ alloy. The red points, black solid line and blue solid lines represent the observed and calculated XRD spectra of the investigated sample, as well as their difference. The short vertical violet and green lines show the positions of the Bragg reflections for $L2_1$ austenite and NM martensite, respectively.

(a) $Ni_{48}Mn_{28}Ga_{20}Co_{3}Fe_{1}$ - water cooled

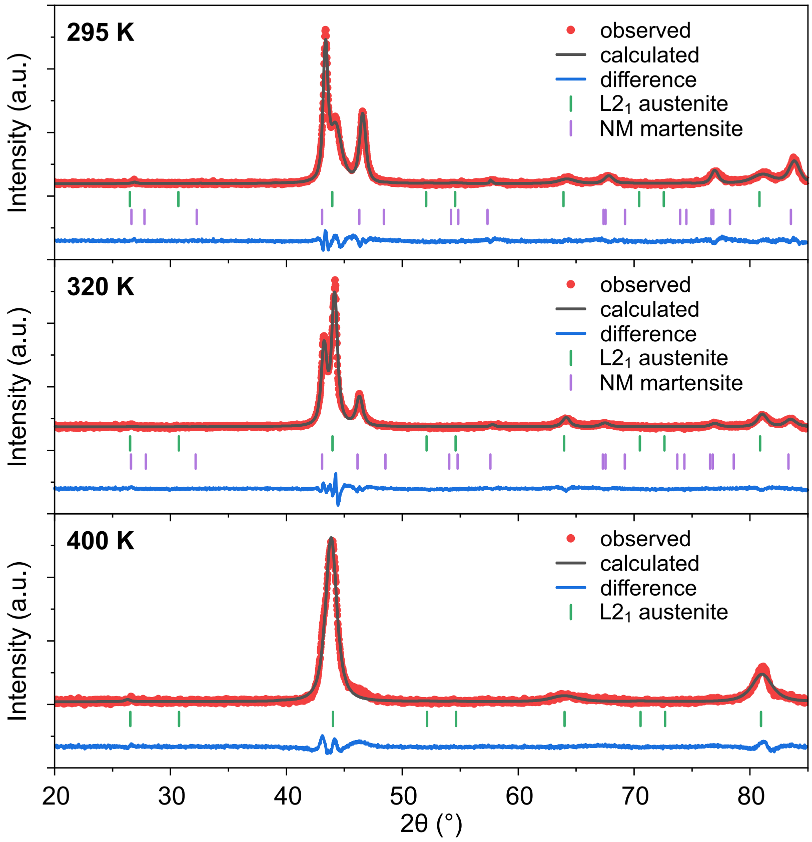

(b) $Ni_{48}Mn_{28}Ga_{20}Co_{3}Fe_{1}$ - air cooled

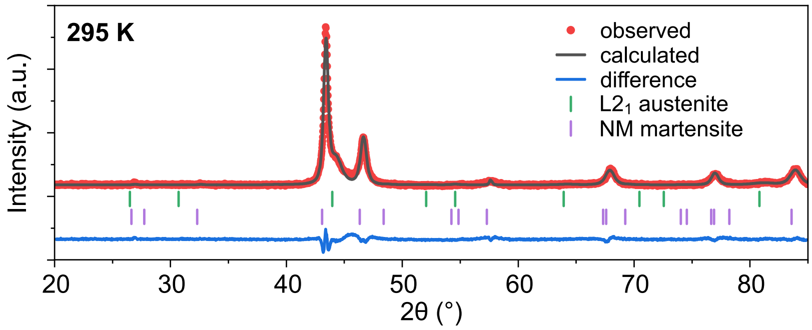

(c) $Ni_{48}Mn_{28}Ga_{20}Co_{3}Fe_{1}$ - furnace cooled

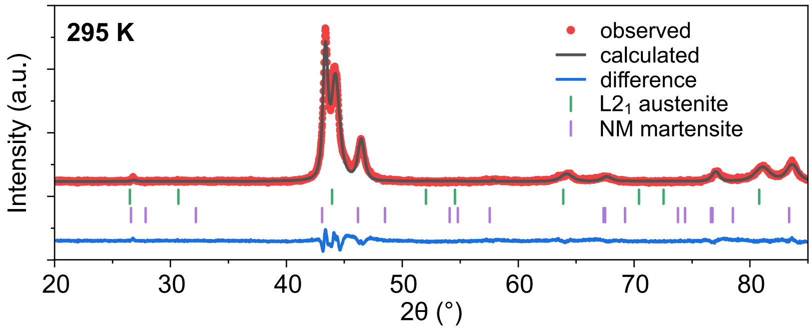

Fig. 3.22. Rietveld refinement of XRD patterns recorded at indicated temperatures for the **(a)** water, **(b)** air and **(c)** furnace cooled $Ni_{48}Mn_{28}Ga_{20}Co_{3}Fe_{1}$ alloy. The red points, black solid line and blue solid lines represent the observed and calculated XRD spectra of the investigated sample, as well as their difference. The short vertical green and violet lines show the positions of the Bragg reflections for L2$_1$ austenite and NM martensite, respectively.

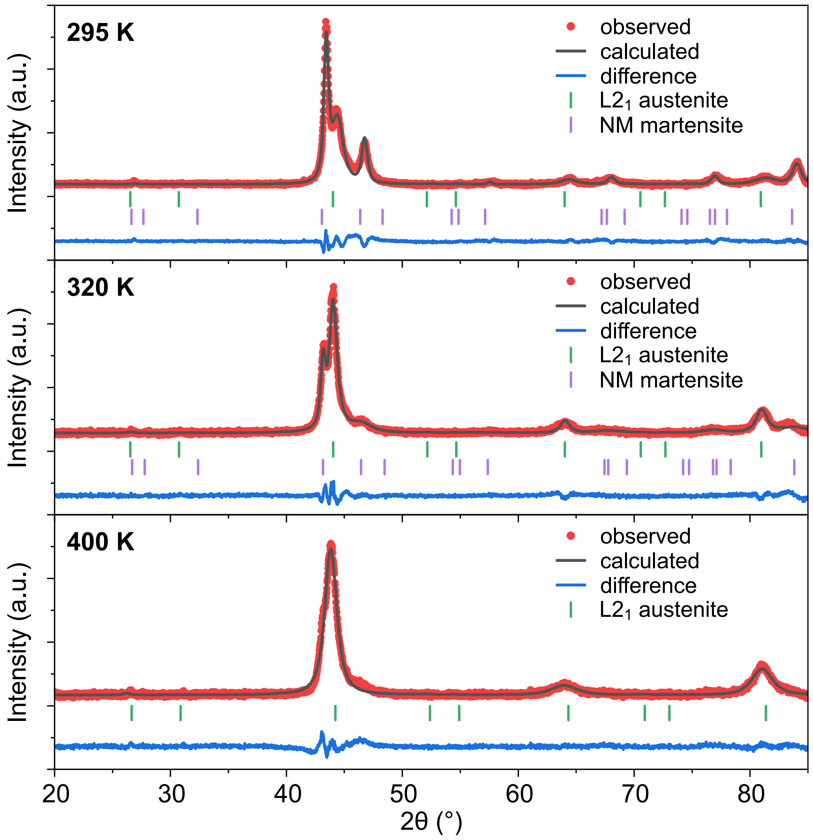
(a) $Ni_{50}Mn_{25}Ga_{21}Co_2Fe_2$ - water cooled

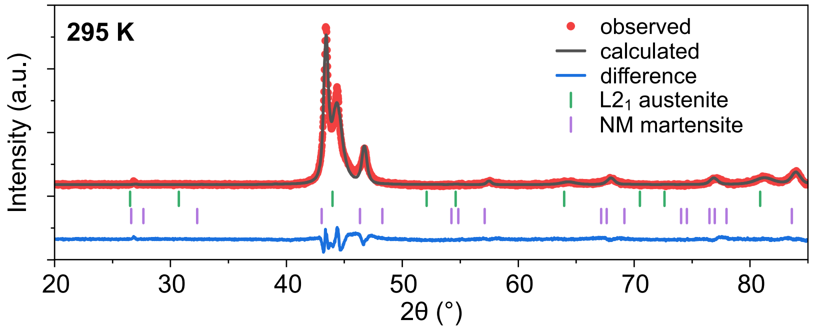
(b) $Ni_{50}Mn_{25}Ga_{21}Co_2Fe_2$ - air cooled

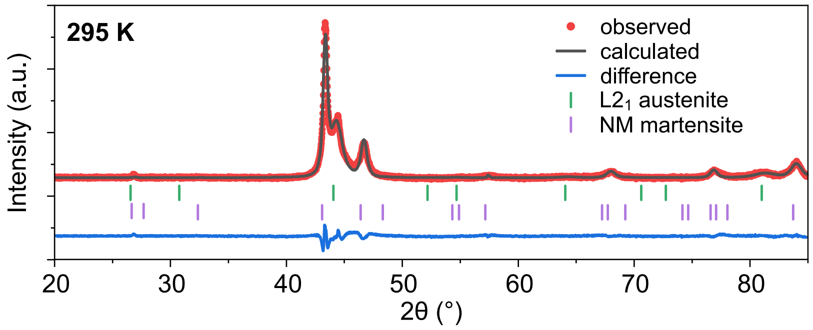
(c) $Ni_{50}Mn_{25}Ga_{21}Co_2Fe_2$ - furnace cooled

Fig. 3.23. Rietveld refinement of XRD patterns recorded at indicated temperatures for the **(a)** water, **(b)** air and **(c)** furnace cooled $Ni_{50}Mn_{25}Ga_{21}Co_2Fe_2$ alloy. The red points, black solid line and blue solid lines represent the observed and calculated XRD spectra of the investigated sample, as well as their difference. The short vertical green and violet lines show the positions of the Bragg reflections for $L2_1$ austenite and NM martensite, respectively.

(a) $Ni_{48}Mn_{28}Ga_{20}Co_1Fe_3$ - water cooled

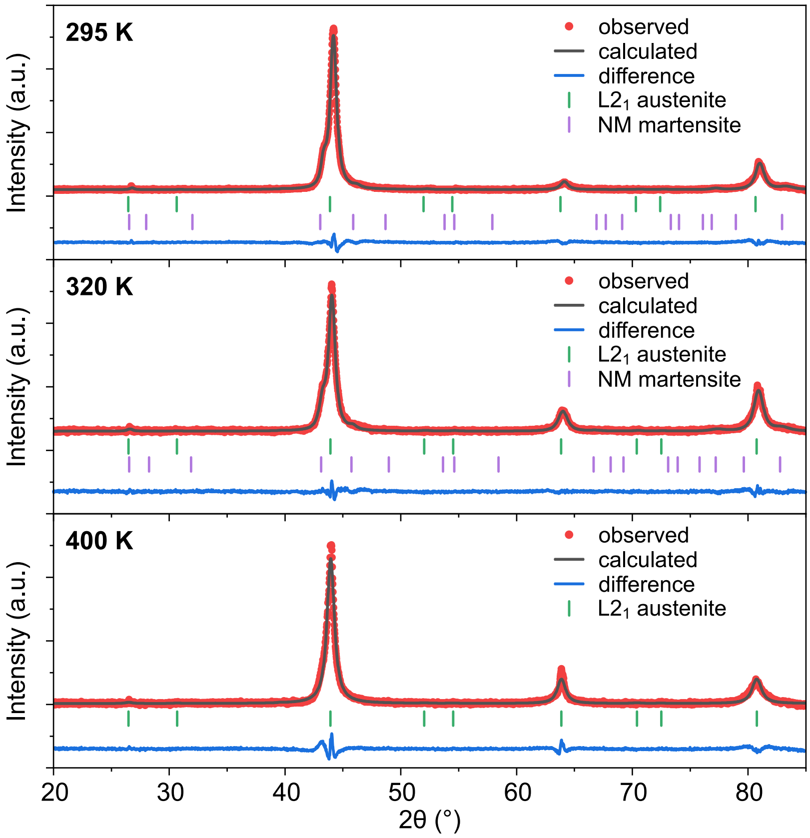

(b) $Ni_{48}Mn_{28}Ga_{20}Co_1Fe_3$ - air cooled

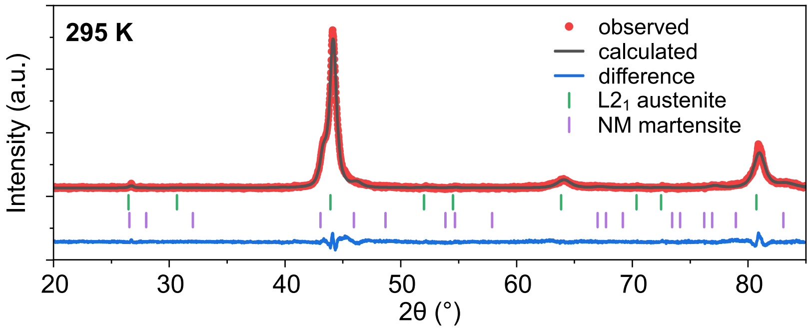

(c) $Ni_{48}Mn_{28}Ga_{20}Co_1Fe_3$ - furnace cooled

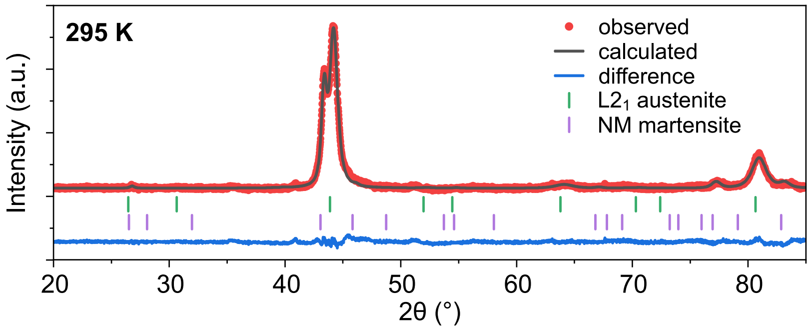

Fig. 3.24. Rietveld refinement of XRD patterns recorded at indicated temperatures for the **(a)** water, **(b)** air and **(c)** furnace cooled $Ni_{48}Mn_{28}Ga_{20}Co_1Fe_3$ alloy. The red points, black solid line and blue solid lines represent the observed and calculated XRD spectra of the investigated sample, as well as their difference. The short vertical green and violet lines show the positions of the Bragg reflections for $L2_1$ austenite and NM martensite, respectively.

(a) $Ni_{48}Mn_{28}Ga_{20}Fe_4$ - water cooled

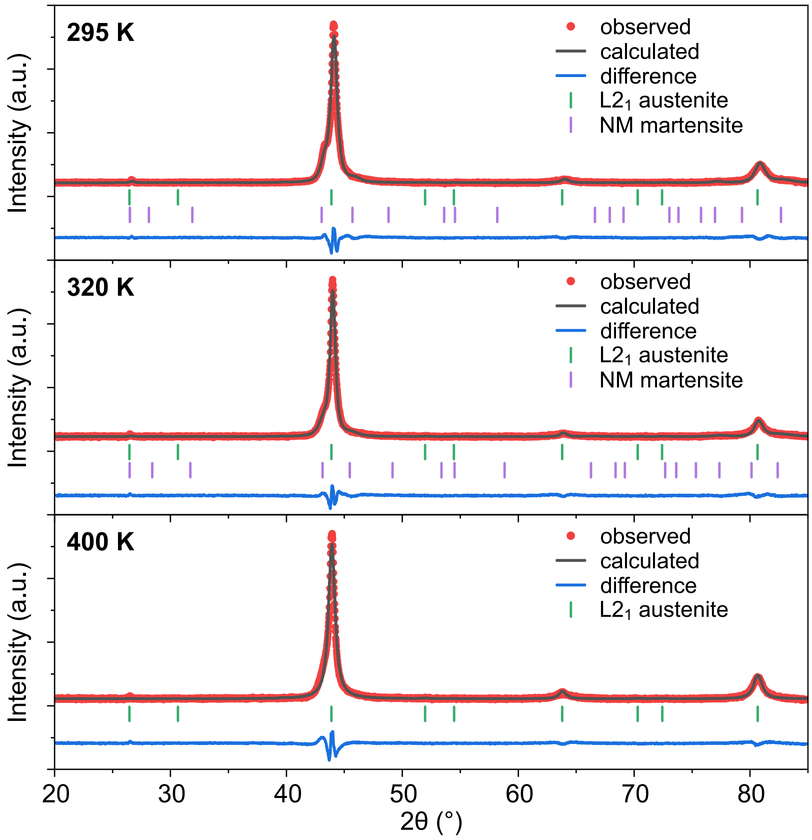

(b) $Ni_{48}Mn_{28}Ga_{20}Fe_4$ - air cooled

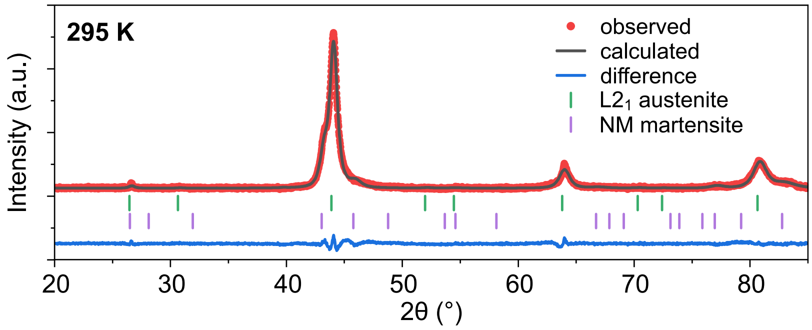

(c) $Ni_{48}Mn_{28}Ga_{20}Fe_4$ - furnace cooled

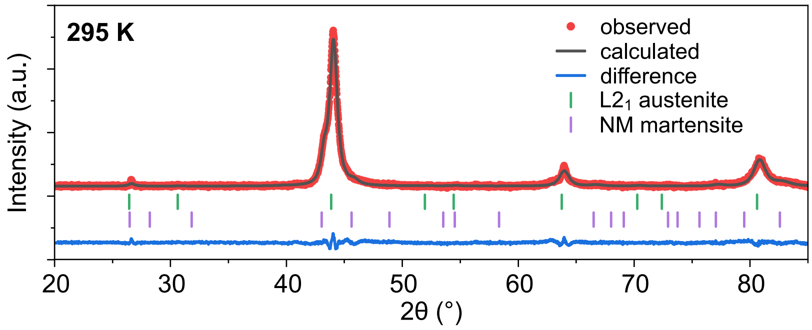

Fig. 3.25. Rietveld refinement of XRD patterns recorded at indicated temperatures for the **(a)** water, **(b)** air and **(c)** furnace cooled $Ni_{48}Mn_{28}Ga_{20}Fe_4$ alloy. The red points, black solid line and blue solid lines represent the observed and calculated XRD spectra of the investigated sample, as well as their difference. The short vertical green and violet lines show the positions of the Bragg reflections for $L2_1$ austenite and NM martensite, respectively.

Fig. 3.18–3.25 are mainly focused on direct comparison of XRD patterns collected for the examined alloys exposed to different cooling conditions. In order to show the structural evolution of the produced NiMnGa-based materials induced by elemental doping, **Fig. 3.26–3.28** provides the XRD spectra obtained at room temperature for all the investigated water, air and furnace cooled alloys, respectively. Following the path of Co and subsequent Fe doping, it is clearly seen that the reference undoped $Ni_{48}Mn_{32}Ga_{20}$ alloy is predominantly characterised by austenitic phase, mainly defined by (220), (400) and (422) peaks of the cubic $Fm\bar{3}m$ structure. Moreover, previously aforementioned presence of NM martensite phase, manifested as a slight (112) peak of tetragonal $I4/mmm$ structure, is also observed for the reference water, air and furnace cooled samples (Fig. 3.26–3.28). With the increasing Co content, the intensity of this (112) martensite peak starts to increase, indicating that the amount of martensite grows at the expanse of austenitic phase. For the $Ni_{48}Mn_{28}Ga_{20}Co_4$ alloy with the highest Co content, the presented XRD spectra reveal the fully martensitic structure identified by its characteristic (112), (200), (004), (220), (204) and (312) peaks. On the contrary, when Co is gradually substituted by Fe, the reverse trend of structural evolution is observed for the produced Heusler materials. This time, the amount of austenite phase starts to increase at the expanse of NM martensite, which is particularly evident in an increase in the (220) austenite peak and simultaneous decrease in the (112) and (200) NM martensite peaks. For the final $Ni_{48}Mn_{28}Ga_{20}Fe_4$ alloy with the highest content of Fe, the XRD spectra reveals the high predominance of austenite phase over the NM martensite phase, comparable to the reference $Ni_{48}Mn_{32}Ga_{20}$ sample.

It should be highlighted that the direct comparison of XRD patterns for alloys with different chemical compositions shown in **Fig 3.26–3.28** allows for more accurate distinction of 5M modulated martensite structure found in the $Ni_{48}Mn_{31}Ga_{20}Co_1$ and $Ni_{48}Mn_{30}Ga_{20}Co_2$ alloys. The existence of the five-layered martensite modulation is manifested as the additional component of XRD spectrum close to (220) austenite peak (close up in **Fig 3.26–3.28**). The other extra components originating from modulated martensite were also noticed closed to (400) and (422) austenite peaks. As it was stated before, the least thermally stable furnace cooled samples shown in **Fig. 3.28** exhibit the strongest signs of the presence of 5M modulated martensite.

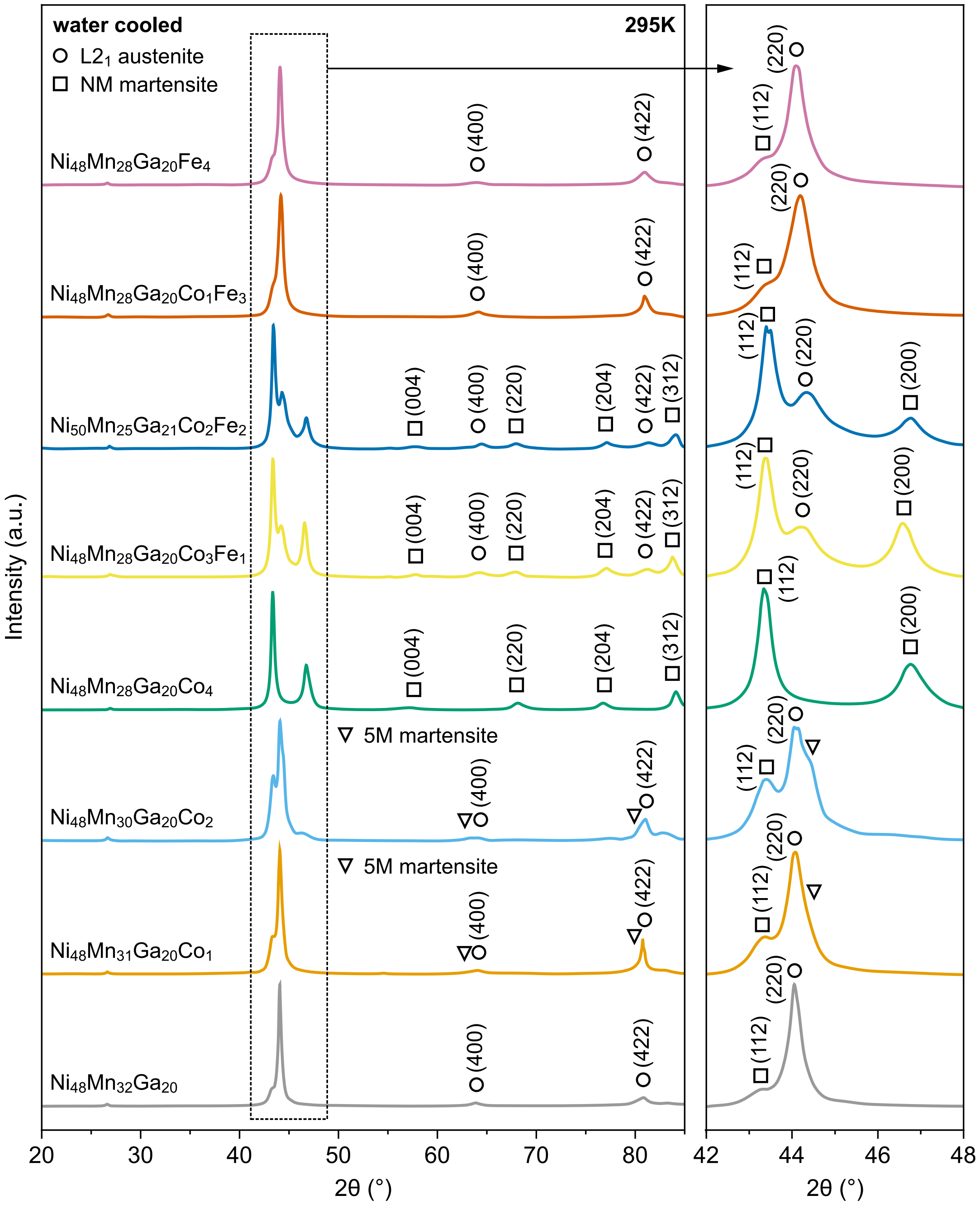

Fig. 3.26. The XRD patterns obtained at room temperature (295 K) for the water cooled $Ni_{48}Mn_{32}Ga_{20}$, $Ni_{48}Mn_{31}Ga_{20}Co_1$, $Ni_{48}Mn_{30}Ga_{20}Co_2$, $Ni_{48}Mn_{28}Ga_{20}Co_4$, $Ni_{48}Mn_{28}Ga_{20}Co_3Fe_1$, $Ni_{50}Mn_{25}Ga_{21}Co_2Fe_2$, $Ni_{48}Mn_{28}Ga_{20}Co_1Fe_3$ and $Ni_{48}Mn_{28}Ga_{20}Fe_4$ magnetic shape memory alloys. The peaks corresponding to the $L2_1$ austenite, NM martensite and 5M modulated martensite are indicated by circle, square and triangle symbol, respectively.

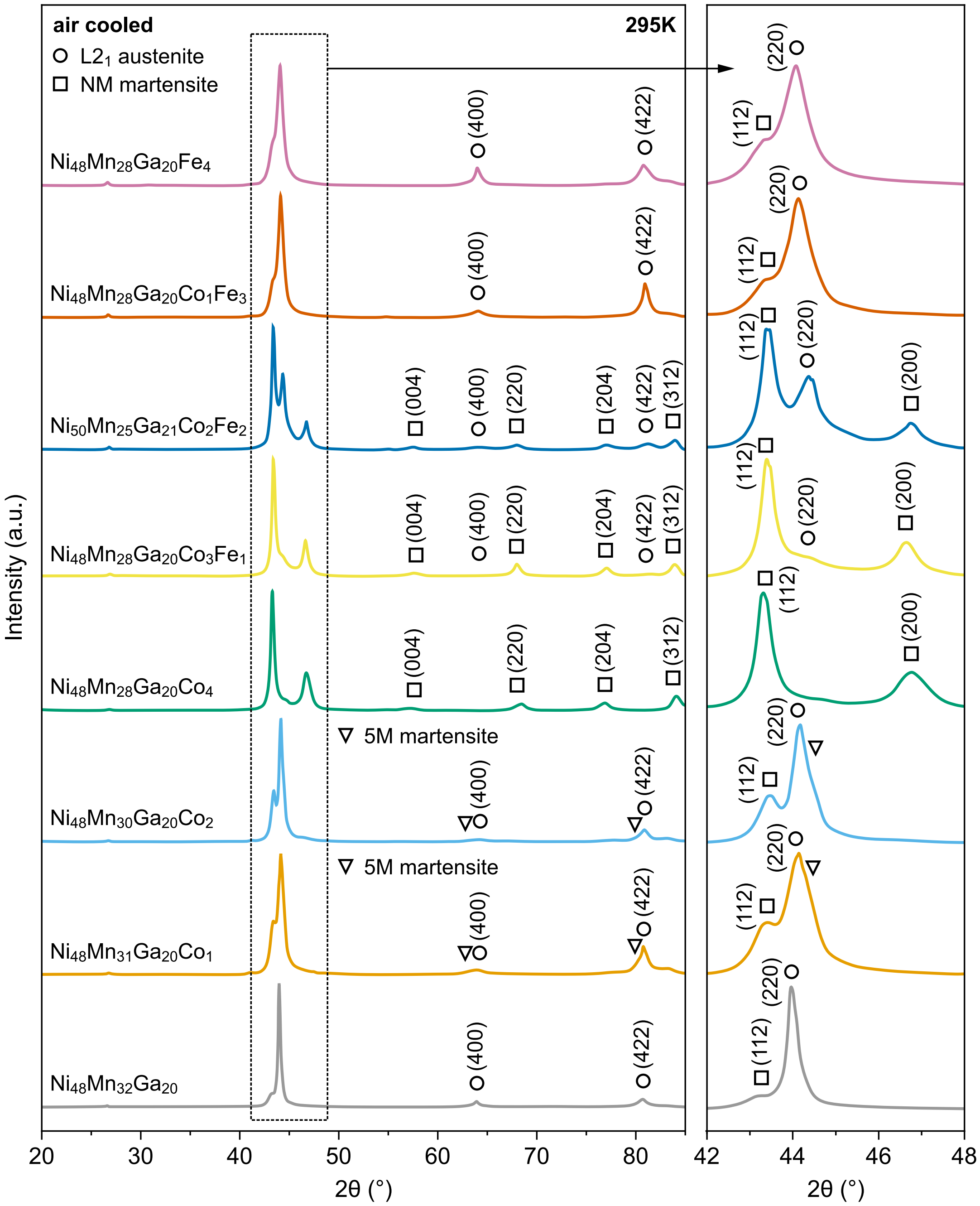

Fig. 3.27. The XRD patterns obtained at room temperature (295 K) for the air cooled $Ni_{48}Mn_{32}Ga_{20}$, $Ni_{48}Mn_{31}Ga_{20}Co_1$, $Ni_{48}Mn_{30}Ga_{20}Co_2$, $Ni_{48}Mn_{28}Ga_{20}Co_4$, $Ni_{48}Mn_{28}Ga_{20}Co_3Fe_1$, $Ni_{50}Mn_{25}Ga_{21}Co_2Fe_2$, $Ni_{48}Mn_{28}Ga_{20}Co_1Fe_3$ and $Ni_{48}Mn_{28}Ga_{20}Fe_4$ magnetic shape memory alloys. The peaks corresponding to the $L2_1$ austenite, NM martensite and 5M modulated martensite are indicated by circle, square and triangle symbol, respectively.

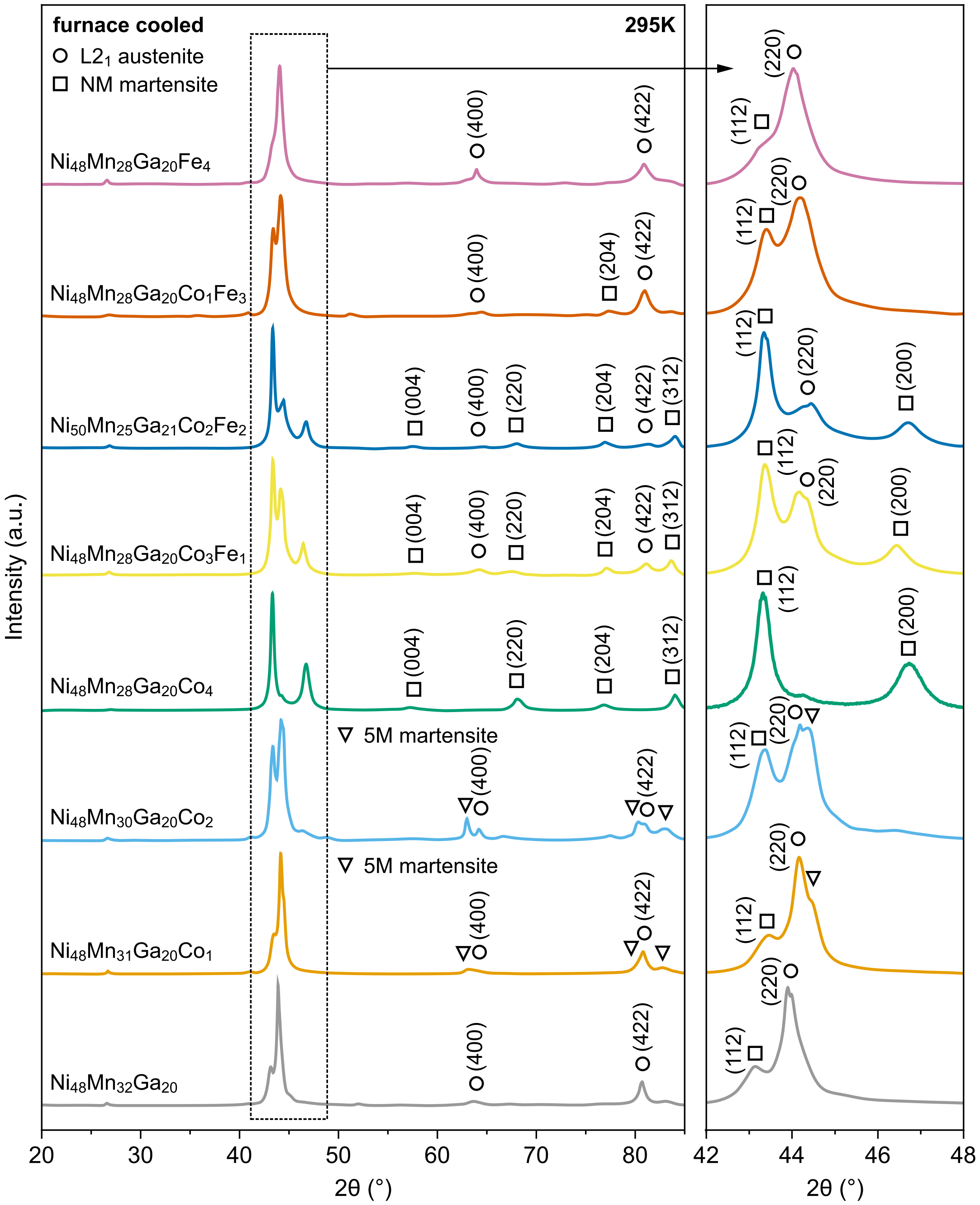

Fig. 3.28. The XRD patterns obtained at room temperature (295 K) for the furnace cooled $Ni_{48}Mn_{32}Ga_{20}$, $Ni_{48}Mn_{31}Ga_{20}Co_1$, $Ni_{48}Mn_{30}Ga_{20}Co_2$, $Ni_{48}Mn_{28}Ga_{20}Co_4$, $Ni_{48}Mn_{28}Ga_{20}Co_3Fe_1$, $Ni_{50}Mn_{25}Ga_{21}Co_2Fe_2$, $Ni_{48}Mn_{28}Ga_{20}Co_1Fe_3$ and $Ni_{48}Mn_{28}Ga_{20}Fe_4$ magnetic shape memory alloys. The peaks corresponding to the L2$_1$ austenite, NM martensite and 5M modulated martensite are indicated by circle, square and triangle symbol, respectively.

In a matter of qualitative description of crystal structure of the produced NiMnGa-based multifunctional alloys, the Rietveld refinement analysis presented in **Fig. 18–25** allowed to estimate the crystal lattice parameters for the individual austenitic and martensitic phases identified in the fabricated water, air and furnace cooled samples. **Table 3.2** shows the summary of the performed Rietveld analysis for all evaluated alloys depicted in **Fig. 18–25**. The refinement results presented in Table 3.2 include the crystal lattice parameters for the cubic austenite, tetragonal NM martensite and monoclinic 5M modulated martensite, as well as the related agreement indices (R_{wp}, R_{exp} and GOF) representing the actual refinement quality. The mathematical definition of each refinement factor is given in the experimental part of the thesis in **Section 2.3.3**.

First of all, it should be emphasised, that according to the presented agreement factors, all performed refinements are characterized by reliable and consistent fits. Regarding R-factors, the low values of R_{exp}, below 2.5 for all the investigated samples, indicates the high-quality data with negligible noise and background influence. Moreover, it is widely accepted in the crystallographic community that a successful fit requires the GOF of less than 4. In the majority of the presented refinements, the GOF is typically less then 2.0, and occasionally only slightly above 2.0, which suggests an excellent convergence between the recorded XRD patterns and proposed crystallographic model of the produced NiMnGa-based materials. Apparently, one has to bear in mind that strictly mathematical background of the abovementioned agreement indices could lead to a scenario in which the wrong crystallographic solution achieves an excellent match that is solely characterized by low values of R_{wp}, R_{exp} and GOF. In a view of this, two things should be prioritized in Rietveld analysis: first, decreasing the discrepancy between predicted and observed XRD patterns, and second, mathematical agreement factors. This complementary approach was used for the presented Rietveld refinements, with particular attention devoted to the discrepancy between crystallographic model and the observed XRD spectrum. These differences in XRD patterns were already depicted as blue solid lines in **Fig. 18–25**, demonstrating the satisfactory accuracy of the proposed crystallographic models. Based on that crystallographic solution, the additional convergence of experimental and recorded XRD patterns were carried out to minimize the aforementioned refinement agreement factors. As a result, the obtained low values of R_{wp}, R_{exp} and GOF, summarized in **Table 3.2**, provides a reliable information about the quality of the accomplished fits.

Table 3.2. Crystal lattice parameters obtained from the Rietveld refinement of the XRD patterns recorded at different temperatures for the produced water, air and furnace cooled NiMnGa-based alloys. The identified and refined phases include cubic austenite ($Fm\bar{3}m$, no. 225), tetragonal martensite ($I4/mmm$, no. 139) and monoclinic 5M modulated martensite ($P2/m$, no. 10). The agreement factors R_{wp}, R_{exp} and GOF specifies the quality of the performed fits.

	$Ni_{48}Mn_{32}Ga_{20}$				
	Water cooled			**Air cooled**	**Furnace cooled**
	295 K	**320 K**	**400 K**	**295 K**	**295 K**
Austenite [$Fm\bar{3}m$]					
a (Å)	5.850	5.844	5.844	5.846	5.843
V_{cell} (Å^3)	200.2	199.6	199.6	199.8	199.5
NM martensite [I4/mmm]					
a (Å)	4.034	3.998		4.039	3.973
c (Å)	6.255	6.285		6.239	6.354
c/a	1.551	1.572		1.545	1.599
V_{cell} (Å^3)	101.8	100.5		101.8	100.3
Agreement factors					
R_{wp}	3.31	3.21	4.66	4.03	3.31
R_{exp}	1.87	2.31	2.26	2.01	2.16
GOF	1.77	1.39	2.06	2.00	1.53

	$Ni_{48}Mn_{31}Ga_{20}Co_1$				
	Water cooled			**Air cooled**	**Furnace cooled**
	295 K	**320 K**	**400 K**	**295 K**	**295 K**
Austenite [$Fm\bar{3}m$]					
a (Å)	5.845	5.841	5.839	5.843	5.839
V_{cell} (Å^3)	199.7	199.3	199.1	199.5	199.1
NM martensite [I4/mmm]					
a (Å)	3.985	3.982		3.996	3.971
c (Å)	6.331	6.328		6.302	6.373
c/a	1.589	1.589		1.577	1.605
V_{cell} (Å^3)	100.5	100.3		100.6	100.5
5M martensite [P2/m]					
a (Å)	4.199			4.197	4.199
b (Å)	5.692			5.636	5.681
c (Å)	20.85			20.97	20.89
β (°)	90.3			90.3	90.3
V_{cell} (Å^3)	498.3			496.1	498.3
Agreement factors					
R_{wp}	3.02	5.00	4.30	2.46	2.95
R_{exp}	1.94	2.30	2.28	1.87	1.92
GOF	1.56	2.17	1.89	1.32	1.54

	$Ni_{48}Mn_{30}Ga_{20}Co_2$				
	Water cooled			**Air cooled**	**Furnace cooled**
	295 K	**320 K**	**400 K**	**295 K**	**295 K**
Austenite [$Fm\bar{3}m$]					
a (Å)	5.838	5.831	5.830	5.835	5.833
V_{cell} (Å^3)	1.990	198.3	198.2	198.7	198.5
NM martensite [I4/mmm]					
a (Å)	3.961	3.952		3.957	3.955
c (Å)	6.372	6.368		6.357	6.383
c/a	1.609	1.611		1.607	1.614
V_{cell} (Å^3)	100.0	99.5		99.5	99.8
5M martensite [P2/m]					
a (Å)	4.197			4.197	4.198
b (Å)	5.638			5.636	5.632
c (Å)	20.949			20.970	21.045
β (°)	90.3			90.3	90.3
V_{cell} (Å^3)	495.7			496.1	497.6
Agreement factors					
R_{wp}	2.79	3.36	4.68	2.74	3.02
R_{exp}	1.99	2.23	2.34	1.92	2.01
GOF	1.40	1.49	2.00	1.43	1.50

	$Ni_{48}Mn_{28}Ga_{20}Co_4$				
	Water cooled			**Air cooled**	**Furnace cooled**
	295 K	**320 K**	**400 K**	**295 K**	**295 K**
Austenite [$Fm\bar{3}m$]					
a (Å)			5.815		
V_{cell} (Å^3)			196.6		
NM martensite [I4/mmm]					
a (Å)	3.902	3.903	5.815	3.900	3.904
c (Å)	6.457	6.444	6.422	6.458	6.452
c/a	1.655	1.651	1.646	1.656	1.653
V_{cell} (Å^3)	98.3	98.2	97.7	98.2	
Agreement factors					
R_{wp}	3.75	4.48	3.02	4.35	4.10
R_{exp}	1.71	2.23	2.32	1.86	1.77
GOF	2.19	2.01	1.30	2.34	2.32

	$Ni_{48}Mn_{28}Ga_{20}Co_3Fe_1$				
	Water cooled			**Air cooled**	**Furnace cooled**
	295 K	**320 K**	**400 K**	**295 K**	**295 K**
Austenite [$Fm\bar{3}m$]					
a (Å)	5.822	5.818	5.814	5.821	5.823
V_{cell} (Å^3)	197.3	196.9	196.5	197.2	197.4
NM martensite [I4/mmm]					
a (Å)	3.920	3.932		3.917	3.929
c (Å)	6.421	6.395		6.426	6.401
c/a	1.638	1.626		1.641	1.629
V_{cell} (Å^3)	98.7	98.9		98.6	98.8
Agreement factors					
R_{wp}	2.94	3.45	3.84	3.60	3.42
R_{exp}	2.05	2.27	2.34	2.03	1.87
GOF	1.43	1.52	1.64	1.77	1.83

	$Ni_{50}Mn_{25}Ga_{21}Co_2Fe_2$				
	Water cooled			**Air cooled**	**Furnace cooled**
	295 K	**320 K**	**400 K**	**295 K**	**295 K**
Austenite [$Fm\bar{3}m$]					
a (Å)	5.815	5.812	5.808	5.818	5.810
V_{cell} (Å^3)	196.6	196.3	195.9	196.9	196.1
NM martensite [I4/mmm]					
a (Å)	3.914	3.908		3.915	3.910
c (Å)	6.443	6.419		6.446	6.441
c/a	1.646	1.642		1.646	1.647
V_{cell} (Å^3)	98.7	98.0		98.8	98.5
Agreement factors					
R_{wp}	3.45	3.02	3.40	4.46	3.64
R_{exp}	1.87	2.31	2.33	1.97	1.83
GOF	1.84	1.31	1.46	2.26	1.99

	$Ni_{48}Mn_{28}Ga_{20}Co_1Fe_3$				
	Water cooled			**Air cooled**	**Furnace cooled**
	295 K	**320 K**	**400 K**	**295 K**	**295 K**
Austenite [$Fm\bar{3}m$]					
a (Å)	5.832	5.826	5.825	5.827	5.832
V_{cell} (Å^3)	198.4	197.8	197.7	197.9	198.4
NM martensite [I4/mmm]					
a (Å)	3.952	3.965		3.947	3.957
c (Å)	6.365	6.312		6.366	6.351
c/a	1.611	1.592		1.613	1.605
V_{cell} (Å^3)	99.4	99.2		99.2	99.4
Agreement factors					
R_{wp}	2.79	2.68	3.84	3.00	2.95
R_{exp}	1.89	2.22	2.28	2.07	2.09
GOF	1.48	1.21	1.68	1.45	1.41

	$Ni_{48}Mn_{28}Ga_{20}Fe_4$				
	Water cooled			**Air cooled**	**Furnace cooled**
	295 K	**320 K**	**400 K**	**295 K**	**295 K**
Austenite [$Fm\bar{3}m$]					
a (Å)	5.836	5.832	5.831	5.832	5.834
V_{cell} (Å^3)	198.8	198.4	198.3	198.4	198.6
NM martensite [I4/mmm]					
a (Å)	3.967	3.986		3.962	3.973
c (Å)	6.336	6.274		6.343	6.321
c/a	1.597	1.574		1.601	1.591
V_{cell} (Å^3)	99.7	99.7		99.6	99.8
Agreement factors					
R_{wp}	3.58	3.32	4.19	2.85	2.65
R_{exp}	1.87	2.18	2.19	1.92	2.02
GOF	1.91	1.52	1.91	1.48	1.31

To visualise some most important crystallographic data attached in **Table 3.2**, the supporting figures were additionally developed and presented below. **Fig. 3.29** depicts the values of crystal lattice parameters for the cubic austenite and tetragonal NM martensite for all the examined alloys exposed to different cooling conditions. The presented plots are expressed as a function of doping elements, *i.e.* the left part of the **Fig 3.29** shows the Co-doped samples, whereas the right part of the plot presents the Fe-Co-doped materials (the exact at.% of doping elements are presented on the *x* axis). The following study ignores the lattice parameters for the 5M modulated martensite since this structure was observed only in two compositions ($Ni_{48}Mn_{31}Ga_{20}Co_1$ and $Ni_{48}Mn_{30}Ga_{20}Co_2$ alloy – **Table 3.2**), thus limiting the ability to draw any valuable conclusions from the few data.

In the cubic austenite $L2_1$ unit cell (**Fig 3.29(a)**), it can be observed that the lattice parameter *a* decrease almost linearly, with the increasing Co content and then increase linearly, when Co is gradually substituted by Fe. The observed changes in estimated lattice parameter are not spectacular, as for the water cooled Co-doped alloys the a drops from 5.850 Å for the $Ni_{48}Mn_{32}Ga_{20}$ sample to 5.838 Å for the $Ni_{48}Mn_{30}Ga_{20}Co_2$ specimen and then increase for the Fe-Co-doped alloys from 5.822 Å for the $Ni_{48}Mn_{28}Ga_{20}Co_3Fe_1$ sample to 5.836 Å for the $Ni_{48}Mn_{28}Ga_{20}Fe_4$ specimen (**Table 3.2**). Interestingly, the slight, but noticeable difference between the austenite lattice parameter are observed for the materials with the same chemical composition, but fabricated using different cooling procedure. In almost all presented cases the highest values of a were estimated for the water cooled samples, whereas for the air and furnace cooled materials the values of a differ between the equivalent chemical compositions. It should be also noted that the $Ni_{50}Mn_{25}Ga_{21}Co_2Fe_2$ alloy clearly stands out from the other produced materials due to a different Ni/Mn ratio (**Fig 3.29(a)**). It shows that the Ni/Mn ratio, as opposed to Fe and Co elemental doping, has a greater influence on the lattice parameter for Fe-Co-doped NiMnGa-based alloys.

The tetragonal unit cell of NM martensite is characterized by two lattice parameters a and c, graphically presented in **Fig. 3.29(b)**. Similarly to the austenite phase (**Fig. 3.29(a)**), the changes in lattice parameters of martensite are also almost linear, which is represented by corresponding dotted lines. Once again, the influence of Fe doping on lattice parameters of NiMnGa-based Heusler alloys is in direct opposition to the effect of Co doping. For the Co-doped samples the basal length a decreases with the increasing Co content and then slightly increases when Co is gradually substituted by Fe. At the same time, the unit cell height c notably increases with the increasing Co content and than decreases with the ongoing Fe doping. When it comes to differences between the water, air and furnace cooled alloys they are mainly observed for the Co-doped samples, as furnace cooled materials exhibits significantly lower changes in both lattice parameters than water and air cooled specimens (**Fig. 3.29(b)**). These differences vanishes for the $Ni_{48}Mn_{28}Ga_{20}Co_4$ alloy and can be disregarded for additional Fe doping. The aforementioned initial increase in c, followed by the gradual decrease, occurs at higher rate than the opposite changes in a. Therefore, as shown in **Fig 3.29(c)**, the variations in lattice parameter c governs the tetragonality (c/a) of the NM martensite unit cell. It can be seen that the tetragonality of the NM martensite for differently cooled alloys behaves analogously as c parameter shown in **Fig. 3.29(b)**. For example, the tetragonality for the water cooled alloys changes from 1.550 for the $Ni_{48}Mn_{32}Ga_{20}$ sample to 1.655 for the $Ni_{48}Mn_{28}Ga_{20}Co_4$ alloy and back to 1.597 for the $Ni_{48}Mn_{28}Ga_{20}Fe_4$ sample.

Lastly, it is worth mentioning that, the $Ni_{50}Mn_{25}Ga_{21}Co_2Fe_2$ alloy differs from other samples in terms of the lattice characteristics and tetragonality of NM martensite, just like it does with the austenitic phase. This is manly due to the previously mentioned differences in Ni/Mn ratio, which are significant in determining the crystal lattice parameters of NiMnGa-base Heusler alloys.

The previously introduced temperature dependent XRD investigations of the water cooled NiMnGa-based alloys, followed by Rietveld refinement summarized in **Table 3.2**, also provide some important information about the crystallographic nature of the fabricated Heusler materials. **Fig. 3.20** presents the lattice parameters of the austenite and NM martensite phase as well as the tetragonality parameter for the water-cooled samples obtained at 295 K, 320 K and 400 K. The figure is arrange in the same way as **Fig. 3.29**, exposing the division between Co-doped and Fe-Co-doped specimens.

As can be clearly seen in **Fig. 3.30(a)**, the cubic austenite phase, which is characterized by parameter a, exhibits the most pronounced differences in lattice characteristics. For all the investigated NiMnGa-based materials, the differences between a estimated at two extreme temperatures, *i.e.* 295 K and 400 K, are relatively constant and close to 0.01 Å (**Table 3.2**).

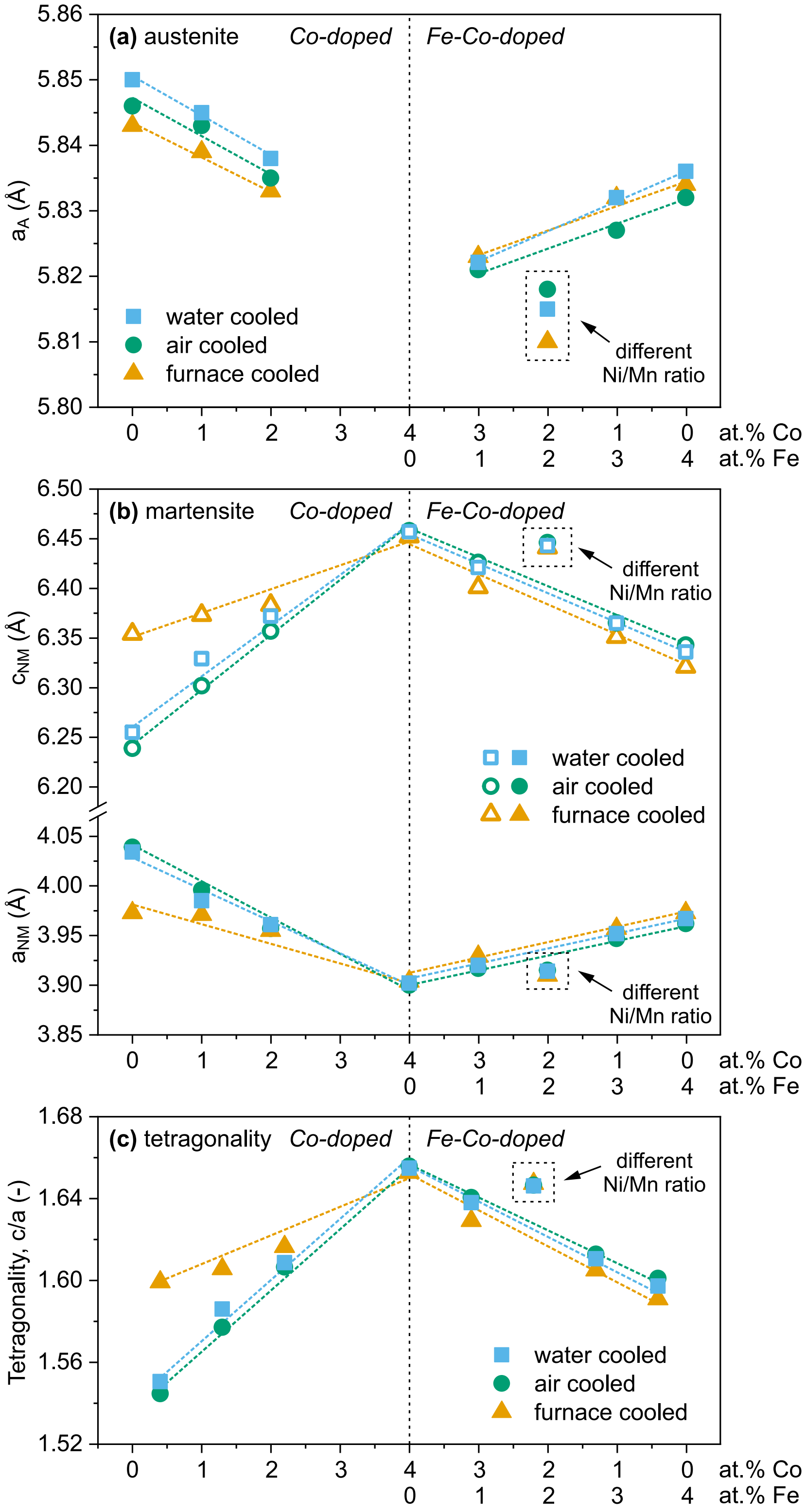

Fig. 3.29. The crystal lattice parameters of **(a)** the cubic austenite (a_A) and **(b)** tetragonal martensite (a_{NM} and c_{NM}), as well as **(c)** the tetragonality of NM martensite (c/a) estimated from the water, air and furnace cooled $Ni_{48}Mn_{32}Ga_{20}$, $Ni_{48}Mn_{31}Ga_{20}Co_1$, $Ni_{48}Mn_{30}Ga_{20}Co_2$, $Ni_{48}Mn_{28}Ga_{20}Co_4$, $Ni_{48}Mn_{28}Ga_{20}Co_3Fe_1$, $Ni_{50}Mn_{25}Ga_{21}Co_2Fe_2$, $Ni_{48}Mn_{28}Ga_{20}Co_1Fe_3$ and $Ni_{48}Mn_{28}Ga_{20}Fe_4$ alloys. The symbols corresponding to the $Ni_{50}Mn_{25}Ga_{21}Co_2Fe_2$ alloys characterized by different Ni/Mn ratio are indicated by frames.

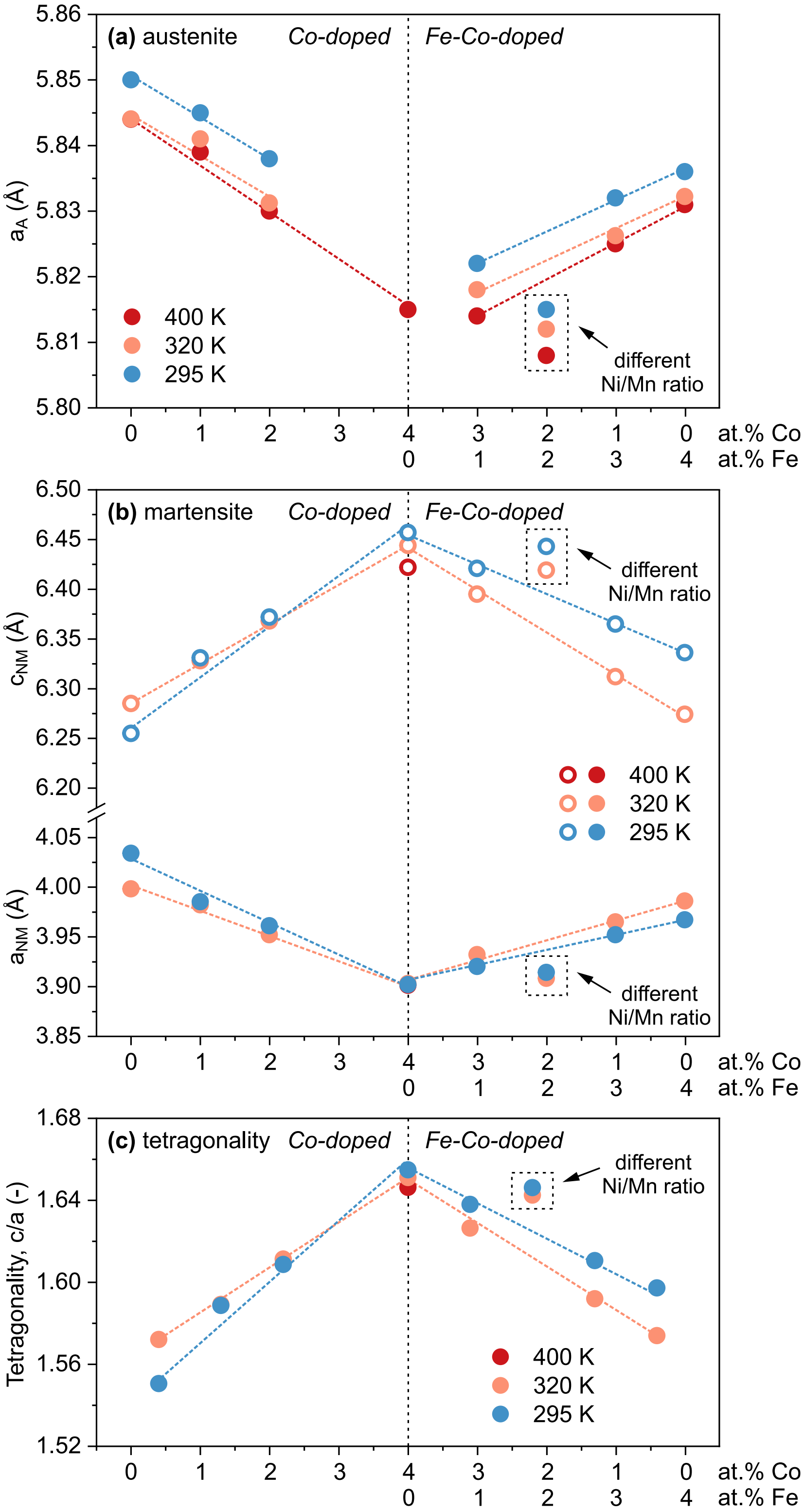

Fig. 3.30. The crystal lattice parameters of **(a)** the cubic austenite (a_A) and **(b)** tetragonal martensite (a_{NM} and c_{NM}), as well as **(c)** the tetragonality of NM martensite (c/a) estimated from the Rietveld refinement at 295 K, 320 K and 400 K for the water cooled $Ni_{48}Mn_{32}Ga_{20}$, $Ni_{48}Mn_{31}Ga_{20}Co_1$, $Ni_{48}Mn_{30}Ga_{20}Co_2$, $Ni_{48}Mn_{28}Ga_{20}Co_4$, $Ni_{48}Mn_{28}Ga_{20}Co_3Fe_1$, $Ni_{50}Mn_{25}Ga_{21}Co_2Fe_2$, $Ni_{48}Mn_{28}Ga_{20}Co_1Fe_3$ and $Ni_{48}Mn_{28}Ga_{20}Fe_4$ alloys. The symbols corresponding to the $Ni_{50}Mn_{25}Ga_{21}Co_2Fe_2$ alloys characterized by different Ni/Mn ratio are indicated by frame.

In consideration of NM martensite phase, the proper comparison of temperature dependent lattice parameters can be carried out only for data obtained at 295 K and 320 K, as at 400 K the martensitic phase was identified only in the $Ni_{48}Mn_{28}Ga_{20}Co_4$ alloy. In such a case, the aforementioned austenite lattice differences becomes neglectable for the tetragonal NM martensite. As can be seen in **Fig. 3.30(b)**, the values of a and c parameters obtained at 295 K and 320 K are very comparable with only minor differences for the Fe-Co-doped samples. Consequently, in **Fig. 3.30(c)** the same negligible differences between tetragonality of the NM martensite phase estimated at various temperatures are also observed for all the examined Heusler materials.

The results presented in **Fig. 3.29** and **3.30** demonstrates the usefulness of the straightforward elemental doping strategy in defining the structural evolution of NiMnGa-based materials. However, this approach works only as a function of one compositional factor, e.g. substitution of Ni/Mn/Ga by selected alloying element. As a result, the discussed method is not universal, because any additional variations in chemical composition of the alloy results in the changes in the overall behaviour of lattice parameters. When Co is replaced by Fe, the increasing or decreasing trend of a particular lattice parameter is abruptly reversed, while any changes in Ni/Mn ratio discard the material form the primary structural trend.

In order to study the potential dependence of crystal lattice parameters with the electronic parameters of the fabricated NiMnGa-based alloys, the crystallographic data from **Table 3**.2 were also investigated as a function of valence electron concentration e/a and the non-bonding electrons concentration N_e/a parameters described in theoretical part of the thesis in **Sections 1.6.1** and **1.6.2.4**. The calculations of both parameters were formerly carried out based on EDS analysis and listed in **Table 3.1** (**Section 3.1.3**).

Fig 3.31 and **3.32** presents the crystal lattice parameters for the austenitic and martensitic phase of the produced water, air and furnace cooled NiMnGa-based alloys express as a function of e/a and N_e/a, respectively. According to **Fig. 3.31**, the general behaviour of austenite and martensite lattice parameters for water, air, and furnace cooled alloys is comparable in terms of valence electron concentration. The a_A of cubic austenite and a_{NM} of tetragonal NM martensite decrease with the increasing e/a, whereas c_{NM} of NM martensite simultaneously increases. Nevertheless, there are some noticeable differences between the variously cooled specimens. Firstly, it is discovered that not all produced samples exhibit a monotonic increase or decrease of a given crystal lattice parameter, resulting in a distinction between Co-doped and Fe-Co-doped alloys. This discrepancy is seen for parameter c for the water cooled alloys, which has slightly lower values for the Fe-Co-doped alloys than for the Co-doped alloys. However, it should be noted that both trends for Co-doped and Fe-Co-doped specimens exhibit the same linear tendency and that these differences are actually quite small when compared to the average value of c_{NM}. These discrepancies between Co-doped and Fe-Co-doped materials become more noticeable only for furnace cooled alloys and show the characteristic non-linear monocity of c_{NM}. For the air cooled alloys both martensite lattice parameters (a_{NM} and c_{NM}) changes linearly, without any significant deviations. However, in this case, the a_A of austenite losses its monotonic behaviour and splits into two distinct trends for Co-doped and Fe-Co-doped samples.

Despite the aforementioned differences in a_A the lattice parameters expressed as a function of e/a for the water and air cooled alloys are comparable and characterizes by the same monotonical changes of a_A as well as the linear dependence of a_{NM} and c_{NM}. The most evident discrepancies in lattice parameters behaviour between differently cooled materials are observed for the furnace cooled alloys presented in **Fig 3.21(c)**. It can be seen that when alloys are slowly cooled in furnace, changes in a_A are more distant from linear dependence than in case of water and air cooled samples. Moreover, the a_{NM} and c_{NM} parameters no longer display their prior obvious linear behaviour. These significant differences stems from the thermal history of the slowest cooled alloys and indicates the lowest stability of crystal lattice parameters both before and after martensitic transformation.

What is important to note, the $Ni_{50}Mn_{25}Ga_{21}Co_2Fe_2$ alloy, which has a different Ni/Mn ratio, do not stands out from the other alloys presented in **Fig. 3.31** and evenly follows the examined structural changes. This implies that for the Fe and/or Co doping the e/a is a more accurate parameter to define the changes in crystal lattice of the NiMnGa-based material, than basic elemental doping approach presented in **Fig. 3.29** and **3.30**. As shown in **Fig. 3.31** and **3.32**, when Heusler alloys with different Ni-Mn-Ga composition are doped by Fe and/or Co the e/a ratio relatively effectively takes into account both the amount of constituent Ni, Mn and Ga atoms, as well as the additional alloying elements.

Another investigated electronic parameter defined as non-bonding electrons concentration is presented in **Fig. 3.32**. The figure is arrange in the same manner as **Fig. 3.31**, however this time the evaluated crystal lattice parameters are plotted against the N_e/a parameter. The first main obvious difference observed for N_e/a dependence is the clear distinction between the crystal lattice parameters behaviour for Co-doped and Fe-Co-doped alloys. This distinction is evident for both cubic austenite and tetragonal martensite for all alloys exposed to different cooling procedures. The general tendency for increasing or decreasing of the individual lattice parameter with the increasing value of N_e/a is the same for both Co-doped and Fe-Co-doped alloys, however the introduction of different atomic element to Ni-Mn-Ga composition substantially decreases (for a_A and a_{NM}) or increases (for c_{NM}) the overall trend (**Fig. 3.32**). This is partially caused by the notable difference between the number of non-bonding electron equal to 3.64 and 2.45 for Co and Fe, respectively. In case of previously discussed e/a parameter (**Fig. 3.31**), the Co and Fe were characterized by 9 and 8 electrons, respectively, making the relative difference between the electronic parameters of neighbouring alloys less significant.

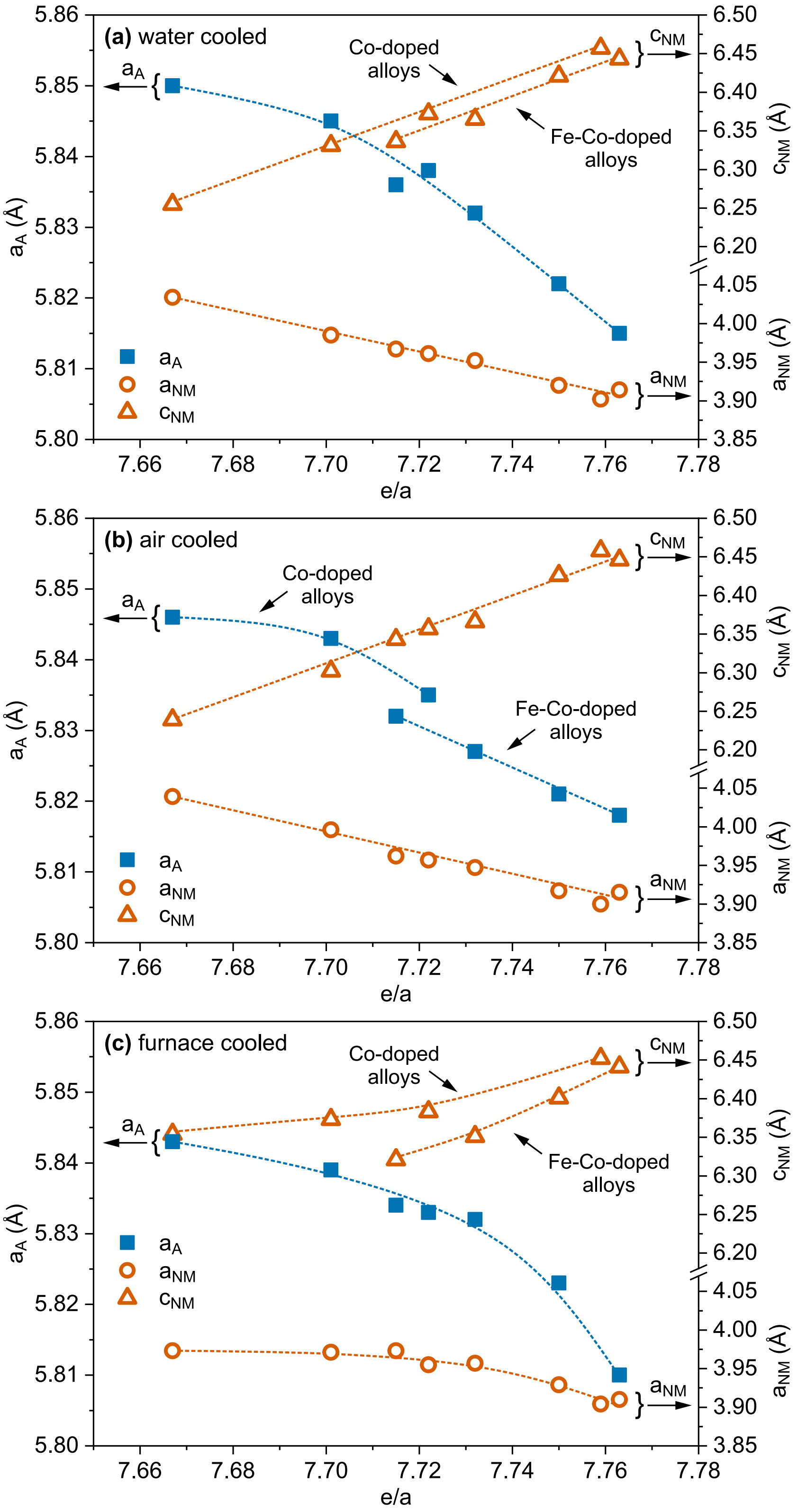

Fig. 3.31. Crystal lattice parameters dependence of the valence electrons concentration *e*/*a* for the cubic austenite (a_A) and tetragonal martensite (a_{NM} and c_{NM}) estimated from the Rietveld refinement at room temperature for the **(a)** water, **(b)** air and **(c)** furnace cooled NiMnGa-based Heusler alloys doped by Co and/or Fe. The dotted lines are guide for an eye to show the trends in lattice parameters.

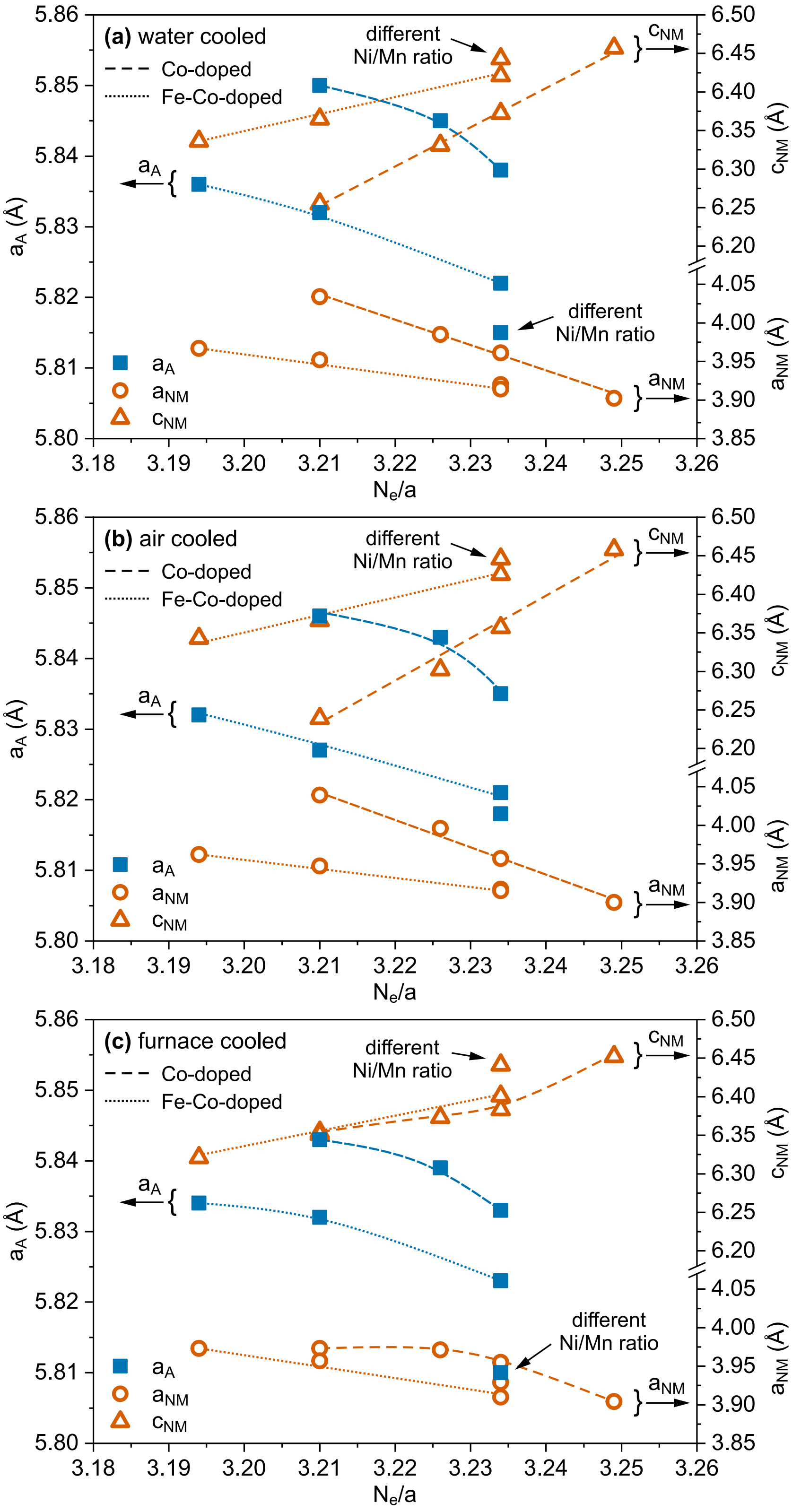

Fig. 3.32. Crystal lattice parameters dependence of the non-bonding electrons concentration N_e/a for the cubic austenite (a_A) and tetragonal martensite (a_{NM} and c_{NM}) estimated for the **(a)** water, **(b)** air and **(c)** furnace cooled NiMnGa-based Heusler alloys doped by Co and/or Fe. The dashed and dotted lines corresponds to Co-doped and Fe-Co-doped alloys, respectively.

Furthermore, it is also seen that the $Ni_{50}Mn_{25}Ga_{21}Co_2Fe_2$ alloy, with a different Ni/Mn ratio, is not consistent with the general trends observed in **Fig. 3.32**. It was discovered that in case of NiMnGa-based alloys doped by Fe and Co, in contrast to the e/a parameter, the N_e/a is sensitive to changes in Ni/Mn ratio. This situation is most evident on the example of lattice parameters estimated for the furnace cooled samples presented in **Fig. 3.31(c)** and **3.32(c)**. For the e/a parameter (**Fig. 3.31(c)**) the $Ni_{50}Mn_{25}Ga_{21}Co_2Fe_2$ alloy follows the general trend of lattice parameter changes, but for the N_e/a parameter (**Fig. 3.32(c)**) the same sample distinguished by different Ni/Mn ratio considerably deviates from the generally established monotonic trends.

Despite the discussed lack of universality in defining the crystal lattice variations with the help of N_e/a parameter, one important advantage of N_e/a should be emphasised. Within a distinguished group of alloys for which only two elements are mutually substituted, *i.e.* Mn for Co in Co-doped samples and Fe for Co in Fe-Co-doped samples, the general almost linear changes in lattice parameters are observed. Similarly to the e/a parameter, this linear monotonicity is particularly evident for the tetragonal martensite unit cell, especially for the water and air cooled materials depicted in **Fig 3.32(a)** and **32(b)**, respectively. It should be noted that the visible changes in austenite unit cell parameter are also very close to linearity, which was not so obvious for the counterpart a/e parameter (**Fig. 3.31**). Once again, the general tendencies for all studied lattice parameters are comparable for NiMnGa-based materials cooled in water or air, but deteriorates for samples slowly cooled in furnace (**Fig. 3.31(c)**). This is caused by the low crystal lattice stability of the furnace cooled alloys obtained after very slow cooling from disorder B2′ phase.

The tetragonality of the NM martensite phase also reflects the discrepancies between e/a and N_e/a parameters. **Fig. 3.33** presents the c/a for the water, air and furnace cooled alloys expressed as a function of both e/a (**Fig. 3.33(a)–(c)**) and N_e/a (**Fig. 3.33(d)–(f)**). It is evident that in case of e/a parameter, the martensite tetragonality follows the same increasing linear trend with the increasing values of e/a for all alloys cooled in water or air. However, this linear behaviour differentiates between Co-doped and Fe-Co-doped alloys for samples that were cooled in a furnace. When it comes to N_e/a parameter, two separate, but almost perfectly linear relationships are observed for the Co-doped and Fe-Co-doped materials cooled in water or air. Once again, the linear dependence deteriorates for the furnace cooled samples (**Fig. 3.33(f)**). Additionally, the tetragonality of the $Ni_{50}Mn_{25}Ga_{21}Co_2Fe_2$ alloy with different Ni/Mn ratio deviates from the general linear trends observed for N_e/a parameter, which is not noticeable for the concurrent e/a parameter.

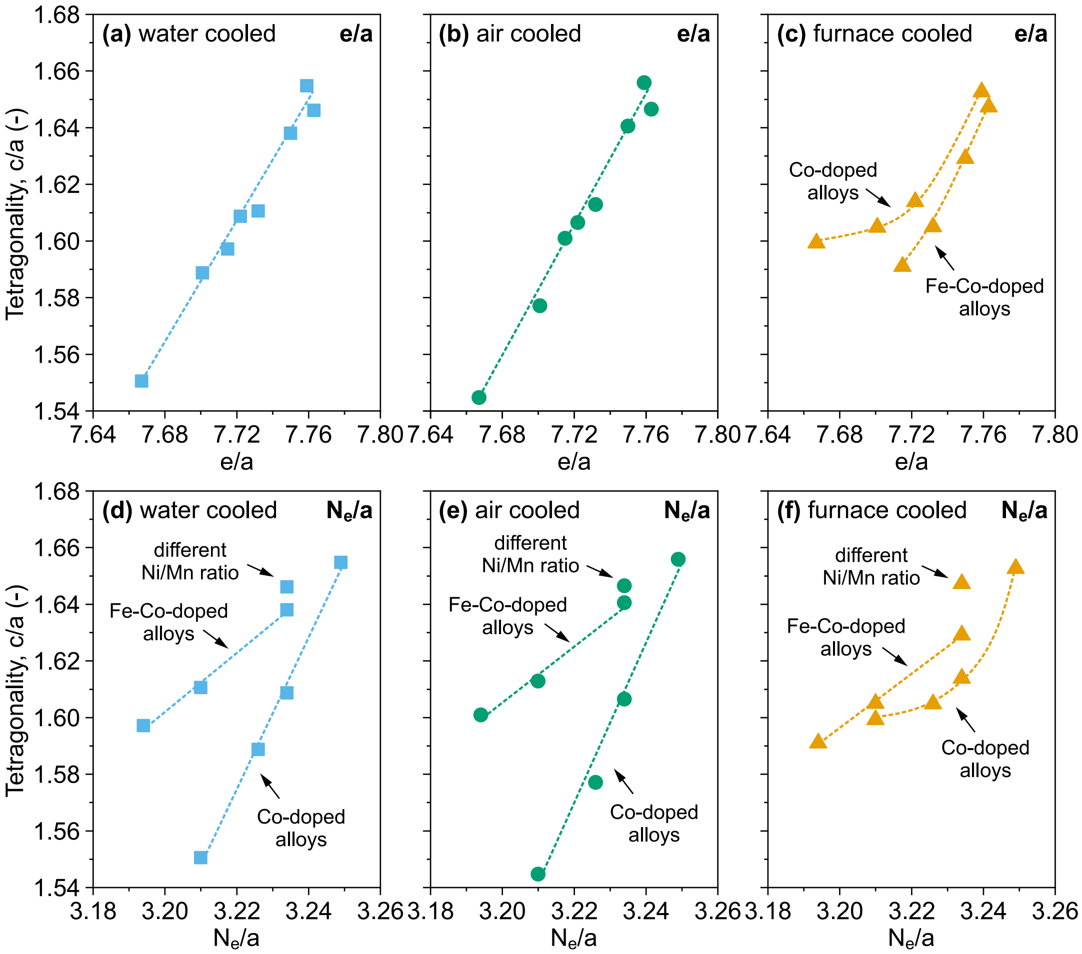

Fig. 3.33. The tetragonality of NM martensite (*c*/*a*) expressed as a function of valence electrons concentration *e*/*a* and non-bonding electrons concentration N_e/a for the **(a)** water, **(b)** air and **(c)** furnace cooled NiMnGa-based Heusler alloys doped by Co and/or Fe. The dotted lines are guide for an eye to show the trends in *c*/*a*.

Considering the influence of increasing temperature on the studied electronic parameters, Fig. 3.34 and 3.35 shows the dependence of the examined crystal lattice parameters estimated at 295 K, 320 K and 400 K for the water cooled NiMnGa-based alloys on the e/a and N_e/a parameter, respectively. As can be observed in Fig. 3.34, the general relationship between a_A and e/a is quite comparable at all investigated temperatures. It is caused by the fact that austenite is a high temperature phase, thus the increasing temperature may only stabilize this particular structure. This effect is partly seen in direct comparison of a_A estimated at two extreme temperatures, *i.e.* 295 K and 400 K. It is seen that a_A refined for the doped alloys ($e/a > 7.7$) follows more linear trend at 400 K than at 295 K. This differences are not very significant, however still well justified by the crystallographic nature of the Ni-Mn-Ga compound.

Significantly more pronounced differences in crystal lattice parameters along the *e*/*a* were found for the NM martensitic phase. In this case, it is clearly seen that at elevated temperature of 320 K, both a_{NM} and c_{NM} splits into two different linear trends related to Co-doped and Fe-Co-doped samples. The first minor signs of this separation are seen for the c_{NM} at 295 K, however they become notably more obvious at 320 K. It should be remembered that martensite is a low temperature phase, so it becomes less stable with increasing temperatures, until it completely transform into austenite. In such situation the crystal lattice characteristics and martensite stability may be significantly impacted by elemental doping. That is way, the general trend of a_{NM} and c_{NM} along the *e*/*a* divides at elevated temperatures, when Co is substituted by different dopant, *i.e.* Fe. Lastly, the $Ni_{48}Mn_{28}Ga_{20}Fe_4$ sample s the only examined alloy that is not entirely austenitic at 400 K, hence no trends in a_{NM} and c_{NM} can be identified.

When it comes to N_e/a dependence, it has already been demonstrated that even at room temperature (295 K) two distinct linear relationships are observed for Co-doped and Fe-Co-doped alloys. As a result, the crystal lattice parameters obtained at elevated temperatures are also divided into two groups, according to the type od alloying element, as presented in **Fig 3.35**. It is seen that the general relationship between a_A, a_{NM}, c_{NM} and N_e/a are analogous at room and at elevated temperatures, with linear or close to linear trends being apparent at 320 K and 400 K. The only notable deviation from general linearity of tetragonal martensite cell parameters is observed for the a_{NM} for the Fe-Cop-doped samples at 320 K (**Fig. 3.35(b)**).

The abovementioned observations are also reflected in the temperature dependent tetragonality of NM martensite phase. Fig. 3.36 presents the tetragonality of martensite estimated at 295 K and 320 K, and expressed as a function of both *e*/*a* (**Fig. 3.36(a)–(b)**) and N_e/a (**Fig. 3.36(c)–(d)**) parameter. Once more, it seemed inevitable that the c/a would inherit the general behaviour of the a_{NM} and c_{NM} parameters depicted in **Fig. 3.34** and **3.35**. This indicates that at room temperature all investigated alloys follow the same linear trend in terms of tetragonality as *e*/*a* increases (**Fig. 3.36(a)**). For Co-doped alloys and Fe-Co-doped alloys, this linear connection separates at 320 K into two independent dependencies.. In case of N_e/a parameter almost perfect linear trends observed independently for the Co-doped and Fe-Co-doped samples are generally preserved at 320 K, with slight deviation for the Co-doped materials.

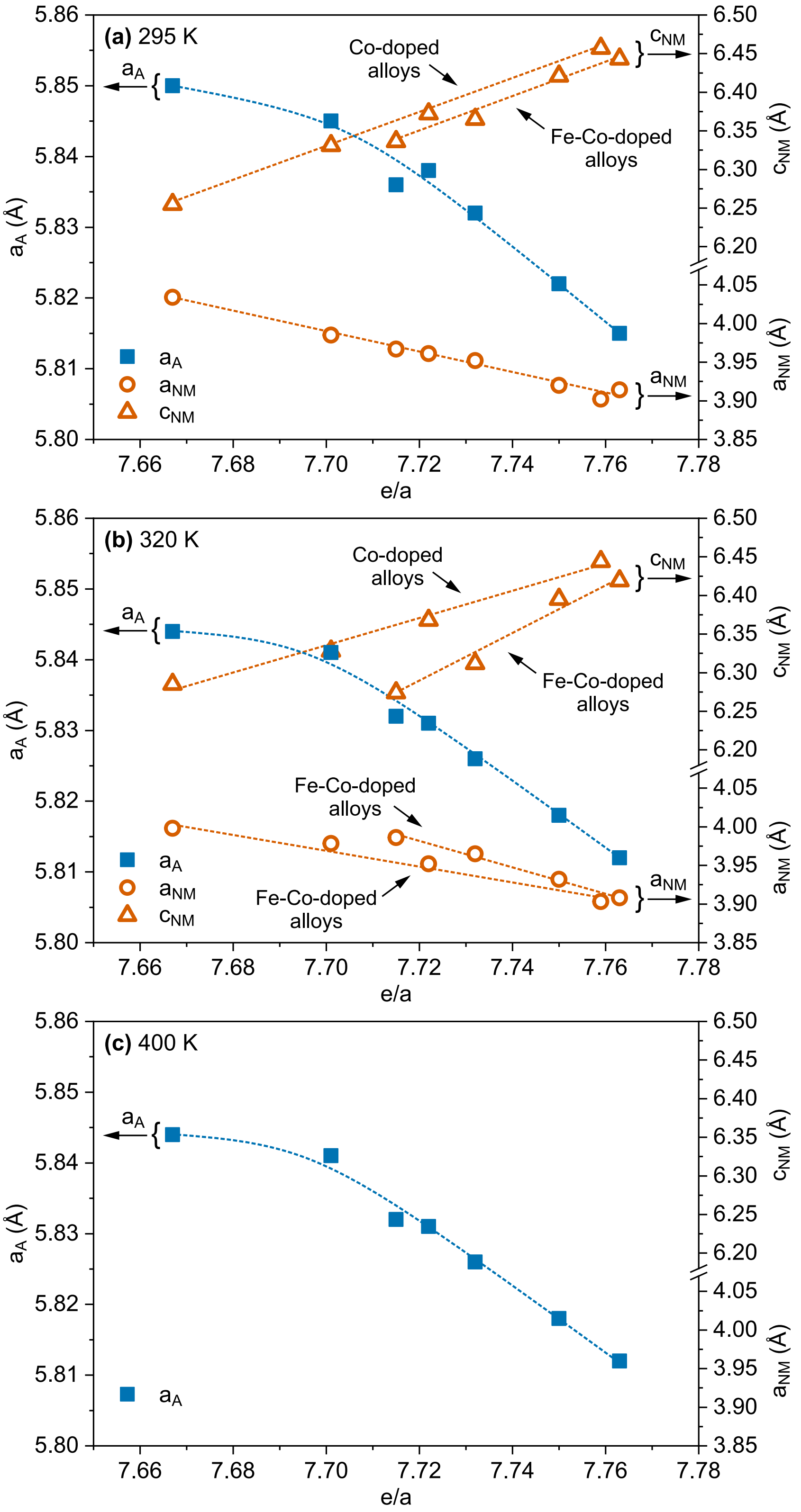

Fig. 3.34. The crystal lattice parameters dependence of the valence electrons concentration *e*/*a* for the cubic austenite (a_A) and tetragonal martensite (a_{NM} and c_{NM}) estimated from the Rietveld refinement at **(a)** 295 K, **(b)** 320 K and **(c)** 400 K for the water cooled NiMnGa-based Heusler alloys doped by Co and/or Fe. The dotted lines are guide for an eye to show the trends in lattice parameters.

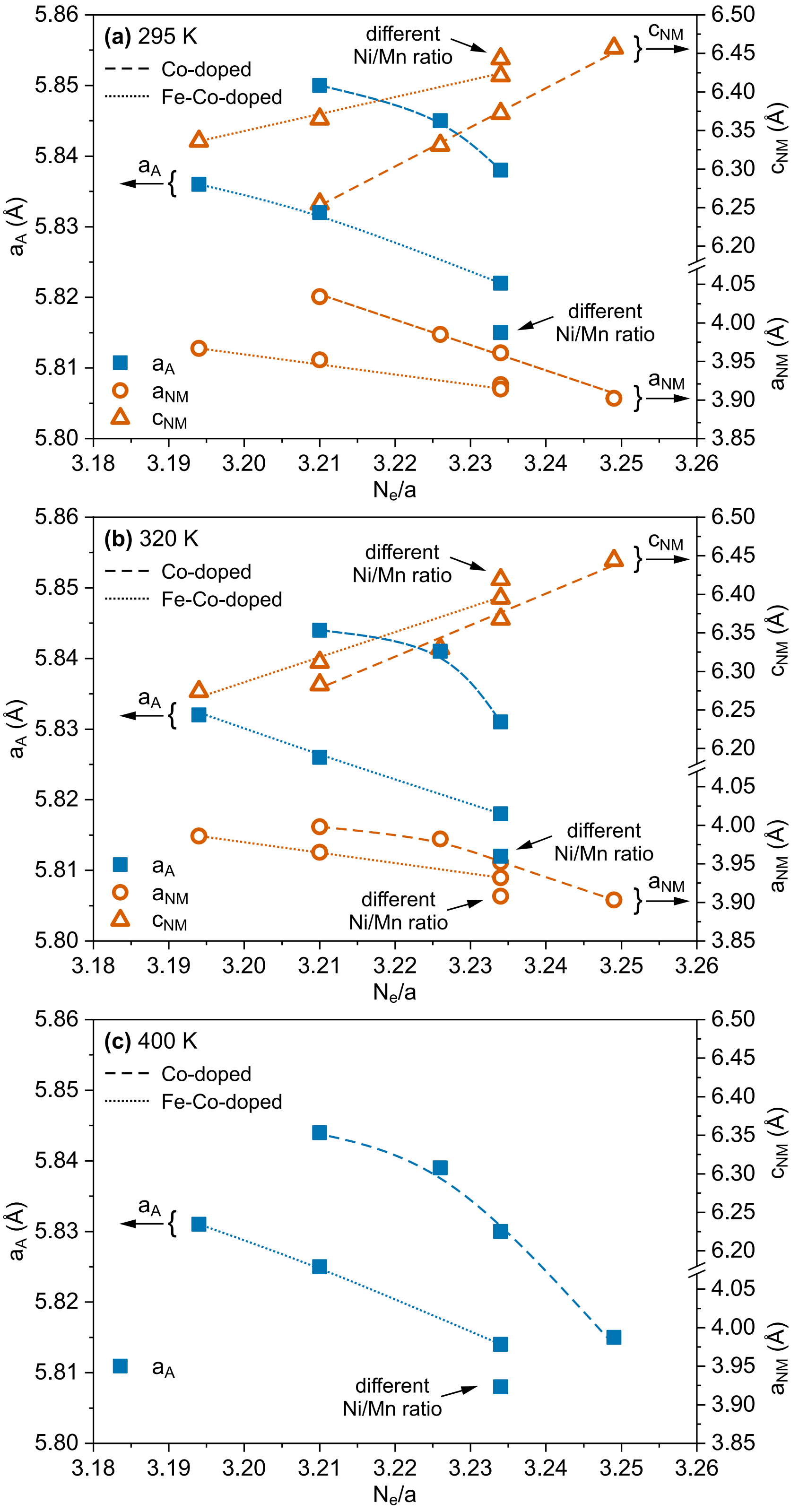

Fig. 3.35. The crystal lattice parameters dependence of the non-bonding electrons concentration N_e/a for the cubic austenite (a_A) and tetragonal martensite (a_{NM} and c_{NM}) estimated from the Rietveld refinement at **(a)** 295 K, **(b)** 320 K and **(c)** 400 K for the water cooled NiMnGa-based Heusler alloys doped by Co and/or Fe. The dashed and dotted lines are guide for an eye to show the trends in lattice parameters for the Co-doped and Fe-Co-doped alloys, respectively.

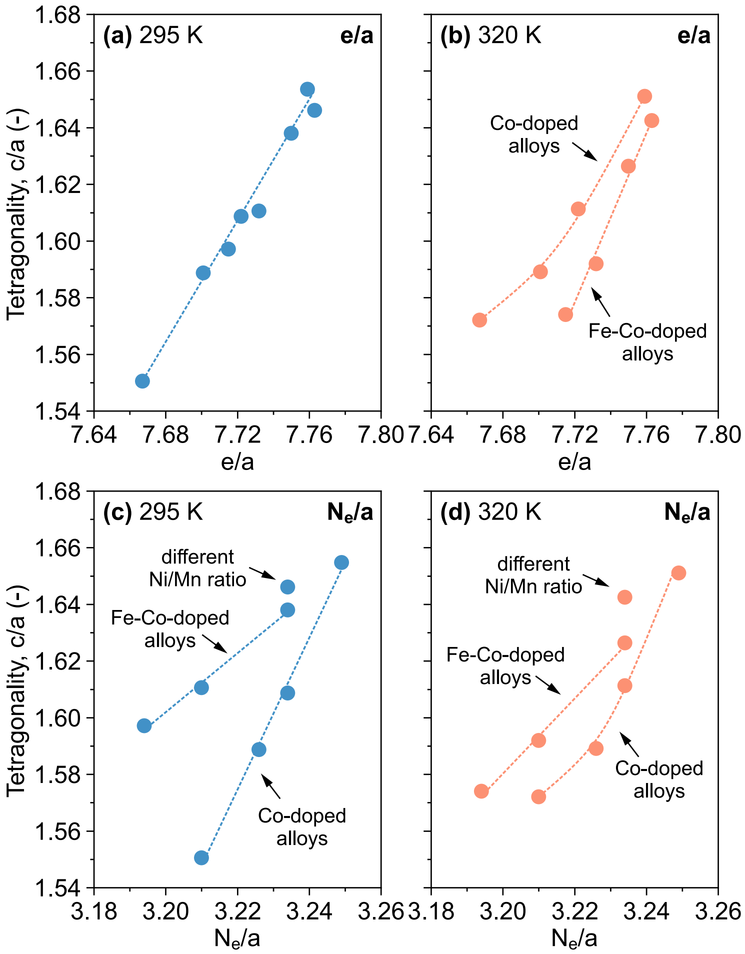

Fig. 3.36. The tetragonality of NM martensite (*c*/*a*) expressed as a function of **(a)–(b)** valence electrons concentration *e*/*a* and **(c)–(d)** non-bonding electrons concentration N_e/a at 295 K and 320 K for the water cooled NiMnGa-based Heusler alloys doped by Co and/or Fe. The dotted lines are guide for an eye to show the trends in *c*/*a*.

3.1.5 Topography of austenite and martensite phases

The previously discussed microstructural characterisation using polarised optical microscopy and SEM shown that at room temperature the $Ni_{48}Mn_{32}Ga_{20}$, $Ni_{48}Mn_{31}Ga_{20}Co_1$, $Ni_{48}Mn_{30}Ga_{20}Co_2$, $Ni_{48}Mn_{28}Ga_{20}Co_1Fe_3$ and $Ni_{48}Mn_{28}Ga_{20}Fe_4$ alloys are in austenitic state, while $Ni_{48}Mn_{28}Ga_{20}Co_4$, $Ni_{48}Mn_{28}Ga_{20}Co_3Fe_1$ and $Ni_{50}Mn_{25}Ga_{21}Co_2Fe_2$ are in martensitic state. The later in-depth XRD studies revealed that residual martensite phase is also present in austenitic alloys and correspondingly the residual austenite is present in the martensitic samples. In order to complement and expand the microstructural analysis of the fabricated NiMnGa-based multifunctional materials the atomic force microscopy studies were carried in contact mode.

The AFM examination may be particularly significant in the case of Ni-Mn-Ga shape memory material since it offers 3D images of the studied surface with all crucial topographical details. For the standard optical microscopy or SEM the obtained images are two dimensional with no quantitative information about the topography. Moreover, the usage of optical microscopy and SEM for the unetched single phase samples is also partially limited, which was already discussed in **Section 3.1.2**. In contrary, the AFM technique allows to identify complex topographical features, such as martensitic reliefs, with the resolution of single nanometres.

Nevertheless, the quantitative analysis of martensite reliefs in the fabricated Ni-Mn-Ga alloys required some basic simplifications. First of all, it should be remembered that two different unit cells are used to defined the NM martensite: (1) one connected with cubic axes of austenite cell and (2) second one arranged in the principle axes of tetragonal martensite, which is in detail explained in **Section 1.2.2**. Because the second method results in a smaller unit cell volume, it is significantly more popular and was also used in the presented thesis for the crystallographic description of manufactured alloys (**Table 3.2**). However, from the geometrical point of view, in order to characterize the martensite twinning, the same *cubic axes system* with the identical lattice vectors should be used for austenite and corresponding martensite cell. Therefore, the relationships between the cubic (index *c*) and tetragonal (index *t*) axes for $L1_0$ martensite phase are $(001)_c.|\ (001)_t$ and $[100]_c.|\ [110]_t$, which corresponds to $a_c = \sqrt{2}a_t$ and $c_c = c_t$ [43].

Secondly, the 5M modulated martensite identified in some of the produced Heusler materials is defined by monoclinic lattice (**Table 3.2**). However, the observed monoclinicity of the 5M modulation is relatively low ($\beta = 90.3°$), which allows for slight simplification and direct translation from *monoclinic axes* to *cubic axes*, taking into consideration that new modulated pseudo-tetragonal unit cell stems from the orthogonal distortion of the former cubic unit cell [43,61]. As a result, the monoclinic cell (index *m*) expressed in cubic axes follows the relationship $a_c = \sqrt{2}a_m$ and $c_c = b_m$ [43].

The described transformation of NM and 5M martensite to cubic axes system were used to estimate the possible twinning angles between neighbouring martensite twins. It should be stressed out that the similar approach for qualitative evaluation of modulated martensitic structures for different types of Ni-Mn-Ga Heusler alloys have been successfully used and reported by various authors [383,524–527].

For the aforementioned tetragonal and pseudo-tetragonal unit cell there is only one possible twinning system: *a*-*c* twinning, which originates according to the (101) twinning plate and is schematically depicted in **Fig 3.37**. This kind of twinning occurs between *a*-type and *c*-type twin, where *a* and *c* prefix defines the crystallographic direction of the twin measured perpendicularly to the observed surface. Using the simple geometrical relations shown in **Fig 3.37**, the twinning angle 2α can be estimated according to the following relation [524]:

$$2\alpha = \arctan\frac{c}{a} - \arctan\frac{a}{c} \tag{3.4}$$

where *a* and *c* are the lattice parameters of martensite unit cell expressed in cubic axes system. Taking into account the lattice parameters estimated from XRD

Rietveld analysis (**Table 3.2**) and transformed into cubic axes, the 2α for the NM and 5M martensite were calculated and summarized in **Table 3.3**. Despite the use of the aforementioned geometrical simplifications, it is seen that significantly differently ranges of 2α are expected for 5M ($2\alpha = 2°–3°$) and NM martensite ($2\alpha = 8°–9°$).

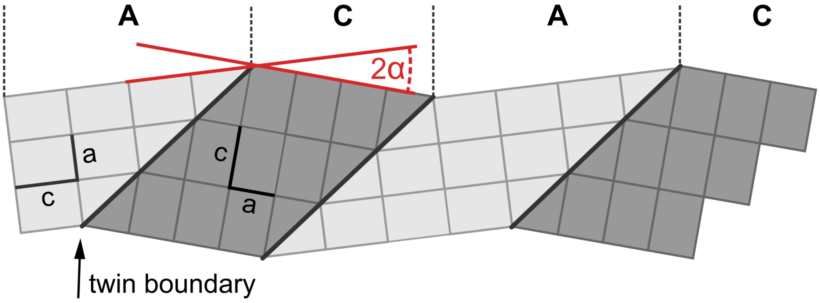

Fig. 3.37. The geometrical model of the martensite relief formed by a-c twinning. The lower case a and c shows the orientation of tetragonal unit cells in neighbouring martensite variants. The capital letters A and C represents the crystallographic direction of each twin variant measured perpendicular to the surface. The 2α indicates the relief angle, which is equal to the twinning angle (based on [524]).

Table 3.3. The theoretical twinning angles calculated for the *a*-*c* twinning system in NM and 5M martensite for the fabricated NiMnGa-based Heusler alloys along with the corresponding experimentally determined relief angles. The table covers only alloys exhibiting martensitic structure during AFM studies for which the relief angle were calculated as an average value from at least 20 twin boundaries.

Alloy composition	**Cooling condition**	**Calculated 2α (°)**		**Measured 2α (°)**
		5M	**NM**	
$Ni_{48}Mn_{31}Ga_{20}Co_1$	Furnace cooled	2.5		2.8
$Ni_{48}Mn_{30}Ga_{20}Co_2$	Water cooled	2.9		3.2
	Air cooled	3.0		2.5
	Furnace cooled	3.0		3.2
$Ni_{48}Mn_{28}Ga_{20}Co_4$	Water cooled		9.0	8.4
$Ni_{48}Mn_{28}Ga_{20}Co_3Fe_1$	Water cooled		8.4	9.1
	Air cooled		8.5	9.0
	Furnace cooled		8.1	7.8
$Ni_{50}Mn_{25}Ga_{21}Co_2Fe_2$	Water cooled		8.7	9.2
	Air cooled		8.7	8.8
	Furnace cooled		8.7	8.2

When it comes to materials in fully austenitic state, **Fig. 3.38** shows the 2D and corresponding 3D AFM images for the water, air and furnace cooled $Ni_{48}Mn_{32}Ga_{20}$ alloys. As expected after previous microstructural investigations, all reference undoped samples are characterized by completely flat surfaces with only neglectable marks and scratches remained after former polishing. Although only one image of each specimen is shown in **Fig. 3.38**, the same results were also obtained by probing multiple distinct areas of the prepared samples.

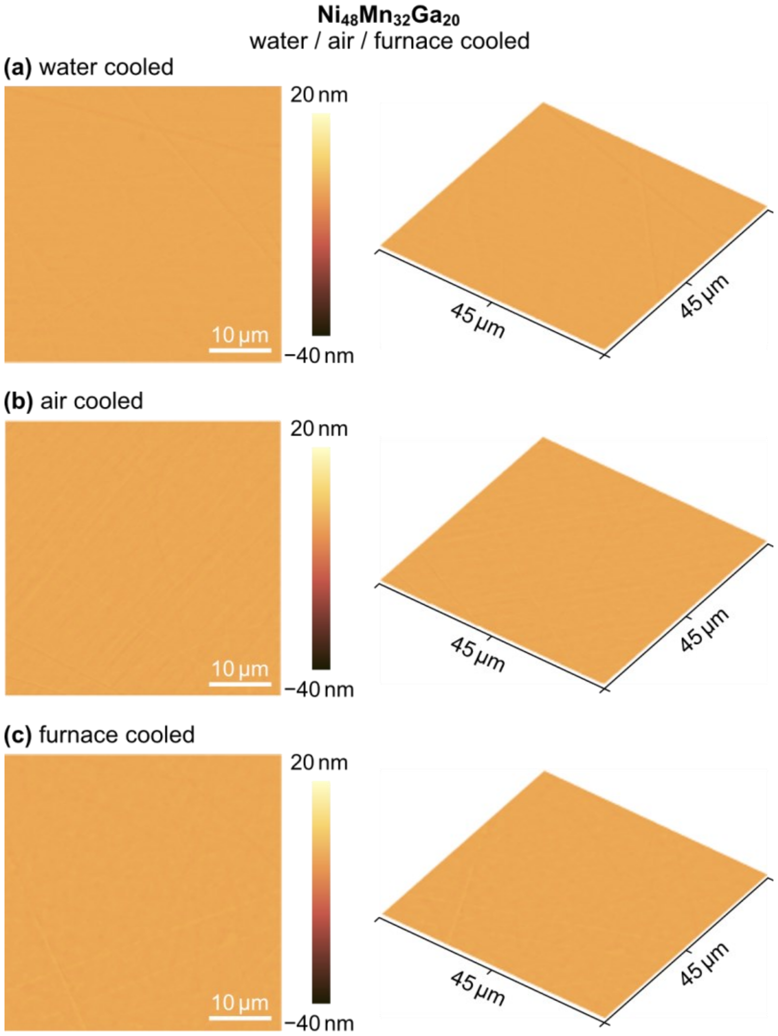

Fig. 3.38. AFM 2D and 3D topographic images of the **(a)** water, **(b)** air and **(c)** furnace cooled $Ni_{48}Mn_{32}Ga_{20}$ alloy. All images are presented in the same scale.

Fig. 3.39 and **3.40** presents the AFM images for the water and air, as well as furnace cooled $Ni_{48}Mn_{31}Ga_{20}Co_1$ alloy, respectively. It is interesting to note that both water and air cooled materials are found fully austenitic (**Fig. 3.39**), whereas early signs of martensitic phase are observed in the furnaced cooled specimen (**Fig. 3.40**) and even the characteristic habit plane between austenite and martensite phase is visible in **Fig. 3.40(a)**. It should be also recalled that the discussed martensitic phase in $Ni_{48}Mn_{31}Ga_{20}Co_1$ alloy was not observed with the help of polarised microscope (**Section 3.1.1**), but the existence of NM and 5M martensite was revealed in XRD analysis (**Section 3.1.4**). As a result, the following AFM results are in line with the discussed XRD studies and provides complementary information concerning the microstructure of the produced Heusler materials.

The morphology of the martensite phase shown in **Fig. 3.40** is characterised by triangular topography with characteristic sharp ridges and valleys representing the hierarchical lamellar twins observed at different length scales. It should be noted that the straightforward description of the investigated martensite at various structural levels might be misleading and is sometimes differently interpreted in literature. Theoretically, single unit cells forms the basic twins, depending on their crystallographic orientation (*e.g. a*-*c* twinning system), which share the same twin boundary [525]. The group of twins with the same twinning system forms the *twin domain* and matching twin domains creates the exact *martensite variant*. On the other hand, recent studies focused on hierarchical [392,528] or adaptive concept [88–90] of martensite demonstrates that there can be more structural levels of twin patterns, which was extensively described in theoretical part of this thesis in **Section 1.2.2**. Taking into consideration the obtained AFM images the author decided to use the prefixes *macro*-, *meso*-, *micro*-, and *nano*- to describe the observed twins at different length scales, similarly to the approach proposed in [294,392,529–531]. According to this nomenclature, the macro-scale corresponds to the largest observed areas characterized by the evenly oriented martensite laminates, whereas the nano-scale considers the twinning mechanism at atomistic scale.

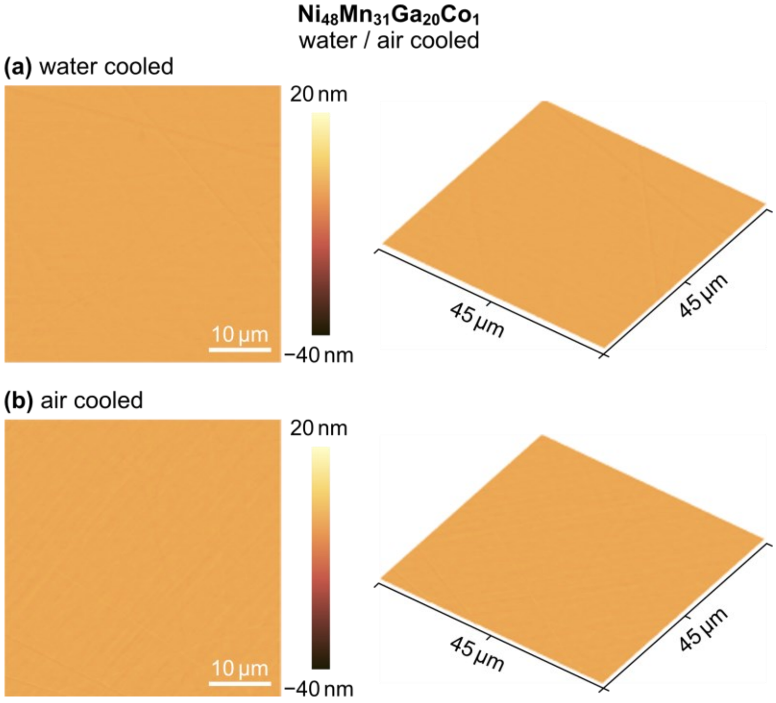

Fig. 3.39. AFM 2D and 3D topographic images of the **(a)** water and **(b)** air cooled $Ni_{48}Mn_{31}Ga_{20}Co_1$ alloy. All images are presented in the same scale.

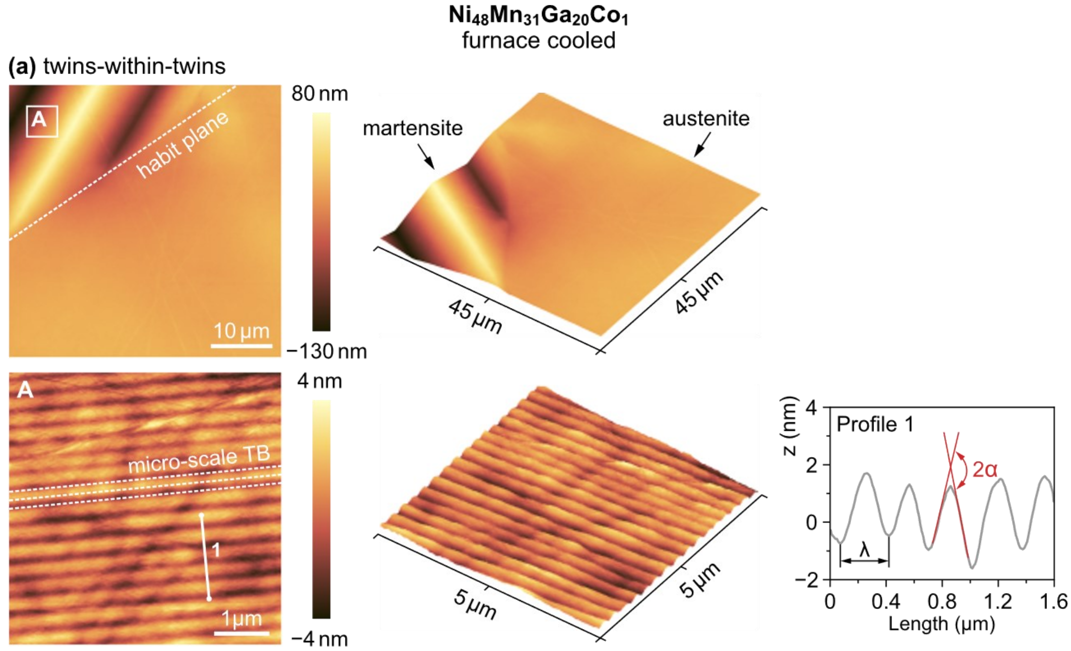
(a) twins-within-twins

(b) twins-within-twins

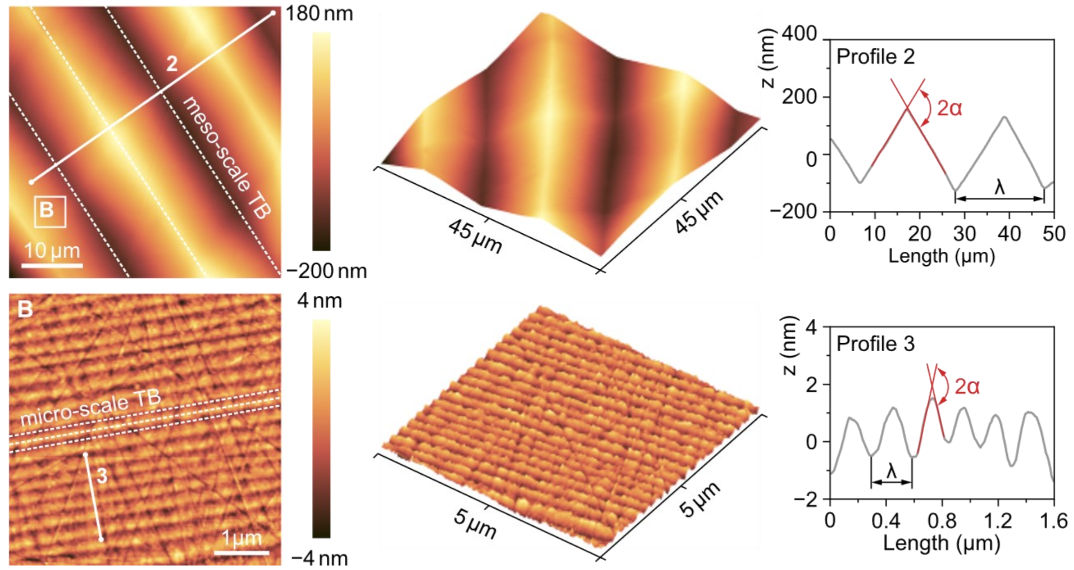

Fig. 3.40. AFM 2D and 3D topographic images of the furnace cooled $Ni_{48}Mn_{31}Ga_{20}Co_1$ alloy showing **(a)** the habit plane between austenite and martensite phase, **(b)** hierarchical twins-within-twins martensite structure. The exemplary meso-scale and micro-scale twin boundaries (TB) are indicated by parallel dashed lines. The close ups are marked with rectangles and annotated by capital letters (A and B). The height profiles along the 1–3 lines are presented in right column, where λ corresponds to twin periodicity and 2α represents the relief angle.

For the furnace cooled $Ni_{48}Mn_{31}Ga_{20}Co_1$ alloy shown in **Fig. 3.40**, the observed hierarchical twins-within-twins structure suggests the existence of at least two levels of twins: (1) meso-scale and (2) micro-scale ones. Both twin scales differ from each other in terms of their *periodicity* λ, which is clearly seen on the specific surface profiles and is also schematically marked by dashed lines indicating the particular twin boundaries (TB). For the $Ni_{48}Mn_{31}Ga_{20}Co_1$ sample λ equals to about 20 μm and 250 nm for the meso- and micro scale twins, respectively. This shows that the distinction between two levels of twins is certainly justified since the examined length scales differs by almost two orders of magnitude. Nevertheless, despite these variations in periodicity, both meso- and micro-scale twins share the same relief angle $2\alpha = 2.8°$, which was calculated as the mean value from over 20 twin boundaries. Considering the simple geometrical representation of martensite relief (**Fig. 3.37**), the measured twinning angle is quite similar to the theoretical value $2\alpha = 3.0°$ estimated for the 5M martensite (**Table 3.3**). This comparison suggest that the observed martensitic relief belongs to the 5M modulated structure, which is consistent with the previous XRD investigation. Certainly, the XRD analysis revealed the 5M martensite in all $Ni_{48}Mn_{31}Ga_{20}Co_1$ samples, whereas AFM studies found it only in furnace cooled specimen. However, one should bear in mind, that the scan area of AFM covers only a small selection of the examined surface, so it is relatively difficult to find the residual martensitic phase across the whole examined surface even after numerous probing. Therefore, the 5M martensite was noticed only for the least thermally stable material, *i.e.* furnace cooled sample.

This situation changes for the $Ni_{48}Mn_{30}Ga_{20}Co_2$ alloy, where all samples exposed to various cooling procedures show both the dominant austenite phase and residual martensite phase. **Fig. 3.41–3.43** presents the example of AFM images obtained for the water, air and furnace cooled $Ni_{48}Mn_{30}Ga_{20}Co_2$ samples, respectively. Each figure shows the flat surface associated to the austenite phase and distinctive triangular relief found for the residual martensite phase. In case of water and air cooled specimens, the observed reliefs are distinguished by meso-scale twins with various periodicity from single to couple micrometres. The hierarchical twins-within-twins microstructure is observed only for the furnace cooled alloy, which is depicted in **Fig. 3.43**. Yet again, the periodicity of meso-scale twins is in the range of couple micrometres, while that of micro-scale twins is close to ~250 nm. Remarkably, all water, air and furnace cooled samples had twinning angle that are close ~3.0°, indicating the presence of 5M modulated structure (**Table 3.3**). These results are also in line with the previous XRD Rietveld analysis.

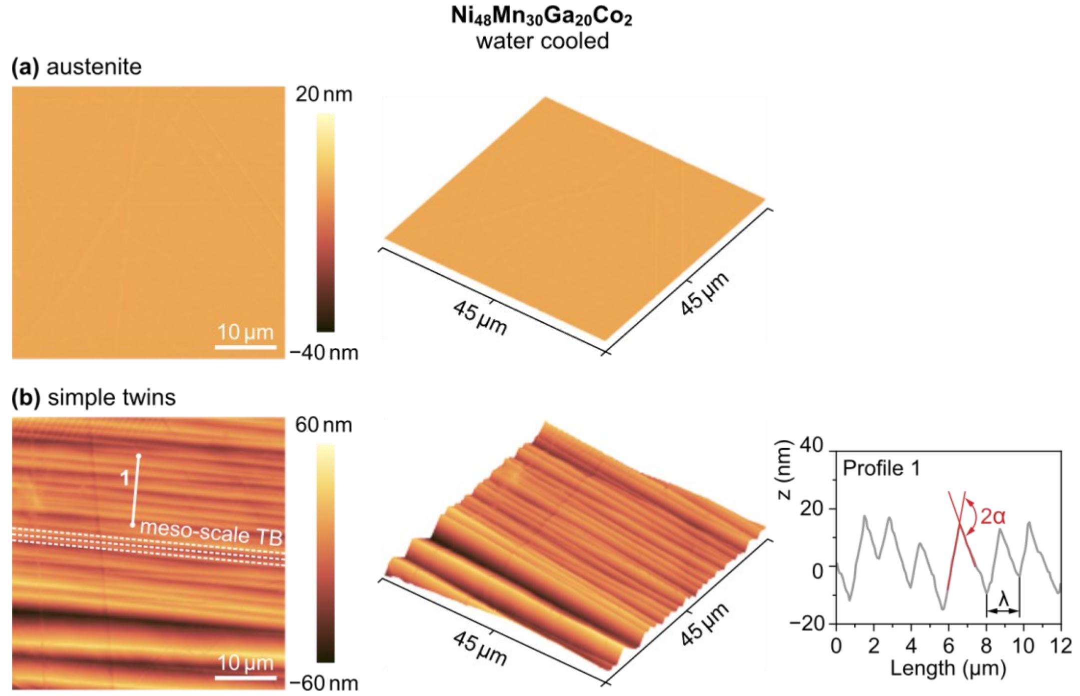

Fig. 3.41. AFM 2D and 3D topographic images of the water cooled $Ni_{48}Mn_{30}Ga_{20}Co_2$ alloy showing **(a)** the austenite phase and **(b)** the martensite phase characterized by simple twins structure. The exemplary meso-scale twin boundaries (TB) are indicated by parallel dashed lines. The height profile along the 1 line is presented in right column.

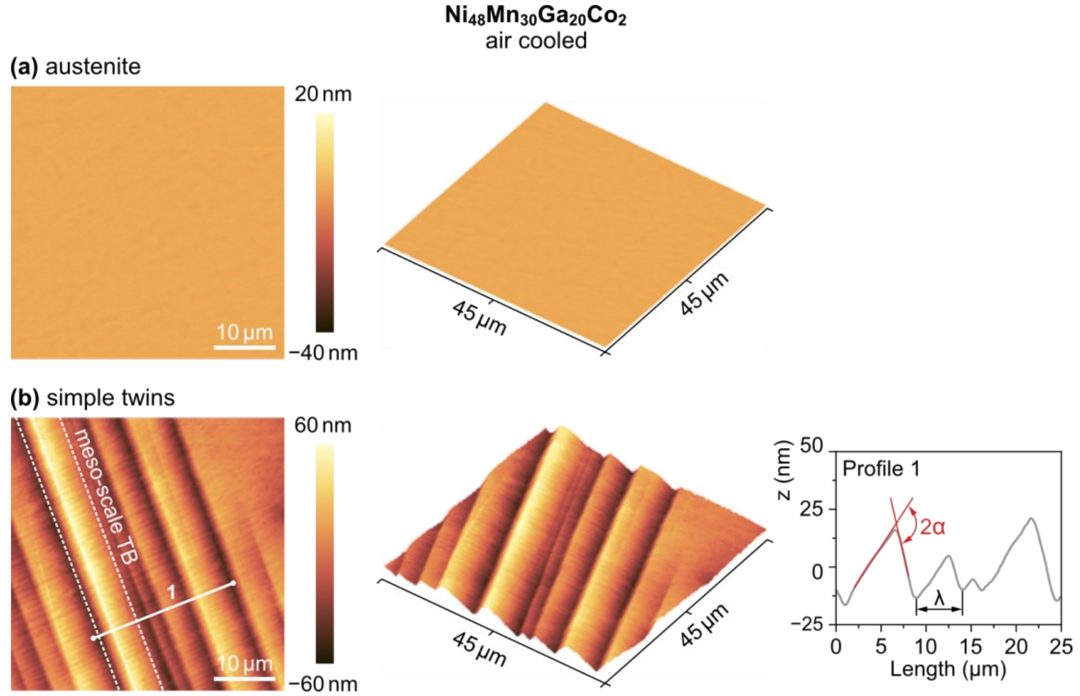

Fig. 3.42. AFM 2D and 3D topographic images of the air cooled $Ni_{48}Mn_{30}Ga_{20}Co_2$ alloy showing **(a)** the austenite phase and **(b)** the martensite phase characterized by simple twins structure. The exemplary meso-scale twin boundaries (TB) are indicated by parallel dashed lines. The height profile along the 1 line is presented in right column, where λ corresponds to twin periodicity and 2α represents the relief angle.

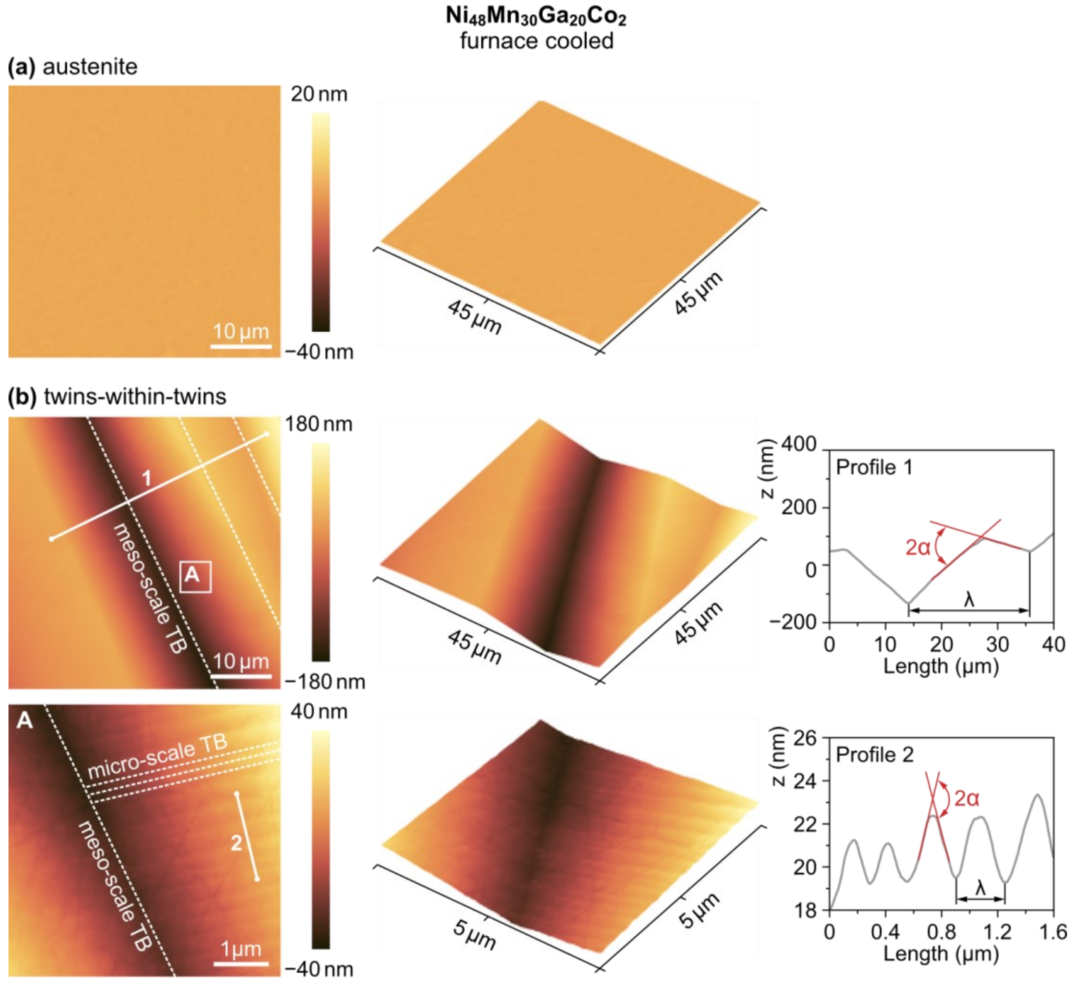

Fig. 3.43. AFM 2D and 3D topographic images of the furnace cooled $Ni_{48}Mn_{30}Ga_{20}Co_2$ alloy showing **(a)** the austenite phase and **(b)** the martensite phase characterized by hierarchical twins-within-twins structure. The exemplary meso-scale and micro-scale twin boundaries (TB) are indicated by parallel dashed lines. The close up is marked with rectangle and annotated by capital letter A. The height profiles along the 1 and 2 lines are presented in right column, where λ corresponds to twin periodicity and 2α represents the relief angle.

In a case involving fully martensitic Heusler materials, **Fig. 3.44** presents the example of AFM images for the water cooled $Ni_{48}Mn_{28}Ga_{20}Co_4$ alloy, while **Fig. 3.45** shows the AFM images for the same alloy after air and furnace cooling. As anticipated from prior microstructural investigations, the $Ni_{48}Mn_{28}Ga_{20}Co_4$ alloy is found to be fully martensitic with various complex martensite morphologies. **Fig. 3.44(a)** depicts the typical example of martensite relief for the water cooled sample, which consist of martensite lamellae that bifurcate or bend due to the reorientations of variants. These different types of simple twins are detected at the meso-scale without any internal micro-scale self-accommodated structure. Alternatively, **Fig. 3.44(b)** shows the example of complex crossing twins structure that was found on the same water cooled $Ni_{48}Mn_{28}Ga_{20}Co_4$ sample. It can be seen that interpenetration between various twin variants results in characteristic pyramidal relief with two distinct periodicity (marked as Profile 2 and 3). What is interesting, The orientation between interpenetrated twins is inherited between the micro- and meso-scales, which is an important feature of the crossing twins microstructure. The quantitative analysis of relief angle for both simple and crossing twins reveals that 2α is approximately equal to $\sim 8{,}4°$ for all types of twinning at different structural levels. The experimentally measured value of 2α is close to the theoretical value $2\alpha = 9.0°$ estimated for the NM martensite (**Table 3.3**), which suggests that the examined martensitic structures belongs to NM martensite phase. Once again, the quantitative analysis of AFM images confirms earlier XRD investigations.

The martensitic structures of air and furnace cooled $Ni_{48}Mn_{28}Ga_{20}Co_4$ shown in **Fig. 3.45** differs from those described for the water cooled specimen. The main difference is seen on the height of the obtained structures

Typically, the height differences in meso-scale twins are measured in hundreds of nanometres, however for the air and furnace $Ni_{48}Mn_{28}Ga_{20}Co_4$ samples, the observed height differences are measured in single nanometres (**Fig. 3.45**). As a result, the recorded profiles are characterized by step-like periodicity without characteristic sharp ridges and valleys. The previous XRD studies did not show any significant microstructural differences between the water, air and furnace cooled samples, thus the observed differences in AFM images may stem from external factors. One possible explanation is that the least thermally stable air and furnace cooled samples are more susceptible to mechanical polishing than water cooled sample, which could lead to the deterioration of characteristic martensite relief.

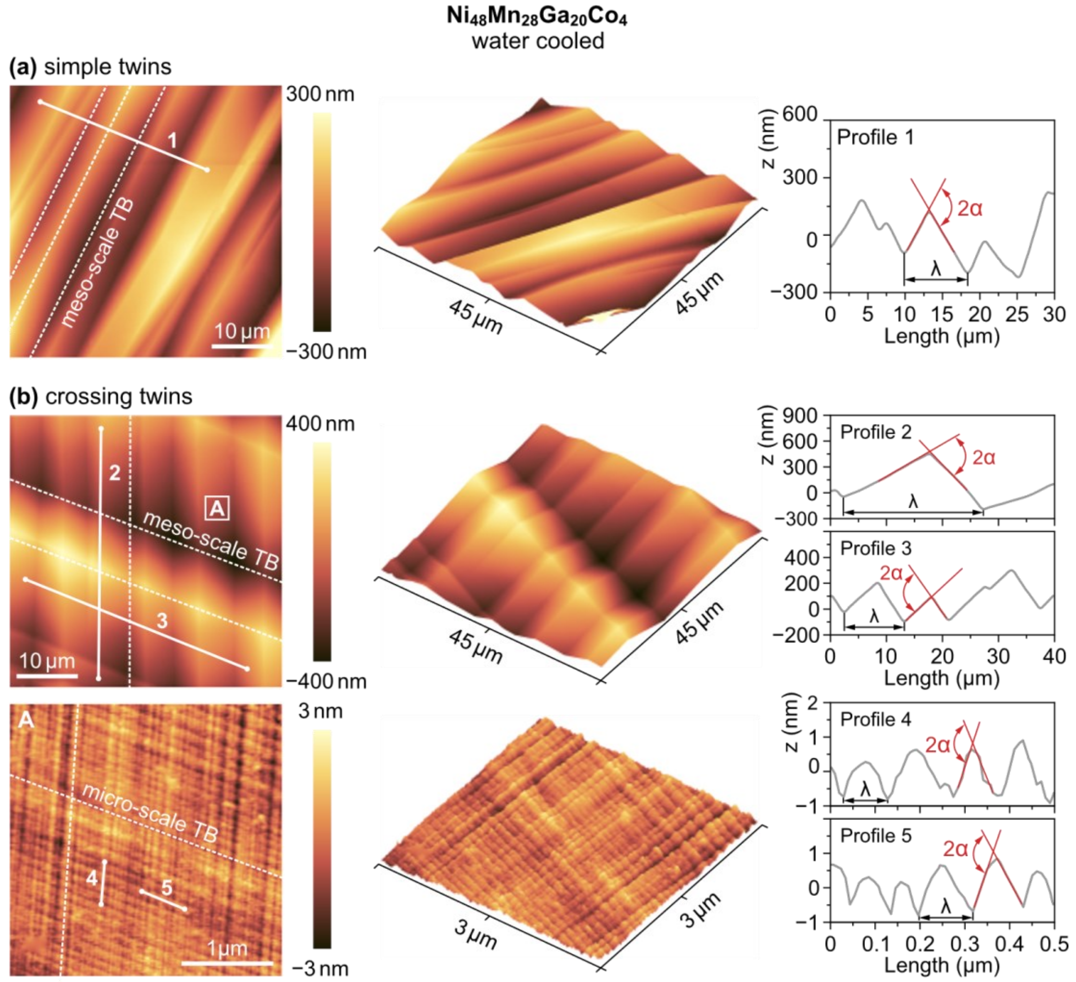

Fig. 3.44. AFM 2D and 3D topographic images of the furnace cooled $Ni_{48}Mn_{28}Ga_{20}Co_4$ alloy showing **(a)** simple twins and **(b)** crossing twins martensitic structure. The exemplary meso-scale and micro-scale twin boundaries (TB) are indicated by parallel dashed lines. The close up is marked with rectangle and annotated by capital letter A. The height profiles along the 1–5 lines are presented in right column, where λ corresponds to twin periodicity and 2α represents the relief angle.

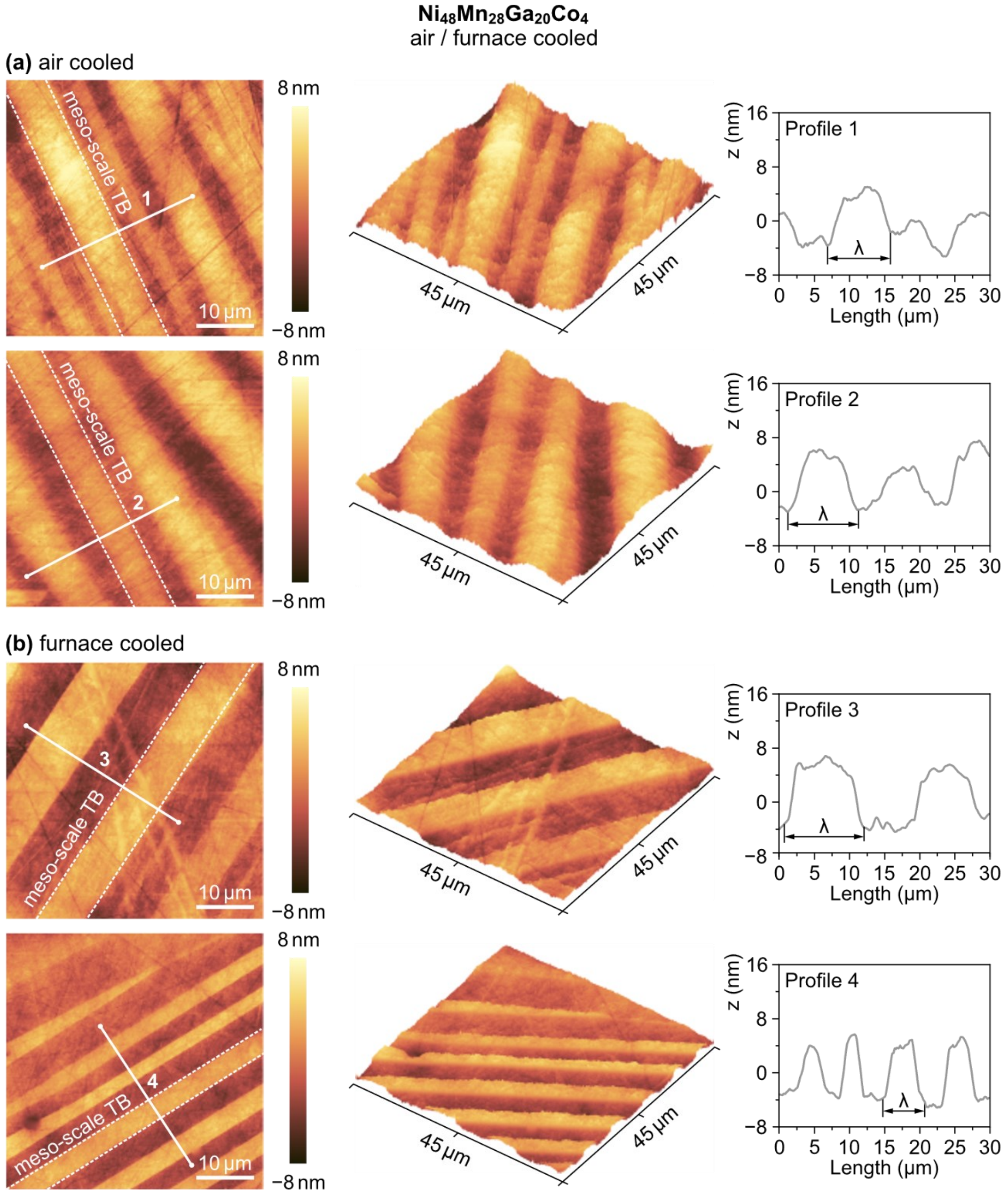

Fig. 3.45. AFM 2D and 3D topographic images of the **(a)** air and **(b)** furnace cooled $Ni_{48}Mn_{28}Ga_{20}Co_4$ alloy showing the deteriorated martensitic structure. The exemplary meso-scale twin boundaries (TB) are indicated by parallel dashed lines. The height profiles along the 1–4 lines are presented in right column, where λ corresponds to twin periodicity.

In regards to the Fe-doped alloys **Fig. 3.46** and **3.47** shows the example of AFM images obtained for the water, as well as air and furnace cooled $Ni_{48}Mn_{28}Ga_{20}Co_3Fe_1$ alloys, respectively. This particular material was also expected to be fully martensitic, which is confirmed by the presented AFM images. The martensitic structures for the water cooled specimen (**Fig. 3.46**) exhibit very similar morphology as previous samples with different chemical compositions. Simple meso-scale twins without internal self-accommodation are depicted **Fig. 3.46(a)**, the characteristic twins-within-twins structure built from hierarchical meso-scale ($\lambda \approx 15$ µm) and micro-scale twins ($\lambda \approx 400$ nm) is shown in **Fig. 3.46(b)**. For the air and furnace cooled alloys presented in **Fig 3.47** only the simple meso-scale martensitic lamellae with different orientations are observed. What should be also noted is that again the martensitic structures for samples cooled in air and furnace cooled are again less sharp than for samples cooled in water cooled. In consideration of experimentally determined relief angle, the value of 2α are equal to 9.1°, 9.0° and 7.8° for the water, air and furnace cooled alloy, respectively. These values are close to the theoretical ones of 8.4°, 8.5° and 8.1°, calculated for the NM martensite found in water, air and furnace cooled $Ni_{48}Mn_{28}Ga_{20}Co_3Fe_1$ alloys, respectively (**Table 3.3**).

$Ni_{48}Mn_{28}Ga_{20}Co_3Fe_1$
water cooled

(a) simple twins

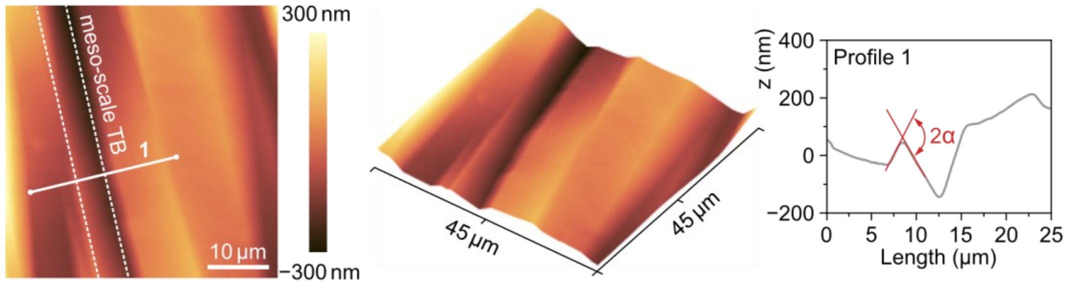

(b) twins-within-twins

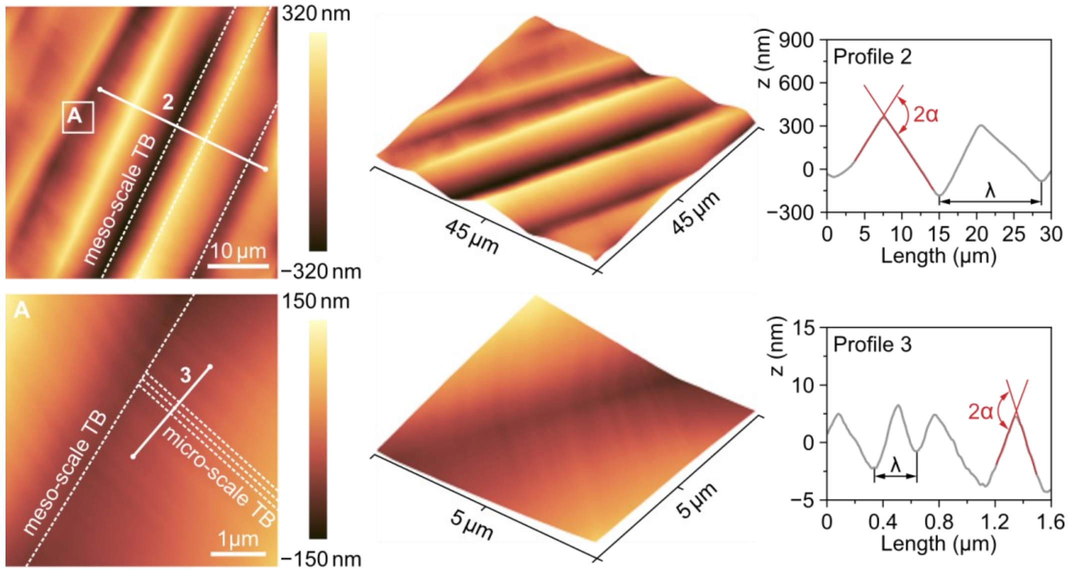

Fig. 3.46. AFM 2D and 3D topographic images of the water cooled $Ni_{48}Mn_{28}Ga_{20}Co_3Fe_1$ alloy showing **(a)** simple twins and **(b)** hierarchical twins-within-twins martensitic structure. The exemplary meso-scale and micro-scale twin boundaries (TB) are indicated by parallel dashed lines. The close ups is marked with rectangles and annotated by capital letter A. The height profiles along the 1–3 lines are presented in right column, where λ corresponds to twin periodicity and 2α represents the relief angle.

$Ni_{48}Mn_{28}Ga_{20}Co_3Fe_1$
air / furnace cooled

(a) air cooled

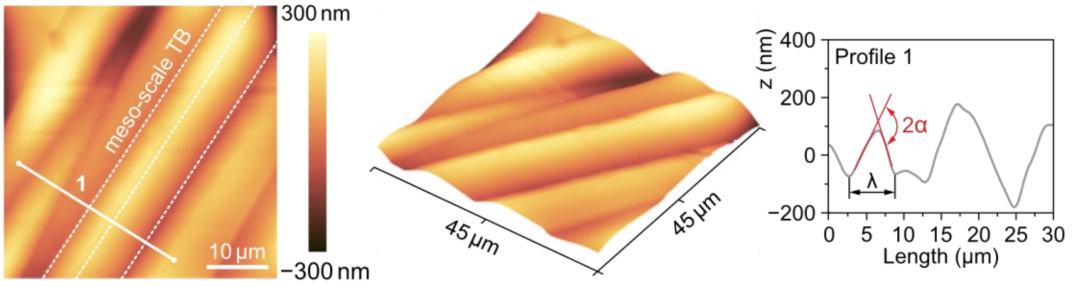

(b) furnace cooled

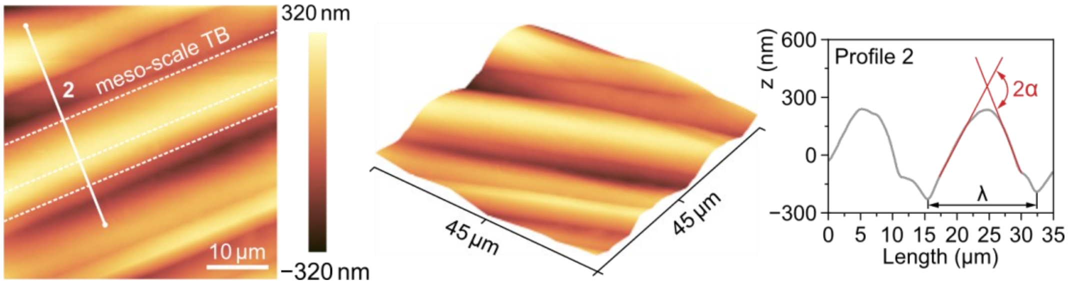

Fig. 3.47. AFM 2D and 3D topographic images of the **(a)** air and **(b)** furnace cooled $Ni_{48}Mn_{28}Ga_{20}Co_3Fe_1$ alloy showing the simple martensitic structure. The exemplary meso-scale twin boundaries (TB) are indicated by parallel dashed lines. The height profiles along the 1 and 2 lines are presented in right column, where λ corresponds to twin periodicity.

The last fully martensitic Heusler materials are water, air and furnace cooled $Ni_{50}Mn_{25}Ga_{21}Co_2Fe_2$ samples presented in **Fig. 3.48** and **3.49**, respectively. **Fig. 3.48** shows the diversity of martensitic reliefs for the water cooled alloy, including the already defined simple meso-scale twinning (**Fig. 3.48(a)**), as well as the characteristic twin-within-twins structure characterized by meso-scale and corresponding micro-scale twins (**Fig. 3.48(b)**). Similar to other Co-doped and Fe-doped alloys, macro-scale twins have an estimated periodicity that ranges from single to couple micrometres. In contrary, the periodicity for micro-scale twins is about ~500 nm, which is comparable to the Fe-doped $Ni_{48}Mn_{28}Ga_{20}Co_3Fe_1$ alloy, but noticeably higher than for samples that only contain Co doping. In regards to air and furnace cooled $Ni_{50}Mn_{25}Ga_{21}Co_2Fe_2$ samples, only simple meso-scale twinning was observed in these materials during AFM investigations, which is presented in **Fig 3.49**. For the air cooled alloy almost perfectly symmetrical meso-scale twinning with $\lambda = 15$ µm is depicted in **Fig. 3.49(a)**. For the furnace cooled specimen, shown in **Fig 3.49(b)**, the previously defined interpenetrating crossing twins structure is depicted. In this case only one profile for single twin variants is presented (Profile 2), as the periodicity for the second twinning variants exceeds the maximum AFM scanning area. Analogous to other investigated NiMnGa-based materials in martensitic state, the relief angle for the examined $Ni_{48}Mn_{28}Ga_{20}Co_3Fe_1$ alloy is characterized by the similar values of 9.2°, 8.8° and 8.2° for the water, air and furnace cooled alloy, respectively. These values are as well comparable to theoretical value of 8.7° estimated for the NM martensite (**Table 3.3**).

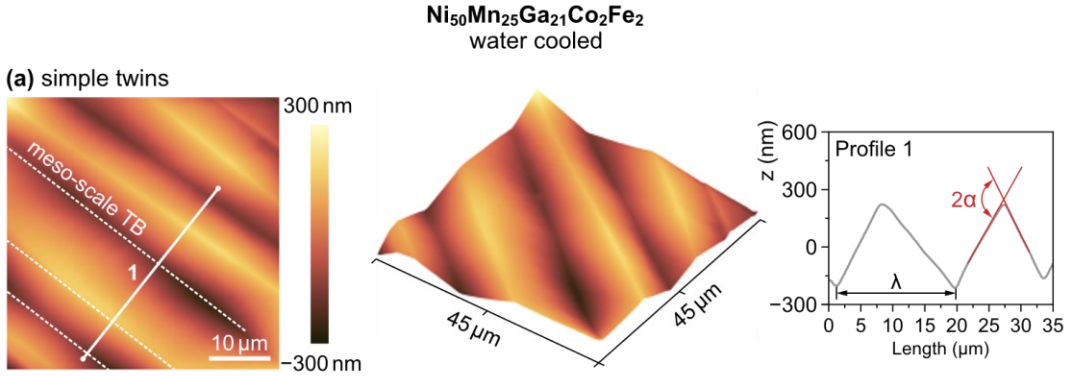

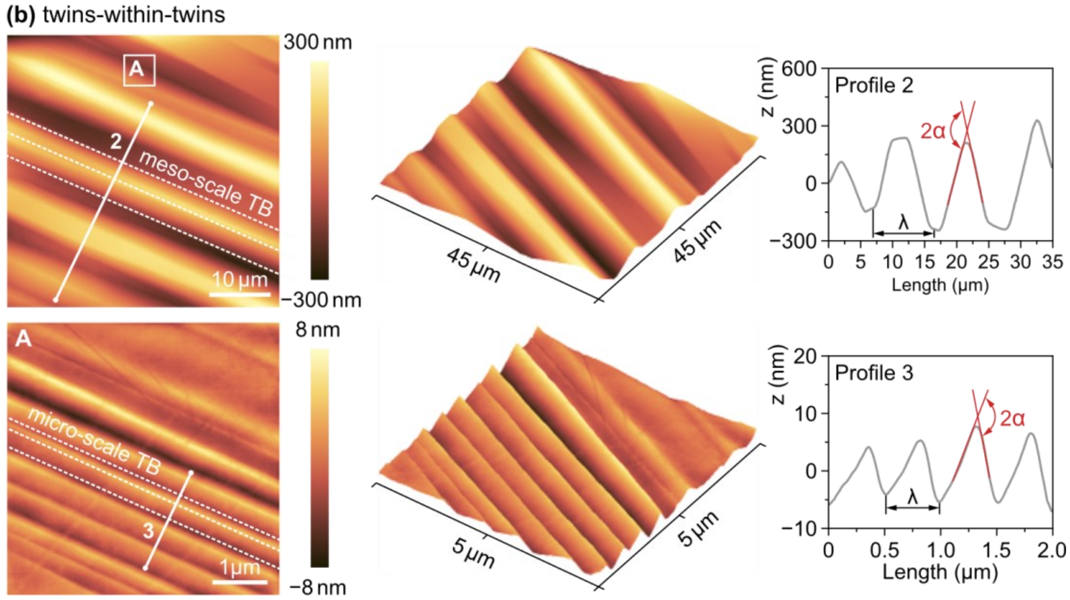

Fig. 3.48. AFM 2D and 3D topographic images of the water cooled $Ni_{50}Mn_{25}Ga_{21}Co_2Fe_2$ alloy showing **(a)** simple twins and **(b)** hierarchical twins-within-twins martensitic structure. The exemplary meso-scale and micro-scale twin boundaries (TB) are indicated by parallel dashed lines. The close up is marked with rectangle and annotated by capital letter A. The height profiles along the 1–3 lines are presented in right column, where λ corresponds to twin periodicity and 2α represents the relief angle.

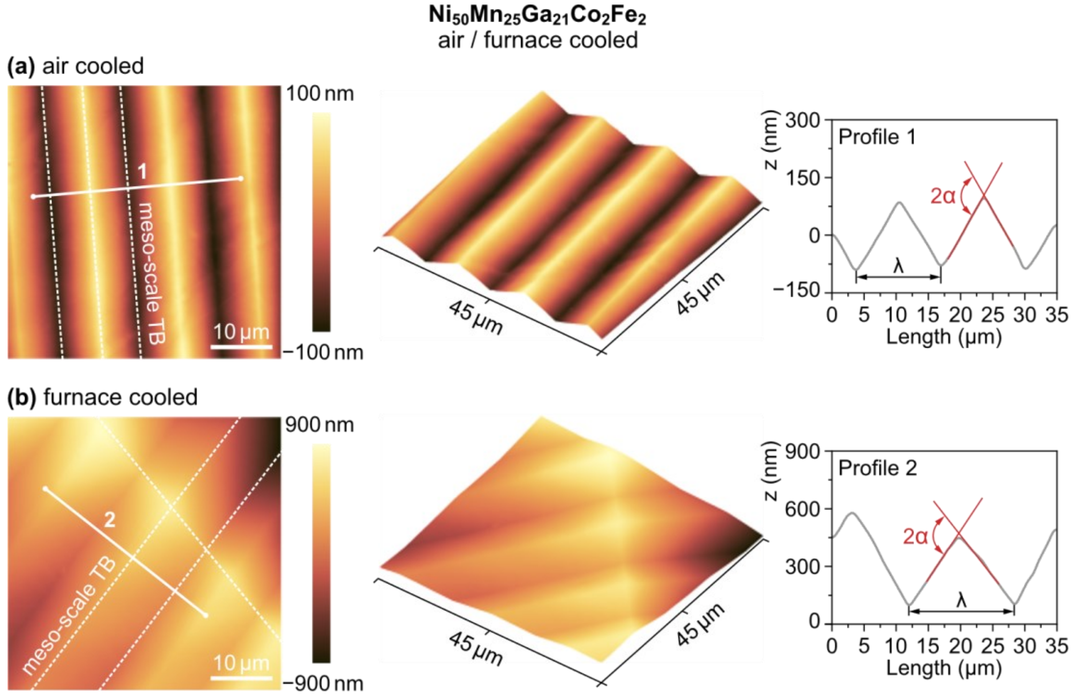

Fig. 3.49. AFM 2D and 3D topographic images of the **(a)** air and **(b)** furnace cooled $Ni_{50}Mn_{25}Ga_{21}Co_2Fe_2$ alloy showing the simple twins **(a)** and crossing twins **(b)** structure. The exemplary meso-scale twin boundaries (TB) are indicated by parallel dashed lines. The height profiles along the 1 and 2 lines are presented in right column, where λ corresponds to twin periodicity.

The last two Fe-doped doped Heusler materials, *i.e.* $Ni_{48}Mn_{28}Ga_{20}Co_1Fe_3$ and $Ni_{48}Mn_{28}Ga_{20}Fe_4$ alloys, produced with a different cooling procedures are shown in **Fig. 3.50** and **3.51**, respectively. It is seen that for these alloys, the AFM images are in line with previous microstructural investigation by polarised microscopy and SEM since only completely flat surfaces were obtained for all examined materials during AFM probing. According to the XRD examination, the described alloys do, in fact, contain residual NM martensite, although this residual phase could be minor as remain undetected throughout the entire cross-section of the prepared specimens. Moreover, taking into account the XRD analysis, it should be noted that the only residual phase that were observed in manufactured NiMnGa-based materials is the 5M modulated martensite revealed in the $Ni_{48}Mn_{31}Ga_{20}Co_1$ and $Ni_{48}Mn_{30}Ga_{20}Co_2$ samples. No residual NM martensite was noticed for these two particular alloys.

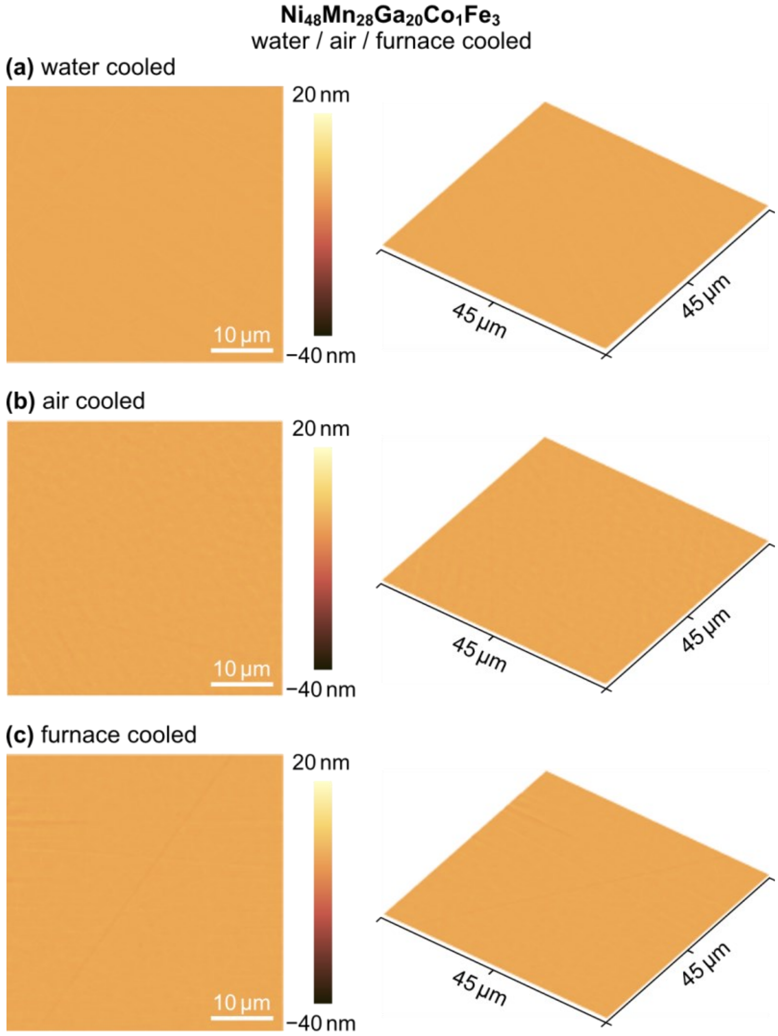

Fig. 3.50. AFM 2D and 3D topographic images of the **(a)** water, **(b)** air and **(c)** furnace cooled $Ni_{48}Mn_{28}Ga_{20}$ Co_1Fe_3 alloy. All images are presented in the same scale.

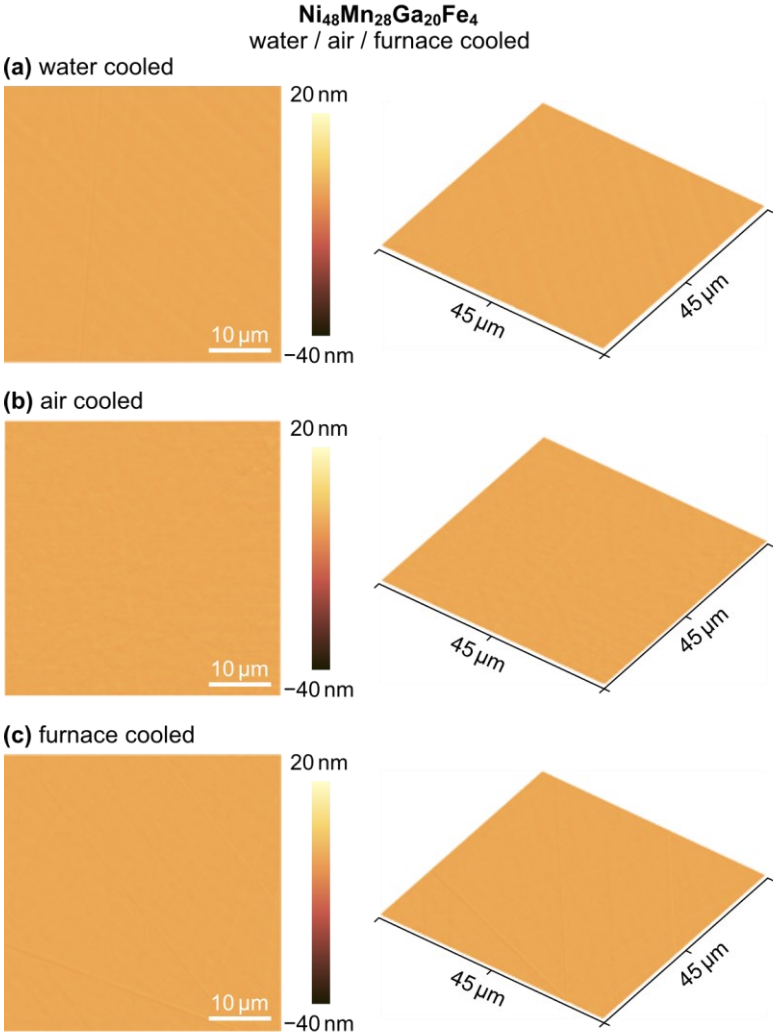

Fig. 3.51. AFM 2D and 3D topographic images of the **(a)** water, **(b)** air and **(c)** furnace cooled $Ni_{48}Mn_{28}Ga_{20}Fe_4$ alloy. All images are presented in the same scale.

In conclusion, the presented AFM investigation is extremely important in microstructural characterisation of fabricated NiMnGa-based materials, especially in the case of complex martensitic structures. The presented studies reveals the hierarchical arrangement of martensite twinning, which stems from the self-accommodation nature of martensite, that need to compensate the orthorhombic distortion during thermoelastic martensitic transformation. The martensite system tends to minimize the strain energy (originating from strain incompatibilities at twin variant boundaries) by deformation of already-existing variants. The previously presented optical microscopy images (**Section 3.1.1**) shows the macro-scale twin boundaries and the discussed AFM examination revealed the meso-scale and micro-scale twinning patterns with various constructions of laminates, which is schematically summarized in **Fig. 3.52**. It is noteworthy that the highest amount of self accommodated structures at different structural levels are observed for the water cooled alloys, which suggest that these alloys perform better at compensating various external and internal stresses. The periodicity of the micro-scale twin boundaries, which is noticeably higher for the Fe-containing alloys, is the only difference in topographical characteristics of martensite structures between Co-doped and Fe-Co-doped alloys that can be attributed to elemental doping. Finally, the quantitative analysis of the examined martensite reliefs at different structural levels allows to identify both NM and 5M martensite structures and reveals the hereditary nature of martensite features over different length scales.

(a) hierarchy of twins

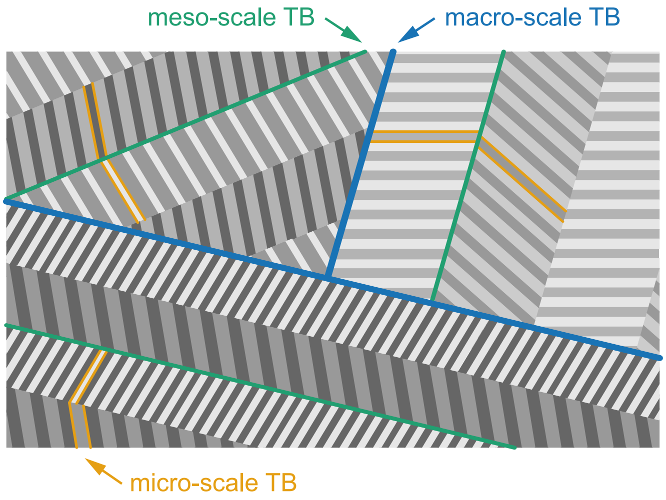

(b) construction of twins


simple twins twins-within-twins crossing twins

Fig. 3.52. The schematic illustration of **(a)** the hierarchy of observed twins at different structural levels, from macro-scale (blue lines) through mesoscale (green lines) up to micro-scale (yellow lines) (based on [525]), **(b)** different constructions of observed martensite laminates, including simple twins, twins-within-twins and crossing twins structures (based on [532]).

3.2 Martensitic and magnetic transformation

3.2.1 Thermal behaviour of phase transitions

The differential scanning calorimetry studies were carried out to estimate the temperatures of the first-order reversible martensitic transition in the produced NiMnGa-based magnetic shape memory alloys. The measurements were performed in at least three heating and cooling cycles to assess the thermal stability of the reversible structural transition. It should be stressed out that no significant differences between each heating and cooling cycle were observed for all investigated alloys. Thus, in order not to obscure the figures with numerous overlapping curves, only the last heating ⇄ cooling cycles are shown in all figures presented in the following section. Moreover, the magneto-thermo-structural properties of all water, air and furnace cooled materials were also investigated by the VSM, which will be discussed in the next section (**Section 3.2.2**). According to preliminary research, there are no significant differences between the temperatures of martensitic transformation estimated from DSC and VSM. Therefore, in view of the time constraints resulting from the long measuring times, only the main group of water cooled alloys were fully investigated by DSC technique and presented in the following section. Additionally, the complementary magnetic thermogravimetry measurements in the vicinity of Curie temperature were also performed to investigate the second-order magnetic transformation in the produced water cooled materials.

Fig. 3.53 presents the recorded DSC and M-TG curves for the reference and Co-doped water cooled $Ni_{48}Mn_{32}Ga_{20}$, $Ni_{48}Mn_{31}Ga_{20}Co_1$, $Ni_{48}Mn_{30}Ga_{20}Co_2$ and $Ni_{48}Mn_{28}Ga_{20}Co_4$ alloys, while **Fig. 3.54** shows the results for materials in which Co was gradually substituted by Fe, *i.e.* $Ni_{48}Mn_{28}Ga_{20}Co_3Fe_1$, $Ni_{50}Mn_{25}Ga_{21}Co_2Fe_2$, $Ni_{48}Mn_{28}Ga_{20}Co_1Fe_3$ and $Ni_{48}Mn_{28}Ga_{20}Fe_4$ alloy. The characteristic exothermic and endothermic peaks observed during cooling and heating process, respectively, indicates the reversible first-order transition that corresponds to the desired martensitic transformation. It was thoroughly explained in **Section 1.3.4** that thermoelastic phase transition driven by Gibbs free energy is characterized by imminent hysteretic behaviour due to the required undercooling or overheating being the driving force of the transformation. As a result, the transformation peaks visible in **Fig. 3.53** and **3.54** are not perfectly sharp and characteristic temperatures representing start and finish of the forward and backward martensitic transformation may be clearly distinguished. In this work the martensite start M_s, martensite finish M_f, austenite start A_s and austenite finish A_f temperatures were estimated using the linear approximation of tangent lines to the DSC curve close to the inflation points, as schematically indicated in **Fig. 3.53** and **3.54**. The obtained transformation temperatures for all investigated materials are summarized in **Table 3.4**, together with the average martensitic transformation temperature T_M, which is determined as follows:

$$T_M = \frac{M_s + M_f + A_s + A_f}{4} \tag{3.5}$$

Furthermore, the thermal hysteresis ΔT_H of the first-order transformation were also quantitatively estimated as temperature difference between forward and backward martensitic transition, according the relation:

$$\Delta T_H = \frac{(A_f + A_s) - (M_s + M_f)}{2} \tag{3.6}$$

When it comes to the second-order magnetic transformation, the Curie temperature is also observed on the recorded DSC curves as a small λ-shape anomalies. This is due to the strong coupling between magnetic and structural properties of the fabricated NiMnGa-based MSMAs. However, the observed kinks in the base-line curves are not so pronounced, thus the Curie temperatures were estimated using the complementary M-TG curves shown in right column in **Fig. 3.53** and **3.54**. It can be seen that in case of M-TG characteristics, the magnetic transformation manifested by abrupt increase or decrease of the weight of the sample is significantly more evident than for the DSC curves. Moreover, the magnetic transition is also characterized by minor hysteresis of about ~2–4 K between heating and cooling cycles, thus the final T_C was evaluated as an average value between this two processes. The resultant T_C for all examined water cooled materials are also summarized in **Table 3.4**.

Table 3.4. The temperatures of martensitic and magnetic transformation estimated from the DSC and M-TG curves for the produced NiMnGa-based Heusler alloys. The A_s/A_f and M_s/M_f are the start/finish temperatures for the austenite and martensite transformation, respectively. The T_C is the average value of Curie temperature determined from heating and cooling M-TG curves. The T_M and ΔT_H corresponds to average temperature of martensitic transition and the thermal hysteresis between the austenite and martensite transformation, respectively.

Alloy composition	**Transformation temperatures**						
	Martensitic						**Magnetic**
	A_s (K)	**A_f (K)**	**M_s (K)**	**M_f (K)**	**T_M (K)**	**ΔT_H (K)**	**T_C (K)**
$Ni_{48}Mn_{32}Ga_{20}$	279	285	273	267	276.0	12.0	374
$Ni_{48}Mn_{31}Ga_{20}Co_1$	285	291	279	274	282.3	11.5	385
$Ni_{48}Mn_{30}Ga_{20}Co_2$	293	304	290	282	292.3	12.5	391
$Ni_{48}Mn_{28}Ga_{20}Co_4$	348	360	339	330	344.3	19.5	400
$Ni_{48}Mn_{28}Ga_{20}Co_3Fe$	284	293	276	266	279.8	17.5	403
$Ni_{50}Mn_{25}Ga_{21}Co_2Fe_{21}$	308	318	296	288	302.5	21.0	399
$Ni_{48}Mn_{28}Ga_{20}Co_1Fe_3$	262	269	255	249	258.8	13.5	410
$Ni_{48}Mn_{28}Ga_{20}Fe_4$	259	264	250	246	254.8	13.5	392

It is seen in **Fig. 3.53** and **3.54** that peaks corresponding to the martensitic transformation significantly shifts to the higher temperatures with the increasing Co-content and then return to lower temperatures as Fe gradually substitutes Co. For the reference undoped $Ni_{48}Mn_{32}Ga_{20}$ sample the $T_M = 276.0$ K and then increase to 344.3 K for the $Ni_{48}Mn_{28}Ga_{20}Co_4$ alloy with the highest content of Co. It shows that adding merely 4 at.% of Co considerably increases the T_M in Ni-Mn-Ga system by over 70 K. On the contrary, the Co substitution by Fe decreases the T_M up to 254.8 K for the $Ni_{48}Mn_{28}Ga_{20}Fe_4$ alloy exhibiting the highest content of Fe. The exchange of 4 at.% of Co to 4 at.% of Fe without altering the Ni/Mn/Ga ratio reduces the TM by almost 90 K, which confirms the contradictory influence of Fe and Co on temperature of martensitic transition. However, it should be emphasized that compared to Co, Fe has a less significant impact on T_M. The direct comparison of the reference undoped sample and $Ni_{48}Mn_{28}Ga_{20}Fe_4$ alloy reveals only 20 K difference in their temperature of martensitic transition, which is 3.5 times less than in case of aforementioned $Ni_{48}Mn_{28}Ga_{20}Co_4$ specimen.

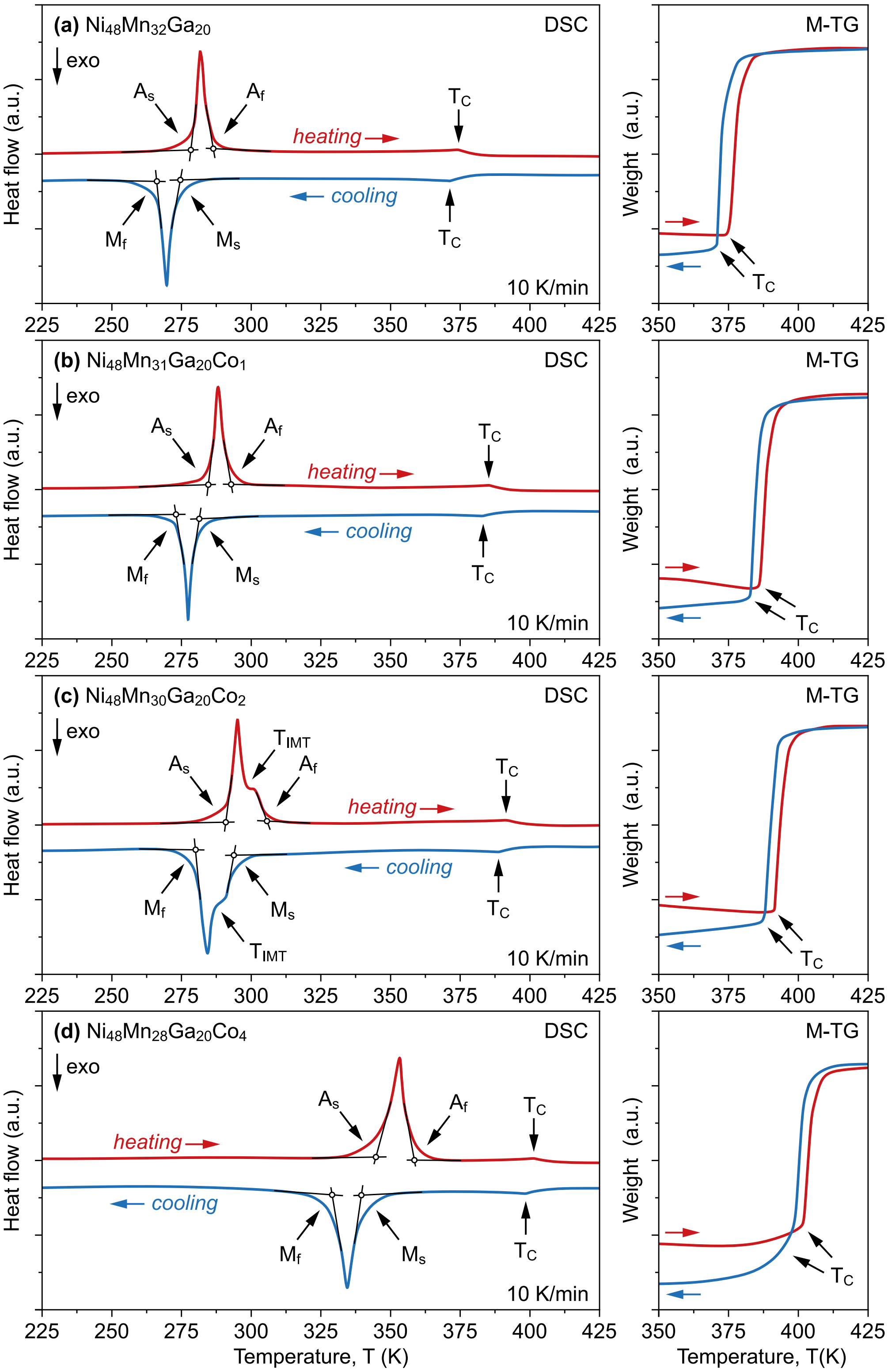

Fig. 3.53. DSC and M-TG curves recorded during heating and cooling cycles for the water cooled **(a)** $Ni_{48}Mn_{32}Ga_{20}$, **(b)** $Ni_{48}Mn_{31}Ga_{20}Co_1$, **(c)** $Ni_{48}Mn_{30}Ga_{20}Co_2$ and **(d)** $Ni_{48}Mn_{28}Ga_{20}Co_4$ magnetic shape memory alloys. The characteristic start and finish temperatures for the martensitic and austenitic transformations are marked with arrows and denoted as M_s, M_f, A_s and A_f, respectively. The T_{IMT} corresponds to intermartensitic transition. The Curie temperature (T_C) during heating and cooling cycle is indicated in both DSC and M-TG curves.

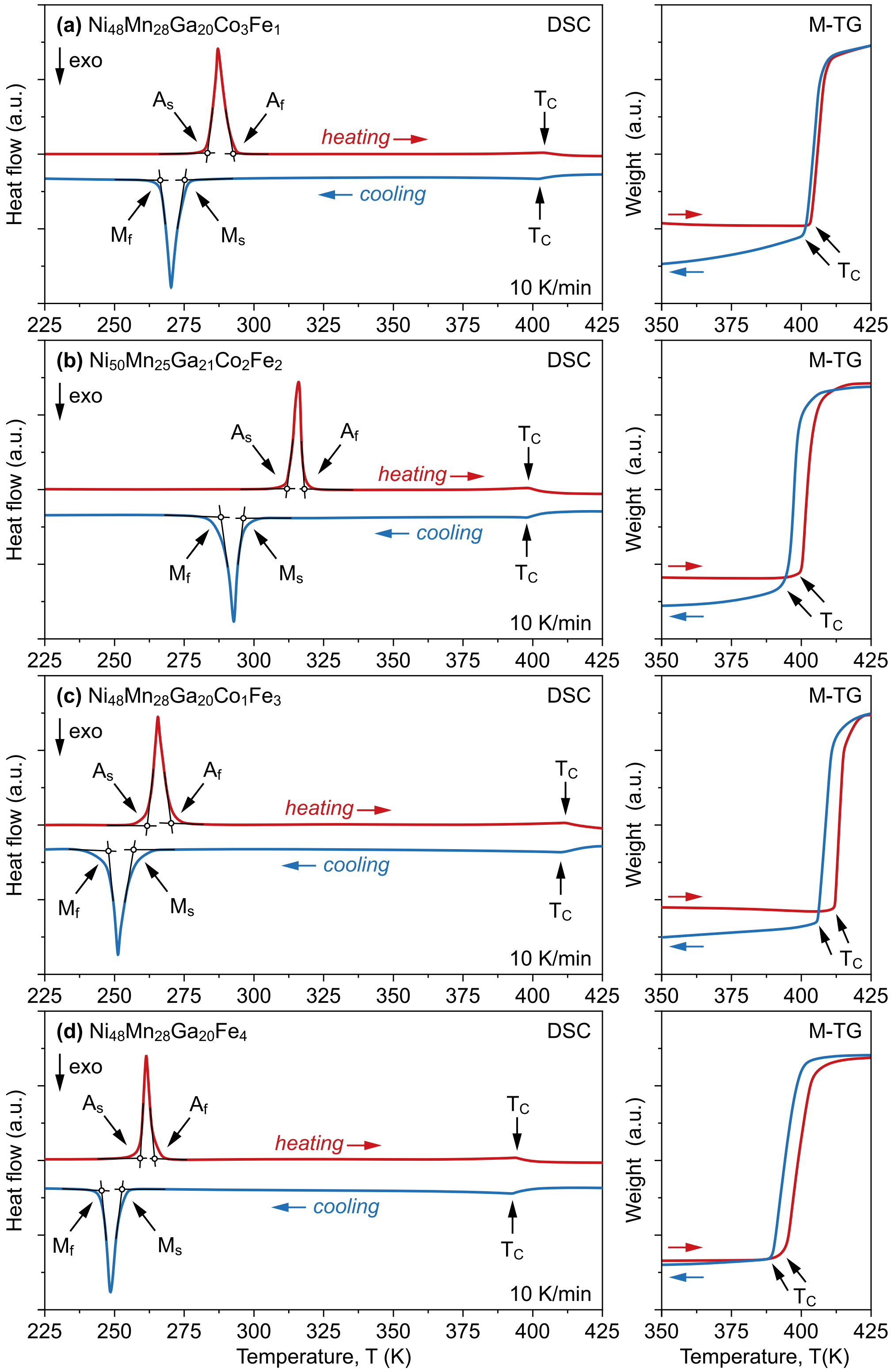

Fig. 3.54. DSC and M-TG curves recorded during heating and cooling cycles for the water cooled **(a)** $Ni_{48}Mn_{28}Ga_{20}Co_3Fe_1$, **(b)** $Ni_{50}Mn_{25}Ga_{21}Co_2Fe_2$, **(c)** $Ni_{48}Mn_{28}Ga_{20}Co_1Fe_3$ and **(d)** $Ni_{48}Mn_{28}Ga_{20}Fe_4$ magnetic shape memory alloys. The characteristic start and finish temperatures for the martensitic and austenitic transformations are marked with arrows and denoted as M_s, M_f, A_s and A_f, respectively. The Curie temperature (T_C) during heating and cooling cycle is indicated in both DSC and M-TG curves.

The obtained values of characteristic temperatures describing the martensitic transformation are also in accordance with the previous microstructural investigation of the fabricated NiMnGa-based materials (**Section 3.1**). As explained in experimental part of this thesis, all investigated samples were firstly cooled down considerably below the martensitic transformation temperature and then slowly warmed up back to room temperature (RT). The proposed procedure allowed to reduce the introduction of additional driving force for a potential first-order martensitic transformation. Consequently, in the following analysis, the reference temperature that implies the diminishing of the formerly induced martensitic phase is then the austenite start temperature. **Table 3.4** shows that the $Ni_{48}Mn_{28}Ga_{20}Co_4$ and $Ni_{50}Mn_{25}Ga_{21}Co_2Fe_2$ alloys, which were actually found fully martensitic during microstructural studies, have A_s that are higher than RT. For the earlier martensitic $Ni_{48}Mn_{28}Ga_{20}Co_1Fe_3$ sample the A_s is slightly below the RT, however the mechanical polishing may induce some internal stresses that stabilize the martensitic phase below the A_s estimated for the stress-free sample. Moreover, the A_s for the $Ni_{48}Mn_{31}Ga_{20}Co_1$ and $Ni_{48}Mn_{30}Ga_{20}Co_2$ alloy is also very close to the RT, supporting earlier findings that suggested the existence of the residual martensitic phase in these particular samples. Special attention should be given to the $Ni_{48}Mn_{30}Ga_{20}Co_2$ alloy presented in **Fig. 3.53** in which both the endothermic and exothermic peaks are characterized by corresponding overlapping bimodal distribution. The observed shape of peaks refer to a two-stage process, which in case of martensitic transformation indicates the occurrence of intermartensitic transition (T_{IMT}), that was previously described in **Section 1.5.3**. The suggested interpretation of the bimodal distribution is consistent with the XRD analysis that revealed the 5M modulated martensite structure in this particular alloy (**Section 3.1.4**).

Furthermore, the increasing content of Co in NiMnGa-based alloys also lead to the shift of Curie temperature to higher values and the subsequent substitution of Co by Fe also maintains this tendency. In order visualize these changes with reference to the examined elemental doping, **Fig. 3.55** presents the temperatures of martensitic and magnetic transformation from **Table 3.4** plotted as a function of alloying addition. The obvious contradictory influence of Co and Fe on the temperature of reversible martensitic transformation is now clearly seen in **Fig. 3.55(a)**. It is worth noticing that again the $Ni_{50}Mn_{25}Ga_{21}Co_2Fe_2$ alloy with different Ni/Mn ratio stands out from the rest of the samples. This implies the stronger influence of Ni/Mn ratio than Co or Fe doping, which was already suggested during XRD analysis (**Section 3.1.4**).

When it comes to magnetic transformation, the unusual anomalies are observed for the Fe-Co-doped samples. Generally, it is reported that the addition of Fe to Ni-Mn-Ga composition increases the Curie temperature [267,284] or occasionally may have negligible influence on the paramagnetic ⇄ ferromagnetic transformation [286,287]. Comparable results are partially seen in this work on the example of the $Ni_{48}Mn_{28}Ga_{20}Co_3Fe_1$ and $Ni_{48}Mn_{28}Ga_{20}Co_1Fe_3$ alloys for which the increasing trend in T_C is almost the exact continuation of the trend emerging for the Co-doped materials (**Fig. 3.55(b)**). What could be expected, the $Ni_{50}Mn_{25}Ga_{21}Co_2Fe_2$

alloy with different Ni/Mn ratio stands out from the other fabricated samples, though the significantly lower T_C observed for last $Ni_{48}Mn_{28}Ga_{20}Fe_4$ alloy is unforeseen. One should bear in mind that the observed increasing characteristic of T_C is simultaneously influenced by both Co and Fe, but the aforementioned anomaly is only discovered in samples doped with Fe. Generally, the increase in T_C observed for alloys doped by Co or Fe can be explained by the fact that Fe or Co has a greater magnetic moment than Mn, resulting in a stronger exchange interaction of the system. Nevertheless, the presented results suggests that for the alloys doped by both Co and Fe the combined effect of these two elements may by remarkably different than individual influences of Fe or Co. In this context, it should be also stated that the unusual non-monotonous trend in T_C in Ni-Mn-Ga-Co-Fe system was previously reported in [269,270], and was described in **Section 1.6.2.2**.

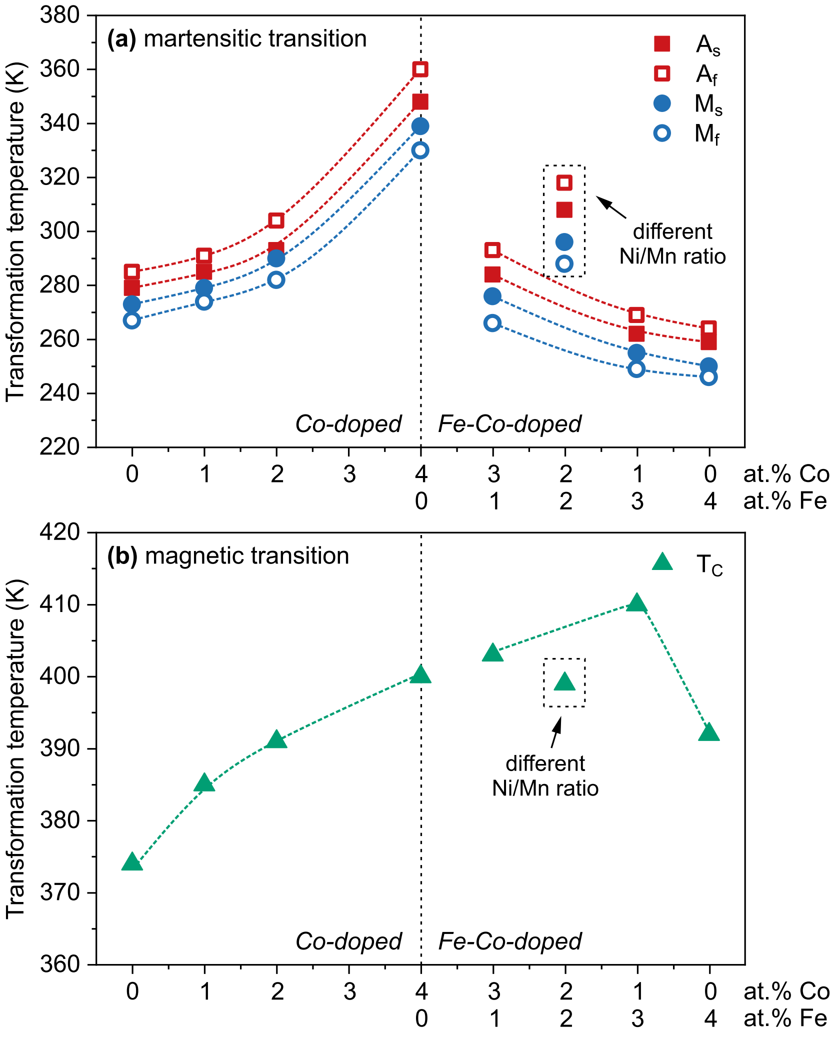

Fig. 3.55. The characteristic temperatures for **(a)** the martensitic transformation (A_s, A_f, M_s and M_f) and **(b)** magnetic transformation (T_C) estimated from the DSC and M-TG curves for the water cooled $Ni_{48}Mn_{32}Ga_{20}$, $Ni_{48}Mn_{31}Ga_{20}Co_1$, $Ni_{48}Mn_{30}Ga_{20}Co_2$, $Ni_{48}Mn_{28}Ga_{20}Co_4$, $Ni_{48}Mn_{28}Ga_{20}Co_3Fe_1$, $Ni_{50}Mn_{25}Ga_{21}Co_2Fe_2$, $Ni_{48}Mn_{28}Ga_{20}Co_1Fe_3$ and $Ni_{48}Mn_{28}Ga_{20}Fe_4$ alloys expressed as a function of Co and Fe doping. The symbols corresponding to the $Ni_{50}Mn_{25}Ga_{21}Co_2Fe_2$ alloy characterized by different Ni/Mn ratio are indicated by additional frames.

The XRD studies presented and discussed in **Section 3.1.4** revealed the partial correlation between the lattice and electronic properties of the fabricated NiMnGa-based multifunctional alloys. Following that fact, **Fig. 3.56** and **3.57** present the estimated temperatures of martensitic transformation, as well as the Curie temperature expressed as a function of e/a and N_e/a parameter, respectively. It is seen in **Fig. 3.56(a)** that the T_M significantly increases with the increasing e/a, indicating the strong mutual dependence between these parameters. Remarkably, the T_M for the $Ni_{50}Mn_{25}Ga_{21}Co_2Fe_2$ alloy, which has a different Ni/Mn ratio than the other alloys, follows the same trends as the rest of the samples, demonstrating the potential universality of e/a ratio. Additionally, the comparable, but distinctive increasing trends are observed separately for Co-doped and Fe-Co-doped samples. The temperature difference between these two individual trends is about ~35 K. This results show that Fe might be employed as a doping element in the quaternary Ni-Mn-Ga-Co system to significantly lower the T_M by a known constant value. Likewise, Co may be used in Ni-Mn-Ga-Fe system to increase the T_M by the same constant value, without influencing the general characteristics of T_M.

In the context of magnetic transformation, **Fig. 3.56(b)** shows the obvious linear relationship between Curie temperature and e/a parameter. Again, Co-doped and Fe-Co-doped materials exhibit two separate linear relationships. It is interesting to note that the previously mentioned $Ni_{48}Mn_{28}Ga_{20}Fe_4$ alloy exhibiting anomalous T_C is now located along the linear trend characterizing the Co-doped samples. This supports the earlier conclusion that the joint influence of Fe and Co is considerably different than the distinct influence of individual elements.

In consideration of the second electronic parameter defining the non-bonding electron concentration, **Fig 3.57(a)** shows the influence of N_e/a on the martensitic transformation temperature for the investigated NiMnGa-based alloys. The relationship between the T_M and N_e/a is clearly comparable to the one shown for the e/a parameter (**Fig. 3.56(a)**), but this time there is no evident distinction between Co-doped and Fe-Co-doped alloys. The T_M for all examined alloys increases in the same manner, although the distribution of measured values are more random than in case of e/a and deviates by around ±15 K from the overall trend. It is particularly notable in comparison to the earlier XRD analysis discussed in **Section 3.1.4**. It should be recalled that for the crystal lattice parameters, the e/a ratio was considered as fairly universal parameter for all investigated materials, whereas the refined crystallographic data for Co-doped and Fe-Co-doped materials were clearly distinguished for N_e/a parameter. This phenomenon was attributed the notable difference between the number of non-bonding electron equal to 3.64 and 2.45 for Co and Fe, respectively. However, the investigated temperature of the martensitic transition now shows the opposite pattern. In the following case, the obvious distinction between Co-doped and Fe-Co-doped samples are found for the e/a ratio, whereas N_e/a parameter suggest to be more universal despite having higher uncertainty.

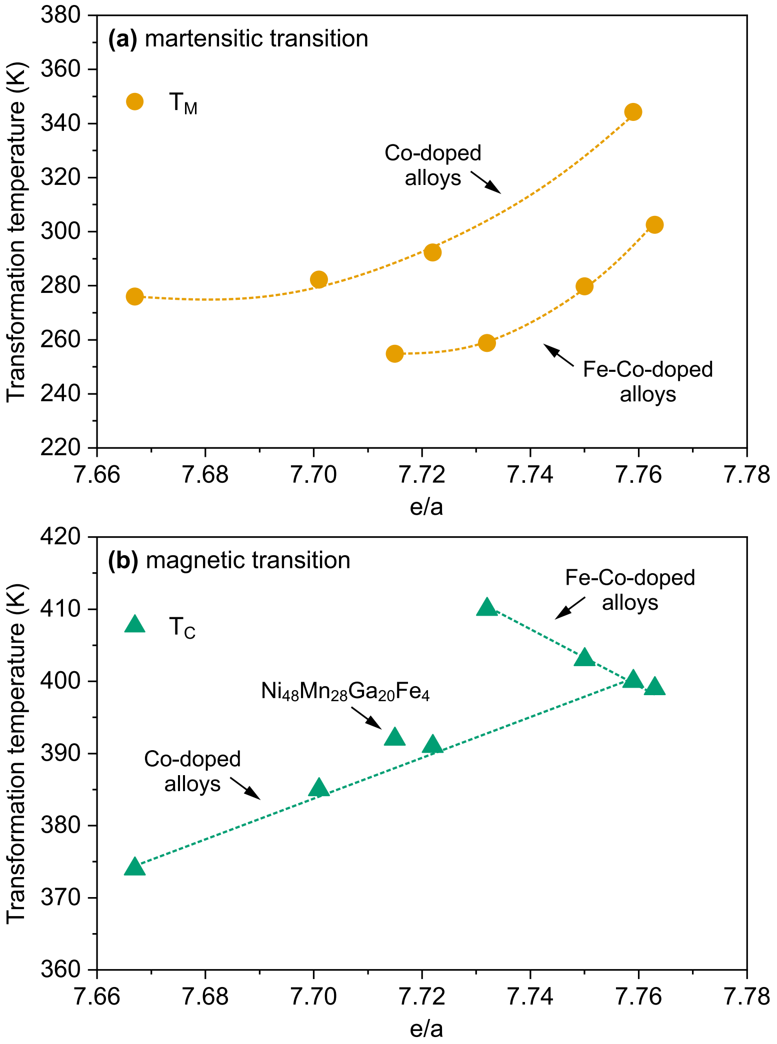

Fig. 3.56. The temperatures of **(a)** the martensitic transformation (T_M) and **(b)** the magnetic transformation (T_C) estimated from DSC and M-TG curves and expressed as a function of the valence electrons concentration e/a for the investigated NiMnGa-based Heusler alloys doped by Co and/or Fe. The dashed lines are guide for an eye to show the trends in T_M and T_C.

For the magnetic transformation temperature depicted in **Fig. 3.57(b)**, Co-doped and Fe-Co-doped alloys exhibit two distinct linear relationships of T_C. The obtained linear characteristics are once more very similar to those presented for the e/a parameter (**Fig. 3.56(b)**), with and the only difference found for the $Ni_{48}Mn_{28}Ga_{20}Fe_4$ sample (marked with an addition arrow in **Fig. 3.56(b)** and **3.57(b)**). It is seen that for the N_e/a parameter the Curie temperature of this specimen do not correspond to other Co-doped or Fe-Co-doped materials. In this case the e/a ratio appears to be a more relevant metric in determining the Curie temperature than N_e/a when taking into account the results shown in both figures.

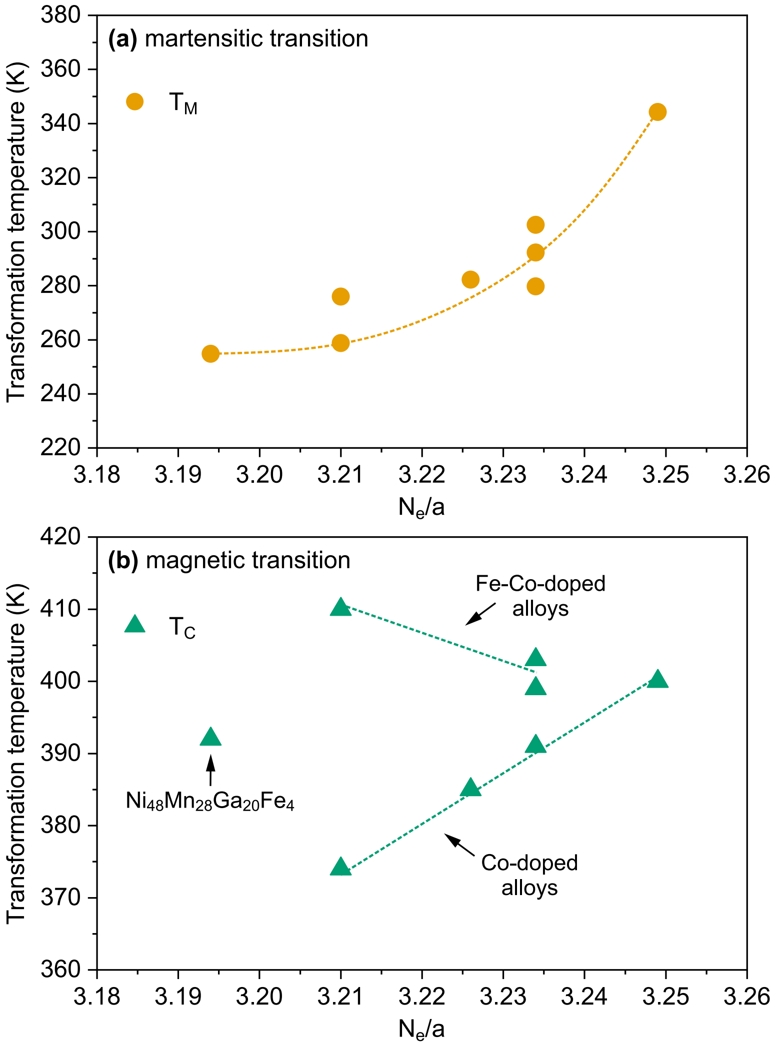

Fig. 3.57. The temperatures of **(a)** the martensitic transformation (T_M) and **(b)** the magnetic transformations (T_C) estimated from DSC and M-TG curves and expressed as a function non-bonding electrons concentration N_e/a for the investigated NiMnGa-based Heusler alloys doped by Co and/or Fe. The dashed lines are guide for an eye to show the trends in T_M and T_C.

Last but not least, the mention should also be made of thermal hysteresis ΔT_H estimated on the basis of **Eq. 3.6** and reported in **Table 3.4**. Firstly, it is worth noticing that there are two distinct ranges in which the acquired values of ΔT_H can be placed. The first range between 11.5 K and 13.5 K is related the alloys which were previously found to be austenitic at room temperature, *i.e.* the $Ni_{48}Mn_{32}Ga_{20}$, $Ni_{48}Mn_{31}Ga_{20}Co_1$, $Ni_{48}Mn_{30}Ga_{20}Co_2$, $Ni_{48}Mn_{28}Ga_{20}Co_1Fe_3$ and $Ni_{48}Mn_{28}Ga_{20}Fe_4$ alloys. The second, noticeably higher region between 17.5 K and 21.0 K corresponds to the fully martensitic samples at room temperatures, *i.e.* the $Ni_{48}Mn_{28}Ga_{20}Co_4$, $Ni_{48}Mn_{28}Ga_{20}Co_3Fe_1$ and $Ni_{50}Mn_{25}Ga_{21}Co_2Fe_2$ alloys. This suggests that the shifting of T_M towards higher temperatures by elemental doping entails the increase of thermal hysteresis, which ultimately influences the potential functional properties of the future magnetic shape memory alloys. This phenomenon is also observed in a matter of the discussed electronic parameters, which is presented in **Fig. 3.58**. According to **Fig. 3.58(a)**, ΔT_H increases steeply with the increase of e/a and all Co-doped and Fe-Co-doped alloys follows the same monotonical trend. In contrary, **Fig. 3.59(b)** shows that the estimated values of ΔT_H are scattered along the N_e/a parameter without any evident relationship. This again favours the e/a parameter in consideration of predicting the temperatures of reversible martensitic transformation.

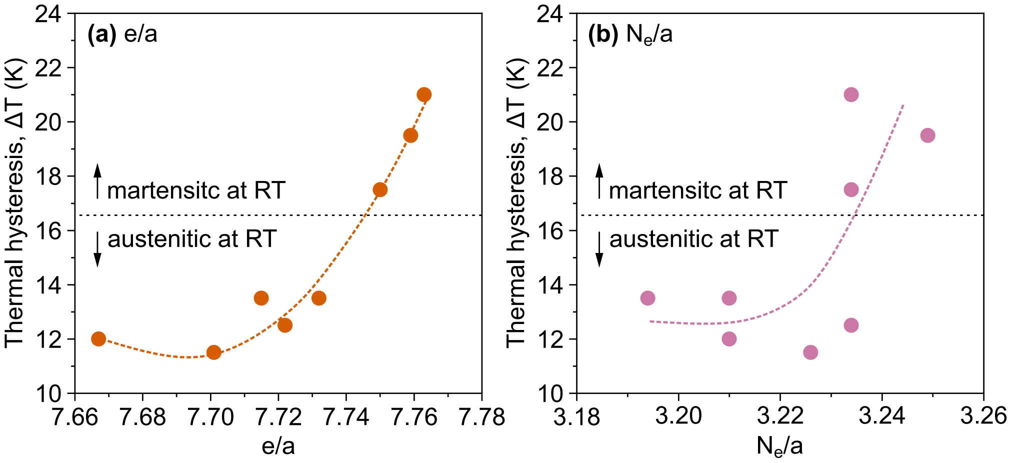

Fig. 3.58. The thermal hysteresis ΔT_H of reversible martensitic transformation expressed as a function of **(a)** e/a and **(b)** N_e/a parameters. The horizontal dashed line shows the schematic division for alloys observed in austenitic and martensitic state at room temperature (RT). The dashed colour lines are guide for an eye to show the trends in ΔT.

3.2.2 Thermomagnetic behaviour

A large part of the theoretical introduction of this thesis was devoted to show and describe the exceptionally strong magneto-thermo-structural coupling characterizing the Ni-Mn-Ga magnetic shape memory alloys. In a view of this information the thermomagnetic behaviour of the fabricated materials were investigated with the help of vibrating sample magnetometer. The temperature-dependent magnetization curves were recorded in heating and cooling cycle following the ZFC an FC protocol, which was in detail described in experimental part of this thesis (**Section 2.3.6**). It should be emphasized that, the measurements were conducted at the same heating/cooling rate of 10 K/min as the previously discussed DSC investigation, which allows for direct comparison of the obtained results.

Fig. 3.59–3.61 shows the temperature dependence of magnetization $M(T)$ recorded for all fabricated water, air and furnace cooled NiMnGa-based alloys, respectively. It should be remembered that for such low value of external magnetic field ($\mu_0 H$ = 10 mT), the quantitative analysis of magnetization may be misleading, as it is strongly influenced by mass and shape of the sample. Hence, the presented $M(T)$ curves were normalized to allow for better comparison of numerous specimens. It is seen in **Fig. 3.59–3.61** that every sample exhibits an abrupt increase in magnetization during heating phase and a following sudden drop in magnetization during the cooling process. The observed rapid change of magnetization is related to the austenitic and martensitic transformation, respectively. The magnetization of the samples changes due to significant difference between magnetic ordering of the austenite and martensite phase, which was extensively discussed in the theoretical introduction (**Section 1.3**). Based on the presented thermomagnetic curves the characteristic temperatures of forward and reverse martensitic transformation were established using the linear approximation of tangent lines to the $M(T)$ curve close to structural transformations, as depicted in **Fig. 3.59–3.61**. The estimated values of A_s, A_f, M_s, and M_f , as well as T_M and ΔT are listed in **Table 3.5**.

It is essential to note that the observed sudden change in magnetization is only connected with structural transformation and should not be confused with the magnetostructural transformation described in **Section 1.3.7**. In case of the produced MSMAs the previously discussed M-TG studies shown that the Curie temperature is above 370 K for all investigated samples. As a results, the T_C is not observed in $M(T)$ curves and martensitic transformation undergoes between two ferromagnetic phases. As a consequence, the following transformation sequence is then valid for all produced materials:

$$\begin{array}{c}\textit{ferromagnetic}\\ \text{austenite}\end{array} \xrightarrow{T_M} \begin{array}{c}\textit{ferromagnetic}\\ \text{martensite}\end{array} \xrightarrow{T_C} \begin{array}{c}\textit{paramagnetic}\\ \text{martensite}\end{array}$$

One characteristic feature that distinguish the heating and cooling part of $M(T)$ curve is the notable difference between the magnetization of the martensite phase. This is due to the strong magnetocrystalline anisotropy of the NiMnGa-based materials as well as the employment of the ZFC and FC mode. At the beginning, during heating in ZFC mode, the examined sample is magnetized at low temperature with no favourable magnetostructural orientation. In the subsequent FC cooling mode the already magnetized sample in austenitic state undergoes the field-assisted martensitic transformation, which induces the preferred magnetostructural orientation of martensite. It is clearly seen in **Fig. 3.59–3.61** that despite the relatively low field of only 10 mT the described phenomenon is still observed in all examined alloys. What is interesting, the aforementioned differences in magnetization are more pronounced in Co-doped samples than in Fe-Co-doped samples, which suggests the greater influence of Co on magnetostructural properties of NiMnGa-based alloys than Fe. Moreover, the stated magnetization differences are less evident for the furnace cooled materials, than for the other of water and air cooled samples. This implies that furnace cooling process may deteriorate the magnetostructural coupling of NiMnGa-based alloys or, in other words, it did not allow for complete structural development of MSMA. This conclusion is also relevant in general direct comparison of temperature-dependent behaviour of magnetization for all fabricated alloys. It is seen in **Fig. 3.61** that the slowest cooled materials are characterized by notably lower changes in magnetization during forward and revered martensitic transformation than quickly cooled samples, *i.e.* water (**Fig. 3.59**) and air cooled (**Fig. 3.60**) ones, which also supports the theory that furnace cooling may reduce the complete magnetostructural evolution of NiMnGa-based Heusler compounds. This is an important finding in light of potential applications of Ni-Mn-Ga-Co-Fe alloys since the appearance of the various functional magnetic field-induced effects discussed in **Sections 1.4** and **1.5** depends on the significant difference in magnetization that emerges during the phase transition.

Table 3.5. The characteristic temperatures of martensitic transformation estimated from the thermomagnetic curves for the produced NiMnGa-based Heusler alloys. The A_s/A_f and M_s/M_f are the start/finish temperatures for the austenite and martensite transformation, respectively. The T_M and ΔT_H corresponds to average temperature of martensitic transition and the thermal hysteresis between the austenite and martensite transformation, respectively.

Alloy composition	**Cooling**	**Martensitic transition**					
		A_s (K)	**A_f (K)**	**M_s (K)**	**M_f (K)**	**T_M (K)**	**ΔT_H (K)**
$Ni_{48}Mn_{32}Ga_{20}$	water	279	283	272	267	275.3	11.5
	air	280	283	271	269	275.8	11.5
	furnace	278	286	274	271	277.3	9.5
$Ni_{48}Mn_{31}Ga_{20}Co_{1}$	water	285	289	277	274	281.3	11.5
	air	286	291	279	276	283.0	11.0
	furnace	292	296	286	283	289.3	9.5
$Ni_{48}Mn_{30}Ga_{20}Co_{2}$	water	294	301	288	280	290.8	13.5
	air	295	300	287	281	290.8	13.5
	furnace	300	303	290	287	295.0	13.0
$Ni_{48}Mn_{28}Ga_{20}Co_{4}$	water	350	360	340	332	345.5	19.0
	air	248	259	342	334	345.8	15.5
	furnace	354	360	342	336	348.0	18.0
$Ni_{48}Mn_{28}Ga_{20}Co_{3}Fe$	water	286	295	277	266	281.0	19.0
	air	287	296	279	267	282.3	18.5
	furnace	294	302	291	282	292.3	11.5
$Ni_{50}Mn_{25}Ga_{21}Co_{2}Fe_{21}$	water	309	318	298	291	304.0	19.0
	air	314	320	301	292	306.8	20.5
	furnace	315	324	306	297	310.5	18.0
$Ni_{48}Mn_{28}Ga_{20}Co_{1}Fe_{3}$	water	262	267	253	249	257.8	13.5
	air	261	256	252	248	256.5	13.0
	furnace	266	270	259	255	262.5	11.0
$Ni_{48}Mn_{28}Ga_{20}Fe_{4}$	water	258	262	249	245	253.5	13.0
	air	257	260	248	245	252.5	12.0
	furnace	264	268	258	253	260.8	10.5

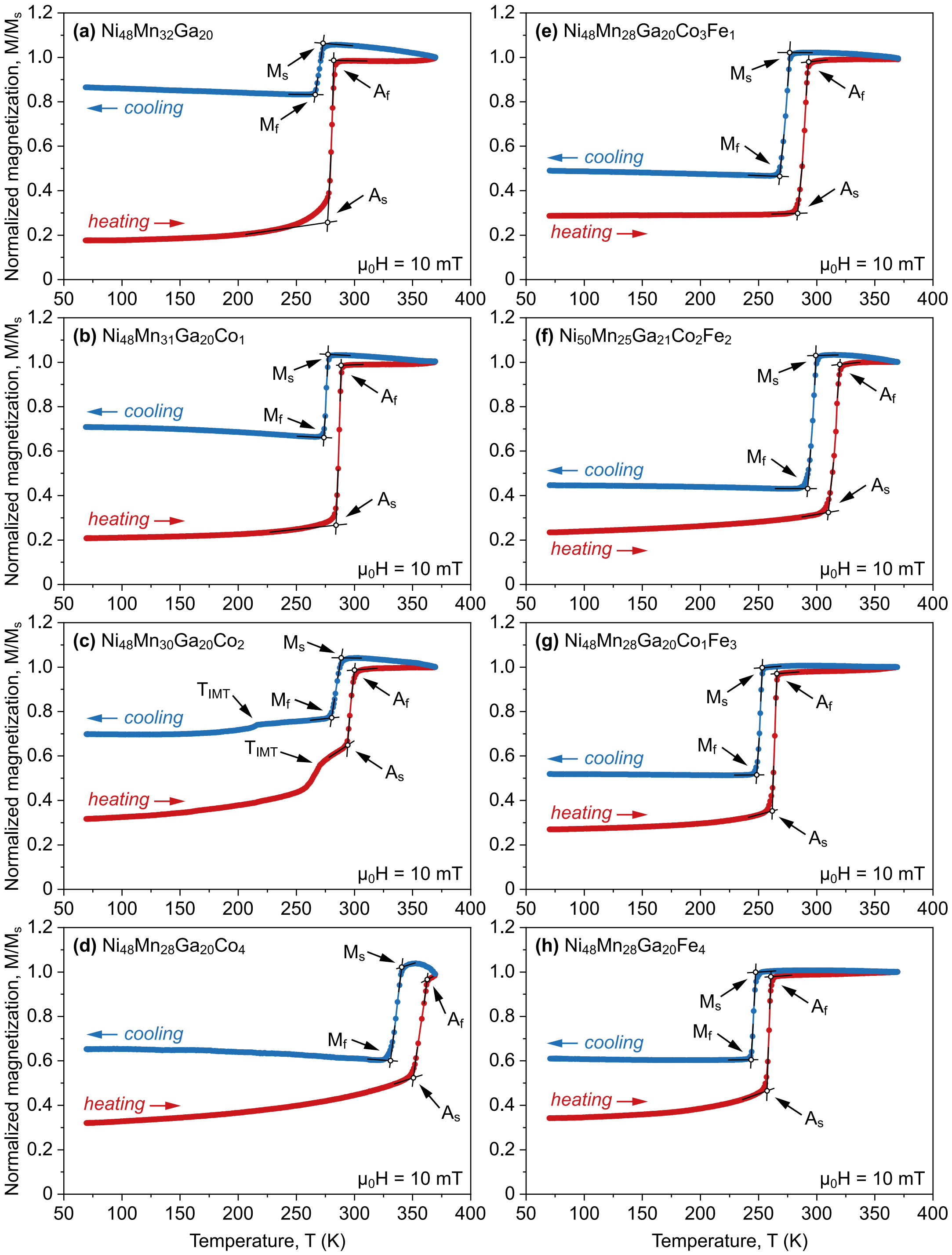

Fig. 3.59. Temperature dependence of magnetization $M(T)$ for the water cooled **(a)** $Ni_{48}Mn_{32}Ga_{20}$, **(b)** $Ni_{48}Mn_{31}Ga_{20}Co_1$, **(c)** $Ni_{48}Mn_{30}Ga_{20}Co_2$ and **(d)** $Ni_{48}Mn_{28}Ga_{20}Co_4$, **(e)** $Ni_{48}Mn_{28}Ga_{20}Co_3Fe_1$, **(f)** $Ni_{50}Mn_{25}Ga_{21}Co_2Fe_2$, **(g)** $Ni_{48}Mn_{28}Ga_{20}Co_1Fe_3$ and **(h)** $Ni_{48}Mn_{28}Ga_{20}Fe_4$ alloys recorded during heating (ZFC) and cooling (FC) cycle under an external magnetic field of 10 mT. The characteristic start and finish temperatures for the martensitic and austenitic transformations are marked with arrows and denoted as M_s, M_f, A_s and A_f, respectively. The T_{IMT} corresponds to intermartensitic transition.

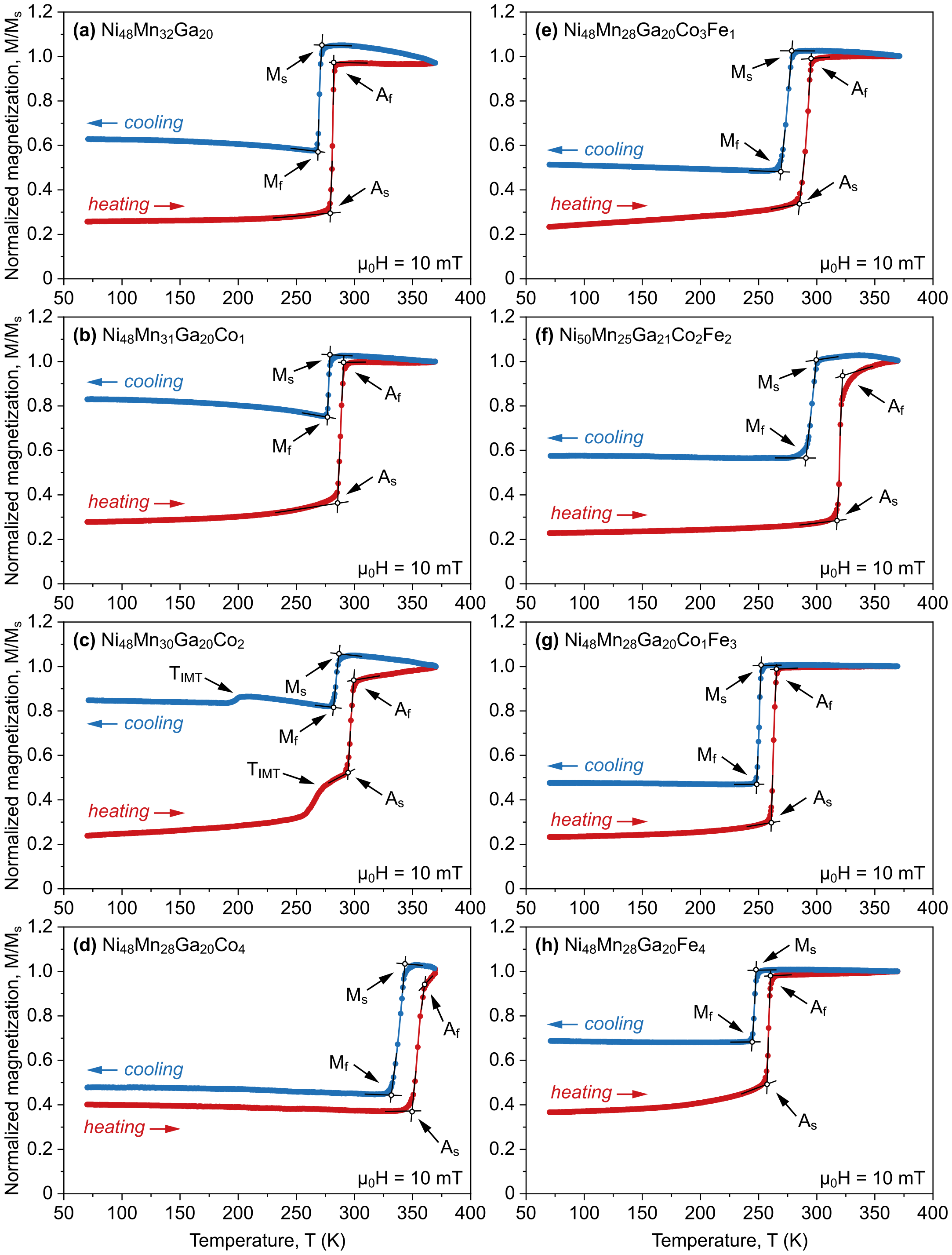

Fig. 3.60. Temperature dependence of magnetization $M(T)$ for the air cooled **(a)** $Ni_{48}Mn_{32}Ga_{20}$, **(b)** $Ni_{48}Mn_{31}Ga_{20}Co_1$, **(c)** $Ni_{48}Mn_{30}Ga_{20}Co_2$ and **(d)** $Ni_{48}Mn_{28}Ga_{20}Co_4$, **(e)** $Ni_{48}Mn_{28}Ga_{20}Co_3Fe_1$, **(f)** $Ni_{50}Mn_{25}Ga_{21}Co_2Fe_2$, **(g)** $Ni_{48}Mn_{28}Ga_{20}Co_1Fe_3$ and **(h)** $Ni_{48}Mn_{28}Ga_{20}Fe_4$ alloys recorded during heating (ZFC) and cooling (FC) cycle under an external magnetic field of 10 mT. The characteristic start and finish temperatures for the martensitic and austenitic transformations are marked with arrows and denoted as M_s, M_f, A_s and A_f, respectively. The T_{IMT} corresponds to intermartensitic transition.

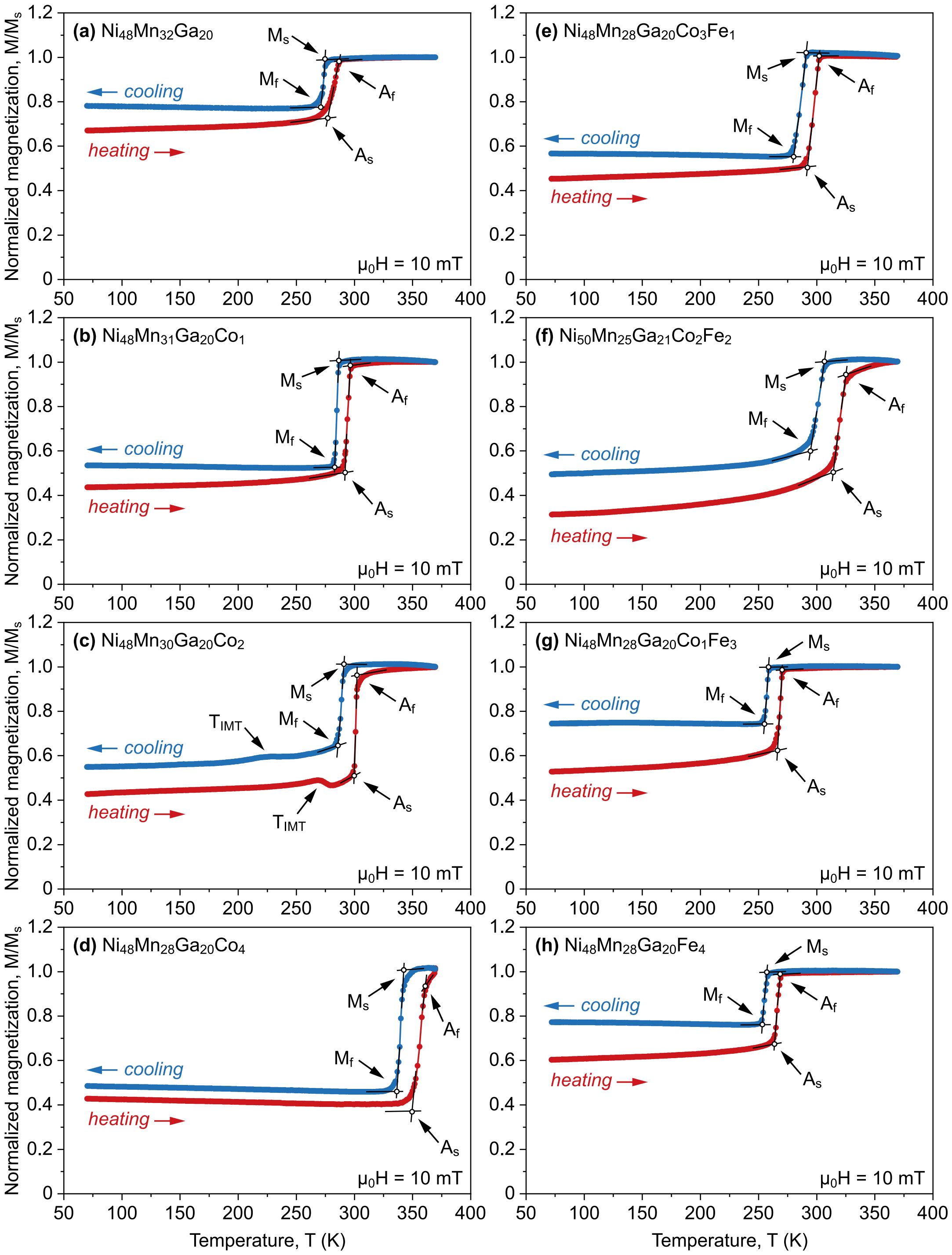

Fig. 3.61. Temperature dependence of magnetization $M(T)$ for the furnace cooled **(a)** $Ni_{48}Mn_{32}Ga_{20}$, **(b)** $Ni_{48}Mn_{31}Ga_{20}Co_1$, **(c)** $Ni_{48}Mn_{30}Ga_{20}Co_2$ and **(d)** $Ni_{48}Mn_{28}Ga_{20}Co_4$, **(e)** $Ni_{48}Mn_{28}Ga_{20}Co_3Fe_1$, **(f)** $Ni_{50}Mn_{25}Ga_{21}Co_2Fe_2$, **(g)** $Ni_{48}Mn_{28}Ga_{20}Co_1Fe_3$ and **(h)** $Ni_{48}Mn_{28}Ga_{20}Fe_4$ alloys recorded during heating (ZFC) and cooling (FC) cycle under an external magnetic field of 10 mT. The characteristic start and finish temperatures for the martensitic and austenitic transformations are marked with arrows and denoted as M_s, M_f, A_s and A_f, respectively. The T_{IMT} corresponds to intermartensitic transition.

In a view of elemental doping, it is seen in **Fig. 3.59–3.61** and in **Table 3.5** that the martensitic transformation follows the same patterns as in the case of previously described DSC investigations. Generally, the temperature of martensitic transformation increases with the increasing Co content and then subsequently decreases when Co is gradually replaced by Fe. The direct comparison between TM obtained with the help of DSC and VSM measurements for the water cooled NiMnGa-based alloys are presented in **Fig. 3.62.** As shown in **Fig. 3.62(a)** the T_M estimated from both DSC and $M(T)$ curves are in almost perfect agreement for all examined samples and the differences in corresponding data do not exceed ±1.5 K (**Fig. 3.62(b)**). Moreover, the comprehensive comparison of all characteristic temperatures of martensitic transition, including A_s, A_f, M_s, and M_f , collected in **Tables 3.4** and **3.5** also demonstrates that the difference in T_M between thermally oriented DSC data and magnetically oriented VSM data do not exceed ±2.0K. It is also worth pointing out that the previously observed intermartensitic transformation revealed in DSC analysis for the $Ni_{48}Mn_{30}Ga_{20}Co_2$ alloy was as well found during VSM measurements. The unusual deflections of $M(T)$ characteristics observed in **Fig. 3.59(c)–3.61(c)** and marked as T_{IMT} are most likely related to the intermartensitic transition, which is consistent with the corresponding DSC studies and former microstructural investigations.

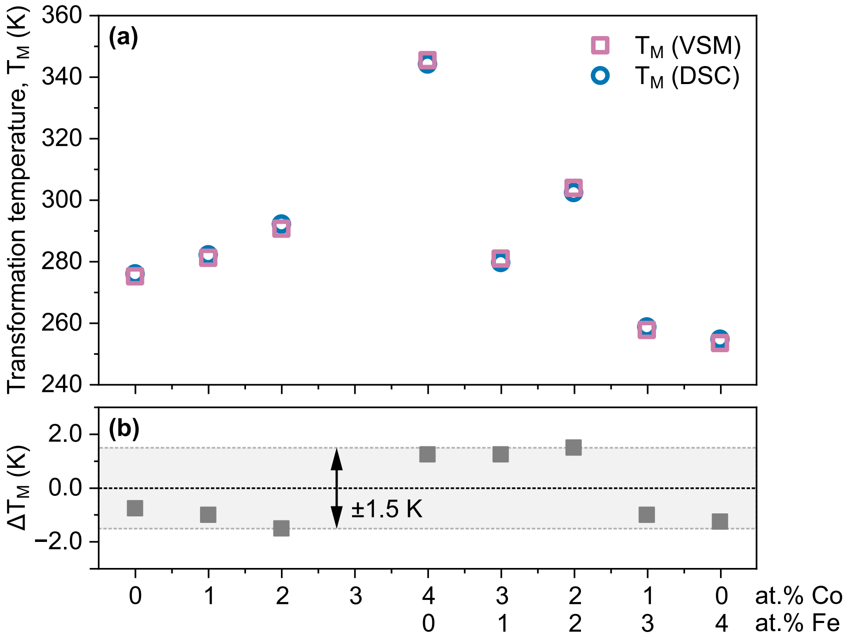

Fig. 3.62. The comparison of the martensitic transformation temperature T_M for the produced water cooled NiMnGa-based alloys expressed as a function of Co and/or Fe doping. **(a)** The T_M estimated on the basis of VSM and DSC measurements, as well as **(b)** the temperature difference ΔT_M between the corresponding T_M obtained by different technique. The calculated ΔT_M do not exceed ±1.5K.

Taking this comparison into consideration, it was decided not to repeat the discussion about the influence of elemental doping and related electronic parameters on the temperature of martensitic transformation for the fabricated NiMnGa-based materials since it was already covered in **Section 3.2.1**. The following part of this section will be instead focused on the observed differences between the materials exposed to a different cooling conditions, which will be complementary to the previous discussion.

Fig. 3.63 presents the average temperature of martensitic transformation for the water, air and furnace cooled alloys represented as a function of simple elemental doping and e/a parameter (e/a was previously found as better predictor of T_M then N_e/a). It can be seen that samples that have been cooled in water and those that have been cooled on air exhibit very comparable martensitic transition temperatures. The T_M for air cooled materials are occasionally slightly lower or slightly higher than T_M obtained for water cooled specimens. The average difference between T_M established for water and air cooled alloys is close to ~1 K, which is fairly low value considering the uncertainties of linear approximations during the prior estimation of A_s, A_f, M_s, and M_f. On the contrary, the furnace cooled samples are characterized by noticeably higher T_M than both water and air cooled specimens. Additionally, elemental doping affects the observed difference in T_M.. For the furnace cooled Co-doped alloys the T_M is about ~4 K higher than T_M estimated for the water cooled samples, whereas for the Fe-Co-doped alloys this difference increase to about ~7.5 K. In addition, the T_M for the furnace cooled alloys are also more scattered from general trends, which is especially evident in the example of e/a dependency shown in **Fig. 3.63(b)**. Despite the aforementioned differences in TM, the general behaviour of martensitic transformation is similar for corresponding water, air and furnace cooled materials since there have been no significant changes in thermal hysteresis of observed structural transition. The ΔT estimated for the $Ni_{48}Mn_{32}Ga_{20}$, $Ni_{48}Mn_{31}Ga_{20}Co_1$, $Ni_{48}Mn_{30}Ga_{20}Co_2$, $Ni_{48}Mn_{28}Ga_{20}Co_1Fe_3$ and $Ni_{48}Mn_{28}Ga_{20}Fe_4$ alloys is about ~12 K, while ΔT for the $Ni_{48}Mn_{28}Ga_{20}Co_4$, $Ni_{48}Mn_{28}Ga_{20}Co_3Fe_1$ and $Ni_{50}Mn_{25}Ga_{21}Co_2Fe_2$ alloys is around ~18 K.

The discussed distinct behaviour of TM for the furnace cooled samples clearly shows that despite the same chemical composition as water and air cooled materials, the magnetostructural properties of furnace cooled MSMAs are not fully developed. These structural differences between differently cooled alloys were partially revealed during XRD investigation (**Section 3.1.4**) and the discussed VSM measurements confirmed the influence of the examined structural order on the reversible martensitic transformation.

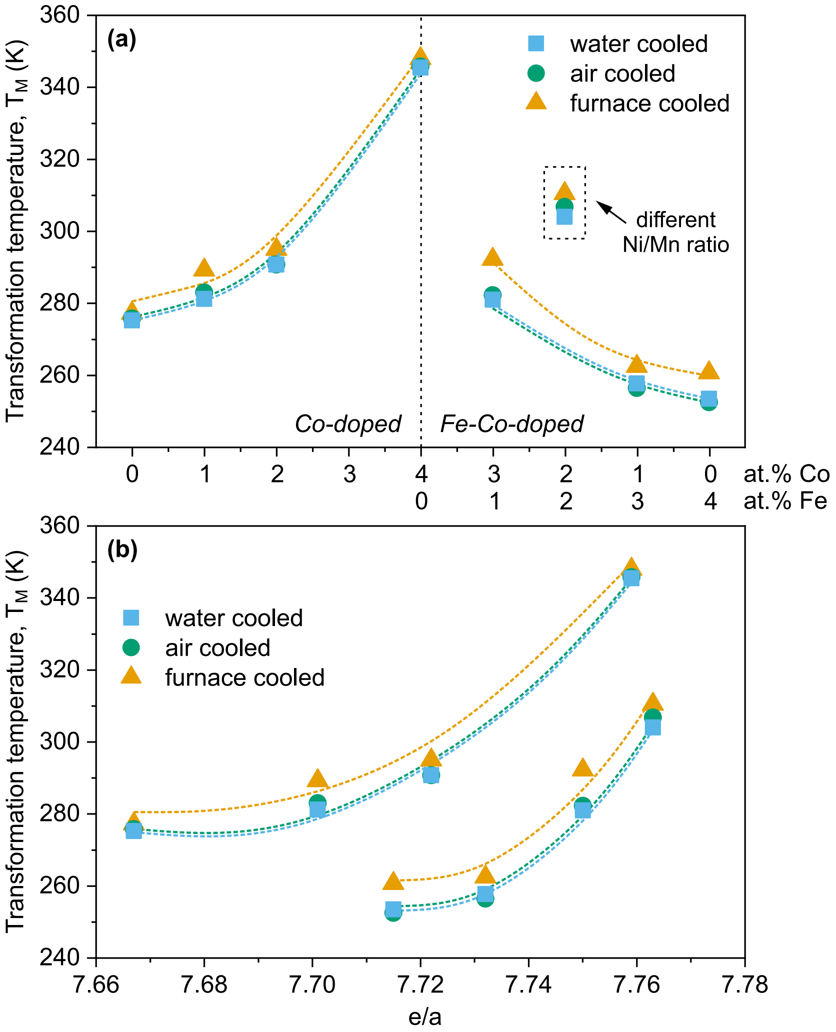

Fig. 3.63. The comparison of the martensitic transformation temperature T_M for the water, air and furnace cooled NiMnGa-based alloys expressed as **(a)** a function of Co and/or Fe doping, as well as **(b)** a function of the valence electrons concentration *e*/*a*.

3.3 Magnetic properties

3.3.1 Thermomagnetic hysteresis

The magnetic properties of the produced NiMnGa-based materials were investigated on the basis of DC hysteresis loops recorded at 100 K for the martensite phase and at 320 K or 360 K for the austenite phase, depend on the established temperature of martensitic transformation for the individual samples. All loops were collected under an external magnetic field up to 2 T.

Fig. 3.64–3.66 presents the obtained hysteresis loops for the fabricated water, air and furnace cooled alloys, respectively. The distinct differences between the magnetization behaviour of the high temperature austenite phase and the low temperature martensite phase can be seen in all of the presented cases. For low values of external magnetic field ($\mu_0H < 0.3$ T) the austenite phase is characterized by higher initial permeability than martensite phase, and therefore, saturates notably faster. It is noteworthy that this is consistent with the $M(T)$ curves shown in the preceding Section (**Fig. 3.59–3.60**), where measurements were conducted at a low external magnetic field of 10 mT and the austenite phase was found to have a significantly higher magnetization than the martensite phase. Nevertheless, the observed situation changes for the higher values of external magnetic field ($\mu_0H > 0.5$ T). In this range of fields the austenite phase becomes almost saturated, whereas the magnetization of martensite phase is still substantially rising. For the high values of magnetic field ($\mu_0H > 1.5$ T), where both austenite and martensite phase are almost completely saturated, the considerable difference of about ~25–30% between the magnetization of individual phases is observed for all investigated materials. This unusual magnetic behaviour of fabricated MSMAs stems from the high magnetocrystalline anisotropy of the poor symmetry martensitic structure, characterized by differently oriented twin variants, that are absent in high symmetry cubic austenite (**Section 3.1.5**). This magnetostructural anisotropy diminishes the initial permeability of the alloy, which may only be overcome by exposure to a strong enough external magnetic field.

The difference in magnetic properties of austenite and martensite phase are also evident on the example of coercivity (or coercive field) H_C derived from the recorded hysteresis loops. The estimated values of H_C for the austenite and martensite phases for all water, air, and furnace cooled NiMnGa-based samples are listed in **Table 3.6**. Additionally, these results are shown in relation to elemental doping in **Fig. 3.67**.

Table 3.6. The coercivity $H_C(T)$ of the martensite and austenite phase estimated from $M(H)$ loops recorded at 100 K and 320 K (or 360 K*), respectively, for the produced water, air and furnace cooled NiMnGa-based Heusler alloys.

Alloy composition	**Coercivity H_C (mT)**					
	Water cooled		**Air cooled**		**Furnace cooled**	
	100 K	**320 K**	**100 K**	**320 K**	**100K**	**320 K**
$Ni_{48}Mn_{32}Ga_{20}$	22.7	0.7	36.7	2.5	4.1	0.6
$Ni_{48}Mn_{31}Ga_{20}Co_1$	20.2	1.7	35.1	3.0	6.3	0.7
$Ni_{48}Mn_{30}Ga_{20}Co_2$	17.3	2.3	34.4	3.4	7.8	1.1
$Ni_{48}Mn_{28}Ga_{20}Co_4$	9.8	3.4*	16.6	4.2*	9.3	1.5*
$Ni_{48}Mn_{28}Ga_{20}Co_3Fe_1$	11.3	0.8	21.6	1.8	8.0	0.4
$Ni_{50}Mn_{25}Ga_{21}Co_2Fe_2$	10.2	0.8	19.7	2.2	8.4	0.5
$Ni_{48}Mn_{28}Ga_{20}Co_1Fe_3$	14.9	0.5	21.4	0.7	6.6	0.3
$Ni_{48}Mn_{28}Ga_{20}Fe_4$	16.2	0.4	22.4	0.5	5.6	0.3

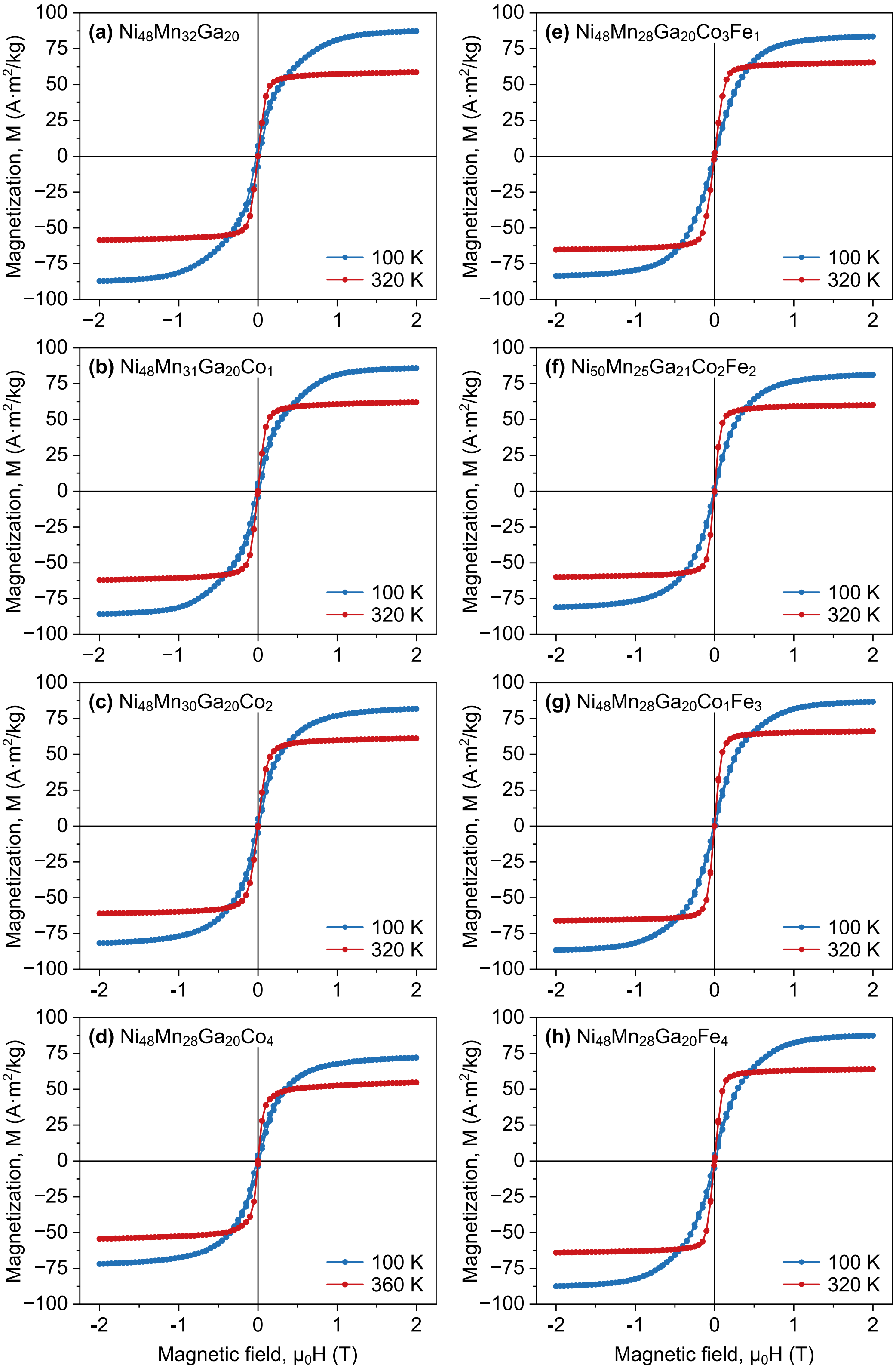

Fig. 3.64. Magnetization hysteresis loops *M*(*H*) obtained for the water cooled **(a)** $Ni_{48}Mn_{32}Ga_{20}$, **(b)** $Ni_{48}Mn_{31}Ga_{20}Co_1$, **(c)** $Ni_{48}Mn_{30}Ga_{20}Co_2$ and **(d)** $Ni_{48}Mn_{28}Ga_{20}Co_4$, **(e)** $Ni_{48}Mn_{28}Ga_{20}Co_3Fe_1$, **(f)** $Ni_{50}Mn_{25}Ga_{21}Co_2Fe_2$, **(g)** $Ni_{48}Mn_{28}Ga_{20}Co_1Fe_3$ and **(h)** $Ni_{48}Mn_{28}Ga_{20}Fe_4$ alloys. The loops recorded at 100 K and 320 K or 360 K corresponds to martensitic corresponds to martensite and austenite phase, respectively.

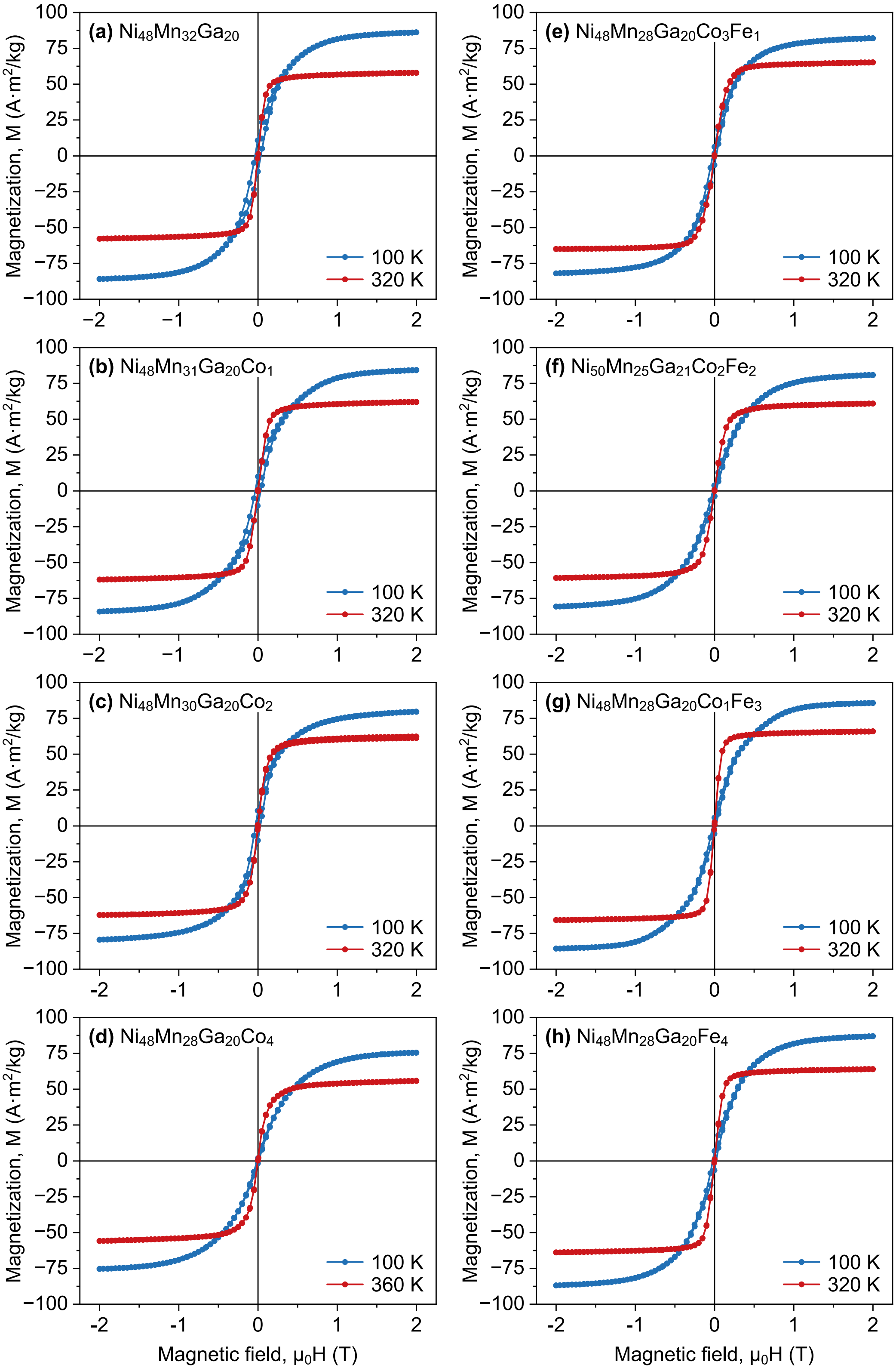

Fig. 3.65. Magnetization hysteresis loops *M*(*H*) obtained for the air cooled **(a)** $Ni_{48}Mn_{32}Ga_{20}$, **(b)** $Ni_{48}Mn_{31}Ga_{20}Co_1$, **(c)** $Ni_{48}Mn_{30}Ga_{20}Co_2$ and **(d)** $Ni_{48}Mn_{28}Ga_{20}Co_4$, **(e)** $Ni_{48}Mn_{28}Ga_{20}Co_3Fe_1$, **(f)** $Ni_{50}Mn_{25}Ga_{21}Co_2Fe_2$, **(g)** $Ni_{48}Mn_{28}Ga_{20}Co_1Fe_3$ and **(h)** $Ni_{48}Mn_{28}Ga_{20}Fe_4$ alloys. The loops recorded at 100 K and 320 K or 360 K corresponds to martensitic corresponds to martensite and austenite phase, respectively.

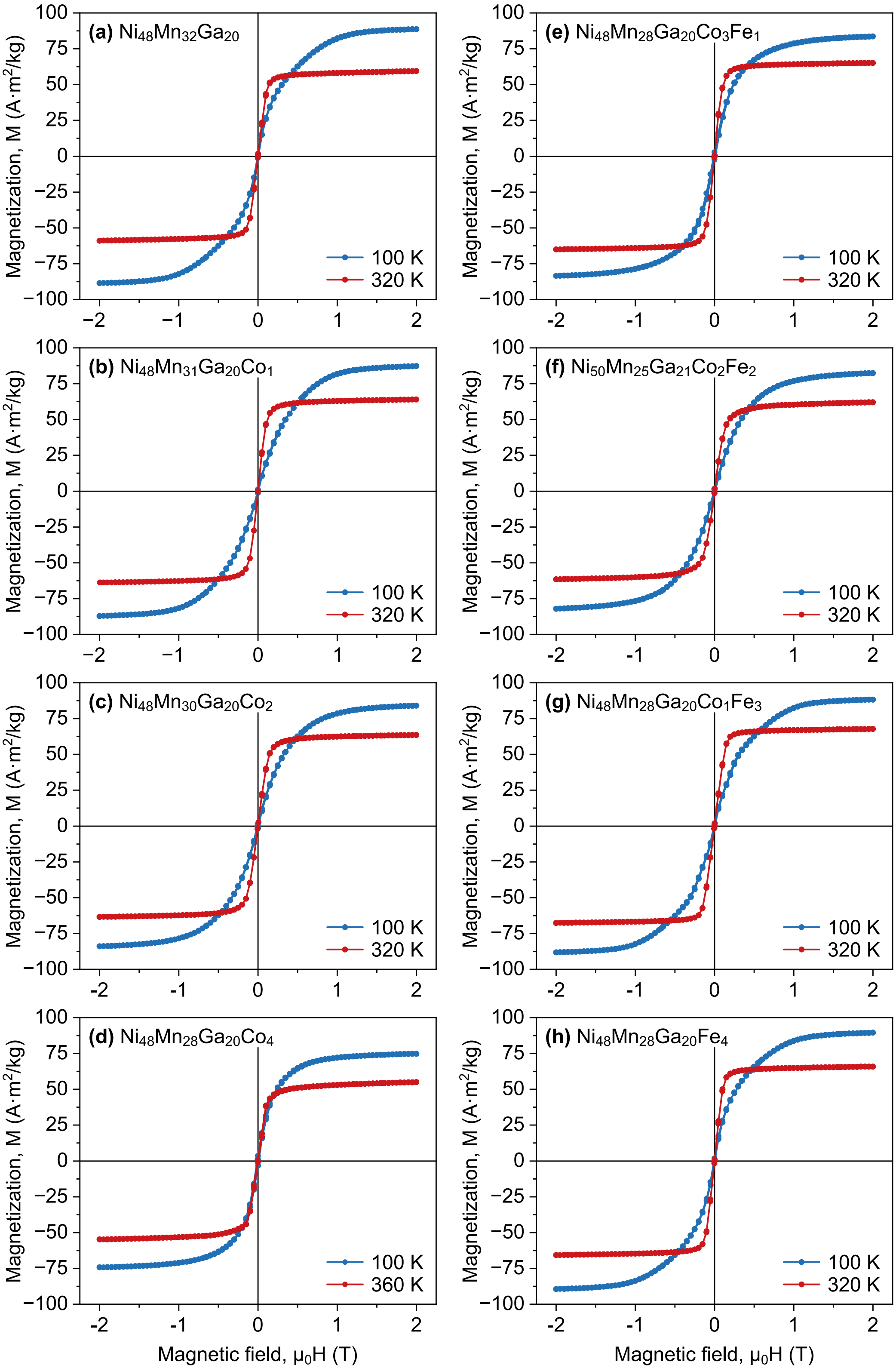

Fig. 3.66. Magnetization hysteresis loops *M*(*H*) obtained for the furnace cooled **(a)** $Ni_{48}Mn_{32}Ga_{20}$, **(b)** $Ni_{48}Mn_{31}Ga_{20}Co_1$, **(c)** $Ni_{48}Mn_{30}Ga_{20}Co_2$ and **(d)** $Ni_{48}Mn_{28}Ga_{20}Co_4$, **(e)** $Ni_{48}Mn_{28}Ga_{20}Co_3Fe_1$, **(f)** $Ni_{50}Mn_{25}Ga_{21}Co_2Fe_2$, **(g)** $Ni_{48}Mn_{28}Ga_{20}Co_1Fe_3$ and **(h)** $Ni_{48}Mn_{28}Ga_{20}Fe_4$ alloys. The loops recorded at 100 K and 320 K or 360 K corresponds to martensitic corresponds to martensite and austenite phase, respectively.

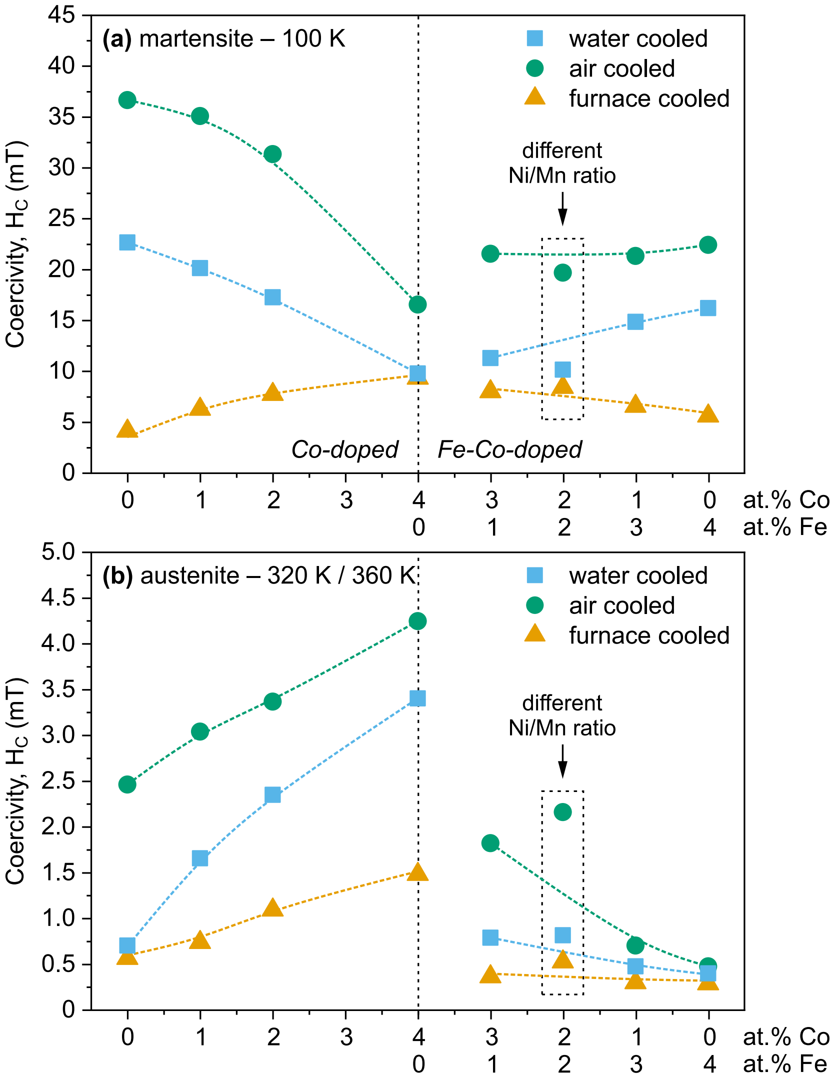

Fig. 3.67. The coercivity H_C of **(a)** the martensite and **(b)** austenite phase estimated from $M(H)$ loops recorded at 100 K and 320 K or 360 K, respectively, for the water, air and furnace cooled $Ni_{48}Mn_{32}Ga_{20}$, $Ni_{48}Mn_{31}Ga_{20}Co_1$, $Ni_{48}Mn_{30}Ga_{20}Co_2$, $Ni_{48}Mn_{28}Ga_{20}Co_4$, $Ni_{48}Mn_{28}Ga_{20}Co_3Fe_1$, $Ni_{50}Mn_{25}Ga_{21}Co_2Fe_2$, $Ni_{48}Mn_{28}Ga_{20}Co_1Fe_3$ and $Ni_{48}Mn_{28}Ga_{20}Fe_4$ alloys expressed as a function of Co and Fe doping. The symbols corresponding to the $Ni_{50}Mn_{25}Ga_{21}Co_2Fe_2$ alloy characterized by different Ni/Mn ratio are indicated by additional frames.

Because of the previously mentioned magnetocrystalline anisotropy of the martensitic structure, it is evident from **Fig. 3.67** and **Table 3.6** that the martensitic phase has a couple times higher coercivity than the austenite phase. However, a direct comparison of H_C obtained for the same alloys in two different states reveals that these variations are significantly influenced by chemical composition. The addition of Co significantly reduces the coercivity of the martensite phase for both water- and air-cooled specimens while simultaneously increasing the coercivity of the austenite phase. In contrast, the subsequent Co substitution by Fe have contradictory effects on examined coercivity and these effects less pronounced than in case of Co addition. As a result, the highest relative difference in H_C is observed for the $Ni_{48}Mn_{28}Ga_{20}Fe_4$ alloy, for which the coercivity of martensite is even more than 40 times higher than coercivity of corresponding austenite phase (**Table 3.6**). In contrary, the $Ni_{48}Mn_{28}Ga_{20}Co_4$, alloy exhibits the lowest relative difference in H_C, with martensite coercivity only being 4 times higher than that of the austenite phase (**Table 3.6**). Overall, the relative differences in H_C are noticeably higher for the Fe-Co-doped alloys than for Co-doped alloys, even despite the fact that Fe-containing alloys are characterized by lower H_C than quaternary Co-doped samples.

It should be noted at this point that the coercivity of the austenite phase (**Fig. 3.67(b)**), which is currently being discussed, and the previously estimated temperature of the martensitic transformation (**Fig. 3.55(a)**), both relate to the Co and Fe doping. Taking this into consideration, it is possible to attribute some of the observed changes in H_C to the magnetostructural stability of the austenite or martensite phases following the austenitic or martensitic transition, respectively. Since the measurements were made far from the structural transformation, the coercivity of austenite is relatively low for alloys with low T_M, such as the $Ni_{48}Mn_{32}Ga_{20}$, $Ni_{48}Mn_{28}Ga_{20}Co_1Fe_3$ or $Ni_{48}Mn_{28}Ga_{20}Fe_4$ sample. When the T_M approaches room temperature (e.g. for the $Ni_{48}Mn_{28}Ga_{20}Co_4$, $Ni_{48}Mn_{28}Ga_{20}Co_3Fe_1$ or $Ni_{50}Mn_{25}Ga_{21}Co_2Fe_2$ sample) the coercivity of austenite phase also increases, as in this case, the hysteresis loops were collected close to the structural transformation. When it comes to martensite phase, the variations in H_C are even more complex since the additional influence of magnetocrystalline anisotropy must also be taken into account. It was reported in literature [253,288,533–535], among others, also by the author of this thesis [319], that magnetocrystalline anisotropy in Ni-Mn-Ga MSMAs is temperature dependent and increases with decreasing temperature.

The significant differences in coercivity are also observed for the samples exposed to different cooling conditions. According to **Fig. 3.67**, the slowest cooled alloys exhibit the lowest values of H_C as well as the smallest changes in H_C, which are almost neglectable in comparison to quickly cooled materials. This discrepancies in H_C between variously cooled alloys seems to originates form the nature of magnetic coercivity. This variation in H_C between different alloys appears to have its origins in the nature of magnetic coercivity. The relatively rapid cooling of water- or air-cooled materials introduces lattice defects and internal stresses that pin the magnetic domain walls, raising the coercivity of the ferromagnetic material. Due to the fact that Ni-Mn-Ga MSMAs are typically prepared using water or air cooling, the H_C values obtained for the martensite structure, which range from 10 to 35 mT, are very similar to those reported in the literature for other NiMnGa-based materials [252,536,537]. Following this concept, the slow furnace cooling do not introduce any internal stresses and allows for slow diffusion processes. Therefore, the furnace cooled structure is relatively free form internal stresses and lattice defects that affects the coercivity of heat-treated alloys. Because of this, samples that have been cooled in a furnace may have significantly lower coercivity than their water- or air-cooled counterparts. Remarkably, the H_C for the furnace cooled samples is even up to 10 times lower than the H_C estimated for the corresponding water or air cooled specimens for the alloys shown in **Fig. 3.67** and summarized in **Table 3.6**. This phenomenon is rarely found in literature, although the comparable remarkable difference in coercivity for differently cooled NiMnGa-based alloys were also recently reported by Straka *et. al.* [253].

In the matter of electronic parameters examined in the following thesis, **Fig. 3.68** and **3.69** presents the H_C obtained for all fabricated NiMnGa-based alloys plotted as a function of e/a and N_e/a parameters. It is clear from both figures that the coercivity and electronic properties of the produced materials have a close relationship.

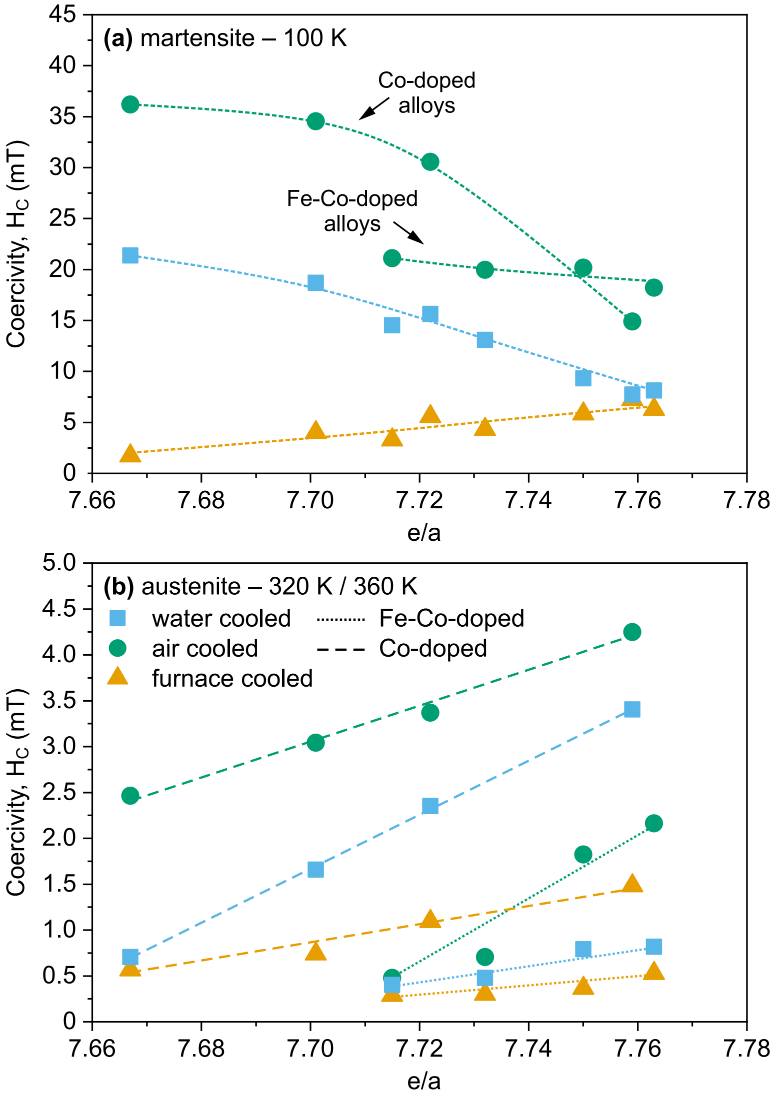

Fig. 3.68. The coercivity H_C of **(a)** the martensite and **(b)** austenite phase estimated from $M(H)$ loops recorded at 100 K and 320 K or 360 K, respectively, for the water, air and furnace cooled $Ni_{48}Mn_{32}Ga_{20}$, $Ni_{48}Mn_{31}Ga_{20}Co_1$, $Ni_{48}Mn_{30}Ga_{20}Co_2$, $Ni_{48}Mn_{28}Ga_{20}Co_4$, $Ni_{48}Mn_{28}Ga_{20}Co_3Fe_1$, $Ni_{50}Mn_{25}Ga_{21}Co_2Fe_2$, $Ni_{48}Mn_{28}Ga_{20}Co_1Fe_3$ and $Ni_{48}Mn_{28}Ga_{20}Fe_4$ alloys expressed as a function valence electron concentration e/a.

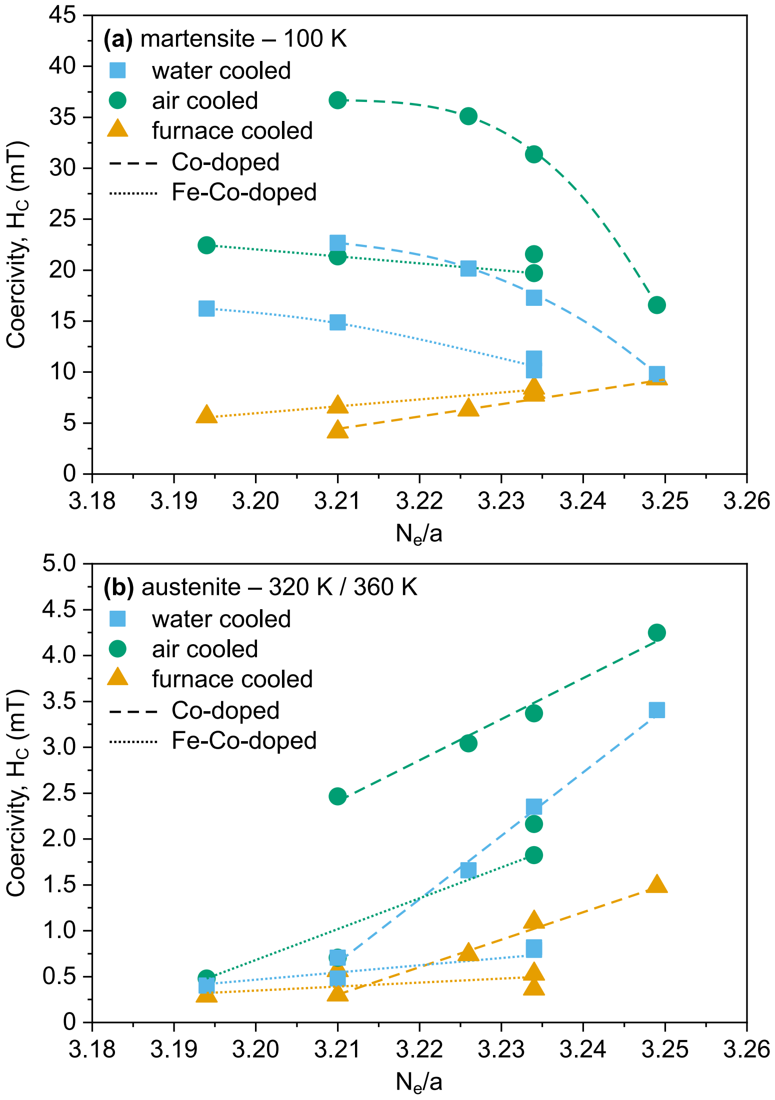

Fig. 3.69. The coercivity H_C of **(a)** the martensite and **(b)** austenite phase estimated from $M(H)$ loops recorded at 100 K and 320 K or 360 K, respectively, for the water, air and furnace cooled $Ni_{48}Mn_{32}Ga_{20}$, $Ni_{48}Mn_{31}Ga_{20}Co_1$, $Ni_{48}Mn_{30}Ga_{20}Co_2$, $Ni_{48}Mn_{28}Ga_{20}Co_4$, $Ni_{48}Mn_{28}Ga_{20}Co_3Fe_1$, $Ni_{50}Mn_{25}Ga_{21}Co_2Fe_2$, $Ni_{48}Mn_{28}Ga_{20}Co_1Fe_3$ and $Ni_{48}Mn_{28}Ga_{20}Fe_4$ alloys expressed as a function non-bonding electron concentration N_e/a.

Fig. 3.68(a) shows that for water and furnace cooled materials the H_C of the martensite phase is well represented by the same trend for both Co-doped and Fe-Co-doped materials, with the exception of samples that were cooled in air. This suggest that for the low-temperature martensite phase the magnetocrystalline anisotropy of multivariant martensitic structure seems to play more important role than the influence of additional doping elements. However this situation drastically changes after the reversible martensitic transformation, as very distinctive division of H_C for Co-doped and Fe-Co-doped samples is observed. Moreover, the revealed relationship between HC and e/a is almost linear which also suggest the substantial effect of doping elements on the coercivity of cubic austenite. It appears that for simple, cubic austenite, a rise in valence electron concentration causes a rise in the pinning of magnetic domain walls, which eventually leads to a rise in coercivity.

In terms of non-bonding electron concentration, **Fig. 3.69** clearly distinguishes between Co-doped and Fe-Co-doped alloys for both the martensite and austenite phases. This again proves that N_e/a parameter is very sensitive to Co and/or Fe doping, which was also discovered during microstructural investigations (**Section 3.1.4**). However, the general H_C vs N_e/a relationships within one group of alloys are still monotonic and, in the vast majority of cases, also very close to linear, despite the fact that elemental doping is not universal.

Last but not least, it should be noted that the discussed influence of elemental doping and cooling conditions on coercivity of Ni-Mn-Ga MSMAs are somewhat unique. Throughout many years, the topic of coercivity were rarely brought up by other authors, as it was not connected with the multifunctional properties of Heusler alloys. However in recent years the multifunctional nature of Ni-Mn-Ga materials has been expanded to many new distinct phenomena, such as mechanically induced demagnetization [252] or mechanically induced remanent magnetization rotation [252,538], that may exploit the tuneable magnetic coercivity. In light of these newly reported effects, the discussed effects of Fe and Co doping, as well as cooling conditions, point to a potential significant alteration of the coercivity in the Ni-Mn-Ga-Co-Fe system.

3.3.2 Law of approach to magnetic saturation

In order to reveal additional information about the magnetocrystalline anisotropy of the fabricated NiMnGa-based alloys, the high field magnetization part of isothermal $M(H)$ loops from **Fig. 3.59–3.61** were used to perform approach-to-saturation fitting in accordance with the law of approach to magnetic saturation. The overall fitting procedure, including the relevant theoretical background was in detail described in **Section 2.3.6.1**.

At first the selected high field magnetization curves were fitted according the LoA model adapted independently for the low-temperature martensite phase and high-temperature austenite phase in order to cover the last ~5% of saturation magnetization. Due to that fact, the $M(H)$ data collected for the martensite phase the was fitted in the magnetic field ranging from 1000 kA/m to 1600 kA/m following the **Eq. 2.10** (**Section 2.3.6.1**):

$$M(H) = M_s\left(1 - \frac{a}{H} - \frac{b}{H^2}\right) \tag{2.10}$$

In case of magnetically softer austenite phase, the fitting procedure was carried out from 500 kA/m to 1600 A/m using the **Eq. 2.9** (**Section 2.3.6.1**):

$$M(H) = M_s\left(1 - \frac{b}{H^2}\right) + \chi H \tag{2.9}$$

Fig. 3.70 presents the selected high field magnetization parts of the *M*(*H*) loops, along with the fitted curves, for all water, air and furnace cooled NiMnGa-based alloys. The fitting parameters, including magnetization saturation and magnetocrystalline anisotropy are also listed in **Table 3.7**. Before the final evaluation, it should be emphasized that the regression models have excellent coefficients of determination R^2 higher than 0.999 for all examined magnetization curves. What is even more important, the additional residual plots do not show any sign of bias model, supporting the employment of the LoA proposed in **Eq 2.9** and **2.10**. This high accuracy of fitting is also clearly evident in **Fig. 3.70**, where all presented fitted curves overlay with the corresponding magnetization data points.

Table 3.7. The magnetization saturation M_S and effective anisotropy constant Keff for the produced NiMnGa-based MSMAs in austenitic (100 K) and martensitic (320 K / 360 K) state estimated from the fitting of high field magnetization data to LoA model.

Alloy composition	**Martensite**		**Austenite**	
	M_S (100 K) ($A{\cdot}m^2/kg$)	**K_{eff} (100 K) (10^5 J/m^3)**	**M_S (320 K) ($A{\cdot}m^2/kg$)**	**K_{eff} (320 K) (10^5 J/m^3)**
Water cooled				
$Ni_{48}Mn_{32}Ga_{20}$	89.1	7.27	56.6	1.23
$Ni_{48}Mn_{31}Ga_{20}Co_1$	87.5	6.04	59.9	1.37
$Ni_{48}Mn_{30}Ga_{20}Co_2$	84.8	4.88	59.5	1.49
$Ni_{48}Mn_{28}Ga_{20}Co_4$	77.1	2.45	52.2	1.67
$Ni_{48}Mn_{28}Ga_{20}Co_3Fe_1$	85.6	5.63	63.8	1.31
$Ni_{50}Mn_{25}Ga_{21}Co_2Fe_2$	83.7	5.30	58.8	1.34
$Ni_{48}Mn_{28}Ga_{20}Co_1Fe_3$	88.1	6.56	64.7	1.20
$Ni_{48}Mn_{28}Ga_{20}Fe_4$	89.1	6.89	62.4	1.12
Air cooled				
$Ni_{48}Mn_{32}Ga_{20}$	87.7	6.81	55.9	1.28
$Ni_{48}Mn_{31}Ga_{20}Co_1$	87.0	5.88	59.8	1.46
$Ni_{48}Mn_{30}Ga_{20}Co_2$	83.5	4.17	59.6	1.61
$Ni_{48}Mn_{28}Ga_{20}Co_4$	75.9	2.28	51.8	1.79
$Ni_{48}Mn_{28}Ga_{20}Co_3Fe_1$	84.7	5.45	63.4	1.38
$Ni_{50}Mn_{25}Ga_{21}Co_2Fe_2$	84.2	5.25	59.0	1.52
$Ni_{48}Mn_{28}Ga_{20}Co_1Fe_3$	87.1	6.23	64.4	1.26
$Ni_{48}Mn_{28}Ga_{20}Fe_4$	88.9	6.76	62.2	1.17
Furnace cooled				
$Ni_{48}Mn_{32}Ga_{20}$	90.5	7.22	57.1	1.05
$Ni_{48}Mn_{31}Ga_{20}Co_1$	89.0	6.56	62.4	1.27
$Ni_{48}Mn_{30}Ga_{20}Co_2$	86.8	5.95	62.1	1.44
$Ni_{48}Mn_{28}Ga_{20}Co_4$	79.5	4.75	53.1	1.63
$Ni_{48}Mn_{28}Ga_{20}Co_3Fe_1$	86.3	6.15	63.8	1.23
$Ni_{50}Mn_{25}Ga_{21}Co_2Fe_2$	85.3	6.01	59.2	1.29
$Ni_{48}Mn_{28}Ga_{20}Co_1Fe_3$	89.8	6.68	66.5	1.14
$Ni_{48}Mn_{28}Ga_{20}Fe_4$	91.1	6.91	64.3	1.07

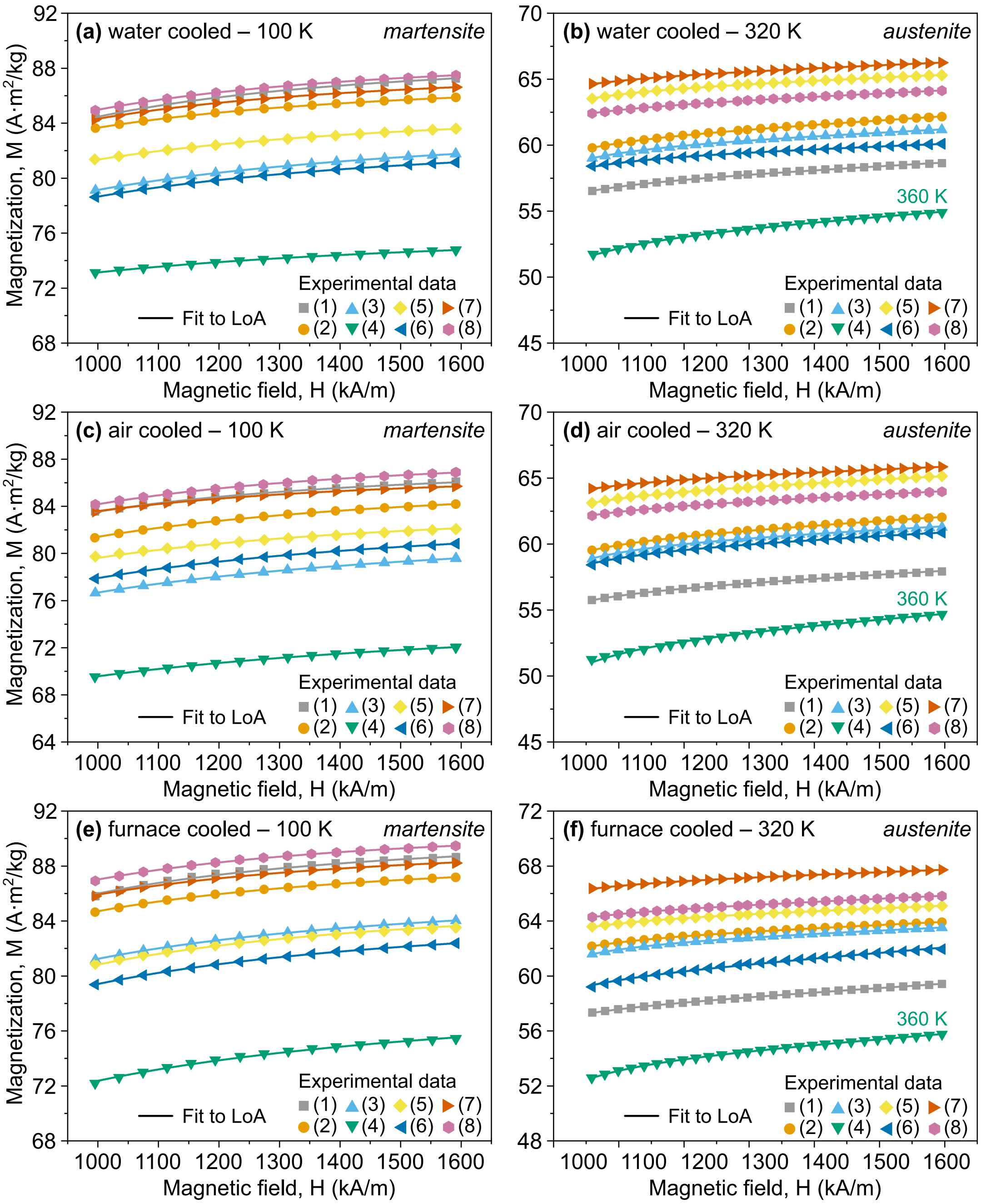

Fig. 3.70. The high field magnetization parts of *M*(*H*) loops fitted to the low of approach to magnetic saturation (LoA) for the **(a–b)** water, **(c–d)** air and **(e–f)** furnace cooled NiMnGa-based alloys in **(a, c, e)** austenitic and **(c, d, f)** martensitic state. The solid lines represents the fitted curves, while the symbols correspond to the raw data for the (1) $Ni_{48}Mn_{32}Ga_{20}$, (2) $Ni_{48}Mn_{31}Ga_{20}Co_1$, (3) $Ni_{48}Mn_{30}Ga_{20}Co_2$, (4) $Ni_{48}Mn_{28}Ga_{20}Co_4$, (5) $Ni_{48}Mn_{28}Ga_{20}Co_3Fe_1$, (6) $Ni_{50}Mn_{25}Ga_{21}Co_2Fe_2$, (7) $Ni_{48}Mn_{28}Ga_{20}Co_1Fe_3$ and (8) $Ni_{48}Mn_{28}Ga_{20}Fe_4$ alloy.

It is worth noting that the magnetic saturation observed in **Fig. 3.70** varies between the investigated samples due to the introduction of additional alloying elements into the Ni-Mn-Ga system. The maximum values of saturation magnetization M_S derived from the considered fittings are presented in **Fig. 3.71** as a function of Co and/or Fe doping.

Firstly, it is evident that, regardless of the cooling conditions, the M_S decreases significantly with the addition of Co the low-temperature martensite phase (**Fig. 3.70(a)**) and then slightly increases with the gradual substitution of Co by Fe. For instance, the M_S decreases from 81.1 A·m^2/kg for the reference water cooled $Ni_{48}Mn_{32}Ga_{20}$ sample to 77.1 A·m^2/kg for the water cooled $Ni_{48}Mn_{28}Ga_{20}Co_4$ sample. It is interesting to note that the M_S for the $Ni_{48}Mn_{28}Ga_{20}Co_3Fe_1$ alloy abruptly increases to 85.6 A·m^2/kg when only 1 at.% of Co is replaced by Fe. Nevertheless, the further increase of M_S with the increasing of Fe content is less spectacular, thus the final $Ni_{48}Mn_{28}Ga_{20}Fe_4$ alloy is identified by the same M_S = 81.1 A·m^2/kg as the reference undoped sample. The analogous relationship between the M_S and chemical composition of NiMnGa-based alloys is also observed for both air and furnace cooled materials. The main distinction is that samples cooled by air or a furnace have slightly lower and slightly higher M_S than those cooled by water. However, assuming the obtained values of M_S, these changes are negligibly minor, differing by only ±1.5–2.0%.

In regards to the magnetically softer austenite phase, the general trends are notably different from those seen for the austenite phase. It is seen that for both Co-doped and Fe-Co-doped alloys the magnetization saturation firstly increase with the increasing content of doping element, but then starting to decrease for the samples with 4 at.% of Co or Fe. However the observed variations is Ms are not so pronounced since the relative difference in Co-doped and Fe-Co doped materials are close to 5% and 2%, respectively. In addition, the Fe-containing samples are distinguished by higher Ms than Co-doped specimens, and this phenomenon is even more pronounced than in the case of the previously discussed martensite phase (**Fig. 71(a)**). Once more, it appears that the M_S is unaffected by the various cooling conditions. The materials that are cooled with water and air have nearly identical Ms values for the corresponding alloys, whereas a few samples that are cooled in a furnace have slightly higher M_S values than their water and air cooled equivalents.

The discovered variation in saturation magnetization for the doped Ni-Mn-Ga alloys are strongly connected with the proposed approach to dopants addition. It was stated in theoretical part of the thesis in **Section 1.3.6** that ferromagnetism of Ni-Mn-Ga Heusler alloys predominantly originates from the localized moment of Mn atoms. In the case of the fabricated NiMnGa-based materials, Mn was initially substituted by Co and then Co was gradually replaced Fe. Taking this into consideration, the substitution of Co for Mn have unusual dual effect on magnetic properties of examined materials, strengthening the magnetic interactions in the austenite phase while weakening them in the martensite phase. Such extraordinary influence of Co on the ferromagnetic interactions in Ni-Mn-Ga alloys were also reported by other authors for compositions with different Ni/Mn/Ga ratio .

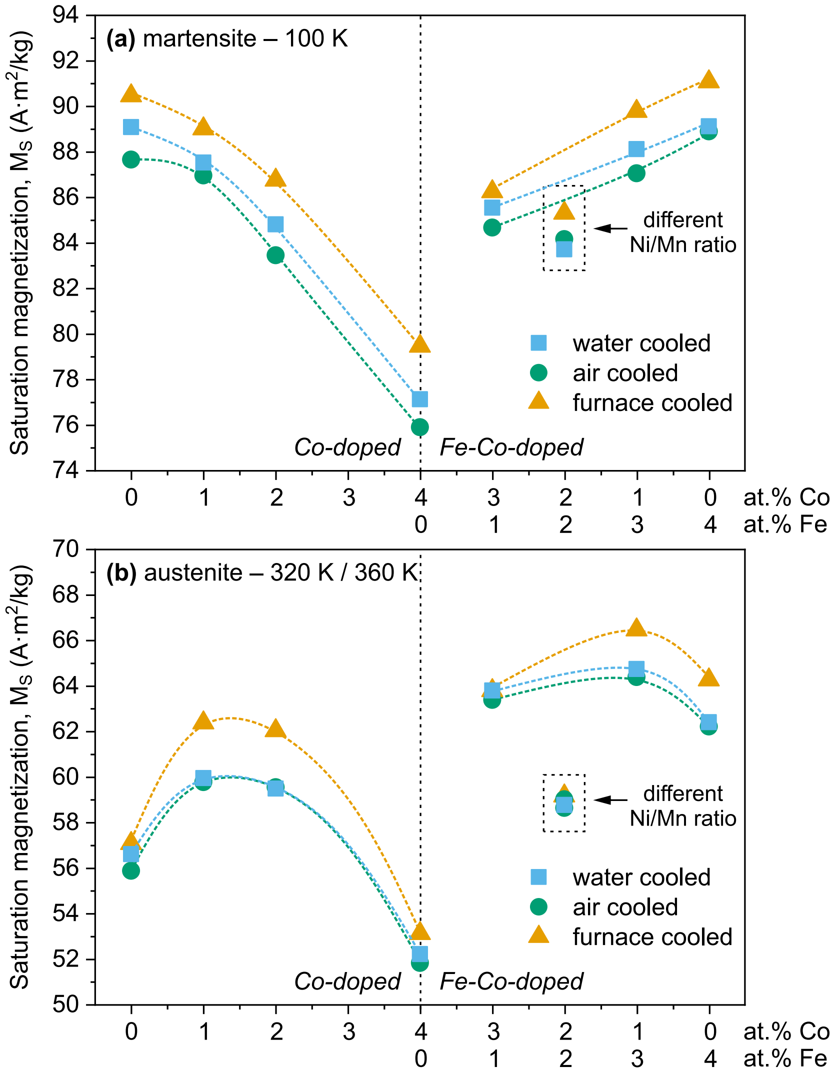

Fig. 3.71. The saturation magnetization M_S of **(a)** martensite and **(b)** austenite phase estimated from the fitting of high field magnetization data to LoA model for the water, air and furnace cooled $Ni_{48}Mn_{32}Ga_{20}$, $Ni_{48}Mn_{31}Ga_{20}Co_1$, $Ni_{48}Mn_{30}Ga_{20}Co_2$, $Ni_{48}Mn_{28}Ga_{20}Co_4$, $Ni_{48}Mn_{28}Ga_{20}Co_3Fe_1$, $Ni_{50}Mn_{25}Ga_{21}Co_2Fe_2$, $Ni_{48}Mn_{28}Ga_{20}Co_1Fe_3$ and $Ni_{48}Mn_{28}Ga_{20}Fe_4$ alloys expressed as a function of Co and Fe doping. The symbols corresponding to the $Ni_{50}Mn_{25}Ga_{21}Co_2Fe_2$ alloy characterized by different Ni/Mn ratio are indicated by additional frames.

Following this assumption, the subsequent gradual replacement of Co by Fe increases the magnetic interaction in both austenite and martensite phases, therefore Fe have a stronger contribution on the ferromagnetism of the Ni-Mn-Ga alloys than Co. This is consistent with earlier research on the Curie temperature of austenite phase, which also increase with the increasing level of Fe doping. However, it should be also remembered that the examined effects are observed for the Mn-rich Heusler alloys. As a result, a possible atomic disorder is also expected to play a significant role in the magnetic properties of the fabricated materials, as it strongly influence the magnetic coupling of Mn atoms [116,234,278,342].

The observed variations in saturation magnetization were also investigated in reference to valence electron concentration, which is presented in **Fig. 3.72**. It is seen that even when using the electronic parameter *e*/*a*, which was previously discovered to be rather universal for both Fe and Co doping, the austenite and martensite phases clearly distinguish between Co-doped and Fe-Co-doped alloys. In M_S behaviour for the martensite phase steadily decreases with increasing *e*/*a* ratio, whereas the M_S behaviour for the austenite phase is more complex but analogous to that seen in **Fig. 3.71(b)**. The integration of alloys with varying Ni/Mn ratios is, once more, the main benefit of employing the *e*/*a* parameter rather of a straightforward doping relation. The M_S for the $Ni_{50}Mn_{25}Ga_{21}Co_2Fe_2$ sample exhibit the same relationship in the M_S vs *e*/*a* plot as other Fe-Co-doped materials.

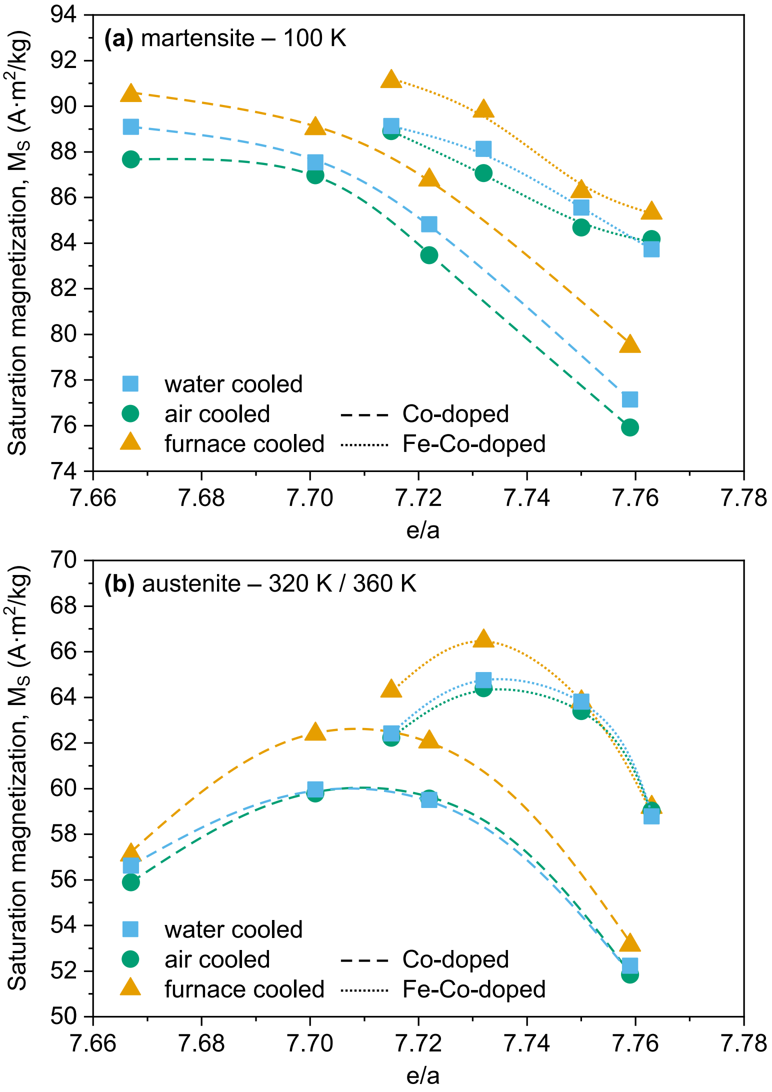

Fig. 3.72. The saturation magnetization M_S of **(a)** martensite and **(b)** austenite phase estimated from the fitting of high field magnetization data to LoA model for the water, air and furnace cooled $Ni_{48}Mn_{32}Ga_{20}$, $Ni_{48}Mn_{31}Ga_{20}Co_1$, $Ni_{48}Mn_{30}Ga_{20}Co_2$, $Ni_{48}Mn_{28}Ga_{20}Co_4$, $Ni_{48}Mn_{28}Ga_{20}Co_3Fe_1$, $Ni_{50}Mn_{25}Ga_{21}Co_2Fe_2$, $Ni_{48}Mn_{28}Ga_{20}Co_1Fe_3$ and $Ni_{48}Mn_{28}Ga_{20}Fe_4$ alloys expressed as a function valence electron concentration *e*/*a*.

Surprising results were obtained in the case of the second electronic parameter describing the non-bonding electron concentration shown in **Fig. 3.73**. It is important to keep in mind that the N_e/a parameter was discovered to be extremely sensitive to a different type of doping element. As a result, the previously discussed microstructural properties, temperatures of phase transformations, as well as some magnetic properties, exhibit different behaviours for Co-doped and Fe-Co-doped samples. In contrary, **Fig 3.73(a)** demonstrates that saturation magnetization exhibits a consistent pattern throughout all produced samples, regardless of the amount and type of alloying elements. Additionally, the measured behaviour of M_S vs N_e/a for the austenite phase shown in **Fig. 3.72(b)** is remarkably similar to that shown for the e/a parameter (**Fig. 3.71(b)**) and for doping relation (**Fig. 3.71(b)**).

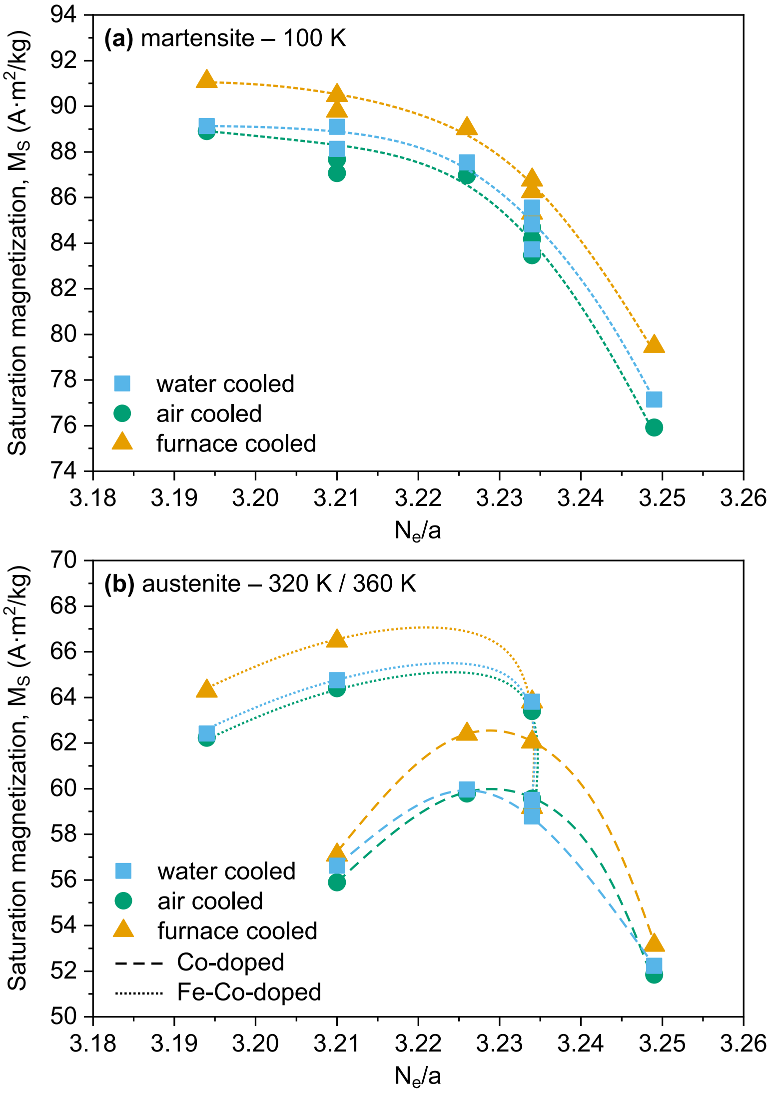

Fig. 3.73. The saturation magnetization M_S of **(a)** martensite and **(b)** austenite phase estimated from the fitting of high field magnetization data to LoA model for the water, air and furnace cooled $Ni_{48}Mn_{32}Ga_{20}$, $Ni_{48}Mn_{31}Ga_{20}Co_1$, $Ni_{48}Mn_{30}Ga_{20}Co_2$, $Ni_{48}Mn_{28}Ga_{20}Co_4$, $Ni_{48}Mn_{28}Ga_{20}Co_3Fe_1$, $Ni_{50}Mn_{25}Ga_{21}Co_2Fe_2$, $Ni_{48}Mn_{28}Ga_{20}Co_1Fe_3$ and $Ni_{48}Mn_{28}Ga_{20}Fe_4$ alloys expressed as a function non-bonding electron concentration N_e/a.

In consideration of magnetocrystalline anisotropy the two most important parameters established from the presented fittings are formerly discussed magnetization saturation M_S and coefficient b, which is directly related to the investigated magnetocrystalline anisotropy. These two fitting parameters were used to estimate the effective magnetic anisotropy constant K_{eff} according to the **Eq. 2.12** (**Section 2.3.6.1**):

$$K_{\text{eff}} = \mu_0 M_{\text{S}} \sqrt{\frac{b}{c}} \tag{3.9}$$

where c is the constant connected to the crystal structure of the material. For the fabricated untextured polycrystalline alloys with cubic anisotropy, that was revealed during microstructural analysis (**Section 3.1**), constant $c = 8/105$ [507]. On the ground of this, the calculated values of K_{eff} along with corresponding M_S are listed in **Table 3.7**.

Fig. 3.74 presents the estimated values of K_{eff} for the produced NiMnGa-based alloys in martensite and austenite state expressed as a function of Co and/or Fe doping. As could be expected from previous investigations the poor symmetry martensite, characterized by different twin variants and multiscale twin boundaries, is generally characterized by notably higher magnetocrystalline anisotropy than high symmetry cubic austenite. It should be recalled that this large discrepancy between the K_{eff} of two existing phases were previously indicated by the separation between ZFC heating and FC cooling $M(T)$ curves (**Fig. 3.64–3.66**). But this time, it is obvious that the observed differences in K_{eff} clearly depend on the actual chemical composition. On the example of the water cooled materials, the addition of Co to Ni-Mn-Ga system decreases the K_{eff} of low temperature martensite from $7.27 \cdot 10^5$ J/m^3 for the reference $Ni_{48}Mn_{32}Ga_{20}$ sample to $2.45 \cdot 10^5$ J/m^3 for the $Ni_{48}Mn_{28}Ga_{20}Co_4$ specimen. Given that magnetocrystalline anisotropy is primarily caused by the intricate structure of the martensite phase, the approximately three times difference in K_{eff} after introduction of single at.% of Co to Ni-Mn-Ga composition is still really remarkable. Nevertheless, the estimated values of K_{eff} for NM martensite are comparable to those reported in literature for both ternary [539–543] and quaternary [288,535,544] NiMn-based alloys, which tends to support the obtained results.

In a view of austenite phase, the addition of Co to Ni-Mn-Ga composition increases the K_{eff} of the high temperature phase from $1.23 \cdot 10^5$ J/m^3 for the undoped material to $1.67 \cdot 10^5$ J/m^3 for the $Ni_{48}Mn_{28}Ga_{20}Co_4$ alloy. What is important, the estimated values of K_{eff} are also in agreement with the ones reported by other researchers for various Ni-Mn-Ga Heusler compounds in austenitic state [230,288,542]. Considering the aforementioned changes in K_{eff} for Co-doped samples, it is evident that the $Ni_{48}Mn_{28}Ga_{20}Co_4$ alloy exhibits substantially less variation in magnetocrystalline anisotropy between austenite and martensite phase than other produced samples.

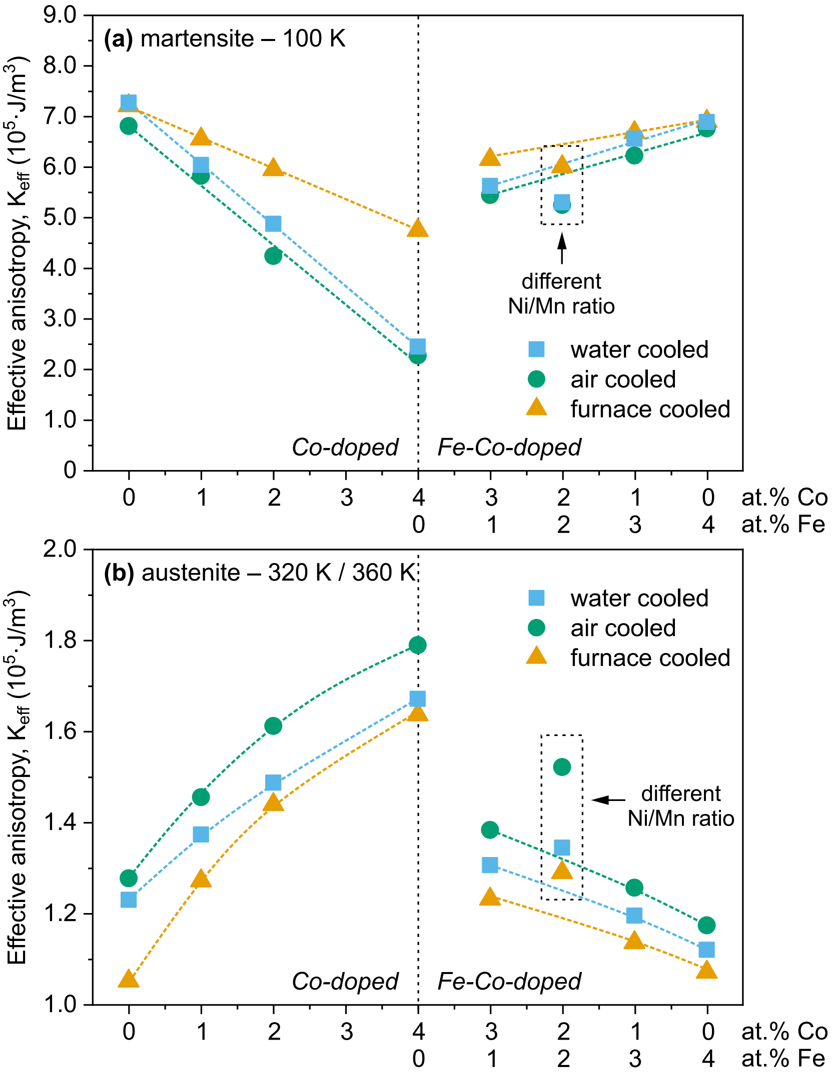

Fig. 3.74. The effective magnetocrystalline anisotropy K_{eff} of **(a)** martensite and **(b)** austenite phase estimated from the fitting of high field magnetization data to LoA model for the water, air and furnace cooled $Ni_{48}Mn_{32}Ga_{20}$, $Ni_{48}Mn_{31}Ga_{20}Co_1$, $Ni_{48}Mn_{30}Ga_{20}Co_2$, $Ni_{48}Mn_{28}Ga_{20}Co_4$, $Ni_{48}Mn_{28}Ga_{20}Co_3Fe_1$, $Ni_{50}Mn_{25}Ga_{21}Co_2Fe_2$, $Ni_{48}Mn_{28}Ga_{20}Co_1Fe_3$ and $Ni_{48}Mn_{28}Ga_{20}Fe_4$ alloys expressed as a function of Co and Fe doping. The symbols corresponding to the $Ni_{50}Mn_{25}Ga_{21}Co_2Fe_2$ alloy characterized by different Ni/Mn ratio are indicated by additional frames.

On the other hand, the substitution of Co by Fe in NiMnGa-based composition have contradictory effect on the examined anisotropies for both considered phases. The K_{eff} of the martensite phase gradually increases for the sequence of water cooled Fe-Co-doped samples, rising from $5.36 \cdot 10^5$ J/m^3 for the first $Ni_{48}Mn_{28}Ga_{20}Co_3Fe_1$ sample to $6.89 \cdot 10^5$ J/m^3 for the final $Ni_{48}Mn_{28}Ga_{20}Fe_4$ sample. Consequently, when the austenite phase is present in the aforementioned samples, the K_{eff} decreases from $1.31 \cdot 10^5$ J/m^3 to $1.12 \cdot 10^5$ J/m^3 for the $Ni_{48}Mn_{28}Ga_{20}Co_3Fe_1$ and $Ni_{48}Mn_{28}Ga_{20}Fe_4$ sample, respectively.

What is noteworthy is that the observed changes in K_{eff} for the martensite phase follows almost perfect linear trends with respect to the changes in Co and/or Fe doping. It is especially valuable due to the possible opportunities for the relatively easy alteration of magnetocrystalline anisotropy by simple Fe and/or Co doping. The obtained trends in K_{eff} for the austenite phase are also almost linear for the Fe-Co-doped samples and nearly linear for the Co-doped specimens. These results are also generally favourable in light of potential alterations of K_{eff}, although it should be remembered that the multifunctional effects exploiting the magnetocrystalline anisotropy are typically connected with the martensitic structures, which was extensively described in **Section 1.4**.

When various cooling conditions are taken into account, it is seen that there is no significant differences between the water and air cooled samples. Depending on the specific alloy, the observed relative variances between these two differently cooled series are about 4–7%. This findings are consistent with the previously discussed saturation magnetization changes, which were also very comparable between corresponding materials cooled in water and air. As could be expected, the most significant variations in magnetocrystalline anisotropy were revealed for the furnaced cooled alloys. It is seen in **Fig. 3.74** and in **Table 3.7** that the slowest cooled samples are characterized be the smallest values of K_{eff} for all alloys in high temperature austenite state. This is most likely a result of the extremely slow cooling rate, which reduced the amount of internal stresses and crystal lattice defects that have an impact on magnetostructural anisotropy. Similar effects of slow cooling were also previously seen in relatively low values of magnetic coercivity (**Fig. 3.67**). The furnace cooling produces the least differences in K_{eff} for alloys with varied chemical compositions when the martensite phase is present in the sample. This is clearly seen on the example of Co-doped alloys for which the K_{eff} of martensite drops from $7.22 \cdot 10^5$ J/m^3 for the reference $Ni_{48}Mn_{32}Ga_{20}$ sample to $4.75 \cdot 10^5$ J/m^3 for the last Co-doped $Ni_{48}Mn_{28}Ga_{20}Co_4$ alloy. Presented characteristics of Keff suggest that very slow cooling rate may be able to limit the influence of alloying components on the overall magnetocrystalline anisotropy in martensitic phase, which may be required in some specific applications.

Taking into account the investigated electronic parameters, **Fig. 3.75** and **3.76** show the estimated values of K_{eff} represented as a function of e/a and N_e/a, respectively. It is clear from both figures that the magnetocrystalline anisotropy constant is strictly dependent on the considered electronic parameters. In case of valence electron concentration, the K_{eff} for the martensite and austenite phase decreases and increases almost linearly with the increasing e/a ratio, respectively. However, the e/a parameter loses its universal character, as Co-doped and Fe-Co-doped materials are characterized by the distinctive trends. What is significant, despite the previously observed differences in the values of K_{eff} for the corresponding variously cooled materials, the general trends observed for water and air cooled samples are comparable to those found for the furnace cooled specimens. Moreover, once again the $Ni_{50}Mn_{25}Ga_{21}Co_2Fe_2$ sample exhibit the same characteristics as other Fe-Co-doped alloys despite having a different Ni/Mn ratio. All of this demonstrates that while e/a may be sensitive to a particular sort of alloying elements, the overall behaviour of Keff is unaffected by the Ni/Mn/Ga ratio.

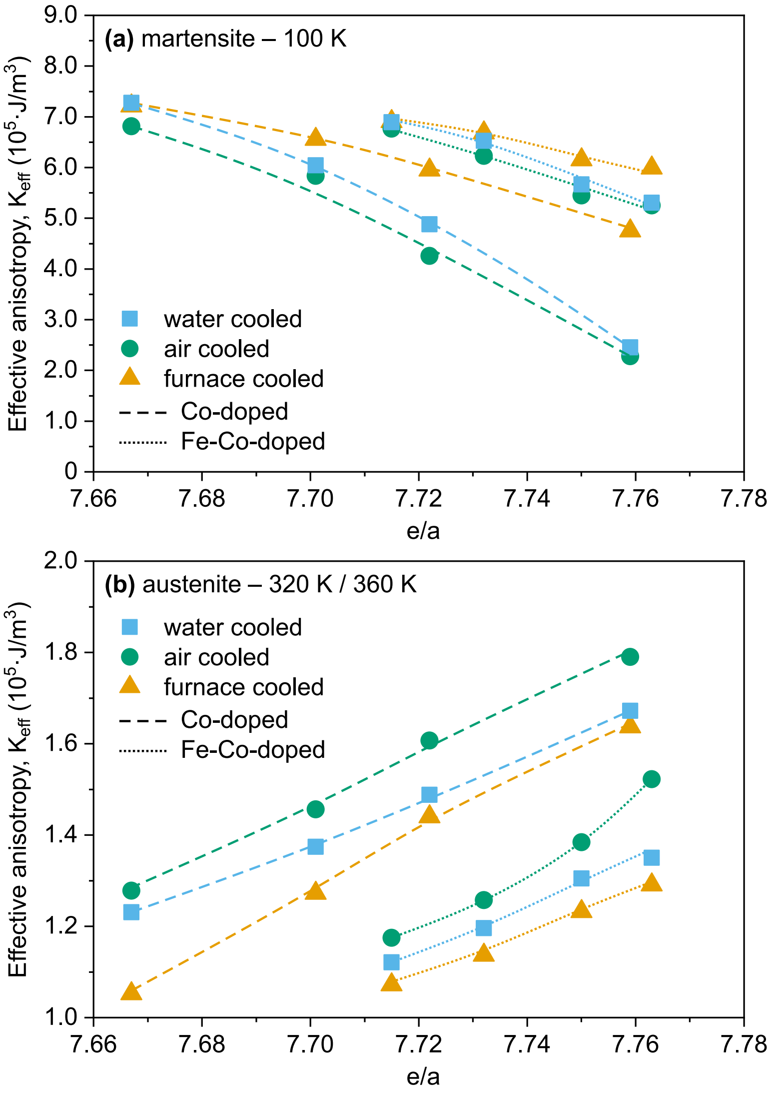

Fig. 3.75. The effective magnetocrystalline anisotropy K_{eff} of **(a)** martensite and **(b)** austenite phase estimated from the fitting of high field magnetization data to LoA model for the water, air and furnace cooled $Ni_{48}Mn_{32}Ga_{20}$, $Ni_{48}Mn_{31}Ga_{20}Co_1$, $Ni_{48}Mn_{30}Ga_{20}Co_2$, $Ni_{48}Mn_{28}Ga_{20}Co_4$, $Ni_{48}Mn_{28}Ga_{20}Co_3Fe_1$, $Ni_{50}Mn_{25}Ga_{21}Co_2Fe_2$, $Ni_{48}Mn_{28}Ga_{20}Co_1Fe_3$ and $Ni_{48}Mn_{28}Ga_{20}Fe_4$ alloys expressed as a function valence electron concentration e/a.

When it comes to the N_e/a parameter, presented in **Fig. 3.76**, the observed relationship between K_{eff} and non-bonding electron concentration are analogous to the ones observed for the valence electron concentration. In contrast to other magnetostructural features examined in this thesis, it is remarkable that for the N_e/a the observed characteristics are relatively universal for both Co-doped and Fe-Co-doped materials in the austenite and martensite phase. Certainly, the depicted common relationship found for all fabricated samples is burdened by the higher dispersion of K_{eff}, particularly for the alloys with the same $N_e/a = 3.234$, *i.e.* $Ni_{48}Mn_{30}Ga_{20}Co_2$, $Ni_{48}Mn_{28}Ga_{20}Co_3Fe_1$ and $Ni_{50}Mn_{25}Ga_{21}Co_2Fe_2$ sample. Nevertheless, this findings imply that N_e/a parameter might in some circumstances be more effective then the widely used e/a ratio.

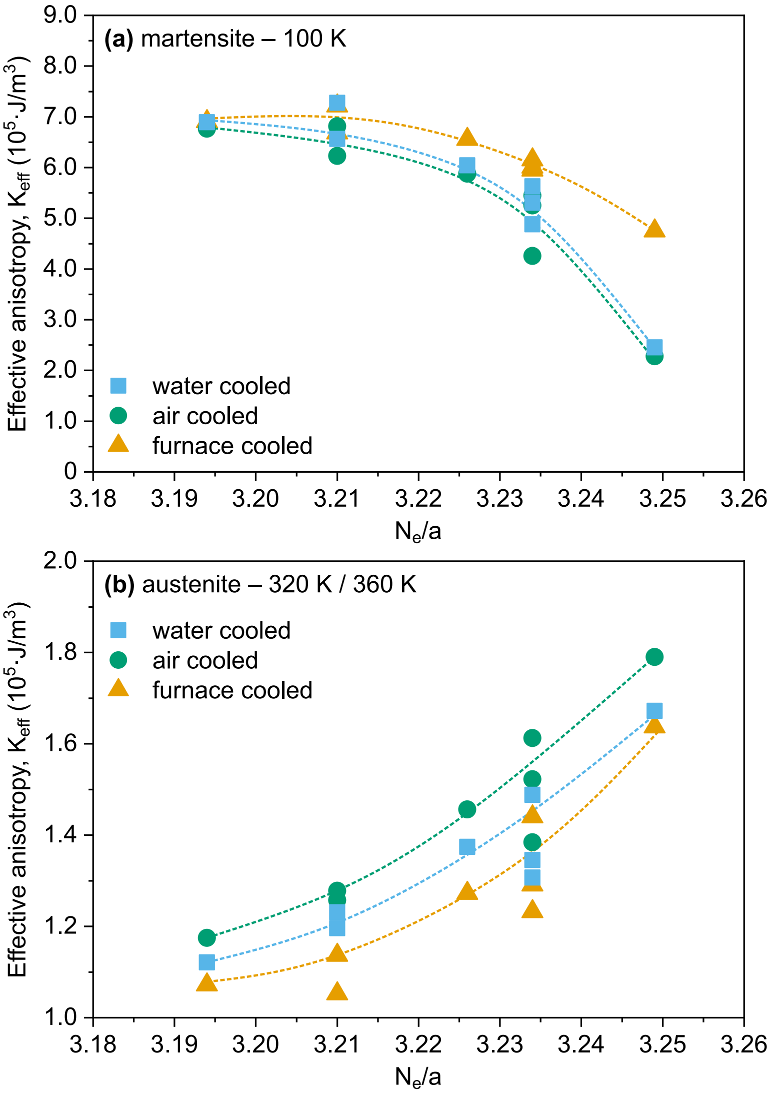

Fig. 3.76. The effective magnetocrystalline anisotropy K_{eff} of **(a)** martensite and **(b)** austenite phase estimated from the fitting of high field magnetization data to LoA model for the water, air and furnace cooled $Ni_{48}Mn_{32}Ga_{20}$, $Ni_{48}Mn_{31}Ga_{20}Co_1$, $Ni_{48}Mn_{30}Ga_{20}Co_2$, $Ni_{48}Mn_{28}Ga_{20}Co_4$, $Ni_{48}Mn_{28}Ga_{20}Co_3Fe_1$, $Ni_{50}Mn_{25}Ga_{21}Co_2Fe_2$, $Ni_{48}Mn_{28}Ga_{20}Co_1Fe_3$ and $Ni_{48}Mn_{28}Ga_{20}Fe_4$ alloys expressed as a function non-bonding electron concentration N_e/a.

Last but not least, it should be noted that the discussed magnetocrystalline anisotropy is found to be strongly related with the previously studied magnetic coercivity, which is graphically depicted in **Fig. 3.77**. It is seen that the low temperature, low symmetry martensite phase is characterized by considerably higher K_{eff} and H_C than high temperature, high symmetry martensite phase. A note of caution here is that the presented figure is plotted in log-log scale, emphasizing the magnetostructural differences between both phases. The obtained results are in line with the well known phenomenon stating that anisotropy energy is one the key elements affecting the coercive field in ferromagnets. Moreover, the same effect was also previously reported by the author of this thesis for other NiMnGa-based MSMAs [319].

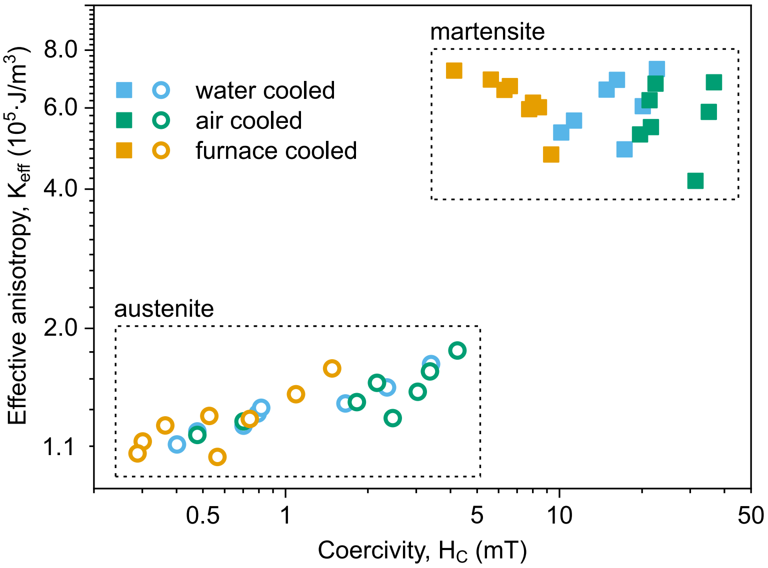

Fig. 3.77. The effective magnetocrystalline anisotropy K_{eff} versus the coercivity H_C for the produced water, air and furnace cooled NiMnGa-based magnetic shape memory alloys.

3.4 Micromechanical properties

3.4.1 Nanoindentation mapping

According to the previously described microstructural characterization of the examined NiMnGa-based alloys, all produced samples are characterized by single phase microstructures that may be seen at room temperature as austenite or martensite phase. Moreover, the utilized production process did introduce any substantial structural texture that may have affected on the physical properties of the final material. However, despite this high uniformity of presented microstructures (especially in austenite state), the preliminary studies revealed that micromechanical properties of the examined samples varies across the studied cross-sections. As a result, the investigation of micromechanical properties were conduced with the help of nanoindentation mapping. which allow to distinguished the differences between the mechanical parameters from different parts of the investigated areas.

As described in the experimental part of this thesis in **Section 2.3.7**, the nanoindentation mapping were performed in 210 μm × 210 μm grid covered with 225 indentations. The size of the grid were adjusted according to the average grain size of austenite phase (**Section 3.1.1**). The single indentation test was performed with a maximum load of 50 mN, preventing the mechanical properties of the adjacent measurements from being influenced by one another. The mechanical parameters of each individual indentation, including hardness H_{IT}, elastic modulus E_{IT} and elastic energy ratio η_{IT}, were then estimated according to the Oliver and Pharr protocol outlined in **Section 2.3.7.1**. Finally, the obtained nanoindentation maps were subjected to the statistical analysis in order to distinguish the mechanical properties of the individual neighbouring grains. The proposed approach to statistical analysis based on the Gaussian mixture model clustering is comprehensively explained in **Section 2.3.7.2**. What is significant, the nanoindentation mapping was carried out at multiple locations on each sample, including the inner and outer parts of the examined cross-section, to cover at least 5 different grains. This approach allows for reliable estimation of the level of micromechanical anisotropy of the produced MSMAs.

Prior to the statistical analysis, the calculated mechanical parameters, including hardness H_{IT}, elastic modulus E_{IT} and elastic energy ratio η_{IT} were plotted with respect to the X and Y coordinates of individual indentations. As a result, **Fig. 3.77–3.82** shows the example of nanoindentation maps generated for the $Ni_{48}Mn_{32}Ga_{20}$, $Ni_{48}Mn_{31}Ga_{20}Co_1$, $Ni_{48}Mn_{30}Ga_{20}Co_2$, $Ni_{48}Mn_{28}Ga_{20}Co_4$, $Ni_{48}Mn_{28}Ga_{20}Co_3Fe_1$, $Ni_{50}Mn_{25}Ga_{21}Co_2Fe_2$, $Ni_{48}Mn_{28}Ga_{20}Co_1Fe_3$ and $Ni_{48}Mn_{28}Ga_{20}Fe_4$ alloys exposed to water, air and furnace cooling, respectively. For each individual alloy, the depicted hardness, elastic modulus and elastic energy ratio corresponds the same indentations, hence the same areas of the samples. As can be seen in all of the presented examples, the significant differences in H_{IT}, E_{IT} and η_{IT} are observed across the analysed regions of the investigated materials, reflecting the microstructural features of produced alloys. These differences in mechanical properties varies between the samples, which is represented by lower or higher contrast of individual austenite grains or martensite variants. Remarkably, the observed micromechanical anisotropy was revealed in the single phase NiMnGa-based MSMAs since the previous microstructural characterization confirms the uniform, relatively untextured microstructure of the produced polycrystalline materials.

The substantial micromechanical anisotropy in the austenitic phase may be plainly observed when two neighbouring grains are directly compared. For instance, one of the highest contrast in mechanical properties can be seen for the water cooled $Ni_{48}Mn_{30}Ga_{20}Co_2$, alloy (**Fig. 3.78(b)**), for which the hardness, elastic modulus and elastic energy ratio changes from 3600 to 4400 MPa, from 86 to 96 MPa and from 23 to 27.5%, respectively. It should be emphasized that regardless of the cooling conditions, the opposite contrast between the H_{IT} and E_{IT} maps is seen for almost all other austenitic samples. This means that the austenite grains with the higher H_{IT} are in the same time characterized by the lower E_{IT}. This behaviour is quite unusual in metallic materials, as typically the higher hardness is followed by higher elastic modulus. However, this general well-known rule is commonly applicable to macro-scale properties, where mechanical parameters of the materials are influenced by the overall microstructure of the bulk sample, which contains many crystal lattice defects, such as simple grain boundaries. In the following work, the individual nanoindentations refers to single grains, thus the obtained mechanical properties are more dependant from the preferred orientation of the particular austenite grain rather than from other microstructural features. This significant anisotropy of mechanical properties of Ni-Mn-based MSMAs were recently reported in [545–547]. For example, in [545] authors demonstrated that the H_{IT} and E_{IT}

of austenite vary by 27.6% and 37.5%, respectively, depending on the crystallographic direction of individual grains.

In the case of martensitic structures illustrated in selected nanoindentation maps in **Fig. 3.77–3.82**, the observed difference in H_{IT}, E_{IT} and η_{IT} contrast corresponds to the individual martensitic lamella, previously defined in **Section 3.1.5**. It is evident that the length scale of the martensite twins has a significant impact on the produced nanoindentation maps. For instance, the furnace cooled $Ni_{48}Mn_{28}Ga_{20}Co_4$ sample in **Fig. 3.82(d)** serves as an example of large macro-scale twins, whereas the water cooled $Ni_{48}Mn_{28}Ga_{20}Co_3Fe_1$ and $Ni_{50}Mn_{25}Ga_{21}Co_2Fe_2$ alloys in **Fig. 3.78(a)–(b)** serve as an example of meso-scale twins. As seen in aforementioned figures, in contrast to the former austenite phase, the martensite lamellae characterized by higher H_{IT} are also characterized by the high E_{IT}. This relationship between hardness and elastic modulus was observed for all samples in martensitic state, regardless of the martensite twin morphology and cooling conditions of fabricated materials.

What is significant, the nanoindentation maps included in **Fig. 3.77–3.82** presents only one selected exemplary measurement collected for each produced NiMnGa-based alloy, which helps to qualitatively illustrate the micromechanical anisotropy of the austenite and martensite phases. However, it should be remembered that for the further quantitative analysis, several different nanoindentation grids for each investigated specimen were additionally measured and included into the statistical analysis.

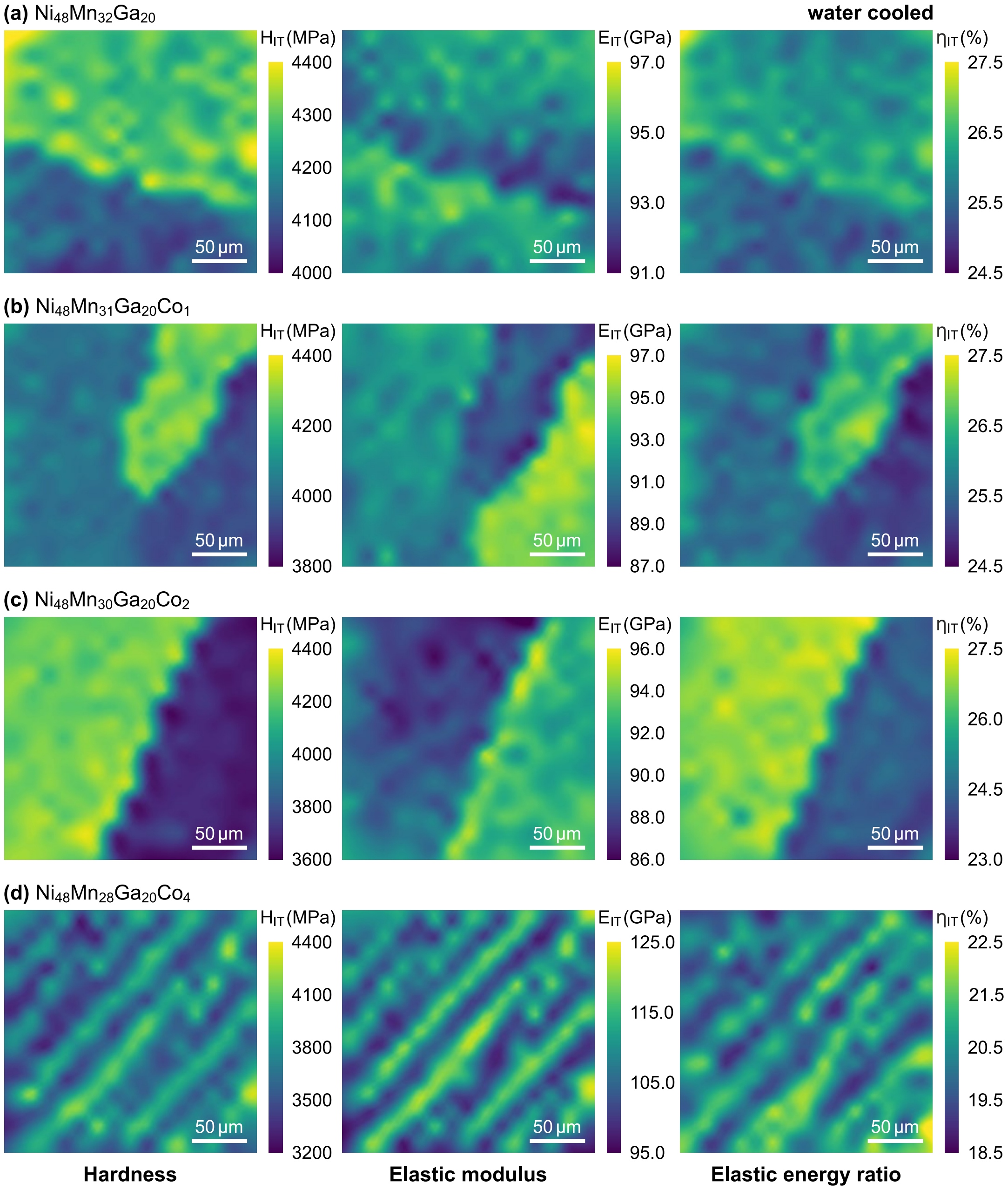

Fig. 3.78. Nanoindentation maps showing hardness (H_{IT}) elastic modulus (E_{IT}) and elastic energy ratio (η_{IT}) for the water cooled **(a)** $Ni_{48}Mn_{32}Ga_{20}$, **(b)** $Ni_{48}Mn_{31}Ga_{20}Co_1$, **(c)** $Ni_{48}Mn_{30}Ga_{20}Co_2$, **(d)** $Ni_{48}Mn_{28}Ga_{20}Co_4$ polycrystalline Heusler alloys. The size of individual map is 210 µm × 210 µm.

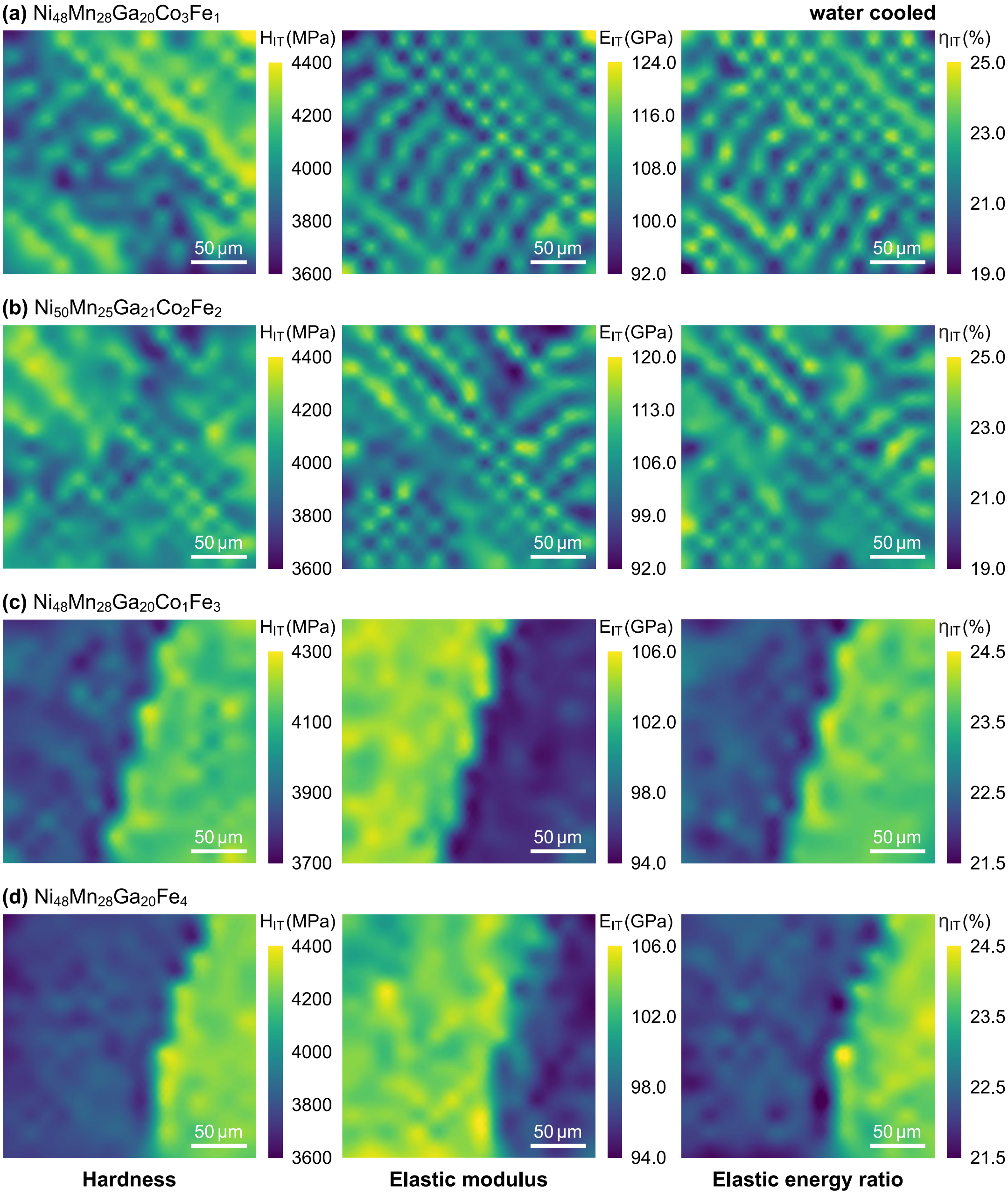

Fig. 3.79. Nanoindentation maps showing hardness (H_{IT}) elastic modulus (E_{IT}) and elastic energy ratio (η_{IT}) for the water cooled **(a)** $Ni_{48}Mn_{28}Ga_{20}Co_3Fe_1$, **(b)** $Ni_{50}Mn_{25}Ga_{21}Co_2Fe_2$, **(c)** $Ni_{48}Mn_{28}Ga_{20}Co_1Fe_3$ and **(d)** $Ni_{48}Mn_{28}Ga_{20}Fe_4$ alloys. polycrystalline Heusler alloys. The size of individual map is 210 µm × 210 µm.

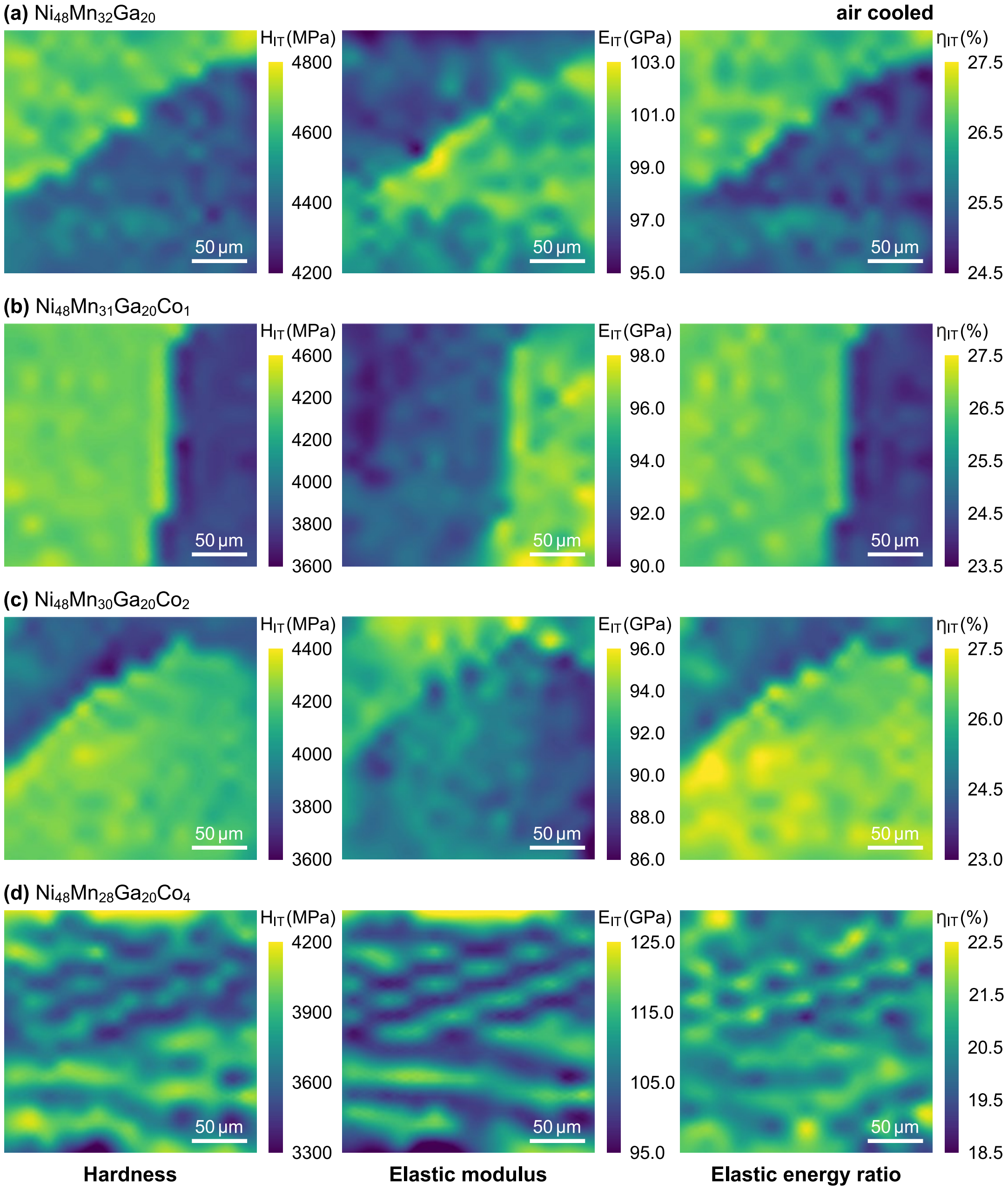

Fig. 3.80. Nanoindentation maps showing hardness (H_{IT}) elastic modulus (E_{IT}) and elastic energy ratio (η_{IT}) for the air cooled **(a)** $Ni_{48}Mn_{32}Ga_{20}$, **(b)** $Ni_{48}Mn_{31}Ga_{20}Co_1$, **(c)** $Ni_{48}Mn_{30}Ga_{20}Co_2$, **(d)** $Ni_{48}Mn_{28}Ga_{20}Co_4$ polycrystalline Heusler alloys. The size of individual map is 210 µm × 210 µm.

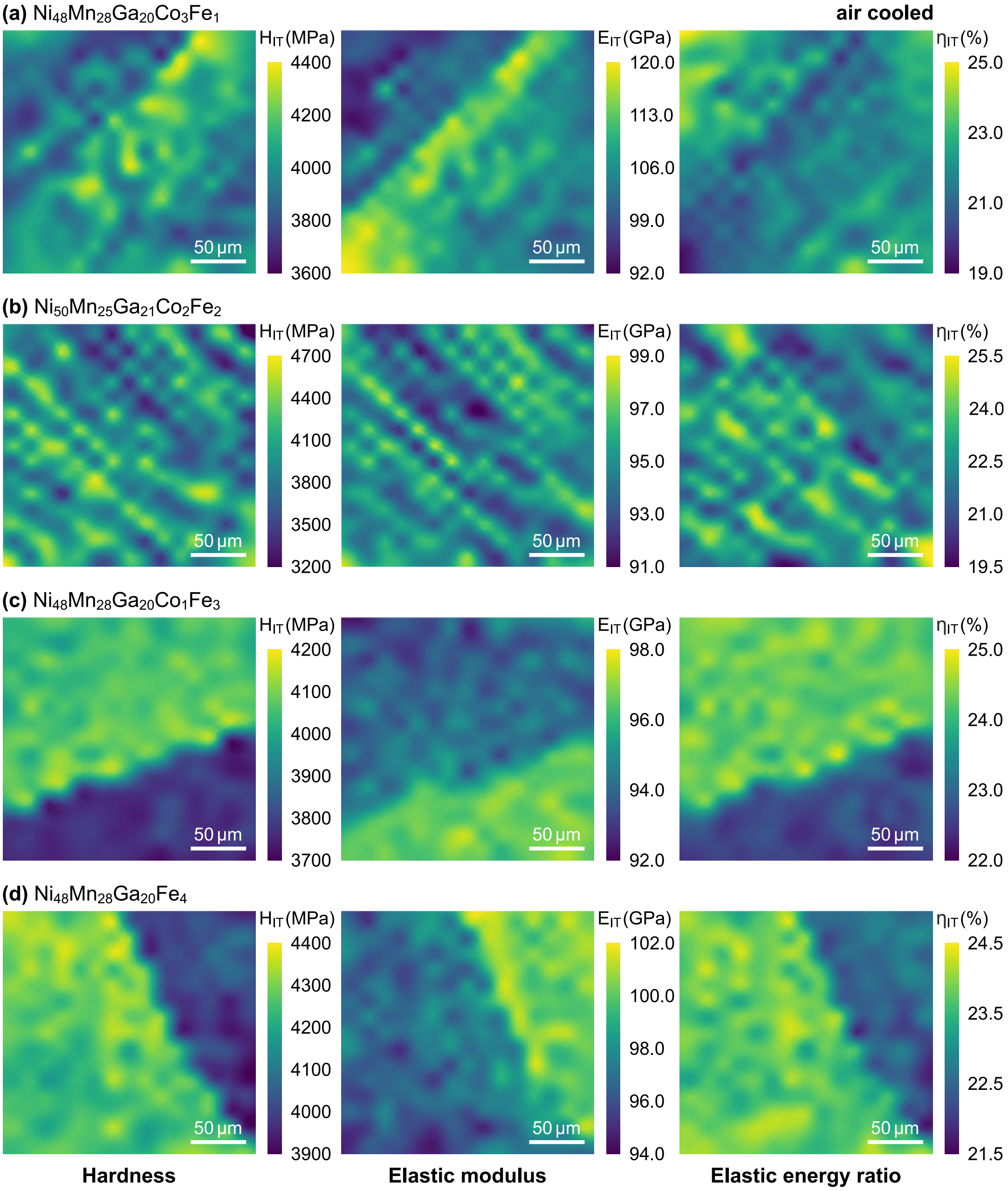

Fig. 3.81. Nanoindentation maps showing hardness (H_{IT}) elastic modulus (E_{IT}) and elastic energy ratio (η_{IT}) for the air cooled **(a)** $Ni_{48}Mn_{28}Ga_{20}Co_3Fe_1$, **(b)** $Ni_{50}Mn_{25}Ga_{21}Co_2Fe_2$, **(c)** $Ni_{48}Mn_{28}Ga_{20}Co_1Fe_3$ and **(d)** $Ni_{48}Mn_{28}Ga_{20}Fe_4$ alloys. polycrystalline Heusler alloys. The size of individual map is 210 µm × 210 µm.

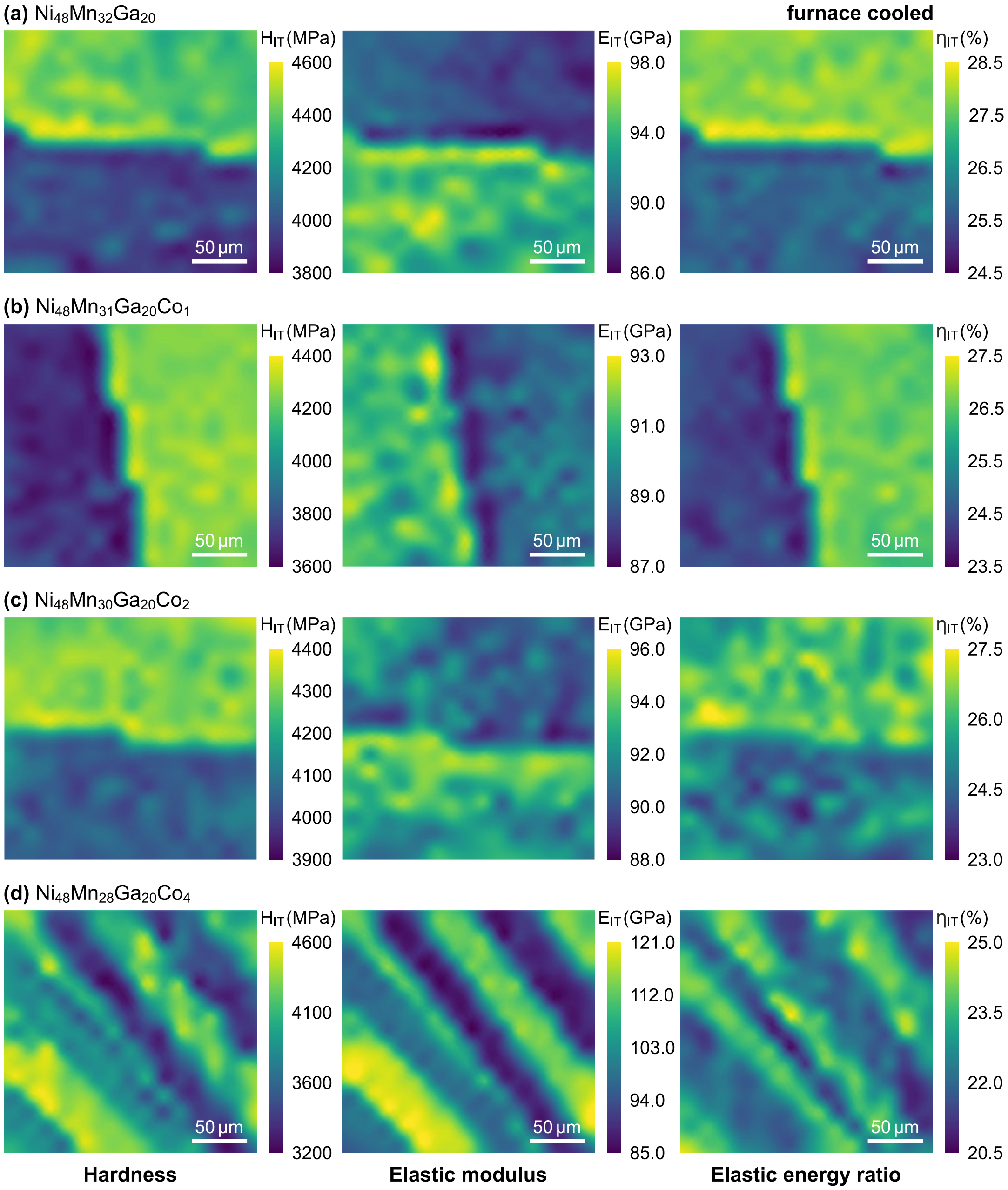

Fig. 3.82. Nanoindentation maps showing hardness (H_{IT}) elastic modulus (E_{IT}) and elastic energy ratio (η_{IT}) for the furnace cooled **(a)** $Ni_{48}Mn_{32}Ga_{20}$, **(b)** $Ni_{48}Mn_{31}Ga_{20}Co_1$, **(c)** $Ni_{48}Mn_{30}Ga_{20}Co_2$, **(d)** $Ni_{48}Mn_{28}Ga_{20}Co_4$ polycrystalline Heusler alloys. The size of individual map is 210 µm × 210 µm.

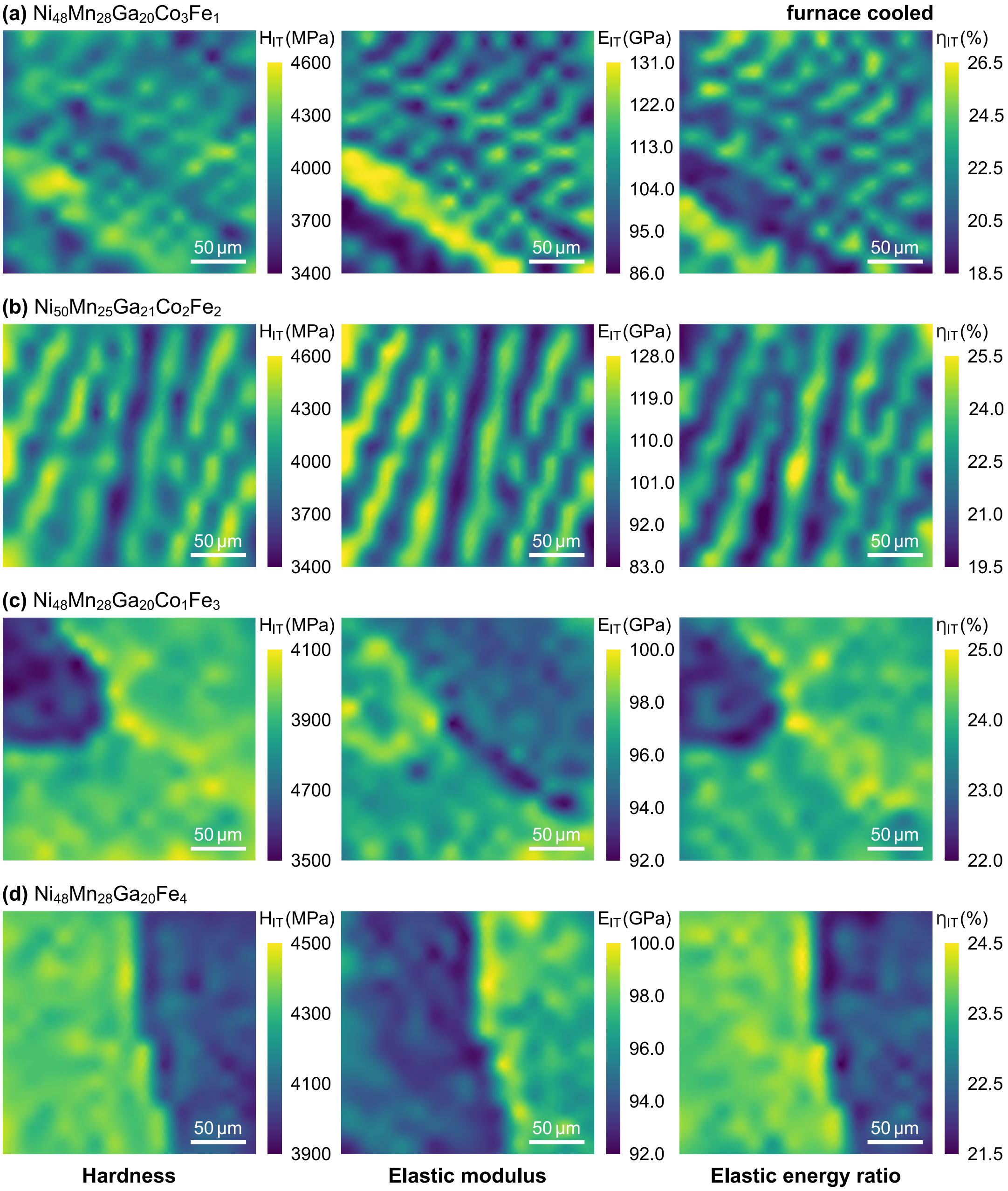

Fig. 3.83. Nanoindentation maps showing hardness (H_{IT}) elastic modulus (E_{IT}) and elastic energy ratio (η_{IT}) for the furnace cooled **(a)** $Ni_{48}Mn_{28}Ga_{20}Co_3Fe_1$, **(b)** $Ni_{50}Mn_{25}Ga_{21}Co_2Fe_2$, **(c)** $Ni_{48}Mn_{28}Ga_{20}Co_1Fe_3$ and **(d)** $Ni_{48}Mn_{28}Ga_{20}Fe_4$ alloys. polycrystalline Heusler alloys. The size of individual map is 210 µm × 210 µm.

To demonstrate the idea of utilizing the 2D GMM in micromechanical properties investigation, **Fig. 3.84–3.87** presents the selected examples of different nanoindentation datasets from **Fig. 3.77–3.82** subjected to the formerly described statistical analysis. According to the flow chart established in **Fig. 2.12** and explained in the Experimental part of the thesis (**Section 2.3.7.1**), all presented figures are organized in the same manner to show the subsequent steps of the analysis. The central part of each figure presents the relationship between hardness and elastic modulus estimated for individual indentations of the examined grid. Additionally, the corresponding neighbouring histograms shows the individual distribution of both H_{IT} and E_{IT}. It is seen in **Fig 3.84**, that in some cases the mechanical properties of neighbouring grains are so dissimilar that the distinction between multimodal one-dimensional histograms is clearly observed. However, during analysis, in the majority of the investigated nanoindentation grinds, the distribution of mechanical properties of individual grains overlaps, which effectively restricts the one-dimension analysis based only on a single selected parameter (H_{IT} or E_{IT}). This overlapping behaviour of H_{IT} and E_{IT} distributions is seen for both austenite and martensite phase, which is for example seen in **Fig. 3.85** and **3.87**, respectively. Considering that fact, the presented clustering of nanoindentation data conducted using the 2D GMM, and the optimal number of clusters (austenite grains or martensite twins) were evaluated according to the Bayesian information criterion (**Section 2.3.7.2**). The clustered datasets are indicated in **Fig. 3.84–3.87** with the individual colours and the corresponding matching ellipses represents the 95% confidence region for each group level. Finally, the grain mapping plots shown in the top right hand corner in **Fig. 3.84–3.87** illustrate the clustered dataset with regard to the individual coordinates of single indentation. In addition, the example of nanoindentation curves recorded for each identified grain are presented at the bottom of the discussed figures, together with the example of 3D AFM image displaying the imprint left by a single indentation with Berkovich indenter.

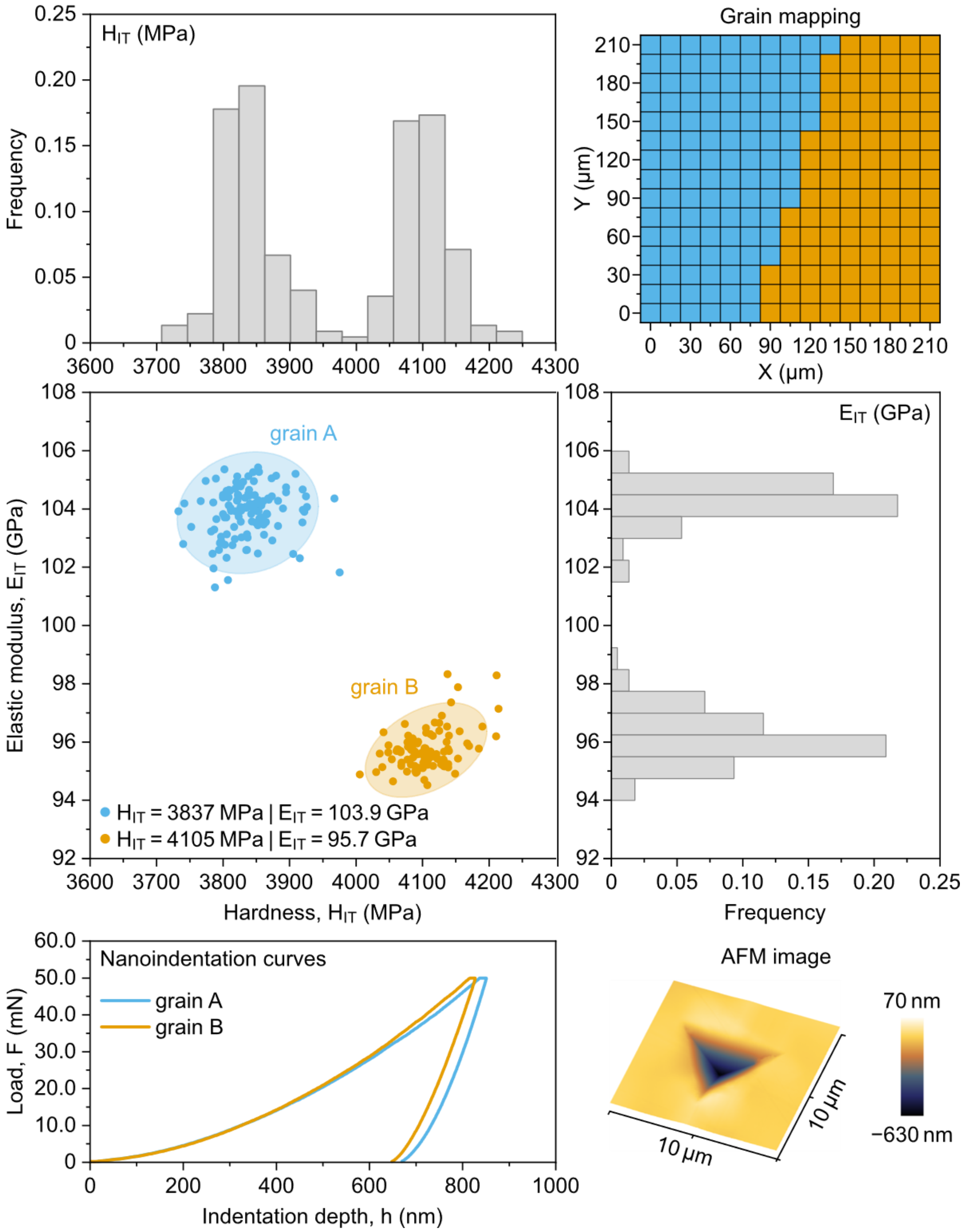

Fig. 3.84. Elastic modulus (E_{IT}) versus hardness plot (H_{IT}) for the water cooled $\mathrm{Ni_{48}Mn_{28}Ga_{20}Co_1Fe_3}$ alloy clustered with 2D GMM. The corresponding histograms presents the individual distributions of E_{IT} and H_{IT}. The grain mapping plot is the outcome of the clustering procedure. The additional nanoindentation curves presents the example plots for the identified grains. The 3D AFM image shows the residual imprint left by a single indentation.

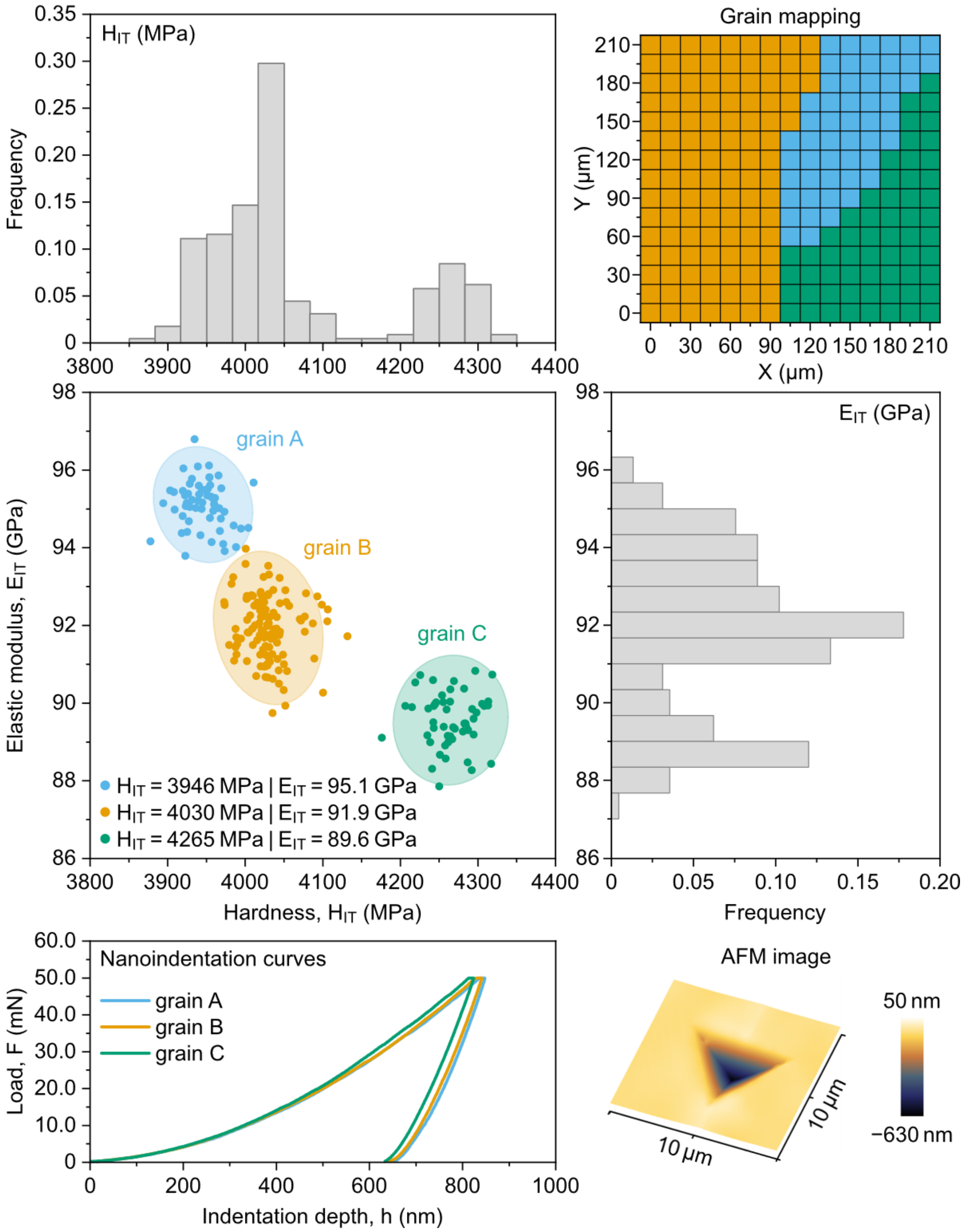

Fig. 3.85. Elastic modulus (E_{IT}) versus hardness plot (H_{IT}) for the water cooled $Ni_{48}Mn_{31}Ga_{20}Co_{1}$ alloy clustered with 2D GMM. The corresponding histograms presents the individual distributions of E_{IT} and H_{IT}. The grain mapping plot is the outcome of the clustering procedure. The additional nanoindentation curves presents the example plots for the identified grains. The 3D AFM image shows the residual imprint left by a single indentation.

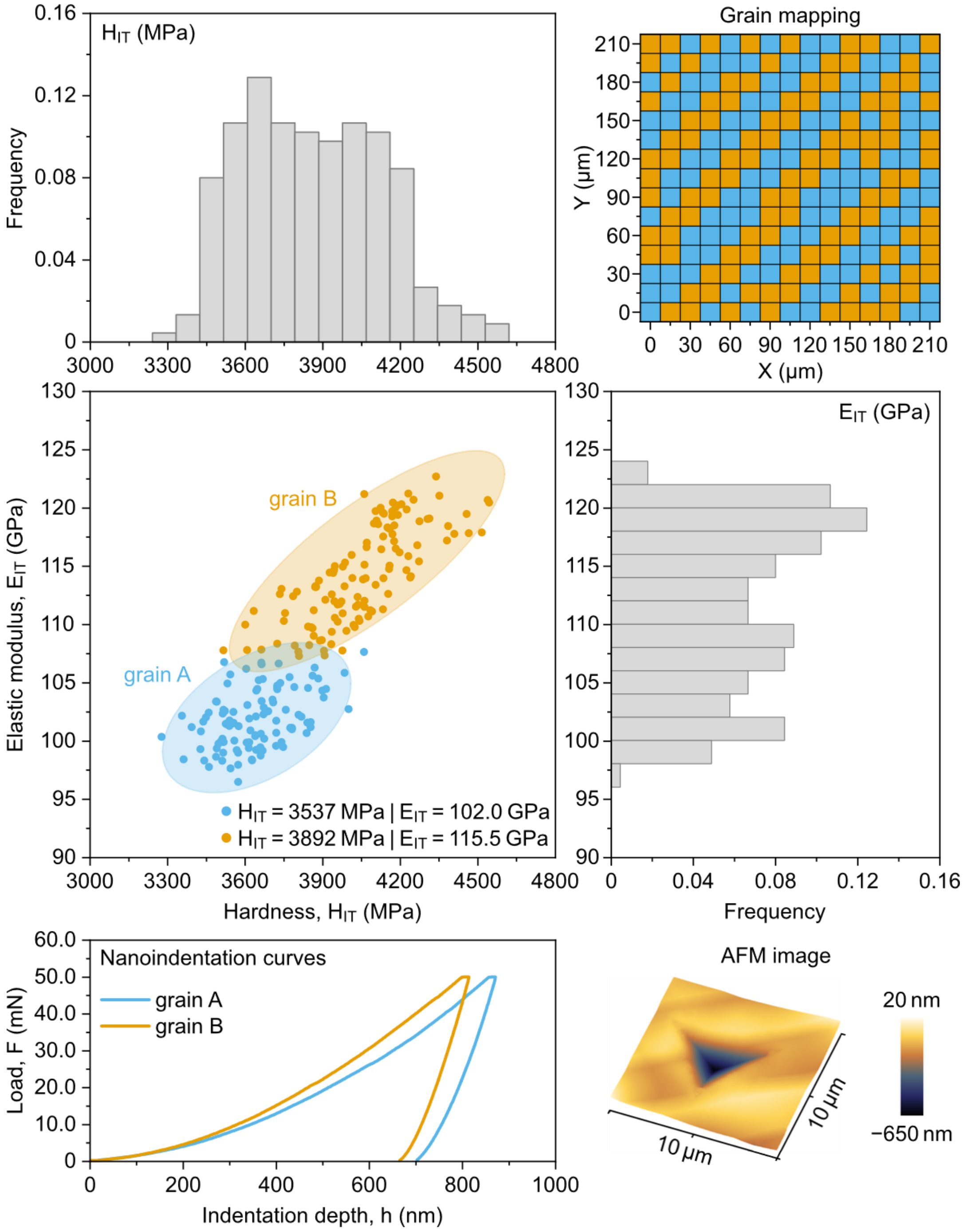

Fig. 3.86. Elastic modulus (E_{IT}) versus hardness plot (H_{IT}) for the water cooled $Ni_{48}Mn_{28}Ga_{20}Co_4$ alloy clustered with 2D GMM. The corresponding histograms presents the individual distributions of E_{IT} and H_{IT}. The grain mapping plot is the outcome of the clustering procedure. The additional nanoindentation curves presents the example plots for the identified grains. The 3D AFM image shows the residual imprint left by a single indentation.

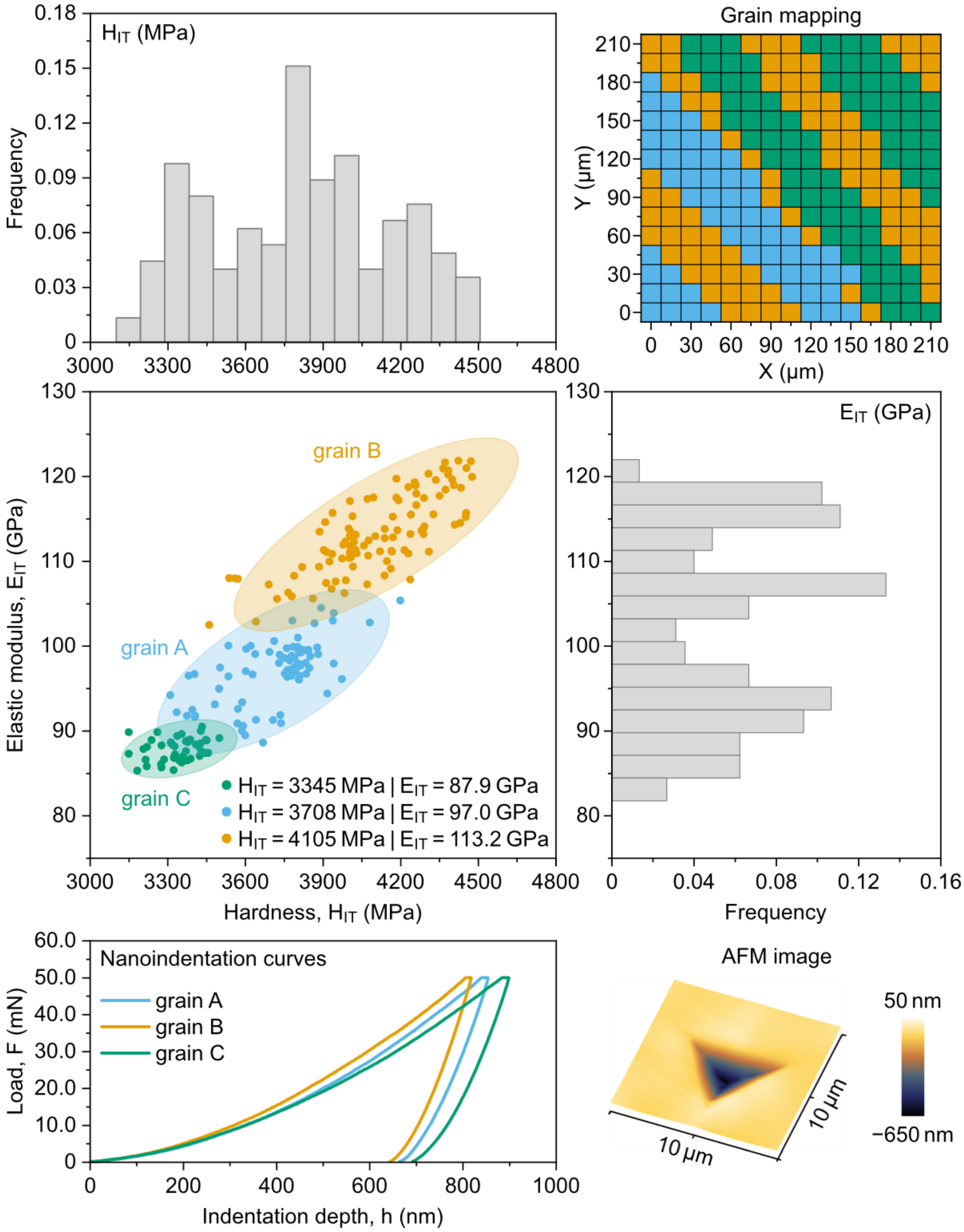

Fig. 3.87. Elastic modulus (E_{IT}) versus hardness plot (H_{IT}) for the air cooled $Ni_{48}Mn_{28}Ga_{20}Co_{4}$ alloy clustered with 2D GMM. The corresponding histograms presents the individual distributions of E_{IT} and H_{IT}. The grain mapping plot is the outcome of the clustering procedure. The additional nanoindentation curves presents the example plots for the identified grains. The 3D AFM image shows the residual imprint left by a single indentation.

The discussed clustering method combined with grain mapping enables a qualitative evaluation of the performed analysis. **Fig 3.84–3.87** demonstrate how closely the final grain mapping resembles the nanoindentation maps displayed in **Fig 3.77–3.82**. For example, for the water-cooled $Ni_{48}Mn_{28}Ga_{20}Co_1Fe_3$ alloy shown in **Fig. 3.78(c)** and **3.84**, both the associated grain mapping plot and the nanoindentation maps clearly depicts the different differences between two neighbouring austenite grains. The vertical grain boundary that is noticed in the middle of the investigated area matches between all figures, which appears to confirm the accuracy of clustering process. With regard to another austenitic sample, *i.e.* the water-cooled $Ni_{48}Mn_{31}Ga_{20}Co_1$ alloy, the nanoindentation maps presented in **Fig. 3.78(b)** demonstrate at least three distinct austenite grains, which illustrates the more complex scenario. The corresponding quantitative analysis presented in **Fig. 3.85** confirmed the existence of three different data clusters and the subsequent grain mapping revealed the same microstructural features as those observed in nanoindentation maps, which ones again validated the accuracy of the clustering process.

In consideration of martensitic structures, **Fig 3.78(d)** and **3.86** presents the nanoindentation maps and corresponding statistical analysis for the water cooled $Ni_{48}Mn_{28}Ga_{20}Co_4$ sample characterized by meso-scale martensite twins. Once more, the clustering procedure followed by the grain mapping converge with the former nanoindentation maps, revealing the same microstructural features of the investigated martensite structure. Furthermore, the clustering procedure showed that this specific meso-scale martensite consist of two twin variations, each with unique mechanical parameters. The effectiveness of the proposed statistical approach is also demonstrated in **Fig. 3.82(d)** and **3.86** for the macro-scale martensite twins using an example of the $Ni_{48}Mn_{28}Ga_{20}Co_4$ alloy exposed to air cooling. The direct comparison of nanoindentation maps and statistical grain mapping yet again shows the same structural features of meso-scale martensite twins. Although, for this particular nanoindentation grid, three different martensite variants are suggested by the clustering procedure.

Very similar results of statistical analysis were also found for other NiMnGa-based alloys observed at room temperature in both austenitic and martensitic state. In the majority of cases the clustering process revealed from one up to three different austenite grains and from one up to four different martensite variants. Each time the clustering procedure was qualitatively verified with the unprocessed nanoindentation data to avoid the interpretation errors. The individual mechanical parameters of the clustered and separated grains (or twins) were then calculated in order to determine the degree of micromechanical anisotropy in the fabricated polycrystalline Heusler alloys. The maximum and minimum values of H_{IT}, E_{IT} and η_{IT} found for each studied material are listed in **Table 3.8**.

Table 3.8. The maximum and minimum mean values (± standard deviation) of mechanical properties obtained from the statistical analysis of nanoindentation mapping for the produced NiMnGa-based alloys. The H_{IT}, E_{IT} and η_{IT} correspond to hardness, elastic modulus and elastic energy ratio.

Alloy	H_{IT} (MPa)		E_{IT} (MPa)		η_{IT} (MPa)	
	min	max	min	max	min	max
Water cooled						
$Ni_{48}Mn_{32}Ga_{20}$	4075±39	4701±46	91.0±0.8	97.2±1.2	24.8±0.3	27.1±0.3
$Ni_{48}Mn_{31}Ga_{20}Co_{1}$	3863±73	4341±45	89.6±0.7	95.2±0.6	24.1±0.4	26.7±0.3
$Ni_{48}Mn_{30}Ga_{20}Co_{2}$	3690±34	4427±46	84.8±0.7	92.7±1.0	24.3±0.2	28.3±0.3
$Ni_{48}Mn_{28}Ga_{20}Co_{4}$	3573±124	4057±118	97.8±2.2	115.4±3.6	19.8±0.5	22.7±0.6
$Ni_{48}Mn_{28}Ga_{20}Co_{3}Fe_{1}$	3784±105	4571±56	83.0±1.4	111.4±6.3	22.3±1.2	28.5±0.5
$Ni_{50}Mn_{25}Ga_{21}Co_{2}Fe_{2}$	3634±164	4255±104	93.8±4.1	116.3±3.5	20.6±0.6	23.7±0.8
$Ni_{48}Mn_{28}Ga_{20}Co_{1}Fe_{3}$	3596±46	4105±37	95.7±0.7	103.9±0.9	22.3±0.3	24.1±0.2
$Ni_{48}Mn_{28}Ga_{20}Fe_{4}$	3778±42	4218±33	96.7±1.0	105.4±1.1	22.3±0.3	24.5±0.2
Air cooled						
$Ni_{48}Mn_{32}Ga_{20}$	4191±44	4771±94	91.4±0.8	100.1±1.2	25.3±0.3	27.7±0.4
$Ni_{48}Mn_{31}Ga_{20}Co_{1}$	3892±39	4381±30	92.5±0.9	97.0±0.8	24.2±0.2	26.5±0.2
$Ni_{48}Mn_{30}Ga_{20}Co_{2}$	3791±39	4449±45	84.8±0.8	88.0±1.5	25.7±0.2	27.8±0.3
$Ni_{48}Mn_{28}Ga_{20}Co_{4}$	3608±168	3879±169	102.4±4.1	112.9±4.1	20.4±0.8	21.5±0.7
$Ni_{48}Mn_{28}Ga_{20}Co_{3}Fe_{1}$	3555±166	4137±158	93.2±4.8	105.7±8.1	20.9±0.9	23.2±1.3
$Ni_{50}Mn_{25}Ga_{21}Co_{2}Fe_{2}$	3651±147	4118±215	93.0±3.4	113.3±9.2	20.7±0.6	24.6±0.8
$Ni_{48}Mn_{28}Ga_{20}Co_{1}Fe_{3}$	3680±26	4103±29	92.8±0.7	96.9±0.8	22.7±0.2	24.4±0.2
$Ni_{48}Mn_{28}Ga_{20}Fe_{4}$	3766±27	4270±45	97.3±0.9	100.4±0.6	22.8±0.2	24.4±0.2
Furnace cooled						
$Ni_{48}Mn_{32}Ga_{20}$	4026±49	4464±62	88.7±0.9	93.8±1.3	25.4±0.3	27.7±0.2
$Ni_{48}Mn_{31}Ga_{20}Co_{1}$	3773±45	4176±25	84.4±0.6	90.3±0.6	24.3±0.2	26.9±
$Ni_{48}Mn_{30}Ga_{20}Co_{2}$	3729±64	4136±64	82.3±0.7	83.4±1.8	26.0±0.3	27.6±0.2
$Ni_{48}Mn_{28}Ga_{20}Co_{4}$	3479±167	3973±184	91.2±3.6	105.1±5.8	20.2±0.7	22.9±1.0
$Ni_{48}Mn_{28}Ga_{20}Co_{3}Fe_{1}$	3728±32	4203±62	84.7±0.8	89.1±1.0	24.9±0.2	27.6±0.3
$Ni_{50}Mn_{25}Ga_{21}Co_{2}Fe_{2}$	3345±91	4245±188	87.9±1.4	113.2±4.7	21.2±0.5	24.0±0.6
$Ni_{48}Mn_{28}Ga_{20}Co_{1}Fe_{3}$	3701±46	4126±39	93.1±1.2	100.9±0.9	22.9±0.2	24.1±0.2
$Ni_{48}Mn_{28}Ga_{20}Fe_{4}$	4007±42	4425±39	93.8±1.1	97.4±0.9	23.9±0.3	25.7±0.2

Fig. 3.88 presents the calculated values of hardness and elastic modulus of various grains examined in the investigated NiMnGa-based materials expressed as a function of Co and/or Fe addition. Each individual symbol denotes a single austenite grain or martensite twin and the colour-filled band shows the rough estimation of magnitude of the change for both E_{IT} and H_{IT} of austenitic phase. Due to the significant scatter of mechanical properties of martensite phase the observed linear trends are only marked for the austenite phase. First and foremost, it should be noted that the observed anisotropy of H_{IT} and E_{IT} is substantial in all produced samples and exceeds the standard mechanical anisotropies reported for conventional metallic materials [548,549]. The magnitude of H_{IT} changes for the water and air cooled samples in austenitic state is similar and approximately equals to 18% and 13% for the Co-doped and Fe-Co-doped specimens, respectively. This dis-

crepancy between the highest and minimum value of H_{IT} is less noticeable for furnace-cooled alloys and equals 13% and 10% for the corresponding Co-doped and Fe-Co-doped specimens, respectively. When it come to elastic modulus, these variations in mechanical properties of austenite phase are less evident and equals to about 10% for all Fe and Co doped alloys after every cooling procedure. It is also important to note that the maximum and minimum values of H_{IT} and E_{IT} for samples that were cooled by air and water are comparable, while the values for samples that were cooled by furnaces are slightly lower. These findings imply that the mechanical properties of the slowest cooled alloys differ from those of the water and air cooled materials, which is particularly evident in the case of the hardness parameter. Generally, the hardness defines the plastic deformation process governed by the slipping mechanism. Taking this into account, in atomistic scale, hardness is then strictly dependant from slip system and direction of slip. In this context According to the prior microstructural analysis outlined in **Section 3.1.4**, materials that are slowly cooled have the most uniform lattice parameters, which appears to lead to the most uniform atomic density of slip planes. This, in turn, led to the lower magnitude of H_{IT} measured for differently oriented grains.

Another important topic is the individual influence of Co and Fe on the total micromechanical parameters of fabricated Heusler alloys. As can be seen in **Fig. 3.88** the addition of Co to Ni-Mn-Ga composition decrease both the H_{IT} and E_{IT}, whereas the subsequent gradual replacement of Co by Fe increases the described parameters. It should be recalled that the evident contradictory influence of Co and Fe was previously also discovered for number of structural and thermomagnetic properties of NiMnGa-based materials, which were discussed in previous Sections of this thesis. These findings point to a strong correlation between magneto-thermo-structural and mechanical properties of the produced materials and, thus, shows the promising approach for simultaneous change of the various functional properties of the alloy by simple Fe-Co doping, which is one of the main idea of multifunctional materials.

The interpretation of micromechanical properties obtained for the various martensitic structures is more complex since it is influenced by many factors. First off, the significant magnitude of H_{IT} and E_{IT} values is observed for all martensitic samples and the average H_{IT} and E_{IT} values obtained for individual martensite twins are distinguished by a noticeably higher standard deviation than for austenite grains. This suggests that mechanical parameters are distributed more randomly, particularly in the case of the elastic modulus. This significant discrepancies stems from the complex morphology of martensite twins. It was discussed in **Section 3.1.5** that the martensitic structures in the produced materials are characterized by at least three different levels of twins that may form different constructions, including the complex crossing twins patterns (**Fig. 3.52**). Taking this into consideration, the crystallographic orientation of particular twins may significantly differs in different areas of the sample, leading to significant differences in obtained mechanical properties. Furthermore, the alloying additions appear to have a significant impact on the measured values of E_{IT} in terms of elastic properties because they alter the bonding characteristics and planar packing density, which are the main determinants of elastic properties in metallic materials.

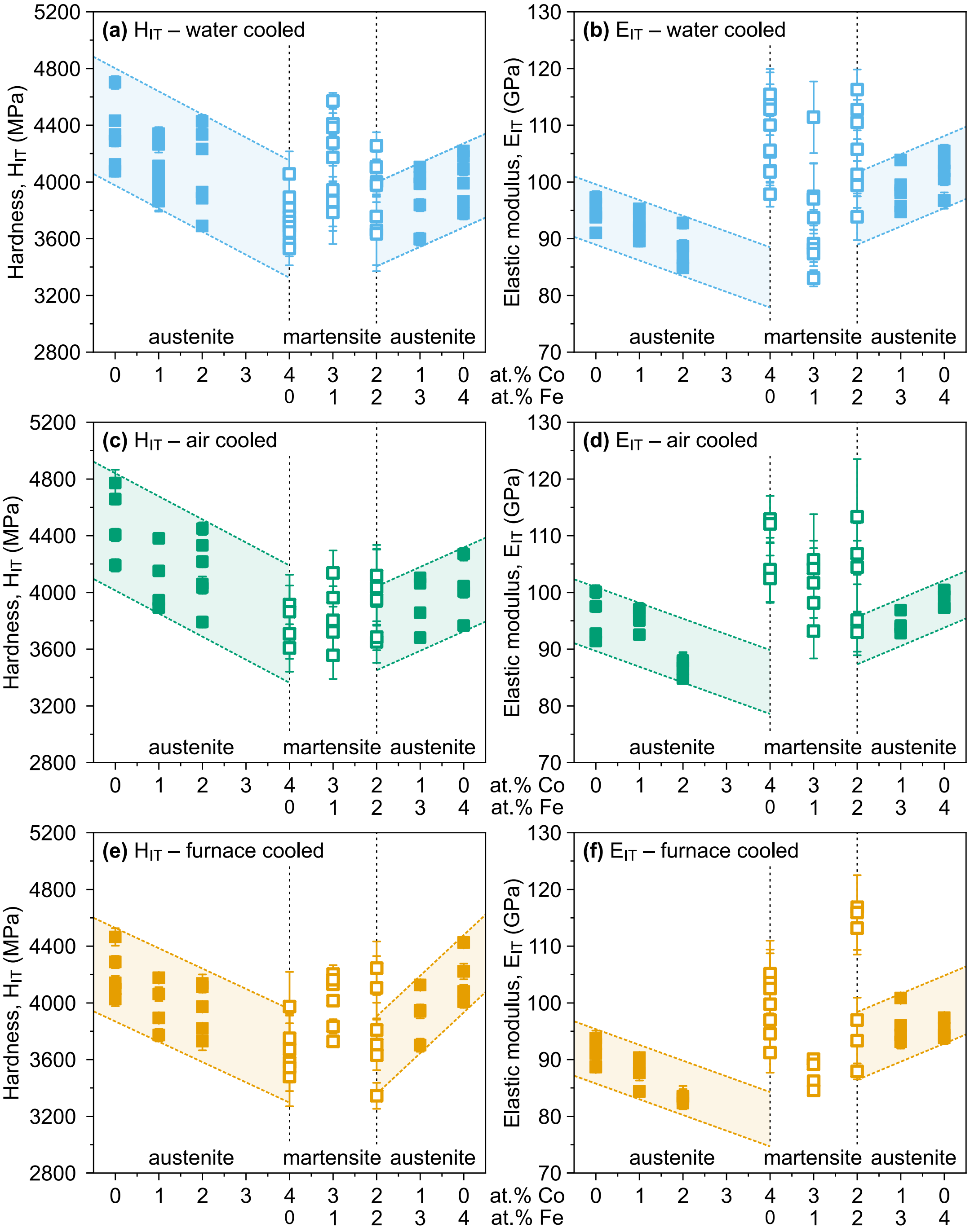

Fig. 3.88. Hardness (H_{IT}) (left column) and elastic modulus (E_{IT}) (right column) of individual grains obtained from statistical analysis for the **(a-b)** water, **(c-d)** air and **(e-f)** furnace cooled $Ni_{48}Mn_{32}Ga_{20}$, $Ni_{48}Mn_{31}Ga_{20}Co_1$, $Ni_{48}Mn_{30}Ga_{20}Co_2$, $Ni_{48}Mn_{28}Ga_{20}Co_4$, $Ni_{48}Mn_{28}Ga_{20}Co_3Fe_1$, $Ni_{50}Mn_{25}Ga_{21}Co_2Fe_2$, $Ni_{48}Mn_{28}Ga_{20}Co_1Fe_3$ and $Ni_{48}Mn_{28}Ga_{20}Fe_4$ alloys expressed as a function of Co and Fe doping. Each symbol corresponding to an individual austenite grain (full symbols) or martensite twin (empty symbols).

Last but not least, the martensitic structures observed in the produced Ni-Mn-Ga materials are prone to self-accommodation mechanism. This means that in order to minimize the internal energy during stress application the rearrangement of martensite twins may by induce in the vicinity of particular indentation due to the significant stress concentration. In order to study the potential rearrangement of martensite patterns, the additional AFM studies were carried on the residual imprints left in martensitic samples. **Fig. 3.89** shows the example of selected nanoindentation curve and corresponding AFM images of the residual imprint for the water cooled $Ni_{48}Mn_{28}Ga_{20}Co_4$ alloy.

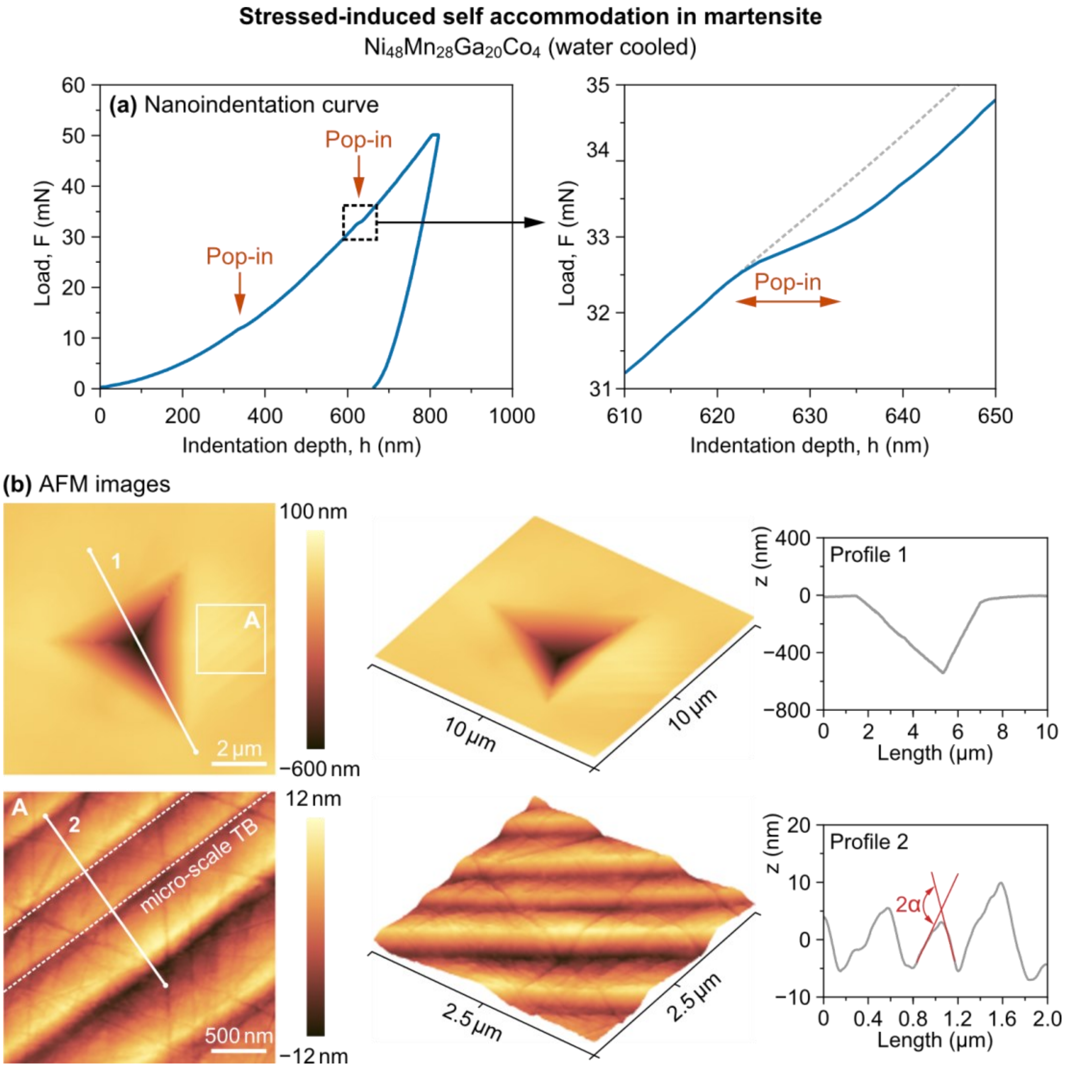

Fig. 3.89. Stress-induced self accommodation mechanism presented on the example of water cooled $Ni_{48}Mn_{28}Ga_{20}Co_4$ alloy. **(a)** Nanoindentation curve with characteristic “pop-ins” indicating twin variant reorientation. **(b)** AFM images of the residual imprint showing the stress-induced micro-scale twins. The close up is marked with rectangle and annotated by capital letter A. The height profiles along imprint (profile 1) and martensite twins (profile 2) are presented in right column, where 2α shows the relief angle.

As demonstrated in **Fig. 3.89(a)**, the characteristic discernible "pop-ins" marked on the loading part of the indentation curve are a manifestation of the potential stress-induced rearrangements of martensite. During stress-induced twins rearrangement the accumulated stress is suddenly relieved due to the twin boundary motion, which is observed as a local abrupt increase in indentation depth, without the proportional increase in applied load. The fact that the described "pop-ins" were only evident in martensitic samples seems to support the proposed explanation for this phenomenon. Additionally, the direct AFM investigation of the residual indentation imprint shown in **Fig 3.89(b)** confirms the existence of nearby micro-scale twins. What should be stressed out, these micro-scale twins were observed only in close proximity to remaining imprints and disappeared after moving 2–4 μm away from the imprint. Remarkably, all stress-induced martensitic reliefs had twinning angles 2α close to 8,0°, which, according to the geometrical model of martensite relief discussed in **Section 3.1.5**, implies the NM nature of induced rearranged martensite. The discussed observations were comparable between all martensitic samples, *i.e.* $Ni_{48}Mn_{28}Ga_{20}Co_4$, $Ni_{48}Mn_{28}Ga_{20}Co_3Fe_1$ and $Ni_{50}Mn_{25}Ga_{21}Co_2Fe_2$ alloys, regardless of their cooling conditions.

The examined stress-induced self accommodation in martensite were observed only in selected nanoindentation tests since the possibility of twin variant reorientation depends on a number of factors, such as intrinsic internal stresses, type of martensite variant, crystallographic orientation of twins or stability of martensitic phase. Taking this into consideration, the presented self accommodation mechanism in part of the performed nanoindentation tests appears to influence on the previously noted substantial differences in mechanical properties between different martensite lamellae.

In consideration of the discussed electronic parameters, **Fig. 3.90** presents the obtained values of H_{IT} and E_{IT} for the water, air and furnace cooled NiMnGa-based alloys plotted with respect to their valence electron density. Apparently, the large scatter of mechanical parameters for each chemical composition is the same as formerly presented in **Fig. 3.88**. However, taking the e/a ratio into consideration, the obtained characteristics for H_{IT} and E_{IT} differs notably. In terms of hardness (**Fig. 3.90(a)**, **(c)** and **(e)**), both the Co-doped and Fe-Co doped samples follows the same decreasing linear trend with the decreasing e/a value in the austenite phase regime ($e/a < \sim 7.75$). Interestingly, despite the considerable scatter of H_{IT} values in the martensite phase regime ($e/a > \sim 7.75$), this decreasing tendency is generally maintained even after martensitic transformation. Moreover, the roughly estimated rate of this change is comparable for the water and air cooled materials and equals to 7300 and 7400 MPa/1, respectively. In this case, the exact linear fitting is restricted by the reference value of H_0, which may be defined as minimum, maximum or mean value, depend on the required interpretation. Yet again, the rate of change is significantly lower for the furnace cooled samples and equals to about 5200 MPa.

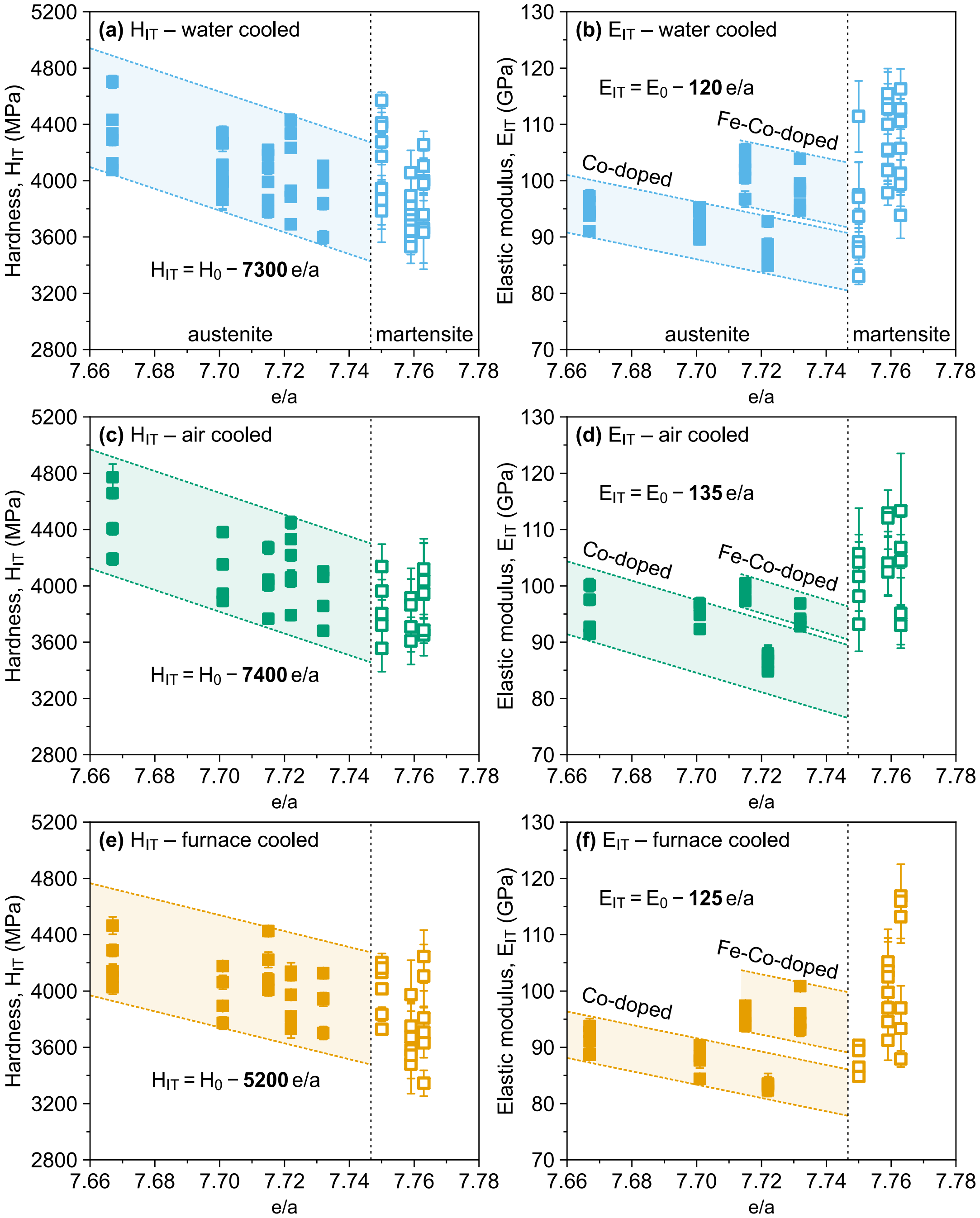

Fig. 3.90. Hardness (H_{IT}) (left column) and elastic modulus (E_{IT}) (right column) of individual grains obtained from statistical analysis for the **(a-b)** water, **(c-d)** air and **(e-f)** furnace cooled $Ni_{48}Mn_{32}Ga_{20}$, $Ni_{48}Mn_{31}Ga_{20}Co_1$, $Ni_{48}Mn_{30}Ga_{20}Co_2$, $Ni_{48}Mn_{28}Ga_{20}Co_4$, $Ni_{48}Mn_{28}Ga_{20}Co_3Fe_1$, $Ni_{50}Mn_{25}Ga_{21}Co_2Fe_2$, $Ni_{48}Mn_{28}Ga_{20}Co_1Fe_3$ and $Ni_{48}Mn_{28}Ga_{20}Fe_4$ alloys expressed as a function of valence electron concentration *e*/*a*. Each symbol corresponding to an individual austenite grain (full symbols) or martensite twin (empty symbols).

What is interesting, in the case of elastic modulus (**Fig. 3.90(b)**, **(d)** and **(f)**), the observed decreasing linear dependence of mechanical parameters on *e*/*a* ratio splits into two individual trends for Co-doped and Fe-Co-doped compositions. This behaviour of E_{IT} is observed for all differently cooled materials in austenite state.

Moreover, the rate of E_{IT} change is relatively comparable between water, air and furnace cooled alloys and varies between 120 and 135 GPa/1. What is also worth noticing, the significant differences between elastic modulus of high symmetry austenite and low symmetry martensite phase are evidently seen in **Fig. 3.90(b)**, **(d)** and **(f)**.

This considerable differences between $H_{\mathrm{IT}}(e/a)$ and $E_{\mathrm{IT}}(e/a)$ characteristics originates from the differences in plastic and elastic properties of the fabricated MSMAs. It was previously stated that plastic deformation during nanoindentation test, defined by hardness parameter, is mainly controlled by the slipping mechanism. On that basis, it can be stated that for the NiMnGa-based materials the slipping mechanism is similarly influenced by Co and Fe addition, which leads to the same e/a tendency. On the other hand, the elastic properties of the material depends on bonding characteristics and crystal lattice parameters. Considering this, the Co and Fe seems to have slightly different influence on the resistance of crystal lattice to bond stretching caused by elastic deformation, which is manifested by the distinctive e/a characteristics for the Co and Fe-Co containing alloys.

Alternatively, **Fig. 3.91** presents the same values of H_{IT} and E_{IT} expressed as a function of second discussed electronic parameter, *i.e.* non-bonding electron concentration. In this case, the observed relationships between investigated mechanical properties and N_e/a parameter are in contrast to those observed for the e/a ratio. According to **Fig. 3.91(a)**, **(c)** and **(e)** the established hardness of individual grains follows the decreasing linear tendency with the increasing N_e/a value. However, the indicated tendency, is now being noticed separately for the Co-doped and Fe-Co-doped alloys. Moreover the observed rate of change between 11500 and 12500 MPa/1 along the N_e/a parameter is generally comparable between water, air and furnace cooled samples. Because of the previously described decline in the maximum measured values of H_{IT}, the independent trends for Co-doped and Fe-Co-doped alloys noticeably overlap (**Fig. 3.91(e)**), which is the only meaning difference seen for the slowest cooling alloys.

The opposite behaviour of N_e/a and e/a parameters was also discovered for the elastic modulus shown in **Fig. 3.91(b)**, **(d)** and **(f)**. In contrary to the previous e/a characteristics, both Co-doped and Fe-Co-doped alloys clearly follow the same linearly decreasing trends with respect to the N_e/a parameter. One important similarity is that the rate of change is comparable between water, air and furnace cooled samples and equals to about 260 GPa/1 in all three cases. These findings suggest that e/a and N_e/a parameters slightly differently describes the structural changes in NiMnGa-based Heusler alloys. The e/a ratio relatively effectively defines the variations in slipping mechanism responsible for plastic deformation, regardless of the type of dopant. On the other hand, the N_e/a parameter appears to be more useful in defining the resistance of crystal lattice to bond stretching by elastic deformation since it remain unaffected by the type of alloying element (Co or Fe).

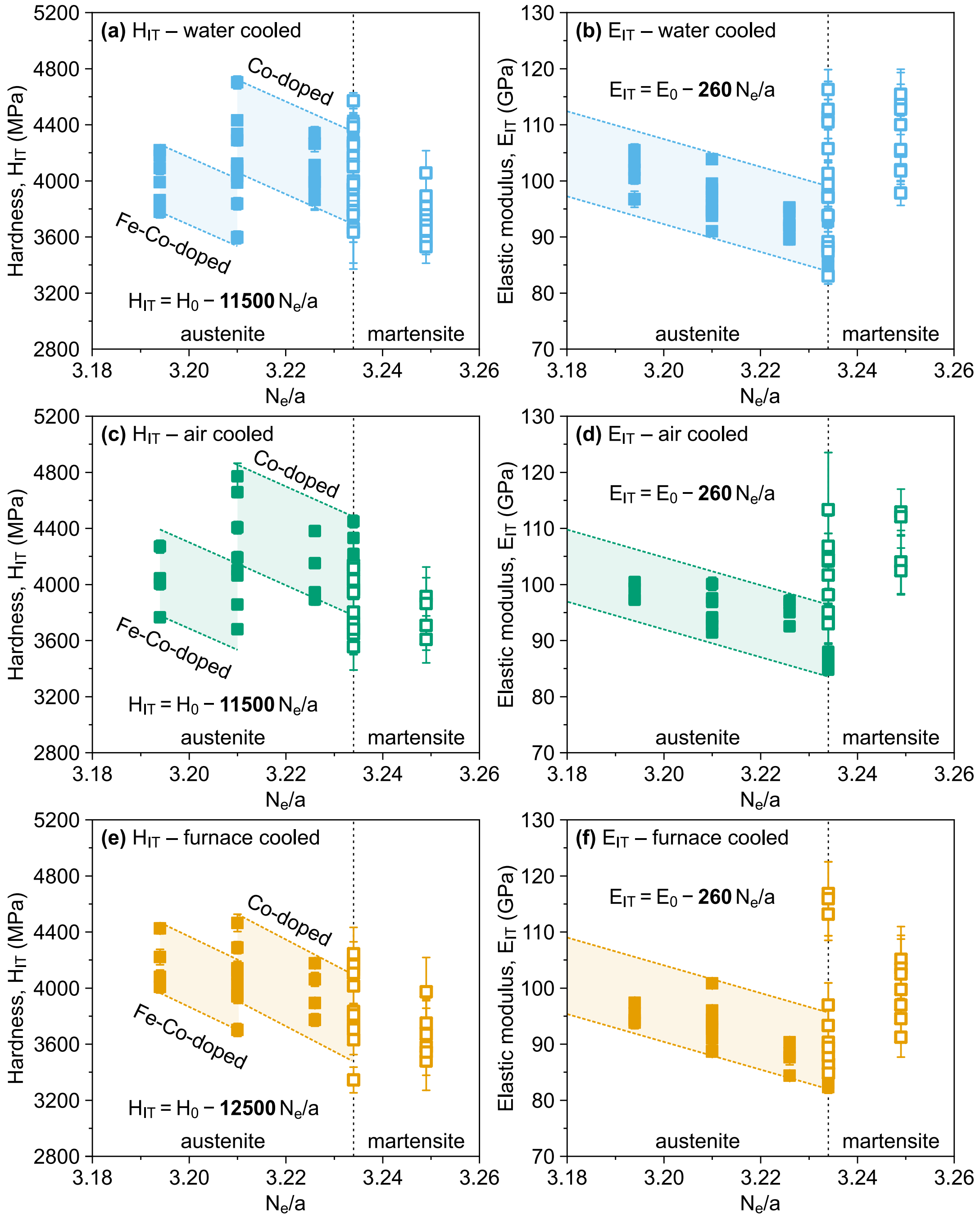

Fig. 3.91. Hardness (H_{IT}) (left column) and elastic modulus(E_{IT}) (right column) of individual grains obtained from statistical analysis for the **(a-b)** water, **(c-d)** air and **(e-f)** furnace cooled $Ni_{48}Mn_{32}Ga_{20}$, $Ni_{48}Mn_{31}Ga_{20}Co_1$, $Ni_{48}Mn_{30}Ga_{20}Co_2$, $Ni_{48}Mn_{28}Ga_{20}Co_4$, $Ni_{48}Mn_{28}Ga_{20}Co_3Fe_1$, $Ni_{50}Mn_{25}Ga_{21}Co_2Fe_2$, $Ni_{48}Mn_{28}Ga_{20}Co_1Fe_3$ and $Ni_{48}Mn_{28}Ga_{20}Fe_4$ alloys expressed as a function of non-bonding electron concentration N_e/a. Each symbol corresponding to an individual austenite grain (full symbols) or martensite twin (empty symbols).

The last important parameter that were established from the obtained nanoindentation data is the elastic energy ratio which defines the elastic recovery energy in the total work of indentation. In many situations, apart from instrumented indentation tests, when the work of deformation is difficult to measure, the elastic deformation is also represented by the dimensionless elastic deformation index H/E [550]. Taking this into account, **Fig. 3.92** presents the calculated elastic energy ratio for the investigated NiMnGa-based alloys expressed as a function doping elements and additionally as a function of elastic deformation index.

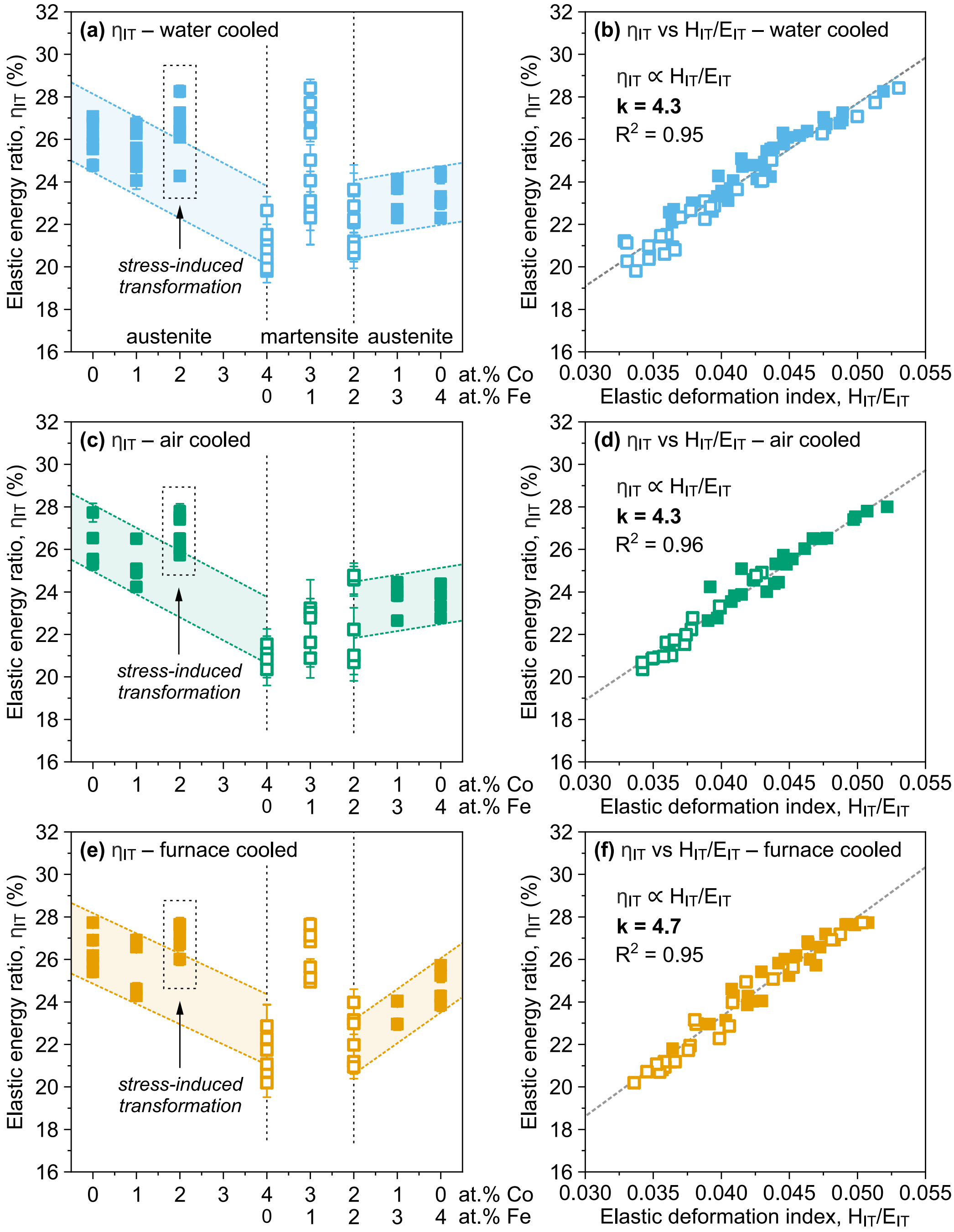

Fig. 3.92. Elastic energy ratio (η_{IT}) obtained from statistical analysis for the **(a-b)** water, **(c-d)** air and **(e-f)** furnace cooled $Ni_{48}Mn_{32}Ga_{20}$, $Ni_{48}Mn_{31}Ga_{20}Co_1$, $Ni_{48}Mn_{30}Ga_{20}Co_2$, $Ni_{48}Mn_{28}Ga_{20}Co_4$, $Ni_{48}Mn_{28}Ga_{20}Co_3Fe_1$, $Ni_{50}Mn_{25}Ga_{21}Co_2Fe_2$, $Ni_{48}Mn_{28}Ga_{20}Co_1Fe_3$ and $Ni_{48}Mn_{28}Ga_{20}Fe_4$ alloys expressed as a function of Co/Fe doping (left column) and elastic deformation index (H_{IT}/E_{IT}) (right column). Each symbol corresponding to an individual austenite grain (full symbols) or martensite twin (empty symbols).

As seen in **Fig. 3.92(a)**, **(c)** and **(e)** the η_{IT} exhibits the same behaviour as the previously discussed H_{IT} and E_{IT}, *i.e.* linearly decreases with the addition of Co to Ni-Mn-Ga system and then slightly increases with the subsequent substitution of Co by Fe. This inheritance of elastic and plastic properties defined by E_{IT} and H_{IT} is also supported by the corresponding $\eta_{\mathrm{IT}} - H_{\mathrm{IT}}/E_{\mathrm{IT}}$ plots shown **Fig. 3.92(b)**, **(d)** and **(f)**. It is shown that all samples exposed to various cooling conditions exhibit the evident proportionality between η_{IT} and $H_{\mathrm{IT}}/E_{\mathrm{IT}}$. Moreover, the proportionality factor $k = 4.3$ is the same for the water and air cooled samples, which provides a foundation for estimating the deformation energies in Ni-Mn-Ga-Co-Fe system directly from the simple $H_{\mathrm{IT}}/E_{\mathrm{IT}}$ relation. As could be expected from previous investigations, the elastic energy behaviour of furnace cooled materials slightly deviates from other alloys, as the proportionality factor between η_{IT} and $H_{\mathrm{IT}}/E_{\mathrm{IT}}$ is equal to 4.7. It is also important to note that, despite the considerable scatter of η_{IT} estimated for the martensitic alloys (empty symbols in **Fig. 3.92**), it is still proportional to the elastic deformation index. This fact significantly extends the universal applicability of the $H_{\mathrm{IT}}/E_{\mathrm{IT}}$ parameter to other NiMnGa-based alloys that undergo reversible martensitic transformation.

What is interesting, it is evident in **Fig. 3.92(a)**, **(c)** and **(e)** that all water, air and furnace cooled $Ni_{48}Mn_{30}Ga_{20}Co_2$ samples significantly stand out from the general linear characteristics obtained for other produced Co-doped materials. In order to account for this anomaly, these particular specimens were carefully studied in term of the unprocessed nanoindentation curves. In addition, In order to look into any potential structural changes, additional AFM experiments were also carried out in the vicinity of the residual indentation imprints. **Fig. 3.93** presents the example of the aforementioned analysis performed for the water cooled $Ni_{48}Mn_{30}Ga_{20}Co_2$ alloy. It is seen in **Fig. 3.92(a)** that the loading part of the nanoindentation curve exhibits a highly distinctive “pop-in” that occurs very close to the maximum applied load. The observed “pop-in” is similar to that previously reported for stress-induced martensite variant reorientation (**Fig. 3.89**). However, the observed "pop-in" is more pronounced in the current case and occurs over a wider range of the plateau phase, when the depth of the indentation increases rapidly without a noticeable increase in the applied load. Furthermore for the $Ni_{48}Mn_{30}Ga_{20}Co_2$ alloys these “pop-ins” were recorded only very close to maximum load and each loading curve had only one characteristic deflection. In contrast, during stress-induced self accommodation in martensite, the characteristic “pop-ins” were observed several times in different parts of the same loading curve. This comparison indicates that the “pop-ins” observed for the $Ni_{48}Mn_{30}Ga_{20}Co_2$ alloy originates from the stress-induced martensitic transformation that occurs when a sufficiently high stress is applied to the examined sample. The external mechanical stress promotes the martensite variant with the higher shear stress than the former austenite phase. As a result, the material may go through a martensitic transformation in order to reduce the accumulated energy. The similar phenomenon of stress-induced martensitic transformation by nanoindentation were previously reported for other shape memory materials, such as Cu-Al-Ni

[551], Cu-Al-Be [552], Ni-Ti [553] alloys. The comprehensive explanation od stressed-induced thermoelastic martensitic transformation was provided in **Section 1.4** of the theoretical part of the thesis.

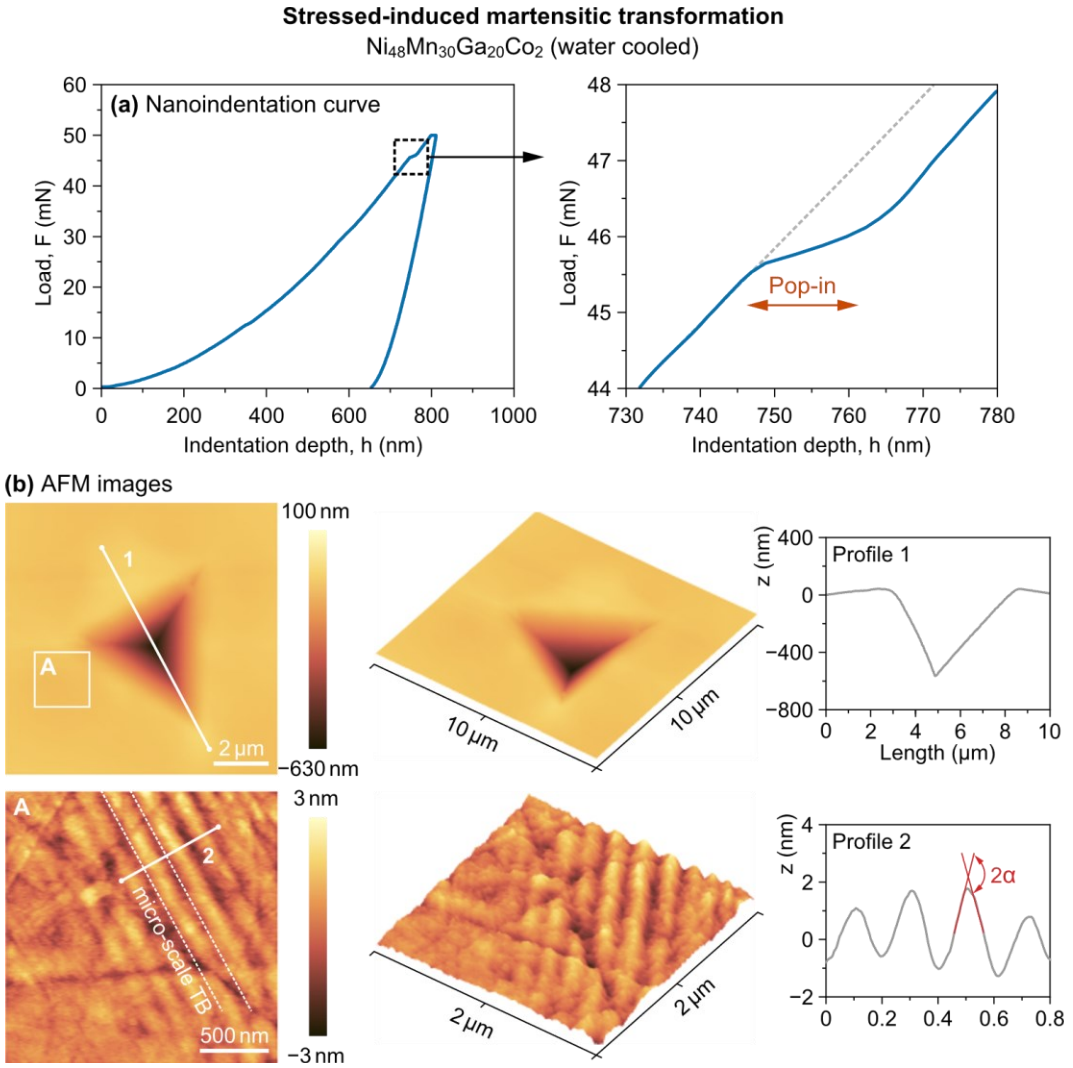

Fig. 3.93. Stress-induced martensitic transformation presented on the example of water cooled $Ni_{48}Mn_{30}Ga_{20}Co_2$ alloy. **(a)** Nanoindentation curve with characteristic “pop-in” indicating phase transformation. **(b)** AFM images of the residual imprint showing the stress-induced micro-scale twins. The close up is marked with rectangle and annotated by capital letter A. The height profiles along the imprint (profile 1) and martensite twins (profile 2) are presented in right column, where 2α shows the relief angle.

The AFM images presented in **Fig. 3.93(b)** seems to confirm the proposed theory regarding stress-induced martensitic transformation. As seen in depicted 2D and 3D AFM images the characteristic martensitic relief is present in the close vicinity of the residual indentation imprint. What should be highlighted, the discussed imprint was left in austenitic phase of $Ni_{48}Mn_{30}Ga_{20}Co_2$ sample and no other signs of martensitic phase were found in this particular area of the examined specimen. In the light of this, the discovered martensite relief must have been formed during indentation as a result of stress-induced phase transformation. Due to the considerable plastic deformation caused by the indenter, the induced martensite remained in the sample after indentation and did not transform back to austenite phase. This plastic deformation blocks the reversible phase transformation, since it may occurs only in the elastic deformation range. The quantitative analysis of the profiles obtained for discovered micro-scale twins shown the same relief angle $2\alpha = 2.9°$ for all water, air and furnace cooled $Ni_{48}Mn_{30}Ga_{20}Co_2$ samples. These findings support earlier AFM research (**Section 3.1.5**), which suggests that the favourable martensite in the $Ni_{48}Mn_{30}Ga_{20}Co_2$ alloy is a 5M regulated structure.

The observed phenomenon of stress-induced martensitic transformation was found only for $Ni_{48}Mn_{30}Ga_{20}Co_2$ alloys. This is due to the fact that this particular alloy is characterized by martensitic transformation temperature very close to room temperature ($M_S = 288$ K) at which all nanoindentation tests were carried out. Because of this, the applied load of 50 mN might provide the sufficient mechanical energy required to trigger the phase transition.

Lastly, it is important to note that the discussed supplementary AFM studies of the residual imprints allowed for a validation of the accuracy of the Oliver and Pharr analysis. As explained in **Section 2.3.7.1** the area of residual imprint is estimated on the basis of penetration depth. The Oliver and Pharr approach consider the characteristic “sink-in” underneath the indenter taking into account the elastic contact mechanics [512]. However, some materials may exhibit abnormal sink-in or pile-up deformation, which can lead to an under- or overestimation of true indentation area by as much as 60% [554]. In this circumstance, the AFM investigation helps to evaluate the true contact area and assess the deformation around the residual imprint. When it comes to the nanoindentation studies discussed in this Section, **Fig. 3.89(b)** and **3.93(b)** shows very typical residual imprints profiles for both martensite and austenite phase, respectively. No significant irregularities that may influence the calculations of true contact area were found in any sample, which supports the accuracy of the micro mechanical properties analysis presented in this Section.

4

Conclusions

The NiMnGa-based magnetic shape memory alloys are one of the most interesting group of modern smart materials. The complex multifunctional behaviour combining the magnetic, thermal and mechanical properties provides a basis for various sophisticated applications. In this context, the understanding of their of the nature of reversible phase transformation, microstructure and related magneto-thermo-structural properties is one of the most important topics in future prospect development of this group of materials. In the presented thesis, comprehensive investigations of microstructure, martensitic transformation, thermomagnetic behaviour and micromechanical properties were carried out in order to establish the relationship between the chemical composition, electronic parameters, atomic ordering and aforementioned functional properties of Ni-Mn-Ga alloys doped by Fe or Co.

The Ni-Mn-Ga-(Co-Fe) alloys, including the $Ni_{48}Mn_{32}Ga_{20}$, $Ni_{48}Mn_{31}Ga_{20}Co_1$, $Ni_{48}Mn_{30}Ga_{20}Co_2$, $Ni_{48}Mn_{28}Ga_{20}Co_4$, $Ni_{48}Mn_{28}Ga_{20}Co_3Fe_1$, $Ni_{50}Mn_{25}Ga_{21}Co_2Fe_2$, $Ni_{48}Mn_{28}Ga_{20}Co_1Fe_3$, $Ni_{48}Mn_{28}Ga_{20}Fe_4$ were successfully produced in bulk polycrystalline form following the proposed fabrication procedure based on the arc-melting method. All samples were then annealed at the same temperature of 1173 K for 24 h and cooled with three different cooling rates realized by water, air or furnace cooling.

The microstructural investigations conducted by polarised light microscopy and SEM shows that all alloys are characterized by single phase microstructure without any undesirable secondary phases. This confirms the good solubility of both Co and Fe in the Ni-Mn-Ga composition, which was also supported by a long annealing process above the order-disorder transformation temperature. Moreover, the proposed fabrication procedure did not introduce any significant microstructural texture to the examined materials, regardless of the cooling conditions.

The EDS studies confirms that the fabricated alloys have the same chemical composition as was initially assumed and that the proposed production method provides perfect homogeneity throughout the entire volume of the bulk samples. The differences between the designed and the obtained compositions do not exceed ±0.5 at.% in case of all single elements. The experimentally established chemical compositions were used to calculate two electronic parameters: (1) valence electron concentration e/a and (2) non-bonding electrons concentration N_e/a, which were examined as a potential estimators for predicting the magneto-thermo-structural properties of Ni-Mn-Ga MSMAs.

The detailed XRD studies shows that at room temperature the $Ni_{48}Mn_{32}Ga_{20}$, $Ni_{48}Mn_{31}Ga_{20}Co_1$, $Ni_{48}Mn_{30}Ga_{20}Co_2$, $Ni_{48}Mn_{28}Ga_{20}Co_1Fe_3$, $Ni_{48}Mn_{28}Ga_{20}Fe_4$ are in austenitic state, whereas the $Ni_{48}Mn_{28}Ga_{20}Co_4$, $Ni_{48}Mn_{28}Ga_{20}Co_3Fe_1$ and $Ni_{50}Mn_{25}Ga_{21}Co_2Fe_2$ are in martensitic state. However, the temperature dependent XRD studies revealed that almost all alloys contain some amount of residual phase inherited after forward and reverse martensitic transformation. These residual phases fully disappear at noticeably higher or lower temperatures than would suggested by the martensitic transformation temperature, which indicates the hysteretic character of the phase transformation. According to the Rietveld refinement analysis, the austenitic phase was identified as a cubic $Fm\bar{3}m$ structure ($L2_1$) and the main martensitic phase was found to be of non-modulated type with a tetragonal $I4/mmm$ structure ($L1_0$). Furthermore, the $Ni_{48}Mn_{31}Ga_{20}Co_1$ and $Ni_{48}Mn_{30}Ga_{20}Co_2$ alloys were also characterized by five-layered modulated martensite defined by a monoclinic $P2/m$ structure. The 5M modulation of martensite was in this case strictly connected with the chemical composition, as it was observed in all differently cooled materials. The examination of particular lattice parameters for cubic and tetragonal phase shows the differences in atomic ordering between water, air and furnace cooled alloys. These differences were most evident for the slowest cooled samples, which were characterized by the less significant changes in lattice parameters with the gradual introduction of doping elements than water and air cooled materials. Regardless of cooling conditions, the decisive factor influencing the final crystal lattice parameters is the type and content of doping elements. It was found that Fe and Co have contradictory influence on lattice parameters of both austenite and martensite phase, though the effect of Co is notably more evident than the effect of Fe. Consequently, in a matter of electronic structure, the e/a parameter was found to be more successful in predicting the crystal lattice parameters than N_e/a, since it incorporates both the influence of Co and Fe doping and the differences in Ni/Mn ratio. In this case, the N_e/a was noticed to be more sensitive to the aforementioned factors.

Microstructural investigations were also supported by the AFM measurements in contact mode. The qualitative AFM analysis revealed the areas with residual martensitic phases in austenitic samples, which was indicated by the former XRD spectra. The examined residual martensite seems to be present in the observed microstructures due to the remaining internal stresses, that may locally stabilize the low temperature phase. For the fully martensitic Heusler alloys, the AFM images revealed complex martensitic structures characterized by self-accommodated twins observed at different length scales. In view of this, three distinctive length scales defining the periodicity of twinning were proposed to describe the martensite phase, *i.e.* macro-scale ($\lambda > 100$ μm), meso-scale ($\lambda < 100$ μm) and micro-scale ($\lambda < 1$ μm) twins. Moreover, each type of twinning may be organized as simple twins, twins-within-twins or complex crossing twins structures. The quantitative analysis of AFM images, based on the proposed geometrical model of the martensite relief, shows that the measured relief angle may be approximated by the theoretical twinning angle calculated on the basis of crystallographic parameters obtained from the Rietveld refinement. Following this assumption, the 5M modulated martensite was identified in the $Ni_{48}Mn_{31}Ga_{20}Co_1$ and $Ni_{48}Mn_{30}Ga_{20}Co_2$ alloys, which is in accordance with XRD studies and presents a potential for identification of martensite modulation without the time-consuming diffraction measurements.

The thermomagnetic behaviour of phase transformations was investigated with the help of DSC, M-TG and VSM. It was shown that the sequence of transformations starts from the martensitic transformation between ferromagnetic austenite and ferromagnetic martensite, which then undergoes the magnetic transformation to paramagnetic martensite at Curie temperature significantly higher than TM. The estimated temperature of martensitic transformation monotonically increases with the increasing content of Co and then slightly decreases with the gradual substitution of Co by Fe. It was shown that substitution of Fe by Co, or Co by Fe, may significantly decrease or increase the T_M by almost 90 K from T_M = 254.8 K for the $Ni_{48}Mn_{28}Ga_{20}Fe_4$ alloy to T_M = 344.3 K for the $Ni_{48}Mn_{28}Ga_{20}Co_4$ alloy, which is a very promising feature considering the future multifunctional applications requiring the particular set of properties at different working temperatures. This contradictory influence of Co and Fe is not observed for Curie temperature, which generally increases with the increasing content of both elements. The differences in cooling conditions have a very minor effect on the temperatures of structural and magnetic transformations. Only the furnace cooled samples were characterized by slightly higher T_M than the corresponding water or air cooled materials.

In case of T_M, the e/a ratio becomes sensitive to a type of alloying addition, but still incorporates the differences in the Ni/Mn ratio. In this situation, the N_e/a parameter seems to be more universal metrics in predicting the T_M, even despite the higher uncertainties.

The investigation of magnetic properties based on magnetization hysteresis loops recorded with the use of VSM revealed the considerable differences between the magnetic behaviour of the austenite and martensite phase, which is ascribed to a high magnetocrystalline anisotropy of the low temperature martensite phase. It was revealed that depending on the particular alloy, the coercivity of martensite is even more than 40 times higher than the coercivity of the corresponding austenite phase. The examination of coercivity expose the differences in atomic ordering between differently cooled materials and shows that the slowest cooled samples are characterised by significantly lower coercivity than the water and air cooled materials. This suggests that post-preparation heat treatment and subsequent cooling rate have considerable influence on the pinning of the magnetic domain walls and, thus, on selected magnetic properties. Furthermore, both the austenite and martensite phases differ significantly when it comes to their saturation magnetization. Because of the high magnetocrystalline anisotropy, the low-symmetry martensite structure saturate significantly slower than high-symmetry austenite. However, at high magnetic field, when anisotropy is compensated by magnetic field, the M_S of martensite phase is about ~25–30% higher than the M_S of austenite phase. Moreover, the contradictory influence of Co and Fe is also evident on the example of M_S for the martensite phase, which significantly decreases with the increase of Co content and then increases with the subsequent substitution of Co by Fe.

What is significant is that the e/a and N_e/a were found to be relatively well predictors of both coercivity and magnetization saturation in produced NiMnGa-based materials. Nevertheless, both parameters are sensitive to the type of doping element and are reliable for the martensite phase than for the austenite phase.

The recorded hysteresis loops were also used to estimate the magnetocrystalline anisotropy of the fabricated Heusler alloys following the low of approach to magnetic saturation. The performed analysis confirmed the significant differences in magnetocrystalline anisotropy of the martensite and austenite phases. Moreover, it was also found that the magnetocrystalline anisotropy is strictly dependent on the chemical composition and is well described by both the e/a and N_e/a parameter. In this particular case, the N_e/a revealed a more universal character incorporating the influence of different doping elements. The presented strong relationship between the elemental doping and Keff shows a promising perspective for future design of multifunctional Ni-Mn-Ga-(Co-Fe) alloys with the desired level of anisotropy, which governs the majority of multifunctional properties observed in MSMAs.

Last but not least, the micromechanical properties of the produced NiMnGa-based materials, including hardness, elastic modulus and elastic energy ratio were investigated on the basis of instrumented nanoindentation mapping. The high anisotropy of the mechanical properties between different neighbouring grains required a statistical approach to distinguish the mechanical parameters of the individual grains. In this work, the author proposed the methodology based on the 2D Gaussian mixture model followed by Bayesian information criterion to cluster and label individual grains and estimate their mechanical properties. Considering the established approach, it was shown that the differences between the minimum and maximum value of the hardness and elastic modulus of the austenite phase measured for the same alloy reaches up to ~20% and ~10%, respectively, which is an uncommon phenomenon compared to conventional polycrystalline alloys. In case of micromechanical properties, the contradictory effects of Co and Fe were one again noticed in all examined materials. Generally, both the hardness and elastic modulus decrease with increasing Co content, and then increase with subsequent increasing Fe content. However, as a result of the strong micromechanical anisotropy, the differences in H_{IT} and E_{IT} for individual grains in the same alloy are more substantial than the variations influenced by the elemental doping. As a consequence, the maximum values of H_{IT} and E_{IT} for the alloys with the lowest mechanical properties are still higher than minimum values of H_{IT} and E_{IT} for the alloys with the highest mechanical properties. The discrepancies between mechanical properties of individual grains are even more pronounced for the martensite phase due to the complex self-accommodated nature of the martensitic structure. Moreover, additional AFM investigations of residual imprints revealed the rearrangement mechanism of martensite twins during indentation, which appears to influence the significant discrepancies between the estimated mechanical properties of individual martensitic lamellae. Similar phenomena were also found for the $Ni_{48}Mn_{30}Ga_{20}Co_2$ alloys for which mechanical stress under the indenter induced the martensitic transformation, which is manifested by a significant increase in the elastic energy ratio.

Despite the large scatter of estimated mechanical properties, both H_{IT} and E_{IT} revealed strong linear relationships with both investigated electronic parameters. The e/a ratio was found to have a universal character incorporating the influence of Co and Fe doping for the hardness estimation, whereas N_e/a was found to be a better predictor in the case of the elastic modulus. Moreover, in a matter of elastic properties of the studied materials, it was shown that for both austenite and martensite phases, the energy of deformation may be expressed by a simple elastic deformation index H/E, which may significantly simplify the mechanical characterisation of this group of MSMAs. Lastly, the different cooling rates do not significantly influence the examined mechanical properties. Only furnace cooled materials exhibit slightly lower values of H_{IT} and E_{IT} than corresponding water and air cooled alloys.

The presented thesis contains a comprehensive evaluation of the microstructure and magneto-thermo-mechanical properties of Ni-Mn-Ga magnetic shape alloys influence by Co and/or Fe doping. On the basis of the obtained results, it was proven that the proper elemental doping leads to a significant change in all important multifunctional properties of the final material, including structural, magnetic and mechanical properties. The exemplified contradictory effect of Co and Fe addition to the Ni-Mn-Ga composition can be used to alter the desired properties required for particular complex application. Moreover, the resultant properties of the alloy may also be, to some extent, influenced by the heat treatment and cooling conditions. What is significant, in this particular Ni-Mn-Ga-Co-Fe system the considered functional properties may be predicted by valence electron concentration e/a and non-bonding electrons concentration Ne/a. However, it should be remembered that non of this electronic parameters are universal and they should be examined together to fully understand the complex nature of the NiMnGa-based alloy. Overall, the wide-ranging research presented in this thesis provides a distinctive and original contribution to the further future development of polycrystalline NiMnGa-based Heusler alloys and constitutes a strong foundation for designing the multifunctional materials in the Ni-Mn-Ga-Co-Fe system.

Appendices

Appendix A: Crystallographic Information Files

A.1 CIF file created for cubic austenite phase

```
# Ni2MnGa - cubic austenite (L21)

_cell_length_a          5.821
_cell_length_b          5.821
_cell_length_c          5.821
_cell_angle_alpha       90.0
_cell_angle_beta        90.0
_cell_angle_gamma       90.0

_symmetry_space_group_name_H-M 'F 4/m -3 2/m'
_symmetry_Int_Tables_number 225
_space_group.reference_setting '225:-F 4 2 3'

loop_
_atom_site_label
_atom_site_type_symbol
_atom_site_symmetry_multiplicity
_atom_site_Wyckoff_label
_atom_site_fract_x
_atom_site_fract_y
_atom_site_fract_z
Ni Ni   8 c 0.25000 0.25000 0.25000
Mn Mn   4 a 0.00000 0.00000 0.00000
Ga Ga   4 b 0.50000 0.50000 0.50000
```

A.2 CIF file created for NM martensite phase

```
# Ni2MnGa - NM martensite (L10)

_cell_length_a          3.908
_cell_length_b          3.908
_cell_length_c          6.458
_cell_angle_alpha       90.0
_cell_angle_beta        90.0
_cell_angle_gamma       90.0

_symmetry_space_group_name_H-M 'I 4/m m m'
_symmetry_Int_Tables_number 139
_space_group.reference_setting '139: -F 4 2'

loop_
_atom_site_label
_atom_site_type_symbol
```

```
_atom_site_symmetry_multiplicity
_atom_site_Wyckoff_label
_atom_site_fract_x
_atom_site_fract_y
_atom_site_fract_z
Ni Ni   4 d 0.00000 0.50000 0.25000
Mn Mn   2 b 0.00000 0.00000 0.50000
Ga Ga   2 a 0.00000 0.00000 0.00000
```

A.3 CIF file created for 5M modulated martensite

```
# Ni2MnGa - 5M modulated martensite

_cell_length_a            4.197
_cell_length_b            5.586
_cell_length_c            20.927
_cell_angle_alpha         90.0
_cell_angle_beta          90.3
_cell_angle_gamma         90.0

_symmetry_space_group_name_H-M 'P 1 2/m 1'
_symmetry_Int_Tables_number 10
_space_group.reference_setting '10: -P 2y'

loop_
_atom_site_label
_atom_site_type_symbol
_atom_site_symmetry_multiplicity
_atom_site_Wyckoff_label
_atom_site_fract_x
_atom_site_fract_y
_atom_site_fract_z
Mn Mn   1 a 0.00000 0.50000 0.25000
Mn Mn   2 m 0.94800 0.00000 0.40000
Mn Mn   2 m 0.04400 0.00000 0.20000
Mn Mn   2 m 0.55200 0.50000 0.10000
Mn Mn   2 n 0.45600 0.50000 0.30000
Mn Mn   1 h 0.50000 0.50000 0.50000
Ni Ni   2 j 0.50000 0.25000 0.00000
Ni Ni   4 o 0.05200 0.25000 0.10000
Ni Ni   4 o 0.54400 0.25000 0.20000
Ni Ni   4 o 0.95600 0.25000 0.30000
Ni Ni   4 o 0.44800 0.25000 0.40000
Ni Ni   2 k 0.00000 0.25000 0.50000
Ga Ga   1 b 0.00000 0.50000 0.00000
Ga Ga   2 m 0.55200 0.00000 0.10000
Ga Ga   2 n 0.04400 0.50000 0.20000
Ga Ga   2 m 0.45600 0.00000 0.30000
Ga Ga   2 n 0.94800 0.50000 0.40000
Ga Ga   1 g 0.50000 0.00000 0.50000
```

List of figures

List of tables

References

[1] F. Heusler, W. Starck, E. Haupt, Magnetisch-chemische studien, Verhandlungen Der Deutschen Physikalischen Gesellschaft. 5 (1903) 220.

[2] F. Heusler, Über magnetische Manganlegierungen, Verhandlungen der Deutschen Physikalischen Gesellschaft. 5 (1903) 119.

[3] H.H. Potter, The X-ray structure and magnetic properties of single crystals of Heusler alloy, Proceedings of the Physical Society. 41 (1928) 135–142. https://doi.org/10.1088/0959-5309/41/1/314.

[4] A.J. Bradley, J.W. Rodgers, The crystal structure of the Heusler alloys, Proceedings of the Royal Society of LLndon. Series A, Containing Papers of a Mathematical and Physical Character. 144 (1934) 340–359.

[5] R.A. de Groot, F.M. Mueller, P.G. van Engen, K.H.J. Buschow, New Class of Materials: Half-Metallic Ferromagnets, Phys Rev Lett. 50 (1983) 2024–2027. https://doi.org/10.1103/PhysRevLett.50.2024.

[6] K.E.H.M. Hanssen, P.E. Mijnarends, L.P.L.M. Rabou, K.H.J. Buschow, Positron-annihilation study of the half-metallic ferromagnet NiMnSb: Experiment, Phys Rev B. 42 (1990) 1533–1540. https://doi.org/10.1103/PhysRevB.42.1533.

[7] M. Julliere, Tunneling between ferromagnetic films, Phys Lett A. 54 (1975) 225–226. https://doi.org/10.1016/0375-9601(75)90174-7.

[8] F. Lei, C. Tang, S. Wang, W. He, Half-metallic full-Heusler compound Ti2NiAl: A first-principles study, J Alloys Compd. 509 (2011) 5187–5189. https://doi.org/10.1016/j.jallcom.2011.02.002.

[9] H. Xie, H. Wang, C. Fu, Y. Liu, G.J. Snyder, X. Zhao, T. Zhu, The intrinsic disorder related alloy scattering in ZrNiSn half-Heusler thermoelectric materials, Sci Rep. 4 (2015) 6888. https://doi.org/10.1038/srep06888.

[10] S. Ouardi, G.H. Fecher, C. Felser, J. Kübler, Realization of Spin Gapless Semiconductors: The Heusler Compound Mn2CoAl, Phys Rev Lett. 110 (2013) 100401. https://doi.org/10.1103/PhysRevLett.110.100401.

[11] T. Graf, C. Felser, S.S.P. Parkin, Simple rules for the understanding of Heusler compounds, Progress in Solid State Chemistry. 39 (2011) 1–50. https://doi.org/10.1016/j.progsolidstchem.2011.02.001.

[12] Y. Zhou, J. Zhang, Y. Huang, X. Wei, The structural, electronic, magnetic and mechanical properties of d0 binary Heusler alloys XF3 (X = Be, Mg, Ca, Sr, Ba), Journal of Physics and Chemistry of Solids. 138 (2020) 109246. https://doi.org/10.1016/j.jpcs.2019.109246.

[13] G.Z. Xu, E.K. Liu, Y. Du, G.J. Li, G.D. Liu, W.H. Wang, G.H. Wu, A new spin gapless semiconductors family: Quaternary Heusler compounds, EPL (Europhysics Letters). 102 (2013) 17007. https://doi.org/10.1209/0295-5075/102/17007.

[14] Z. Bai, L. Shen, G. Han, Y.P. Feng, Data Storage: Review of Heusler Compounds, SPIN. 02 (2013) 1230006. https://doi.org/10.1142/S201032471230006X.

[15] F.A. Hames, Ferromagnetic-Alloy Phases Near the Compositions Ni2MnIn, Ni2MnGa, Co2MnGa, Pd2MnSb, and PdMnSb, J Appl Phys. 31 (1960) S370–S371. https://doi.org/10.1063/1.1984753.

[16] M. Elfazani, M. DeMarco, S. Jha, G.M. Julian, J.W. Blue, Hyperfine magnetic field at cadmium impurity in Heusler alloys Ni2MnGa, Ni2MnIn, Cu2MnIn, and Au2MnIn, J Appl Phys. 52 (1981) 2043–2045. https://doi.org/10.1063/1.329609.

[17] T. Kanomata, K. Shirakawa, T. Kaneko, Effect of hydrostatic pressure on the Curie temperature of the Heusler alloys Ni2MnZ(Z = Al, Ga, In, Sn and Sb), J Magn Magn Mater. 65 (1987) 76–82. https://doi.org/10.1016/0304-8853(87)90312-X.

[18] S. Jha, H.M. Seyoum, M. Demarco, G.M. Julian, D.A. Stubbs, J.W. Blue, M.T.X. Silva, A. Vasquez, Site and probe dependence of hyperfine magnetic field in L21 Heusler alloys X2MnZ (X=Ni, Cu, Rh, Pd and Z=Ga, Ge, In, Sn, Pb), Hyperfine Interact. 16 (1983) 685–688. https://doi.org/10.1007/BF02147342.

[19] S. Jha, H.M. Seyoum, M. de Marco, G.M. Julian, G.K. Shenoy, R.A. Dunlap, Hyperfine-magnetic-field measurements in the Heusler alloy Ni2MnGa, Phys Rev B. 32 (1985) 6104–6107. https://doi.org/10.1103/PhysRevB.32.6104.

[20] P.J. Webster, K.R.A. Ziebeck, S.L. Town, M.S. Peak, Magnetic order and phase transformation in Ni2MnGa, Philosophical Magazine B. 49 (1984) 295–310. https://doi.org/10.1080/13642817408246515.

[21] V. v. Kokorin, V.A. Chernenko, Martensitic transformation in a ferromagnetic Heusler alloy, The Physics of Metals and Metallography. 68 (1989) 111–115.

[22] V.A. Chernenko, V. v Kokorin, A.N. Vasil'Ev, Y.I. Savchenko, The behaviour of the elastic constants at the transformation between the modulated phases in Ni2MnGa, Phase Transitions. 43 (1993) 187–191. https://doi.org/10.1080/01411599308207818.

[23] K. Ullakko, J.K. Huang, C. Kantner, R.C. O'Handley, V. v. Kokorin, Large magnetic-field-induced strains in Ni2MnGa single crystals, Appl Phys Lett. 69 (1996) 1966–1968. https://doi.org/10.1063/1.117637.

[24] M.B. Moffett, A.E. Clark, M. Wun-Fogle, J. Linberg, J.P. Teter, E.A. McLaughlin, Characterization of Terfenol-D for magnetostrictive transducers, J Acoust Soc Am. 89 (1991) 1448–1455. https://doi.org/10.1121/1.400678.

[25] T. Tadaki, K. Shimizu, High tetragonality of the thermoelastic Fe3Pt martensite and small volume change during the transformation, Scripta Metallurgica. 9 (1975) 771–776. https://doi.org/10.1016/0036-9748(75)90238-0.

[26] S. Kajiwara, W.S. Owen, The reversible martensite transformation in iron-platinum alloys near Fe3Pt, Metallurgical and Materials Transactions B. 5 (1974) 2047–2061. https://doi.org/10.1007/BF02644498.

[27] D.P. Dunne, C.M. Wayman, The effect of austenite ordering on the martensite transformation in Fe-Pt alloys near the composition Fe3Pt: I. Morphology and transformation characteristics, Metallurgical Transactions. 4 (1973) 137–145. https://doi.org/10.1007/BF02649612.

[28] R. Oshima, Successive martensitic transformations in Fe-Pd alloys, Scripta Metallurgica. 15 (1981) 829–833. https://doi.org/10.1016/0036-9748(81)90260-X.

[29] R. Oshima, M. Sugiyama, F.E. Fujita, Tweed structures associated with Fcc-Fct transformations in Fe-Pd alloys, Metallurgical Transactions A. 19 (1988) 803–810. https://doi.org/10.1007/BF02628361.

[30] R. Kainuma, W. Ito, R.Y. Umetsu, V.V. Khovaylo, T. Kanomata, Metamagnetic Shape Memory Effect and Magnetic Properties of Ni-Mn Based Heusler Alloys, Materials Science Forum. 684 (2011) 139–150. https://doi.org/10.4028/www.scientific.net/MSF.684.139.

[31] V.D. Buchelnikov, P. Entel, S. v. Taskaev, V. v. Sokolovskiy, A. Hucht, M. Ogura, H. Akai, M.E. Gruner, S.K. Nayak, Monte Carlo study of the influence of antiferromagnetic exchange interactions on the phase transitions of ferromagnetic Ni-Mn-X alloys (X=In,Sn,Sb), Phys Rev B. 78 (2008) 1–11. https://doi.org/10.1103/PhysRevB.78.184427.

[32] Y. Tanaka, T. Ohmori, K. Oikawa, R. Kainuma, K. Ishida, Ferromagnetic Co-Ni-Al Shape Memory Alloys with $\beta + \gamma$ Two-Phase Structure, Mater Trans. 45 (2004) 427–430. https://doi.org/10.2320/matertrans.45.427.

[33] Z. Liu, S. Yu, H. Yang, G. Wu, Y. Liu, Phase separation and magnetic properties of Co–Ni–Al ferromagnetic shape memory alloys, Intermetallics (Barking). 16 (2008) 447–452. https://doi.org/10.1016/j.intermet.2007.12.004.

[34] V.A. Chernenko, J. Pons, E. Cesari, A.E. Perekos, Martensitic transformation in a ferromagnetic Co–Ni–Ga single crystal, Materials Science and Engineering: A. 378 (2004) 357–360. https://doi.org/10.1016/j.msea.2003.10.361.

[35] J. Dadda, H.J. Maier, I. Karaman, H.E. Karaca, Y.I. Chumlyakov, Pseudoelasticity at elevated temperatures in [001] oriented Co49Ni21Ga30 single crystals under compression, Scr Mater. 55 (2006) 663–666. https://doi.org/10.1016/j.scriptamat.2006.07.005.

[36] Y. Kishi, C. Craciunescu, M. Sato, T. Okazaki, Y. Furuya, M. Wuttig, Microstructures and magnetic properties of rapidly solidified CoNiGa ferromagnetic shape memory alloys, J Magn Magn Mater. 262 (2003) L186–L191. https://doi.org/10.1016/S0304-8853(03)00195-1.

[37] R. Kainuma, N. Satoh, X.J. Liu, I. Ohnuma, K. Ishida, Phase equilibria and Heusler phase stability in the Cu-rich portion of the Cu–Al–Mn system, J Alloys Compd. 266 (1998) 191–200. https://doi.org/10.1016/S0925-8388(97)00425-8.

[38] M.O. Prado, P.M. Decorte, F. Lovey, Martensitic transformation in Cu-Mn-Al alloys, Scripta Metallurgica et Materialia. 33 (1995) 877–883. https://doi.org/10.1016/0956-716X(95)00292-4.

[39] K. Oikawa, T. Ota, T. Ohmori, Y. Tanaka, H. Morito, A. Fujita, R. Kainuma, K. Fukamichi, K. Ishida, Magnetic and martensitic phase transitions in ferromagnetic Ni–Ga–Fe shape memory alloys, Appl Phys Lett. 81 (2002) 5201–5203. https://doi.org/10.1063/1.1532105.

[40] R. Santamarta, J. Font, J. Muntasell, F. Masdeu, J. Pons, E. Cesari, J. Dutkiewicz, Effect of ageing on the martensitic transformation of Ni–Fe–Ga alloys, Scr Mater. 54 (2006) 1105–1109. https://doi.org/10.1016/j.scriptamat.2005.11.062.

[41] H.X. Zheng, M.X. Xia, J. Liu, J.G. Li, Martensitic transformation of highly undercooled Ni–Fe–Ga magnetic shape memory alloys, J Alloys Compd. 388 (2005) 172–176. https://doi.org/10.1016/j.jallcom.2004.07.028.

[42] V.A. Chernenko, C. Seguí, E. Cesari, J. Pons, V. v Kokorin, Sequence of martensitic transformations in Ni-Mn-Ga alloys, Phys Rev B. 57 (1998) 2659–2662. https://doi.org/10.1103/PhysRevB.57.2659.

[43] J. Pons, V.A. Chernenko, R. Santamarta, E. Cesari, Crystal structure of martensitic phases in Ni–Mn–Ga shape memory alloys, Acta Mater. 48 (2000) 3027–3038. https://doi.org/10.1016/S1359-6454(00)00130-0.

[44] Z. Ding, D. Liu, Q. Qi, J. Zhang, Y. Yao, Y. Zhang, D. Cong, J. Zhu, Multistep superelasticity of Ni-Mn-Ga and Ni-Mn-Ga-Co-Cu microwires under stress-temperature coupling, Acta Mater. 140 (2017) 326–336. https://doi.org/10.1016/j.actamat.2017.08.035.

[45] Z.L. Wang, P. Zheng, Z.H. Nie, Y. Ren, Y.D. Wang, P. Müllner, D.C. Dunand, Superelasticity by reversible variants reorientation in a Ni–Mn–Ga microwire with bamboo grains, Acta Mater. 99 (2015) 373–381. https://doi.org/10.1016/j.actamat.2015.08.002.

[46] A. Sozinov, N. Lanska, A. Soroka, W. Zou, 12% magnetic field-induced strain in Ni-Mn-Ga-based non-modulated martensite, Appl Phys Lett. 102 (2013) 021902. https://doi.org/10.1063/1.4775677.

[47] W.H. Wang, Z.H. Liu, Z.W. Shan, J.L. Chen, G.H. Wu, W.S. Zhan, Effect of post-growth annealing and magnetic field on the two-way shape memory effect of Ni52Mn24Ga24 single crystals, J Phys D Appl Phys. 35 (2002) 492–496. https://doi.org/10.1088/0022-3727/35/5/313.

[48] V.A. Chernenko, E. Villa, S. Besseghini, J.M. Barandiaran, Giant two-way shape memory effect in high-temperature Ni–Mn–Ga single crystal, Phys Procedia. 10 (2010) 94–98. https://doi.org/10.1016/j.phpro.2010.11.081.

[49] F. Hu, B. Shen, J. Sun, G. Wu, Large magnetic entropy change in a Heusler alloy Ni52.6Mn23.1Ga24.3 single crystal, Phys Rev B. 64 (2001) 132412. https://doi.org/10.1103/PhysRevB.64.132412.

[50] P.O. Castillo-Villa, D.E. Soto-Parra, J.A. Matutes-Aquino, R.A. Ochoa-Gamboa, A. Planes, L. Mañosa, D. González-Alonso, M. Stipcich, R. Romero, D. Ríos-Jara, H. Flores-Zúñiga, Caloric effects induced by magnetic and mechanical fields in a Ni50Mn25−xGa25Cox magnetic shape memory alloy, Phys Rev B. 83 (2011) 174109. https://doi.org/10.1103/PhysRevB.83.174109.

[51] L. Mañosa, E. Stern-Taulats, A. Planes, P. Lloveras, M. Barrio, J.-L. Tamarit, B. Emre, S. Yüce, S. Fabbrici, F. Albertini, Barocaloric effect in metamagnetic shape memory alloys, Physica Status Solidi (b). 251 (2014) 2114–2119. https://doi.org/10.1002/pssb.201350371.

[52] L. Mañosa, A. Planes, Materials with Giant Mechanocaloric Effects: Cooling by Strength, Advanced Materials. 29 (2017) 1603607. https://doi.org/10.1002/adma.201603607.

[53] V.O. Golub, V.A. Chernenko, A. Apolinario, I.R. Aseguinolaza, J.P. Araujo, O. Salyuk, J.M. Barandiaran, G.N. Kakazei, Negative Magnetoresistance in Nanotwinned NiMnGa Epitaxial Films, Sci Rep. 8 (2018) 15730. https://doi.org/10.1038/s41598-018-34057-8.

[54] D. Pal, K. Mandal, O. Gutfleisch, Large negative magnetoresistance in nickel-rich Ni–Mn–Ga Heusler alloys, J Appl Phys. 107 (2010) 09B103. https://doi.org/10.1063/1.3350912.

[55] T. Paramanik, I. Das, Near room temperature giant magnetocaloric effect and giant negative magnetoresistance in Co, Ga substituted Ni–Mn–In Heusler alloy, J Alloys Compd. 654 (2016) 399–403. https://doi.org/10.1016/j.jallcom.2015.09.096.

[56] A. Çakır, M. Acet, M. Farle, Kinetic arrest and exchange bias in L10 Ni-Mn-Ga, Physica Status Solidi (b). 251 (2014) 2120–2125. https://doi.org/10.1002/pssb.201451301.

[57] F. Tian, K. Cao, Y. Zhang, Y. Zeng, R. Zhang, T. Chang, C. Zhou, M. Xu, X. Song, S. Yang, Giant spontaneous exchange bias triggered by crossover of superspin glass in Sb-doped Ni50Mn38Ga12 Heusler alloys, Sci Rep. 6 (2016) 30801. https://doi.org/10.1038/srep30801.

[58] Y. Ma, Y. Yang, Y. Gao, Y. Hu, Optimization of spontaneous exchange bias in Mn-rich Heusler alloys, Physical Chemistry Chemical Physics. 23 (2021) 17365–17373. https://doi.org/10.1039/D1CP01797G.

[59] Y. Wang, C. Huang, J. Gao, S. Yang, X. Ding, X. Song, X. Ren, Evidence for ferromagnetic strain glass in Ni-Co-Mn-Ga Heusler alloy system, Appl Phys Lett. 101 (2012) 101913. https://doi.org/10.1063/1.4751250.

[60] P. Entel, M.E. Gruner, D. Comtesse, V. v. Sokolovskiy, V.D. Buchelnikov, Interacting magnetic cluster-spin glasses and strain glasses in Ni-Mn based Heusler structured in-

termetallics, Physica Status Solidi (b). 251 (2014) 2135–2148. https://doi.org/10.1002/pssb.201451059.

[61] Y. Ge, O. Söderberg, N. Lanska, A. Sozinov, K. Ullakko, V.K. Lindroos, Crystal structure of three Ni-Mn-Ga alloys in powder and bulk materials, Journal de Physique IV. 112 (2003) 921–924. https://doi.org/10.1051/jp4:20031031.

[62] P.J. Brown, J. Crangle, T. Kanomata, M. Matsumoto, K.U. Neumann, B. Ouladdiaf, K.R.A. Ziebeck, The crystal structure and phase transitions of the magnetic shape memory compound Ni2MnGa, Journal of Physics Condensed Matter. 14 (2002) 10159–10171. https://doi.org/10.1088/0953-8984/14/43/313.

[63] R.W. Overholser, M. Wuttig, D.A. Neumann, Chemical ordering in Ni-Mn-Ga Heusler alloys, Scr Mater. 40 (1999) 1095–1102. https://doi.org/10.1016/S1359-6462(99)00080-9.

[64] V. v Khovailo, T. Takagi, A.N. Vasil'ev, H. Miki, M. Matsumoto, R. Kainuma, On Order-Disorder (L21→B2′) Phase Transition in Ni2+xMn1−xGa Heusler Alloys, Physica Status Solidi (a). 183 (2002) R1–R3. http://arxiv.org/abs/cond-mat/0209547.

[65] I. Aaltio, O. Söderberg, M. Friman, I. Glavatskyy, Y. Ge, N. Glavatska, S.-P. Hannula, Determining the liquidus and ordering temperatures of the ternary NiMn-Ga and quaternary Ni-Mn-Ga-Fe/Cu alloys, in: 8th European Symposium on Martensitic Transformations (ESOMAT 2009), EDP Sciences, Les Ulis, France, 2009: p. 04001. https://doi.org/10.1051/esomat/200904001.

[66] X. Xu, M. Nagasako, W. Ito, R.Y. Umetsu, T. Kanomata, R. Kainuma, Magnetic properties and phase diagram of Ni50Mn50−xGax ferromagnetic shape memory alloys, Acta Mater. 61 (2013) 6712–6723. https://doi.org/10.1016/j.actamat.2013.07.033.

[67] J. Enkovaara, A. Ayuela, A.T. Zayak, P. Entel, L. Nordström, M. Dube, J. Jalkanen, J. Impola, R.M. Nieminen, Magnetically driven shape memory alloys, Materials Science and Engineering: A. 378 (2004) 52–60. https://doi.org/10.1016/j.msea.2003.10.330.

[68] D.Y. Cong, P. Zetterström, Y.D. Wang, R. Delaplane, R.L. Peng, X. Zhao, L. Zuo, Crystal structure and phase transformation in Ni53Mn25Ga22 shape memory alloy from 20K to 473K, Appl Phys Lett. 87 (2005) 111906. https://doi.org/10.1063/1.2043250.

[69] B. Wedel, M. Suzuki, Y. Murakami, C. Wedel, T. Suzuki, D. Shindo, K. Itagaki, Low temperature crystal structure of Ni–Mn–Ga alloys, J Alloys Compd. 290 (1999) 137–143. https://doi.org/10.1016/S0925-8388(99)00198-X.

[70] M.E. Gruner, R. Niemann, P. Entel, R. Pentcheva, U.K. Rößler, K. Nielsch, S. Fähler, Modulations in martensitic Heusler alloys originate from nanotwin ordering, Sci Rep. 8 (2018) 8489. https://doi.org/10.1038/s41598-018-26652-6.

[71] M. Zelený, Nanotwinning and Modulation of Martensitic Structures in Ni2MnGa Alloy: An ab inito Study, Acta Phys Pol A. 134 (2018) 658–661. https://doi.org/10.12693/APhysPolA.134.658.

[72] M. Zelený, L. Straka, A. Sozinov, O. Heczko, Transformation Paths from Cubic to Low-Symmetry Structures in Heusler Ni2MnGa Compound, Sci Rep. 8 (2018) 1–8. https://doi.org/10.1038/s41598-018-25598-z.

[73] V. v. Martynov, X-Ray Diffraction Study of Thermally and Stress-Induced Phase Transformations in Single Crystalline Ni-Mn-Ga Alloys, Journal de Physique IV. 05 (1995) C8-91-C8-99. https://doi.org/10.1051/jp4:1995810.

[74] V. v. Martynov, V. v. Kokorin, The crystal structure of thermally- and stress-induced Martensites in Ni2MnGa single crystals, Journal de Physique III. 2 (1992) 739–749. https://doi.org/10.1051/jp3:1992155.

[75] V.A. Chernenko, E. Cesari, J. Pons, C. Seguí, Phase Transformations in Rapidly Quenched Ni–Mn–Ga Alloys, J Mater Res. 15 (2000) 1496–1504. https://doi.org/10.1557/JMR.2000.0215.

[76] S. Morito, K. Otsuka, Electron microscopy of new martensites with long period stacking order structures in Ni50AlxMn50-x alloys I. Structures and morphologies, Materials Science and Engineering: A. 208 (1996) 47–55. https://doi.org/10.1016/0921-5093(95)10051-2.

[77] J. Pons, R. Santamarta, V.A. Chernenko, E. Cesari, Structure of the layered martensitic phases of Ni–Mn–Ga alloys, Materials Science and Engineering: A. 438–440 (2006) 931–934. https://doi.org/10.1016/j.msea.2006.02.179.

[78] J. Pons, R. Santamarta, V.A. Chernenko, E. Cesari, Long-period martensitic structures of Ni-Mn-Ga alloys studied by high-resolution transmission electron microscopy, J Appl Phys. 97 (2005) 083516. https://doi.org/10.1063/1.1861137.

[79] L. Righi, F. Albertini, E. Villa, A. Paoluzi, G. Calestani, V. Chernenko, S. Besseghini, C. Ritter, F. Passaretti, Crystal structure of 7M modulated Ni–Mn–Ga martensitic phase, Acta Mater. 56 (2008) 4529–4535. https://doi.org/10.1016/j.actamat.2008.05.010.

[80] L. Righi, F. Albertini, L. Pareti, A. Paoluzi, G. Calestani, Commensurate and incommensurate “5M” modulated crystal structures in Ni–Mn–Ga martensitic phases, Acta Mater. 55 (2007) 5237–5245. https://doi.org/10.1016/j.actamat.2007.05.040.

[81] L. Righi, F. Albertini, A. Paoluzi, S. Fabbrici, E. Villa, G. Calestani, S. Besseghini, Incommensurate and Commensurate Structural Modulation in Martensitic Phases of FSMA, Materials Science Forum. 635 (2009) 33–41. https://doi.org/10.4028/www.scientific.net/MSF.635.33.

[82] L. Righi, F. Albertini, G. Calestani, L. Pareti, A. Paoluzi, C. Ritter, P.A. Algarabel, L. Morellon, M. Ricardo Ibarra, Incommensurate modulated structure of the ferromagnetic shape-memory Ni2MnGa martensite, J Solid State Chem. 179 (2006) 3525–3533. https://doi.org/10.1016/j.jssc.2006.07.005.

[83] I. Glavatskyy, N. Glavatska, I. Urubkov, J.-U. Hoffman, F. Bourdarot, Crystal and magnetic structure temperature evolution in Ni–Mn–Ga magnetic shape memory martensite, Materials Science and Engineering: A. 481 (2008) 298–301. https://doi.org/10.1016/j.msea.2007.02.139.

[84] C.P. Opeil, B. Mihaila, R.K. Schulze, L. Mañosa, A. Planes, W.L. Hults, R.A. Fisher, P.S. Riseborough, P.B. Littlewood, J.L. Smith, J.C. Lashley, Combined experimental and theoretical investigation of the premartensitic transition in Ni2MnGa, Phys Rev Lett. 100 (2008) 1–4. https://doi.org/10.1103/PhysRevLett.100.165703.

[85] P.J. Brown, J. Crangle, T. Kanomata, M. Matsumoto, K.-U. Neumann, B. Ouladdiaf, K.R.A. Ziebeck, The crystal structure and phase transitions of the magnetic shape memory compound Ni2MnGa, Journal of Physics: Condensed Matter. 14 (2002) 10159–10171. https://doi.org/10.1088/0953-8984/14/43/313.

[86] S. Singh, S.R. Barman, D. Pandey, Incommensurate modulations in stoichiometric Ni2MnGa ferromagnetic shape memory alloy: an overview, Z Kristallogr Cryst Mater. 230 (2015) 13–22. https://doi.org/10.1515/zkri-2014-1784.

[87] A.G. Khachaturyan, S.M. Shapiro, S. Semenovskaya, Adaptive phase formation in martensitic transformation, Phys Rev B. 43 (1991) 10832–10843. https://doi.org/10.1103/PhysRevB.43.10832.

[88] R. Niemann, S. Fähler, Geometry of adaptive martensite in Ni-Mn-based Heusler alloys, J Alloys Compd. 703 (2017) 280–288. https://doi.org/10.1016/j.jallcom.2017.01.189.

[89] S. Kaufmann, U.K. Rößler, O. Heczko, M. Wuttig, J. Buschbeck, L. Schultz, S. Fähler, Adaptive Modulations of Martensites, Phys Rev Lett. 104 (2010) 145702. https://doi.org/10.1103/PhysRevLett.104.145702.

[90] R. Niemann, U.K. Rößler, M.E. Gruner, O. Heczko, L. Schultz, S. Fähler, The Role of Adaptive Martensite in Magnetic Shape Memory Alloys, Adv Eng Mater. 14 (2012) 562–581. https://doi.org/10.1002/adem.201200058.

[91] J.P. Liu, E. Fullerton, O. Gutfleisch, D.J. Sellmyer, Nanoscale Magnetic Materials and Applications, Springer, 2009. https://doi.org/10.1007/978-0-387-85600-1.

[92] A. Planes, E. Obradó, A. Gonzàlez-Comas, L. Mañosa, Premartensitic Transition Driven by Magnetoelastic Interaction in bcc Ferromagnetic Ni2MnGa, Phys Rev Lett. 79 (1997) 3926–3929. https://doi.org/10.1103/PhysRevLett.79.3926.

[93] A.N. Vasil'ev, V.D. Buchel'nikov, T. Takagi, V. v Khovailo, E.I. Estrin, Shape memory ferromagnets, Physics-Uspekhi. 46 (2003) 559–588. https://doi.org/10.1070/PU2003v046n06ABEH001339.

[94] V.A. Chernenko, J. Pons, C. Seguí, E. Cesari, Premartensitic phenomena and other phase transformations in Ni–Mn–Ga alloys studied by dynamical mechanical analysis and electron diffraction, Acta Mater. 50 (2002) 53–60. https://doi.org/10.1016/S1359-6454(01)00320-2.

[95] U. Stuhr, P. Vorderwisch, V. v. Kokorin, P.-A. Lindgård, Premartensitic phenomena in the ferro- and paramagnetic phases of Ni2MnGa, Phys Rev B. 56 (1997) 14360–14365. https://doi.org/10.1103/PhysRevB.56.14360.

[96] A. Zheludev, S.M. Shapiro, P. Wochner, L.E. Tanner, Precursor effects and premartensitic transformation in Ni2MnGa, Phys Rev B. 54 (1996) 15045–15050. https://doi.org/10.1103/PhysRevB.54.15045.

[97] T. Fukuda, H. Kushida, M. Todai, T. Kakeshita, H. Mori, Crystal structure of the martensite phase in the ferromagnetic shape memory compound Ni2MnGa studied by electron diffraction, Scr Mater. 61 (2009) 473–476. https://doi.org/10.1016/j.scriptamat.2009.04.046.

[98] S.W. D′Souza, J. Nayak, M. Maniraj, A. Rai, R.S. Dhaka, S.R. Barman, D.L. Schlagel, T.A. Lograsso, A. Chakrabarti, Ni2MnGa(100) ferromagnetic shape memory alloy: A surface study, Surf Sci. 606 (2012) 130–136. https://doi.org/10.1016/j.susc.2011.07.023.

[99] H. Bhadeshia, R. Honeycombe, Steels: Microstructure and Properties, Butterworth-Heinemann, 2017. https://linkinghub.elsevier.com/retrieve/pii/B9780750680844X50006.

[100] G. Grimvall, Thermophysical Properties of Materials, Elsevier, 1999. https://doi.org/10.1016/B978-0-444-82794-4.X5000-1.

[101] C. Lexcellent, P. Butaud, E. Foltête, M. Ouisse, Advances in Shape Memory Materials, Springer International Publishing, Cham, 2017. https://doi.org/10.1007/978-3-319-53306-3.

[102] J.M. Jani, S. Huang, M. Leary, A. Subic, Numerical modeling of shape memory alloy linear actuator, Comput Mech. 56 (2015) 443–461. https://doi.org/10.1007/s00466-015-1180-z.

[103] J. Ortfn, A. Planes, L. Delaey, Hysteresis in Shape-Memory Materials, in: The Science of Hysteresis, Elsevier, 2006: pp. 467–553. https://doi.org/10.1016/B978-012480874-4/50023-3.

[104] B. Dutta, A. Çakır, C. Giacobbe, A. Al-Zubi, T. Hickel, M. Acet, J. Neugebauer, Ab initio Prediction of Martensitic and Intermartensitic Phase Boundaries in Ni-Mn-Ga, Phys Rev Lett. 116 (2016) 025503. https://doi.org/10.1103/PhysRevLett.116.025503.

[105] Z. Li, B. Yang, Y. Zhang, C. Esling, N. Zou, X. Zhao, L. Zuo, Crystallographic insights into the intermartensitic transformation in Ni–Mn–Ga alloys, Acta Mater. 74 (2014) 9–17. https://doi.org/10.1016/j.actamat.2014.04.025.

[106] O. Söderberg, A. Sozinov, N. Lanska, Y. Ge, V.K. Lindroos, S.-P. Hannula, Effect of intermartensitic reaction on the co-occurrence of the magnetic and structural transition in Ni–Mn–Ga alloys, Materials Science and Engineering: A. 438–440 (2006) 957–960. https://doi.org/10.1016/j.msea.2006.02.052.

[107] L. Dai, J. Cullen, M. Wuttig, Intermartensitic transformation in a NiMnGa alloy, J Appl Phys. 95 (2004) 6957–6959. https://doi.org/10.1063/1.1687203.

[108] V.V. Kokorin, A.O. Perekos, A.A. Tshcherba, O.M. Babiy, T.V. Efimova, Intermartensitic phase transitions in Ni–Mn–Ga alloy, magnetic field effect, J Magn Magn Mater. 302 (2006) 34–39. https://doi.org/10.1016/j.jmmm.2005.08.010.

[109] A. Çakır, L. Righi, F. Albertini, M. Acet, M. Farle, S. Aktürk, Extended investigation of intermartensitic transitions in Ni-Mn-Ga magnetic shape memory alloys: A detailed phase diagram determination, J Appl Phys. 114 (2013) 183912. https://doi.org/10.1063/1.4831667.

[110] C. Seguí, V.A. Chernenko, J. Pons, E. Cesari, V. Khovailo, T. Takagi, Low temperature-induced intermartensitic phase transformations in Ni–Mn–Ga single crystal, Acta Mater. 53 (2005) 111–120. https://doi.org/10.1016/j.actamat.2004.09.008.

[111] W.H. Wang, Z.H. Liu, J. Zhang, J.L. Chen, G.H. Wu, W.S. Zhan, T.S. Chin, G.H. Wen, X.X. Zhang, Thermoelastic intermartensitic transformation and its internal stress dependency in Ni52Mn24Ga24 single crystals, Phys Rev B. 66 (2002) 052411. https://doi.org/10.1103/PhysRevB.66.052411.

[112] Z. Li, B. Yang, Y. Zhang, C. Esling, N. Zou, X. Zhao, L. Zuo, Crystallographic insights into the intermartensitic transformation in Ni-Mn-Ga alloys, Acta Mater. 74 (2014) 9–17. https://doi.org/10.1016/j.actamat.2014.04.025.

[113] V.A. Chernenko, V. L'vov, J. Pons, E. Cesari, Superelasticity in high-temperature Ni–Mn–Ga alloys, J Appl Phys. 93 (2003) 2394–2399. https://doi.org/10.1063/1.1539532.

[114] A. Pramanick, X.P. Wang, K. An, A.D. Stoica, J. Yi, Z. Gai, C. Hoffmann, X.-L. Wang, Structural modulations and magnetic properties of off-stoichiometric Ni-Mn-Ga magnetic shape memory alloys, Phys Rev B. 85 (2012) 144412. https://doi.org/10.1103/PhysRevB.85.144412.

[115] B.L. Ahuja, B.K. Sharma, S. Mathur, N.L. Heda, M. Itou, A. Andrejczuk, Y. Sakurai, A. Chakrabarti, S. Banik, A.M. Awasthi, S.R. Barman, Magnetic Compton scattering study of Ni2+xMn1−xGa ferromagnetic shape-memory alloys, Phys Rev B. 75 (2007) 134403. https://doi.org/10.1103/PhysRevB.75.134403.

[116] P. Lázpita, J.M. Barandiarán, J. Gutiérrez, J. Feuchtwanger, V.A. Chernenko, M.L. Richard, Magnetic moment and chemical order in off-stoichiometric Ni–Mn–Ga ferromagnetic shape memory alloys, New J Phys. 13 (2011) 033039. https://doi.org/10.1088/1367-2630/13/3/033039.

[117] B.L. Ahuja, G. Ahmed, S. Banik, M. Itou, Y. Sakurai, S.R. Barman, Compton scattering studies of Mn-rich Ni-Mn-Ga ferromagnetic shape memory alloys, Phys Rev B. 79 (2009) 214403. https://doi.org/10.1103/PhysRevB.79.214403.

[118] N. Xu, J.M. Raulot, Z.B. Li, J. Bai, B. Yang, Y.D. Zhang, X.Y. Meng, X. Zhao, L. Zuo, C. Esling, Composition-dependent structural and magnetic properties of Ni–Mn–Ga alloys

studied by ab initio calculations, J Mater Sci. 50 (2015) 3825–3834. https://doi.org/10.1007/s10853-015-8951-y.

[119] A.N. Vasil'ev, A.D. Bozhko, V. v. Khovailo, I.E. Dikshtein, V.G. Shavrov, V.D. Buchelnikov, M. Matsumoto, S. Suzuki, T. Takagi, J. Tani, Structural and magnetic phase transitions in shape-memory alloys Ni2+xMn1-xGa, Phys Rev B. 59 (1999) 1113–1120. https://doi.org/10.1103/PhysRevB.59.1113.

[120] T. Eto, X. Xu, T. Ito, F. Honda, D.X. Li, G. Oomi, F. Nakamura, H. Masumoto, R. Kainuma, T. Kanomata, Martensitic and magnetic transitions in Ni2+MnGa1− ferromagnetic shape memory alloys, J Alloys Compd. 871 (2021) 159480. https://doi.org/10.1016/j.jallcom.2021.159480.

[121] P. Entel, V.D. Buchelnikov, M.E. Gruner, A. Hucht, V. v. Khovailo, S.K. Nayak, A.T. Zayak, Shape Memory Alloys: A Summary of Recent Achievements, Materials Science Forum. 583 (2008) 21–41. https://doi.org/10.4028/www.scientific.net/MSF.583.21.

[122] N. Lanska, O. Söderberg, A. Sozinov, Y. Ge, K. Ullakko, V.K. Lindroos, Composition and temperature dependence of the crystal structure of Ni–Mn–Ga alloys, J Appl Phys. 95 (2004) 8074–8078. https://doi.org/10.1063/1.1748860.

[123] A. Çakır, L. Righi, F. Albertini, M. Acet, M. Farle, S. Aktürk, Extended investigation of intermartensitic transitions in Ni-Mn-Ga magnetic shape memory alloys: A detailed phase diagram determination, J Appl Phys. 114 (2013) 183912. https://doi.org/10.1063/1.4831667.

[124] V. v. Khovailo, V. Novosad, T. Takagi, D.A. Filippov, R.Z. Levitin, A.N. Vasil'ev, Magnetic properties and magnetostructural phase transitions in Ni 2+xMn1-xGa shape memory alloys, Phys Rev B. 70 (2004) 1–6. https://doi.org/10.1103/PhysRevB.70.174413.

[125] V.D. Buchelnikov, V. v. Sokolovskiy, H.C. Herper, H. Ebert, M.E. Gruner, S. v. Taskaev, V. v. Khovaylo, A. Hucht, A. Dannenberg, M. Ogura, H. Akai, M. Acet, P. Entel, First-principles and Monte Carlo study of magnetostructural transition and magnetocaloric properties of Ni2+xMn1-xGa, Phys Rev B. 81 (2010) 1–19. https://doi.org/10.1103/PhysRevB.81.094411.

[126] F. Albertini, S. Fabbrici, A. Paoluzi, J. Kamarad, Z. Arnold, L. Righi, M. Solzi, G. Porcari, C. Pernechele, D. Serrate, P. Algarabel, Reverse Magnetostructural Transitions by Co and In Doping NiMnGa Alloys: Structural, Magnetic, and Magnetoelastic Properties, Materials Science Forum. 684 (2011) 151–163. https://doi.org/10.4028/www.scientific.net/MSF.684.151.

[127] J. Marcos, Ll. Mañosa, A. Planes, F. Casanova, X. Batlle, A. Labarta, B. Martínez, Magnetic field induced entropy change and magnetoelasticity in Ni–Mn–Ga alloys, J Magn Magn Mater. 272–276 (2004) E1595–E1596. https://doi.org/10.1016/j.jmmm.2003.12.1002.

[128] B. Ingale, R. Gopalan, M.M. Raja, V. Chandrasekaran, S. Ram, Magnetostructural transformation, microstructure, and magnetocaloric effect in Ni-Mn-Ga Heusler alloys, J Appl Phys. 102 (2007) 5–10. https://doi.org/10.1063/1.2751489.

[129] J. Mohd Jani, M. Leary, A. Subic, M.A. Gibson, A review of shape memory alloy research, applications and opportunities, Mater Des. 56 (2014) 1078–1113. https://doi.org/10.1016/j.matdes.2013.11.084.

[130] V. Antonucci, A. Martone, Phenomenology of Shape Memory Alloys, in: Shape Memory Alloy Engineering, Elsevier, 2015: pp. 33–56. https://doi.org/10.1016/B978-0-08-099920-3.00002-4.

[131] A. Planes, L. Mãosa, M. Acet, Magnetocaloric effect and its relation to shape-memory properties in ferromagnetic Heusler alloys, Journal of Physics Condensed Matter. 21 (2009). https://doi.org/10.1088/0953-8984/21/23/233201.

[132] J.M.D. Coey, Magnetism and Magnetic Materials, Cambridge University Press, Cambridge, 2010.

[133] A.A. Likhachev, A. Sozinov, K. Ullakko, Modeling the strain response, magneto-mechanical cycling under the external stress, work output and energy losses in Ni–Mn–Ga, Mechanics of Materials. 38 (2006) 551–563. https://doi.org/10.1016/j.mechmat.2005.05.022.

[134] Y.W. Lai, N. Scheerbaum, D. Hinz, O. Gutfleisch, R. Schäfer, L. Schultz, J. McCord, Absence of magnetic domain wall motion during magnetic field induced twin boundary motion in bulk magnetic shape memory alloys, Appl Phys Lett. 90 (2007) 192504. https://doi.org/10.1063/1.2737934.

[135] O. Heczko, Magnetic shape memory effect and magnetization reversal, J Magn Magn Mater. 290–291 (2005) 787–794. https://doi.org/10.1016/j.jmmm.2004.11.397.

[136] P. Müllner, V.A. Chernenko, G. Kostorz, Large cyclic magnetic-field-induced deformation in orthorhombic (14M) Ni–Mn–Ga martensite, J Appl Phys. 95 (2004) 1531–1536. https://doi.org/10.1063/1.1639144.

[137] X. Wang, F. Li, Q. Hu, An anisotropic micromechanical-based model for characterizing the magneto-mechanical behavior of NiMnGa alloys, Smart Mater Struct. 21 (2012) 065021. https://doi.org/10.1088/0964-1726/21/6/065021.

[138] O. Heczko, Magnetic shape memory effect and highly mobile twin boundaries, Materials Science and Technology. 30 (2014) 1559–1578. https://doi.org/10.1179/1743284714Y.0000000599.

[139] E. Pagounis, R. Chulist, M.J. Szczerba, M. Laufenberg, Over 7% magnetic field-induced strain in a Ni-Mn-Ga five-layered martensite, Appl Phys Lett. 105 (2014) 052405. https://doi.org/10.1063/1.4892633.

[140] A. Sozinov, A.A. Likhachev, N. Lanska, K. Ullakko, Giant magnetic-field-induced strain in NiMnGa seven-layered martensitic phase, Appl Phys Lett. 80 (2002) 1746–1748. https://doi.org/10.1063/1.1458075.

[141] A.-G. Olabi, Encyclopedia of Smart Materials, Elsevier, 2022.

[142] D.C. Dunand, P. Müllner, Size Effects on Magnetic Actuation in Ni-Mn-Ga Shape-Memory Alloys, Advanced Materials. 23 (2011) 216–232. https://doi.org/10.1002/adma.201002753.

[143] M. Pötschke, S. Weiss, U. Gaitzsch, D. Cong, C. Hürrich, S. Roth, L. Schultz, Magnetically resettable 0.16% free strain in polycrystalline Ni–Mn–Ga plates, Scr Mater. 63 (2010) 383–386. https://doi.org/10.1016/j.scriptamat.2010.04.027.

[144] U. Gaitzsch, J. Romberg, M. Pötschke, S. Roth, P. Müllner, Stable magnetic-field-induced strain above 1% in polycrystalline Ni–Mn–Ga, Scr Mater. 65 (2011) 679–682. https://doi.org/10.1016/j.scriptamat.2011.07.011.

[145] Z. Li, D. Li, J. Chen, B. Yang, N. Zou, Y. Zhang, C. Esling, X. Zhao, L. Zuo, Crossing twin of Ni–Mn–Ga 7M martensite induced by thermo-mechanical treatment, Acta Mater. 185 (2020) 28–37. https://doi.org/10.1016/j.actamat.2019.11.065.

[146] Z. Zhou, P. Wu, G. Ma, B. Yang, Z. Li, T. Zhou, D. Wang, Y. Du, Large reversible magnetic-field-induced strain in a trained Ni49.5Mn28Ga22.5 polycrystalline alloy, J Alloys Compd. 792 (2019) 399–404. https://doi.org/10.1016/j.jallcom.2019.04.038.

[147] Z. Li, Z. Li, B. Yang, X. He, W. Gan, Y. Zhang, Z. Li, Y. Zhang, C. Esling, X. Zhao, L. Zuo, Over 2% magnetic-field-induced strain in a polycrystalline Ni50Mn28.5Ga21.5 alloy prepared by directional solidification, Materials Science and Engineering: A. 780 (2020) 139170. https://doi.org/10.1016/j.msea.2020.139170.

[148] U. Gaitzsch, M. Pötschke, S. Roth, B. Rellinghaus, L. Schultz, A 1% magnetostrain in polycrystalline 5M Ni–Mn–Ga, Acta Mater. 57 (2009) 365–370. https://doi.org/10.1016/j.actamat.2008.09.017.

[149] A.A. Mendonça, J.F. Jurado, S.J. Stuard, L.E.L. Silva, G.G. Eslava, L.F. Cohen, L. Ghivelder, A.M. Gomes, Giant magnetic-field-induced strain in Ni2MnGa-based polycrystal, J Alloys Compd. 738 (2018) 509–514. https://doi.org/10.1016/j.jallcom.2017.12.197.

[150] M. Chmielus, C. Witherspoon, R.C. Wimpory, A. Paulke, A. Hilger, X. Zhang, D.C. Dunand, P. Müllner, Magnetic-field-induced recovery strain in polycrystalline Ni–Mn–Ga foam, J Appl Phys. 108 (2010) 123526. https://doi.org/10.1063/1.3524503.

[151] C. Witherspoon, P. Zheng, M. Chmielus, D.C. Dunand, P. Müllner, Effect of porosity on the magneto-mechanical behavior of polycrystalline magnetic shape-memory Ni–Mn–Ga foams, Acta Mater. 92 (2015) 64–71. https://doi.org/10.1016/j.actamat.2015.03.038.

[152] C. Witherspoon, P. Zheng, M. Chmielus, S.C. Vogel, D.C. Dunand, P. Müllner, Texture and training of magnetic shape memory foam, Acta Mater. 61 (2013) 2113–2120. https://doi.org/10.1016/j.actamat.2012.12.032.

[153] M. Chmielus, X.X. Zhang, C. Witherspoon, D.C. Dunand, P. Müllner, Giant magnetic-field-induced strains in polycrystalline Ni–Mn–Ga foams, Nat Mater. 8 (2009) 863–866. https://doi.org/10.1038/nmat2527.

[154] V. Laitinen, A. Saren, A. Sozinov, K. Ullakko, Giant 5.8% magnetic-field-induced strain in additive manufactured Ni-Mn-Ga magnetic shape memory alloy, Scr Mater. 208 (2022) 114324. https://doi.org/10.1016/j.scriptamat.2021.114324.

[155] T. Sakon, Y. Adachi, T. Kanomata, Magneto-Structural Properties of Ni2MnGa Ferromagnetic Shape Memory Alloy in Magnetic Fields, Metals (Basel). 3 (2013) 202–224. https://doi.org/10.3390/met3020202.

[156] L. Chen, F.X. Hu, J. Wang, J. Shen, J. Zhang, J.R. Sun, B.G. Shen, J.H. Yin, L.Q. Pan, Magnetoresistance and magnetocaloric effect in metamagnetic alloys Ni45Co5Mn36.5In13.5, J Appl Phys. 107 (2010) 09A940. https://doi.org/10.1063/1.3359806.

[157] T. Krenke, E. Duman, M. Acet, E.F. Wassermann, X. Moya, L. Mañosa, A. Planes, E. Suard, B. Ouladdiaf, Magnetic superelasticity and inverse magnetocaloric effect in Ni-Mn-In, Phys Rev B. 75 (2007) 104414. https://doi.org/10.1103/PhysRevB.75.104414.

[158] N. v. Rama Rao, M. Manivel Raja, S. Esakki Muthu, S. Arumugam, S. Pandian, Pressure-magnetic field induced phase transformation in Ni46Mn41In13 Heusler alloy, J Appl Phys. 116 (2014) 223904. https://doi.org/10.1063/1.4903958.

[159] K. Dadda, S. Alleg, S. Souilah, J.J. Suňol, E. Dhahri, L. Bessais, E.K. Hlil, Critical behavior, magnetic and magnetocaloric properties of melt-spun Ni50Mn35Sn15 ribbons, J Alloys Compd. 735 (2018) 1662–1672. https://doi.org/10.1016/j.jallcom.2017.11.277.

[160] J. Kaštil, J. Kamarád, O. Isnard, Y. Skourski, M. Míšek, Z. Arnold, Effect of pressure and high magnetic field on phase transitions and magnetic properties of Ni1.92Mn1.56Sn0.52 and Ni2MnSn Heusler compounds, J Alloys Compd. 650 (2015) 248–255. https://doi.org/10.1016/j.jallcom.2015.07.284.

[161] P. Lázpita, V.A. Chernenko, J.M. Barandiarán, I. Orue, J. Gutiérrez, J. Feuchtwanger, J.A. Rodriguez-Velamazán, Influence of Magnetic Field on Magnetostructural Transi-

tion in Ni46.4Mn32.8Sn20.8 Heusler Alloy, Materials Science Forum. 635 (2009) 89–95. https://doi.org/10.4028/www.scientific.net/MSF.635.89.

[162] F. Hu, S. Wei, Y. Cao, X. He, K. Xu, Z. Li, Y. Zhang, Y. Kang, C. Tao, Effect of magnetic field on thermal strain, thermal expansion and negative thermal expansion property in a polycrystalline Ni55Mn18Ga27 alloy, Physica B Condens Matter. 638 (2022) 413933. https://doi.org/10.1016/j.physb.2022.413933.

[163] T. Sakon, H. Nagashio, K. Sasaki, S. Susuga, D. Numakura, M. Abe, K. Endo, S. Yamashita, H. Nojiri, T. Kanomata, Thermal strain and magnetization of the ferromagnetic shape memory alloy Ni52Mn25Ga23 in a magnetic field, Journal of Physics and Chemistry of Solids. 74 (2013) 158–165. https://doi.org/10.1016/j.jpcs.2012.09.004.

[164] S. Jeong, K. Inoue, S. Inoue, K. Koterazawa, M. Taya, K. Inoue, Effect of magnetic field on martensite transformation in a polycrystalline Ni2MnGa, Materials Science and Engineering: A. 359 (2003) 253–260. https://doi.org/10.1016/S0921-5093(03)00359-9.

[165] S.Y. Yu, Z.X. Cao, L. Ma, G.D. Liu, J.L. Chen, G.H. Wu, B. Zhang, X.X. Zhang, Realization of magnetic field-induced reversible martensitic transformation in NiCoMnGa alloys, Appl Phys Lett. 91 (2007) 102507. https://doi.org/10.1063/1.2783188.

[166] N.A. Spaldin, M. Fiebig, The Renaissance of Magnetoelectric Multiferroics, Science (1979). 309 (2005) 391–392. https://doi.org/10.1126/science.1113357.

[167] H. Gu, X. Zhang, H. Wei, Y. Huang, S. Wei, Z. Guo, An overview of the magnetoresistance phenomenon in molecular systems, Chem Soc Rev. 42 (2013) 5907. https://doi.org/10.1039/c3cs60074b.

[168] D. Faurie, A.O. Adeyeye, F. Zighem, Prospects toward flexible magnonic systems, J Appl Phys. 130 (2021) 150901. https://doi.org/10.1063/5.0055976.

[169] J.M. Barandiarán, V.A. Chernenko, P. Lázpita, J. Gutiérrez, J. Feuchtwanger, Effect of martensitic transformation and magnetic field on transport properties of Ni-Mn-Ga and Ni-Fe-Ga Heusler alloys, Phys Rev B. 80 (2009) 104404. https://doi.org/10.1103/PhysRevB.80.104404.

[170] S. Singh, R. Rawat, S.R. Barman, Existence of modulated structure and negative magnetoresistance in Ga excess Ni-Mn-Ga, Appl Phys Lett. 99 (2011) 021902. https://doi.org/10.1063/1.3604015.

[171] C. Biswas, R. Rawat, S.R. Barman, Large negative magnetoresistance in a ferromagnetic shape memory alloy: Ni2+xMn1−xGa, Appl Phys Lett. 86 (2005) 202508. https://doi.org/10.1063/1.1925757.

[172] J. Gao, J. Xuan, F. Li, Y. Wan, J. Zhu, Study on magnetoresistance of Ni48Mn22Ga22Co4Cu4 microwires, Solid State Commun. 323 (2021) 114112. https://doi.org/10.1016/j.ssc.2020.114112.

[173] M. Zeng, S.W. Or, Z. Zhu, S.L. Ho, Twin-variant reorientation-induced large magnetoresistance effect in Ni50Mn29Ga21 single crystal, J Appl Phys. 108 (2010) 053716. https://doi.org/10.1063/1.3480794.

[174] S. Bhatti, R. Sbiaa, A. Hirohata, H. Ohno, S. Fukami, S.N. Piramanayagam, Spintronics based random access memory: a review, Materials Today. 20 (2017) 530–548. https://doi.org/10.1016/j.mattod.2017.07.007.

[175] B.M. Wang, Y. Liu, P. Ren, B. Xia, K.B. Ruan, J.B. Yi, J. Ding, X.G. Li, L. Wang, Large Exchange Bias after Zero-Field Cooling from an Unmagnetized State, Phys Rev Lett. 106 (2011) 077203. https://doi.org/10.1103/PhysRevLett.106.077203.

[176] Z.D. Han, B. Qian, D.H. Wang, P. Zhang, X.F. Jiang, C.L. Zhang, Y.W. Du, Magnetic phase separation and exchange bias in off-stoichiometric Ni-Mn-Ga alloys, Appl Phys Lett. 103 (2013) 172403. https://doi.org/10.1063/1.4826654.

[177] L. González-Legarreta, W.O. Rosa, J. García, M. Ipatov, M. Nazmunnahar, L. Escoda, J.J. Suñol, V.M. Prida, R.L. Sommer, J. González, M. Leoni, B. Hernando, Annealing effect on the crystal structure and exchange bias in Heusler Ni45.5Mn43.0In11.5 alloy ribbons, J Alloys Compd. 582 (2014) 588–593. https://doi.org/10.1016/j.jallcom.2013.08.078.

[178] J. Sharma, K.G. Suresh, Observation of giant exchange bias in bulk Mn50Ni42Sn8 Heusler alloy, Appl Phys Lett. 106 (2015) 072405. https://doi.org/10.1063/1.4913268.

[179] W. Zhang, K.M. Krishnan, Epitaxial exchange-bias systems: From fundamentals to future spin-orbitronics, Materials Science and Engineering: R: Reports. 105 (2016) 1–20. https://doi.org/10.1016/j.mser.2016.04.001.

[180] A. Kitanovski, Energy Applications of Magnetocaloric Materials, Adv Energy Mater. 10 (2020) 1903741. https://doi.org/10.1002/aenm.201903741.

[181] P. Debye, Einige Bemerkungen zur Magnetisierung bei tiefer Temperatur, Ann Phys. 386 (1926) 1154–1160. https://doi.org/10.1002/andp.19263862517.

[182] W.F. Giauque, A thermodynamic treatment of certain magnetic effects. A proposed method of producing temperatures considerably below 1° absolute, J Am Chem Soc. 49 (1927) 1864–1870. https://doi.org/10.1021/ja01407a003.

[183] V.K. Pecharsky, K.A. Gschneidner, Jr., Giant Magnetocaloric Effect in Gd5(Si2Ge2), Phys Rev Lett. 78 (1997) 4494–4497. https://doi.org/10.1103/PhysRevLett.78.4494.

[184] V. Franco, J.S. Blázquez, B. Ingale, A. Conde, The magnetocaloric effect and magnetic refrigeration near room temperature: Materials and models, Annu Rev Mater Res. 42 (2012) 305–342. https://doi.org/10.1146/annurev-matsci-062910-100356.

[185] R. Varga, T. Ryba, Z. Vargova, S. Michalik, V. Zhukova, A. Zhukov, J.L. Sanchez Llamazares, A. Quintana-Nedelcos, Magnetocaloric effects in magnetic microwires for magnetic refrigeration applications, in: Magnetic Nano- and Microwires, Elsevier, 2015: pp. 569–587. https://doi.org/10.1016/B978-0-08-100164-6.00019-9.

[186] A. Smith, C.R.H. Bahl, R. Bjørk, K. Engelbrecht, K.K. Nielsen, N. Pryds, Materials Challenges for High Performance Magnetocaloric Refrigeration Devices, Adv Energy Mater. 2 (2012) 1288–1318. https://doi.org/10.1002/aenm.201200167.

[187] V. Chaudhary, X. Chen, R.V. Ramanujan, Iron and manganese based magnetocaloric materials for near room temperature thermal management, Prog Mater Sci. 100 (2019) 64–98. https://doi.org/10.1016/j.pmatsci.2018.09.005.

[188] N.A. de Oliveira, P.J. von Ranke, Magnetocaloric effect around a magnetic phase transition, Phys Rev B. 77 (2008) 214439. https://doi.org/10.1103/PhysRevB.77.214439.

[189] H. Wada, Y. Tanabe, Giant magnetocaloric effect of MnAs1−xSbx, Appl Phys Lett. 79 (2001) 3302–3304. https://doi.org/10.1063/1.1419048.

[190] N.T. Trung, Z.Q. Ou, T.J. Gortenmulder, O. Tegus, K.H.J. Buschow, E. Brück, Tunable thermal hysteresis in MnFe(P,Ge) compounds, Appl Phys Lett. 94 (2009) 102513. https://doi.org/10.1063/1.3095597.

[191] N.T. Trung, L. Zhang, L. Caron, K.H.J. Buschow, E. Brück, Giant magnetocaloric effects by tailoring the phase transitions, Appl Phys Lett. 96 (2010) 172504. https://doi.org/10.1063/1.3399773.

[192] A. Fujita, S. Fujieda, Y. Hasegawa, K. Fukamichi, Itinerant-electron metamagnetic transition and large magnetocaloric effects in La(FexSi1-x)13 compounds and their hydrides, Phys Rev B. 67 (2003) 104416. https://doi.org/10.1103/PhysRevB.67.104416.

[193] R. Kainuma, Y. Imano, W. Ito, Y. Sutou, H. Morito, S. Okamoto, O. Kitakami, K. Oikawa, A. Fujita, T. Kanomata, K. Ishida, Magnetic-field-induced shape recovery by reverse phase transformation, Nature. 439 (2006) 957–960. https://doi.org/10.1038/nature04493.

[194] T. Krenke, E. Duman, M. Acet, E.F. Wassermann, X. Moya, L. Mañosa, A. Planes, Inverse magnetocaloric effect in ferromagnetic Ni–Mn–Sn alloys, Nat Mater. 4 (2005) 450–454. https://doi.org/10.1038/nmat1395.

[195] J. Liu, T. Gottschall, K.P. Skokov, J.D. Moore, O. Gutfleisch, Giant magnetocaloric effect driven by structural transitions, Nat Mater. 11 (2012) 620–626. https://doi.org/10.1038/nmat3334.

[196] X. Zhou, W. Li, H.P. Kunkel, G. Williams, A criterion for enhancing the giant magnetocaloric effect: (Ni–Mn–Ga)—a promising new system for magnetic refrigeration, Journal of Physics: Condensed Matter. 16 (2004) L39–L44. https://doi.org/10.1088/0953-8984/16/6/L02.

[197] S.K. Sarkar, Sarita, P.D. Babu, A. Biswas, V. Siruguri, M. Krishnan, Giant magnetocaloric effect from reverse martensitic transformation in Ni–Mn–Ga–Cu ferromagnetic shape memory alloys, J Alloys Compd. 670 (2016) 281–288. https://doi.org/10.1016/j.jallcom.2016.02.039.

[198] Z. Li, Y. Zhang, C.F. Sánchez-Valdés, J.L. Sánchez Llamazares, C. Esling, X. Zhao, L. Zuo, Giant magnetocaloric effect in melt-spun Ni-Mn-Ga ribbons with magneto-multistructural transformation, Appl Phys Lett. 104 (2014) 044101. https://doi.org/10.1063/1.4863273.

[199] B. Ingale, R. Gopalan, M.M. Raja, V. Chandrasekaran, S. Ram, Magnetostructural transformation, microstructure, and magnetocaloric effect in Ni-Mn-Ga Heusler alloys, J Appl Phys. 102 (2007) 013906. https://doi.org/10.1063/1.2751489.

[200] V. v. Khovaylo, K.P. Skokov, S. v. Taskaev, D.Y. Karpenkov, E.T. Dilmieva, V. v. Koledov, Yu.S. Koshkid’ko, V.G. Shavrov, V.D. Buchelnikov, V. v. Sokolovskiy, I. Bobrovskij, A. Dyakonov, R. Chatterjee, A.N. Vasiliev, Magnetocaloric properties of Ni2+xMn1-xGa with coupled magnetostructural phase transition, J Appl Phys. 127 (2020) 173903. https://doi.org/10.1063/5.0003327.

[201] Z. Li, K. Xu, Y. Zhang, C. Tao, D. Zheng, C. Jing, Two successive magneto-structural transformations and their relation to enhanced magnetocaloric effect for Ni55.8Mn18.1Ga26.1Heusler alloy, Sci Rep. 5 (2015) 1–7. https://doi.org/10.1038/srep15143.

[202] V.D. Buchelnikov, V. v. Sokolovskiy, Magnetocaloric effect in Ni-Mn-X (X = Ga, In, Sn, Sb) Heusler alloys, The Physics of Metals and Metallography. 112 (2011) 633–665. https://doi.org/10.1134/S0031918X11070052.

[203] V. Basso, C.P. Sasso, K.P. Skokov, O. Gutfleisch, V. v. Khovaylo, Hysteresis and magnetocaloric effect at the magnetostructural phase transition of Ni-Mn-Ga and Ni-Mn-Co-Sn Heusler alloys, Phys Rev B. 85 (2012) 014430. https://doi.org/10.1103/PhysRevB.85.014430.

[204] V. Khovaylo, Inconvenient magnetocaloric effect in ferromagnetic shape memory alloys, J Alloys Compd. 577 (2013) S362–S366. https://doi.org/10.1016/j.jallcom.2012.03.035.

[205] V.V. Kokorin, S.M. Konoplyuk, A.E. Perekos, Yu.S. Semenova, Martensitic transformation temperature hysteresis narrowing and magnetocaloric effect in ferromagnetic shape memory alloys Ni–Mn–Ga, J Magn Magn Mater. 321 (2009) 782–785. https://doi.org/10.1016/j.jmmm.2008.11.077.

[206] X. Moya, S. Kar-Narayan, N.D. Mathur, Caloric materials near ferroic phase transitions, Nat Mater. 13 (2014) 439–450. https://doi.org/10.1038/nmat3951.

[207] E. Bonnot, R. Romero, L. Mañosa, E. Vives, A. Planes, Elastocaloric Effect Associated with the Martensitic Transition in Shape-Memory Alloys, Phys Rev Lett. 100 (2008) 125901. https://doi.org/10.1103/PhysRevLett.100.125901.

[208] L. Mañosa, D. González-Alonso, A. Planes, E. Bonnot, M. Barrio, J.-L. Tamarit, S. Aksoy, M. Acet, Giant solid-state barocaloric effect in the Ni–Mn–In magnetic shape-memory alloy, Nat Mater. 9 (2010) 478–481. https://doi.org/10.1038/nmat2731.

[209] C. Cazorla, Novel mechanocaloric materials for solid-state cooling applications, Appl Phys Rev. 6 (2019) 041316. https://doi.org/10.1063/1.5113620.

[210] L. Mañosa, A. Planes, M. Acet, Advanced materials for solid-state refrigeration, J Mater Chem A Mater. 1 (2013) 4925. https://doi.org/10.1039/c3ta01289a.

[211] L. Mañosa, A. Planes, Solid-state cooling by stress: A perspective, Appl Phys Lett. 116 (2020) 050501. https://doi.org/10.1063/1.5140555.

[212] D. Li, Z. Li, J. Yang, Z. Li, B. Yang, H. Yan, D. Wang, L. Hou, X. Li, Y. Zhang, C. Esling, X. Zhao, L. Zuo, Large elastocaloric effect driven by stress-induced two-step structural transformation in a directionally solidified Ni55Mn18Ga27 alloy, Scr Mater. 163 (2019) 116–120. https://doi.org/10.1016/j.scriptamat.2019.01.014.

[213] H. Hou, S. Qian, I. Takeuchi, Materials, physics and systems for multicaloric cooling, Nat Rev Mater. 7 (2022) 633–652. https://doi.org/10.1038/s41578-022-00428-x.

[214] Y. Hu, Z. Li, B. Yang, S. Qian, W. Gan, Y. Gong, Y. Li, D. Zhao, J. Liu, X. Zhao, L. Zuo, D. Wang, Y. Du, Combined caloric effects in a multiferroic Ni–Mn–Ga alloy with broad refrigeration temperature region, APL Mater. 5 (2017) 046103. https://doi.org/10.1063/1.4980161.

[215] Z. Li, Z. Li, D. Li, J. Yang, B. Yang, Y. Hu, D. Wang, Y. Zhang, C. Esling, X. Zhao, L. Zuo, Achieving a broad refrigeration temperature region through the combination of successive caloric effects in a multiferroic Ni50Mn35In15 alloy, Acta Mater. 192 (2020) 52–59. https://doi.org/10.1016/j.actamat.2020.03.043.

[216] H. Qian, J. Guo, Z. Wei, J. Liu, Multicaloric effect in synergic magnetostructural phase transformation Ni-Mn-Ga-In alloys, Phys Rev Mater. 6 (2022) 054401. https://doi.org/10.1103/PhysRevMaterials.6.054401.

[217] E. Stern-Taulats, T. Castán, L. Mañosa, A. Planes, N.D. Mathur, X. Moya, Multicaloric materials and effects, MRS Bull. 43 (2018) 295–299. https://doi.org/10.1557/mrs.2018.72.

[218] T. Gottschall, A. Gràcia-Condal, M. Fries, A. Taubel, L. Pfeuffer, L. Mañosa, A. Planes, K.P. Skokov, O. Gutfleisch, A multicaloric cooling cycle that exploits thermal hysteresis, Nat Mater. 17 (2018) 929–934. https://doi.org/10.1038/s41563-018-0166-6.

[219] P. Entel, V.D. Buchelnikov, V. v. Khovailo, A.T. Zayak, W.A. Adeagbo, M.E. Gruner, H.C. Herper, E.F. Wassermann, Modelling the phase diagram of magnetic shape memory Heusler alloys, J Phys D Appl Phys. 39 (2006) 865–889. https://doi.org/10.1088/0022-3727/39/5/S13.

[220] S. Banik, R. Ranjan, A. Chakrabarti, S. Bhardwaj, N.P. Lalla, A.M. Awasthi, V. Sathe, D.M. Phase, P.K. Mukhopadhyay, D. Pandey, S.R. Barman, Structural studies of Ni2+x

Mn1-x Ga by powder x-ray diffraction and total energy calculations, Phys Rev B. 75 (2007) 1–9. https://doi.org/10.1103/PhysRevB.75.104107.

[221] S. Banik, A. Chakrabarti, U. Kumar, P.K. Mukhopadhyay, A.M. Awasthi, R. Ranjan, J. Schneider, B.L. Ahuja, S.R. Barman, Phase diagram and electronic structure of Ni2+xMn1−xGa, Phys Rev B. 74 (2006) 085110. https://doi.org/10.1103/PhysRevB.74.085110.

[222] S. Banik, P.K. Mukhopadhyay, A.M. Awasthi, S.R. Barman, Structural Studies on Mn Excess and Ga Deficient Ni-Mn-Ga, Adv Mat Res. 52 (2008) 109–114. https://doi.org/10.4028/www.scientific.net/AMR.52.109.

[223] C.M. Li, H. bin Luo, Q.M. Hu, R. Yang, B. Johansson, L. Vitos, First-principles investigation of the composition dependent properties of Ni2+x Mn1+x Ga shape-memory alloys, Phys Rev B. 82 (2010) 1–9. https://doi.org/10.1103/PhysRevB.82.024201.

[224] C. Jiang, G. Feng, S. Gong, H. Xu, Effect of Ni excess on phase transformation temperatures of NiMnGa alloys, Materials Science and Engineering: A. 342 (2003) 231–235. https://doi.org/10.1016/S0921-5093(02)00288-5.

[225] V. v. Khovaylo, V.D. Buchelnikov, R. Kainuma, V. v. Koledov, M. Ohtsuka, V.G. Shavrov, T. Takagi, S. v. Taskaev, A.N. Vasiliev, Phase transitions in Ni2+xMn1-xGa with a high Ni excess, Phys Rev B. 72 (2005) 1–10. https://doi.org/10.1103/PhysRevB.72.224408.

[226] F. Albertini, F. Canepa, S. Cirafici, E.A. Franceschi, M. Napoletano, A. Paoluzi, L. Pareti, M. Solzi, Composition dependence of magnetic and magnetothermal properties of Ni–Mn–Ga shape memory alloys, J Magn Magn Mater. 272–276 (2004) 2111–2112. https://doi.org/10.1016/j.jmmm.2003.12.883.

[227] Y. Ma, C. Jiang, Y. Li, H. Xu, C. Wang, X. Liu, Study of Ni50+xMn25Ga25-x (x = 2-11) as high-temperature shape-memory alloys, Acta Mater. 55 (2007) 1533–1541. https://doi.org/10.1016/j.actamat.2006.10.014.

[228] S. Singh, S. Bhardwaj, A.K. Panda, V.K. Ahire, A. Mitra, A.M. Awasthi, S.R. Barman, Structural, Thermal and Magnetic Properties of Ga Excess Ni-Mn-Ga, Materials Science Forum. 635 (2009) 43–47. https://doi.org/10.4028/www.scientific.net/MSF.635.43.

[229] S.R. Barman, A. Chakrabarti, S. Singh, S. Banik, S. Bhardwaj, P.L. Paulose, B.A. Chalke, A.K. Panda, A. Mitra, A.M. Awasthi, Theoretical prediction and experimental study of a ferromagnetic shape memory alloy: Ga2MnNi, Phys Rev B. 78 (2008) 1–6. https://doi.org/10.1103/PhysRevB.78.134406.

[230] C. Jiang, Y. Muhammad, L. Deng, W. Wu, H. Xu, Composition dependence on the martensitic structures of the Mn-rich NiMnGa alloys, Acta Mater. 52 (2004) 2779–2785. https://doi.org/10.1016/j.actamat.2004.02.024.

[231] M.L. Richard, J. Feuchtwanger, S.M. Allen, R.C. O’Handley, P. Lázpita, J.M. Barandiaran, J. Gutierrez, B. Ouladdiaf, C. Mondelli, T. Lograsso, D. Schlagel, Chemical order in off-stoichiometric Ni-Mn-Ga ferromagnetic shape-memory alloys studied with neutron diffraction, Philosophical Magazine. 87 (2007) 3437–3447. https://doi.org/10.1080/14786430701297582.

[232] P. Lázpita, J.M. Barandiarán, J. Gutiérrez, M. Richard, S.M. Allen, R.C. O’Handley, Magnetic and structural properties of non-stoichiometric Ni-Mn-Ga ferromagnetic shape memory alloys, European Physical Journal: Special Topics. 158 (2008) 149–154. https://doi.org/10.1140/epjst/e2008-00668-0.

[233] V.A. Chernenko, Compositional instability of β-phase in Ni-Mn-Ga alloys, Scr Mater. 40 (1999) 523–527. https://doi.org/10.1016/S1359-6462(98)00494-1.

[234] J. Chaboy, P. Lázpita, J.M. Barandiarán, J. Gutiérrez, M.L. Fernández-Gubieda, N. Kawamura, XAS and XMCD study of the influence of annealing on the atomic ordering and magnetism in an NiMnGa alloy, Journal of Physics: Condensed Matter. 21 (2009) 016002. https://doi.org/10.1088/0953-8984/21/1/016002.

[235] J. Enkovaara, O. Heczko, A. Ayuela, R.M. Nieminen, Coexistence of ferromagnetic and antiferromagnetic order in Mn-doped Ni2MnGa, Phys Rev B. 67 (2003) 14–17. https://doi.org/10.1103/PhysRevB.67.212405.

[236] M. Khan, I. Dubenko, S. Stadler, N. Ali, Magnetic and structural phase transitions in Heusler type alloys Ni 2MnGa1-xinx, Journal of Physics Condensed Matter. 16 (2004) 5259–5266. https://doi.org/10.1088/0953-8984/16/29/017.

[237] P. Cejpek, P. Doležal, P. Opletal, J. Valenta, K. Vlášková, M. Dopita, Temperature versus composition phase diagram and temperature evolution of structure and modulation of Ni2MnGa1-xInx single crystals, J Alloys Compd. 855 (2021) 157327. https://doi.org/10.1016/j.jallcom.2020.157327.

[238] P. Cejpek, P. Proschek, L. Straka, O. Heczko, Dependence of martensite transformation temperature on magnetic field in Ni2MnGa and Ni2MnGa0.95In0.05 single crystals, J Alloys Compd. 908 (2022) 164514. https://doi.org/10.1016/j.jallcom.2022.164514.

[239] J. Liu, J. Wang, L. Zhang, X. Wang, H. Hua, C. Jiang, Effect of isoelectronic substitution on phase transition and magnetic properties of Ni57Mn18Ga25-xInx (0≤x≤8) alloys with Ni excess, J Appl Phys. 117 (2015) 0–4. https://doi.org/10.1063/1.4916804.

[240] L. Zhang, J. Wang, H. Hua, C. Jiang, H. Xu, Tailoring the magnetostructural transition and magnetocaloric properties around room temperature: In-doped Ni-Mn-Ga alloys, Appl Phys Lett. 105 (2014) 1–5. https://doi.org/10.1063/1.4895929.

[241] S. Chatterjee, S. Giri, S. Majumdar, S.K. De, V. v. Koledov, Effect of Sn doping on the martensitic and premartensitic transitions in Ni 2MnGa, J Magn Magn Mater. 324 (2012) 1891–1896. https://doi.org/10.1016/j.jmmm.2012.01.018.

[242] L.S. Barton, R.T. Lazott, E.R. Marsten, Magnetic properties of full Heusler alloys Ni MnGa1−xZx with Z = Sn or Zn, J Appl Phys. 115 (2014) 17A908. https://doi.org/10.1063/1.4861217.

[243] F. Li, M. Su, D. Zhao, J. Liu, Q. Sun, L. Ma, C. Zhen, D. Hou, Exploring a synergistic-type magnetostructural transformation in Ni-Mn-Ga-X (X = Sn, Sb) Heusler alloys, Intermetallics (Barking). 136 (2021) 107262. https://doi.org/10.1016/j.intermet.2021.107262.

[244] Z.Y. Gao, C. Liu, D. Wu, W.J. Ma, J. Zhang, W. Cai, Martensitic transformation and magnetocaloric properties of Sn doping Mn-Ni-Ga alloys, J Magn Magn Mater. 322 (2010) 2488–2492. https://doi.org/10.1016/j.jmmm.2010.03.006.

[245] L. Mañosa, A. Planes, M. Acet, E. Duman, E.F. Wassermann, Magnetic shape memory in Ni–Mn–Ga and Ni–Mn–Al, J Magn Magn Mater. 272–276 (2004) 2090–2092. https://doi.org/10.1016/j.jmmm.2003.12.850.

[246] H. Ishikawa, R.Y. Umetsu, K. Kobayashi, A. Fujita, R. Kainuma, K. Ishida, Atomic ordering and magnetic properties in Ni2Mn(GaxAl1-x) Heusler alloys, Acta Mater. 56 (2008) 4789–4797. https://doi.org/10.1016/j.actamat.2008.05.034.

[247] Y. Xin, Y. Li, C.B. Jiang, H. bin Xu, Martensitic Transformations of Ni54Mn25Ga21-xAlx Shape Memory Alloys, in: Materials Science Forum, 2005: pp. 1991–1994. https://doi.org/10.4028/0-87849-960-1.1991.

[248] A.C. Abhyankar, Y.T. Yu, Y.K. Kuo, G.W. Huang, C.S. Lue, Thermal and transport properties of Ni2MnGa1-xAl x alloys, Intermetallics (Barking). 18 (2010) 2090–2095. https://doi.org/10.1016/j.intermet.2010.06.014.

[249] S. Singh, R.K. Roy, M. Ghosh, A. Mitra, A.K. Panda, Martensitic transformation and magneto-strain in melt spun NiMnGaAl Ferromagnetic Shape Memory Alloys, Intermetallics (Barking). 43 (2013) 147–151. https://doi.org/10.1016/j.intermet.2013.07.018.

[250] B.R. Gautam, I. Dubenko, A.K. Pathak, S. Stadler, N. Ali, The structural and magnetic properties of Ni2Mn1-xBxGa Heusler alloys, J Magn Magn Mater. 321 (2009) 29–33. https://doi.org/10.1016/j.jmmm.2008.07.010.

[251] M. Ramudu, A. Satish Kumar, V. Seshubai, Influence of boron addition on the microstructure, structural and magnetic properties of Ni53.5Mn26.0Ga20.5 alloy, Intermetallics (Barking). 28 (2012) 51–57. https://doi.org/10.1016/j.intermet.2012.03.060.

[252] L. Straka, A. Soroka, O. Heczko, H. Hänninen, A. Sozinov, Mechanically induced demagnetization and remanent magnetization rotation in Ni–Mn–Ga (–B) magnetic shape memory alloy, Scr Mater. 87 (2014) 25–28. https://doi.org/10.1016/j.scriptamat.2014.05.017.

[253] L. Straka, L. Fekete, M. Rameš, E. Belas, O. Heczko, Magnetic coercivity control by heat treatment in Heusler Ni–Mn–Ga(–B) single crystals, Acta Mater. 169 (2019) 109–121. https://doi.org/10.1016/j.actamat.2019.02.045.

[254] Y. Aydogdu, A.S. Turabi, M. Kok, A. Aydogdu, H. Tobe, H.E. Karaca, Effects of the substitution of gallium with boron on the physical and mechanical properties of Ni–Mn–Ga shape memory alloys, Applied Physics A. 117 (2014) 2073–2078. https://doi.org/10.1007/s00339-014-8621-y.

[255] X. Zhang, Q. Liu, X. Zeng, J. Sui, W. Cai, H. Wang, Y. Feng, Microstructure, mechanical properties and shape memory effect of Ni-Mn-Ga-B high-temperature shape memory alloy, Intermetallics (Barking). 68 (2016) 113–117. https://doi.org/10.1016/j.intermet.2015.10.003.

[256] S. Stadler, M. Khan, J. Mitchell, N. Ali, A.M. Gomes, I. Dubenko, A.Y. Takeuchi, A.P. Guimarães, Magnetocaloric properties of Ni2Mn1-xCuxGa, Appl Phys Lett. 88 (2006) 33–36. https://doi.org/10.1063/1.2202751.

[257] A.M. Gomes, M. Khan, S. Stadler, N. Ali, I. Dubenko, A.Y. Takeuchi, A.P. Guimarães, Magnetocaloric properties of the Ni2Mn1-x(Cu,Co)xGa Heusler alloys, J Appl Phys. 99 (2006) 10–13. https://doi.org/10.1063/1.2164415.

[258] C. Jiang, J. Wang, P. Li, A. Jia, H. Xu, Search for transformation from paramagnetic martensite to ferromagnetic austenite: NiMnGaCu alloys, Appl Phys Lett. 95 (2009) 23–26. https://doi.org/10.1063/1.3155199.

[259] M. Kataoka, K. Endo, N. Kudo, T. Kanomata, H. Nishihara, T. Shishido, R.Y. Umetsu, M. Nagasako, R. Kainuma, Martensitic transition, ferromagnetic transition, and their interplay in the shape memory alloys Ni2Mn1-xCuxGa, Phys Rev B. 82 (2010) 1–14. https://doi.org/10.1103/PhysRevB.82.214423.

[260] V. Sokolovskiy, V. Buchelnikov, K. Skokov, O. Gutfleisch, D. Karpenkov, Yu. Koshkid'ko, H. Miki, I. Dubenko, N. Ali, S. Stadler, V. Khovaylo, Magnetocaloric and magnetic properties of Ni2Mn1-x CuxGa Heusler alloys: An insight from the direct measurements and ab inito and Monte Carlo calculations, J Appl Phys. 114 (2013) 183913. https://doi.org/10.1063/1.4826366.

[261] C. Seguí, E. Cesari, Ordering mechanism and kinetics in Ni2Mn1−CuGa ferromagnetic shape memory alloys, J Alloys Compd. 887 (2021) 161302. https://doi.org/10.1016/j.jallcom.2021.161302.

[262] C. Seguí, J. Torrens-Serra, E. Cesari, P. Lázpita, Optimizing the Caloric Properties of Cu-Doped Ni–Mn–Ga Alloys, Materials. 13 (2020) 419. https://doi.org/10.3390/ma13020419.

[263] S.K. Sarkar, Sarita, P.D. Babu, A. Biswas, V. Siruguri, M. Krishnan, Giant magnetocaloric effect from reverse martensitic transformation in Ni–Mn–Ga–Cu ferromagnetic shape memory alloys, J Alloys Compd. 670 (2016) 281–288. https://doi.org/10.1016/j.jallcom.2016.02.039.

[264] C.L. Tan, G.F. Dong, L. Gao, J.H. Sui, Z.Y. Gao, W. Cai, Microstructure, martensitic transformation and mechanical properties of Ni50Mn30Ga20−xCux ferromagnetic shape memory alloys, J Alloys Compd. 538 (2012) 1–4. https://doi.org/10.1016/j.jallcom.2012.05.121.

[265] X. Liao, Y. Wang, G. Fan, E. Liu, J. Shang, S. Yang, H. Luo, X. Song, X. Ren, K. Otsuka, High damping capacity of a Ni-Cu-Mn-Ga alloy in wide ambient-temperature range, J Alloys Compd. 695 (2017) 2400–2405. https://doi.org/10.1016/j.jallcom.2016.11.132.

[266] D.Y. Cong, S. Wang, Y.D. Wang, Y. Ren, L. Zuo, C. Esling, Martensitic and magnetic transformation in Ni–Mn–Ga–Co ferromagnetic shape memory alloys, Materials Science and Engineering: A. 473 (2008) 213–218. https://doi.org/10.1016/j.msea.2007.03.088.

[267] I. Glavatskyy, N. Glavatska, O. Söderberg, S.-P. Hannula, J.-U. Hoffmann, Transformation temperatures and magnetoplasticity of Ni–Mn–Ga alloyed with Si, In, Co or Fe, Scr Mater. 54 (2006) 1891–1895. https://doi.org/10.1016/j.scriptamat.2006.02.010.

[268] X. Wang, J.-M. Wang, H. Hua, C.-B. Jiang, Phase transition of Ni55−xCoxMn20Ga25 ($8.5 \leq x \leq 11.0$) alloys with different compositions and magnetic fields, Rare Metals. (2016) 1–7. https://doi.org/10.1007/s12598-016-0828-y.

[269] M. Khan, I. Dubenko, S. Stadler, N. Ali, The structural and magnetic properties of Ni2Mn1−xMxGa (M=Co, Cu), J Appl Phys. 97 (2005) 10M304. https://doi.org/10.1063/1.1847131.

[270] V. Sánchez-Alarcos, J.I. Pérez-Landazábal, V. Recarte, C. Gómez-Polo, J.A. Rodríguez-Velamazán, Correlation between composition and phase transformation temperatures in Ni–Mn–Ga–Co ferromagnetic shape memory alloys, Acta Mater. 56 (2008) 5370–5376. https://doi.org/10.1016/j.actamat.2008.07.017.

[271] T. Kanomata, S. Nunoki, K. Endo, M. Kataoka, H. Nishihara, V. v Khovaylo, R.Y. Umetsu, T. Shishido, M. Nagasako, R. Kainuma, K.R.A. Ziebeck, Phase diagram of the ferromagnetic shape memory alloys Ni2MnGa1−xCox, Phys Rev B. 85 (2012) 134421. https://doi.org/10.1103/PhysRevB.85.134421.

[272] M. Zelený, A. Sozinov, L. Straka, T. Björkman, R.M. Nieminen, First-principles study of Co- and Cu-doped Ni2MnGa along the tetragonal deformation path, Phys Rev B. 89 (2014) 184103. https://doi.org/10.1103/PhysRevB.89.184103.

[273] D. Zheng, Z. Li, Y. Zhang, P. Huang, K. Xu, C. Jing, Magnetostructural transformation and its multiple functional properties for Co-doped Ni56Mn18Ga26 Heusler alloy, J Alloys Compd. 694 (2017) 532–538. https://doi.org/10.1016/j.jallcom.2016.10.020.

[274] Y. Ma, S. Yang, Y. Liu, X. Liu, The ductility and shape-memory properties of Ni–Mn–Co–Ga high-temperature shape-memory alloys, Acta Mater. 57 (2009) 3232–3241. https://doi.org/10.1016/j.actamat.2009.03.025.

[275] S. Fabbrici, J. Kamarad, Z. Arnold, F. Casoli, A. Paoluzi, F. Bolzoni, R. Cabassi, M. Solzi, G. Porcari, C. Pernechele, From direct to inverse giant magnetocaloric effect in Co-doped NiMnGa multifunctional alloys, Acta Mater. 59 (2011) 412–419. https://doi.org/10.1016/j.actamat.2010.09.059.

[276] S.Y. Yu, Z.X. Cao, L. Ma, G.D. Liu, J.L. Chen, G.H. Wu, B. Zhang, X.X. Zhang, Realization of magnetic field-induced reversible martensitic transformation in NiCoMnGa alloys, Appl Phys Lett. 91 (2007) 102507. https://doi.org/10.1063/1.2783188.

[277] S. Fabbrici, G. Porcari, F. Cugini, M. Solzi, J. Kamarad, Z. Arnold, R. Cabassi, F. Albertini, Co and In Doped Ni-Mn-Ga Magnetic Shape Memory Alloys: A Thorough Structural, Magnetic and Magnetocaloric Study, Entropy. 16 (2014) 2204–2222. https://doi.org/10.3390/e16042204.

[278] C. Segui, E. Cesari, Composition and atomic order effects on the structural and magnetic transformations in ferromagnetic Ni–Co–Mn–Ga shape memory alloys, J Appl Phys. 111 (2012) 043914. https://doi.org/10.1063/1.3688019.

[279] K. Rolfs, M. Chmielus, R.C. Wimpory, A. Mecklenburg, P. Müllner, R. Schneider, Double twinning in Ni-Mn-Ga-Co, Acta Mater. 58 (2010) 2646–2651. https://doi.org/10.1016/j.actamat.2009.12.051.

[280] S. Yang, Y. Ma, H. Jiang, X. Liu, Microstructure and shape-memory characteristics of Ni56Mn25−xCoxGa19 (x = 4, 8) high-temperature shape-memory alloys, Intermetallics (Barking). 19 (2011) 225–228. https://doi.org/10.1016/j.intermet.2010.08.009.

[281] S. Yang, Y. Liu, C. Wang, X. Liu, Martensite stabilization and thermal cycling stability of two-phase NiMnGa-based high-temperature shape memory alloys, Acta Mater. 60 (2012) 4255–4267. https://doi.org/10.1016/j.actamat.2012.04.029.

[282] A. Nespoli, C.A. Biffi, E. Villa, A. Tuissi, Effect of heating/cooling rate on martensitic transformation of NiMnGa-Co high temperature ferromagnetic shape memory alloys, J Alloys Compd. 690 (2017) 478–484. https://doi.org/10.1016/j.jallcom.2016.08.143.

[283] Z.H. Liu, M. Zhang, W.Q. Wang, W.H. Wang, J.L. Chen, G.H. Wu, F.B. Meng, H.Y. Liu, B.D. Liu, J.P. Qu, Y.X. Li, Magnetic properties and martensitic transformation in quaternary Heusler alloy of NiMnFeGa, J Appl Phys. 92 (2002) 5006–5010. https://doi.org/10.1063/1.1511293.

[284] K. Koho, O. Söderberg, N. Lanska, Y. Ge, X. Liu, L. Straka, J. Vimpari, O. Heczko, V.K. Lindroos, Effect of the chemical composition to martensitic transformation in Ni–Mn–Ga–Fe alloys, Materials Science and Engineering: A. 378 (2004) 384–388. https://doi.org/10.1016/j.msea.2003.10.363.

[285] A. Armstrong, F. Nilsén, M. Rameš, R.H. Colman, P. Veřtát, T. Kmječ, L. Straka, P. Müllner, O. Heczko, Systematic Trends of Transformation Temperatures and Crystal Structure of Ni–Mn–Ga–Fe–Cu Alloys, Shape Memory and Superelasticity. 6 (2020) 97–106. https://doi.org/10.1007/s40830-020-00273-3.

[286] D.E. Soto-Parra, X. Moya, L. Mañosa, A. Planes, H. Flores-Zúñiga, F. Alvarado-Hernández, R.A. Ochoa-Gamboa, J.A. Matutes-Aquino, D. Ríos-Jara, Fe and Co selective substitution in Ni2MnGa: Effect of magnetism on relative phase stability, Philosophical Magazine. 90 (2010) 2771–2792. https://doi.org/10.1080/14786431003745393.

[287] D. Soto, F.A. Hernández, H. Flores-Zúñiga, X. Moya, L. Mañosa, A. Planes, S. Aksoy, M. Acet, T. Krenke, Phase diagram of Fe-doped Ni-Mn-Ga ferromagnetic shape-memory alloys, Phys Rev B. 77 (2008) 1–7. https://doi.org/10.1103/PhysRevB.77.184103.

[288] Y. Zhang, Z. Li, X. He, Y. Huang, K. Xu, C. Jing, Evolution of phase transformation and magnetic properties with Fe content in Ni55− xFexMn20Ga25 Heusler alloys, J Phys D Appl Phys. 51 (2018) 075004. https://doi.org/10.1088/1361-6463/aaa58e.

[289] S. Guo, Y. Zhang, B. Quan, J. Li, Y. Qi, X. Wang, The effect of doped elements on the martensitic transformation in Ni–Mn–Ga magnetic shape memory alloy, Smart Mater Struct. 14 (2005) S236–S238. https://doi.org/10.1088/0964-1726/14/5/010.

[290] Y. Hayasaka, S. Aoto, H. Date, T. Kanomata, X. Xu, R.Y. Umetsu, M. Nagasako, T. Omori, R. Kainuma, T. Sakon, H. Nishihara, K.R.A. Ziebeck, Magnetic phase diagram of ferromagnetic shape memory alloys Ni2MnGa1-xFex, J Alloys Compd. 591 (2014) 280–285. https://doi.org/10.1016/j.jallcom.2013.12.035.

[291] C. Huang, Y. Wang, H. Wu, X. Liao, S. Yang, S. Wei, J. Wang, X. Song, Fe substitution induced intermartensitic transition and its internal stress dependent transforming behavior in Ni–Mn–Ga based alloy, J Alloys Compd. 581 (2013) 812–815. https://doi.org/10.1016/j.jallcom.2013.07.200.

[292] P. Veřtát, H. Seiner, L. Straka, M. Klicpera, A. Sozinov, O. Fabelo, O. Heczko, Hysteretic structural changes within five-layered modulated 10M martensite of Ni–Mn–Ga(–Fe), Journal of Physics: Condensed Matter. 33 (2021) 265404. https://doi.org/10.1088/1361-648X/abfb8f.

[293] M. Klicpera, T. Kovaliuk, K. Drastichová, P. Cejpek, K. Uhlířová, M. Kratochvílová, B. Vondráčková, J. Valenta, R.H. Colman, Synthesis and characterisation of Fe-substituted Ni50Mn25Fe Ga25- single crystals—Development of the phase transformations with Fe content, J Alloys Compd. 908 (2022) 164543. https://doi.org/10.1016/j.jallcom.2022.164543.

[294] R.I. Barabash, O.M. Barabash, D. Popov, G. Shen, C. Park, W. Yang, Multiscale twin hierarchy in NiMnGa shape memory alloys with Fe and Cu, Acta Mater. 87 (2015) 344–349. https://doi.org/10.1016/j.actamat.2015.01.010.

[295] R.K. Singh, M. Manivel Raja, R.P. Mathur, M. Shamsuddin, Effect of Fe substitution on the phase stability and magnetic properties of Mn-rich NiMnGa ferromagnetic shape memory alloys, J Magn Magn Mater. 323 (2011) 574–578. https://doi.org/10.1016/j.jmmm.2010.10.014.

[296] J.M. Guldbakke, M. Chmielus, K. Rolfs, R. Schneider, P. Müllner, A. Raatz, Magnetic, mechanical and fatigue properties of a Ni45.4Mn29.1Ga21.6Fe3.9 single crystal, Scr Mater. 62 (2010) 875–878. https://doi.org/10.1016/j.scriptamat.2010.02.032.

[297] R. Fayzullin, V.D. Buchelnikov, S. Taskaev, M. Drobosyuk, V. v. Khovaylo, Experimental Study of Magnetocaloric Effect in Ni-Fe-Mn-Ga and Ni-Co-Mn-Ga Heusler Alloys, Materials Science Forum. 738–739 (2013) 456–460. https://doi.org/10.4028/www.scientific.net/MSF.738-739.456.

[298] A. Tekgül, K. Şarlar, İ. Küçük, Structural, magnetic and magnetocaloric properties of Ni54Mn14Ga27Fe5: the impact of annealing time, J Therm Anal Calorim. 144 (2021) 1109–1114. https://doi.org/10.1007/s10973-020-09625-8.

[299] N. Singh, R. Arróyave, Magnetocaloric effects in Ni-Mn-Ga-Fe alloys using Monte Carlo simulations, J Appl Phys. 113 (2013) 183904. https://doi.org/10.1063/1.4803544.

[300] Y. Liu, X. Zhang, D. Xing, H. Shen, D. Chen, J. Liu, J. Sun, Magnetocaloric effect (MCE) in melt-extracted Ni–Mn–Ga–Fe Heusler microwires, J Alloys Compd. 616 (2014) 184–188. https://doi.org/10.1016/j.jallcom.2014.07.077.

[301] H.B. Xu, Y. Li, C.B. Jiang, Ni–Mn–Ga high-temperature shape memory alloys, Materials Science and Engineering: A. 438–440 (2006) 1065–1070. https://doi.org/10.1016/j.msea.2006.02.187.

[302] E. Villa, E. Villa, M. Melzi D'Eril, A. Nespoli, F. Passaretti, The role of γ-phase on the thermo-mechanical properties of NiMnGaFe alloys polycrystalline samples, J Alloys Compd. 763 (2018) 883–890. https://doi.org/10.1016/j.jallcom.2018.06.028.

[303] B. Tian, R. Ji, Y.X. Tong, L. Li, Y.F. Zheng, Microstructure, phase transformation and mechanical property of Nb-doped Ni–Mn–Ga alloys, Intermetallics (Barking). 64 (2015) 37–43. https://doi.org/10.1016/j.intermet.2015.04.015.

[304] Z. Ni, X. Guo, Q. Li, Z. Liang, H. Luo, F. Meng, Effect of Zn-doping on the phase transition and magnetic properties of Heusler alloys Ni2MnGa1−xZnx ($x = 0, 0.25, 0.5, 0.75$ and 1), J Magn Magn Mater. 464 (2018) 65–70. https://doi.org/10.1016/j.jmmm.2018.05.044.

[305] J. Janovec, L. Straka, A. Sozinov, O. Heczko, M. Zelený, First-principles study of Zn-doping effects on phase stability and magnetic anisotropy of Ni-Mn-Ga alloys, Mater Res Express. 7 (2020) 026101. https://doi.org/10.1088/2053-1591/ab6925.

[306] T. Sakon, N. Fujimoto, T. Kanomata, Y. Adachi, Magnetostriction of Ni2Mn1-xCrxGa heusler alloys, Metals (Basel). 7 (2017) 1–13. https://doi.org/10.3390/met7100410.

[307] M. Khan, J. Brock, I. Sugerman, Anomalous transport properties of Ni2Mn1−xCrxGa Heusler alloys at the martensite-austenite phase transition, Phys Rev B. 93 (2016) 054419. https://doi.org/10.1103/PhysRevB.93.054419.

[308] U. Devarajan, M. Kannan, R. Thiyagarajan, M. Manivel Raja, N. v. Rama Rao, S. Singh, D. Venkateshwarlu, V. Ganesan, M. Ohashi, S. Arumugam, Coupled magnetostructural transition in Ni-Mn-V-Ga Heusler alloys and its effect on the magnetocaloric and transport properties, J Phys D Appl Phys. 49 (2016) 065001. https://doi.org/10.1088/0022-3727/49/6/065001.

[309] J.I. Pérez-Landazábal, V. Recarte, V. Sánchez-Alarcos, V.A. Chernenko, J.M. Barandiarán, P. Lázpita, J. Rodriguez Fernández, L. Righi, Transformation behavior of Ni–Mn–Ga in the low-temperature limit, Journal of Physics: Condensed Matter. 24 (2012) 276004. https://doi.org/10.1088/0953-8984/24/27/276004.

[310] Y. Xin, Y. Zhou, Martensitic transformation and mechanical properties of Ni-Mn-Ga-V high-temperature shape memory alloys, Intermetallics (Barking). 73 (2016) 50–57. https://doi.org/10.1016/j.intermet.2016.03.005.

[311] Z. Gao, B. Chen, X. Meng, W. Cai, Site preference and phase stability of Ti doping Ni–Mn–Ga shape memory alloys from first-principles calculations, J Alloys Compd. 575 (2013) 297–300. https://doi.org/10.1016/j.jallcom.2013.05.193.

[312] G.F. Dong, Z.Y. Gao, C.L. Tan, J.H. Sui, W. Cai, Phase transformation and magnetic properties of Ni–Mn–Ga–Ti ferromagnetic shape memory alloys, J Alloys Compd. 508 (2010) 47–50. https://doi.org/10.1016/j.jallcom.2010.04.157.

[313] A. Łaszcz, M. Hasiak, J. Kaleta, Effects of Ti and Gd for Ga substitution on microstructure, magnetic and mechanical properties of polycrystalline Ni-Mn-Ga magnetic shape memory alloy, J Magn Magn Mater. 476 (2019) 497–505. https://doi.org/10.1016/j.jmmm.2019.01.031.

[314] D. Li, Z. Li, X. Zhang, B. Yang, D. Wang, X. Zhao, L. Zuo, Enhanced cyclability of elastocaloric effect in a directionally solidified Ni55Mn18Ga26Ti1 alloy with low hysteresis, Scr Mater. 189 (2020) 78–83. https://doi.org/10.1016/j.scriptamat.2020.08.010.

[315] A. Łaszcz, M. Hasiak, J. Kaleta, Structural, magnetic and mechanical properties of dual-phase Ni50Mn25Ga20Gd5 magnetic shape memory alloy, Acta Phys Pol A. 135 (2019) 301–303. https://doi.org/10.12693/APhysPolA.135.301.

[316] A. Łaszcz, M. Hasiak, J. Kaleta, Microstructure, magnetism and nanomechanical properties of Ni50Mn25Ga20Gd5 magnetic shape memory alloy before and after heat treatment, Journal of Rare Earths. 37 (2019) 1224–1229. https://doi.org/10.1016/j.jre.2019.01.004.

[317] J. Sui, X. Zhang, X. Zheng, Z. Yang, W. Cai, X. Tian, Two-way shape memory effect of polycrystalline Ni-Mn-Ga-Gd high-temperature shape memory alloys, Scr Mater. 68 (2013) 679–682. https://doi.org/10.1016/j.scriptamat.2013.01.022.

[318] X. Zhang, J. Sui, Z. Yu, W. Cai, Structure and shape memory effect in a Ni54Mn25Ga20Gd1 alloy with a high transformation temperature, J Alloys Compd. 509 (2011) 8032–8037. https://doi.org/10.1016/j.jallcom.2011.04.144.

[319] A. Łaszcz, M. Hasiak, J. Kaleta, Temperature Dependence of Anisotropy in Ti and Gd Doped NiMnGa-Based Multifunctional Ferromagnetic Shape Memory Alloys, Materials. 13 (2020) 2906. https://doi.org/10.3390/ma13132906.

[320] T. Kovaliuk, B. Vondráčková, J. Valenta, R.H. Colman, M. Klicpera, Evolution of magnetic and structural phase transitions in solid solutions Ni2MnGa1-xGex, J Alloys Compd. 894 (2022) 162441. https://doi.org/10.1016/j.jallcom.2021.162441.

[321] Y. Wu, J. Wang, Y. He, H. Wu, C. Jiang, H. Xu, Microstructure and the correlated martensitic transformation of melt spinning Ni50Mn29Ga21-xTbx (x = 0-1) ribbons, Acta Mater. 104 (2016) 91–100. https://doi.org/10.1016/j.actamat.2015.11.043.

[322] R. Wroblewski, M. Leonowicz, Z. Zengqi, J. Liping, Structure and properties of Ni–Mn–Ga magnetic shape memory alloys containing minor addition of terbium, J Magn Magn Mater. 316 (2007) e595–e598. https://doi.org/10.1016/j.jmmm.2007.03.031.

[323] Y. Wu, J. Wang, H. Hua, C. Jiang, H. Xu, Phase transition and magnetocaloric effect of Ni50Mn29Ga21-xTbx (0 ≤ x ≤ 1) alloys, J Alloys Compd. 632 (2015) 681–685. https://doi.org/10.1016/j.jallcom.2015.01.279.

[324] K. Tsuchiya, A. Tsutsumi, H. Ohtsuka, M. Umemoto, Modification of Ni–Mn–Ga ferromagnetic shape memory alloy by addition of rare earth elements, Materials Science and Engineering: A. 378 (2004) 370–376. https://doi.org/10.1016/j.msea.2003.11.076.

[325] L. Gao, J.H. Sui, W. Cai, Z.Y. Gao, Study of the precipitate phases and martensitic transformation in quaternary Heusler alloys of NiMnGaDy, Solid State Commun. 149 (2009) 257–260. https://doi.org/10.1016/j.ssc.2008.10.030.

[326] W. Tong, L. Liang, J. Xu, H.J. Wang, J. Tian, L.M. Peng, Achieving enhanced mechanical, pseudoelastic and elastocaloric properties in Ni-Mn-Ga alloys via Dy micro-alloying and isothermal mechanical cyclic training, Scr Mater. 209 (2022) 114393. https://doi.org/10.1016/j.scriptamat.2021.114393.

[327] L. Gao, G.F. Dong, Z.Y. Gao, W. Cai, Effect of Dy addition on mechanical and magnetic properties of Mn-rich Ni–Mn–Ga ferromagnetic shape memory alloys, J Alloys Compd. 520 (2012) 281–286. https://doi.org/10.1016/j.jallcom.2012.01.048.

[328] J. Sui, X. Zhang, L. Gao, W. Cai, Microstructure, phase transformation and mechanical properties of Ni-Mn-Ga-Y magnetic shape memory alloys, J Alloys Compd. 509 (2011) 8692–8699. https://doi.org/10.1016/j.jallcom.2011.06.013.

[329] V. Franco, J.S. Blázquez, J.J. Ipus, J.Y. Law, L.M. Moreno-Ramírez, A. Conde, Magnetocaloric effect: From materials research to refrigeration devices, Prog Mater Sci. 93 (2018) 112–232. https://doi.org/10.1016/j.pmatsci.2017.10.005.

[330] M. Ramudu, A.S. Kumar, V. Seshubai, T. Rajasekharan, Correlation of martensitic transformation temperatures of Ni- Mn-Ga/Al-X alloys to non-bonding electron concentration, IOP Conf Ser Mater Sci Eng. 73 (2015) 012074. https://doi.org/10.1088/1757-899X/73/1/012074.

[331] L. Pauling, Electron Transfer in Intermetallic Compounds, Proceedings of the National Academy of Sciences. 36 (1950) 533–538. https://doi.org/10.1073/pnas.36.10.533.

[332] A.R. Miedema, F.R. de Boer, P.F. de Chatel, Empirical description of the role of electronegativity in alloy formation, Journal of Physics F: Metal Physics. 3 (1973) 1558–1576. https://doi.org/10.1088/0305-4608/3/8/012.

[333] A.R. Miedema, P.F. de Châtel, F.R. de Boer, Cohesion in alloys - fundamentals of a semi-empirical model, Physica B+C. 100 (1980) 1–28. https://doi.org/10.1016/0378-4363(80)90054-6.

[334] M. Klicpera, T. Kovaliuk, K. Drastichová, P. Cejpek, K. Uhlířová, M. Kratochvílová, B. Vondráčková, J. Valenta, R.H. Colman, Synthesis and characterisation of Fe-substituted Ni50Mn25FexGa25-x single crystals—Development of the phase transformations with Fe content, J Alloys Compd. 908 (2022). https://doi.org/10.1016/j.jallcom.2022.164543.

[335] V. Kopecký, M. Rameš, P. Veřtát, R.H. Colman, O. Heczko, Full variation of site substitution in ni-mn-ga by ferromagnetic transition metals, Metals (Basel). 11 (2021) 1–18. https://doi.org/10.3390/met11060850.

[336] W. Wang, H. Li, J. Ren, J. Fu, Q. Zhai, Z. Luo, H. Zheng, Enhanced magnetocaloric properties in annealed Heusler Ni–Mn–Sn ribbons, J Magn Magn Mater. 374 (2015) 153–156. https://doi.org/10.1016/j.jmmm.2014.08.042.

[337] P. Czaja, M. Fitta, J. Przewoźnik, W. Maziarz, J. Morgiel, T. Czeppe, E. Cesari, Effect of heat treatment on magnetostructural transformations and exchange bias in Heusler Ni48Mn39.5Sn9.5Al3 ribbons, Acta Mater. 103 (2016) 30–45. https://doi.org/10.1016/j.actamat.2015.10.001.

[338] G. Crouïgneau, L. Porcar, P. Courtois, S. Pairis, E. Mossang, E. Eyraud, D. Bourgault, Annealing effect on the magnetic induced austenite transformation in polycrystalline freestanding Ni-Co-Mn-In films produced by co-sputtering, J Appl Phys. 117 (2015) 035302. https://doi.org/10.1063/1.4906224.

[339] S. Agarwal, E. Stern-Taulats, L. Mañosa, P.K. Mukhopadhyay, Effect of low temperature annealing on magneto-caloric effect of Ni–Mn–Sn–Al ferromagnetic shape memory alloy, J Alloys Compd. 641 (2015) 244–248. https://doi.org/10.1016/j.jallcom.2015.04.069.

[340] F. Chen, W.L. Liu, Y.G. Shi, P. Müllner, Influence of annealing on martensitic transformation and magnetic entropy change in Ni37.7Co12.7Mn40.8Sn8.8 magnetic shape memory alloy ribbon, J Magn Magn Mater. 377 (2015) 137–141. https://doi.org/10.1016/j.jmmm.2014.10.077.

[341] A.S. Kalbfleisch, G. Matthews, P.J. Jacques, On the influence of the cooling rate on the martensitic transformation of Ni-Mn-Sn Heusler alloys, Scr Mater. 114 (2016) 121–124. https://doi.org/10.1016/j.scriptamat.2015.12.005.

[342] V. Sánchez-Alarcos, V. Recarte, J.I. Pérez-Landazábal, G.J. Cuello, Correlation between atomic order and the characteristics of the structural and magnetic transformations in Ni–Mn–Ga shape memory alloys, Acta Mater. 55 (2007) 3883–3889. https://doi.org/10.1016/j.actamat.2007.03.001.

[343] L. Sturz, A. Drevermann, U. Hecht, E. Pagounis, M. Laufenberg, Production and characterization of large single crystals made of ferromagnetic shape memory alloys Ni–Mn–Ga, Phys Procedia. 10 (2010) 81–86. https://doi.org/10.1016/j.phpro.2010.11.079.

[344] D.L. Schlagel, Y.L. Wu, W. Zhang, T.A. Lograsso, Chemical segregation during bulk single crystal preparation of Ni–Mn–Ga ferromagnetic shape memory alloys, J Alloys Compd. 312 (2000) 77–85. https://doi.org/10.1016/S0925-8388(00)01161-0.

[345] D. Kellis, A. Smith, K. Ullakko, P. Müllner, Oriented single crystals of Ni–Mn–Ga with very low switching field, J Cryst Growth. 359 (2012) 64–68. https://doi.org/10.1016/j.jcrysgro.2012.08.014.

[346] J. Wang, C. Jiang, Single-crystal growth of NiMnGa magnetic shape memory alloys, J Cryst Growth. 310 (2008) 865–869. https://doi.org/10.1016/j.jcrysgro.2007.11.197.

[347] J. Liu, J. Wang, H. Zhang, C. Jiang, H. Xu, Effect of directional solidification rate on the solidified morphologies and phase transformations of Ni50.5Mn25Ga24.5 alloy, J Alloys Compd. 541 (2012) 477–482. https://doi.org/10.1016/j.jallcom.2012.07.011.

[348] L. Hou, Y. Dai, Y. Fautrelle, Z. Li, Z. Ren, C. Esling, X. Li, Evolution of microstructure and microsegregation in Ni-Mn-Ga alloys directionally solidified under axial magnetic field, J Alloys Compd. 758 (2018) 54–61. https://doi.org/10.1016/j.jallcom.2018.05.136.

[349] Z. Li, Z. Li, B. Yang, Y. Yang, Y. Zhang, C. Esling, X. Zhao, L. Zuo, Large low-field magnetocaloric effect in directionally solidified Ni55Mn18+xGa27−x (x = 0, 1, 2) alloys, J Magn Magn Mater. 445 (2018) 71–76. https://doi.org/10.1016/j.jmmm.2017.08.090.

[350] Y. Dai, L. Hou, R. Chulist, Y. Fautrelle, Z. Li, B. Yang, C. Esling, Z. Ren, X. Li, A special single variant zone in directionally solidified Ni-Mn-Ga alloy, Scr Mater. 167 (2019) 105–109. https://doi.org/10.1016/j.scriptamat.2019.04.005.

[351] Y. Dai, L. Hou, Y. Fautrelle, Z. Li, C. Esling, Z. Ren, X. Li, Martensitic transformation and detwinning in directionally solidified two-phase Ni-Mn-Ga alloys under uniaxial compression, J Alloys Compd. 722 (2017) 721–728. https://doi.org/10.1016/j.jallcom.2017.06.129.

[352] L. Hou, Y. Dai, Y. Fautrelle, Z. Li, Z. Ren, C. Esling, X. Li, Correlation of microsegregation and variant distribution in directionally solidified Ni-Mn-Ga alloys, Scr Mater. 156 (2018) 95–100. https://doi.org/10.1016/j.scriptamat.2018.07.019.

[353] Y. Zhu, T. Shi, Y. Teng, Micromechanical modeling of stress-induced strain in polycrystalline Ni–Mn–Ga by directional solidification, J Alloys Compd. 645 (2015) 328–334. https://doi.org/10.1016/j.jallcom.2015.05.123.

[354] U. Gaitzsch, M. Pötschke, S. Roth, B. Rellinghaus, L. Schultz, Mechanical training of polycrystalline 7M Ni50Mn30Ga20 magnetic shape memory alloy, Scr Mater. 57 (2007) 493–495. https://doi.org/10.1016/j.scriptamat.2007.05.026.

[355] Y. Zhu, T. Chen, Y. Teng, B. Liu, L. Xue, Experimental study of directionally solidified ferromagnetic shape memory alloy under multi-field coupling, J Magn Magn Mater. 417 (2016) 249–257. https://doi.org/10.1016/j.jmmm.2016.05.097.

[356] L. Wei, X. Zhang, J. Liu, L. Geng, Orientation dependent cyclic stability of the elastocaloric effect in textured Ni-Mn-Ga alloys, AIP Adv. 8 (2018) 055312. https://doi.org/10.1063/1.5028212.

[357] D. Li, Z. Li, X. Zhang, B. Yang, D. Wang, X. Zhao, L. Zuo, Enhanced cyclability of elastocaloric effect in a directionally solidified Ni55Mn18Ga26Ti1 alloy with low hysteresis, Scr Mater. 189 (2020) 78–83. https://doi.org/10.1016/j.scriptamat.2020.08.010.

[358] C. Yu, T. Chen, H. Yin, G. Kang, D. Fang, Modeling the anisotropic elastocaloric effect of textured NiMnGa ferromagnetic shape memory alloys, Int J Solids Struct. 191–192 (2020) 509–528. https://doi.org/10.1016/j.ijsolstr.2019.12.020.

[359] A.S. Kumar, M. Ramudu, V. Seshubai, The role of quenched-in disorder in polycrystalline bulk and melt-spun ribbons of Ni 50 Mn 29 Ga 21, Phase Transitions. 94 (2021) 183–191. https://doi.org/10.1080/01411594.2021.1928125.

[360] J. Wang, C. Jiang, R. Techapiesancharoenkij, D. Bono, S.M. Allen, R.C. O'Handley, Anomalous magnetizations in melt spinning Ni–Mn–Ga, J Appl Phys. 106 (2009) 023923. https://doi.org/10.1063/1.3183947.

[361] N.V. Rama Rao, R. Gopalan, M. Manivel Raja, J. Arout Chelvane, B. Majumdar, V. Chandrasekaran, Magneto-structural transformation studies in melt-spun Ni–Mn–Ga ribbons, Scr Mater. 56 (2007) 405–408. https://doi.org/10.1016/j.scriptamat.2006.10.037.

[362] A.S. Kumar, M. Ramudu, V. Seshubai, Microstructural Evolution on Annealing and its Correlation to Structural and Magnetic Properties of Melt-Spun Ni50Mn29Ga21 Ribbons, J Supercond Nov Magn. 34 (2021) 479–487. https://doi.org/10.1007/s10948-020-05710-z.

[363] F. Chen, M. Zhang, Y. Chai, C. Gong, Martensitic structure and magnetic domain transformation in melt-spun Ni-Mn-Ga ferromagnetic ribbons, Physica Status Solidi (a). 209 (2012) 1557–1561. https://doi.org/10.1002/pssa.201228085.

[364] Z. Li, Y. Jiang, Z. Li, Y. Yang, B. Yang, Y. Zhang, C. Esling, X. Zhao, L. Zuo, Texture inheritance from austenite to 7 M martensite in Ni–Mn–Ga melt-spun ribbons, Results Phys. 6 (2016) 428–433. https://doi.org/10.1016/j.rinp.2016.07.012.

[365] S.Y. Yu, S.S. Yan, S.S. Kang, X.D. Tang, J.F. Qian, J.L. Chen, G.H. Wu, Magnetic field-induced martensite–austenite transformation in Fe-substituted NiMnGa ribbons, Scr Mater. 65 (2011) 9–12. https://doi.org/10.1016/j.scriptamat.2011.03.027.

[366] A. Wójcik, R. Chulist, P. Czaja, M. Kowalczyk, P. Zackiewicz, N. Schell, W. Maziarz, Evolution of microstructure and crystallographic texture of Ni-Mn-Ga melt-spun ribbons exhibiting 1.15% magnetic field-induced strain, Acta Mater. 219 (2021). https://doi.org/10.1016/j.actamat.2021.117237.

[367] J. Wang, C. Jiang, R. Techapiesancharoenkij, D. Bono, S.M. Allen, R.C. O'Handley, Microstructure and magnetic properties of melt spinning Ni–Mn–Ga, Intermetallics (Barking). 32 (2013) 151–155. https://doi.org/10.1016/j.intermet.2012.08.021.

[368] Z.B. Li, J.L. Sánchez Llamazares, C.F. Sánchez-Valdés, Y.D. Zhang, C. Esling, X. Zhao, L. Zuo, Microstructure and magnetocaloric effect of melt-spun Ni52Mn26Ga22 ribbon, Appl Phys Lett. 100 (2012) 174102. https://doi.org/10.1063/1.4704780.

[369] M.J. Szczerba, Giant magnetic-field-induced bending effect in Ni-Mn-Ga-Co-Cu melt-spun ribbons, Scr Mater. 205 (2021) 114203. https://doi.org/10.1016/j.scriptamat.2021.114203.

[370] N.V.R. Rao, R. Gopalan, V. Chandrasekaran, K.G. Suresh, Microstructure, magnetic properties and magnetocaloric effect in melt-spun Ni–Mn–Ga ribbons, J Alloys Compd. 478 (2009) 59–62. https://doi.org/10.1016/j.jallcom.2008.12.015.

[371] M.F. Qian, X.X. Zhang, C. Witherspoon, J.F. Sun, P. Müllner, Superelasticity and shape memory effects in polycrystalline Ni–Mn–Ga microwires, J Alloys Compd. 577 (2013) S296–S299. https://doi.org/10.1016/j.jallcom.2011.10.117.

[372] Y. Zhang, M. Li, Y.D. Wang, J.P. Lin, K.A. Dahmen, Z.L. Wang, P.K. Liaw, Superelasticity and Serration Behavior in Small-Sized NiMnGa Alloys, Adv Eng Mater. 16 (2014) 955–960. https://doi.org/10.1002/adem.201300518.

[373] M.F. Qian, X.X. Zhang, L.S. Wei, L. Geng, H.X. Peng, Effect of chemical ordering annealing on martensitic transformation and superelasticity in polycrystalline Ni–Mn–Ga microwires, J Alloys Compd. 645 (2015) 335–343. https://doi.org/10.1016/j.jallcom.2015.05.118.

[374] M.F. Qian, X.X. Zhang, X. Li, R.C. Zhang, P.G. Martin, J.F. Sun, L. Geng, T.B. Scott, H.X. Peng, Magnetocaloric effect in bamboo-grained Ni-Mn-Ga microwires over a wide working temperature interval, Mater Des. 190 (2020) 108557. https://doi.org/10.1016/j.matdes.2020.108557.

[375] Z. Ding, D. Liu, Q. Qi, J. Zhang, Y. Yao, Y. Zhang, D. Cong, J. Zhu, Multistep superelasticity of Ni-Mn-Ga and Ni-Mn-Ga-Co-Cu microwires under stress-temperature coupling, Acta Mater. 140 (2017) 326–336. https://doi.org/10.1016/j.actamat.2017.08.035.

[376] P. Zheng, N.J. Kucza, C.L. Patrick, P. Müllner, D.C. Dunand, Mechanical and magnetic behavior of oligocrystalline Ni–Mn–Ga microwires, J Alloys Compd. 624 (2015) 226–233. https://doi.org/10.1016/j.jallcom.2014.11.067.

[377] N. Scheerbaum, O. Heczko, J. Liu, D. Hinz, L. Schultz, O. Gutfleisch, Magnetic field-induced twin boundary motion in polycrystalline Ni–Mn–Ga fibres, New J Phys. 10 (2008) 073002. https://doi.org/10.1088/1367-2630/10/7/073002.

[378] L. Shao, Y. Zhao, A. Jiménez, M. Vázquez, Y. Zhang, Shape Memory and Huge Superelasticity in Ni–Mn–Ga Glass-Coated Fibers, Coatings. 7 (2017) 5. https://doi.org/10.3390/coatings7010005.

[379] Z. Ding, J. Zhu, D. Liu, H. Jiang, Q. Qi, Y. Zhang, D. Cong, Ni-Mn-Ga microwire twist caused by stress-magnetic coupling, Mater Des. 130 (2017) 521–527. https://doi.org/10.1016/j.matdes.2017.05.026.

[380] Y. Zhao, M. Kang, J. Xue, J. Ju, M. Wang, S. Wang, Y. Zhang, M. Vázquez, H. Gao, J. Wang, Strain-magnetization effect in superelastic Ni-Mn-Ga microfiber, Scr Mater. 162 (2019) 397–401. https://doi.org/10.1016/j.scriptamat.2018.12.002.

[381] M. Qian, X. Zhang, L. Wei, P. Martin, J. Sun, L. Geng, T.B. Scott, H.X. Peng, Tunable Magnetocaloric Effect in Ni-Mn-Ga Microwires, Sci Rep. 8 (2018). https://doi.org/10.1038/s41598-018-35028-9.

[382] S. Miyazaki, Y.Q. Fu, W.M. Huang, eds., Thin Film Shape Memory Alloys, Cambridge University Press, 2009. https://doi.org/10.1017/CBO9780511635366.

[383] A. Backen, S.R. Yeduru, M. Kohl, S. Baunack, A. Diestel, B. Holzapfel, L. Schultz, S. Fähler, Comparing properties of substrate-constrained and freestanding epitaxial Ni–Mn–Ga films, Acta Mater. 58 (2010) 3415–3421. https://doi.org/10.1016/j.actamat.2010.02.016.

[384] S.R. Yeduru, A. Backen, S. Fähler, L. Schultz, M. Kohl, Large superplastic strain in non-modulated epitaxial Ni–Mn–Ga films, Phys Procedia. 10 (2010) 162–167. https://doi.org/10.1016/j.phpro.2010.11.093.

[385] J.W. Dong, J.Q. Xie, J. Lu, C. Adelmann, C.J. Palmstrøm, J. Cui, Q. Pan, T.W. Shield, R.D. James, S. McKernan, Shape memory and ferromagnetic shape memory effects in single-crystal Ni2MnGa thin films, J Appl Phys. 95 (2004) 2593–2600. https://doi.org/10.1063/1.1643199.

[386] O. Heczko, M. Thomas, J. Buschbeck, L. Schultz, S. Fähler, Epitaxial Ni-Mn-Ga films deposited on SrTi O3 and evidence of magnetically induced reorientation of martensitic variants at room temperature, Appl Phys Lett. 92 (2008) 10–13. https://doi.org/10.1063/1.2883961.

[387] M. Thomas, O. Heczko, J. Buschbeck, Y.W. Lai, J. McCord, S. Kaufmann, L. Schultz, S. Fähler, Stray-Field-Induced Actuation of Free-Standing Magnetic Shape-Memory Films, Advanced Materials. 21 (2009) 3708–3711. https://doi.org/10.1002/adma.200900469.

[388] B. Yang, Y. Zhang, Z. Li, G. Qin, X. Zhao, C. Esling, L. Zuo, Insight into variant selection of seven-layer modulated martensite in Ni–Mn–Ga thin films grown on MgO(0 0 1) substrate, Acta Mater. 93 (2015) 205–217. https://doi.org/10.1016/j.actamat.2015.04.024.

[389] B. Yang, T. Liu, X. Hao, Z. Li, Y. Zhang, G. Qin, M.J. Philippe, C. Esling, X. Zhao, L. Zuo, Crystallography of Martensitic Transformation in Epitaxial Ni50Mn30Ga20 Thin Film, Adv Eng Mater. 20 (2018) 1–7. https://doi.org/10.1002/adem.201700171.

[390] P. Ranzieri, S. Fabbrici, L. Nasi, L. Righi, F. Casoli, V.A. Chernenko, E. Villa, F. Albertini, Epitaxial Ni-Mn-Ga/MgO(1 0 0) thin films ranging in thickness from 10 to 100 nm, Acta Mater. 61 (2013) 263–272. https://doi.org/10.1016/j.actamat.2012.09.056.

[391] B. Yang, I. Soldatov, F. Chen, Y. Zhang, Z. Li, H. Yan, R. Schäfer, D. Wang, C. Esling, X. Zhao, L. Zuo, Observation of magnetic domain evolution in constrained epitaxial Ni–Mn–Ga thin films on MgO(0 0 1) substrate, J Mater Sci Technol. 102 (2022) 56–65. https://doi.org/10.1016/j.jmst.2021.06.029.

[392] R. Niemann, A. Backen, S. Kauffmann-Weiss, C. Behler, U.K. Rößler, H. Seiner, O. Heczko, K. Nielsch, L. Schultz, S. Fähler, Nucleation and growth of hierarchical mar-

tensite in epitaxial shape memory films, Acta Mater. 132 (2017) 327–334. https://doi.org/10.1016/j.actamat.2017.04.032.

[393] P. Ranzieri, M. Campanini, S. Fabbrici, L. Nasi, F. Casoli, R. Cabassi, E. Buffagni, V. Grillo, C. Magén, F. Celegato, G. Barrera, P. Tiberto, F. Albertini, Achieving Giant Magnetically Induced Reorientation of Martensitic Variants in Magnetic Shape-Memory Ni-Mn-Ga Films by Microstructure Engineering, Advanced Materials. 27 (2015) 4760–4766. https://doi.org/10.1002/adma.201502072.

[394] M. Campanini, L. Nasi, S. Fabbrici, F. Casoli, F. Celegato, G. Barrera, V. Chiesi, E. Bedogni, C. Magén, V. Grillo, G. Bertoni, L. Righi, P. Tiberto, F. Albertini, Magnetic Shape Memory Turns to Nano: Microstructure Controlled Actuation of Free-Standing Nanodisks, Small. 14 (2018) 1–9. https://doi.org/10.1002/smll.201803027.

[395] K. Lünser, A. Diestel, K. Nielsch, S. Fähler, Self-Patterning of Multifunctional Heusler Membranes by Dewetting, Adv Mater Interfaces. 8 (2021) 2100966. https://doi.org/10.1002/admi.202100966.

[396] M. Takhsha Ghahfarokhi, J.A. Arregi, F. Casoli, M. Horký, R. Cabassi, V. Uhlíř, F. Albertini, Microfabricated ferromagnetic-shape-memory Heuslers: The geometry and size effects, Appl Mater Today. 23 (2021) 101058. https://doi.org/10.1016/j.apmt.2021.101058.

[397] O. Heczko, H. Seiner, P. Stoklasová, P. Sedlák, J. Sermeus, C. Glorieux, A. Backen, S. Fähler, M. Landa, Temperature dependence of elastic properties in austenite and martensite of Ni-Mn-Ga epitaxial films, Acta Mater. 145 (2018) 298–305. https://doi.org/10.1016/j.actamat.2017.12.011.

[398] O. Heczko, A. Soroka, S.-P. Hannula, Magnetic shape memory effect in thin foils, Appl Phys Lett. 93 (2008) 022503. https://doi.org/10.1063/1.2957675.

[399] D. Musiienko, A. Saren, K. Ullakko, Magnetic shape memory effect in single crystalline Ni-Mn-Ga foil thinned down to 1μm, Scr Mater. 139 (2017) 152–154. https://doi.org/10.1016/j.scriptamat.2017.06.027.

[400] G. Murasawa, S.R. Yeduru, M. Kohl, Macroscopic inhomogeneous deformation behavior arising in single crystal Ni–Mn–Ga foils under tensile loading, Opt Lasers Eng. 87 (2016) 139–145. https://doi.org/10.1016/j.optlaseng.2015.12.014.

[401] V. Pinneker, R.Yin, C. Eberl, A. Sozinov, Y. Ezer, M. Kohl, Evolution of local strain bands of different orientation in single crystalline Ni–Mn–Ga foils under tension, J Alloys Compd. 577 (2013) S358–S361. https://doi.org/10.1016/j.jallcom.2012.03.004.

[402] V. Pinneker, M. Gueltig, A. Sozinov, M. Kohl, Single phase boundary actuation of a ferromagnetic shape memory foil, Acta Mater. 64 (2014) 179–187. https://doi.org/10.1016/j.actamat.2013.10.025.

[403] M. Reinhold, D. Kiener, W.B. Knowlton, G. Dehm, P. Müllner, Deformation twinning in Ni–Mn–Ga micropillars with 10M martensite, J Appl Phys. 106 (2009) 053906. https://doi.org/10.1063/1.3211327.

[404] D. Musiienko, A. Saren, L. Straka, M. Vronka, J. Kopeček, O. Heczko, A. Sozinov, K. Ullakko, Ultrafast actuation of Ni-Mn-Ga micropillars by pulsed magnetic field, Scr Mater. 162 (2019) 482–485. https://doi.org/10.1016/j.scriptamat.2018.12.009.

[405] D. Musiienko, L. Straka, L. Klimša, A. Saren, A. Sozinov, O. Heczko, K. Ullakko, Giant magnetic-field-induced strain in Ni-Mn-Ga micropillars, Scr Mater. 150 (2018) 173–176. https://doi.org/10.1016/j.scriptamat.2018.03.020.

[406] Y. Boonyongmaneerat, M. Chmielus, D.C. Dunand, P. Müllner, Increasing Magnetoplasticity in Polycrystalline Ni-Mn-Ga by Reducing Internal Constraints through Porosity, Phys Rev Lett. 99 (2007) 247201. https://doi.org/10.1103/PhysRevLett.99.247201.

[407] X.X. Zhang, C. Witherspoon, P. Müllner, D.C. Dunand, Effect of pore architecture on magnetic-field-induced strain in polycrystalline Ni–Mn–Ga, Acta Mater. 59 (2011) 2229–2239. https://doi.org/10.1016/j.actamat.2010.12.026.

[408] P. Gao, B. Tian, J. Xu, Y. Tong, L. Li, Microstructure, phase transformation and mechanical property of porous NiMnGa alloys prepared by one-step sintering, Materials Science and Engineering: A. 788 (2020) 139583. https://doi.org/10.1016/j.msea.2020.139583.

[409] K. Wang, R. Hou, J. Xuan, X. Li, J. Zhu, Shape memory effect and superelasticity of Ni50Mn30Ga20 porous alloy prepared by imitation casting method, Intermetallics (Barking). 149 (2022) 107668. https://doi.org/10.1016/j.intermet.2022.107668.

[410] A.E. Perekos, V.A. Chernenko, S.A. Bunyaev, V.P. Zalutskiy, T. v. Ruzhitskaya, O.F. Boitsov, G.N. Kakazei, Structure and magnetic properties of highly dispersed Ni-Mn-Ga powders prepared by spark-erosion, J Appl Phys. 112 (2012) 093909. https://doi.org/10.1063/1.4764017.

[411] V.C. Solomon, J.-I. Hong, Y. Tang, A.E. Berkowitz, D.J. Smith, Electron microscopy investigation of spark-eroded Ni–Mn–Ga ferromagnetic shape-memory alloy particles, Scr Mater. 56 (2007) 593–596. https://doi.org/10.1016/j.scriptamat.2006.12.034.

[412] P. Ochin, A. v. Gilchuk, G.E. Monastyrsky, Y. Koval, A.A. Shcherba, S.N. Zaharchenko, Martensitic Transformation in Spark Plasma Sintered Compacts of Ni-Mn-Ga Powders Prepared by Spark Erosion Method in Cryogenic Liquids, Materials Science Forum. 738–739 (2013) 451–455. https://doi.org/10.4028/www.scientific.net/MSF.738-739.451.

[413] F. Nilsén, I. Aaltio, Y. Ge, T. Lindroos, S.P. Hannula, Characterization of Gas Atomized Ni-Mn-Ga Powders, Mater Today Proc. 2 (2015) S879–S882. https://doi.org/10.1016/j.matpr.2015.07.422.

[414] B. Tian, F. Chen, Y.X. Tong, L. Li, Y.F. Zheng, Phase Transformation and Magnetic Property of Ni-Mn-Ga Powders Prepared by Dry Ball Milling, J Mater Eng Perform. 21 (2012) 2530–2534. https://doi.org/10.1007/s11665-012-0365-2.

[415] K. Vallal Peruman, M. Mahendran, Ball milling effect on structural and magnetic properties of Ni–Mn–Ga ferromagnetic nanoparticles, Pure and Applied Chemistry. 83 (2011) 2071–2077. https://doi.org/10.1351/PAC-CON-11-04-04.

[416] G. Cavazzini, F. Cugini, D. Delmonte, G. Trevisi, L. Nasi, S. Ener, D. Koch, L. Righi, M. Solzi, O. Gutfleisch, F. Albertini, Multifunctional Ni-Mn-Ga and Ni-Mn-Cu-Ga Heusler particles towards the nanoscale by ball-milling technique, J Alloys Compd. 872 (2021) 159747. https://doi.org/10.1016/j.jallcom.2021.159747.

[417] Y.D. Wang, Y. Ren, Z.H. Nie, D.M. Liu, L. Zuo, H. Choo, H. Li, P.K. Liaw, J.Q. Yan, R.J. McQueeney, J.W. Richardson, A. Huq, Structural transition of ferromagnetic Ni2MnGa nanoparticles, J Appl Phys. 101 (2007). https://doi.org/10.1063/1.2713370.

[418] B. Tian, F. Chen, Y.X. Tong, L. Li, Y.F. Zheng, Y. Liu, Q.Z. Li, Phase transition of Ni-Mn-Ga alloy powders prepared by vibration ball milling, J Alloys Compd. 509 (2011) 4563–4568. https://doi.org/10.1016/j.jallcom.2011.01.104.

[419] M. Qian, X. Zhang, Z. Jia, X. Wan, L. Geng, Enhanced magnetic refrigeration capacity in Ni-Mn-Ga micro-particles, Mater Des. 148 (2018) 115–123. https://doi.org/10.1016/j.matdes.2018.03.062.

[420] P. Czaja, R. Chulist, A. Wójcik, M. Kowalczyk, P. Zackiewicz, A. Szewczyk, N. Schell, W. Maziarz, Suppression and Recovery of Martensitic Transformation and Magnetism in Mechanically and Thermally Treated Magnetic Shape-Memory Ni−Mn−Ga Melt-Spun Ribbons, Adv Eng Mater. 23 (2021) 2100075. https://doi.org/10.1002/adem.202100075.

[421] M. Qian, X. Zhang, Z. Jia, X. Wan, L. Geng, Enhanced magnetic refrigeration capacity in Ni-Mn-Ga micro-particles, Mater Des. 148 (2018) 115–123. https://doi.org/10.1016/j.matdes.2018.03.062.

[422] B. Tian, F. Chen, Y.X. Tong, L. Li, Y.F. Zheng, Bending properties of epoxy resin matrix composites filled with Ni–Mn–Ga ferromagnetic shape memory alloy powders, Mater Lett. 63 (2009) 1729–1732. https://doi.org/10.1016/j.matlet.2009.05.004.

[423] J. Liu, N. Scheerbaum, S. Kauffmann-Weiss, O. Gutfleisch, NiMn-Based Alloys and Composites for Magnetically Controlled Dampers and Actuators, Adv Eng Mater. 14 (2012) 653–667. https://doi.org/10.1002/adem.201200038.

[424] M. Lahelin, I. Aaltio, O. Heczko, O. Söderberg, Y. Ge, B. Löfgren, S.-P. Hannula, J. Seppälä, DMA testing of Ni–Mn–Ga/polymer composites, Compos Part A Appl Sci Manuf. 40 (2009) 125–129. https://doi.org/10.1016/j.compositesa.2008.10.011.

[425] S. Kauffmann-Weiss, N. Scheerbaum, J. Liu, H. Klauss, L. Schultz, E. Mäder, R. Häßler, G. Heinrich, O. Gutfleisch, Reversible Magnetic Field Induced Strain in Ni2MnGa-Polymer-Composites, Adv Eng Mater. 14 (2012) 20–27. https://doi.org/10.1002/adem.201100128.

[426] B. Tian, F. Chen, Y. Tong, L. Li, Y. Zheng, Magnetic field induced strain and damping behavior of Ni–Mn–Ga particles/epoxy resin composite, J Alloys Compd. 604 (2014) 137–141. https://doi.org/10.1016/j.jallcom.2014.03.100.

[427] S. Glock, V. Michaud, Thermal and damping behaviour of magnetic shape memory alloy composites, Smart Mater Struct. 24 (2015) 065025. https://doi.org/10.1088/0964-1726/24/6/065025.

[428] J. Feuchtwanger, E. Seif, P. Sratongon, H. Hosoda, V.A. Chernenko, Vibration damping of Ni-Mn-Ga/silicone composites, Scr Mater. 146 (2018) 9–12. https://doi.org/10.1016/j.scriptamat.2017.10.028.

[429] F. Nilsén, I. Aaltio, S.-P. Hannula, Comparison of magnetic field controlled damping properties of single crystal Ni-Mn-Ga and Ni-Mn-Ga polymer hybrid composite structures, Compos Sci Technol. 160 (2018) 138–144. https://doi.org/10.1016/j.compscitech.2018.03.026.

[430] P. Sratong-on, V.A. Chernenko, J. Feuchtwanger, H. Hosoda, Magnetic field-induced rubber-like behavior in Ni-Mn-Ga particles/polymer composite, Sci Rep. 9 (2019) 3443. https://doi.org/10.1038/s41598-019-40189-2.

[431] D. Goswami, K.S. Anand, P.P. Jana, S.K. Ghorai, S. Chattopadhyay, J. Das, Synthesis of a robust multifunctional composite with concurrent magnetocaloric effect and enhanced energy absorption capabilities through a tailored processing route, Mater Des. 187 (2020) 108399. https://doi.org/10.1016/j.matdes.2019.108399.

[432] P. Gao, B. Tian, J. Xu, Y. Tong, F. Chen, L. Li, Investigation on porous NiMnGa alloy and its composite with epoxy resin, J Alloys Compd. 892 (2022) 162248. https://doi.org/10.1016/j.jallcom.2021.162248.

[433] T. DebRoy, H.L. Wei, J.S. Zuback, T. Mukherjee, J.W. Elmer, J.O. Milewski, A.M. Beese, A. Wilson-Heid, A. De, W. Zhang, Additive manufacturing of metallic components – Process, structure and properties, Prog Mater Sci. 92 (2018) 112–224. https://doi.org/10.1016/j.pmatsci.2017.10.001.

[434] F. Nilsén, I.F. Ituarte, M. Salmi, J. Partanen, S.-P. Hannula, Effect of process parameters on non-modulated Ni-Mn-Ga alloy manufactured using powder bed fusion, Addit Manuf. 28 (2019) 464–474. https://doi.org/10.1016/j.addma.2019.05.029.

[435] V. Laitinen, A. Salminen, K. Ullakko, First investigation on processing parameters for laser powder bed fusion of Ni-Mn-Ga magnetic shape memory alloy, J Laser Appl. 31 (2019) 022303. https://doi.org/10.2351/1.5096108.

[436] V. Laitinen, A. Sozinov, A. Saren, M. Chmielus, K. Ullakko, Characterization of as-built and heat-treated Ni-Mn-Ga magnetic shape memory alloy manufactured via laser powder bed fusion, Addit Manuf. 39 (2021) 101854. https://doi.org/10.1016/j.addma.2021.101854.

[437] I.F. Ituarte, F. Nilsén, V.K. Nadimpalli, M. Salmi, J. Lehtonen, S.-P. Hannula, Towards the additive manufacturing of Ni-Mn-Ga complex devices with magnetic field induced strain, Addit Manuf. 49 (2022) 102485. https://doi.org/10.1016/j.addma.2021.102485.

[438] W. Maziarz, P. Czaja, R. Chulist, A. Wójcik, Ł. Żrodowski, B. Morończyk, R. Wróblewski, M. Kowalczyk, Microstructure and Magnetic Properties of Selected Laser Melted Ni-Mn-Ga and Ni-Mn-Ga-Fe Powders Derived from as Melt-Spun Ribbons Precursors, Metals (Basel). 11 (2021) 903. https://doi.org/10.3390/met11060903.

[439] M.P. Caputo, A.E. Berkowitz, A. Armstrong, P. Müllner, C.V. Solomon, 4D printing of net shape parts made from Ni-Mn-Ga magnetic shape-memory alloys, Addit Manuf. 21 (2018) 579–588. https://doi.org/10.1016/j.addma.2018.03.028.

[440] S.L. Taylor, R.N. Shah, D.C. Dunand, Ni-Mn-Ga micro-trusses via sintering of 3D-printed inks containing elemental powders, Acta Mater. 143 (2018) 20–29. https://doi.org/10.1016/j.actamat.2017.10.002.

[441] M.P. Caputo, D.R. Waryoba, C. v. Solomon, Sintering effects on additive manufactured Ni–Mn–Ga shape memory alloys: a microstructure and thermal analysis, J Mater Sci. 55 (2020) 5311–5321. https://doi.org/10.1007/s10853-020-04352-9.

[442] I. Suorsa, E. Pagounis, K. Ullakko, Position dependent inductance based on magnetic shape memory materials, Sens Actuators A Phys. 121 (2005) 136–141. https://doi.org/10.1016/j.sna.2005.01.001.

[443] N. Sarawate, M. Dapino, Experimental characterization of the sensor effect in ferromagnetic shape memory Ni–Mn–Ga, Appl Phys Lett. 88 (2006) 121923. https://doi.org/10.1063/1.2189452.

[444] N.N. Sarawate, M.J. Dapino, Dynamic sensing behavior of ferromagnetic shape memory Ni–Mn–Ga, Smart Mater Struct. 18 (2009) 104014. https://doi.org/10.1088/0964-1726/18/10/104014.

[445] J.M. Stephan, E. Pagounis, M. Laufenberg, O. Paul, P. Ruther, A Novel Concept for Strain Sensing Based on the Ferromagnetic Shape Memory Alloy NiMnGa, IEEE Sens J. 11 (2011) 2683–2689. https://doi.org/10.1109/JSEN.2011.2157489.

[446] J.M. Stephan, K. Retan, P. Ruther, O. Paul, On the influence of thermal treatment on strain sensors based on the ferromagnetic shape memory alloy NiMnGa, in: 2011 IEEE SENSORS Proceedings, IEEE, 2011: pp. 85–88. https://doi.org/10.1109/ICSENS.2011.6126996.

[447] A. Hobza, C.L. Patrick, K. Ullakko, N. Rafla, P. Lindquist, P. Müllner, Sensing strain with Ni-Mn-Ga, Sens Actuators A Phys. 269 (2018) 137–144. https://doi.org/10.1016/j.sna.2017.11.002.

[448] B. Holz, L. Riccardi, H. Janocha, D. Naso, MSM Actuators: Design Rules and Control Strategies, Adv Eng Mater. 14 (2012) 668–681. https://doi.org/10.1002/adem.201200045.

[449] R. Techapiesancharoenkij, J. Kostamo, S.M. Allen, R.C. O’Handley, The effect of magnetic stress and stiffness modulus on resonant characteristics of Ni–Mn–Ga ferromagnetic shape memory alloy actuators, J Magn Magn Mater. 323 (2011) 3109–3116. https://doi.org/10.1016/j.jmmm.2011.06.066.

[450] E. Faran, L. Riccardi, D. Shilo, Inertia-Controlled Twinning in Ni–Mn–Ga Actuators: A Discrete Twin-Boundary Dynamics Study, Shape Memory and Superelasticity. 3 (2017) 206–217. https://doi.org/10.1007/s40830-017-0112-5.

[451] K. Matsunaga, N. Niguchi, K. Hirata, Study on Starting Performance of Ni-Mn-Ga Magnetic Shape Memory Alloy Linear Actuator, IEEE Trans Magn. 49 (2013) 2225–2228. https://doi.org/10.1109/TMAG.2013.2240445.

[452] P.G. Lindquist, P. Müllner, Working Ni–Mn–Ga Single Crystals in a Magnetic Field Against a Spring Load, Shape Memory and Superelasticity. 1 (2015) 69–77. https://doi.org/10.1007/s40830-015-0010-7.

[453] J. Ziske, F. Ehle, H. Neubert, A.D. Price, J. Lienig, A Simple Phenomenological Model for Magnetic Shape Memory Actuators, IEEE Trans Magn. 51 (2015) 1–8. https://doi.org/10.1109/TMAG.2014.2338833.

[454] H. Shi, K. Tan, J. Xu, X. Mei, Design and Performance Analysis of Magnetic Shape Memory Alloy Actuator With a Compact Electromagnetic Coil Configuration, IEEE Trans Magn. 56 (2020) 1–13. https://doi.org/10.1109/TMAG.2020.3000039.

[455] K. Schlüter, B. Holz, A. Raatz, Principle Design of Actuators Driven by Magnetic Shape Memory Alloys, Adv Eng Mater. 14 (2012) 682–686. https://doi.org/10.1002/adem.201200078.

[456] K. Wegener, P. Blumenthal, A. Raatz, Development of a miniaturized clamping device driven by magnetic shape memory alloys, J Intell Mater Syst Struct. 25 (2014) 1062–1068. https://doi.org/10.1177/1045389X13505784.

[457] A. Hubert, N. Calchand, Y. le Gorrec, J.-Y. Gauthier, Magnetic shape memory alloys as smart materials for micro-positioning devices, Advanced Electromagnetics. 1 (2012) 75–84. http://aemjournal.org/index.php/AEM/article/view/10.

[458] V. Pinneker, M. Gueltig, A. Sozinov, M. Kohl, Single phase boundary actuation of a ferromagnetic shape memory foil, Acta Mater. 64 (2014) 179–187. https://doi.org/10.1016/j.actamat.2013.10.025.

[459] A. Backen, S.R. Yeduru, A. Diestel, L. Schultz, M. Kohl, S. Fähler, Epitaxial Ni⍰Mn⍰Ga Films for Magnetic Shape Memory Alloy Microactuators, Adv Eng Mater. 14 (2012) 696–709. https://doi.org/10.1002/adem.201200069.

[460] E. Kalimullina, A. Kamantsev, V. Koledov, V. Shavrov, V. Nizhankovskii, A. Irzhak, F. Albertini, S. Fabbrici, P. Ranzieri, P. Ari-Gur, Magnetic shape memory microactuator, Physica Status Solidi (c). 11 (2014) 1023–1025. https://doi.org/10.1002/pssc.201300718.

[461] M. Kohl, M. Schmitt, A. Backen, L. Schultz, B. Krevet, S. Fähler, Ni-Mn-Ga shape memory nanoactuation, Appl Phys Lett. 104 (2014) 043111. https://doi.org/10.1063/1.4863667.

[462] F. Lambrecht, N. Sagardiluz, M. Gueltig, I.R. Aseguinolaza, V.A. Chernenko, M. Kohl, Martensitic transformation in NiMnGa/Si bimorph nanoactuators with ultra-low hysteresis, Appl Phys Lett. 110 (2017) 213104. https://doi.org/10.1063/1.4984058.

[463] C. Lay, I. Aseguinolaza, V. Chernenko, M. Kohl, In-situ characterization of ferromagnetic shape memory alloy / silicon bimorph nanoactuators, in: 14th IEEE International Conference on Nanotechnology, IEEE, 2014: pp. 192–195. https://doi.org/10.1109/NANO.2014.6967989.

[464] E.T. Dilmieva, A. v. Irzhak, A.P. Kamantsev, V. v. Koledov, V.G. Shavrov, R.M. Grechishkin, E.P. Krasnoperov, V.A. Dikan, F. Albertini, S. Fabbrici, L. González-Legarreta, B. Hernando, Rapidly quenched ferromagnetic ribbons with shape memory for magnetically controlled micromechanic devices, Journal of Communications Tech-

nology and Electronics. 62 (2017) 809–819. https://doi.org/10.1134/S106422691707004X.

[465] ETO Magnetic GmbH, MAGNETOSHAPE, (n.d.). https://www.etogruppe.com/en/company/magnetoshape-r.html.

[466] S. Flaga, A. Sioma, Characteristics of Experimental MSMA-Based Pneumatic Valves, in: Conference on Smart Materials, Adaptive Structures and Intelligent Systems (ASME2013), American Society of Mechanical Engineers, 2013. https://doi.org/10.1115/SMASIS2013-3323.

[467] T. Schiepp, E. Pagounis, M. Laufenberg, Magnetic Shape Memory Actuators for Fluidic Applications, in: 9th International Fluid Power Conference (9th IFK), 2014: pp. 24–27.

[468] T. Schiepp, R. Schnetzler, L. Riccardi, M. Laufenberg, E.T.O.M. Gmbh, Energy-efficient multistable valve driven by magnetic shape memory alloys, in: 10th International Fluid Power Conference (10th IFK), 2016: pp. 491–502.

[469] J. Happel, R. Schnetzler, M. Laufenberg, Multistable valve technology with magnetic shape memory alloy as passive element activated by a bidirectional solenoid actuator, in: 12th International Fluid Power Conference (12th IFK), Technische Universität Dresden, 2020: pp. 315–320. https://doi.org/10.25368/2020.8.

[470] J. Happel, E. Pagounis, R. Schnetzler, J. Heider, M. Laufenberg, Multistable proportional valve: An energy efficient approach for high temperature passive magnetic shape memory applications, in: ACTUATOR: International Conference and Exhibition on New Actuator Systems and Applications 2021, 2021: pp. 1–3.

[471] A. Effner, T. Zawada, J. Weber, A Design Approach for a Valve Based on a Magnetic Shape Memory Actuator, Shape Memory and Superelasticity. 6 (2020) 107–114. https://doi.org/10.1007/s40830-020-00274-2.

[472] H. Shi, Z. Liu, H. Wang, X. Mei, Design and performance analysis of hydraulic switching valve driven by magnetic shape memory alloy, Advances in Mechanical Engineering. 13 (2021) 1–15. https://doi.org/10.1177/16878140211016985.

[473] S. Flaga, A. Nowak, F. Stefański, B. Minorowicz, Magnetic Shape Memory Alloys Modelling and Pneumatic Applications, Solid State Phenomena. 248 (2016) 235–242. https://doi.org/10.4028/www.scientific.net/SSP.248.235.

[474] K. Ullakko, L. Wendell, A. Smith, P. Müllner, G. Hampikian, A magnetic shape memory micropump: contact-free, and compatible with PCR and human DNA profiling, Smart Mater Struct. 21 (2012) 115020. https://doi.org/10.1088/0964-1726/21/11/115020.

[475] A.R. Smith, A. Saren, J. Järvinen, K. Ullakko, Characterization of a high-resolution solid-state micropump that can be integrated into microfluidic systems, Microfluid Nanofluidics. 18 (2015) 1255–1263. https://doi.org/10.1007/s10404-014-1524-6.

[476] S. Barker, E. Rhoads, P. Lindquist, M. Vreugdenhil, P. Müllner, Magnetic Shape Memory Micropump for Submicroliter Intracranial Drug Delivery in Rats, J Med Device. 10 (2016). https://doi.org/10.1115/1.4034576.

[477] A. Saren, A.R. Smith, K. Ullakko, Integratable magnetic shape memory micropump for high-pressure, precision microfluidic applications, Microfluid Nanofluidics. 22 (2018) 38. https://doi.org/10.1007/s10404-018-2058-0.

[478] I. Kulagin, M. Li, V. Laitinen, H. Handroos, Review of MSM Actuators: Applications, Challenges, and Potential, IEEE Access. 10 (2022) 83841–83850. https://doi.org/10.1109/ACCESS.2022.3197278.

[479] M.-L. Ku, W. Li, Y. Chen, K.J. Ray Liu, Advances in Energy Harvesting Communications: Past, Present, and Future Challenges, IEEE Communications Surveys & Tutorials. 18 (2016) 1384–1412. https://doi.org/10.1109/COMST.2015.2497324.

[480] S. Rashidi, M.H. Ehsani, M. Shakouri, N. Karimi, Potentials of magnetic shape memory alloys for energy harvesting, J Magn Magn Mater. 537 (2021) 168112. https://doi.org/10.1016/j.jmmm.2021.168112.

[481] M.A.A. Farsangi, H. Sayyaadi, M.R. Zakerzadeh, A novel inertial energy harvester using magnetic shape memory alloy, Smart Mater Struct. 25 (2016) 105024. https://doi.org/10.1088/0964-1726/25/10/105024.

[482] Y. Jing, W. Luping, X. Jin, Design and Implementation of Vibration Energy Harvester Based on MSMA Cantilever Beam, Transactions on Electrical and Electronic Materials. 21 (2020) 399–405. https://doi.org/10.1007/s42341-020-00192-1.

[483] M.A.A. Farsangi, F. Cottone, H. Sayyaadi, M.R. Zakerzadeh, F. Orfei, L. Gammaitoni, Energy harvesting from structural vibrations of magnetic shape memory alloys, Appl Phys Lett. 110 (2017) 103905. https://doi.org/10.1063/1.4978258.

[484] I. Karaman, B. Basaran, H.E. Karaca, A.I. Karsilayan, Y.I. Chumlyakov, Energy harvesting using martensite variant reorientation mechanism in a NiMnGa magnetic shape memory alloy, Appl Phys Lett. 90 (2007) 172505. https://doi.org/10.1063/1.2721143.

[485] M. Kohl, R.Z. Yin, V. Pinneker, Y. Ezer, A. Sozinov, A Miniature Energy Harvesting Device Using Martensite Variant Reorientation, Materials Science Forum. 738–739 (2013) 411–415. https://doi.org/10.4028/www.scientific.net/MSF.738-739.411.

[486] H. Sayyaadi, H. Rostami Najafabadi, M.A. Askari Farsangi, Modeling and parametric studies of magnetic shape memory alloy–based energy harvester, J Intell Mater Syst Struct. 29 (2018) 563–573. https://doi.org/10.1177/1045389X17711817.

[487] A. Saren, D. Musiienko, A.R. Smith, J. Tellinen, K. Ullakko, Modeling and design of a vibration energy harvester using the magnetic shape memory effect, Smart Mater Struct. 24 (2015) 095002. https://doi.org/10.1088/0964-1726/24/9/095002.

[488] A.J. Niskanen, I. Laitinen, Design and Simulation of a Magnetic Shape Memory (MSM) Alloy Energy Harvester, in: State-of-the-Art Research and Application of SMAs Technologies (4th CIMTEC), 2012: pp. 58–62. https://doi.org/10.4028/www.scientific.net/AST.78.58.

[489] G.J. D'Silva, H.P. Feigenbaum, C. Ciocanel, On the power and efficiency of Ni 2 MnGa magnetic shape memory alloy power harvesters, Smart Mater Struct. 31 (2022) 075013. https://doi.org/10.1088/1361-665X/ac72da.

[490] P. Lindquist, T. Hobza, C. Patrick, P. Müllner, Efficiency of Energy Harvesting in Ni–Mn–Ga Shape Memory Alloys, Shape Memory and Superelasticity. 4 (2018) 93–101. https://doi.org/10.1007/s40830-018-0158-z.

[491] M. Gueltig, H. Ossmer, M. Ohtsuka, H. Miki, K. Tsuchiya, T. Takagi, M. Kohl, High Frequency Thermal Energy Harvesting Using Magnetic Shape Memory Films, Adv Energy Mater. 4 (2014) 1400751. https://doi.org/10.1002/aenm.201400751.

[492] M. Gueltig, M. Ohtsuka, H. Miki, T. Takagi, M. Kohl, Thermal energy harvesting by high frequency actuation of magnetic shape memory alloy films, in: 2015 18th International Conference on Solid-State Sensors, Actuators and Microsystems (TRANSDUCERS), IEEE, 2015: pp. 718–721. https://doi.org/10.1109/TRANSDUCERS.2015.7181024.

[493] M.A.A. Farsangi, H. Zohoor, Acoustic energy harvesting via magnetic shape memory alloys, J Phys D Appl Phys. 52 (2019) 135501. https://doi.org/10.1088/1361-6463/aafe99.

[494] A. Greco, C. Aprea, A. Maiorino, C. Masselli, A review of the state of the art of solid-state caloric cooling processes at room-temperature before 2019, International Journal of Refrigeration. 106 (2019) 66–88. https://doi.org/10.1016/j.ijrefrig.2019.06.034.

[495] Magnetocaloric Refrigerator/Freezer, (n.d.). https://www.energy.gov/eere/buildings/downloads/magnetocaloric-refrigeratorfreezer.

[496] C.L. Yaws, The Yaws Handbook of Vapor Pressure, Gulf Professional Publishing, 2015. https://doi.org/10.1016/C2014-0-03590-3.

[497] G.W.H. Höhne, W.F. Hemminger, H.-J. Flammersheim, Differential Scanning Calorimetry, Springer, 2013. http://link.springer.com/10.1007/978-3-662-06710-9.

[498] J.I. Goldstein, D.E. Newbury, J.R. Michael, N.W.M. Ritchie, J.H.J. Scott, D.C. Joy, Scanning Electron Microscopy and X-Ray Microanalysis, Springer, 2018. https://doi.org/10.1007/978-1-4939-6676-9.

[499] B.D. Cullity, S.R. Stock, Elements of X-ray Diffraction, Third Edition, Pearson, 2001.

[500] H.M. Rietveld, A profile refinement method for nuclear and magnetic structures, J Appl Crystallogr. 2 (1969) 65–71. https://doi.org/10.1107/S0021889869006558.

[501] N. Doebelin, R. Kleeberg, Profex: a graphical user interface for the Rietveld refinement program BGMN, J Appl Crystallogr. 48 (2015) 1573–1580. https://doi.org/10.1107/S1600576715014685.

[502] I.D. Brown, B. McMahon, CIF: the computer language of crystallography, Acta Crystallogr B. 58 (2002) 317–324. https://doi.org/10.1107/S0108768102003464.

[503] B.H. Toby, R factors in Rietveld analysis: How good is good enough?, Powder Diffr. 21 (2006) 67–70. https://doi.org/10.1154/1.2179804.

[504] D. Nečas, P. Klapetek, Gwyddion: an open-source software for SPM data analysis, Open Physics. 10 (2012) 181–188. https://doi.org/10.2478/s11534-011-0096-2.

[505] D.E. Laughlin, Magnetic Transformations and Phase Diagrams, Metallurgical and Materials Transactions A. 50 (2019) 2555–2569. https://doi.org/10.1007/s11661-019-05214-z.

[506] V.A. Chernenko, V.A. L'vov, E. Cesari, Martensitic transformation in ferromagnets: experiment and theory, J Magn Magn Mater. 196–197 (1999) 859–860. https://doi.org/10.1016/S0304-8853(98)00980-9.

[507] S. Chikazumi, Physics of Ferromagnetism, 2nd ed, Oxford University Press, 2009. http://link.springer.com/10.1007/978-3-642-25583-0.

[508] H. Kronmüller, General Micromagnetic Theory, in: Handbook of Magnetism and Advanced Magnetic Materials, John Wiley & Sons, Ltd, 2007. https://doi.org/10.1002/9780470022184.hmm201.

[509] H. Zhang, D. Zeng, Z. Liu, The law of approach to saturation in ferromagnets originating from the magnetocrystalline anisotropy, J Magn Magn Mater. 322 (2010) 2375–2380. https://doi.org/10.1016/j.jmmm.2010.02.040.

[510] S.V. Andreev, M.I. Bartashevich, V.I. Pushkarsky, V.N. Maltsev, L.A. Pamyatnykh, E.N. Tarasov, N.V. Kudrevatykh, T. Goto, Law of approach to saturation in highly anisotropic ferromagnets Application to Nd-Fe-B melt-spun ribbons, J Alloys Compd. 260 (1997) 196–200. https://doi.org/10.1016/S0925-8388(97)00127-8.

[511] W.C. Oliver, G.M. Pharr, An improved technique for determining hardness and elastic modulus using load and displacement sensing indentation experiments, J Mater Res. 7 (1992) 1564–1583. https://doi.org/10.1557/JMR.1992.1564.

[512] W.C. Oliver, G.M. Pharr, Measurement of hardness and elastic modulus by instrumented indentation: Advances in understanding and refinements to methodology, J Mater Res. 19 (2004) 3–20. https://doi.org/10.1557/jmr.2004.19.1.3.

[513] G. Constantinides, K.S. Ravi Chandran, F.-J. Ulm, K.J. van Vliet, Grid indentation analysis of composite microstructure and mechanics: Principles and validation, Materials Science and Engineering: A. 430 (2006) 189–202. https://doi.org/10.1016/j.msea.2006.05.125.

[514] N.X. Randall, M. Vandamme, F.-J. Ulm, Nanoindentation analysis as a two-dimensional tool for mapping the mechanical properties of complex surfaces, J Mater Res. 24 (2009) 679–690. https://doi.org/10.1557/jmr.2009.0149.

[515] V. Hrbek, V. Koudelková, Grid Indentation and Statistic Deconvolution: Limitations and Accuracy, Key Eng Mater. 731 (2017) 15–22. https://doi.org/10.4028/www.scientific.net/KEM.731.15.

[516] F.-J. Ulm, M. Vandamme, C. Bobko, J. Alberto Ortega, K. Tai, C. Ortiz, Statistical Indentation Techniques for Hydrated Nanocomposites: Concrete, Bone, and Shale, Journal of the American Ceramic Society. 90 (2007) 2677–2692. https://doi.org/10.1111/j.1551-2916.2007.02012.x.

[517] H. Besharatloo, J.M. Wheeler, Influence of indentation size and spacing on statistical phase analysis via high-speed nanoindentation mapping of metal alloys, J Mater Res. 36 (2021) 2198–2212. https://doi.org/10.1557/s43578-021-00214-5.

[518] B. Vignesh, W.C. Oliver, G.S. Kumar, P.S. Phani, Critical assessment of high speed nanoindentation mapping technique and data deconvolution on thermal barrier coatings, Mater Des. 181 (2019) 108084. https://doi.org/10.1016/j.matdes.2019.108084.

[519] K. Wieczerzak, J. Michler, J.M. Wheeler, S. Lech, R. Chulist, Ł. Gondek, J. Czub, A. Hoser, N. Schell, P. Bała, An in situ and ex situ study of χ phase formation in a hypoeutectic Fe-based hardfacing alloy, Mater Des. 188 (2020) 108438. https://doi.org/10.1016/j.matdes.2019.108438.

[520] C.M. Magazzeni, H.M. Gardner, I. Howe, P. Gopon, J.C. Waite, D. Rugg, D.E.J. Armstrong, A.J. Wilkinson, Nanoindentation in multi-modal map combinations: a correlative approach to local mechanical property assessment, J Mater Res. 36 (2021) 2235–2250. https://doi.org/10.1557/s43578-020-00035-y.

[521] C.M. Bishop, Pattern Recognition and Machine Learning, Elsevier, 2006.

[522] T.K. Moon, The expectation-maximization algorithm, IEEE Signal Process Mag. 13 (1996) 47–60. https://doi.org/10.1109/79.543975.

[523] G.J. McLachlan, S. Rathnayake, On the number of components in a Gaussian mixture model, Wiley Interdiscip Rev Data Min Knowl Discov. 4 (2014) 341–355. https://doi.org/10.1002/widm.1135.

[524] M. Reinhold, C. Watson, W.B. Knowlton, P. Müllner, Transformation twinning of Ni-Mn-Ga characterized with temperature- controlled atomic force microscopy, J Appl Phys. 107 (2010). https://doi.org/10.1063/1.3429090.

[525] P. Müllner, G. Kostorz, Microstructure of Magnetic Shape-Memory Alloys: Between Magnetoelasticity and Magnetoplasticity, Materials Science Forum. 583 (2008) 43–65. https://doi.org/10.4028/www.scientific.net/MSF.583.43.

[526] A. Diestel, A. Backen, U.K. Rler, L. Schultz, S. Fhler, Twin boundary energy of hierarchically twinned magnetic shape memory alloys, Appl Phys Lett. 99 (2011) 1–4. https://doi.org/10.1063/1.3635382.

[527] J. Buschbeck, R. Niemann, O. Heczko, M. Thomas, L. Schultz, S. Fähler, In situ studies of the martensitic transformation in epitaxial Ni-Mn-Ga films, Acta Mater. 57 (2009) 2516–2526. https://doi.org/10.1016/j.actamat.2009.02.008.

[528] S. Schwabe, R. Niemann, A. Backen, D. Wolf, C. Damm, T. Walter, H. Seiner, O. Heczko, K. Nielsch, S. Fähler, Building Hierarchical Martensite, Adv Funct Mater. 31 (2021) 2005715. https://doi.org/10.1002/adfm.202005715.

[529] A. Saren, A. Sozinov, S. Kustov, K. Ullakko, Stress-induced a/b compound twins redistribution in 10M Ni-Mn-Ga martensite, Scr Mater. 175 (2020) 11–15. https://doi.org/10.1016/j.scriptamat.2019.09.001.

[530] H. Seiner, L. Straka, O. Heczko, A microstructural model of motion of macro-twin interfaces in Ni–Mn–Ga 10M martensite, J Mech Phys Solids. 64 (2014) 198–211. https://doi.org/10.1016/j.jmps.2013.11.004.

[531] R. Chulist, L. Straka, N. Lanska, A. Soroka, A. Sozinov, W. Skrotzki, Characterization of mobile type I and type II twin boundaries in 10M modulated Ni–Mn–Ga martensite by electron backscatter diffraction, Acta Mater. 61 (2013) 1913–1920. https://doi.org/10.1016/j.actamat.2012.12.012.

[532] H. Seiner, Two-dimensional laminates in monoclinic-II modulated martensites, Int J Solids Struct. 221 (2021) 92–102. https://doi.org/10.1016/j.ijsolstr.2020.04.016.

[533] L. Caron, B. Dutta, P. Devi, M. Ghorbani Zavareh, T. Hickel, R. Cabassi, F. Bolzoni, S. Fabbrici, F. Albertini, C. Felser, S. Singh, Effect of Pt substitution on the magnetocrystalline anisotropy of Ni2MnGa: A competition between chemistry and elasticity, Phys Rev B. 96 (2017) 3–8. https://doi.org/10.1103/PhysRevB.96.054105.

[534] H.C. Herper, Ni-based Heusler compounds: How to tune the magnetocrystalline anisotropy, Phys Rev B. 98 (2018) 1–11. https://doi.org/10.1103/PhysRevB.98.014411.

[535] M. Zelený, L. Straka, M. Rameš, A. Sozinov, O. Heczko, Origin of magnetocrystalline anisotropy in Ni-Mn-Ga-Co-Cu tetragonal martensite, J Magn Magn Mater. 503 (2020). https://doi.org/10.1016/j.jmmm.2020.166522.

[536] M. Kök, Y. Aydoğdu, Electron concentration dependence of phase transition and magnetic properties in NiMnGa alloys, J Supercond Nov Magn. 26 (2013) 1691–1696. https://doi.org/10.1007/s10948-012-1849-x.

[537] O. Heczko, J. Drahokoupil, L. Straka, Enhanced magnetic hysteresis in Ni-Mn-Ga single crystal and its influence on magnetic shape memory effect, J Appl Phys. 117 (2015) 17E703. https://doi.org/10.1063/1.4913726.

[538] Q. Peng, J. Huang, M. Chen, Q. Sun, Phase-field simulation of magnetic hysteresis and mechanically induced remanent magnetization rotation in Ni-Mn-Ga ferromagnetic shape memory alloy, Scr Mater. 127 (2017) 49–53. https://doi.org/10.1016/j.scriptamat.2016.08.033.

[539] O. Heczko, L. Straka, V. Novak, S. Fähler, Magnetic anisotropy of nonmodulated Ni-Mn-Ga martensite revisited, J Appl Phys. 107 (2010) 21–24. https://doi.org/10.1063/1.3357409.

[540] Z.P. Yang, B. Sun, Z.Y. Gao, W. Cai, Surface modifications and tailoring magnetism in Ni 48·4 Mn 28.8 Ga 22.8 films by 120 keV proton irradiation, Intermetallics (Barking). 98 (2018) 106–114. https://doi.org/10.1016/j.intermet.2018.04.015.

[541] V. Golub, K.M. Reddy, V. Chernenko, P. Müllner, A. Punnoose, M. Ohtsuka, Ferromagnetic resonance properties and anisotropy of Ni-Mn-Ga thin films of different thicknesses deposited on Si substrate, J Appl Phys. 105 (2009) 07A942. https://doi.org/10.1063/1.3075395.

[542] C. Gómez-Polo, J.I. Pérez-Landazabal, V. Recarte, V. Sánchez-Alarcos, V.A. Chernenko, Temperature and time dependent magnetic phenomena in a nearly stoichiometric Ni 2 MnGa alloy, Journal of Physics: Condensed Matter. 21 (2009) 026020. https://doi.org/10.1088/0953-8984/21/2/026020.

[543] R. Modak, B. Samantaray, P. Mandal, A. Srinivasan, Low Gilbert damping and in-plane magnetic anisotropy in Ni–Mn–Sn thin film with high L21 order, Appl Phys A Mater Sci Process. 122 (2016) 1–7. https://doi.org/10.1007/s00339-016-9765-8.

[544] L. Yi, T. Zhang, B. Zhang, Y. Xu, H. Piao, L. Pan, Induced magnetic anisotropy of Ni42Co8Mn39Sn11 Heusler alloy under magnetic-field-annealing, J Magn Magn Mater. 495 (2020) 165843. https://doi.org/10.1016/j.jmmm.2019.165843.

[545] A. Jayaraman, M.S.R.N. Kiran, U. Ramamurty, Mechanical Anisotropy in Austenitic NiMnGa Alloy: Nanoindentation Studies, Crystals (Basel). 7 (2017) 254. https://doi.org/10.3390/cryst7080254.

[546] L. Zhou, A. Giri, K. Cho, Y. Sohn, Mechanical anomaly observed in Ni-Mn-Ga alloys by nanoindentation, Acta Mater. 118 (2016) 54–63. https://doi.org/10.1016/j.actamat.2016.07.029.

[547] L. Zhou, A. Mehta, A. Giri, K. Cho, Y. Sohn, Martensitic transformation and mechanical properties of Ni49+xMn36−xIn15 (x=0, 0.5, 1.0, 1.5 and 2.0) alloys, Materials Science and Engineering: A. 646 (2015) 57–65. https://doi.org/10.1016/j.msea.2015.08.034.

[548] A. Kumar, U. Rabe, S. Hirsekorn, W. Arnold, Elasticity mapping of precipitates in polycrystalline materials using atomic force acoustic microscopy, Appl Phys Lett. 92 (2008) 1–4. https://doi.org/10.1063/1.2919730.

[549] J.J. Vlassak, W.D. Nix, Measuring the elastic properties of anisotropic materials by means of indentation experiments, J Mech Phys Solids. 42 (1994) 1223–1245. https://doi.org/10.1016/0022-5096(94)90033-7.

[550] Y.-T. Cheng, C.-M. Cheng, Scaling, dimensional analysis, and indentation measurements, Materials Science and Engineering: R: Reports. 44 (2004) 91–149. https://doi.org/10.1016/j.mser.2004.05.001.

[551] W.C. Crone, H. Brock, A. Creuziger, Nanoindentation and Microindentation of CuAlNi Shape Memory Alloy, Exp Mech. 47 (2007) 133–142. https://doi.org/10.1007/s11340-006-8884-0.

[552] S. Montecinos, A. Cuniberti, S. Simison, Instrumented indentation of transforming and no-transforming phases in Cu–Al–Be shape-memory alloys, Intermetallics (Barking). 28 (2012) 58–64. https://doi.org/10.1016/j.intermet.2012.03.057.

[553] M. Arciniegas, Y. Gaillard, J. Peña, J.M. Manero, F.J. Gil, Thermoelastic phase transformation in TiNi alloys under cyclic instrumented indentation, Intermetallics (Barking). 17 (2009) 784–791. https://doi.org/10.1016/j.intermet.2009.03.020.

[554] A. Bolshakov, G.M. Pharr, Influences of pileup on the measurement of mechanical properties by load and depth sensing indentation techniques, J Mater Res. 13 (1998) 1049–1058. https://doi.org/10.1557/JMR.1998.0146.